WARSAW UNIVERSITY OF TECHNOLOGY

DISCIPLINE OF SCIENCE – MATERIALS ENGINEERING
FIELD OF SCIENCE – ENGINEERING AND TECHNOLOGY

Ph.D. Thesis

Diana C. Martinez G., M.Sc.

Mg-based bioabsorbable implants: From surface characterization to tissue-implant interface evaluation after *in vitro* and *in vivo* degradation

Supervisor
Professor Wojciech Święszkowski, Ph.D.,
Co-supervisor
Tomasz Płociński, Ph.D.,

WARSAW 2024

ABSTRACT

Bone fractures are a global public health concern, with an annual incidence of over 179 million new fractures. A large number of these bone fractures are treated with internal fixation implants, which are preferred among young and elderly patients. Most fracture-fixing implants are permanent and made of cobalt alloys, stainless steel, titanium, and its alloys. These materials are chosen due to their high mechanical strength, corrosion resistance, and proven biocompatibility. However, after the fracture has healed, a secondary surgical procedure is required to remove the implants. This increases discomfort for patients and healthcare costs, in addition to possible complications such as interference with skeletal growth in children, the stress shielding effect, and foreign body reactions.

To overcome these disadvantages, absorbable metals such as magnesium (Mg) and its alloys have recently gained attention for their use in the orthopedic field. These absorbable metals are considered an alternative for internal fixation implants because they possess mechanical properties close to human cortical bone. Nevertheless, the unpredictable corrosion rate of Mg-based devices, which could compromise their mechanical stability before fracture repair, has restricted their wide clinical use.

Therefore, this doctoral thesis seeks to gather information using high-resolution imaging techniques on Mg-based specimens, focusing on understanding the bone-implant interface's composition, structure, topography, and properties through *in vitro* and *in vivo* investigations. The goal is *to gain an insight into the corrosion mechanisms that take place throughout the degradation of Mg-based implants.*

To accomplish the overall objective of this thesis and validate the following hypothesis: i) The composition of the corrosion layer on Mg-based materials is significantly affected by cell viability, proliferation, and cell adhesion under *in vitro* conditions, and ii) The composition of corrosion layers on implants varies according to their *in vivo* location, the research approaches were divided into three subprojects, each with its specific objectives:

Objective 1: Provide a baseline information of the as received Mg-based implants;

The surface properties and microstructure of the as-received Mg-implants were characterized by the importance of the surface integrating with the surrounding tissues and evaluating the influence of the manufacturing methods on the corrosion resistance of these medical implants.

Objective 2: Determine the corrosion rate of Mg-based devices without and with the presence of osteoblast (OB) and osteoclast (OC) cells. Additionally, analyze the kinetic changes in the composition of the degradation products as the corrosion of the Mg materials proceeds.

By performing *in vitro* tests under physiological conditions, the impact of the Mg degradation on pH and osmolality changes in the surrounding *in vitro* environment was investigated. Similarly, the Mg-cell interface was analyzed to evaluate the extent to which bone cells influence the corrosion behavior of Mg implants and their corrosion layers´composition.

Objective 3: Characterize the corrosion layers formed at the implant-tissue interfaces when using Mg-based devices from *in vivo* research to assess the corrosion performance in various tissue compartments.

This section of the thesis focuses on analyzing retrieved implants from small and large animal studies. The aim was to investigate the dynamic changes that occurred in the protective corrosion layers as the Mg implants degraded. Additionally, the research seeks to understand the dynamic and highly complex interface changes, which are crucial for bone ingrowth and remodeling.
In conclusion, the multimodal approach to the study of the Mg implants demonstrated that the investigated Mg medical implants meet the threshold necessary for biodegradable implants to have an appropriate lifespan, with corrosion rates *in vivo* below 0.5 mm/year. The Mg implants exhibited smooth, anisotropic, and free of contaminant surfaces as received, highlighting the importance of proper cleaning, sterilization, packaging, and storage to maintain the surface qualities of the Mg implants for therapeutic purposes. In addition, the corrosion products that formed *in vitro* exhibited a similar elemental composition (including O, Mg, P, and Ca) to what was observed *in vivo*. However, the thickness of the corrosion layer and the distribution of elements were Mg-substrate dependent, varied in the presence of OB and OC cells, and were implantation site dependent. This emphasizes the significance of comprehending the factors that contribute to the discrepancy between the *in vitro* and *in vivo* corrosion rates. The multicellular and multimodal *in vitro* model aims to mimic the outcomes from *in vivo* research while minimizing the need for animal testing. However, for biological relevance, animal studies are still required not only to obtain regulatory approval for medical use but also to provide insights into the behavior of the Mg material within physiological environments and the tissue response as the Mg material degrades.

Keywords: Magnesium alloys, absorbable metals, orthopedic implants, implant-tissue interface, corrosion behavior, osteoblasts (OB), osteoclasts (OC), *in vitro*, *in vivo*.

STRESZCZENIE

Złamania kości są globalnym problemem zdrowia publicznego, z roczną częstością występowania ponad 179 milionów nowych złamań. Duża liczba tych złamań kości jest leczona za pomocą implantów do stabilizacji wewnętrznej, które są preferowane wśród młodych i starszych pacjentów. Większość implantów mocujących złamania jest trwała i wykonana ze stopów kobaltu, stali nierdzewnej, tytanu i jego stopów. Materiały te są wybierane ze względu na ich wysoką wytrzymałość mechaniczną, odporność na korozję i sprawdzoną biokompatybilność. Jednak po zagojeniu się złamania wymagana jest dodatkowa procedura chirurgiczna w celu usunięcia implantów. Zwiększa to dyskomfort pacjentów i koszty opieki zdrowotnej, a także możliwe powikłania, takie jak zakłócenie wzrostu szkieletu u dzieci, efekt ekranowania naprężeń i reakcje na ciała obce.

Aby przezwyciężyć te wady, wchłanialne metale, takie jak magnez (Mg) i jego stopy, zyskały ostatnio uwagę ze względu na ich zastosowanie w dziedzinie ortopedii. Te absorbowalne metale są uważane za alternatywę dla wewnętrznych implantów mocujących, ponieważ posiadają właściwości mechaniczne zbliżone do ludzkiej kości korowej. Niemniej jednak, dużym ograniczeniem stosowania Mg i jego stopów na implanty jest ich nieprzewidywalna szybkość korozji, poprzez co, implant może utracić stabilność mechaniczną.

W związku z tym niniejsza praca doktorska ma na celu zebranie kompleksowych informacji na temat zachowania się Mg i jego stopów w trakcie implantacji przy użyciu technik obrazowania o wysokiej rozdzielczości. Nacisk kładziony jest na zrozumienie składu i struktury produktów korozji, topografii i właściwości interfejsu kość-implant po badaniach *in vitro* i *in vivo*. *Celem jest uzyskanie wiedzy o mechanizmach korozyjnych zachodzących podczas degradacji implantów na bazie Mg*.

Aby osiągnąć główny cel niniejszej rozprawy i zweryfikować następujące hipotezy: i) Na skład warstwy korozyjnej na materiałach na bazie Mg znacząco wpływa obecność komórek, proliferacja i adhezja komórek w warunkach in vitro, oraz ii) Skład warstw korozyjnych na implantach różni się w zależności od ich lokalizacji in vivo, podejścia badawcze zostały podzielone na trzy części, dla których określono następujące cele badawcze:

Cel 1: Dostarczenie podstawowych informacji o badanych implantach na bazie Mg.

Właściwości powierzchni i mikrostruktura badanych implantów magnezowych zostały scharakteryzowane pod kątem znaczenia integracji powierzchni z otaczającymi tkankami oraz oceny wpływu metod produkcji na odporność tych implantów na korozję.

Cel 2: Określenie szybkości korozji implantów na bazie Mg bez i z obecnością komórek osteoblastów (OB) i osteoklastów (OC). Analiza zmian kinetycznych w składzie produktów degradacji w miarę postępu korozji materiału Mg;

Przeprowadzając testy *in vitro* w warunkach fizjologicznych, zbadano wpływ degradacji Mg na zmiany pH i osmolalności w otaczającym środowisku *in vitro*. Podobnie przeanalizowano interfejs Mg-komórka, aby ocenić zakres, w jakim komórki kostne wpływają na zachowanie korozyjne implantów Mg i ich skład warstw korozyjnych.

Cel 3: Scharakteryzowanie interfejsu tkanka-warstwa korozyjna-implant Mg przy użyciu badań *in vivo* w celu oceny działania korozyjnego w różnych obszarach tkankowych.

Ta część rozprawy koncentruje się na analizie odzyskanych implantów z badań na małych i dużych zwierzętach. Celem było zbadanie dynamicznych zmian zachodzących w warstwach korozyjnych w trakcie degradacji implantów Mg. Ponadto badania mają na celu zrozumienie dynamicznych i wysoce złożonych zmian interfejsu, które są kluczowe dla wrastania i przebudowy kości.

Podsumowując, kompleksowe podejście do badania implantów Mg wykazało, że badane implanty Mg spełniają wymagania niezbędne dla biodegradowalnych implantów; posiadają odpowiednią żywotność, oraz szybkość korozji in vivo poniżej 0,5 mm/rok. Implanty Mg wykazywały gładkie, anizotropowe i wolne od zanieczyszczeń powierzchnie, co podkreśla znaczenie właściwego czyszczenia, sterylizacji, pakowania i przechowywania w celu utrzymania jakości powierzchni implantów Mg do celów terapeutycznych. Produkty korozji, które powstały *in vitro*, wykazywały podobny skład chemiczny (w tym O, Mg, P i Ca) do składu produktów powstałych w trakcie badań *in vivo*. Grubość warstwy korozyjnej i rozkład pierwiastków były zależne od podłoża Mg, różniły się w zależności od obecności komórek OB i OC oraz były zależne od miejsca implantacji. Podkreśla to znaczenie zrozumienia czynników, które przyczyniają się do rozbieżności między szybkością korozji *in vitro* i *in vivo*. Wielokomórkowy i kompleksowy model *in vitro* ma na celu naśladowanie wyników badań *in vivo* przy jednoczesnym zminimalizowaniu potrzeby przeprowadzania testów na zwierzętach. Jednak ze względu na znaczenie biologiczne, badania na zwierzętach są nadal wymagane nie tylko w celu uzyskania zgody organów regulacyjnych na zastosowanie implantów, ale także w

celu zapewnienia wglądu w zachowanie Mg w środowisku fizjologicznym i reakcję tkanki, gdy materiał ulega degradacji.

Słowa kluczowe: Stopy magnezu, metale biodegradowalne, implanty ortopedyczne, interfejs implant-tkanka, zachowanie korozyjne, osteoblasty (OB), osteoklasty (OC), *in vitro*, *in vivo*.

TABLE OF CONTENTS

List of abbreviations and symbols

Abbreviations

2D	Two-dimensional
3D	Three-dimensional
AgCl	Silver chloride
ALP	Alkaline phosphatase
AO	Acridine Orange
ASTM	American Society for Testing and Materials
ATR-FTIR	Attenuated total reflectance-Fourier transform infrared spectroscopy
AZ31	Magnesium Aluminum Zinc alloy
BIB	Broad argon ion beam milling
BIC	Bone-to-implant contact
BMPs	Bone morphogenetic proteins
BSA	Bovine serum albumin
BSE	Backscattered electrons
$CaCO_3$	Calcium carbonate
$CaMg(CO_3)_2$	Calcium magnesium carbonate
CB	Cortical bone
CL	Corrosion layer
CLSM	Confocal laser scanning microscopy
CM	Culture medium
Co-Cr	Cobalt-chromium alloy
CO_3^{2-}	Carbonate ion
CO_2	Carbon dioxide
CPD	Critical point drying
CPE	Constant phase element
CPE_{diff}	Constant phase element of corrosion products diffusion capacitance
CR	Corrosion rate
DAPI	4´,6-Diamidino-2-Phenylindole Dihydrochloride
d_{avg}	Average grain size
DKK1	Dickkopf WNT signaling pathway inhibitor
DMEM	Dulbecco´s Modified Eagle´s Medium
DPBS	Dulbecco´s phosphate buffered saline solution without Ca and Mg
DRX	Dynamic recrystallization grains
EB	Ethidium bromide
Eb	Breakdown potential
EBSS	Earle´s balanced salt solution
ECC	Electrical equivalent circuit
E_{corr}	Corrosion potential
EDTA	Ethylenediaminetetraacetic acid
EDX	Energy-dispersive X-ray spectroscopy
EIS	Electrochemical impedance spectroscopy
FBS	Fetal bovine serum
FCS	Fetal calf serum
FD	Freeze-drying
FGF23	Fibroblast growth factor 23
Fib	fibrinogen
FIB	Focus Ion beam

G-CSF	Growth colony stimulating factor
GIS	Gas-injection system
GRO-C/CXCL1	Grow-regulated oncogene (GRO)-keratinocyte chemoattractant (KC)/ chemokine (CXC motif) ligand
HA	Hydroxyapatite
HBSS	Hanks-balanced salt solution
HCO3–	Hydrogen carbonate ion
HCP	Hexagonal close packed
HgO	Mercury oxide
HMDS	Hexamethyldisilane
hOBs	Human primary osteoblast cells
HP-Mg	High-purity magnesium
HPO_4^{2-}	Hydrogen phosphate ion
HUCPV	Human umbilical cord perivascular cells
H&E	Hematoxylin and eosin
i_{corr}	Corrosion current density
IFNγ	Interfero-gamma
IL	Interleukin (IL-10, IL-6, IL-1β)
IMC	Intramedullary cavity
IMPs	Intermetallic particles
IPF	Inverse pole figure
ISO	International Organization for Standardization
KAM	Kernel average misorientation
kGy	kilo Grays
KIM-1	Kidney injury molecule 1
kt	kilotonnes
kV	kilovolt
L929	Adherent type of mouse fibroblast cell line
LPSO	Long-period stacking ordered phase
MCP-1	Monocyte chemoattractant protein-1
M-CSF	Macrophage-colony stimulating factor
m-SBF	Modified simulated body fluid
M3TC3-E1	Murine preosteoblastic cell line
MEM	Minimum essential medium eagle
mg	milligram
Mg-10Gd	Magnesium-Gadolinium alloy
Mg-2Ag	Magnesium-silver alloy
Mg-3Zn	Magnesium-Zinc alloy
Mg-4Y	Magnesium-Yttrium alloy
Mg-Zn-Mn	Magnesium-Zinc-Manganese alloy
$Mg(OH)_2$	Magnesium hydroxide
$Mg(PO_4)_2$	Magnesium phosphate
$Mg_{12}Nd$	Magnesium-Neodymium intermetallic phase
$Mg_{41}Nd_5$	Magnesium-Neodymium intermetallic phase
MG63	Human osteosarcoma cell line
MgCaZnYMn	Magnesium-calcium-zinc-yttrium-manganese alloy
$MgCl_2$	Magnesium chloride
$MgCO_3$	Magnesium carbonate
MgO	Magnesium oxide
$MgSO_4$	Magnesium sulfate

MgYREZr	Magnesium-yttrium-rare earth-zirconium alloy
mL	Milliliter
mM	Millimolar
mmol/L	Millimoles per liter
MSCs	Mesenchymal stem cells
NaCl	Sodium chloride
NC	No cells
nm	nanometers
OB	Osteoblast
OC	Osteoclast
OCP	Open circuit potential
OD	Optical density
OPG	Osteoprotegerin
OPN	Osteopontin
P/S	Penicillin/streptomycin
PB	Pilling-Bedworth coefficient
PBMC	peripheral blood monocyte cells
PBS	Phosphate-buffered saline
PEO	Plasma electrolytic oxidation
PLGA	Poly(L-lactic acid)
PLLA	Poly(lactic-co-glycolic acid)
PO_4^{3-}	Phosphate ion
PP	Potentiodynamic polarization
ppm	Parts per million
RANK	Receptor activator of nuclear factor κB
RANKL	Receptor activator NFκB-ligand
RAW264.7	Macrophage cell line
R_{ct}	Charge transfer resistance
R_{diff}	Diffuse layer resistance
ROI	Region of interest
R_p	Polarization resistance
R_s	Electrolyte resistance
SBF	Simulated body fluids
SD	Sprague-Dawley® rats
SE	Secondary electron
SEM	Scanning electron microscopy
SiC	Silicon carbide
SS	Stainless steel
Ti	Titanium
Ti-6Al-7Nb	Titanium-aluminum-niobium alloy
Ti-6Al-4V	Titanium-aluminum-vanadium alloy
TIMP-1	Tissue inhibitor of metalloproteinases 1
TNFα	Tumour necrosis factor alpha
TRAP	Tartrate-resistance acid phosphatase
UV	Ultraviolet radiation
V_{SCE}	Potential versus saturated calomel electrode
WE43	Magnesium-yttrium-rare earth elements alloy
XHP-Mg	Ultrahigh-purity magnesium
XPS	X-ray photoelectron spectroscopy
XRD	X-ray diffraction analysis

Y_2O_3	Yttrium oxide
ZK60	Zinc-zirconium-magnesium alloy
ZX00	Magnesium-zinc-calcium alloy
α-MEM	Alpha-minimum essential medium
$\alpha\text{-MEM}_C$	Alpha-minimum essential medium supplemented with 10% FBS and 1% P/S
µCT	Microcomputed tomography
µg	Micrograms
µL	Microliter
µmol/L	Micromoles per liter
VEGF	Vascular endothelial growth factor

Chapter 1

Introduction

1.1.Bone fractures and the need for orthopedic implants

The prevalence of bone fractures and the long-term impact of their complications represent a global public health concern [1,2]. Fractures can result from high-energy trauma (bike, motorcycle, or vehicle accidents) or sports injuries, workplace accidents [3], diseases that impair the bone (osteoporosis, bone cancer) [4], or nutritional deficiencies or hormonal disorders [5]. The most frequently anatomical sites for bone fractures include the femur, patella, tibia, fibula, radius, ulna, clavicle, scapula, humerus, vertebrae, jawbone, and calvaria bones [1,3] (Figure.1.1). This decreased productivity due to work absence causes disability and

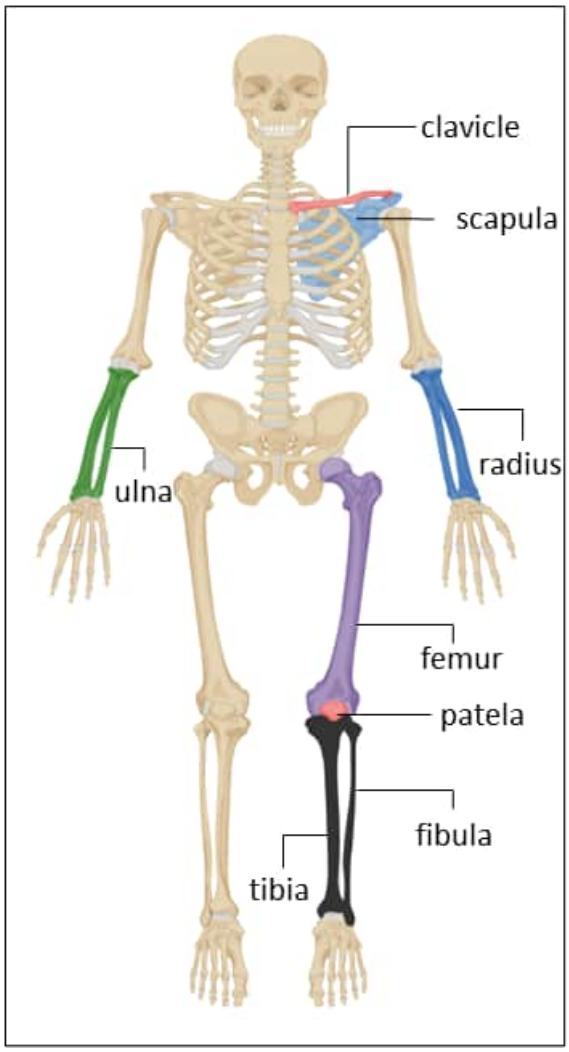

Figure 1.1. The most frequently anatomical sites for bone fractures. *Image created with Biorender.com*

impaired quality of life in addition to high healthcare costs for patients, their families, society, and the healthcare systems. For example, in 2019, there were 179 million new fracture cases. Age-related fractures cause more than nine million fragility injuries worldwide [6], including an estimated 4.3 million in European Union (EU) countries in 2019. In EU countries, this leads to a cumulative fracture-related cost of € 56,9 million [7].

Numerous bone fractures are treated with internal fixation procedures, which refers to the surgical applications of implants (such as plates, screws, nails, and wires) to stabilize fractured bones [8]. The most commonly used metals for internal fixation constituted of cobalt-chromium-based (Co-Cr) alloys, stainless steel (316L), titanium (Ti) and Ti-6Al-4V [9]. These materials have been widely used in orthopedic applications due to their high mechanical strength, corrosion resistance, and biocompatibility [10]. However, several long-term implantation disadvantages of permanent metallic implants, including stress shielding, periprosthetic infections, immune response and inflammation caused by metallosis, foreign body reactions [9–12] and interference with skeletal development in children, have been reported [9,13]. This results in the need for a second surgery for implant retrieval and/or replacement, increasing the patient´s and health care provider´s financial burden [14–17].

As a temporary support alternative for orthopedic applications, absorbable biomaterials such as natural and synthetic polymers and metals (zinc, iron, and magnesium) have emerged to overcome the disadvantages of permanent inert metal implants [14,15,18]. These bioabsorbable materials are temporary structures that break down and are eliminated from the body [19]. They should maintain structural integrity for a predetermined period of time before being degraded, absorbed, and excreted by the body [20]. Synthetic polymers are easy to produce with reasonable cost [21], their degradation can be controlled by adjusting their composition or by processing techniques [22], and they can be manufactured in a variety of sizes and shapes [23]. Poly(L-lactic acid) (PLLA) and poly(lactic-co-glycolic acid) (PLGA) are two of the most frequently used synthetic bioabsorbable polymers in the orthopedics [19]. However, these polymers have been associated with delayed inflammatory reactions [19] and transient local fluid accumulation [24].

Iron (Fe), zinc (Zn), and magnesium (Mg) are biodegradable metals that support tissue healing as demonstrated by recent advances in biomedical engineering [25]. Among these, Mg has attracted attention worldwide, with research focusing on the design and preparation of novel magnesium materials for their potential use in the manufacturing of implantable medical devices for cardiovascular and orthopedic applications [26]. Mg and its allow are characterized by their Young modulus, which closely resembles that of the human cortical bone, thereby reducing the stress shielding effect [27]. In addition, Mg-based devices used as temporary orthopedic implants undergo degradation in biological environments (*in vivo*) without interfering with bone formation, therefore eliminating the necessity of a subsequent surgical reintervention to remove the implants [28]. However, the varied and unpredictable corrosion

of Mg-based implants in physiological conditions has restricted their wide use in clinics. In addition, despite the extensive Mg research conducted *in vitro* and *in vivo* in the past few decades, there is still a lack of understanding regarding the biological interaction between Mg-based implants and the surrounding tissue. This knowledge gap hinders Mg's target-oriented implant development processes. To address these challenges and further optimize Mg implants, this thesis aims *to investigate the composition, topography, and the Mg degradation process at the Mg-implant-tissue interfaces using high-resolution imaging techniques to understand the degradation process of Mg-based implants under physiological conditions from in vitro and in vivo investigations.*

This introductory chapter comprehensively describes Mg and its alloys, including their properties, alloying elements, and their development as biodegradable materials. Subsequently, a brief timeline of the development of Mg as a suitable implantable material is presented, outlining the various forms of corrosion that can occur in Mg-based implants when exposed to physiological conditions. Following that, a section of this chapter will focus on the bone tissue as an implantation site, providing an explanation of its hierarchical structure and main cellular components. Moreover, a thorough examination of the bone fracture healing process will be presented. Finally, a concise overview of the state of the art of Mg research, covering both *in vivo* and *in vitro* investigations, is presented.

1.2. Magnesium and its alloys

1.2.1. Properties of pure Mg

Magnesium (Mg) is an alkaline earth metal [29,30], as 2.7% of Earth's crust is composed of Mg [31,32]. Mg has an atomic number of 12 [30,33], an atomic mass of 24.305 u, an atomic radius 1.50 Å [34], and its most common oxidation state is +2 [35]. Pure Mg has a density of 1.738 g/cm3 [25,36,37], a Young modulus of 45 GPa, a 3.5 Poisson's ratio [33], and a melting point of approximately 650 ^{o}C [38]. It possesses a hexagonal closed-packed (HCP) crystal structure with lattice parameters a= 0.320 nm, c= 0.520 nm, and c/a ratio = 1.624. The 0.320 nm atomic diameter is a favorable size for a variety of solute elements such as zinc (Zn), yttrium (Y), silver (Ag), and zirconium (Zr) [36] (Figure 1.2a).

1.2.2. Mg production

Mg is predominantly used in the automotive industry (44%) to decrease vehicle weight in response to consumer demand for improved fuel efficiency. In addition to the automotive industry, Mg primarily utilized in packaging (10%), construction (12%), desulfurization (11%),

transportation (air, maritime, and railway transport) (4%), and other industries (10%) [30]. China is the wealthiest country in Mg [39] with more than 70% of the world´s Mg resources, the world´s raw Mg reserves, the world´s largest raw Mg production, and the world´s raw Mg export [31]. China produced approximately 900 kilotonnes (kt) of metal and 21 kt of Mg compounds. Other major sources of metallic magnesium include Russia (50kt), Brazil (20 kt), Israel (20kt), Kazakhstan (15kt), Türkiye (13kt), and Ukraine (2kt) [40]. The principal sources of magnesium minerals are the carnallite, magnesite, dolomite, brucite, olivine, and bischofite. Currently, the production of Mg per tonne is extremely costly, ranging from $ 2000 per tonne in recent years to more than $11,000 per tonne in September 2021 (Figure 1.2b). This enormous shift in global prices results from the high energy demand required (approximately 4 kg of coal to produce 1 kg of Mg) and China's recent implementation of carbon neutrality policies [41].

1.2.3. Alloying elements

Pure Mg is soft, mechanically weak with a tensile strength of 20 MPa [42], and is one of the most active metals with a standard electrode potential of -2.372 V. This contributes to a low corrosion resistance [27,43,44], particularly in saline environments such as the one found in the human body. Alloying, surface treatment, and coatings are among the techniques for enhancing the corrosion resistance, mechanical properties, and production cost of pure Mg [27,45,46].

Numerous elements have very limited or no solubility in Mg. Most elements have less than 0.05 wt.% solubility in pure Mg (Figure 1.3). Factors such as electronegativity, valency, atomic size, and crystal structure similarity determined solid solubility [47]. Consequently, three types of insolubilities can be summarized:

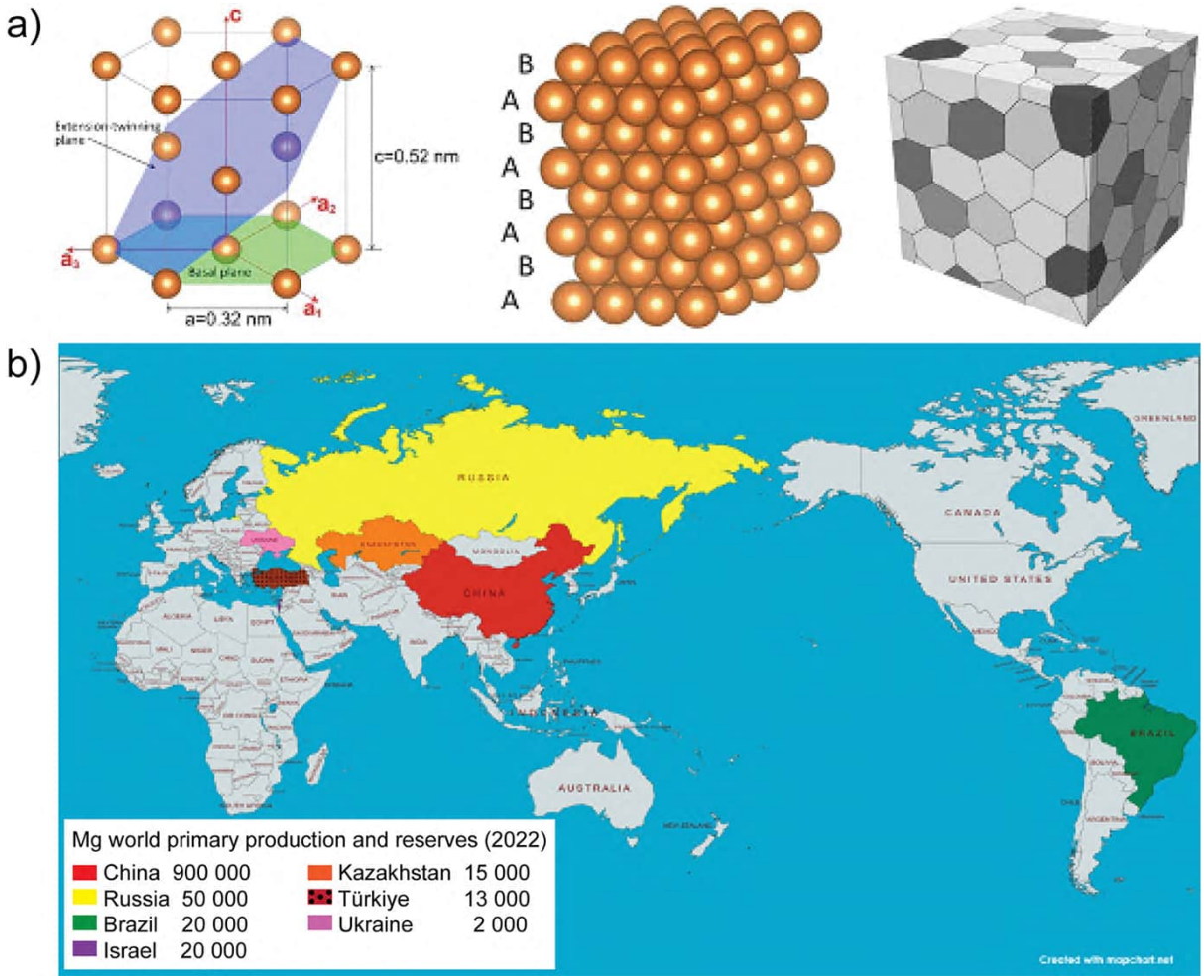

Figure 1.2. Structure of magnesium. a) Mg cell unit (left), hexagonal close-packed (center), polycrystalline Mg (right) [29]. b) Global Mg production in tons. *Image created with mapchart.net.*

(i) elements with some solubility that do not contain Mg-intermetallic. In this instance, elements will get into the solid solution to a limited extent, and any further alloying will result in a distinct, pure phase of the elements. It is feasible with elements such as Zr.

(ii) Elements without solubility and forming an intermetallic Mg-X compound.

(iii) Elements that are complete and full insolubility. Here, neither a solid solution nor a Mg-intermetallic compound is formed with the alloying element. This may occur with elements such as Mo, Nb, or Fe, where the elements form a pure second phase of these metals [42,47].

The limited solubility of most elements in crystalline Mg has minimal effects on the electrochemical potential of the Mg (α) phase [42,47]. As a result, most of the Mg-alloys have a potential near -1.55 V_{SCE}, and most are below –1.4 V_{SCE} [47].

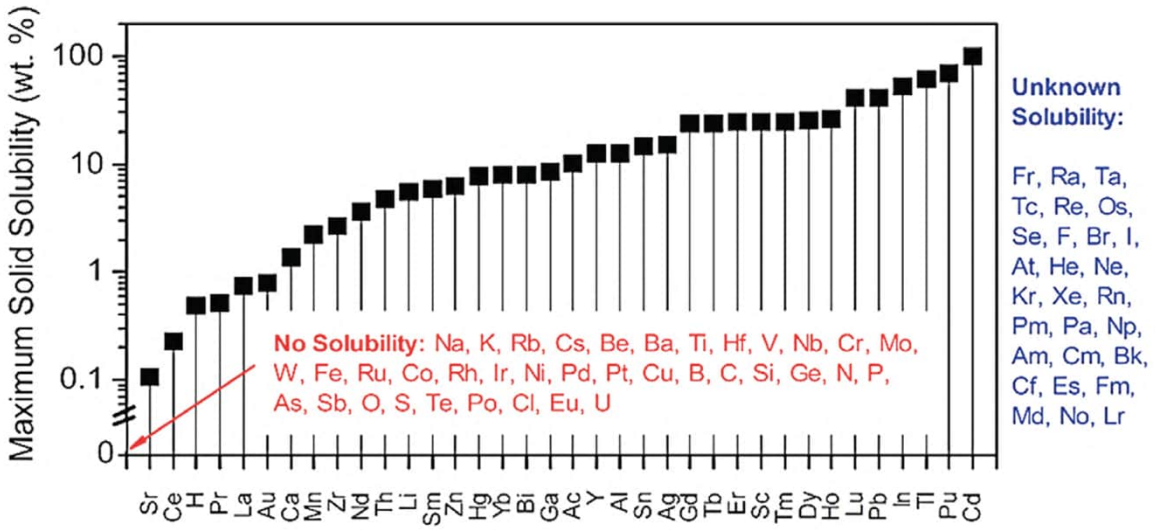

Figure 1. 3. Maximum solubility of alloying elements in Mg [42].

Mg alloys are typically multiphase materials, with intermetallic particles dispersed in the α-Mg matrix [42]. The microstructure, particle size and distribution, and phase distribution have a significant impact on the corrosion behavior of Mg alloys. Through solid solution strengthening and grain refinement, adding alloying elements can increase Mg's strength [48], where the grain refinement enhances the primary and secondary phase distribution [49]. However, from the biomedical point of view, elements should be selected not only to improve the mechanical properties of Mg but also to consider their biocompatibility and degradation in the human body [27,48].

The American Society for Testing and Materials (ASTM) coding system [50] has been the most extensively used in industry and research to date. It is an alphanumeric system in which each alloy designation consists of the following four components: two letters indicating the main alloying elements; two numbers representing the percentage of each of the main alloying elements; one letter to differentiate between alloys that differ only in type and amount of minor alloying elements, and temper designation [50–52]. Table 1.1 provides a summary of the abbreviation letters for the alloying elements commonly referred to as magnesium alloys.

Witte et al. [53] classified Mg alloys into three main categories: (i) pure Mg with traces of other elements, (ii) Mg alloys containing aluminium (Al), and (iii) those alloys without Al. Esmaily et al. [42] instead show the progression of Mg alloys by strengthening their characteristics (Figure 1.4). The compositions of the vast majority of commercial Mg-alloys are typically characterized by the following features: (i) the total alloy loading is <10 wt.%, (ii) they contain second phase particles, (iii) alloying with Al to maintain a low density, and (iv),

alloying with rare-earth elements (REEs) for strengthening [42]. Aluminium (Al), calcium (Ca), zinc (Zn), strontium (Sr), and REEs such as yttrium (Y) and gadolinium (Gd) are the most commonly used alloying elements [54]. They can be used for solid solution strengthening if the alloying elements remain in solid solution [53]. If alloying elements react with Mg or with each other, intermetallic phases will form [53,55]. These intermetallic phases can dissolve in the Mg matrix or distribute along the grain boundaries, thereby influencing the mechanical properties, microstructure, and corrosion performance of Mg alloys [55].

Table 1.1. ASTM designation system of magnesium alloys [27,51–53]

Alloying element	Abbreviation letter		Alloying element	Abbreviation letter
Aluminium	A		Nickel	N
Bismuth	B		Lead	P
Copper	C		Silver	Q
Cadmium	D		Chromium	R
Rare earth metals	E		Silicon	S
Iron	F		Tin	T
Thorium	H		Gadolinium	V
Strontium	J		Ytrium	W
Zirconium	K		Antimony	Y
Lithium	L		Zinc	Z
Manganese	M			

In comparison to various Mg alloys, high-purity Mg has the lowest corrosion rate [25,53,56]. This is because additional phases associated with impurity ions (Fe, Ni, Cu, Co, Be) in Mg alloys can accelerate the corrosion of the Mg α-matrix, if their concentration exceeds the impurity limits [25,37,53]. Therefore, these impurities are particularly detrimental to Mg alloys [56]. The quantity of impurities depends on the alloy's composition, production technology, and alloy development progress. The quantity of these impurities must be tightly controlled for biomedical applications. Be and Ni should be avoided, despite the fact their concentrations are minimal in comparison to the physiological range of the body [53] (Table 2).

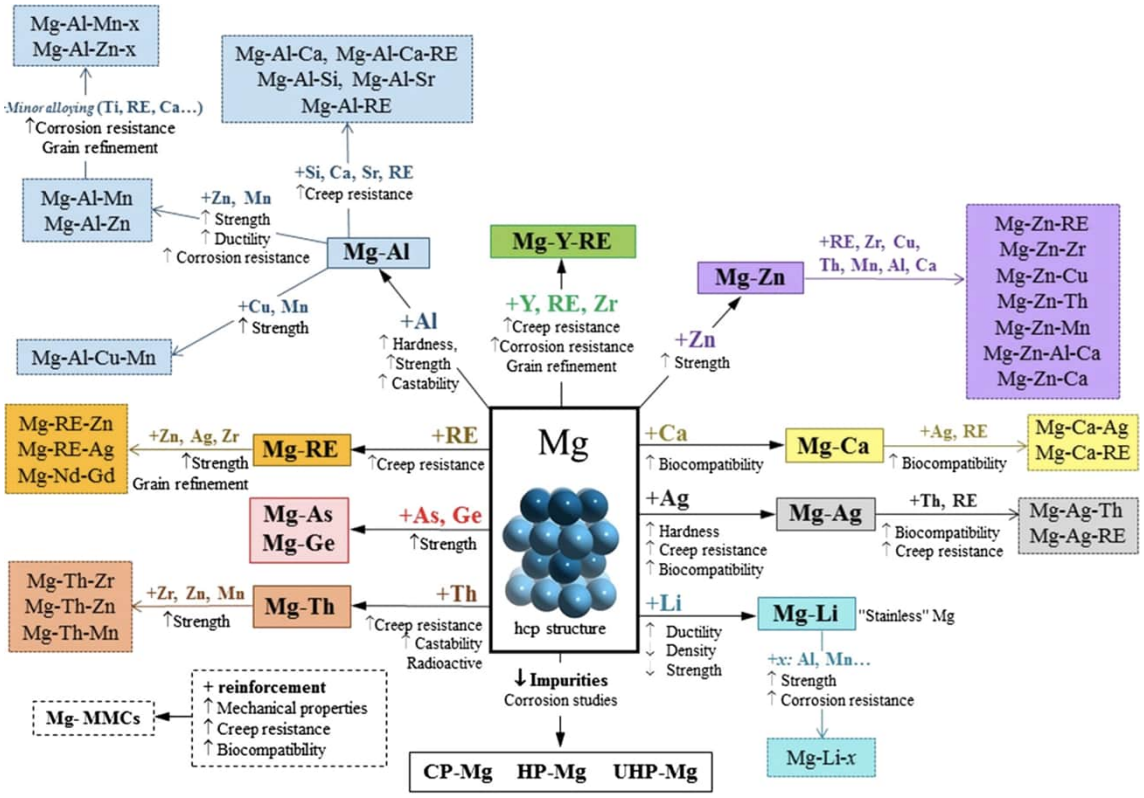

Figure 1.4. Mg **alloys development** [42]

Table 1.2. Impurity tolerance limits of Be, Cu, Fe, and Ni in Mg alloys [53,57]

Element	Impurity tolerance limits	Normal blood serum level
Be	4-5 ppm	0.05 o 0.23 µg/L
Cu	100-300 ppm	Toxic dosage >2 µg/m^3
Fe	35-50 ppm	5.0–17.6 g/L
Ni	20-50ppm	74–131 mol/L

The role of alloying elements investigated for the purpose of this research, both in terms of enhancing the corrosion resistance of Mg and emphasizing their relevance to the human body are described below.

- **Calcium (Ca)**

Its atomic radius is 1.80 Å [34] and its solubility in Mg is approximately 1.34%. Ca contributes to solid strengthening in solution and precipitation [46,49,53,58] as well as to grain refinement at concentrations below 1% [43]. Ca also increases the Mg alloys' elasticity, compressive yield strength, ultimate strength, creep resistance and hardness. Ca in Mg alloys forms Mg-Ca binary phases that are distributed in the grain boundaries and grain interior, reducing the corrosion potential difference between grain boundaries and the Mg α-matrix [59]. Minor addition of Ca improves the corrosion resistance of Mg alloys while higher percentages of Ca lead to brittle Mg alloys, resulting in irregular and more widespread corrosion [43,60].

As the most abundant element in the human body [53], Ca has a density of 1.55 g/cm^3 [49], and a normal serum level between 0.919 and 0.993 mg/L [25,53]. Ca is predominantly stored in bones and teeth [43] in the form of hydroxyapatite [55]. Ca ions are involved in bone growth and maintenance, muscle contraction, blood coagulation, nerve impulse, heartbeat regulation, and blood pressure lowering [25]. Ca also participates in the co-activation and stabilization of enzymes within the human body [43]. Ca deficiencies causes osteoporosis, osteopenia and rickets [61].

- **Manganese (Mn)**

Mn as alloying element has little influence on the mechanical properties of Mg alloys [27]. It refines grain size at concentrations below 0.4 % [49] and improves Mg alloys' ductility [46,53]. Moreover, Mn removes impurities by forming new phases with metals such as Fe [55]. As Mn by itself cannot enhance the corrosion resistance of Mg alloys, it is typically incorporated with other alloying elements [49].

The human body contains approximately 12 mg of Mn [25], with normal blood serum level between 0.05 and 0.23 μg/L [27]. It is an essential trace mineral that is involved in a numerous cellular system, metalloenzymes and cofactors [43]. Mn is involved in blood coagulation, antioxidant defence, immune response, energy production, digestion, bone growth, and the regulation of neural activity [25]. Also serve vital function in the metabolic cycle of carbohydrates, lipids and amino acids [46]. However, it has been reported that Mn has a cytotoxic effect on sensory hair cells [55] and that excessive exposure to it causes "Manganism" a neurological disorder comparable to Parkinson's disease [43]. Therefore, use of Mn in Mg alloys is restricted to less than 1% wt [25].

- **Zinc (Zn)**

Zn has an atomic radius of 1.35 Å [34] and is one of the most frequently used alloying elements in Mg alloys. Zn reacts with Mg and form secondary phases distributed along the grain boundaries. At concentrations below 4% wt. and 5% wt., respectively, Zn increases the ultimate tensile strength and elongation [46] as well as the corrosion resistance of Mg alloys [25,51,53,55]. Excessive Zn addition to Mg alloys results in the formation of Mg-Zn secondary phases that serve as cathodes sites, thereby accelerating the corrosion of the Mg α-matrix [55]. Additionally, Zn enhance the solution strengthening and aging strengthening [25,51,53,55]. It is also reported that Zn reduced the H_2 gas accumulation [25,49].

Approximately 2gr of Zn is found as a trace mineral element in the human body [25]. Normal blood serum levels of Zn range from 12.4 to 17.4 μmol/L [53], and about 85% of Zn is also present in muscles and bones [49]. Zn is also an essential element for transcription factors and biological enzymes [49]. Zn promotes wound healing and deficiencies in Zn have been found to delay the T- cell-independent and dependent antigen response [25].

- **Zirconium (Zr)**

In Mg alloys, Zr contributes to grain refinement [55]. Typically, it is utilized in Mg alloys containing Zn and Y. However, Zr cannot be used concurrently in alloys containing Al because it forms stable compounds with it [46]. Despite the low solubility of Zr in Mg (3.8 % wt.), adding less than 1% wt., enhances the Mg alloy's ductility and strength and decreases the corrosion rate by almost 50% [49]. In addition, Zr slightly increases the ultimate compressive strength. During Mg alloy solidification, Zr also inhibits the growth of crystal grains, resulting in a Mg microstructure comprised of fine equiaxed grains with their characteristic hexagonal shape [55]. Zr concentrations below 0.4 wt.% have typically been observed in biodegradable alloys, and such low levels of Zr are not expected to cause any local or systemic toxicity [62].

Less than 250 mg of Zr is found in the human body, and it tends to accumulate in the bone tissue [25]. Zr ions have been found to be able to cross cell membranes, resulting in the formation of reactive oxygen species (ROS), causing oxidative damage, and binding to lipids, proteins, and DNA [63]. However, Zr has exhibited excellent biocompatibility *in vivo*, no evidence of mutagenicity or carcinogenicity, good corrosion resistance, and bone biocompatibility equal to or greater than Ti [64].

- **Rare-earth elements (REEs)**

ASTM nomenclature for magnesium alloys comprises the REE designated by the letter E, except for the yttrium, which is represented by the letter W [49]. REE are extracted in the form of oxide for rare minerals [55], and they are used to enhance the mechanical properties of Mg alloys [46]. LAE443, Mg-4Y, and WE43 are among the most investigated alloys for biomedical applications [27,58], where neodymium and yttrium are frequently alloyed into Mg alloys.

Neodymium (Nd) has an electrochemical potential similar to Mg (-2.43 V) [65], an atomic radius of 0.1814 nm [62], and is also used for grain refinement in Mg alloys despite its low solubility in Mg (0.63 at. %) [51]. Nd improves the tensile and tensile yield strength of Mg alloys [55] due to the significant difference in atomic radius between Nd and Mg, which results in Nd atoms substituting Mg atoms, impeding dislocation movements. In addition, Nd forms

$Mg_{41}Nd_5$ and $Mg_{12}Nd$ secondary phases. This $Mg_{12}Nd$ phase improves the high-temperature creep resistance of the Mg alloy [51]. Furthermore, Nd is biocompatible as various cell types can tolerate comparatively high concentrations of Nd [66].

Yttrium has a high solubility in Mg (12.4% wt.) [49,58,62], a similar hexagonal closed-packed lattice and lattice parameters (atomic radius 1.80 Å) [62], and the same electrochemical potential as Mg [55]. Y refines grain size and enhances Mg alloys' tensile strength [49]. During the degradation of Mg alloys containing Y, it migrates to the metal surface. It is oxidized, forming Yttrium oxide (Y_2O_3) that accumulates in the degradation layer, thereby slowing down the Mg alloy corrosion. However, if the corrosion layer is unstable, Y will promote micro galvanic corrosion [67]. There have been reports of low levels of Y in the human body (<47µg) [25,27]. However, it has been found that high levels of Y tend to accumulate in the gallbladder and liver, causing an increase in eosinocyte levels and eosinophil infiltration. These may have a negative impact on the biocompatibility [49].

Yttrium and REEs are the primary alloying elements in the WE series of Mg alloys. In addition, trace amounts of Zn and Zr are includes in this WE series. WE43 alloy is the most well-known WE alloy for biomedical applications [51]. However, even though the use of REEs in Mg alloys contributes to the improvement of their corrosion resistance, the use of REEs in the biomedical field requires further investigation to determine their potential cytotoxicity. Excessive levels of Y, for instance, have adverse effects on the DNA transcription factors and alter the gene expression in rodents [58].

Among Mg-REEs alloys, the long-period stacking ordered (LPSO) phase enhances the corrosion and mechanical properties of these alloys [49]. The LPSO phase is a periodic arrangement of close-packed atomic layers enriched by RE elements (RE = Y, Gd, Dy, Ho, Er, Tm, and Tb) and transition metals (TM = Al, Zn, Cu, and Ni) in the Mg lattice [68,69]. This LPSO has a fine lamellar shape distributed in the grain boundaries or extended into inner grains from the grain boundaries and is chemical-ordered (Zn/Y enrichments) as well as stacking-ordered [70]. According to the number of stacking layers, the following LPSO phase types have mainly been described: 6H,10H,14H,18R, and 24R. The H and R, respectively, described the hexahedral and rhombus structures [71]. The LPSO improves corrosion behavior by generating an oxidation film, modifying the corrosion layers, and their uniform distribution, and these LPSO phases improve the mechanical properties of Mg alloys by restricting dislocation movement [49] (Figure 1.5).

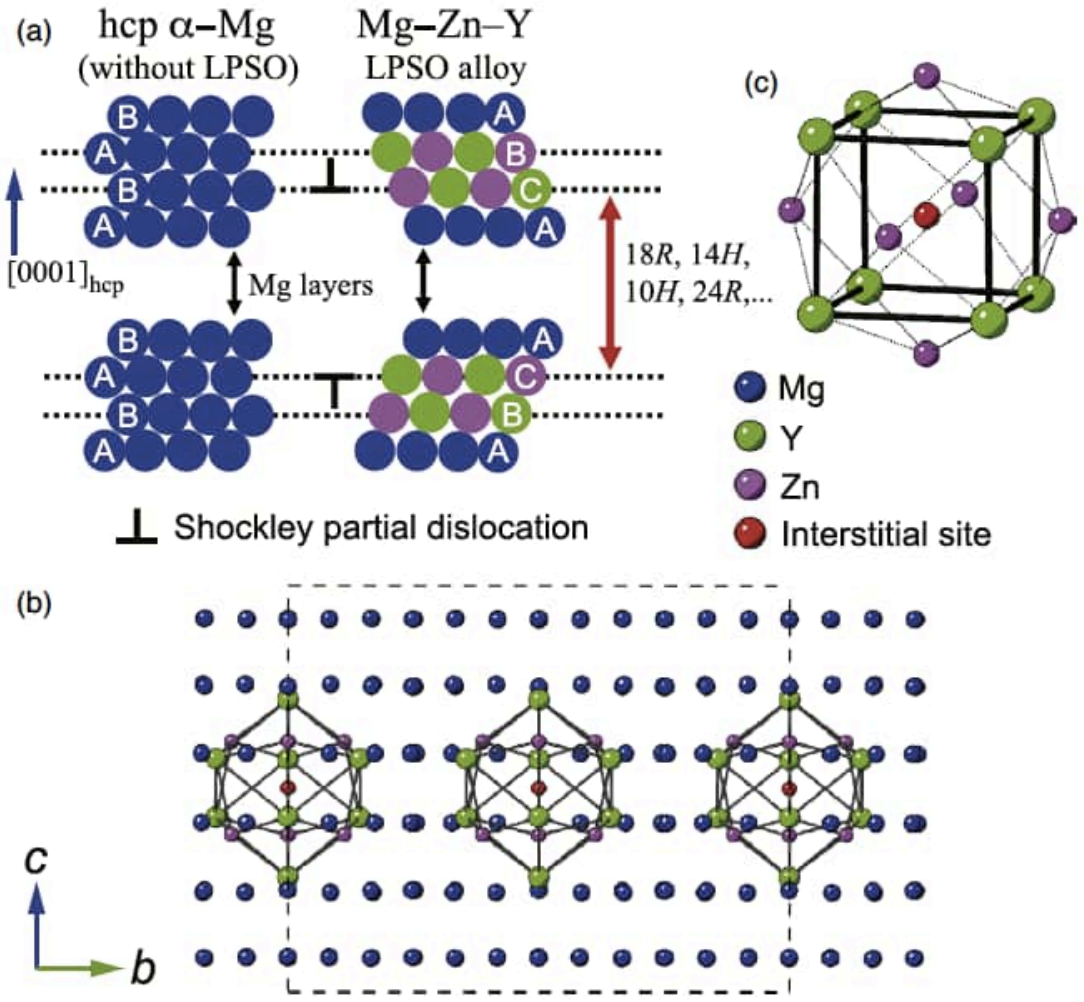

Figure 1.5. Mg-LPSO model structures. a) Schematic hcp α and LPSO structure ina Mg-Zn-Y alloy: Mg Mg site (blue circles), Zn/Y occupation site (purple and green circles, respectively). b) LPSO structure in the MgZnY alloy. The dashed line represents the unit cell. c) Detailed cluster from b) depicting the arrangement of Zn atoms in a Y plane (denoted by bold lines) [72].

To summarize, the alloying elements influence the mechanical properties and corrosion resistance of Mg and its alloys by modifying the grain size, the matrix with various solid solutions, and the fraction and volume of secondary phases (discontinuous or continuous along grain boundaries) [46,55]. In addition, the concentration of alloying elements in the human body will vary depending on the local environment surrounding the Mg-based device, the distance to the Mg-based implant, and the tissue repair as a function of time [25]. All these factors must be considered when designing Mg alloys for biomedical applications, which is why more *in vitro* and *in vivo* experiments still are required [46].

1.2.4. Mg as a biodegradable material

Mg is regarded as one of the essential metals for humans [73], with healthy humans requiring between 250 and 420 mg per day [16,18,37,74]. It is the fourth most abundant cation

in the human body [18,37,73] involved in more than 300 enzymatic reactions in the formation of bone and soft tissues [18]. ~65% of Mg is stored in bones, 34% is distributed intracellularly in soft tissues and muscles, 10 % is available as free ion [75], and 1% is found in the extracellular fluids [76]. Normal blood serum concentration is between 0.73 and 1.06 mmol/L [53].

Mg has been used in the biomedical field for over a century (Figure 1.6). Dr. Nehemiah Grew identified magnesium sulfate ($MgSO_4$) as the primary component of Epsom salt to treat abdominal pain, constipation, muscle strains, and cerebral edema in 1697 [77]. Joseph Black identified Mg^{2+} as an element for the first time in 1755 [27]. Sir Humphrey Davy isolated Mg in 1808 from a mercury oxide (HgO) and magnesium oxide (MgO) mixture. Michael Faraday successfully extracted Mg using electrolysis of fused anhydrous $MgCl_2$ in 1833 [27,46,78]. Dr. Edward C. Huse reported the first biomedical use of Mg in 1878 when he used Mg wires to ligate blood vessels to stop bleeding [79]. In 1900, the physician Erwin Payr inserted Mg tubes into the femoral artery of an animal [46]. He proposed that tissue oxygen, water content carbon dioxide, blood minerals, and cell chemical processes were mainly responsible for the corrosion of Mg *in vivo* [27]. Parallel to his animal research, he successfully treated the hemangioma of a 14 years-old girl and introduced the concept of using Mg plates and sheets in joint arthroplasties to fix traumatic bones [80].

In contrast to Hopfner's use of Mg cylinders for vessel anastomosis in 1903, Lespinasse et al. [46,81] used Mg metallic ring plates with punched holes for extravasal sutures in 1910. Andrews et al. [46,82] utilized Mg absorbable clips and staples for cerebral and deep wounds hemostasis and intestinal anastomosis in 1917. Willey Glover Denis described the role of Mg^{2+} in blood plasma in 1920, while Jehan Leroy demonstrated in 1926 that Mg^{2+} is essential for the well-being of rodents [77]. In 1934, Verbrugge et al. [80] treated a child's diaphyseal humeral fracture with Mg plates and screws. In 1938, McBride et al. [83]reported the first use of an Mg alloy to treat bone fractures with Mg-Al-Mn alloy screws, bolts, and plates. Maier used spindle-shaped Mg sheets to repair two humeral fractures in humans in 1940. One patient's implant was removed owing to the continued formation of gas cavities in the tissues [84]. In 1948, Troitskii et al. [84] reported the successful treatment of 34 cases of pseudarthrosis with Mg-Cd alloy plates and screws.

Despite the significant advancements at that time and successfully reported cases in the use of Mg for vascular, orthopedic, and general surgery [80], the rapid degradation and large amount of hydrogen accumulated in subcutaneous tissues, interrupted the investigations of Mg

and its use as biomaterial for biomedical applications. As an indicative of this fact, there were no clinical studies reported using Mg for orthopedic applications between 1948 and 2010 [27,84]. With the rapid advances in science and technology, significant progress has been made in developing Mg for biomedical applications [80,83]. Since 2002, more than 4000 Mg-related papers have been published, with most of these papers focusing on the corrosion resistance of Mg and its alloys and the mechanical properties of Mg [26,85,86] (Figure 1.7). All these research efforts worldwide have led to some Mg alloys reaching their use in clinics. In 2013, compression screws made of MgYREZr alloy (MAGNEZIX®, Syntellix AG, Germany) were the first Mg biodegradable implant approved by Conformité Européen (CE) to treat hallux vagus [27,60,79]. In 2015, South Korea authorized the use of a Mg alloy screw (K-MET, U&I, Korea) to treat knuckle fractures [79]. In 2016, Magmaris® (Biotronik, Germany) became the first biodegradable stent to receive CE approval. In 2023, Mg-Zn-Ca screws (Bioretec Ltd., Finland) were the most recent Mg-based device to receive FDA approval for clinical use in the US to treat surgical internal fixation of bone fractures in adults [87] (Figure 1.8). Despite these accomplishments, Mg implants are not routinely used in clinics mainly due to challenges related to magnesium degradation. Before discussing these obstacles, it is essential to comprehend the mechanisms of Mg degradation.

1.2.5. Corrosion of Mg

Magnesium (Mg) is one of the metals whose high chemical activity renders it susceptible to oxidation in air and corrosion under aqueous environments [88–91]. The formation of this oxide layer prevents further oxidation of the material [92]. When exposed to air for 10 sec and 10 months, pure magnesium formed a ~2.2 to 5 nm oxide layer (MgO), respectively, whereas Mg alloys could develop an oxide film with a thickness of 1 to 15 nm thickness [93–95]. This MgO has a Pilling-Bedworth (PB) coefficient of 0.81, indicating that the oxide film formed under tension is porous and not dense [42,89–91,96] and is not particularly protective [97]. The corrosion of metals is an electrochemical process where the metal's oxidation state changes because of its interaction with the environment. This process occurs via electron transfer at the electrode interface and entails the oxidation of metal atoms to form ionic species, along with the release of electrons [42]. In contrast to the oxidation process in the air, where specimens display a black surface [98], magnesium degradation in aqueous environments is typically accomplished through an anodic (Equation 1.1) and cathodic (Equation 1.2) reaction that results in the formation of precipitates of crystalline magnesium hydroxide $Mg(OH)_2$, hydrogen gas formation and the alkalinization of the local environment [53,60,97–99] (Equation 1.3):

Anodic reaction: $Mg \rightarrow Mg^{2+} + 2e^-$ (Eq. 1.1)

Cathodic reaction: $2H_2O + 2e^- \rightarrow H_2 + 2OH^-$ (Eq. 1.2)

Overall reaction and product formation: $Mg^{2+} + 2H_2O \leftrightharpoons Mg^{2+}2OH^- + H_2$ (Eq. 1.3)

Due to its low solubility in water (12 mg/L), $Mg(OH)_2$ is the first product to precipitate during the degradation process [98]. This $Mg(OH)_2$ has a PB ratio of 1.77, indicating that it is a compressible protective oxide film [42,97]. In addition, the pH will play a significant role in these reactions. As can be seen in Figure 1.9a Mg reacts with water at all pH levels, reducing it through the evolution of hydrogen and dissolving as Mg^{2+} ions. At a pH between 8.5 to 11.5, it can cover itself with an oxide or hydroxide film. At lower pH values, this passivation layer will be less thin and more permeable, providing limited protection [15,100,101].

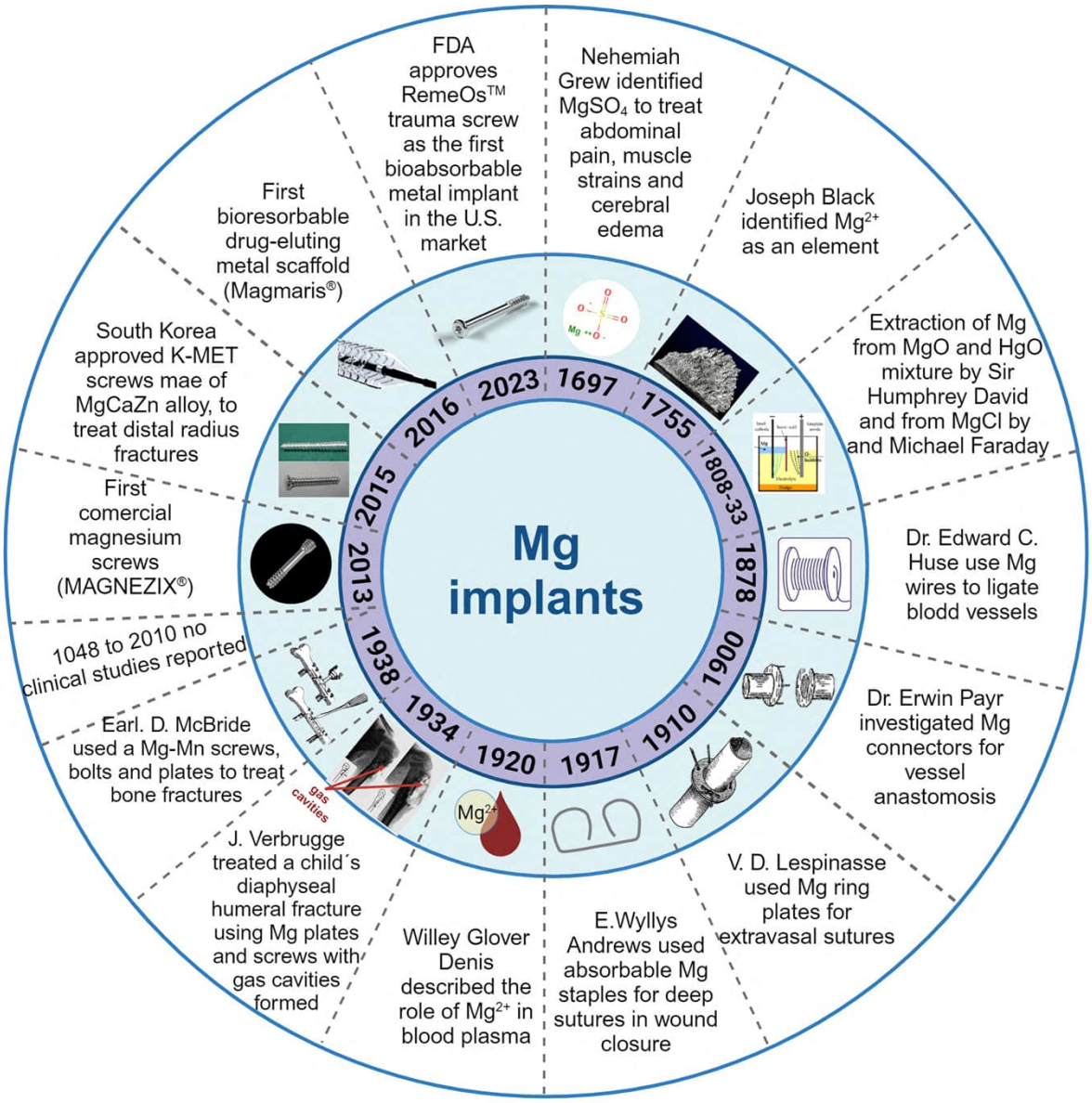

Figure 1.6. Timeline of magnesium development for clinical applications**.** *Image created with Biorender.com*.

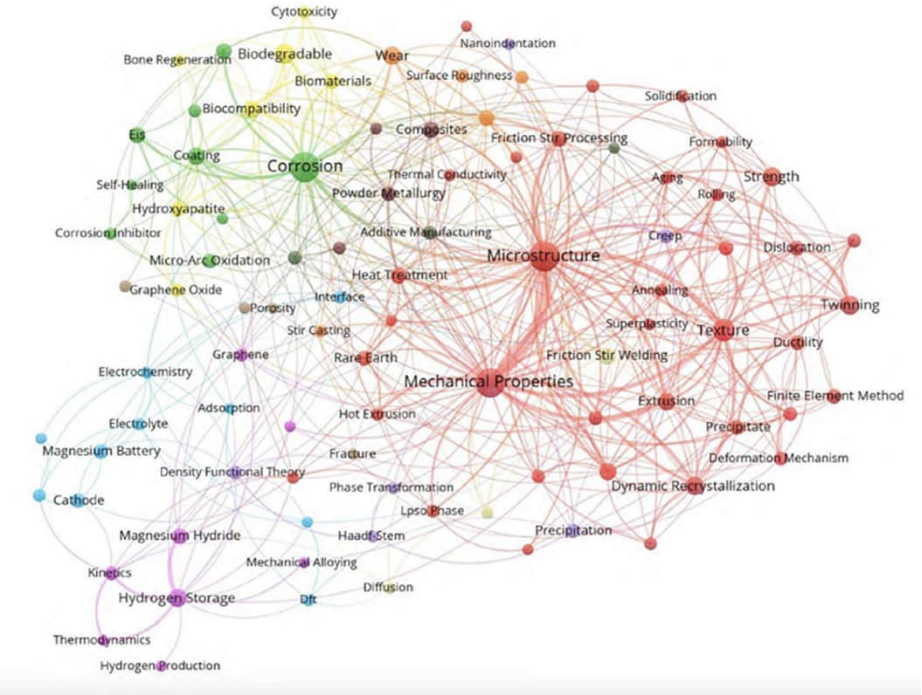

Figure 1.7. Network visualization map of Mg research hotspots [85].

Figure 1.8. Mg medical implants commercially available. *Image adapted from* [87,102]

Because of the narrow pH range under physiological conditions (7.4 - 7.7), Mg and its alloys for biomedical applications will comprise a small portion of the Pourbaix diagram. Liu et al. [103] illustrated the Pourbaix diagrams of Mg in physiological concentration (1 x 10^{-3} M)

(Figure 1.9b-d). They predicted Mg reactions in the presence of human blood plasma concentration of HCO_3^- (CO_2(aq)) and HPO_4^{2-} (0.027 mol L^{-1} and 0.001 mol L^{-1}, respectively) at 0.78 V tissue fluid´s potential. Initially, Mg will undergo anodic reactions, resulting in the formation of $MgCO_3$ and $Mg(OH)_2$ in an ideal scenario. However, as a result of the non-uniform corrosion of Mg, an increase in pH typically results in the formation of $Mg(OH)_2$ rather than $MgCO_3$. In addition, HPO_4^{2-}, PO_4^{3-}, CO_3^{2-} species can react with Ca either from alloying elements or bodily fluids. These reactions result in the formation of corrosion products composed of calcium-phosphate/carbonates.

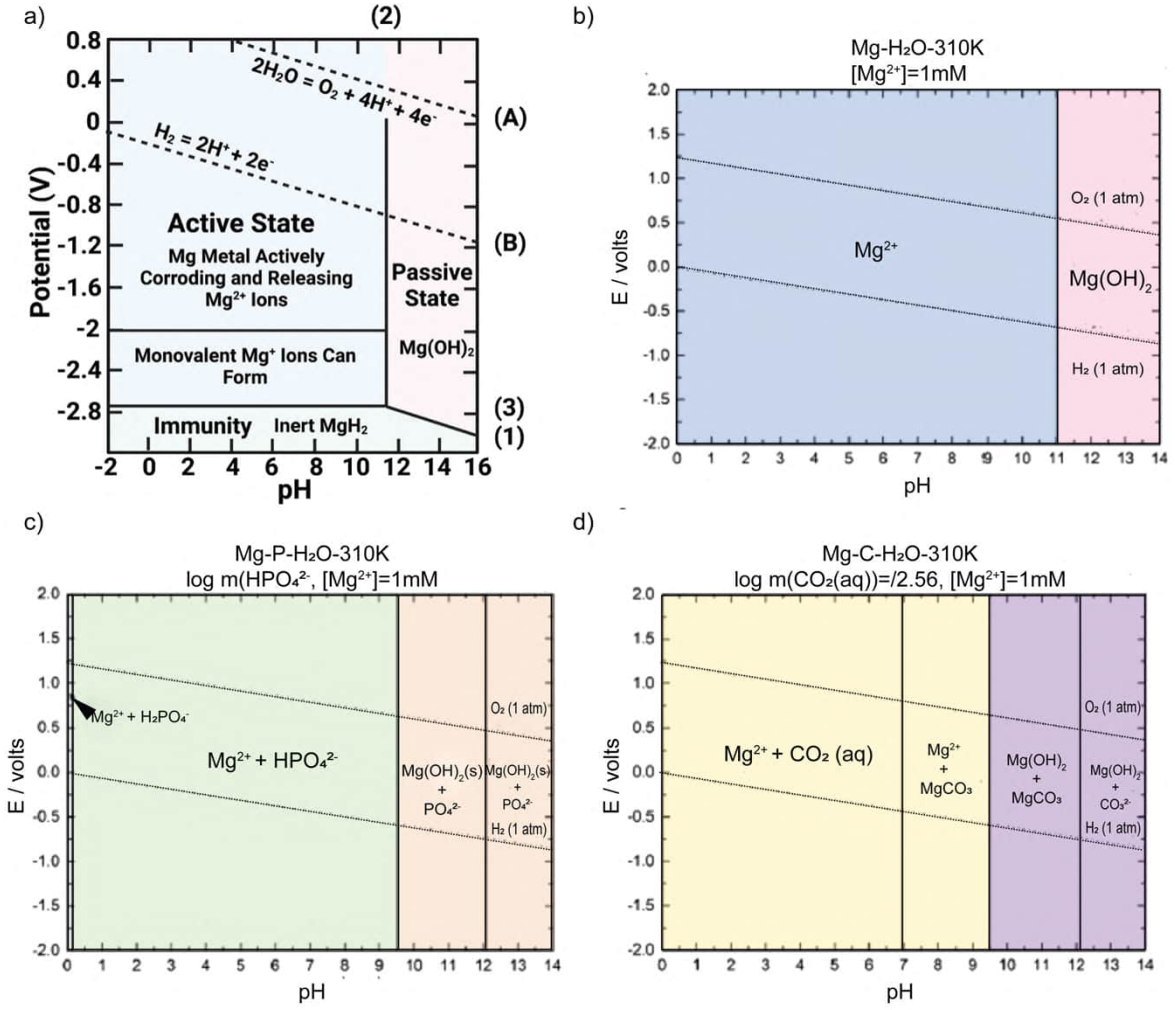

Figure 1.9. Pourbaix diagram of Mg in a) water at 25ºC [100]**, and b-d in physiological concentrations.** *Images in b-d adapted from* [103]**.**

In a complex physiological environment such as the human body, with a high concentration of aggressive ions such as chloride ions, the formed protective layer is converted into soluble magnesium chloride, resulting in accelerated corrosion of Mg-based devices [60,95,104–107]:

$$Mg(OH)_2 + 2Cl^- \rightarrow MgCl_2 + 2OH^- \qquad (\text{Eq. } 1.4)$$

In addition, the presence of numerous organic compounds, such as amino acids, proteins, lipids, enzymes, and cell-tissue interactions, influences the corrosion behavior of absorbable Mg and the composition of the corrosion layer (Figure 1.10) [60,95,104–108]. Amukarimi et al. [24] illustrate the possible chemical reactions that Mg biomaterials may undergo in physiological conditions: at the initial stage of Mg degradation, both anodic and cathodic reactions take place (Figure 1.10a). This is followed by the subsequent formation of $Mg(OH)_2$ and H_2 gas release (Figure 1.10b). According to the equation 4, the presence of Cl^- ions in the body fluids causes the disruption of the $Mg(OH)_2$ film, resulting in the formation of $MgCl_2$ Figure 1.10c). Following this, the OH- and Mg^{+2} ions will undergo a chemical reaction with carbonates and phosphates present in bodily fluids, resulting in the $MgCO_3$ and $Mg(PO_4)_2$ formation (Figure 1.10d-g). Similarly, the presence of Ca carbonates in the body will lead to $CaCO_3$ formation (Figure 1.10h) , and eventually, some kind of carbonate-phosphate can be formed as corrosion products during Mg implant degradation within the human body (Figure 1.10i). Additionally, the protein adsorption will be followed by cell attachment, migration, proliferation (Figure 1.10j), and new tissue formation. The degradation process will have a dual impact, influencing not only the biocompatibility with cells (Figure 1.10k) but also the pH in the tissues adjacent to the implant surface.

As a result, different forms of Mg corrosion can occur under physiological conditions. In general, uniform and localized corrosion are two types of corrosion that occur in Mg alloys [109]. The occurrence of general corrosion is less deleterious to the magnesium implant material and is frequently observed in the process of self-dissolution of unalloyed metals and alloys with a homogeneous composition [110]. However, Mg alloys very rarely displayed uniform corrosion [59]. As Mg alloys contain precipitates, secondary phases, and/or impurities that serve as cathodic sites relative to the α-matrix, the anodic reaction will be accelerated, resulting in faster corrosion of the Mg alloy. If the passivation layer is compromised, the surrounding solution will continuously permeate the porous corrosion layer, thereby accelerating the corrosion of the Mg alloy. Therefore, the following types of corrosion are likely to occur:

Localized corrosion can occur in single-phase magnesium (Mg) alloys, where the magnesium is partially shielded by the presence of magnesium hydroxide ($Mg(OH)_2$) [111]. During the phenomenon of localized corrosion, the corrosion rate observed in a specific area of a magnesium alloy is significantly higher than in the surrounding regions. This discrepancy in corrosion rates leads to a more severe and destructive form of corrosion. Several types of

localized corrosion include galvanic corrosion, intergranular corrosion, stress-cracking corrosion, and fatigue corrosion [110].

Galvanic corrosion refers to a specific form of corrosion that arises when two dissimilar metals, characterized by distinct electrochemical potentials, encounter one other in the presence of an electrolyte solution. Metals with lower nobility will function as the anode and undergo corrosion at a comparatively accelerated rate (Figure 1.11a) [23,45,60,108,112]. The occurrence of this form of corrosion represents a significant challenge in the use of magnesium in orthopedic applications, particularly when employed alongside titanium screws [23]. Galvanic corrosion also occurs due to the inclusion of intermetallic elements, namely Al, Mn, and Fe, or the presence of impurities such as Fe, Ni, Co, or Cu (Figure 1.11b). The aforementioned elements exhibit more nobility than magnesium (Mg) and can locally boost the hydrogen evolution reaction, thereby leading to an accelerated corrosion rate observed in Mg alloys [23,45,113].

Pitting corrosion is a form of localized corrosion that emerges in environments containing hostile ions, such as chloride, inside the human body. These ions contribute to the local degradation of the protective corrosion barrier and the formation of cavities. The observation of this type of corrosion is often challenging due to the existence of the corrosion products/layer. Pits are generated, and impurities facilitate subsequent corrosion by promoting the creation of micro-galvanic cells within these pits (Figure 1.12). As a result, accelerated corrosion will take place [23,110,114].

Crevice corrosion is a form of corrosion that has a close relationship with pitting corrosion. this type of localized corrosion occurs in narrow gaps that are generated between two magnesium (Mg) implants or at the contact between the Mg implants and the surrounding tissues. In a study conducted by Wu et al [115] was observed that high-purity magnesium (HP-Mg) exhibited an increased rate of corrosion because of crevice corrosion, both *in vitro* and *in vivo*. In the proposed model, the immersion of HP-Mg in a PBS solution resulted in the formation of corrosion products that were stable at the crevice during the first stage. The presence of chlorine ions leads to a localized enrichment of them in the crevice. The elevated presence of chloride ions within the crevice will stimulate an increased formation of corrosion products with more chloride absorption, resulting in an accelerated corrosion rate of Mg and its alloys, even within an alkaline environment (Figure 1.13) [45,112,114,115].

Filiform corrosion is a specific type of corrosion that initiates with the formation of microscopic pits inside the Mg matrix. While pitting corrosion refers to the formation of deep cavities in localized regions inside the Mg matrix, filiform corrosion involves the spread of corroded regions along specific paths on the surface of the alloy, typically occurring in shallow and extensive areas [110]. The occurrence of this form of corrosion was noticed by Wang et al. [116] when immersed Mg-3Zn alloy in a 0.01 M NaCl solution for 6 h. Their findings demonstrated the presence of an arborescent structure consisting of filaments that diverge in various directions (Figure 1.14). When a filament meets another filament, it will either change its direction or stop its growth.

1.3.Bone as implantation site

As previously stated, Mg medical implants are currently used for cardiovascular and orthopedic applications. This implies that the mechanical properties should be application specific. The primary purpose of employing bone implants in clinical practice is to facilitate the healing of bone injuries [117]. This means that bone biomaterials play a crucial role in bone regeneration by providing the substrate for cell adhesion, proliferation, and differentiation and regulating cell activity and function [118]. It is anticipated that Mg absorbable devices undergo degradation *in vivo* by electrochemical reactions, afterward being metabolized by cells and assimilated by tissues [102]. Therefore, it is necessary to understand the hierarchical arrangement and chemical composition of human bone tissue and the bone fracture healing process to develop Mg medical implants. Table 1.3 summarizes the density and some mechanical properties of bone and Mg metallic materials.

1.3.1. Hierarchical structure of human bone

Bone is a crucial and complex load-bearing tissue within the human body. The different bones in the human body exhibit distinct mechanical properties based on their location, position, and orientation [119]. At the macroscopic level (At a scale of 1–10 mm) [120] bone consists of cortical bone (often referred to as compact bone) and trabecular bone (also known as cancellous or spongy bone) [121,122]. Both are types of lamellar bone [123]. The cortical bone exhibits a predominantly solid structure, with only 3 – 15% [120,124,125] space allocated to osteocytes cells, canaliculi, and blood vessels [124], providing mainly mechanical support [119]. It demonstrates superior mechanical strength when subjected to longitudinal loading, displaying greater strength in compression compared to tension [124]. Furthermore, the cortical bone serves as a protective outer shell for both the trabecular bone and the bone marrow [126] (Figure 1.15a).

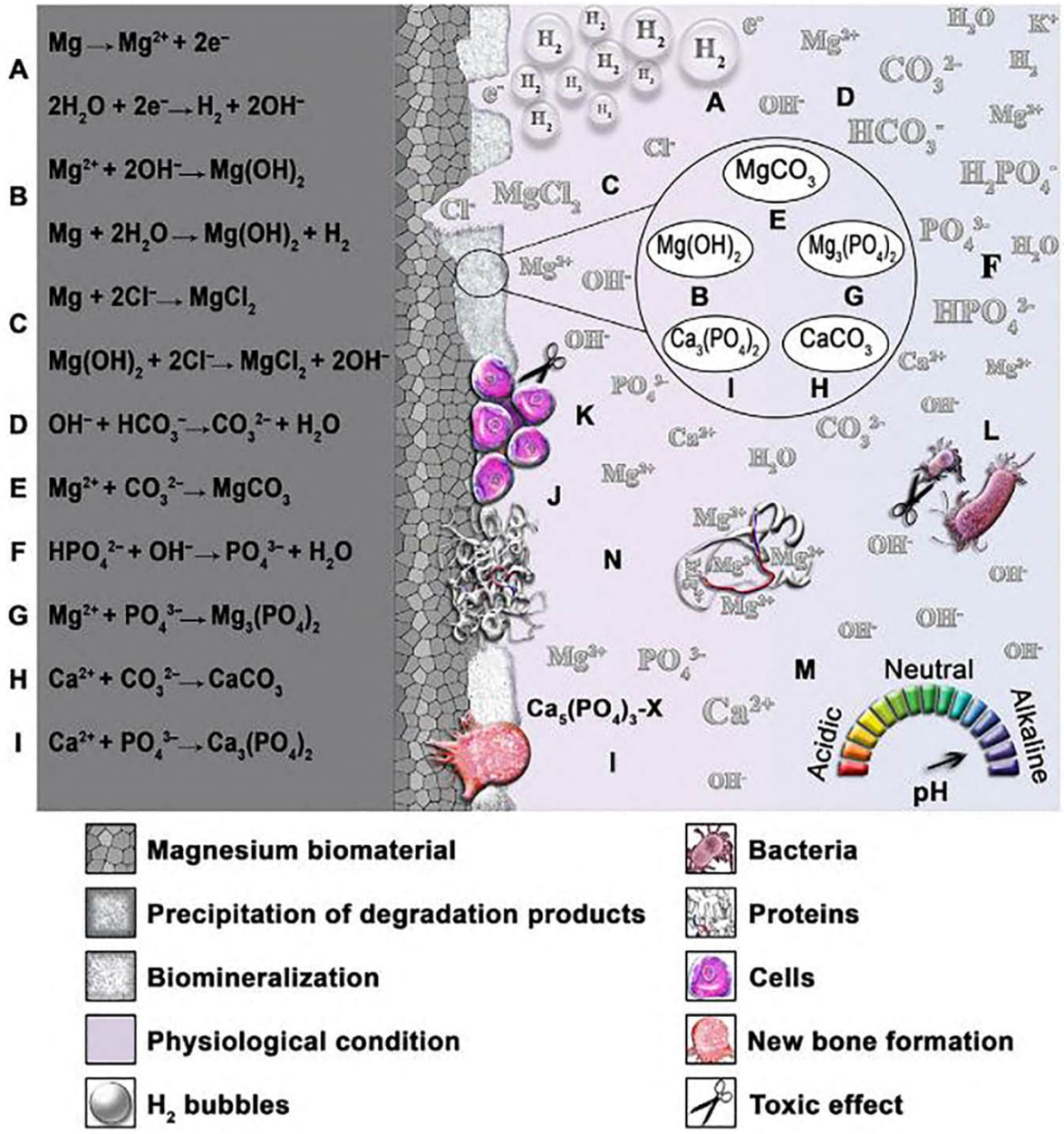

Figure 1.10. Corrosion performance of Mg-based device in physiological conditions [25].

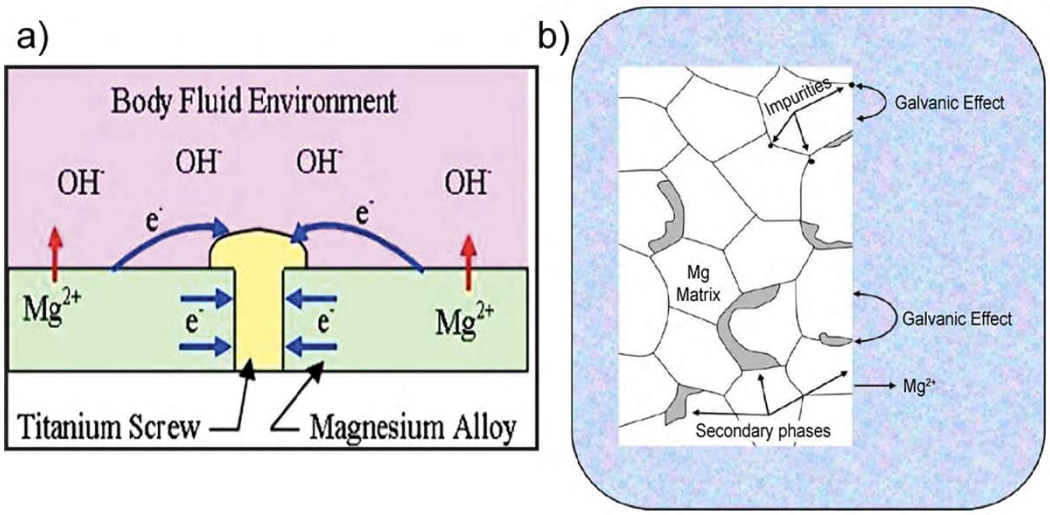

Figure 1.11. Galvanic corrosion. a) between dissimilar metals [112] and b) resulting from impurities and secondary phases [127].

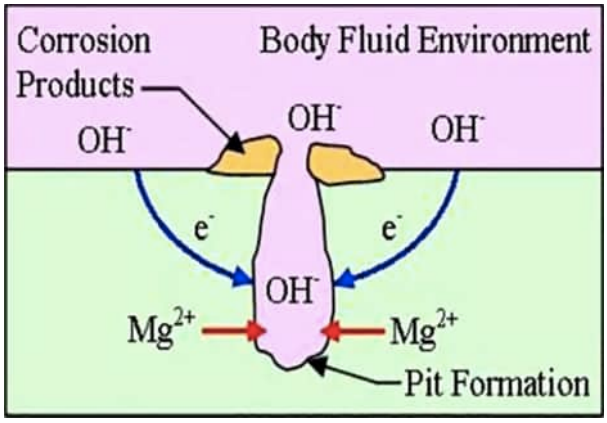

Figure 1.12. Pitting corrosion [112]**.**

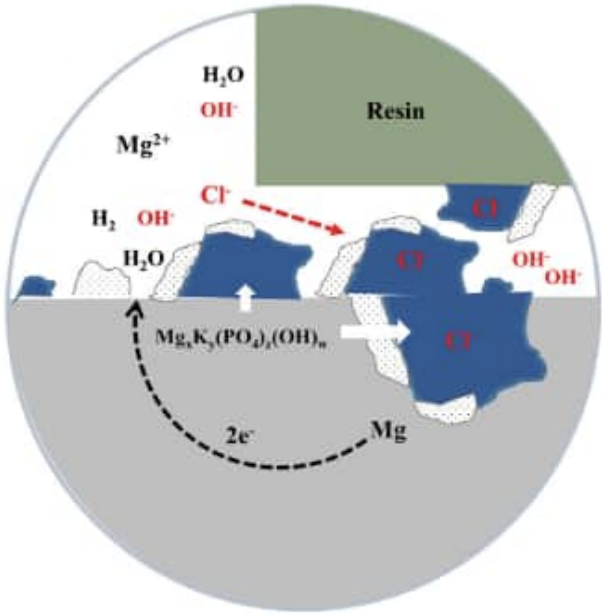

Figure 1.13. Crevice corrosion in presence of chloride ions [115].

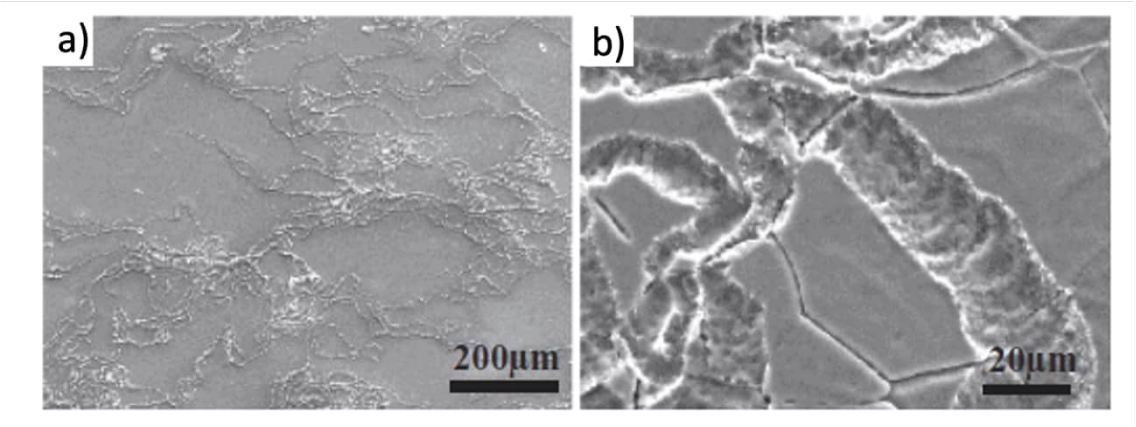

Figure 1.14. Filiform corrosion [116].

On the other hand, the trabecular bone exhibits lower density characterized by a porous structure (ranging from 50 to 95%) [120,124,125]. However, it should be noted that the trabecular bone has a significantly higher surface area per unit volume in comparison to compact bone, with a ratio of twenty-fold [125]. This structure is organized in a honeycomb network [128] that occupies much of the medullary cavity [125]. This network is characterized by its permeability, accommodating a network of blood vessels, and housing the bone marrow. The bone marrow is a versatile tissue that encompasses several types of cells, including stem, progenitor, and fully differentiated cells of multiple lineages [128,129]. In addition, the trabecular bone possesses a relatively low mechanical strength but provides appropriate space for hematopoietic function and bone metabolism. Additionally, it facilitates the support and

transmission of multidirectional stresses during body movement [128]. Moreover, the trabecular bone has a time-dependent performance and is susceptible to injury under cyclic loading conditions [124].

Table 1.3. Mechanical properties of bone and Mg metals [119–121,130–135]

Material	Density (g/cm^3)	Young modulus (GPa)		Strength (MPa)		Poisson´s ration
Human femoral cortical bone	1.8 – 2.0	Longitudinal direction	17.9 ± 3.9	Tensile ultimate stress	135 ± 15.6	0.4 ± 0.16
				Compression ultimate stress	205 ± 17.3	
				Shear ultimate stress	65 ± 4.0	
		Transverse direction	10.1 ± 2.4	Tension ultimate stress	53 ± 10.7	
				Compression ultimate stress	131 ± 20.7	
Human femoral trabecular bone	1.0 – 1.4	Femur	0.44 ± 0.27	Tensile strength	30 – 40	0.62 ± 0.26
				Compression strength	118-142	
		Tibia	0.44 ± 0.25	Tensile Ultimate strength	165.3	
				Compression Ultimate strength	200	
Bone collagen		10 – 20				
Collagen fiber		0.1 – 1				
Calcium phosphate		100				
Pure Mg	1.74	45				
(MgYREZr) WE43	1.84	44				
Mg-Zn-Ca (ZX00)	1.74*	MgZnCa glasses	48	Tensile yield strength	283 ±5.0	
				Ultimate tensile strength	285.7 ±3.1	

* Determined by Archimedes method

At the microscopic level (Figure 1.15a), the cortical bone is comprised of osteons that are organized in alignment with the longitudinal axis of the bone. The osteon, (with a size ranging from 10 to 500 μm [124] is recognized as a fundamental unit of bone tissue and consists of concentrically structured lamellar bone [121,128], containing nerve fibers and blood vessels [128,136].

At the nanoscale level (Figure 1.15a), bone has a composite structure consisting of organic proteins and inorganic minerals [118,122]. As a composite, bone is constituted of about 30 wt.% matrix, 60% mineral, and the remaining 10% is water [121,125]. The organic component of bone primarily consists of collagen protein fibers, specifically type collagen I, which make up ~55-60% of the bone matrix [119,122]. Additionally, noncollagenous proteins including osteocalcin, osteopontin, osteonectin, fibronectin, bone sialoprotein II, as well as bone morphogenetic proteins (BMPs), and growth factors are also present [137]. The inorganic components of bone contribute to its mechanical properties, specifically to its strength and stiffness [125]. The mineral of bone primarily consists of calcium, (Ca) and phosphorus (P) in the form of hydroxyapatite (HA) crystals. Additionally, potassium (K), sodium (Na), fluoride (F), chlorine (Cl), carbonate (CO_2^{3-}), magnesium (Mg), and some trace elements of strontium (Sr), zinc (Zn), iron (Fe), silicon (Si), and copper (Cu), which contribute to the bone´s strength [118,137]. The HA represents around 40 - 45% of the bone matrix [119,122]. It plays a crucial role in enhancing the mechanical properties of the bone matrix [119]. Additionally, approximately 67% of Mg is stored in bone where 30% is exchangeable from the bone surface providing a dynamic supply to maintain extra and intra-cellular Mg concentrations. It has been reported that Mg induces osteoblast differentiation thereby promoting bone regeneration. Low levels of Mg will lead to an increase in osteoclast resorption and a decrease in osteoblast cells [80].

The collagen fibers undergo cross-linked and self-assembled, resulting in the formation of sheets or bundles of fibers. The HA crystals are situated within and between these fibers [122]. This calcium phosphate crystals are found in the form of elongated polycrystalline plates that exhibit a consistent thickness of ~5 nm, length of up to 200 nm, and width between 60 to 80 nm. These plates display either a curved configuration surrounding the collagen fibrils or a stacked arrangement of planar sheets [138].

1.3.2. Main cellular components of bone

Bone, as a mineralized form of connective tissue, has a diverse array of cells (Figure 1.15b) that play a crucial role in the maintenance and restoration of bone under normal physiological circumstances as well as in the presence of injury or damage [139]. The bone cells are derived from two distinct cell lineages, specifically hematopoietic and mesenchymal stem cells [125].

Undifferentiated mesenchymal stem cells (MSCs) can undergo differentiation into preosteoblasts and osteoblasts [139,140]. These cells exhibit a characteristic arrangement

wherein each cell is closely juxtaposed to its neighboring cell [125]. They constitute approximately 4–6% of the overall bone cells [137] and are primarily recognized for their role in bone formation [137,139]. The medullary cavities of bone are the primary location where osteoblasts are more densely concentrated [125]. Additionally, osteoblasts are also situated along the bone surface [137,139] within the periosteum (the outmost layer of bone), which contains significant amounts of osteoblasts as well as osteoprogenitor cells [125]. The process of bone matrix production by osteoblasts can be divided into two primary stages: the initial deposition of the organic matrix, involving the secretion of collagen and non-collagen proteins followed by its subsequent mineralization [137]. A portion of these osteoblasts will undergo programmed cell death (apoptosis), while some of them will continue the secretion of extracellular matrix components and get embedded within the matrix of the bone, forming osteocytes [139].

The osteocytes, which comprise approximately 90–95% of the overall bone cells, are the predominant and long-lived cell population inside the skeletal tissue [125,137]. These cells have a lifespan of up to 25 years [137]. The osteocytes are embedded in the bone mineralized matrix enclosed in lacunae with an elongated and rounded dendritic morphology in the cortical and trabecular bone, respectively. The cytoplasmatic prolongations of osteocytes establish connections with other osteocytes, osteoblasts, and bone lining cells, creating an intricate network that enables the intercellular transportation of small signaling molecules [125,137]. The network of osteocytes is believed to have a crucial function in detecting stress (as a mechanical sensor and regulating the transport of ions within the mineralized matrix [125].

The bone lining cells are also derived from osteoblasts. They possess a flattened and elongated morphology, separating the bone surface and the bone marrow. As a result, bone lining cell safeguards the bone surfaces against undesired resorption [125,137].

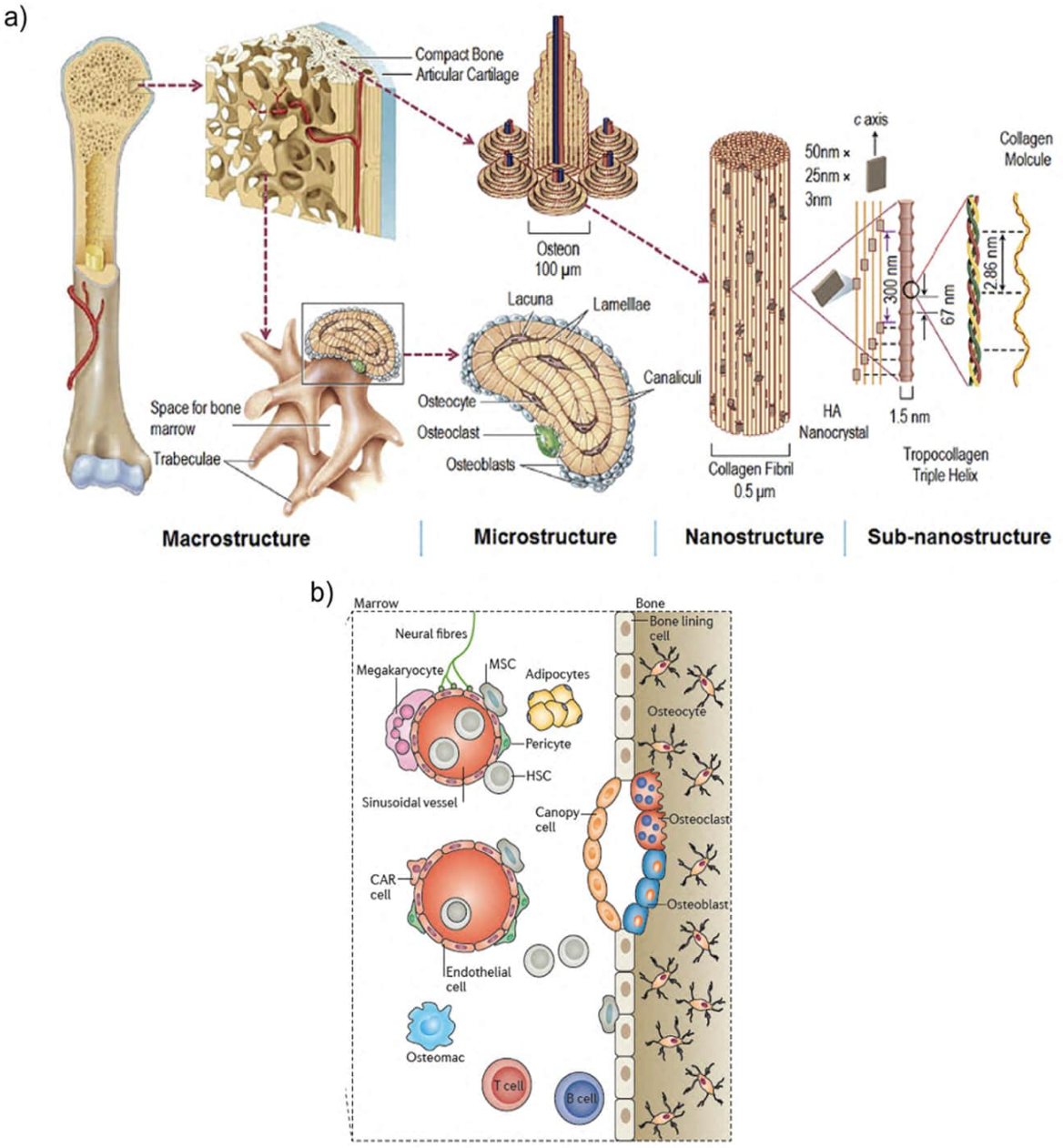

Figure 1.15. a) Bone structure and composition [124]**. b) Main cellular components of bone** [129]**.**

Osteoclasts are a type of differentiated multinucleated cells that have reached the final stage of differentiation. These cells are derived from mononuclear cells that belong to the hematopoietic stem cell lineage [137]. Monocytes, together with macrophages, represent among the initial cellular entities that engage with implanted medical devices [141]. The process of their formation involves the fusing of hematopoietic precursor cells, leading to the development of multinucleated cells with diameters reaching up to 100 µm. The monocyte-macrophage lineage cells undergo differentiation into osteoclast precursors in close proximity to osteoblastic cells [142]. Osteoclasts as antagonists to matrix synthetizing cells, primarily serve the function of bone resorption [140]. They have distinctive features, notably the presence

of a ruffled border, which serves to enhance the processes of demineralization and degradation of the bone matrix [143]. During their non-resorbing phase, osteoclasts exhibit dot-like structures and podosomes of actin filaments (F-actin). Conversely, osteoclasts can be identified during their resorbing phase by the presence of actin rings and the ruffled border [144].

1.3.3. Bone fracture healing process

Bone, being a highly adaptable tissue, undergoes continuous remodeling. In the case of bone injury, it possesses the capability to regenerate and restore its biological and mechanical properties to their pre-damaged state. Two distinct mechanisms of bone fracture repair are observed in the human body, namely primary and secondary bone healing [102,145,146]. Primary repair is a rather infrequent occurrence [145]. It involves the remodeling of cortical bone without the callus formation [102], taking place in fractures when bone fragments exhibit "absolute stability" and there is a close proximity between the bone fragments (less than 0.15 mm) [146]. Indirect or secondary fracture healing is the prevalent type of fracture healing [147]. The treatment for these fractures involves realignment and fixation to facilitate the appropriate healing. The orthopedic implants must be surgically placed to stabilize the fracture fragments and restrict their movements [8]. In addition, it is imperative that implant materials do not hinder the inherent physiological mechanism of bone repair. Therefore, it is important to understand the bone fracture healing process.

The successful healing of a fracture is contingent upon the presence of 4 factors outlined in the conceptual framework known as the diamond concept (Figure 1.16a). These factors include the presence of a robust population of osteogenic cells, the availability of growth factors, an osteoconductive scaffold, a good mechanical environment, and stability [8,146,148] considering the health history of the patient.

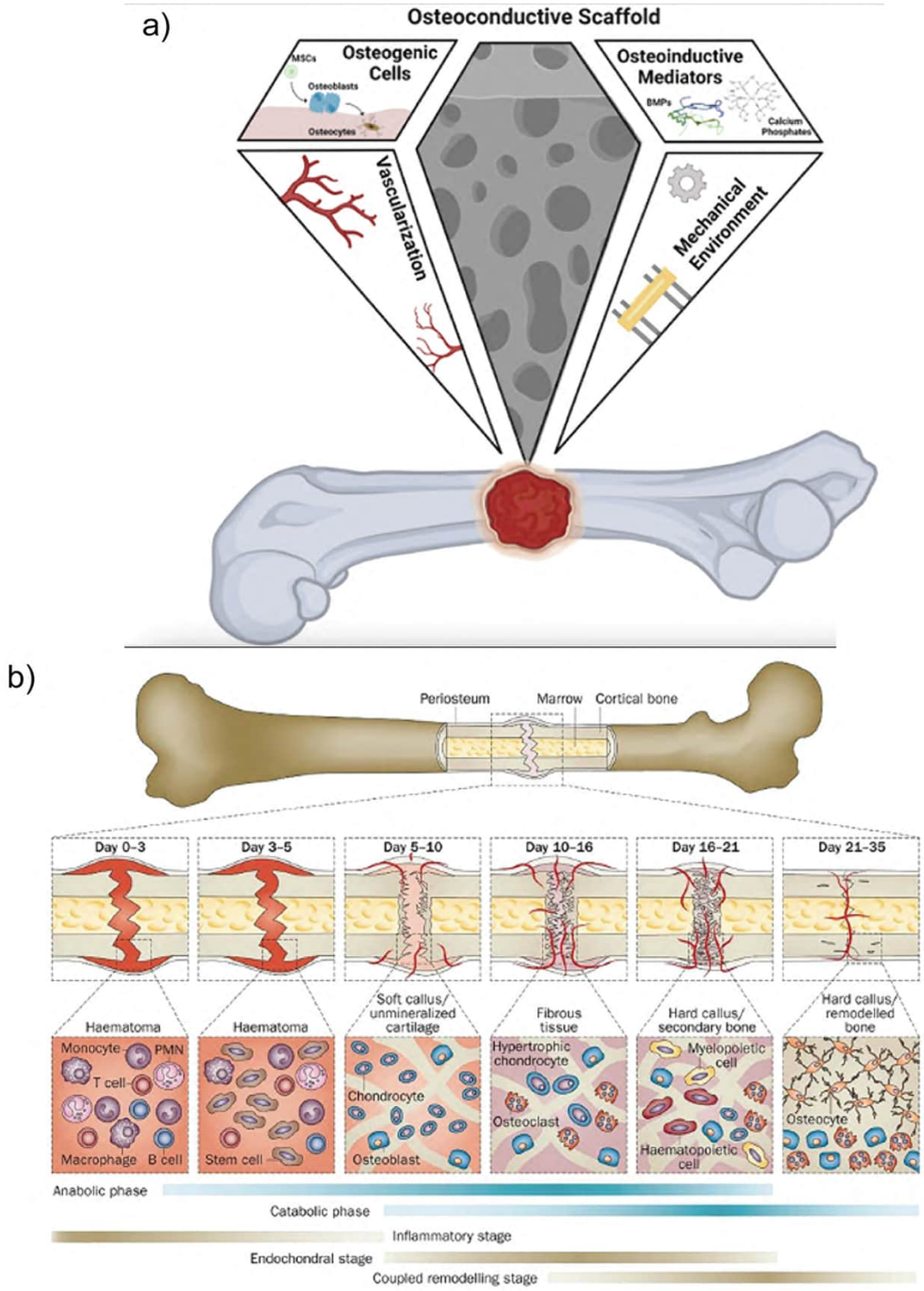

Figure 1.16. a) Diamond concept of bone healing [149]**. b)** Fracture healing process [150].

All these factors are essential during the four phases of the fracture healing process which include (Figure 1.16b): (1) the fracture hematoma formation, inflammation, cell proliferation and differentiation, (2) the reparative phase characterized by callus formation, (3) the hard callus formation, and (4) the remodeling phase [8,102,145–147]. Immediately following a traumatic event, specifically during the first week, various blood cells in the periphery and

within the medullary cavity and bone marrow cells form a hematoma [8,145,146,151]. Subsequently, the reparative phase is initiated by the formation of a fibrocartilaginous callus [145,151], which functions as a stabilizing structure for the fracture area, over a three to four-week period. During this time interval, the process of neovascularization starts, wherein fresh capillaries initiate their growth into the hematoma, thereafter, accompanied by the infiltration and removal of debris by phagocytic cells at the injury site. Fibroblasts and osteoblasts migrate towards the site of damage, while additional cells are recruited to facilitate neovascularization, a process essential for increasing blood flow within the area of tissue repair [147], which is crucial in ensuring the efficacy of bone repair [102]. This reparative phase involves the substitution of the callus with bone formation, which occurs through two distinct mechanisms that resemble embryonic developmental processes [147]. These mechanisms, known as endochondral and intramembranous ossification, occur within a period of three to four weeks after injury [8,102,145]. Throughout this process, there is a proliferation of osteoblasts, resulting in the turning of fibrocartilaginous calluses into bony calluses [145].

The ultimate stage of the process involves bone remodeling when the hard callus undergoes mineralization and is subsequently replaced with mineralized bone [102,145]. This last stage of bone healing starts in the third week after a bone fracture and may continue for several years. This process is subject to various influencing factors, including age, gender, and overall health condition of the patient, as well as the fracture severity and the specific anatomical site of the fracture. The remodeling phase aims to restore the structure and function of the bone to its pre-fracture state, ensuring proper biomechanical integrity [8,102].

The process of bone healing in the presence of an Mg implant closely resembles that observed in cases where no implant is present [8]. Upon placement of an implant within the body, blood encounters it, resulting in the arrival of platelet cells and their subsequent activation. This initiates an inflammatory response, ultimately leading to the hematoma formation. The recruitment of MSCs to the implant surface will subsequently take place. These cells will undergo differentiation into osteoblast cells, initiating the process of bone formation. This bone formation will occur in two directions: toward the edges of the existing bone (contact osteogenesis) and in the opposite direction from the implant (distance osteogenesis) [152]. Consequently, the outcome will be the formation of woven bone. Finally, bone remodeling will occur where peri-implant bone will be replaced with mature bone, therefore enhancing the “bonding” between the implant and the bone [8].

It is necessary for the Mg-based implant to maintain its mechanical integrity until the healing process is complete, after which it will gradually degrade within the human body [84,153]. The interaction between Mg and bone is a complex scenario in which biochemical, biomechanical, and biological processes interact and will impact the biodegradation behavior of Mg devices. As the implant degrades, there is a concomitant decrease in its mechanical strength. Similarly, the bone strength increases in conjunction with the progression of healing stages. It is anticipated that the implant will not undergo complete degradation throughout the four phases of fracture repair [151]. This leads to the importance of the manufacturing process, encompassing the implant design and accuracy throughout its production, to yield an implant with suitable mechanical strength for a degradation rate that does not interfere with bone fracture repair.

1.4. State of the art of Mg research in vitro and in vivo

In the field of Mg research, it is common to conduct *in vitro* and *in vivo* assessments as preliminary steps before initiating clinical trials, with the aim of developing an absorbable implant. Although it is recognized that *in vitro* testing cannot fully replicate the complexity of *in vivo* environments, it continues to play a vital role in the evaluation process required for the clinical application of medical devices [154]. Numerous *in vitro* investigations have provided evidence that Mg and its alloys exhibit a wide range of corrosion rates. These results can be attributed to analyzing various magnesium alloys, immersion solutions with dissimilar compositions, various laboratory methodologies [155], and different experimental time points, all designed to simulate the complex and dynamic electrochemical reactions occurring within a biological environment. Different variables in solutions (Figure 1.17), such as the presence of inorganic ions, organic components (amino acids, proteins, and vitamins), and experimental parameters (pH, buffer system, and flow rate), influence Mg corrosion *in vitro* [107,156–159].

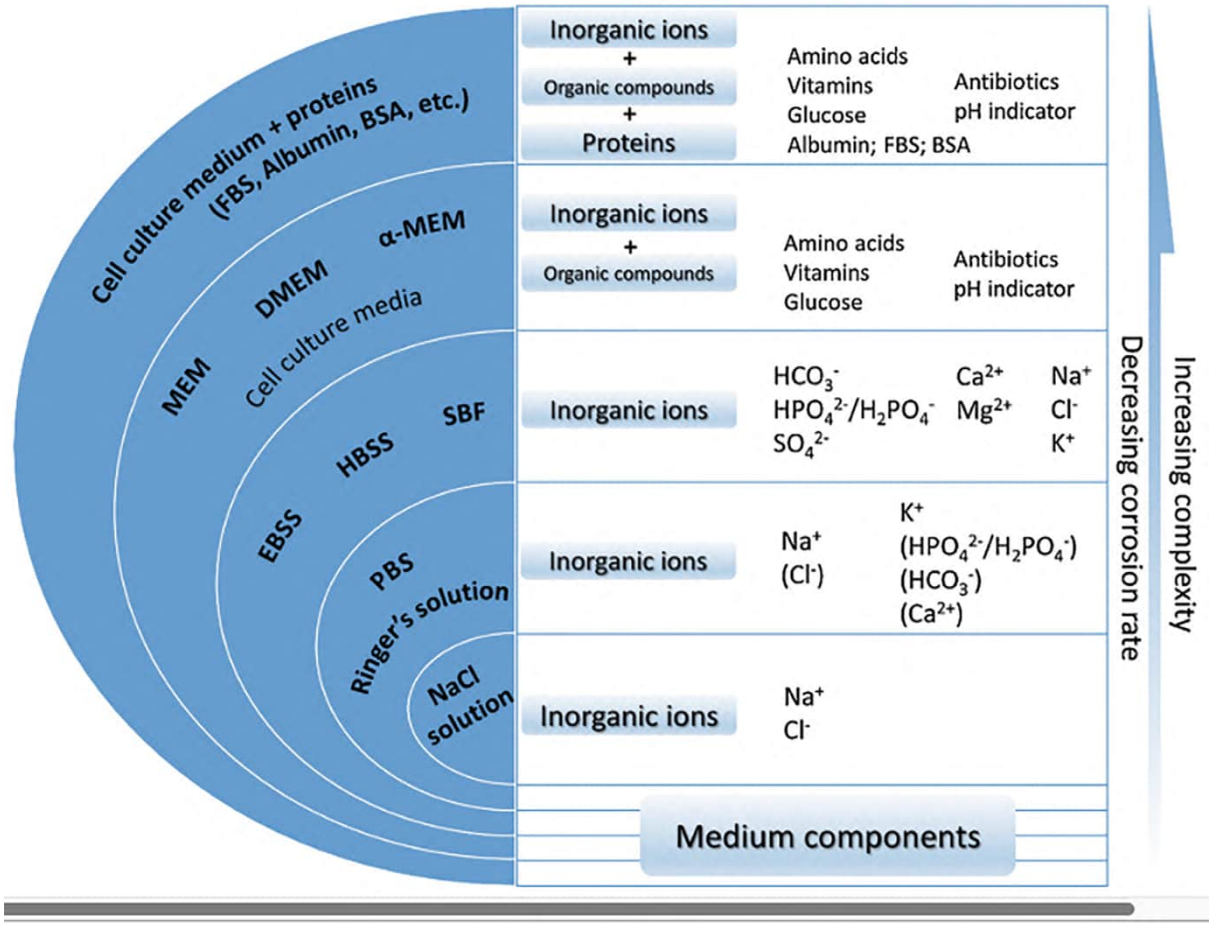

Figure 1.17. Immersion solutions employed for testing Mg-based devices *in vitro* [107].

The absorption of the Mg medical device is accompanied by the formation of corrosion products, which serve as a kinetic barrier. This corrosion product/layer prevents Mg cations from migrating into aqueous environments [25]. The surface morphologies, compositions, and sublayers of the corrosion products display differences that depend on the immersion solution utilized [160] (as summarized in Table S1 and Figure 1.18), which imply distinct degradation mechanisms for Mg and its alloys.

Furthermore, the impact of cells on the corrosion layer's formation and composition has been observed alongside the utilization of immersion media and *in vitro* procedures, which involve using extracts to investigate biocompatibility and cytotoxicity. However, limited research has been conducted to elucidate studies on the role of cells in corrosion products/layer formation (Figure 1.19a-e). Most of the research employed a single-cell type for direct-cell culture, specifically mouse fibroblasts (L929) (Figure 1.19a) [161], human primary osteoblasts (hOBs) (Figure 1.19b) [162], the osteoblastic cell line M3TC3-E1 (Figure 1.19c) [163], or macrophages (RAW264.7) (Figure 1.19d-e) [164]. From these cell lines, the presence of human osteoblasts (hOBs) influenced the thickness and composition of the corrosion layer formed

after 14 days of *in vitro* testing [161,162]. Nevertheless, because osteoblasts and osteoclasts maintain bone tissue homeostasis [144], it is necessary to conduct further *in vitro* cell culture studies with the inclusion of osteoclasts or osteoblast-osteoclast coculture models. This type of *in vitro* research, which attempts to simulate a closer physiological environment, can enhance comprehension of the cell's function in the development and structure of the degradation interface, as well as the degradation patterns exhibited by Mg-based implants.

The research for Mg medical implants through *in vitro* testing is essential to provide baseline knowledge of degradation mechanisms. However, it is worth noting that the corrosion rate of Mg absorbable materials may be significantly high in certain instances. This can result in an increased concentration of corrosion products, which in turn can lead to changes in the pH and osmolality of the *in vitro* biological system. The susceptibility of Mg devices i*n vitro* tests to pH and osmolality variations may not accurately reflect the *in vivo* response, which involves the presence of perfusion and carbonate equilibria. This has resulted in the need for animal research to evaluate the biological response alongside the concurrent degradation of the magnesium medical implants [156] due to the non-uniform degradation performance of Mg implants.

Various animal models and animal bone defects have been employed to investigate bone regeneration in the vicinity of implantable devices. The corrosion behavior of Mg-based devices has predominantly focused on small animal models, with limited attention given to large animal models. Mice, rats, and rabbits are frequently used in orthopedics research to determine bone healing and the safety of Mg-based devices.

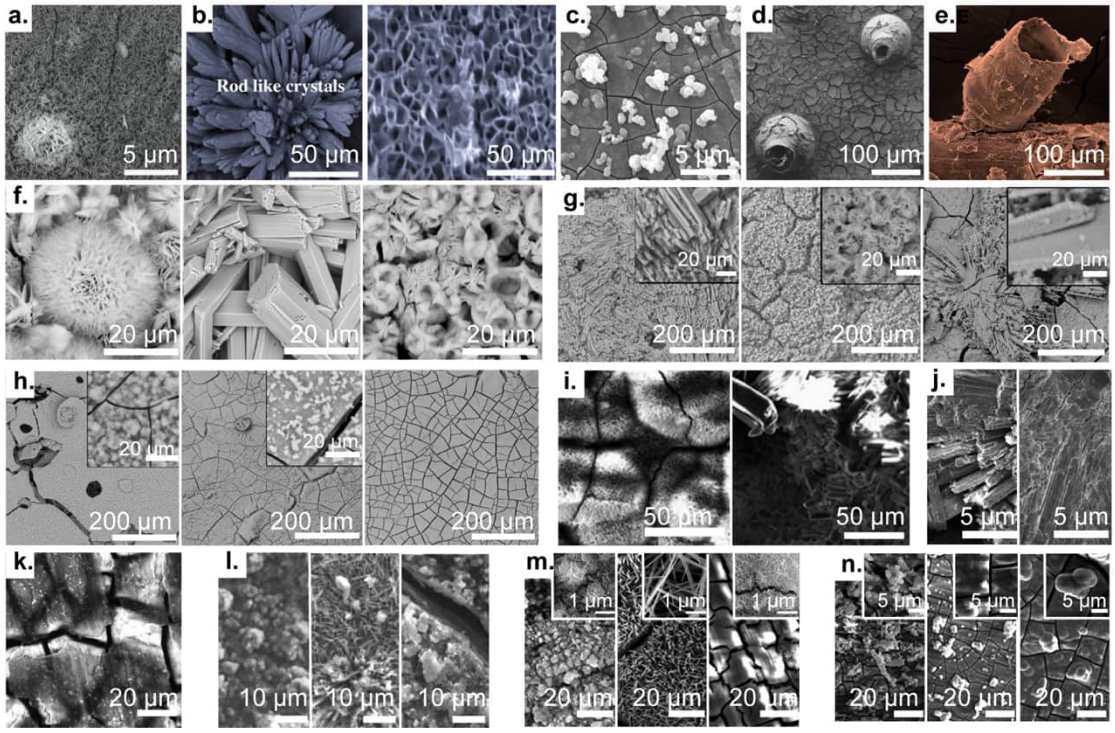

Figure 1.18. Different surface morphologies of corrosion products on Mg and its alloys from *in vitro* studies. **a)** needle-like and mushroom-like appearance on Mg-0.41Dy alloy after 2 h immersion in 3.5% NaCl solution [165]. **b)** rod-like (left) and platelet-like crystals (right) on ZK60 after 36 h immersion in Ringer's solution [166]. **c)** globular and planar apatite deposits formed on pure Mg after 15 days immersion in EBSS [167]. **d)** A volcano-like deposit formed on WE43 after 8 h immersion in m-SBF [95]. **e)** Calcium orthophosphate tube formed on pure Mg wire after 48 h degradation in α-MEM + FBS and antibiotics [168]. **f)** thin platelet conglomerate (left), needle-like (centre), and conglomerates (right) deposits on pure Mg after 14 days of immersion in HBSS with one and two organic components, and in presence of FBS, respectively [104]. **g)** needle-like (left), thin conglomerates (centre) and a mixed of both precipitates formed on pure Mg immersed for 14 in HBSS +BSA, HBSS + BSA +Fibrinogen (Fib), and HBSS + Fib, respectively [169]. **h)** cracked surface and white deposits observed on Pure Mg immersed for 14 days in HBSSCa + BSA (left) and HBSSCa + Fib (centre), respectively. Only crack surface observed when BSA and Fib were added to HBSSCa (right image) [169]. **i)** intergrown needles (left) and flake-like (right) shape crystals formed on pure Mg after 72 h immersion in HBSS and DMEM, respectively [170]. **j)** Porous structure (left) and planar compact (right) structure of corrosion products formed on pure Mg and Mg-Ca alloys after 11 days immersion in DMEM + 10% FCS + L-glutamine + antibiotics [99]. **k)** cracked surface with additional layer formed on ZK21-0.2Sc alloy after 168 h immersion in Hank's solution + BSA [171]. **l)** irregular dense spherical particles (left), acicular clusters (centre), and white precipitates (right) formed on Mg-1.35Ca after 72 h immersion in 0.9 % with 0.0 % 2,5 and 5.0% glucose, respectively [172]. **m)** irregular nanoparticles and flack-like particles (left), cracked surface and nanowires (centre), and honeycomb-like morphology observed on pure Mg immersed for 24 h in 0.9 % NaCl without, 2.5% and 5.0% glucose, respectively [173]**. n)** inhomogeneous deposits (left) and cracked surfaces with spherical particles (centre and right) formed on pure Mg immersed for 72 h in Hank's solution with 0.0%, 2.5%, and 5.0% glucose [173].

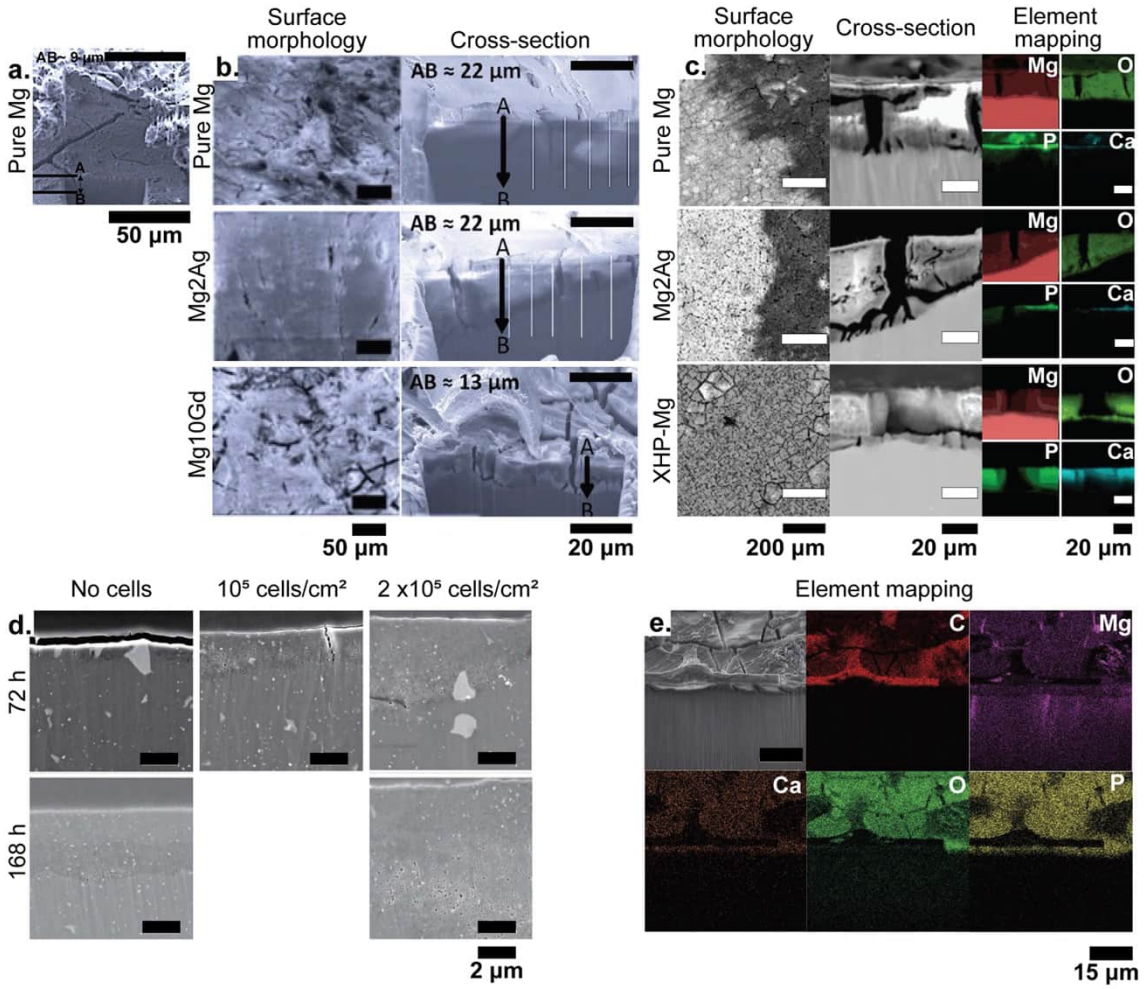

Figure 1.19. Images of cross-sectional morphologies of Mg and its alloys from *in vitro* immersion tests in direct contact with cells. a) SEM images of the cross-section processed by Focus Ion Beam (FIB) showed a ~9 µm corrosion layer thickness when L929 cells were directly seeded for 14 days on pure Mg discs [161]. **b)** SEM images of the surface and processed FIB cross sections when can show the different corrosion layer thicknesses formed in various Mg alloys after 2 weeks of hOBs directly seeded on pure Mg in DMEM + 10% FBS and 1% P/S [162]. **c)** SEM images of the surface morphology, ion-milled cross sections and elemental mappings from corrosion layers formed on different Mg alloys after 2 weeks of direct cell culture of MC3T3-E1 preosteoblasts [163]. **d)** Corrosion layers formed on Mg-Nd-Zn-Zr alloy when no cells or different cell densities of RAW264.7 cells were cultured on the alloy and e) elemental mapping illustrating elements composing the corrosion products formed beneath the cell body after 72 h [164].

Given the variability in animal selection, implant preparation, and evaluation procedures, there is still a notable lack of a universally accepted standardized reference animal model [174]. In previous *in vivo* investigations, it has been observed that a corrosion layer is formed with new bone growth (Figure 1.20). *In vivo* trials on Sprague-Dawley® (SD) rats have analyzed the degradation layer formed on Mg-based implants. Different Mg alloys have been implanted at different time points but at the same implant sites (femoral bone). Marco et al. [115] examined the corrosion layer formed on three Mg-alloys (pure Mg, Mg-10Gd, and Mg-2Ag) 7 days after implantation using SEM/EDX (Figure 1.20a). For pure Mg pins implanted in the femoral bone, the thickest degradation layer (~ 67.5 µm) was observed in the bone marrow cavity, while the

thinnest corrosion layer (~16 µm) was observed on the outer part of the cortical bone with some exceptions. In terms of composition, EDX measurements indicated that the degradation layers were primarily comprised of $Mg(OH)_2$, carbonates (Mg,Ca)-CO_3, and Ca-PO_4 with Ca and P tending to be found in the outer portion of the corrosion layer, which was mainly observed on Mg-10Gd implants.

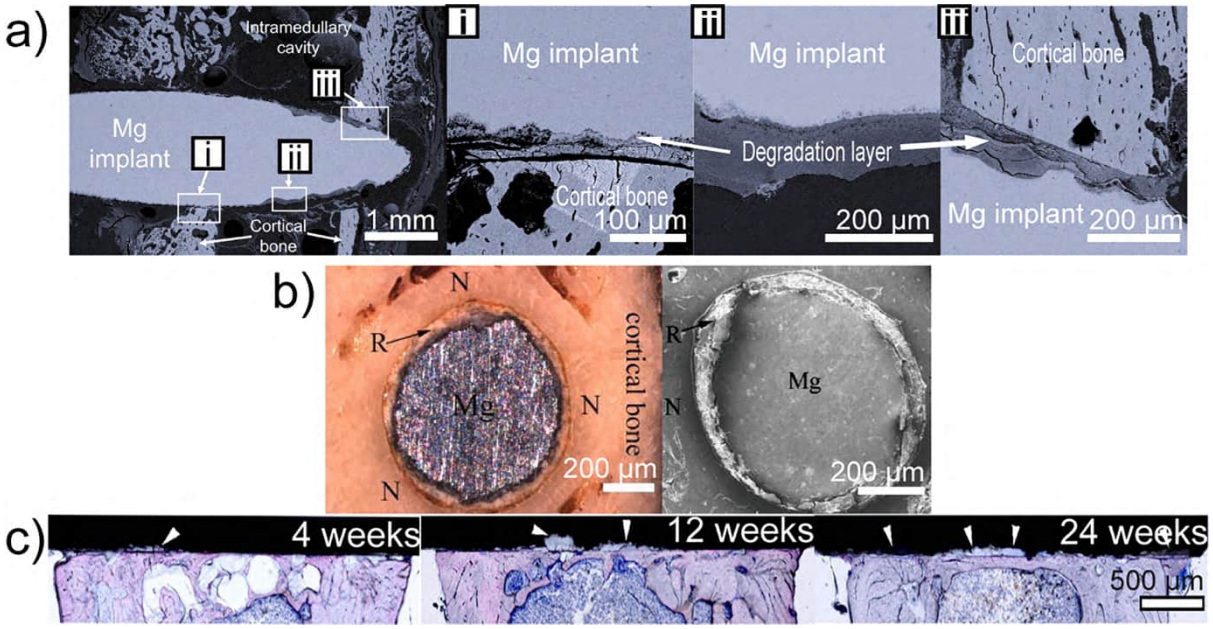

Figure 1.20. Cross-sectional images of the degradation layer from *in vivo* studies in rats: a) BSE images of a pure Mg pin implanted in the femoral bone of rats. (i) and (iii) denoted pin contact with cortical bone, while (iii) depicted degradation of the pin in the intramedullary cavity [175]. **b)** Optical (left) and SEM (right) images of the bone-implant interface of a Mg-Zn-Mg alloy after 10 weeks of implantation in the femora bone of SD rats. The reaction layer (R) is denoted between the remanent Mg implant and the newly formed bone (N) [176]. **c)** Histological sections of WE43 pin after 4, 12, and 24 weeks of implantation in the diaphysis of rats. Newly formed bone covering the surface of the Mg implant with the presence of degradation products is denoted by white arrows at all time points [177].

Zhang et al. [176] showed comparable implant site degradation on an Mg-Zn-Mn alloy after 26 weeks of *in vivo* rod implantation perpendicularly into the SD® rats' femora. When part of the implant was in the bone marrow, the corrosion layer contained more C and O with a small amount of Ca and P, and the implant corroded faster. Identical elemental composition was observed in the corrosion layer in contact with cortical bone, indicating that the corrosion products were a layer of Mg-Ca phosphate. In addition, the corrosion layer was still visible in direct contact with the newly formed bone 26 weeks after implantation (Figure 1.20b), although its thickness did not increase as implantation time increased. In contrast, Lindtner et al. [177] reported that as the implantation time increased, there was a variation in the distribution, extension, and especially in the thickness (50-200 µm) of the corrosion layer formed on WE43 pins (Figure 1.20c) where new bone was formed on the degradation layer after 4 weeks of implantation.

The corrosion layer formation and composition have also been evaluated in New Zealand rabbits (Figure 1.21). Krause et al. [178] implanted cylindrical pins of three Mg alloys (Mg-0.8Ca, LAE442, and WE43) into the medullary cavity of rabbits' tibia and evaluated the degradation behavior 4 and 7 months after implantation. Cross-sectional analysis revealed that as implantation time increased, the corrosion layer increased from 100 to 250μm, varying among the different Mg-alloy implanted and the different implantation periods. Niu et al. [179] described a corrosion layer with a two-layer structure: The inner portion was a C and O rim with a thickness of 150 to 250 μm, while the outer layer was a very dense nanoporous layer containing primarily Ca and P elements with a thickness of 10 to 250 μm (Figure 1.21a). The authors observed the formation of new bone on the corrosion products/layers.

Ma et al. [180] observed dry riverbed-like cracked lumps and needle-like precipitates on the surface of Mg screws implanted in rabbits' femurs 1-, 3-, 5-, and 7-days post-implantation (Figure 1.21b). They detailed how the degradation products formed a three-layer structure, with the inner rim primarily composed of Mg $(OH)_2$, the intermediate region containing dypingite and kovdorskite, and the outer layer consisting of monohydrocalcite with hydroxyapatite. Yang et al. [181] and Tan et al. [182] implanted uncoated and coated AZ31 and AZ31B in rabbit femoral bones for 8 and 21 weeks, respectively. After 8 weeks, the new bone-corrosion layer formed on AZ31 had a thickness of 30 μm [39], whereas, after 21 weeks, the thickness of corrosion products varies between 10-28 μm with local regions having a thickness of ~50μm According to both studies, the corrosion products primarily consisted of O, Mg, Ca, and P. Lastly, Lee et al. [183] described a ~100 μm three-structure layer formed on the surface of Mg-5wt%Ca-1wt%Zn. The inner part was composed primarily of Mg $(OH)_2$, while the middle and outer zones were rich in Ca and P, and the Mg concentration decreased as the distance from the remanent implant increased (Figure 1.21c). Furthermore, gas cavities primarily occur within the intramedullary cavity, and the presence of corrosion products does not interfere with the process of bone formation [184,185].

When evaluating biological performance and developing surgical techniques similar to those used in humans, it is best to select animal models with comparable weight characteristics, such as sheep or minipigs. Imwinkelried et al. [186] observed a ~30 μm corrosion products/layer on uncoated and plasma electrolytic (PEO) coated WE43 plates implanted subcutaneously on the nasal bones of minipigs for 24 weeks. O, Mg, and C mainly composed the corrosion layer of uncoated plates, while increased Ca and P content was detected on PEO-coated plates. Grün et al. [187] (Figure 1.22a) and Holweg et al. [188] (Figure 1.22b) investigated the corrosion

behavior of ZX00 screws implanted in lamb tibia bones. After 12 weeks of implantation, histological analysis revealed new bone ingrowth on the corrosion layer formed on the screw surfaces with a similar thickness (~50 µm and ~43 µm, respectively). However, no information regarding the chemical composition of the degradation products is provided by the lamb studies.

The evidence from *in vivo* research supports the role of Mg-based implants in promoting fracture repair [174] primarily focusing on the degradation pattern and responsiveness of peri-implant bone tissues in animal models [18]. However, when examining the corrosion rates between *in vitro* and *in vivo*, it has been reported in pre-clinical investigations that the corrosion rate *in vivo* was 1 – 4 times lower compared to that *in vitro* [155]. This highlights the necessity to enhance *in vitro* testing to replicate *in vivo* conditions more accurately to minimize the need for *in vivo* trials.

The studies conducted on medical implants made of Mg in the field of orthopedics have undergone significant development, evolving into translational research. The clinical assessment of Mg absorbable implants has been examined in clinical orthopedic trials, encompassing case reports, case series, retrospective observational studies, and prospective controlled clinical trials involving the use of screws for internal fixation to stabilize fractures [189]. Screws mostly composed of pure Mg, Mg-Zn-Ca alloys, and Mg-REEs alloys have been found to be effective in treating hallux valgus and fractures in various parts of the body such as the foot, ankle, mandible, elbow, and wrist [153,189,190]. Xie et al. [191] conducted the first clinical study on the use of Mg-Nd-Zn-Zr alloy calcium phosphate coated (JDBM screws) to treat medial malleolar fractures.

Despite the significant advancements in clinical applications, there are still technical and scientific challenges that need to be addressed to ensure appropriate degradation behavior of Mg-based implants and improve their mechanical properties before conducting large-scale clinical studies [190]. There are surgical areas in humans that have not been thoroughly investigated in preclinical and clinical trials, demanding further research regarding the degradation behavior of Mg absorbable implants [153]. Furthermore, Mg implants have demonstrated potential as absorbable metals in orthopedic applications. However, they are associated with a complication rate of 13.3%. These complications encompass many issues, such as swelling and moderate hyperemia, the collapse of the femoral head, the formation of resorption cysts, postoperative infection, and patient discomfort. Therefore, it is important to

investigate the underlying factors contributing to these clinical issues and develop strategies to enhance the corrosion resistance of Mg-based implants to address these issues [190].

Summary

The number of bone fractures requiring surgical interventions has increased because of sport-related injuries, accidents, diseases, and life expectancy. Most of these fractures are fixed by using permanent metallic implants made of Ti and its alloys, Co-Cr alloys, and SS implants. Then, when the bone fracture healed, a second surgery is usually required to remove these implants, increasing the patient's discomfort and healthcare costs. As a result, Mg-based materials have emerged as an alternative for temporary medical implants due to their close mechanical properties to human cortical bone, as well as its biocompatibility.

As soon a Mg implant is exposed to aqueous and physiological environments, an oxide layer is formed. This corrosion product/layer is a dynamic interface, serving as a bridge between the Mg implants and the near tissues. Extensive *in vitro* research has been conducted to determine the changes at this interface as the Mg materials degrade. However, the multiple experimental setups and variety of Mg alloys investigated have resulted in a wide range of corrosion rates and corrosion product compositions. Additionally, when investigating the material-cell interaction, most of the i*n vitro* findings have focused primarily on the influence of the degradation products on cell viability through monoculture studies. This highlights the limited research addressing how the presence of cells influences the composition of the corrosion products and the degradation of Mg implants, particularly using coculture models with bone cells. Furthermore, the difficulty of mimicking the complex biological environments *in vitro*, such as the complex nature of human bone, leads to the necessity of assessing the corrosion behavior of Mg-based devices employing small and, to a lesser extent, large animal models. However, the variety of animal models, implant geometries, and implant resulted in unpredictable corrosion rates of Mg implants *in vivo*. Therefore, further *in vitro* and *in vivo studies* are required to address strategies for enhancing the corrosion resistance of Mg-based implants for their safety use in clinics.

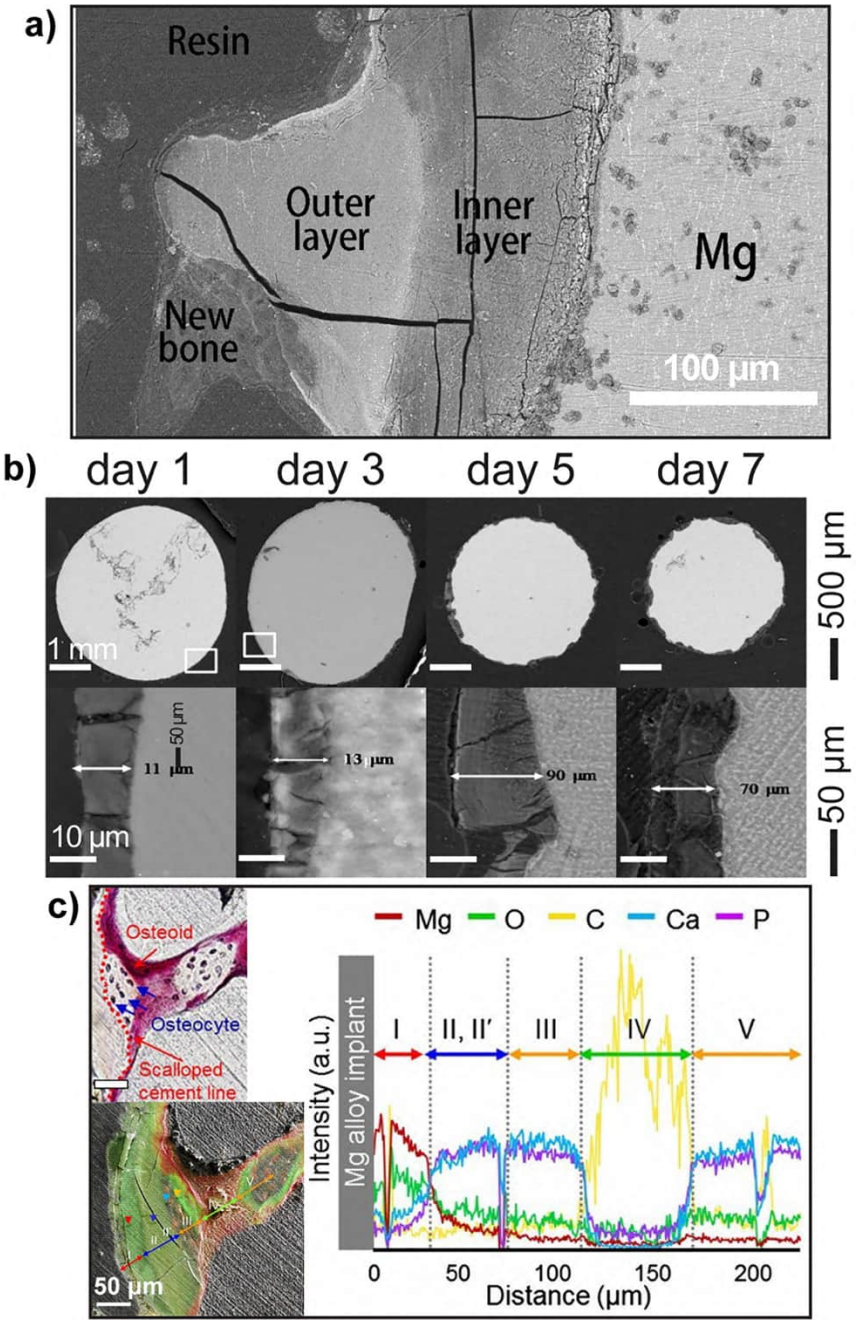

Figure 1.21. a) SEM image of the bone-implant interface of Mg-Nd-Zn-Zr screw implanted in rabbit mandible after 18 months of implantation. It can be seen two-layer structure degradation products denoted as an outer and inner layer with new bone tissue connected with the outer part of the degradation products [179]. **b)** SEM images where changes in the corrosion layer thickness of pure Mg screw implanted for 1, 3, 5, and 7 days can be observed [180]. **c)** Histological section (above) and merged SEM fluorescence microscopy (below) images of a Mg-Ca-Zn implant-bone interface after 8 weeks of implantation in the femoral condyle of New Zealand Rabbits. The histological image showed a scalloped cement line in the calcified matrix, indicating bone formation and resorption activities by osteoblasts and osteoclasts, respectively. The fluorescence/SEM merged image and line scan graph showed the different chemical compositions within the degradation layer [183].

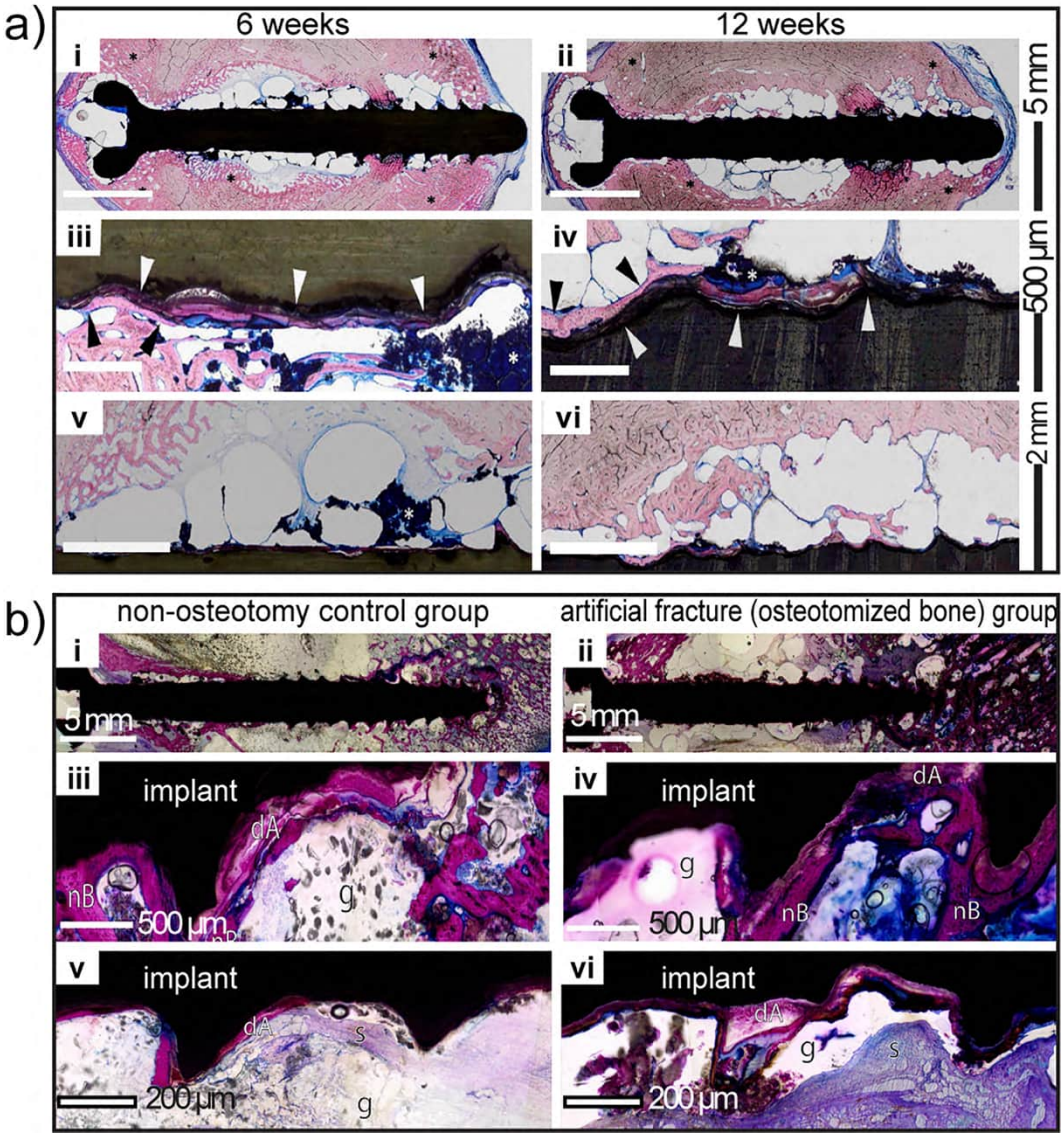

Figure 1.22. Histological evaluation at the Mg implant -bone interface from large animal models. a) Modified Giemsa staining on histological sections of ZX00 screws after 6 (i) and 12 (ii) weeks of implantation in the diaphysis of sheep's tibiae. White arrows denote corrosion products in (iii) and (iv) while black arrows indicate thin layers of bone. Accumulation of gas bubbles is observed after 6 (v) and 12 (vi) weeks of implantation [187]. **b)** Methylene Blue and Basic Fuchsine staining on histological slides of control (i) and artificial (ii) groups after 12 weeks of implantation of ZX00 screws in the tibia of sheep. New bone formed (nB) on corrosion products (dA), and gas pockets (g) surrounded by soft tissue (s) can be seen in (iii), (iv), (v), and (iv) [188].

Table S1.1. Summary of *in vitro* corrosion layer's surface morphology and composition.

Surface morphology	Material composition	Immersion solution	Immersion time	Composition	Ref.
Cracked surface	Pure Mg	HBSSCa + BSA + Fib	14 days	Mg/Ca-PO_4 Ca/Mg-CO_3	[169]
	Pure Mg	HBSSCa + FBS			
	AZ80E	PBS	24 h	Mg, O, Al, traces of Zn	[17]
	AZ31	$NaHCO_3$ (1,3,5,7,9 wt%)	6 h	$MgCO_3$	[192]
Needle-like precipitates Or flake-like particles	Pure Mg	HBSS with two organic compounds	14 days	Nesqueonite	[104]
	Pure Mg	HBSS +BSA	14 days	Nesqueonite	[169]
	Pure Mg	HBSS	7 days	$Mg(OH)_2$ Nesqueonite	[170]
	Pure Mg	0.9 % NaCl	24 h	Mg, O, C	[173]
	Mg-1.35Ca	0.9 % NaCl + 2.5 % glucose	72 h	Mg, O and trace amounts of Cl	[172]
	Mg-0.41Dy Mg-1.3La	3.5% NaCl	24 h	Mg, O, Cl	[165]
Mushroom-like deposits	Mg-0.41Dy Mg-1.3La	3.5% NaCl	24 h	Mg, O, Cl	[165]
Rod-like crystals	ZK 60 WE 43	Ringer's solution at 37 ºC	Up to 96 h	Mg, O, Ca	[166]
Platelet-like crystals	ZK 60 WE 43	Ringer's solution at 37 ºC	Up to 96 h	Mg, O, Ca	[166]
Globular and planar apatite precipitates	Pure Mg	EBSS	30 days	Mg, O, Ca, P	[167]
White rounded volcano-like deposits	WE43	m-SBF	1h	C, O, Mg, high Ca-P ratio content	[95]
Thin platelet conglomerate	Pure Mg	HBSS + one organic compound	14 days	dypingite hydromagnesite	[104]
		HBSS	14 days	dypingite hydromagnesite	[169]
		HBSS + BSA + Fib	14 days	nesqueonite dypingite hydromagnesite	[169]
Needle-like and thin-platelet	Pure Mg	HBSS + Fib	14 days	dypingite hydromagnesite	[169]
Flocculent precipitates	Pure Mg	HBSSCa	14 days	dypingite hydromagnesite	[169]
Tube-like	Pure Mg wire	α-MEM + FBS + antibiotics	48 h	calcium orthophosphate	[168]
Interconnected needles	Pure Mg	DMEM	7 days	$Mg(OH)_2$ nesqueonite	[170]
Planar compact crystals	Mg-Ca	DMEM +10% FBS + 1% P/S	11 days	$MgCO_3$ and traces of Na, K	[99]
Porous deposits	Pure Mg	DMEM +10% FBS + 1% P/S	11 days	$MgCO_3$	[99]
Nano wire deposits	Pure Mg	0.9 % NaCl + 2.5% glucose	24 h	$Mg(OH)_2$ and traces of Cl	[173]
Honeycomb like	Pure Mg	0.9% NaCl + 5% glucose content	72 h	$Mg(OH)_2$ and traces of Cl	[173]
White spherical particles	Pure Mg	0.9% NaCl + 2g/L or 3g/L glucose	72 h	$Mg(OH)_2$ and Ca-P deposits	[173]
	Mg-1.35Ca	0.9 % NaCl	72 h	Mg, O, traces of Cl	[172]
White deposits	Mg-1.35Ca	0.9% NaCl + 5% glucose	72 h	Mg, O, low content Ca and Cl	[172]

Chapter 2

Context, objective, hypothesis, and scope of the thesis

2. Context, objective, hypothesis, and scope of the thesis

2.1. Context

This thesis was conducted as part of the MgSafe project, which is supported by the Marie Sklodowska-Curie Actions of the European Union´s Horizon 2020 program, under REA grant agreement nº 811226. The MgSafe project aims to investigate a novel combination of imaging technologies for biodegradable magnesium implants to promote patient safety. This project is an interdisciplinary collaboration involving 15 doctoral candidates located in 8 European countries, affiliated with 12 different organizations. This project entailed the investigation of four different Mg materials (pure Mg, XHP-Mg, MgZnCa, and the MgYREZr (WE43) magnesium medical alloy). The investigations were conducted through four research work packages (WP), three training WPs, and one management WP. The research work packages are structured to focus on imaging hard tissue remodeling (WP1), soft tissue remodeling and inflammation (WP2), bone-implant interface (WP3), and guaranteeing the inclusion of translational and patient safety considerations (WP4). The WUT team study objective in the MgSafe project was to characterize the structure and composition of the corrosion layers in explants.

2.2. Objective, hypothesis, and scope of the thesis

The overall objectives of this thesis are:

1. To provide a baseline information of the as received Mg based implants.
2. Determine the corrosion rate of Mg-based devices *in vitro* without and with the presence of osteoblast (OB) and osteoclast (OC) cells. Additionally, analyze the kinetic changes in the composition of the degradation products as the corrosion of the Mg material proceeds.
3. Characterize the corrosion layers formed at the implant-tissue interfaces when using Mg-based devices from *in vivo* research to assess the corrosion performance in various tissue compartments.

The following hypotheses have been derived:

1. The composition of the corrosion layer on Mg-based materials is significantly affected by cell viability, proliferation, and cell adhesion under *in vitro* conditions, suggesting

that the biological interaction between cells and Mg implants plays a crucial role in the corrosion behavior of these materials.

2. The composition of corrosion layers on implants varies according to their *in vivo* location, indicating that the local biological environment is a key determinant in the degradation process of the material.

To achieve the objective and validate the hypotheses, the following research scopes were conducted:

- **Stage 1: Material characterization**

- To analyze the as-received surface of four Mg-based devices (pure Mg, ultra-high purity Mg (XHP-Mg), Mg-Y-RE-Zr (WE43), Mg-Zn-Ca (ZX00), providing baseline information regarding the surface morphology, roughness, and chemical composition.

- **Stage 2**: **Degradation**
  - To determine the most probable initial degradation of the Mg-based devices by *in vitro* immersion tests under physiological conditions.
  - To assess the corrosion rates of pure Mg, Mg-Zn-Ca, and WE43 *in vitro*
  - To analyze the effects of Mg degradation on pH, osmolality, and implant-surface changes.

- **Stage 3: Cellular response**
  - To investigate whether bone cells have an influence on the corrosion layers composition and degradation of Mg-based devices when exposed to monoculture and coculture of osteoblasts (OB) and osteoclasts (OC) cells.

- **Stage 4**: ***In vivo*** **examination**
  - To characterize the *in vivo* degradation behavior of the Mg-based materials designed for temporary biodegradable implants in terms of corrosion layers chemical composition, implant-tissue interface, and associated tissue response after *in vivo* implantation in the soft and bone tissues in small and large animal models.

2.3. Description of the chapters

Chapter 1 includes an introduction section regarding bone fractures and highlights the necessity for orthopedic implants in their treatment. Subsequently, a comprehensive literature

review of Mg as a biomaterial is provided, covering alloying elements and various corrosion types that Mg undergoes when exposed to aqueous environments. Additionally, this chapter includes a concise overview of bone as an implantation site and the process of bone fracture repair. Finally, the current start-of-the-art of Mg from *in vitro* and *in vivo* research is reviewed.

Chapter 2 overviews this thesis's context, objective, hypotheses, and scopes. The MgSafe project´s context is explained to provide the reader with a comprehensive understanding of the rationale behind the decisions made using the Mg materials investigated. In addition, a detailed summary of the methods used in both *in vitro* and *in vivo* experiments discussed in the subsequent chapters, will be provided. This will offer insight into the methodologies employed to validate the thesis´s aim and hypothesis. Finally, the key findings from the investigations conducted are presented.

Chapter 3 explores the interaction between pure Mg and the MgYREZr (WE43) alloy with osteoblasts (OB) and osteoclasts (OC) cells. This *in vitro* study examined how the cells influence the composition of the corrosion layer that forms as both Mg materials degraded. This is accomplished by conducting surface characterization, alongside electrochemical techniques and characterization methods (FIB/SEM/EDX).

Chapter 4 elucidates the degradation process of MgYREZr (WE43) pins following *in vivo* implantation in Wistar rats. The main focus of this research work was on the dynamic changes observed in the corrosion layers formed at different tissue compartments as the implantation time progresses. These findings were correlated with the monitoring of systemic biomarkers of inflammation and bone regeneration, alongside the detection of rare earth elements in distant organs.

Chapter 5 describes the findings of the degradation of human-sized screws composed of a rare-earth element-free Mg-based alloy (ZX00 alloy) through both *in vitro* and *in vivo* investigations. Initially, the microstructure at various screw regions was analyzed *in vitro*, followed by a detailed analysis of the surface and cross-sectional morphologies of the corrosion layers formed, along with the examination of the bone-corrosion-layer-implant interfaces.

Chapter 6 presents the findings regarding the kinetic changes in the corrosion of pure Mg disc-shaped implants, as observed through *in vitro* and *in vivo* investigations. The chapter discusses the corrosion behavior of the Mg discs and the associated transient inflammatory response.

Chapter 7 explores an alternative method for Mg medical implants, employing a high purity Mg to minimize impurities that might potentially cause adverse reactions when implanted into the human body. Therefore, the corrosion performance of ultrahigh-purity Mg and ZX00 pins was assessed when implanted for 6 and 24 weeks in male Sprague–Dawley® rats.

Chapter 8 presents a concise overview and conclusions of the research conducted, as well as outline future areas of investigations regarding the use of Mg implants for orthopedic applications.

2.4.Overview of the material and methods employed for the in vitro and in vivo research

2.4.1. Materials

The Mg materials examined in this thesis are presented in Table 2.1 and Figure 2.1. The Institute of Metallic Biomaterials, Helmholtz – Zentrum Hereon GmbH provided the pure Mg specimens, while the XHP-Mg and ZX00 alloy were supplied through a collaboration of the ETH Zürich with Cavis AG. Syntellix AG supplied the MgYREZr (WE43) alloy.

Table 2.1. Chemical composition of Mg materials assessed in this thesis.

Material / Element	Mg	Fe	Cu	Ni	Zn	Ca	RE	Y	Zr	Mn
Pure Mg (wt.%)	99.998	0.0021	0.0013	<0.0002	-	-	-	-	-	-
XHP-Mg (ppm wt.)	Bal.	0.36	0.08	-	-	-	-	-	-	-
Mg-Zn-Ca (at.%)	Bal.	-	-	-	0.45	0.45	-	-	-	-
WE43 (wt.%)	85.2 – 95.9	-	-	-	0.01- 0.8	-	2.5 – 5	1.5 -5	0.1 – 2.5	-

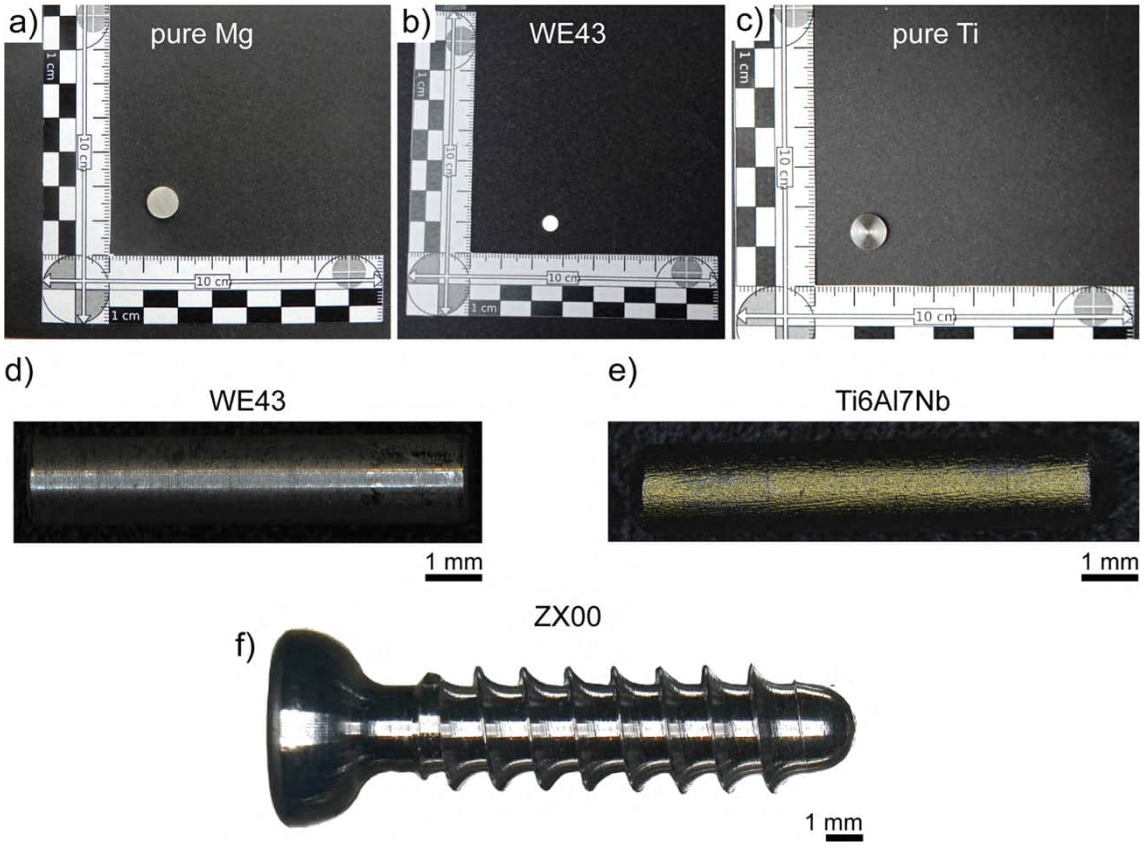

Figure 2.1. Stereomicrographs of the Mg-based devices investigated in this work. Disc-shaped: a) pure Mg, b) WE43, and c) pure Ti; pin-shaped: d) WE43. e) Ti6Al7Nb; screw-shaped: f) ZX00.

2.4.2. Methods

2.4.2.1.Surface characterization

To characterize the surface topography and the physical properties of the sterilized Mg discs, pins, and screws (n = 3/per shaped material), the above-mentioned Mg-based devices were analyzed using a stereomicroscope (Olympus SZ61, Japan, coupled with an OPTA-Tech HDMI camera), as well as scanning electron microscopy (SEM, Hitachi, SU-8000, Japan) equipped with an energy dispersive X-ray detector (EDX, UltraDry EDS Detector, Thermo Scientific™) (Figure 2.2). SEM images were acquired at 5kV using secondary and backscattered electron detectors. The chemical composition of the Mg-based devices was assessed using EDX point, line scans, or maps at various accelerating voltages (15kV – 30kV), at a working distance of 15 mm. The surface roughness was determined following the standard EN ISO 25178-2 [193]. Three random areas of 100 µm × 100 µm were examined for each Mg-based implant (n = 3/per shaped material) using either a confocal laser scanning microscope (CLSM, Keyence, VK-1000 or VHX-7100, Japan) or a Sensofar metrology S optical profilometer (Lynx®, Sensofar Metrology, Spain).

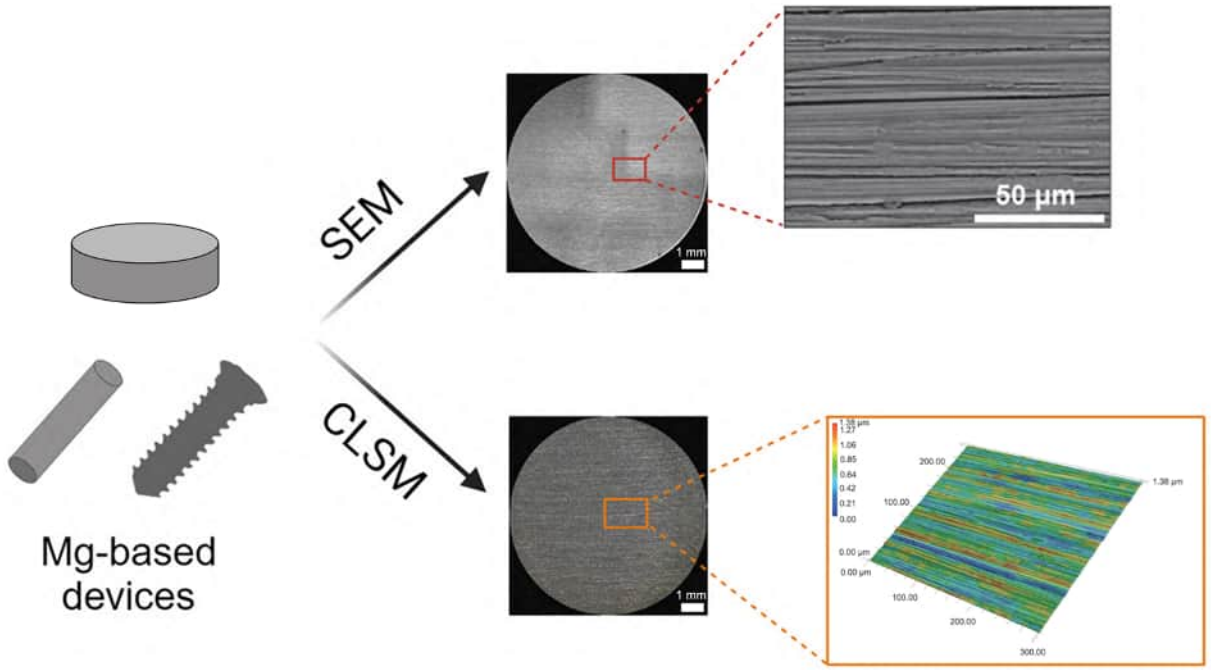

Figure 2.2. Representative scheme of surface characterization techniques employed to analyze the as received Mg-based devices.

The wetting behavior of pure Mg and the MgYREZr (WE43) alloy was investigated to determine the influence of wettability and surface energy, in addition to surface topography and surface chemistry, on the cellular response [194]. Using the OCA 20 optical goniometer (Dataphysics, Filderstadt, Germany), the surface wettability was evaluated employing the static sessile drop method (n = 3/material, 4 zones/sample). This was accomplished by dispensing 1 µL water drop onto Mg samples at room temperature and determining the average contact angles using the SCA20.2.0 software (firmware version 2.05). The surface energy of the Mg materials was determined by applying the Fowkes equation [195], based on the contact angles measured with polar (deionized water) and non-polar (diiodomethane) liquids.

2.4.2.2.Microstructure characterization

To examine the microstructure, a metallographic cutting device (MICRACUT 151, Metkon), was employed to cut pure Mg discs, XHP-Mg pins, and MgZnCa screws. A 1:3 (v/v) solution of glycerol and ethanol was used as a coolant solution for all Mg materials. The cross sections were then mechanically ground and ultimately polished using an Ar^+ low-energy broad ion beam (BIB, IM 4000, Hitachi, Japan) (Figure 2.3). An ion milling system was employed to mitigate artifacts and deformation resulting from mechanically grinding and polishing of the samples, and to prepare a flawless and smooth surface suitable for high-resolution imaging under SEM. Table 2.2. provides a summary of the cross-section milling parameters.

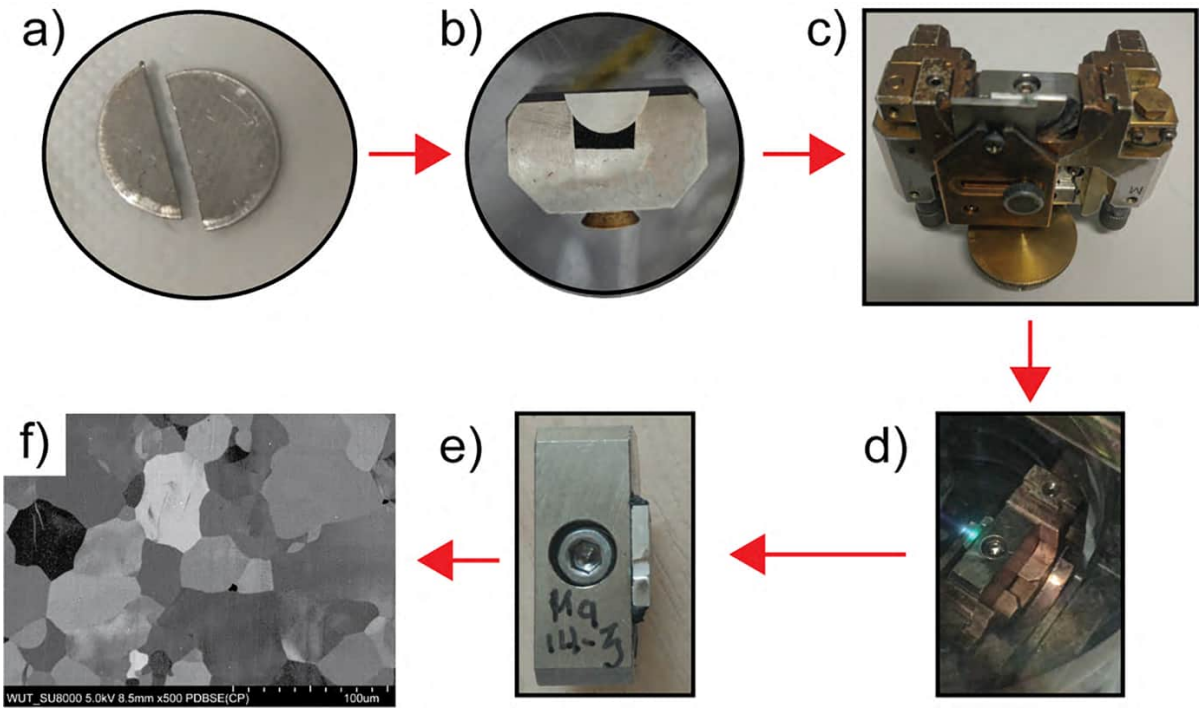

Figure 2.3. Procedure of sample preparation for microstructure analysis. a) Mg sample sectioning, b) specimen mounted in the sample stub, c) sample stub positioned in the cross-section stage, d) broad ion beam milling (BIB) of the sample, e) sample after BIB, f) overview of the BIB-SEM image of a Mg sample.

Table 2.2. Ion milling parameters for cross-section preparation

Cross-section milling	
Speed	3.0 reciprocation/min
Discharge voltage	1.5 kV
Acceleration voltage	6.0 kV
Swing angle	± 30°
Gas flow	0.09 ~ 0.01 cm^3/min
Milling time	4 hrs

Using a backscattered detector (BSE, SU-8000, Hitachi, Japan), the cross-sections perpendicular to the extrusion direction of pure Mg discs, XHP-Mg pins, as well as various regions of the MgZnCa screw (head, valley, and tip) were imaged. In addition, the cross sections of pure Mg, and MgZnCa devices were also analyzed using electron backscattered diffraction (EBSD), which was performed using SEM (SU-70, Hitachi, Japan) equipped with an e−FlashHD detector (Bruker Microanalysis System) at 20 kV and 0.2 μm step size. Subsequently, the collected data was processed using the HKL Channel 5 software.

It is important to highlight that the microstructure of the WE43 alloy (MgYREZr) was not characterized due to its status as a commercially patented alloy [196,197].

2.4.2.3.Electrochemical measurements

To determine the corrosion performance and corrosion resistance of the investigated Mg materials, measurements were conducted using an electrochemical setup. This setup consisted of a 3-electrode configuration consisting of a silver chloride (Ag/AgCl) reference electrode (RE), a counter electrode (CE, platinum electrode), and a working electrode (WE, which consisted of the investigated Mg samples), in connection with a potentiostat (Gamry`s 600+, Gamry Instruments, USA). Each of these electrodes relates to the potentiostat using the corresponding current carrying (WE, CE) or voltage measuring (RE) leads (terminals) [198] (Figure 2.4).

The Mg samples used for electrochemical tests were embedded in metallurgical resin (Cold Mounting Material KEM 35, ATM Qness GmbH, Mammelzen, Germany). The electrical contact was made to the back of the Mg specimen (Cu wire), typically enclosed within the metallurgical resin. The one-well-defined Mg surface exposed was ground and polished. The electrolytes used for the tests include phosphate-buffered saline solution (PBS, tablets purchased from Sigma Aldrich), alpha-minimum essential medium (α-MEM; Life Technologies) supplemented with 10% fetal bovine serum (Gibco, Life Technologies) and 1% penicillin/streptomycin (P/S; Invitrogen). All solutions possess a pH within the physiological range (7.4-7.6). Different regions of a MgZnCa screw were subjected to an electrochemical test in PBS at 37^{o}C, while pure Mg and WE43 specimens underwent electrochemical in supplemented α-MEM under sterile cell culture conditions (37^{o}C, 5%CO_2, and 95% controlled humidity). The conducted electrochemical tests included open circuit potential (OCP), electrochemical impedance spectroscopy (EIS), and potentiodynamic polarization (PDP) measurements (the detailed methodology is described in chapter 3 and 5).

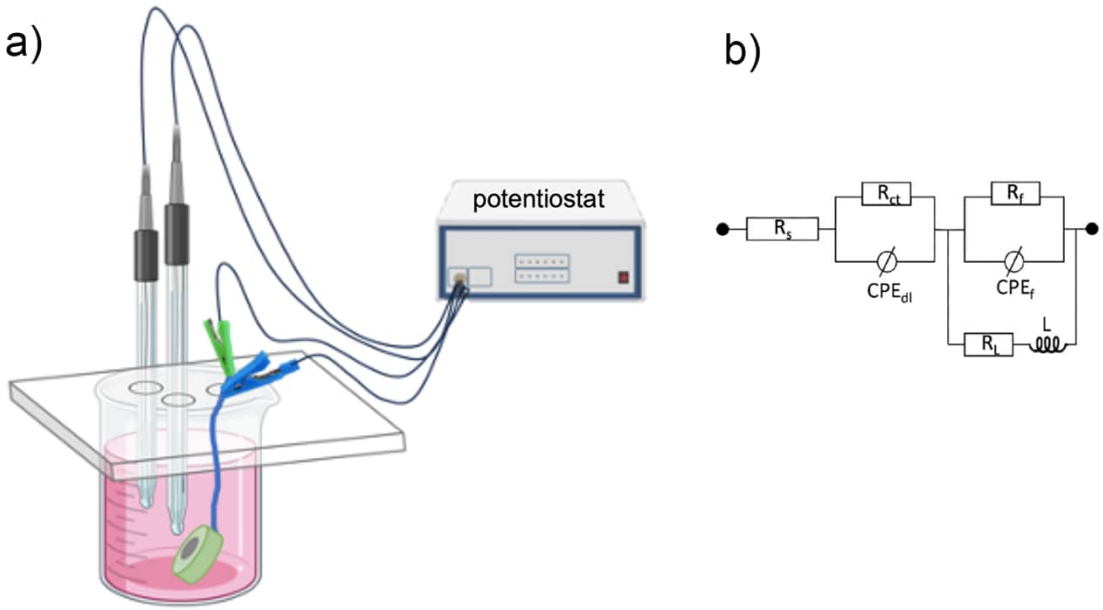

Figure 2.4. a) Schematic diagram of the three-electrode setup. b) Example of an electrical equivalent circuit (EEC) used to fit electrochemical impedance spectroscopy (EIS). Image in a) partially created with Biorender.com.

2.4.2.4.In vitro corrosion test

The Mg-based materials underwent *in vitro* testing in α-MEM supplemented with 10% fetal bovine serum (FBS, Gibco, Life Technologies, Germany) and 1 % penicillin/streptomycin (P/S, Invitrogen, Germany). The exact composition of the α-MEM is compared with the blood fluid plasma in Table 2.3. The selected solution for the immersion test were chosen to provide baseline information on the degradation behavior of the Mg materials. These solutions aim to simulate physiological conditions that closely resemble the clinical scenarios in which Mg materials are intended to be used.

Pure Mg (n =54), WE43 (n =54), and MgZnCa (ZX00, n=30) screws were immersed in α-MEM solution at an Mg sample weight to medium volume ratio of 0.2 g/mL for 1, 3, 6, 14, 21, and 28 days (n = 6 – 9 samples/time point). All experiments were performed under cell culture conditions (37°C, 5%CO_2, 95% relative humidity). One sample was placed in each well of sterilized 12- or 24-well culture plates (Greiner Bio-One, Germany). Three empty wells filled with immersion solution were used as controls. The immersion medium was replaced every 2 – 3 days. The pH and osmolality of the initial culture medium and the supernatants were measured after each cell culture medium change, both with and without samples. At the determined time of immersion (1, 3, 6, 14, 21, and 28 days), samples were rinsed with deionized water and ethanol and then air-dried for further surface and cross-sectional analysis. Figure 2.5

provides an overview of the *in vitro* immersion test workflow and analytical methods employed to characterize the corroded surfaces (the detailed methodology is described in chapters 5 and 6).

Table 2.3. Comparative table of main components of body plasma and electrolyte solutions employed for *in vitro* immersion tests.

Ingredient	**Blood Plasma** [98,107]	**α-MEM (mM)** [199]
Na+	142	144.4
K+	5.0	5.3
Ca^{2+}	2.5	1.8
Mg^{2+}	1.5	0.8
Cl^-	103	124.3
HCO_3-	22-30	26.2
HPO_4^{2-}/ H_2PO_4-	1.0	1.0
SO_4^{2-}	0.5	0.8
Aminoacids	Unknown	8.42
Vitamins	Unknowm	0.32
Proteins (g/L)	63-80	-
Dex/glucose(g/L)	3-6-5.2	5.5
Phenol Red (g/L)	-	0.02

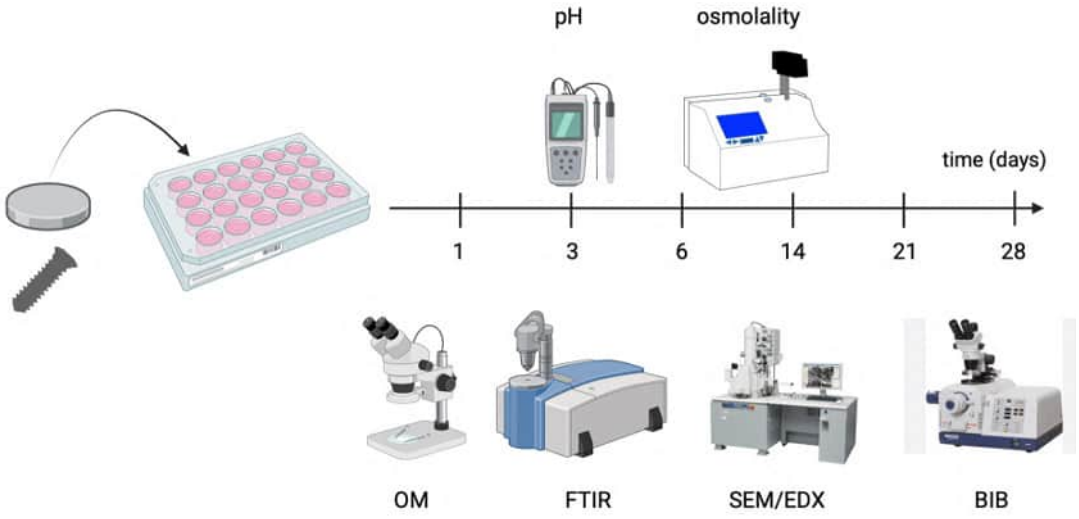

Figure 2.5. Immersion test workflow and analytical techniques employed to characterize the corroded Mg surfaces. *Image created with Biorender.com.*

2.4.2.5.Characterization of the Mg-cell interface using FIB-SEM

The Institute of Metallic Biomaterials characterization laboratory (Helmholtz-Zentrum Hereon GmbH, 21502, Geesthacht, Germany) conducted direct cell culture testing using pure Mg and WE43 materials. The detailed methodology is described in chapter 3. From specimens prepared for electron microscopy analysis, the morphology of OB and OC in direct contact with Mg substrates were analyzed using SEM (Hitachi, SU-8000, Japan). After surface observations,

cross-sections were prepared by focus ion beam (FIB) (Figure 2.6). Firstly, a protective tungsten (W) layer was deposited on the region of interest (ROI). Subsequently a sequence of FIB milling was performed to selectively remove Mg material from the surface to characterize the corrosion formed beneath the cells. After the final FIB polishing step, the cross-section was SEM imaging, and EDX analysis was performed.

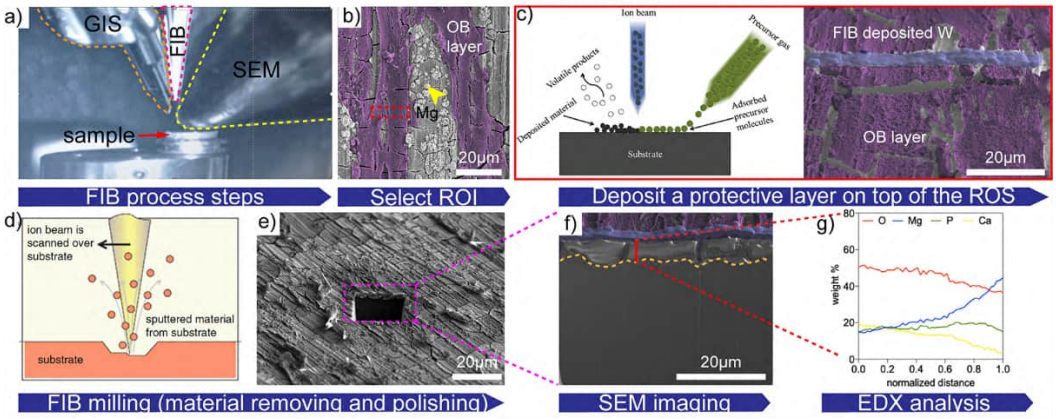

Figure 2.6. FIB/SEM/EDX preparation of cross-sections from Mg specimens after *in vitro* direct cell culture. a) Interior of a FIB/SEM chamber. b) Sample top view of OB layer on Mg substrate with some osmium tetroxide particles (yellow arrow) and the selected region of interest (ROI, red dotted rectangle). c) The gas injection system deposited a tungsten (W) protective layer on ROI. d) FIB milling process. e) FIB milled cross section overview. f) SEM image denoted the corrosion layer (limited by orange dotted line). g) EDX lines scan performed on the corrosion layer. Image in c) and d) adapted from [200,201], respectively.

2.4.2.6. In vivo studies

Common approaches for assessing the tissue response to biomaterials include performing *in vitro* cell culture experiments, animal investigations and analyzing explants [202]. *In vitro* studies offer advantages such as cost-effectiveness, relatively easy methodology, and reduced reliance on *in vivo* animal testing for assessing biocompatibility. Furthermore, *in vitro* studies in the field of Mg and its alloys yield insights into cytotoxicity and cytocompatibility, as well as the degradation behavior of Mg-based devices. However, the primary drawback of *in vitro* research is the challenge of replicating the complex biomaterial-cell-tissue interactions of *in vivo* organisms [203]. It is imperative to conduct *in vivo* investigations on Mg-based devices to acquire a more comprehensive understanding of the degradation interface, the gas void formation, the local and systemic responses resulting from the presence of corrosion products, and their impact on the inflammatory response [174] in the presence of Mg absorbable metals. Consequently, the corrosion behavior of Mg-based devices has been predominantly investigated in small animal models and, to a lesser extent, in large animal models. Mice, rats, and rabbits are commonly employed in orthopedics research to examine bone healing and evaluate the safety of Mg-based devices. Animals with human-like weights, such as sheep or

minipigs, are preferred to determine human-like surgical techniques. This enables a more realistic extrapolation of the findings from animal studies to the human translation [186]. In addition, investigating the corrosion of Mg alloys in living organisms could potentially enable the wide use of degradable metal implants in orthopedics. Therefore, *in vivo* studies are crucial to assess the degradation behavior of Mg-based devices to promote safety information regarding the therapeutic application of Mg implants. In the following chapters (4 to 7), the corrosion performance of Mg-based implants has been evaluated with the aim of ***acquiring information based on high-resolution imaging techniques from Mg-explants regarding the composition, structure, topography, and tissue-implant interface properties to have a comprehensive knowledge of the reactions that occur throughout the degradation of Mg-based implants***.

To accomplish this, 4 animal models were conducted for project partners of the MgSafe project (Table 2.4) in both small animals (rats) and large animal (sheep) models employing different Mg alloy implants disc-, pin-, and screw-shaped. Each animal surgery received ethical approval from the respective institution's ethical committee. In addition, animal experiments followed the guidelines for the accommodation and care of animals established by the European Convention to protect vertebrate animals used for experimental and other scientific purposes. The trials were conducted in accordance with the 3R principles (replace, reduce, and refine). Then, explant samples from small and large animal models (rats and sheep) were received from MgSafe partners (Figure 2.7) from different implantation times. Two types of explant samples were requested: Retrieval implant without surrounding tissue and retrieved Mg-implant with surrounding tissue embedded in resin. (Figure 2.8 and Table 2.5). The aim was *to* ***assess the corrosion layer-Mg implant-soft and bone tissue interface and tissue responses to the different Mg-based implants.*** The retrieved implants underwent sample preparation for surface and cross section analysis, which will be detailed in chapter 4, 5, 6, and 7.

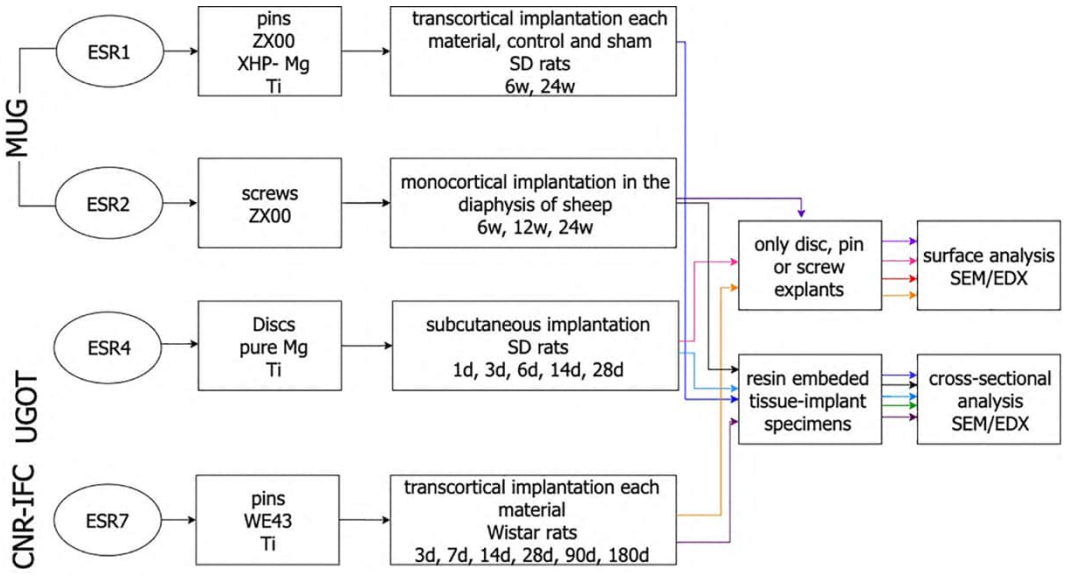

Figure 2.7. The research roadmap of explant specimens from *in vivo* studies. ESR: Early-stage researcher; MUG: Medical University of Graz; UGOT: University of Gothenburg, Sweden; CNF-IFC: National Research Council Institute of Clinical; SD®: Sprague Dawley rats.

Table 2.4. Summary of small and large animal experiments performed for MgSafe partners.

Animal study	Institution	Animal model	Implant placement	Mg material	Implant shape and dimensions	Ethical approval
I	UGOT*	Male Sprague-Dawley® rats	Soft tissue (Implant placed in the back of rats)	Pure Mg	Discs Ø: 9 mm Thickness: 1.5 mm	Dnr-02437/2018 approved by Local Ethical Committee for Laboratory Animals at the University of Gothenburg, Sweden.
II	CNR*	Wistar female rats	Bone tissue (implant placed in the diaphysis of rats)	WE43	Pins Ø: 1.6 mm Length: 8 mm	Prot. nº 299/2020-PR approved by the Instituto Superiore di Sanitá on behalf of the Italian Ministry of Health and Ethics Panel.
III	MUG*	Female Sprague–Dawley® rats	Bone tissue (implant placed in the diaphysis of rats)	XHP-Mg ZX00	Pins Ø: 1.6 mm Length: 8 mm	GZ 66.010/0066-V/ 3b/2019 approved by the Austrian Federal Ministry for Science and Research.
IV	MUG*	Sheep (*Ovis aries*)	Bone tissue (implant placed in the diaphysis of sheep)	Mg-Zn-Ca (ZX00)	Screws Ø: 2 mm Length: 2.3 mm	BMBWF-66.010-0107-V-3b-2019 approved by the Austrian Federal Ministry for Science and Research.

* UGOT: University of Gothenburg, Sweden MUG; CNF-IFC: National Research Council Institute of Clinical; Medical University of Graz.

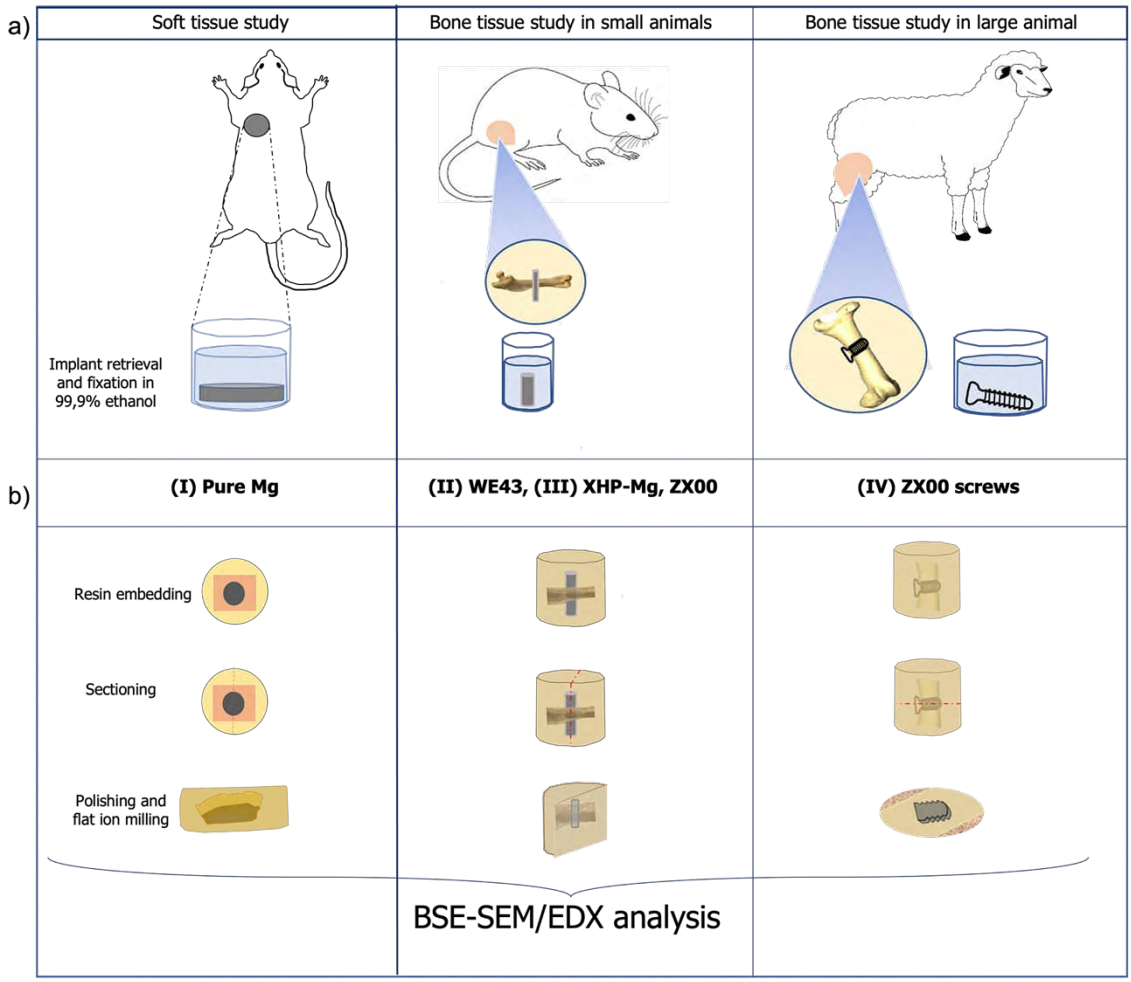

Figure 2.8. Workflow diagram of Mg-based retrieval specimens. a) Mg implants without surrounded tissue were fixed in ethanol and dried for subsequent *ex vivo* surface morphology and chemical composition analysis by SEM/EDX. b) Sample processing steps for Mg implants + tissue blocks for BSE-SEM imaging and elemental distribution analysis to characterize the Mg implant-tissue interface.

2.5. Overview of the results from in vitro and in vivo research

2.5.1. Surface characterization

Before conducting *in vitro* and *in vivo* investigations, the surface roughness and chemical composition of the pure Mg (in Chapters 3 and 6), WE43 (in Chapters 3 and 4), and ZX00 (in Chapters 5 and 7) devices were analyzed. The findings indicated that the initial surface of the Mg-based devices was smooth, anisotropic, and free of contaminants. The surfaces exhibited a thin oxide layer resulting from air and moisture exposure throughout the manufacturing and cleaning procedure and the natural aging process during storage. No signs of surface degradation were seen on the pure Mg and WE43 discs, as well as the ZX00 screws, in relation to their packing and storage. Enriched O regions were only observed on WE43 pins. This highlighted the importance of packaging and storage conditions for Mg-medical devices.

Implants must adhere to the cleaning and sterilizing standards while maintaining their quality and safety from a medical perspective.

After being implanted in the human body, a biomaterial interacts with extracellular fluids and blood from the implant site. The initial molecular-level reactions that occur are water and protein adsorption. The wettability of the material is regulated by the surface free energy, which is influenced by the functional groups and electrical charges present [204]. The pure Mg discs displayed more hydrophilicity and surface energy than the WE43. However, both Mg materials exhibited hydrophilic surfaces, as evidenced by contact angles ranging from 20° to 36°. It has been demonstrated that contact angles between 35° and 80° may benefit applications such as bone regeneration [66,205]. (in Chapter 3).

Table 2.5. Summary of retrieved implants analyzed for the purpose of this thesis.

Animal study	Institution	Animal model	Implant placement	Mg material	Only implant samples	Tissue-implantresin embedded specimens
I	UGOT*	Male Sprague-Dawley® rats	Soft tissue (Implant placed in the back of rats)	Pure Mg	n = 3/time point (Total 15)	n = 5-7/ time point (Total 40) .
II	CNR*	Wistar female rats	Bone tissue (implant placed in the diaphysis of rats)	WE43 Ti6Al7Nb	n = 3 per time point and material) (Total 24)	WE43 (n = 16) Ti6Al7Nb (n = 5)
III	MUG*	Female Sprague–Dawley® rats	Bone tissue (implant placed in the diaphysis of rats)	XHP-Mg ZX00 Ti	-	n = 3-5/time point /material (Total 20)
IV	MUG*	Sheep (*Ovis aries*)	Bone tissue (implant placed in the diaphysis of sheep)	Mg-Zn-Ca (ZX00)	n = 3/time point (Total 9)	n = 3/time point (Total 9)

2.5.2. Microstructure characterization

The microstructure of pure Mg discs (in Chapter 6), XHP Mg pins (in Chapter 7), and ZX00 pins and screws (in Chapters 7 and 5, respectively) were examined. The findings indicated that the grain size order for the various analyzed Mg-based materials, ranging from smaller to coarse grains, is as follows: ZX00 valley and tip region < ZX00 pin and screw's head <pure Mg < XHP-Mg alloy (~1.90 µm < 2.15 – 2.54 µm < 16.87 µm < 37.8 µm). The addition of Ca to the ZX00 alloy clearly revealed the achievement of grain refining. However, differences in grain size were even observed at different zones in ZX00 screws (head, valley, and tip). This

clearly indicated that the recrystallization and the recovery processes differ in the head, tip, and valley regions due to prolonged exposure to the diamond tool during CNC processing. It is important to note that ZX00 screws were produced using polycrystalline diamond tools without the use of lubrication to prevent possible contamination and corrosive damage. Friction, when turning, results in the production of uncontrolled heat. Even a little localized temperature increase can lead to the reformation of the microstructure in Mg alloys.

2.5.3. In vitro immersion tests

The differences in pure Mg, WE43, and ZX00 corrosion resistance *in vitro* could be attributed to their chemical composition and microstructure. When immersed in α-MEM+10%FBS+1%P/S, ZX00 screws corroded at a rate of 1.04 mm/year after 28 days of immersion (In Chapter 5). The WE43 alloy exhibited a higher corrosion rate (CR) during the entire immersion test to reach similar CR behavior as pure Mg after 28 days of immersion (0.16 ± 0.02 mm/year and 0.14 ± 0.05 mm /year, respectively) (briefly shown In Chapter 3). While both the WE43 and ZX00 are clinical-grade alloys that are commercially available and recognized by their good corrosion resistance, the faster degradation observed in the performed *in vitro* tests may be attributed to the susceptibility of certain Mg materials to medium changes carried out in the *in vitro* tests.

2.5.4. The cell-Mg biomaterial interface

The growing demand for improved biomaterials for medical applications emphasizes the importance of expanding our knowledge of cell-material interactions [206]. Despite progress in translational research regarding Mg materials, there remains a limited comprehension of the interaction between Mg materials and cells. The importance of cell-material interactions in the corrosion of Mg *in vivo* has been acknowledged, although its precise roles are still not completely understood [207]. An *in vitro* for assessing the compatibility of Mg-based devices involves culturing cells directly on the surface of the Mg materials. This method enables a more precise evaluation of cell interaction with Mg-based materials. The relevance of understanding the direct interactions between cells and the surface of Mg implants lies in achieving implant integration and tissue regeneration. This accomplishment depends on the initial adherence and cell spreading following the implant placement. To the best of our knowledge, no research is currently available on the impact of coculturing bone cells (osteoblasts (OB) and osteoclasts (OC)) on the composition and degradation performance of Mg-based materials through direct cell culture *in vitro* under physiological conditions. Hence, Chapter 3 investigated the influence

of direct monoculture and coculture of OB and OC cells on the surface morphology, composition, and thickness of the corrosion layers formed on pure Mg and WE43 alloy. The findings revealed that there were changes in cell spread and attachment between OB and OC, which were dependent on the Mg substrates. The results showed that both Mg materials supported effective adhesion and viability of OB and OC cells. However, changes in cell morphology and attachment in response to the different Mg substrates seemed to be influenced by the corrosion of the Mg substrates. Although both pre-differentiated OB and OC cells adhered to the Mg materials, there were differences in the cell density and spread that were seen after 7 and 14 days of cell culture. On pure Mg, OB exhibited enhanced adhesion, leading to greater cell density and confluency after 14 days of monoculture and coculture compared to the WE43 group. Meanwhile, the OC cells exhibited more filopodia, indicating their strong attachment to the pure Mg surface compared to what was observed on the WE43 alloy. Fluorescence microscopy revealed positive staining for differentiated OC. However, non-resorption pits were observed despite the presence of OC in monoculture or coculture in both Mg group surfaces. In addition, the corrosion layer thickness gradually increased on both Mg materials. The thickness of the corrosion layers on WE43 groups, regardless of the presence of the OB and OC cells, were thicker than those formed on pure Mg (~10 μm vs ~5 μm, respectively). The corrosion product layers on pure Mg and WE43 consisted of O, P, Ca, and Mg with traces of the alloying elements of the WE alloy. However, the chemical composition of these layers displayed variations among monoculture, coculture, and Mg substrates. The findings indicate that after 14 days, the coculture group's outer part and middle zones of the corrosion layers exhibited enriched P and Ca on the pure Mg samples. In contrast, this Ca-P enrichment was noticed in the middle part of the corrosion layer in the coculture on the WE43 alloy.

2.5.5. Corrosion performance of Mg-based absorbable implants using animal models

2.5.5.1. Corrosion performance of MgYREZr pins when implanted in the tibial bone of Wistar rats

The corrosion performance of the MgYREZr (WE43) alloy was assessed by implanting pin-shaped devices into the femur bone of Wistar rats (Chapter 4). Initially, the surface evaluation of explanted implants revealed that they maintained their structural integrity for up to 90 days and had a gradual but uneven degradation pattern. The WE43 pin regions exposed to the intramedullary cavity environment exhibited more degradation, characterized by a corroded, cracked, and rougher surface, in contrast to the pin regions that were in the cortical bone compartment. SEM analysis revealed that the bone-implant interface of MgYREZr pins underwent degradation over time, but the main body was still present after 180 days. Since day 3, the implanted pins had a high level of stability, as they were in early direct contact between the bone and the implant. The corrosion layers formed over time consisted of O, Mg, P, Ca, and trace of the alloying elements, whose chemical nature differed depending on the implantation location. At 7 days of *in vivo* implantation, the WE43 pin areas situated within the intramedullary cavity showed corrosion layers with higher P, Ca, and REE content. After 14 and 28 days following pin implantation, the corrosion layers were mainly composed of $Mg(OH)_2$ in both compartments. However, after 90 and 180 days, higher O, Ca, and P were noticed in the corrosion layer at both bone compartments.

As different regions of the pins were exposed to different biological environments (cortical bone, intramedullary cavity, or soft tissues), the formation of corrosion layers of varying thickness (from 1 to 155 μm) was observed. Thicker corrosion layers were formed within the intramedullary cavity (18-155 μm) and at the interface between the soft tissue and the cortical bone (30-89 μm), while thinner corrosion layers formed in the cortical bone compartment (2-18 μm). Furthermore, the mean corrosion rates increased during the initial stages of implantation (1.53 ± 0.56 mm/year after 3 days of implantation). However, these corrosion layers formed on the WE43 pins effectively slow down the degradation of the pins, resulting in a corrosion rate of 0.24 ± 0.00 mm/year after 90 days.

2.5.5.2. Assessment of the corrosion behavior of ZX00 human-sized implants using sheep model

The corrosion resistance of ZX00 screws was evaluated when implanted in the diaphysis of sheep (Chapter 5). The retrieved screws after 6, 12, and 24 weeks of implantation were analyzed using SEM/EDX analysis. After 12 weeks, the threads of the screws began to lose their sharpness, particularly in the areas where the threads and valleys beneath the screw´s head were more corroded. After 24 weeks, the threads were worn away, although the main body of the screw remained. The corrosion layers formed on the screw´s surfaces varied in thickness and composition depending on the implantation site. Thicker and uneven corrosion layers were seen on the regions of the implant within the intramedullary cavity compartment, with some areas measuring up to approximately 174 μm thickness. On the other hand, the screw zones located within the cortical bone showed thinner corrosion layers (39.8 ± 27.4 μm after 12-weeks and 61.9 ± 34 μm after 24 weeks of implant placement). At all-time points, the corrosion layers consistently contained O, Mg, P, and Ca, with variations in composition observed across the different bone compartments. The primary corrosion product observed composing the corrosion layers formed within the cortical bone after 6 and 12 weeks of implantation was $Mg(OH)_2$. In contrast, the corrosion layers within the intramedullary cavity showed a homogeneous distribution of O, Mg, and lower content of Ca and P. Interestingly, the new bone formed in direct contact with the corrosion layers and exhibited similar dark pink histological staining as the newly formed bone.

2.5.5.3.Corrosion behavior of pure Mg discs when implanted in soft tissues

When Mg implants are placed within the human body, they begin to degrade immediately upon contact with physiological body fluids and tissues. This process is followed by an inflammatory response in the nearby soft tissues. To determine the corrosion performance of pure Mg when in contact with soft tissue, Mg discs were surgically implanted into the back of rats for 1, 3, 6, 14, and 28 days. The degradation-induced changes were characterized by surface and cross-sectional analysis of retrieved Mg discs after each determined time point. It was noted that for a period of up to 6 days after implantation, some biological tissue remained attached to the corroded pure Mg disc surfaces, suggesting that at the early stage of implantation, the degradation of the Mg surfaces promoted an inflammatory response. However, after 14 and 28 days of implant placement, the corrosion products formed on the Mg discs were mainly composed of Mg, O, P, and Ca, where Ca and P tend to be located at the

outer part of the corrosion layer at the tissue-implant interface. This was accompanied by a reduced expression of inflammatory genes.

2.5.5.4.A 24-week follow-up comparative study on corrosion performance of XHP-Mg and ZX00 pins

The degradation of ZX00 and XHP-Mg pins and the related bone response to these Mg devices were compared when implanted in juvenile healthy rats over a study period of 6 and 24 weeks. To determine the bone-implant interface morphologies of the ZX00 and XHP-Mg, as well as bone morphologies of the sham and control groups, SEM-EDX analysis was performed 6 and 24 weeks after implantation (Chapter 7). At both designated time points, a corrosion layer formed on the surface of the Mg-based implants with varying thicknesses at different bone compartments (cortical bone (CB) and intramedullary cavity (IMC)). The ZX00 group displayed thicker corrosion layers at CB and IMC (82-86 μm) compared to XHP-Mg implants (52-74 μm). Although both Mg implants formed corrosion layers containing O, Mg, P, and Ca, their distribution within the corrosion varied between the implanted Mg materials. Both Mg materials showed an outer corrosion layer rich in Ca and P. However, the XHP-Mg group exhibits higher Ca and lower P concentrations than the ZX00 group, with a Ca/P ratio of 1.4 ± 0.4 and 0.7 ± 0.1, respectively. New bone formed directly with the corrosion products formed on both Mg materials despite the moderate gas accumulation in the intramedullary cavity and surrounding tissues.

Overall, this thesis is based on the below-enlisted papers:

- **Martinez, D. C**., Borkam-Schuster, A.; Helmholz, H.; Dobkowska, A.; Luthringer - Feyerabend, B.; Plocinski, T.; WIllumeit-Römer, R., Swieszkowski, W. (2024) *Bone cells influence the degradation interface of Mg-based materials: Insights from multimodal in vitro analysis. Manuscript accepted in Acta Biomaterialia (Available online 19 August 2024) https://doi.org/10.1016/j.actbio.2024.08.015.*

- **Martinez, D. C.,** Dobkowska, A., Marek, R., Cwieka, H., & Swi, W. (2023). *In vitro and in vivo degradation behavior of Mg-0.45Zn-0.45Ca (ZX00) screws for orthopedic applications*. **Bioactive Materials**, 28, 132–154. https://doi.org/10.1016/j.bioactmat.2023.05.004.

- Ben, H., **Martinez, D. C**., Shah, F. A., Johansson, A., Emanuelsson, L., Norlindh, B., Willumeit-r, R., Swieszkowski, W., Palmquist, A., Omar, O., & Thomsen, P. (2023). *Magnesium implant degradation provides immunomodulatory and proangiogenic effects and attenuates peri-implant fibrosis in soft tissues*. **Bioactive Materials**, 26, 353–369. https://doi.org/10.1016/j.bioactmat.2023.02.014.

- Okutan B, Schwarze UY, Berger L, **Martinez D.C**., Herber V, Suljevic O, Plocinski T, Swieszkowski W, Santos SG, Schindl R, Löffler JF, Weinberg AM, Sommer NG. (2023). *The combined effect of zinc and calcium on the biodegradation of ultrahigh-purity magnesium implants*. **Biomater Adv. Mar**; 146: 213–287. doi: 10.1016/j.bioadv.2023.213287.

Manuscript under review:

- Mota-Silva, E*.; **Martinez, D.C***.; Basta, G.; Babonni, S.; del Turco, S., Fragnito, D.; Salvatore, S.; Kusmic, C.; Leon, R.; Panetta, D.; Campanella, B.; Onor, M., T Plocinski, W Swieszkowski, L Menichetti. Monitoring osseointegration and degradation of Mg-Alloy implants through plasma biomarkers of inflammation and bone regeneration (* both authors equally contribute to this work) (*Under review in Journal of Tissue Engineering*).

Chapter 3

Bone cells influence the degradation interface of Mg-based materials: Insights from multimodal in vitro analysis

***Diana C. Martinez**, Anke Borkam-Schuster, Heike Helmholz, Anna Dobkowska, Bérengère Luthringer-Feyerabend, Tomasz Plociński, Regine Willumeit-Römer, Wojciech Święszkowski*

*Manuscript accepted in **Acta Biomaterialia**, (Available online 19 August 2024): https://doi.org/10.1016/j.actbio.2024.08.015*

ABSTRACT:

In this study, the interaction of Mg and WE43 alloy under the presence of osteoblast (OB) and osteoclast (OC) cells and their influence on the degradation of materials have been deeply analyzed. Since OB and OC interaction has an important role in bone remodeling, we examined the surface morphology and dynamic changes in the chemical composition and thickness of the corrosion layers formed on Mg and WE43 alloy by direct monoculture and coculture of pre-differentiated OB and OC cells *in vitro*. Electrochemical techniques examined the corrosion performance. The corrosion products were characterized using a combination of the focused ion beam (FIB), scanning electron microscopy (SEM), and energy-dispersive X-ray spectroscopy (EDX). Cell viability and morphology were assessed by fluorescent microscopy and SEM. Our findings demonstrate cell spread and attachment variations, which differ depending on the Mg substrates. It was clearly shown that cell culture groups delayed degradation processes with the lowest corrosion rate observed in the presence of OBOC coculture for WE43. Ca-P enrichment was observed in the outer-middle region of the corrosion layer but only after 7 days of OBOC coculture on WE43 and after 14 days on the Mg specimens.

STATEMENT OF SIGNIFICANCE:

Degradable Mg as biomaterial provides distinct opportunities for orthopedic application. However, there is still a lack, especially in elucidating cell-material interface characterization. The present study provides data on the influence of osteoblast-osteoclast coculture in direct Mg-material contact. Our findings demonstrated that pre-differentiated osteoblasts and osteoclasts cocultured on Mg substrates influenced the chemistry of the corrosion layers. At the same time, the cell spread, and attachment were Mg substrate-dependent, and the corrosion layer thickness increased as the corrosion of Mg materials proceeded regardless of the presence of cells on the Mg surfaces. The findings of coculturing bone cells directly on Mg materials within an *in vitro* model provide an effective approach for studying the dynamic degradation processes of Mg alloys while also elucidating cell behavior and their potential contribution to the degradation of these alloys.

Keywords: Degradable magnesium, in vitro, Osteoblast, Osteoclast, Coculture, Corrosion layer

Graphical abstract

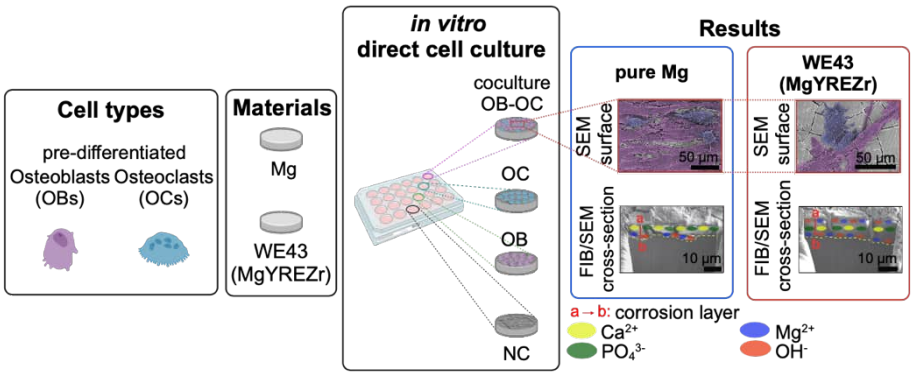

3.1. Introduction

The application of magnesium (Mg) implants for medical purposes has garnered significant attention in recent years [208,209]. Mg and its alloys have distinct characteristics, including biocompatibility, biodegradability, and mechanical performance [27,184]. These features make them particularly suitable for temporary structural biomaterials such as orthopedic implants or cardiovascular stents [26]. In addition, the degradability of Mg-based implants in the physiological environment without causing harm to nearby tissues has opened up new possibilities for addressing complications associated with non-degradable temporary implants, such as foreign body reactions and stress shielding phenomena [9–12]. Despite these encouraging attributes, Mg implants still encounter major challenges in controlling their degradation behavior in physiological environments, which is associated with high corrosion rates and the release of hydrogen gas [25,60,210]. This has prompted researchers to study the development of Mg alloys, such as the WE43-containing rare earth elements (MgYREZr) alloy. This alloy has demonstrated *in vitro* cytocompatibility [211] and has been used for clinical purposes, receiving regulatory approval for specific medical applications, such as orthopedic implants or cardiovascular stents [212,213]. In orthopedic applications, WE43 implants have been used to treat hallux valgus [214,215], medial malleolar fracture [216], tibial spine [217], elbow [218], wrist [183,219], or mandible [220] fractures.

Despite this progress in translational research on Mg materials, there is still a limited understanding of the interaction between Mg materials and cells. Evaluating the biocompatibility of biomaterials requires studying the cellular reaction to materials [213]. The impact of cell-material interactions on the corrosion of Mg *in vivo* has been acknowledged, although its precise roles are not yet fully understood [207]. Traditionally, indirect cell monoculture testing has assessed the interaction between Mg materials and cells using extracting methods [221–229]. Ezechieli et al. [211] demonstrated that the released ions and corrosion products from the MgYREZr alloy were non-toxic to human primary osteoblasts (HOB) and mouse fibroblasts (L929) after 24 h of exposure to the alloy extracts. However, limited studies have been conducted to evaluate the interaction of Mg materials with multiple cell types using coculture methods. Wu et al. [228] examined the impact of supplemented Mg in the form of Mg-based material extracts on the proliferation and differentiation of human osteoblasts (OB) and osteoclasts (OC) from human telomerase reverse transcriptase (hTERT) transduced mesenchymal stem cells (SCP-1) and peripheral blood mononucleated cells (PBMC) in a coculture model. Their research uncovered that highly concentrated Mg extract

encourages OB formation while delaying the differentiation of OC. On the contrary, the coculture of peripheral blood monocyte cells (PBMCs) with OB exhibited a greater tolerance when exposed to a highly concentrated Mg extract. In addition, Maradze et al. [230] revealed that while the viability and proliferation of mesenchymal stem cells (MSCs) decreased when exposed to corrosion product granules, these granules prompted the MSCs to differentiate into OB. Conversely, they observed that the metabolic activity of RAW-osteoclast cells decreased when they were exposed to Mg corrosion granules.

Another *in vitro* approach to examine the compatibility of Mg-based devices involves directly culturing cells on the surface of the Mg materials. This method allows for a more realistic assessment of cell interaction with Mg-based materials. The relevance of comprehending the direct interactions between cells and the surface of Mg implants lies in the success of implant integration and tissue regeneration. This achievement depends on the initial adhesion and cell spreading after implant placement [231]. Previous *in vitro* investigations exploring the direct cellular interactions with Mg materials have yielded inconsistent findings. In several *in vitro* studies, a lack of cell growth or restricted cell adherence to Mg surfaces has been documented [99,232]. On the contrary, other researchers reported variances in cell viability across various Mg alloys, which might be related to changes in surface morphology and chemical composition of the corrosion products formed on Mg-based materials [161–163,233]. However, most *in vitro* direct cell culture experiments employing Mg implants have primarily used monocultures [66,161,163,164,206,207,227,233–243]. Since both OB and OC play crucial roles in bone remodeling and regeneration [140,144], such experimental setups may not comprehensively reflect the complex cell interactions within a physiological context. Therefore, *in vitro* studies involving both types of cells are necessary to evaluate the behavior of Mg materials in orthopedic applications [164].

In addition, most *in vitro* tests primarily examine the effects of Mg degradation products on cells, while there is limited research on the impact of living cells on the degradation of Mg materials [162,244–246]. Previous investigations have indicated that the corrosion rate of Mg materials can be either slowed down [239,247] or accelerated [164,207,244] in the presence of cells. Kannan et al. [244] examined the influence of L929 cells on the corrosion behavior of a Mg-Ca alloy after 48h of cell culture. Their findings revealed an accelerated degradation of the Mg-Ca alloy due to L929 metabolic activity, which caused a decrease in the pH of the culture media and an increase in the Mg dissolution. Agha et al. [162] demonstrated that OB modified the chemical composition of the degradation interface. Specifically, they noticed that the corrosion layers formed near OB cell layers had higher Ca-P concentration after 14 days of

direct cell culture on pure Mg and Mg-10Gd alloy. In addition, they revealed that pure Mg and Mg-10Gd had a decreased corrosion rate when exposed to cells, whereas the Mg-2Ag alloy showed an increased corrosion rate. These contrasting outcomes highlight the need to investigate whether the presence of bone cells might modify the environment at the interface between the cells and the Mg implants, thereby impacting the degrading behavior of Mg-based devices [244]. Previous coculture models assessed the effects of degradable pure Mg involving single and triple cocultures of OB, OC, and osteocytes. The authors demonstrated that Mg degradation products do not disrupt the functioning of OB, OC, and osteocytes *in vitro* [248]. Globig et al. [245,246] found that the corrosion rate of extruded Mg and Mg-6Ag alloy was not noticeably influenced by the coculture of green fluorescent osteosarcoma cells (Saos-eGFP) and red fluorescent dermal fibroblasts (RF fibroblasts) at varying cell densities. Their research highlighted the importance of employing a direct model with Mg-based materials instead of relying on Mg extracts to achieve similar outcomes from *in vivo* studies.

To our knowledge, no research has investigated the impact of cocultured bone cells (OB and OC) on the composition and degradation behavior of Mg-based materials through direct cell culture *in vitro* under physiological conditions. Therefore, the present study aimed to analyze the surface morphology and dynamic changes in composition and thickness of the corrosion layers formed on a Mg and WE43 alloy influenced by direct monoculture and coculture of OB and OC cells.

3.2. Materials and Methods

3.2.1. Materials

The Mg discs (diameter = 9 mm, thickness = 1.5 mm) were fabricated as described previously in [43], while WE43 (MgYREZr) alloy in the shape of discs (diameter = 5 mm, thickness = 1.5 mm) was manufactured by Syntellix AG (Hannover, Germany) as described in [196,197]. The WE43 alloy is a rare-earth (RE) element Mg alloy containing beside Mg, yttrium (Y, zirconium (Zr), and zinc (Zn) [196,249]. The chemical composition of both Mg materials is shown in Table S3.1. Both Mg and WE43 discs were polished with a 2500# silicon carbide abrasive paper (SiC, Hermes Schleifmittel GmbH, Germany) at 50 rotations per minute on both sides using a twin wheel grinder/ polisher (SAPHIR 360, ATH Qness GmbH, Germany). Afterward, they were ultrasonically cleaned with n-hexane for 20 min, acetone for 20 min, and 100% ethanol for 3 min (all chemicals, Merck KGaA, Germany). Following cleaning, the samples were dried, weighed, individually packaged, gamma sterilized with a

total dose of 33.5 kGy (BBF Sterilisation Service GmbH, Germany), and stored under an oxygen-free atmosphere until use.

3.2.2. Surface characterization

The surface morphology of Mg and WE43 discs (n = 3/material) was analyzed by scanning electron microscopy (SEM, Hitachi, SU-8000, Japan). The chemical composition of the surface of both Mg materials was investigated by energy dispersive X-ray spectroscopy (EDX, UltraDry EDS Detector, Thermo Scientific™) at 5, 15, and 30 kV acceleration voltage. The surface roughness (mean arithmetic height (Sa)) was determined following the standard EN ISO 25178-2 [193] using an optical profiler (VHX-7100 digital microscope, Keyence) equipped with a VHX-E500 lens. Three 100 x 100 μm^2 areas/sample/material were analyzed at 1000x magnification. The measurement´s results evaluation filters were selected following EN ISO 25178-3 [250]. Surface wettability was evaluated via static sessile drop method (contact angle measurements on four random zones/sample/Mg material on three independent samples) using the OCA 20 optical goniometer (Dataphysics, Filderstadt, Germany). For this, 1 µL water drop was dispensed on the Mg samples at room temperature, and the average contact angles were calculated using the SCA20.2.0 software (firmware version 2.05). The surface energy of both Mg materials was calculated using the Fowkes equation [195] from contact angles measured using deionized water (polar) and diiodomethane (non-polar) liquids.

3.2.3. Electrochemical measurements

The electrochemical tests were performed under cell culture conditions (37°C, 5% CO_2, 95% controlled humidity) in a completed cell culture medium (α-MEM, Gibco, UK) supplemented with 10% FBS (Biological Industries Ltd, Israel) and 1% penicillin/streptomycin (10 000 U/mL – 10 mg/mL, Sartorius, Israel) designated as α-MEMc in this study. A Gamry FAS1 potentiostat with three electrodes was used: platinum as the counter electrode, Ag/AgCl as the reference electrode, and the measured sample as the working electrode. The electrochemical open-circuit potential (E_{OCP}) was measured for 6 hours. The electrochemical impedance spectroscopy (EIS) was initially recorded after 1 hour of immersion and subsequently after 6 hours of immersion. Electrochemical impedance spectroscopy (EIS) was recorded in a frequency range from 10 mHz to 10 kHz with an AC amplitude of 10 mV. To ensure reproducibility, at least three tests were conducted. The EIS data was fitted using the Gamry Echem Analyst software (version 6.33).

3.2.4. Cell culture

3.2.4.1. Pre – Differentiation of osteoblasts and osteoclasts

Osteoblasts were obtained by exposing human umbilical cord perivascular (HUCPV) cells to osteogenic supplements, as described previously in [251,252]. The cells were isolated from the umbilical cord provided by the Bethesda Hospital Hamburg Bergedorf (approval by the ethical commission of the Ärztekammer Hamburg (PV5991)). The HUCPVs were cultivated in α-MEMc in the presence of osteogenic supplements for 21 days.

Osteoclasts were differentiated from peripheral blood mononuclear cells (PBMC). The isolation of PBMC was performed as described [253]. The differentiation was performed for 21 days in α-MEMc with M-CSF and RANKL. The differentiation was monitored microscopically. The experiments were performed with the same HUCPV donor; however, the PBMCs were pooled from different donors. For the direct exposition experiments, both cell types were carefully removed from the tissue culture (TC) well surface by adding 0.25% Trypsin-EDTA, counted by CASY cell counter, and applied in a ratio of 1:2 (OB: OC) for the coculture.

3.2.4.2. Osteoblasts and osteoclasts single cell type and coculture in the presence of pure Mg and WE43 specimens

The cleaned and sterilized Mg and WE43 specimens were preincubated in α-MEMc for 24 hours under cell culture conditions (37°C, 5% CO_2, 20% O_2, 95% controlled humidity [254] to mimic the immediate body fluid/blood interaction with biomaterial directly after implantation [234]. On experimental day 0, the discs were removed and placed into a 12-well plate (pure Mg) and 24-well plate (WE43) agarose pre-coated. Cells were directly seeded onto each disc at a density of either 20 000 OB and 40 000 OC cells per cm^2 for pure Mg and 10 000 OB and 20 000 OC for WE43 per $cm^{2,}$ representing the ratio 1:2. The cells were then left to adhere to the Mg-based discs for 20 minutes. Then, 2 mL and 1 mL of culture media were added to each well for pure Mg and WE43 samples, respectively. In addition, 10 000 cells/well and 5 000 cells/well were seeded on glass slides placed on 12- and 24 well-plates as cell control included in the experimental layout. Mg samples without cells (NC group) were also immersed as Mg control. Specimens were incubated at 37°C, 5% CO_2, 20% O_2, and 95% relative humidity for 7 and 14 days. The culture medium was changed every 2-3 days, and the pH (Sentron® SI600, Sentrom Europe BV, The Netherlands) and osmolality OSMOMAT® auto, Gonotec GmbH, Germany) of the immersion medium before cell seeding and the supernatants after each cell culture medium change was measured. The subsequent corrosion products of 3 samples per

cell condition, per time point, were removed on the WE group by treating them with fresh chromic acid (180g/L in distilled water, VMR International, Germany) for 10 min on each side. Afterward, samples were rinsed with deionized water and 100% ethanol, dried and weighed. The corrosion rate (CR) in mm/year was calculated according to the equation (ASTM G1-03 2017) [255]:

$$Corrosion\ rate = (K \times \Delta g)/(A \times t \times \rho) \qquad (3.5)$$

Where K is a conversion factor, Δg is the weight change in grams (weight before immersion − weight after cleaning), A is the sample surface area in cm^2, t is immersion time in hours, and **ρ** is the density of the disc in g/cm^3. The density of the discs was determined by the Archimedes method.

3.2.4.3. In vitro viability staining assay

After 7 and 14 days of cell culture, the number of live and dead cells was observed using the LIVE/DEAD staining protocol. Briefly, the medium was removed from each well, and 1mL of assay solution containing 4 µM calcein AM (C1430, Life Technologies GmbH, Germany), 2 µM Ethidium homodimer (46043, Sigma-Aldrich, Germany), and 1 µg/mL Höchst 33342 (14533, Sigma-Aldrich, Germany) in cell culture medium without supplements. Then, the discs and cell controls were incubated for 20 minutes. The staining solution was removed and replaced by 1 mL of α-MEM prior to visualization by fluorescent microscope (Nikon, Eclipse Ni-E) applying FIC, Texas, and DAPI filters. Images were taken at 4x and 10x magnification.

3.2.4.4. Cell adhesion staining assay

The actin filaments of the cytoskeleton were visualized with Phalloidin conjugated with Texas Red (TR-Phalloidin). The nuclei were counterstained with 1µg/mL Höchst 33342 (Merck, Germany). The materials with cells fixed with 3.7% paraformaldehyde (Alfa Aesar GmbH & Co KG, Germany) for 10 min, washed with HBSS containing 1% BSA (Merck, Germany), and permeabilized with 0.1% Triton X-100 (Merck, Germany) for 10 min at room temperature. Staining with TR-Phalloidin was performed for 1 h at room temperature in the dark, followed by final nuclei staining for 15 minutes. The microscopic images were taken using an epifluorescence microscope (Nikon Eclipse Ni-E, Nikon, Germany) and analyzed using NIS Elements viewer software (version 5.21, Nikon, Japan).

3.2.5. Cell morphology and adhesion observations by Scanning Electron Microscope (SEM)

The surface and morphology of OB and OC seeded on the Mg, and WE43 alloy specimens in monoculture and coculture were observed by SEM. The specimens were fixed overnight in 2.5% glutaraldehyde (Sigma-Aldrich, Germany). Subsequently, samples were incubated in 1% osmium tetroxide for 30 minutes. Ascending alcohol series of 20%, 40%, 60%, 80%, and 100% for 1 h each were employed to dehydrate the samples. Mg samples underwent two methods for drying specimens: (critical point drying (CPD, Leica EM CPD030, Germany) and freeze-drying (FD, alpha 1-2 LD plus, Germany) to determine which preparative procedure for SEM induces less qualitative artifacts to the cell surface morphology. WE43 samples only were prepared by CPD. The detailed protocol for both CPD and FD is summarized in the supplementary information. Afterward, to alleviate the charging effect and imaging artifacts, the specimens were coated with a 10 nm gold layer (Leica EM SCD 500, Leica Microsystems, Germany), minimizing the specimen damage and enhancing the topographical contrast [256]. SEM observations were performed at a 5kV acceleration voltage with a secondary electron detector (SE) (SEM, SU-8000, Hitachi, Japan).

3.2.6. Overview of the cell culture experimental design

A schematic representation of the experimental design is shown in Figure. 3.1. Osteoblast (OB) and osteoclast (OC) cells were pre-differentiated for 21 days from human umbilical cord perivascular (HUCPV) cells and peripheral blood mononuclear cells (PBMC), respectively. Then, cells were directly seeded on Mg and WE43 specimens preincubated surfaces in monoculture (OB and OC) and coculture (OB-OC) for 7 and 14 days in α-MEM supplemented with 10% FBS and 1% penicillin/streptomycin. Monoculture and coculture of OB and OC were also seeded on glass as cell control, while Mg samples without cells (NC) were also immersed as Mg control. After 7 and 14 days, cell viability and morphology were evaluated by LIVE/DEAD and actin-DAPI staining while SEM/FIB/EDX surface and cross-sectional analysis were performed on the Mg materials.

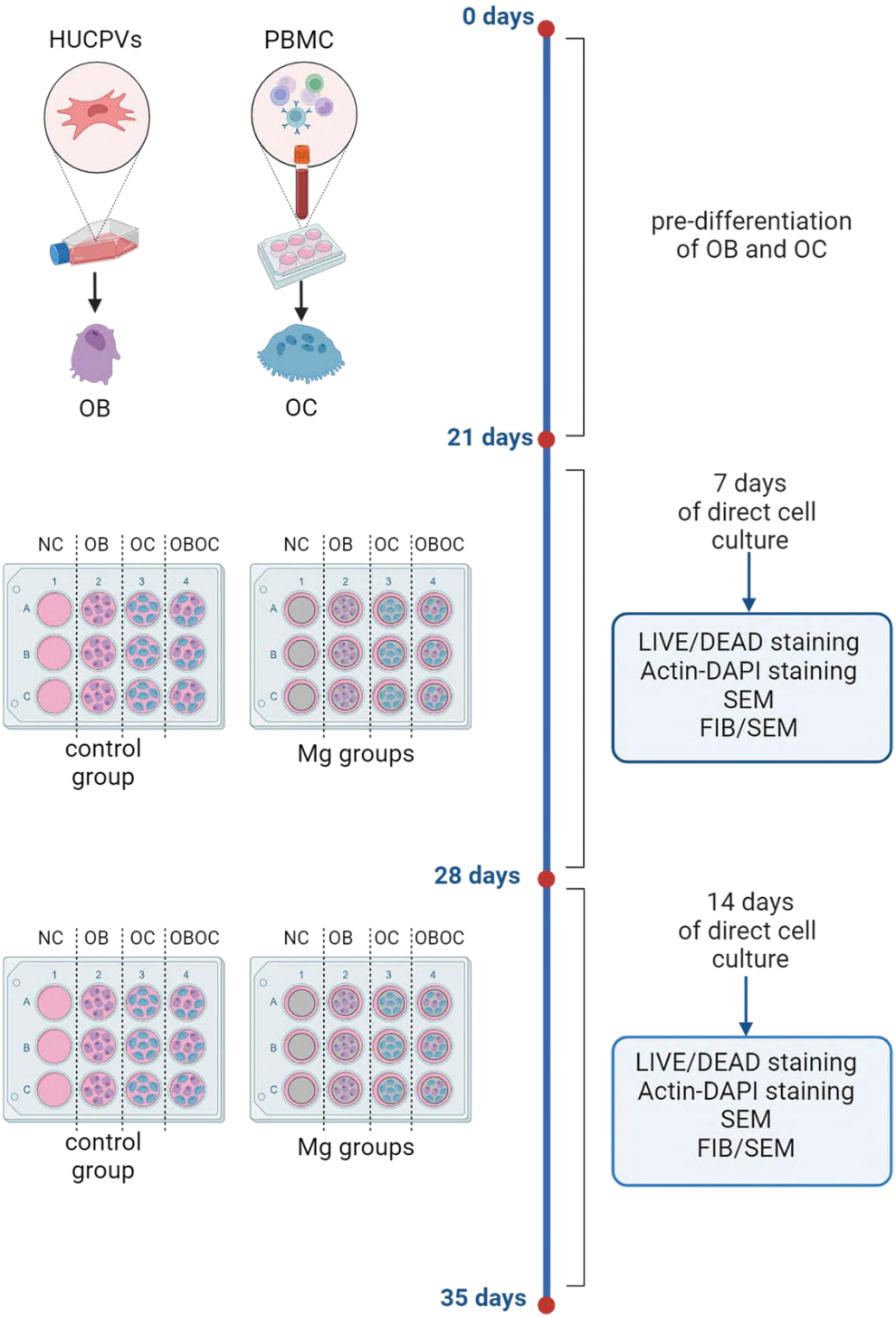

Figure 3.1. Schematic overview of the experimental design. *Image created with Biorender. com*

3.2.7. Corrosion layer interface analysis by Scanning Electron Microscope equipped with a Focus Ion Beam and Energy X-ray Spectroscopy (SEM/FIB/EDX)

After SEM surface observations, the cell-corrosion layer interface was analyzed using a FIB-SEM system (NB-5000 dual-beam, Hitachi, Japan). A thin tungsten layer was deposited using a Gas-Injection-System (GIS) on a selected region of interest (ROI) to protect the sample

surface and prevent cell damage during the next FIB milling steps. The FIB milling of cross-sections of the different cell culture condition specimens (NC, OB, OC, OB-OC coculture, prepared by Critical Point Drying (CDP) after 7- and 14- days of cell culture) was performed using 40 kV acceleration voltage from high-(58.59 nA) to low-(0.73 nA) gallium beam current. SEM images of cross-sections were acquired at 5kV acceleration voltage. Additionally, the vertical distribution of elements composing the corrosion layers was obtained by acquiring five EDX line scans per zone analyzed on the milled cross-sections at 15 kV and 30 kV acceleration voltage for Mg and WE43, respectively. 1-2 random zones of 3 independent samples per cell culture condition per group and time point were analyzed following the described method. Fiji software [257] was employed to measure the corrosion layer thickness (n = 40 – 150 measurements/time point/cell culture condition/3 independent samples/Mg material).

To compare with EDX results, the Hydra-Medusa software [258] was used to predict the chemical equilibrium diagram fraction of Mg and WE43 after 14 days of immersion, based on the ionic concentration of the cell culture medium composition. The Mg concentration was calculated using mass loss measurements to predict the compounds that could form throughout the cell culture assay.

3.2.8. Statistical Analysis

All data are presented as mean ± standard deviation (SD). Statistical analysis was performed using two-way ANOVA followed by Tukey´s post-hoc test. Comparison of independent samples (from different cell conditions, different time points, or different materials) was performed using unpaired Kruskal-Wallis and Mann-Whitney U tests. Statistical analyses were performed in GraphPad Prism 8.0 software (version 8.2.1 GraphPad Software, San Diego USA) and SPSS (v.27; IBM Corporation).

3.3. Results

3.3.1. Surface Morphology and Roughness

Figure 3.2 depicts the surface morphology and the three-dimensional (3D) reconstruction surface of both Mg materials, along with their corresponding EDX analysis. BSE-SEM images of the surface of Mg (Figure 3.2a) and WE43 (Figure 3.2b) discs revealed the grinding texture with a horizontal line pattern. Figure 3.2c-d illustrates the 3D surface profiles of both materials, including the average arithmetical mean height (S_a) and root mean square height (S_q), revealing that both materials exhibited comparable smooth surfaces. There was no statistically significant difference between the maximum peak height (S_z) of the Mg surface and that of the WE43

surface (1.37 ± 0.26 µm and 1.05 ± 0.22 µm, respectively). EDX analysis also revealed that a thin oxide layer was formed on the surface of both Mg materials (Figure 3.2e-f). In addition, Y, Zn, and RE were detected in the case of WE43 (denoted in red color in the EDX panel in Figure 3.2f), and bright, fine, uniformly distributed precipitates rich in Y (denoted in blue color in the EDX panel in Figure 3.2f) [235,259,260]. To investigate the hydrophilicity at the surface interface of the as-polished Mg surfaces and the related surface energy, static contact angle measurements were performed. The contact angle measurements of the polished Mg samples depicted in Figure 3.g indicated that the Mg surface exhibited higher hydrophilicity and greater surface energy (20.6º ± 4.9 and 68.3 mN/m) compared to WE43 (36.3º ± 5.7, and 60.2 mN/m). Furthermore, the polar component of the surface energy in Mg was significantly higher than that of WE43, as seen in Figure 3.2h.

3.3.2. Electrochemical measurements

The evolution of potential recorded under open circuit conditions during 6 hours of immersion under cell culture conditions is presented in Figure 3.3a. The E_{OCP} recorded for the Mg samples has rather a stable curve oscillating around -1.8 V/Ref during the entire experiment. The initial rise of E_{OCP} for WE43 is observed during 1 hour of the immersion; during the first hour of immersion, the E_{OCP} increased from -1.55 V/Ref, reaching a stable value of -1.49 V/Ref for the rest of the experiment. The EIS data shown in the form of Nyquist and Bode plots are depicted in Figure 3.3b and c, respectively. Three well-defined loops are visible on the Nyquist plots, suggesting three-time constants. The capacitive loop defined at the high-frequency region is related to the charge transfer resistance, and the capacitive loop at medium frequency is associated with the mass

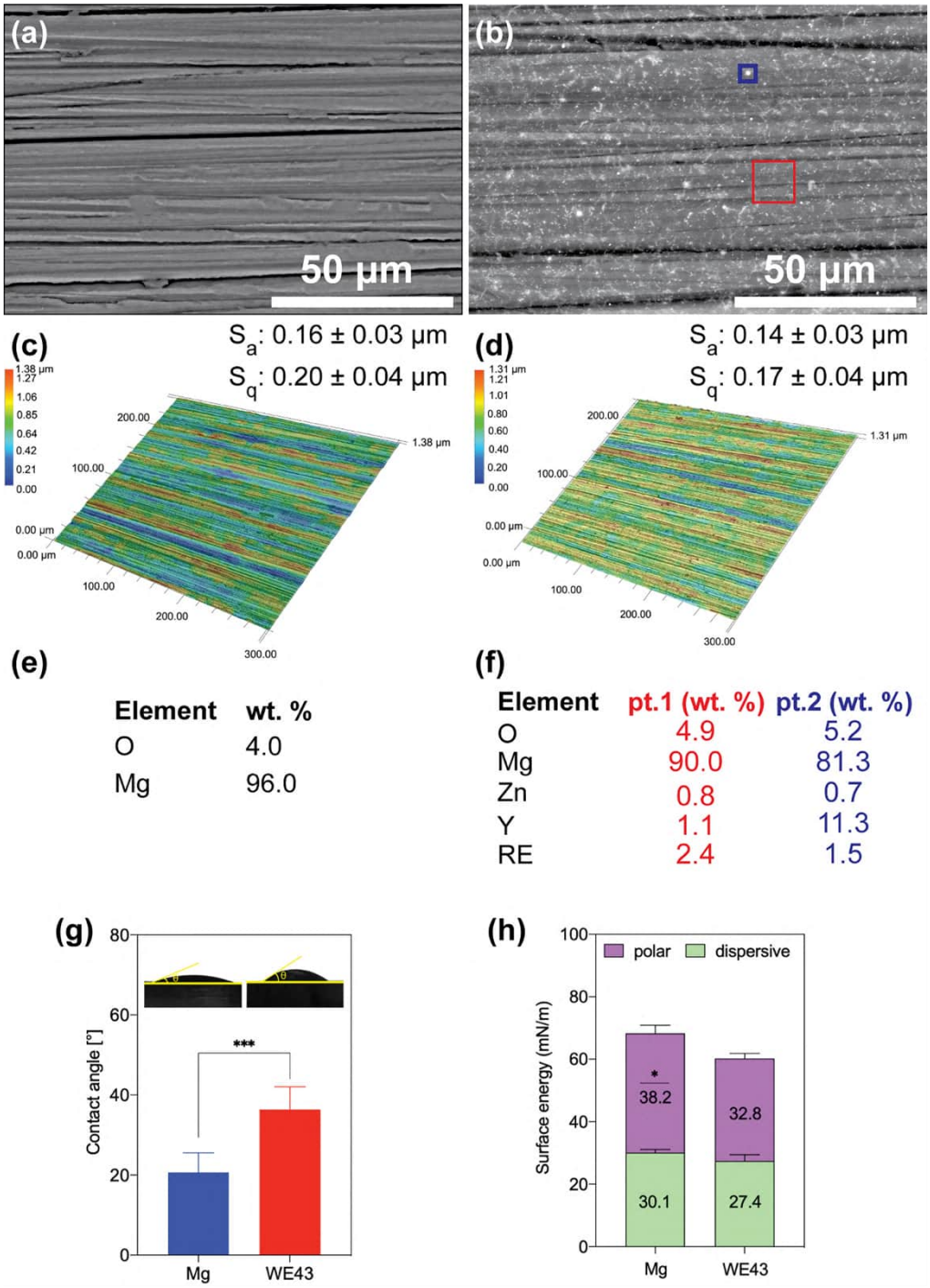

Figure 3.2. Surface characterization of Mg (left) and WE43 alloy (right) before *in vitro* tests. Representative BSE-SEM image of (a) Mg and (b) WE43 surface. The reconstructed three-dimensional (3D) surface of (c) Mg and (d) WE43 with and their corresponding surface roughness (arithmetical mean height (Sa)). EDX profile analysis of (e) Mg and (f) WE43 surface. (g) static contact angle measurements, (h) Polar and dispersive components of the estimated surface energy. The semi-quantitative analysis performed in points (pt.) of the selected areas 1 and 2 in (f) is depicted in red and blue, respectively, displaying oxygen (O), magnesium (Mg), zinc (Zn), yttrium (Y), and rare earth elements (RE). Data in (c), (d), (g), and (h) are presented as mean ± standard deviation. (g) ** $P \leq 0.001$, unpaired Mann-Whitney U test: (h) Two-way ANOVA analysis: *$P \leq 0.05$ polar component of pure Mg *versus* polar component of WE43.

transport at the interface between the surface of the metal and the α-MEMc. In contrast, the inductive loop refers to the relaxation of the adsorption processes of $Mg(OH)_{ads}$ or $Mg(OH)_2$.

The electrical equivalent circuit (EEC) shown in Figure 3.3d has been chosen to fit the EIS data. In the selected EEC, the R_s represent solution resistance. R_{ct} reveals charge transfer resistance; Rf is the resistance of corrosion products formed on the surface, while RL and inductive resistance are often related to pitting corrosion. Constant phase elements (CPE) were employed instead of capacitors to reveal the system's inhomogeneity [261].

The diameters of capacitive loops vary due to different corrosion rates of the investigated materials (Figure 3.3b). After 1 hour of immersion under cell culture conditions, the widest capacitive loops are observed for the WE43. This strongly indicates that WE43 has higher corrosion resistance than Mg at the beginning of the tests. After 6 hours of immersion, the corrosion resistance of the WE43 suddenly decreased, while in the case of Mg samples, an increase in corrosion resistance was observed. Those differences are related to the microstructural heterogeneity, which in the case of WE43 at short immersion times gave the possibility of the Mg species being, while with the time extension, it tends to suffer from localized corrosion. The opposite situation was observed in the case of Mg specimens. At the beginning of immersion, the dissolution reactions overwhelmed film formation reactions. At the same time, with the time extension, the adsorbed species formed a more stable film on the surface of Mg, giving the possibility of better surface protection. For Mg samples, after 1 hour of immersion, a phase angle close to -60° over a wide frequency range is observed, which, with time extension, decreased to -50° and is observed in the narrower frequency range (Figure 3.3c). Two distinct capacitive are visible for WE43 after 1 hour of immersion, and they may relate to the formation of a new layer in addition to the barrier layer on the alloy surface [96]. With the time extension, the resistivity of the passive layer decreased. The EIS parameters obtained from the fitting of the EEC shown in Figure 3.3d are presented in Table 3.1. A reliable agreement between experimental and calculated data was obtained, as evidenced by the χ^2 test that gave values lower than 10^{-3}.

EIS results allow to calculate the corrosion rate of the Mg-based alloys accurately. This approach was validated by King et al. [262] and based on our experience, is the best practice to calculate corrosion rate of the investigated herein alloys under cell culture conditions, as the measurements will not be disturbed by intense hydrogen evolution or local changes of pH at the metal/solution interface [263]. As shown in Refs [262–264], the corrosion rate inversely scales with polarization resistance.

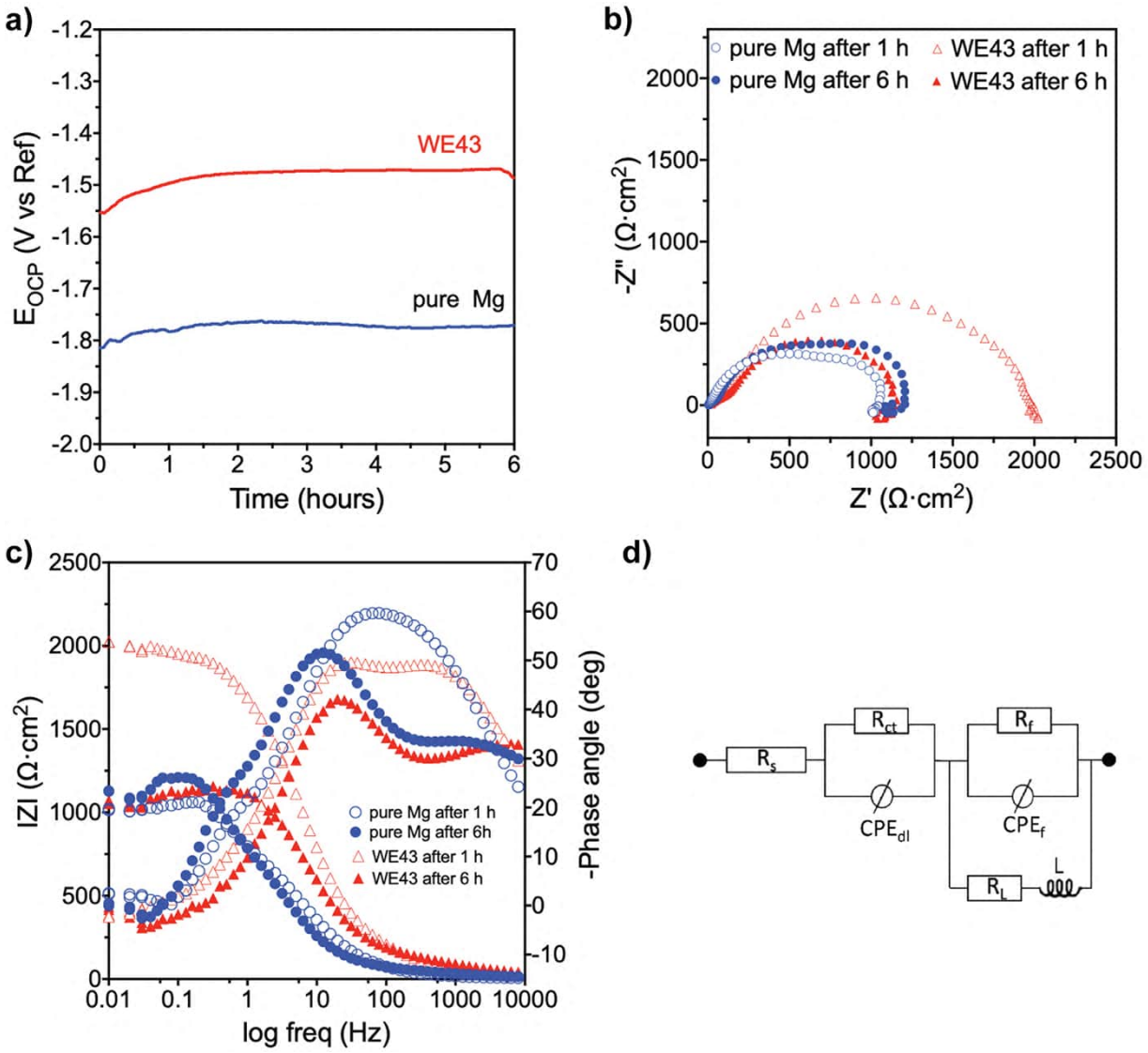

Figure 3.3. Electrochemical measurements of pure Mg and WE43 samples immersed in α-MEM + 10% FBS + 1% P/S under cell culture conditions (37oC, 5%CO2, 95% controlled humidity). a) OCP recorded for 6 h; b) Nyquist plot recorded after 1 and 6 h of immersion; c) Blode plots recorded after 1 and 6 h of immersion, and d) Electrical equivalent circuit (EEC) used to fit EIS spectra shown in b) and c).

Thus, to provide a detailed information about the corrosion response of the investigated materials, the corrosion for both samples was calculated using the simplified equation provided based on EEC shown in Figure 3.3d:

$$\frac{1}{R_p} = \frac{1}{R_{ct}+R_f} + \frac{1}{R_L} \qquad (3.2)$$

As shown in Table 3.2, the apparent corrosion rate for Mg after 1 h of immersion was higher than the corrosion rate calculated for WE43. With the extension of immersion time, the reverse trend occurred, and the apparent corrosion rate for Mg samples decreased twice, while WE43 increased 3 times.

Table 3.1. The electrochemical parameters obtained from electronic equivalent circuit fitting (EEC shown in Figure 3.3c).

Material	R_s (Ω cm^2)	R_{ct} (Ω cm^2)	Q_{ct} (Ss^a·cm^{-2}) X 10^{-5}	n_1	R_f (Ω cm^2)	Q_f (Ss^a·cm^{-2}) X 10^{-5}	n_2	L (H·cm^2)	R_L (Ω cm^2)
after 1 hour of immersion									
Mg	18 ± 2	2839 ± 110	3.0 ± 0.1	0.77 ± 0.01	2081 ± 123	81.5 ± 2.2	0.54 ± 0.01	2954 ± 171	847 ± 22
WE43	12 ± 1	1801 ± 57	4.7 ± 0.1	0.79 ± 0.01	188 ± 11	16.9 ± 1.0	0.58 ± 0.01	135 ± 17	2719 ± 76
after 6 hours of immersion									
Mg	18 ± 1	3633 ± 110	4.9 ± 0.2	0.77 ± 0.01	162 ± 6	7.1 ± 0.3	0.56 ± 0.01	1776 ± 111	653 ± 32
WE43	13 ± 1	960 ± 23	3.9 ± 0.1	0.91 ± 0.01	218 ± 15	9.2 ± 0.3	0.52 ± 0.02	1992 ± 97	550 ± 22

Table 3.2. The reciprocal of linear polarization ($1/R_p$) calculated based on EIS fitting shown in Table 4.1.

Material	$1/R_p$ after 1 hour of immersion ($\times 10^{-4}$)	$1/R_p$ after 6 hours of immersion ($\times 10^{-4}$)
Mg	14 ± 0.2	8 ± 0.1
WE43	9 ± 0.1	27 ± 1.1

3.3.3. Dynamic fluctuations of pH and osmolality

The pH and osmolality were determined during the direct cell culture experiment, as shown in Fig. 4. The pH values ranged from 7.6 to 8.2 for both materials without and in the presence of cells in monoculture and coculture (Figure 3.4a-b). Regardless of the cell culture groups, higher pH was observed for Mg compared to WE43 after 3 and 7 days of incubation (compare Figure 3.4a and Figure 3.4b). By 10 days, the pH for Mg and WE43 was comparable, while by day 14, WE43 showed higher pH values. Consistent and steady osmolality values ranging from 0.303 Osm/Kg to 0.309 Osm/Kg) were observed for Mg specimens when incubated with OC and OB monoculture, regardless of the experiment´s duration (Figure 3.4c). Slightly higher osmolality was recorded for Mg in the presence of OB-OC coculture at 7 days. The osmolality values for WE43 ranged from 0.309 Osm/Kg to 0.333 Osm/Kg. For this alloy, the osmolality rose with extended incubation time with and without the presence of cells (Figure 3.4d).

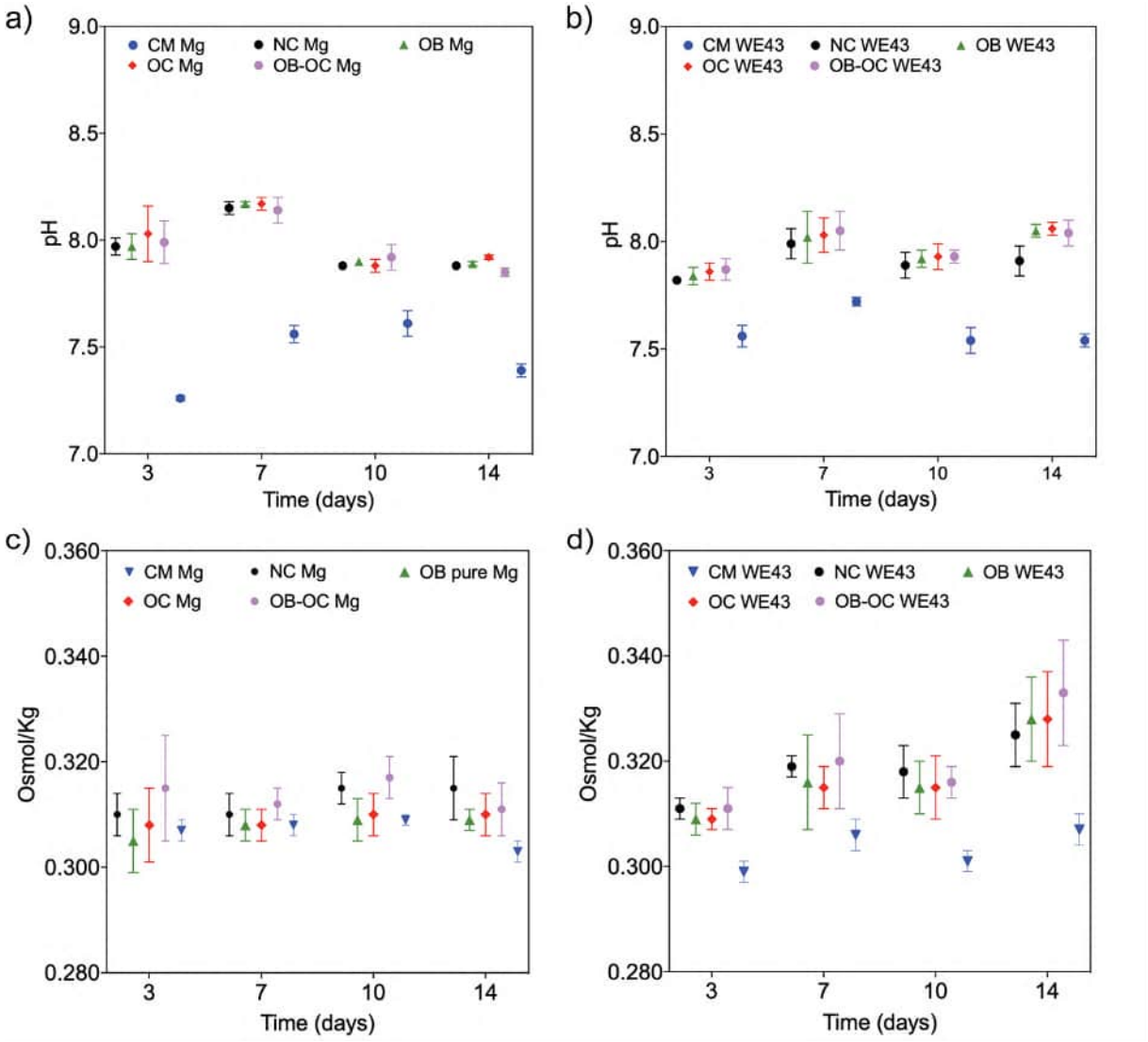

Figure 3.4. Degradation parameters for Mg and WE43 during the *in vitro* direct cell culture in monoculture and coculture conditions. a) pH of the Mg group, b) pH of the WE43 group, c) Mg osmolality, and d) WE43 osmolality. All measurements were recorded at 3, 7, 10, and 14 days. (n = 4/time point/group). Data presented as mean ± standard deviation. NC (No cells), OB (Osteoblasts), OC (Osteoclasts), OBOC (coculture Osteoblast-Osteoclast), CM (culture medium control without material).

3.3.4. Mg degradation in direct contact with OB, OC in monoculture and coculture

Fluorescence microscopy images obtained from LIVE/DEAD staining after 7 and 14 days of OB and OC cells mono and coculturing on Mg and WE43 are presented in Figure 3.5a and Figure 3.5b, respectively. LIVE/DEAD images taken from glass control are displayed in Figure S3.1. After 7 days of cell culture, more viable OB (green fluorescent staining) were observed on Mg compared to the WE43 group. In contrast, comparable viable cells were observed on each Mg surface for the other cell conditions at 7 and 14 days. Moreover, only a few dead cells (red fluorescent staining) were detected on each Mg substrate, regardless of the incubation time. There was no obvious difference in the susceptibility of the different cell types. To

characterize cell interaction with the Mg samples, OB and OC were cultured in monoculture and coculture on the Mg substrates, and their morphological appearance was evaluated using fluorescence staining of cytoskeleton compartments (Figure 3.5, Actin-DAPI) and SEM (Figure 3.6). After 7 and 14 days of monoculture and coculture, elongated OB cells were well spread on the Mg surface (Figure 3.5, Actin-DAPI panel). OC-like cells (highlighted by yellow dotted circles or yellow arrowheads in the coculture group images in the Actin-DAPI panel in Figure 3.5a) were observed as rounded multinucleated cells at 7 days with few multinucleated (blue) TRAP (green) expressing cells (white arrowheads in Figure 3.5a). On the WE43 substrate, in contrast, although OBs are visibly well spread after 7 and 14 days, the actin structure is less developed after 7 days of OB monoculture. In contrast, better spread and elongated morphology were observed in OB monoculture after 14 days and coculture at both time points. OC-like cells on WE43 appeared as small multinucleated cells. They only lightly expressed TRAP after 14 days of culture (OC in coculture denoted by yellow arrowheads in the Actin-DAPI panel in Figure 3.5b).

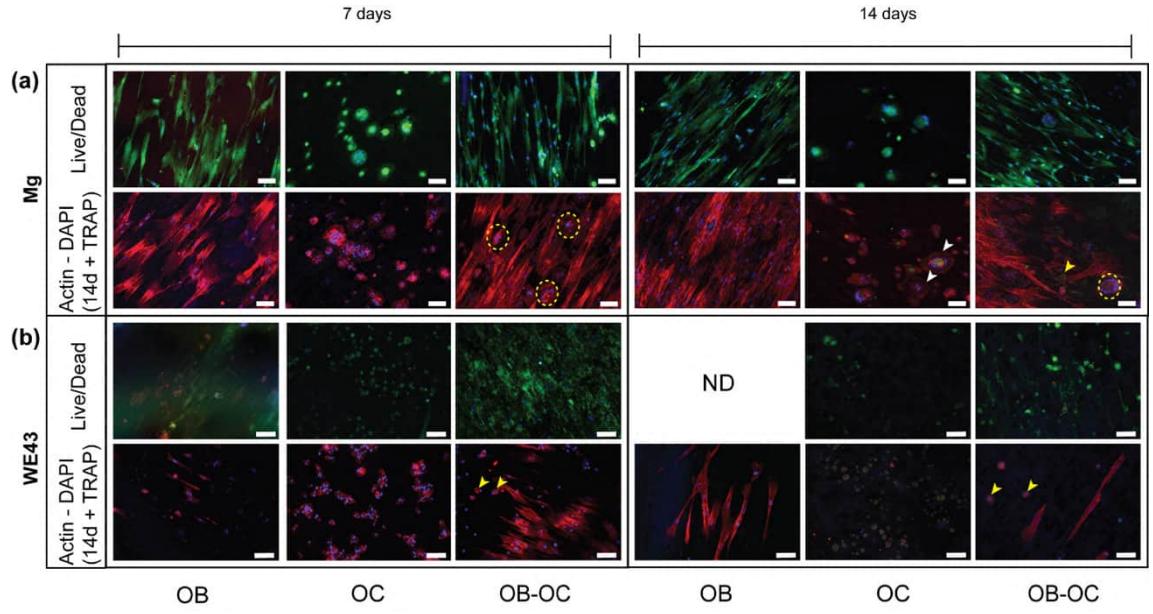

Figure 3.5. Fluorescence microscopy of the cell viability and morphology on Mg (a) and WE43 (b) substrates after 7- and 14- days. In the Live/Dead panels, live cells – green, and dead cells - red. ND = not determined. In the Actin-DAPI-TRAP panels, Actin - red, cell nuclei - blue, and tartrate-resistant acidic phosphatase (TRAP) expression in osteoclasts (OCs) at 14 days - green. Yellow arrowheads or yellow-dotted circles denote Osteoclast multinucleated cells. OB: osteoblast, OC: osteoclast, OB-OC: osteoblast-osteoclast coculture. Scale bar = 100 μm.

While in Figure 3.5, the viability of cells was imaged, with SEM, the cell morphology can be seen in detail in Figure 3.6 adjacent to the Actin visualization. The Mg specimens were taken to compare the feasibility and different outcomes between CPD and FD on the morphological changes of cells during the preparation of biological specimens for electron

microscopy. SEM images were taken at various magnifications after 7- and 14- days of monoculture and coculture. On the Mg surfaces prepared by CPD, cell spreading, and proliferation of differentiated OB and cell attachment of OC were observed after 7 and 14 days of cell culture (Figure 3.6a, third row).

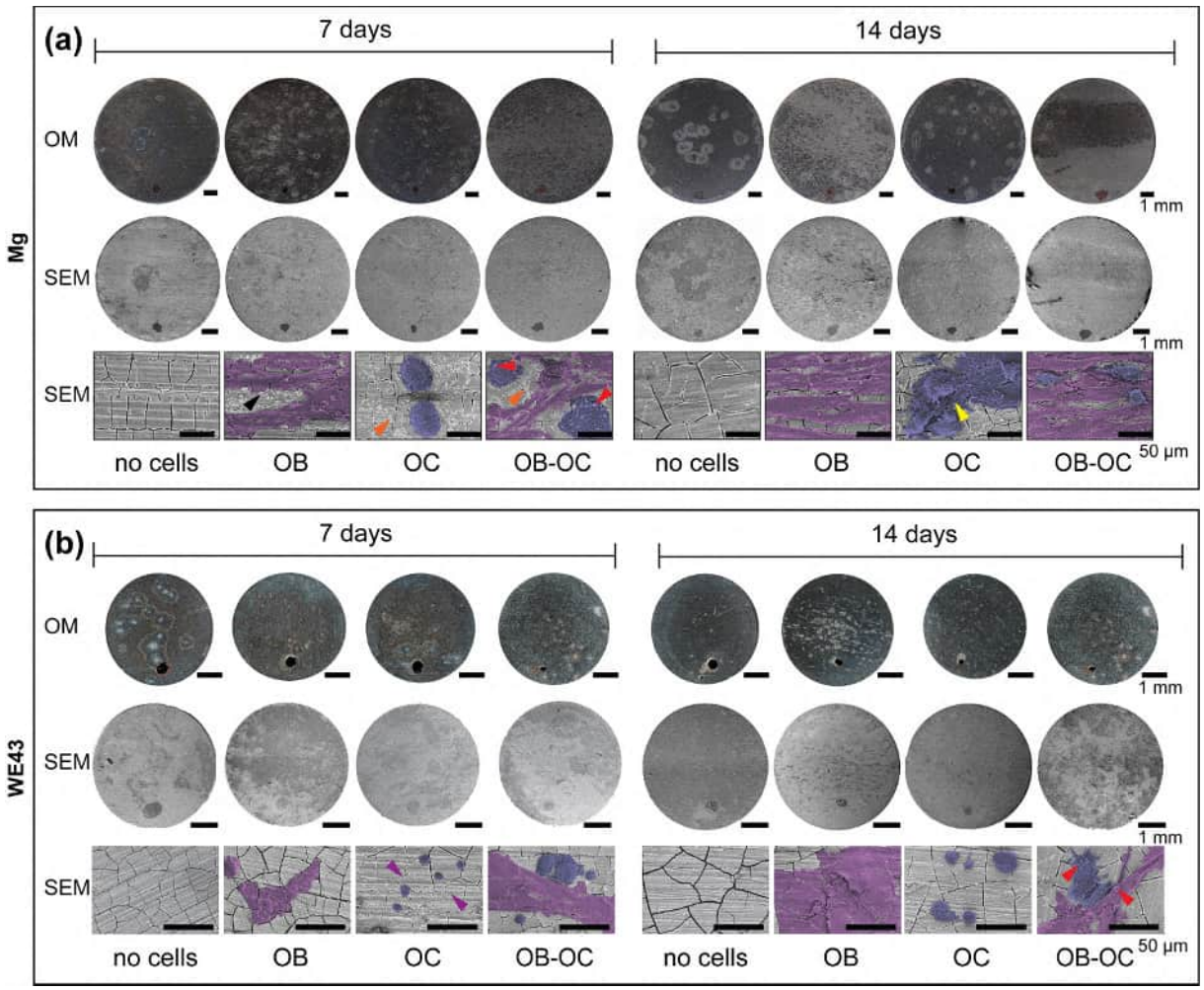

Figure 3.6. Representative stereomicroscope and color-enhanced SE-SEM images of the various cell culture conditions on Mg (a) and WE43 (b) after 7- and 14-day of cell culture. *First rows* in (a) and (b): The overall stereomicroscope images (OM) of the Mg materials, *second rows* in (a) and (b): The overall secondary-electron images (SE) SEM of both Mg discs and *third rows* in (a) and (b): high magnification SE images displaying the cell morphology. The black spots in (a) and (b) were marked to define a coordinated position. OB: osteoblast, OC: osteoclast, OB-OC: osteoblast-osteoclast coculture, osteoblast-cell layer (dyed purple), osteoclast-like cells (dyed blue), osmium particles (black arrow), rounded corrosion products (orange arrows), blebs (red arrows), cytoplasmatic extensions (yellow arrow), and some flat filopodia (purple arrows).

After 7 days of cell culture, some osmium particles (Figure 3.6a, black arrow, EDX point analysis in Figure S3.2), and rounded corrosion products (Figure 3.6a, orange arrows) were observed on the Mg surface. OB extensively proliferated as elongated cells, forming multiple layers covering the Mg surface. OC-like cells displayed their typical plump morphology, with some blebs (Figure 3.6a, red arrows), characteristically dorsal villus-like processes, and

adhesion to the Mg surface with distinct cytoplasmatic extensions (Figure 3.6a, yellow arrow). After 7 days, the OC adhered well to the Mg surface, while after 14 days, the OC showed reduced size and was found on the OB cell layers in the coculture group.

In contrast, the FD method did not preserve the cell morphology on Mg specimens, as shown in the SEM images in Figure S3.3. OB layers appeared to have small, isolated cracks and detach easily. In the monoculture, remnants of OC-like cells were observed where their typical surface morphology was lost. In both monoculture and coculture, OB and OC-like cells displayed increased blebbing. Consequently, since CPD better preserved the cell morphology, WE43 specimens were only prepared by CPD for SEM observations. Concerning cell attachment on WE43 (Figure 3.6b), fewer OB cells were attached to the disc surface. In contrast, OC-like cells exhibited a smaller size, fewer microvilli processes, and a flatter morphology than those observed on the Mg specimens, with flat filopodia edges (Figure 3.6b, purple arrows). Interestingly, a more variable morphology of OC-like cells with more filopodia was observed in the coculture compared to monoculture. In addition, some blebs were also observed on the surface of OB and OC. No resorption pits were detected by SEM analysis in Mg or WE 43 specimens in the presence of OC-like cells.

3.3.5. Corrosion layer characterization by FIB/SEM/EDX beneath the cells in monoculture and coculture

Figure 3.7 displays FIB/SEM images of the cell-corrosion layer interface after 7 (Figure 3.7a) and 14 (Figure 3.7b) days of immersion and corresponding EDX line scan charts from the Mg group. Corrosion layers of ~4 µm thickness were observed after 7 days in all cell culture conditions, increasing to ~5.8 µm thickness after 14 days with no statistically significant differences between cell culture groups or time intervals (Figure S3.4). The corrosion layers formed on all Mg cell groups were primarily composed of oxygen (O), magnesium (Mg), phosphorus (P), and calcium (Ca), as determined by the EDX line and point (Figure S3.5a,c) analysis. However, despite the formed corrosion layers comprising the same elements, the elemental distribution varied between cell culture groups and time points. After 7 days of direct cell culture, higher O concentration (in weight percent, (wt.%)) was noticed throughout the corrosion layer in the no cells group. In contrast, a higher P and Ca wt.% content were observed in the outer-middle region beneath the OC and OB-OC coculture, respectively. After 14 days, the corrosion layer formed under OC contained a slightly higher and uniform oxygen concentration distribution. Similarly, P and Ca were slightly higher in content and

homogeneously distributed throughout the corrosion layer formed beneath the OB-OC coculture.

Similarly, Figure 3.8 displayed FIB/SEM images of the cell-corrosion layer interface after 7 (Figure 3.8a) and 14 (Figure 3.8b) days of immersion and corresponding EDX line scan charts from the WE43 alloy group. It can be noticed that the corrosion layer thickness was 2-fold thicker after 14 days compared to the 7 days of cell culture and, in comparison, to the Mg group. The thickness was irrelevant to the presence of cells, with no statistically significant differences between groups and Mg materials (Figure S3.4).

As determined by EDX analysis (Figure 3.8 and Figure S3.5b,d), the corrosion layers formed on all WE43 alloy cell culture conditions were mainly composed of O, Mg, P, and Ca with traces of sodium (Na), Zn, Y, Zr, and RE. For comparison with the Mg cell groups, the line scans of O, Mg P, and Ca were displayed in Figure 3.8, while the EDX point analysis and line scan charts for the trace elements are presented in Figure S3.5b,d, and Figure S3.6, respectively. After 7 days of cell culture, a higher O concentration homogeneously distributed in the corrosion layer was observed under OC monoculture, while a slightly increased content of P and Ca was noticed in the outer region of the corrosion layer beneath the OB-OC coculture. After 14 days, The O concentration was similar throughout the corrosion layer in the absence of cells and in the presence of OC. In contrast, the Ca and P content was slightly increased in the middle region of the corrosion layers in the OB-OC coculture. Compared to the other cell culture conditions, the corrosion layer formed in the OB monoculture had the lowest O, P, and Ca concentrations.

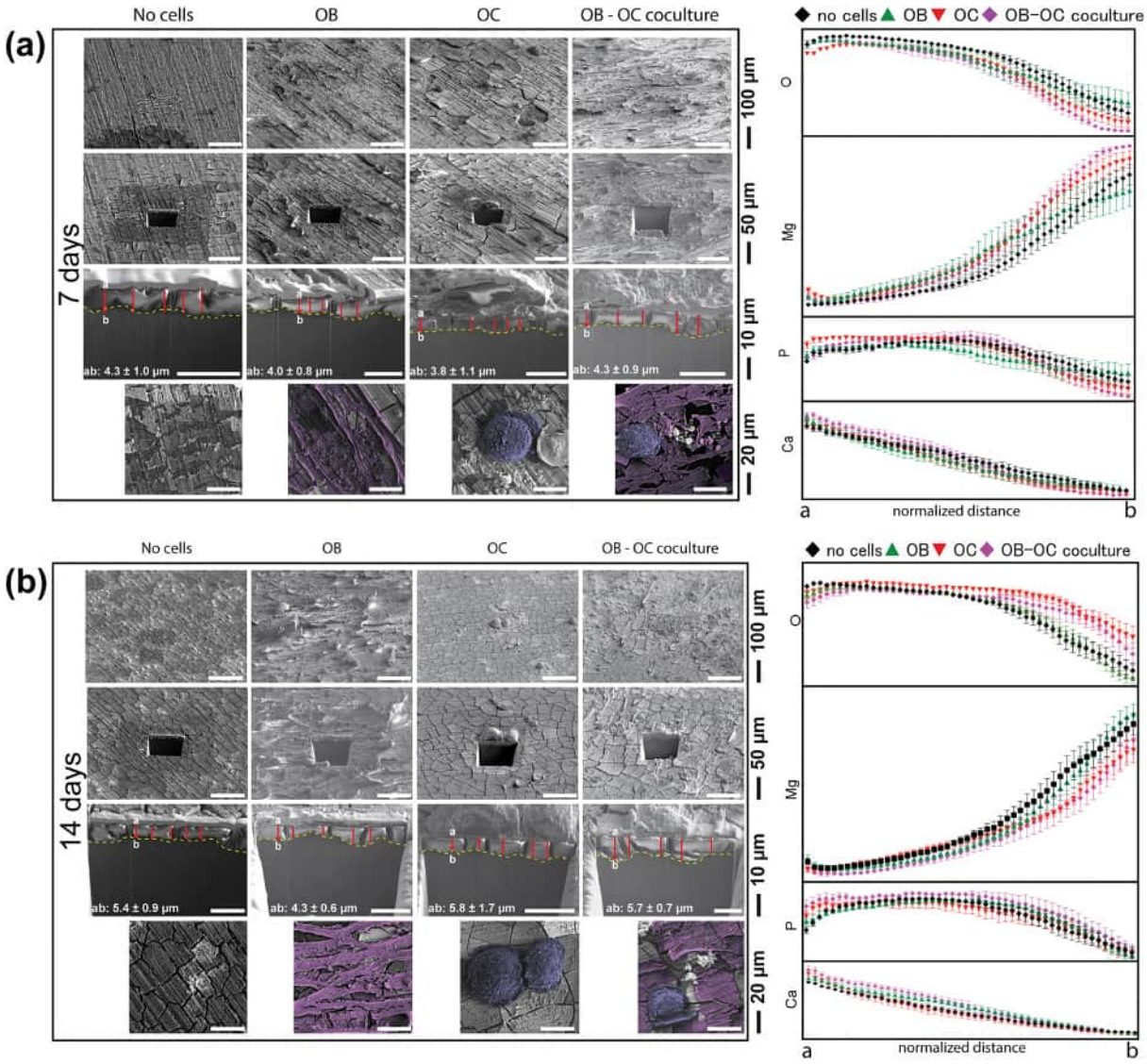

Figure 3.7. FIB/SEM/EDX images of the corrosion layer interface for Mg after 7- and 14- days of cell culture with and without the presence of cells. *First rows* in (a) and (b): Plan-view (tilted surface) of selected ROI before FIB, *second rows* in (a) and (b): plan-view of the processed cross-sections by FIB, *third rows* in (a) and (b): cross-sectional SE-SEM micrographs; corrosion layer (denoted by yellow dotted lines). EDX line scans (denoted by red arrows and lines) performed from the outer to the inner layer of the corrosion layer; *fourth rows* in (a) and (b) high magnification color-enhanced SE-SEM images of the selected ROI for FIB. The line charts (on the right of FIB/SEM images present the EDX line scan measurements of the corrosion layer on the processed FIB cross-sections normalized by distance starting from the outer (a) to the inner (b) region of the corrosion layers. Lines scan data presented as mean ± standard error of the mean (SEM) (n = 5-line scans/sample/cell culture condition/timepoint from 3 independent samples). OB: osteoblast, OC: osteoclast, OB-OC: osteoblast-osteoclast coculture, osteoblast-cell layer (dyed purple), osteoclast-like cells (dyed blue).

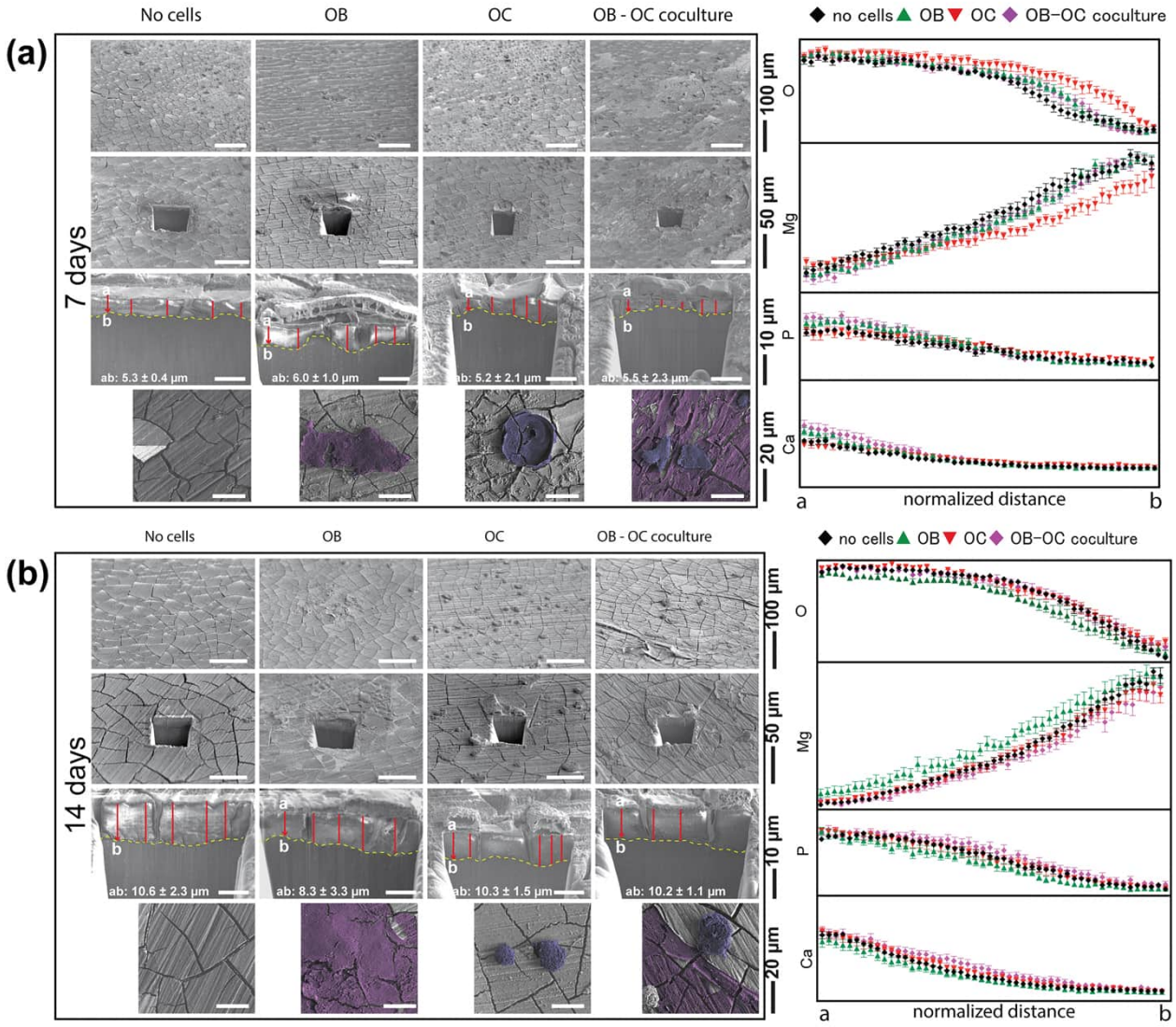

Figure 3.8. FIB/SEM/EDX images of the corrosion layer interface for WE43 alloy after 7- and 14- days of cell culture with and without the presence of cells. *First rows* in (a) and (b): Plan-view (tilted surface) of selected ROI before FIB, *second rows* in (a) and (b): plan-view of the processed cross-sections by FIB, *third rows* in (a) and (b): cross-sectional SE-SEM micrographs; corrosion layer (denoted by yellow dotted lines). EDX line scans (denoted by red arrows and lines) performed from the outer to the inner layer of the corrosion layer; *fourth rows* in (a) and (b) high magnification color-enhanced SE-SEM images of the selected ROI for FIB. The line charts (on the right of FIB/SEM images present the EDX line scan measurements of the corrosion layer on the processed FIB cross-sections normalized by distance starting from the outer (a) to the inner (b) region of the corrosion layers. Lines scan data presented as mean ± standard error of the mean (SEM) (n = 5-line scans/sample/cell culture condition/timepoint from 3 independent samples). OB: osteoblast, OC: osteoclast, OB-OC: osteoblast-osteoclast coculture, osteoblast-cell layer (dyed purple), osteoclast-like cells (dyed blue).

The Ca/P ratio in the outer region of the corrosion layers ranged from 0.78 to 1.02 in the Mg group, with the highest Ca/P ratio in the coculture group at both time points (0.96 and 1.02 after 7 and 14 days of culture, respectively, Figure S3.5e-f). In the WE43 group, the Ca/P ratio ranged from 0.23 to 0.88, which was lower compared to the Mg group at both time points. The OB monoculture group exhibited the lowest Ca/P ratio (0.45 and 0.65 after 7 and 14 days of

culture, respectively), while the OC monoculture and no cells group exhibited a similar ratio (0.88 and 0.86 after 14 days, respectively). For further comparison with EDX results, a simulated Hydra-Medusa diagram was calculated to predict the corrosion products formed on the Mg and WE43 substrates. The predicted compounds as the function of pH for the Mg and WE43 alloy after 14 days fitted similarly; therefore, one predicted fraction diagram is shown in Figure S3.7. In α-MEMc, within the pH range throughout the cell culture, the corrosion products comprised mainly of $CaMg(CO_3)_2$.

3.4. Discussion

Mg and its alloys are being investigated as absorbable metals for temporary orthopedic implants. They have demonstrated biocompatibility and mechanical properties that closely resemble those of human cortical bone, rendering them highly promising biomaterials in the field of orthopedics. It is important to examine the corrosion performance and the material-cell interaction to predict the behavior of Mg-based implants in the biological environment. When Mg materials are immersed in aqueous solutions, a layer of degradation products is formed [53]. The corrosion layer acts as a boundary between the bodily fluids and the surface of the Mg implant [181]. Previous research has primarily investigated the interaction between cells and Mg-based absorbable materials using either Mg extracts or single monoculture *in vitro* experiments. However, it is imperative to establish *in vitro* coculture models incorporating OB and OC cells, given the importance of their interaction in bone remodeling. Therefore, the present study assessed the surface morphology and dynamic changes in composition and thickness of the corrosion layers formed on pure Mg and WE43 alloy influenced by direct monoculture and coculture of OB and OC cells.

3.4.1. Surface preparation

The surface properties of both Mg materials were investigated based on SEM/EDX, profilometry, and surface wettability analysis. These parameters are crucial in compatibility, better protein absorption, and cell activity in direct contact with the host tissue surface *in vivo* [60,265]. Upon examination of the SEM and 3D roughness images, it was noted that both Mg materials displayed a pattern of horizontal grooves and smooth surfaces. A smooth surface benefits corrosion resistance due to a relatively homogeneous structure [66]. In addition, both Mg materials exhibited hydrophilic surfaces, with a contact angle ranging from 20^{o} to 35^{o}. The contact angle of the WE43 alloy, as determined by our research, closely resembled the one

reported by Jin et al. [66]. It has been demonstrated that a contact angle between 35° and 80° may benefit applications such as bone regeneration [66,205]. When the contact angle exceeded 50°, the AZ31B Mg alloy had lower wettability and limited the cell growth of MC3T3 cells [266]. Conversely, when the contact angle was below 40° on the AZ31B-hydroxylapatite composite, it encouraged cell spreading, influenced by the enhancement of the surface hydrophilicity caused by hydroxyapatite coating. In contrast, Bonyadi et al. [163] found a lower rate of MC3T3 dead cells on XHP-Mg samples with a hydrophobic surface (CA ~131°). This wide variation in contact angles across various Mg alloys highlights the influence of surface wettability, along with other surface properties, such as surface roughness, in determining the biological response at the cell/material interface. This emphasizes the importance of tailoring Mg material properties according to the intended clinical application.

3.4.2. Corrosion behavior of pure Mg and WE43 alloy

It is important to highlight that both Mg materials' corroded surfaces lack crystal formation, which could hinder cell adhesion. However, the dissimilarities in cell attachment observed between both Mg materials may be attributed to their contrasting degradation performance. In our previous work [267], it was found that the corrosion rate of the WE43 alloy was nearly twice as high as that of pure Mg (0.23 ± 0.07 mm/year and 0.14 ± 0.01 mm/year, respectively) when immersed in α-MEMc for 14 days. However, after 28 days, no notable disparities were observed in the corrosion rates between the two materials (WE43: 0.16 ± 0.02 mm/year and pure Mg: 0.14 ± 0.05 mm/year). Furthermore, a high corrosion rate was also observed with other WE43 alloys [235,268,269]. As per our results, both materials exhibited corrosion rates lower than 0.5 mm/year, a threshold necessary for biodegradable implants to ensure an effective lifetime [270]. These results and the electrochemical tests agree with our osmolality measurements, indicating a higher osmolality in the WE43 groups than in the Mg groups after 14 days. It was previously stated that the presence of cells and the extracellular matrix they produce may be a physical barrier and modify the interface's microenvironment, resulting in a slow substrate degradation [164,247]. Our osmolality results indicated that the presence of cells led to a slightly decreased release of degradation products compared to materials without cells. This proves that the presence of cells slowed down the corrosion of the Mg materials, as demonstrated in Figure S3.8 for the WE43 alloy. However, due to the lack of homogeneous spread of cells in the WE43 alloy, certain surface areas were more susceptible to corrosion, leading to varying corrosion patterns over time [207] as denoted by the high standard deviation. The EIS results clearly indicate that at the beginning of immersion, WE43 had higher corrosion

resistance than Mg samples; however, with the test extension, it significantly decreased. This data agrees with osmolality results. The EIS data also demonstrated that more stable corrosion products are formed on the Mg than the WE43 surface, and its susceptibility to localized corrosion is lower. Those differences may be related to the microstructural heterogeneity, which in the case of WE43 at short immersion time gave the possibility of the Mg species being adsorbed, while with the time extension, it tends to suffer from localized corrosion. The opposite situation was observed in the case of the Mg samples. At the beginning of immersion, the dissolution reactions overwhelmed film formation reactions. At the same time, with the time extension, the adsorbed species formed a more stable film on the Mg surface, allowing better surface protection. Therefore, the degradation of the WE43 alloy is time-dependent on the protective corrosion layer formed during the immersion test, as demonstrated by Esmaily et al. [271] in WE43 alloys manufactured by selective laser melting and exposed to 0.1 M NaCl solution.

3.4.3. Cell adhesion and spread on the Mg substrates

Since the influence of cells on the degradation behavior of bioabsorbable Mg alloys is an important but relatively understudied topic [164,244], we conducted *in vitro* experiments using monoculture and coculture models involving pre-differentiated OB and OC cells. Direct cell culture on Mg materials employing bone cells closely mimics *in vivo* scenarios [272] and can offer valuable insights regarding material-cell interaction [243]. The crosstalk between OB and OC during the initial bone formation phase is vital for bone formation and absorption [272]. Our findings revealed successful OB and OC cell attachment and viability on both Mg materials. However, changes in cell morphology and attachment in response to the various Mg substrates appeared to be influenced by the corrosion of the substrates, which correlates with the findings of Brooks et al. [207]. While both pre-differentiated OB and OC cells adhered to the Mg materials, the cell density and spread exhibited variations after 7 and 14 days of cell culture. OB exhibited stronger adhesion on the Mg surface, resulting in higher cell density and confluency after 14 days of monoculture and coculture compared to the WE43 group. Similarly, Agha et al. [162] has shown that OB´s cell attachment and proliferation were successful on pure Mg substrates, Mg-2Ag, and Mg-10Gd alloys. Conversely to our findings, Lee et al. [273] suggested that pure Mg samples are unsuitable for long-term direct integration with stem cells during *in vitro* cell viability tests because of their fast corrosion rate. Due to the already high cell density in the coculture at the WE43 surface observed after 7 days, it might

be hypothesized that the cell monolayer was unstable enough to attach at the material surface for 14 days and lost its integrity.

Meanwhile, the OC cells displayed more filopodia, evidencing their adherence to the Mg surface as opposed to what was observed on the WE43 alloy. The filopodia formation enhances cell attachment, suggesting that the cells recognize the morphology of the substrate. This allows the cell-material interaction and proliferation of the cells [274]. Although fluorescence microscopy displayed positive staining for differentiated OC, non-resorption pits were observed in the presence of OC in monoculture or coculture in both Mg group surfaces. The reason for that may be related to the detrimental effect that high concentrations of Mg and corrosion byproducts can have on OC adhesion [228] and mature OC cell function [230], leading to a decrease in cell metabolism as previously demonstrated [275]. In addition, since OC are terminally differentiated cells, it is likely that the pre-differentiated cells did not fully develop their cellular activities under *in vitro* conditions, inhibited by high Mg concentrations, which was particularly evident in the WE43 alloy [228]. In addition, the pH can also have an impact on the OC activity. The findings of our study indicated that the pH levels in both monoculture and coculture exhibited periodic fluctuations within the range of 7.6 to 8.2. It has been demonstrated that when the pH level exceeds 7.5, the number of OC and their function tends to decrease [276]. Additionally, the high P ions in the corrosion layer in OC monoculture observed on the Mg specimens after 7 days of cell culture could inhibit OC activity and explain the absence of resorption pits, as has been previously demonstrated [277]. Interestingly, within the WE43 group, OC-like cells exhibited a cell morphology with larger cell diameter and more filopodia in the coculture than in monoculture, consistent with previous findings [228]. This may be attributed to the Ca/P enrichment observed in the coculture's outer region of the corrosion layer. It has been demonstrated that an appropriate Ca/P ratio promotes signaling pathways for OC differentiation, leading to enhanced bone osseointegration *in vivo* [277].

While previous researchers employed diverse cell types, *in vitro* parameters, and different WE43 alloys containing Y and rare-earth elements, which unenabled straight comparisons, our findings about the dissimilar cell attachment observed on the WE43 align with some of these studies, as discussed below. Dvorsky et al. [235] observed an increased corrosion rate and reduced viability of L929 cells on the surface of a WE43 alloy after 24 h of cell culture in MEM + 10% FBS. Jin et al. [66] noted decreased cell adherence and spreading of MC3T3-E1 preosteblast cells on the bare WE43 (Mg-Y-Nd-Gd) alloy after incubation for 5h in DMEM supplemented with 10% FBS. Lukyanova et al. [278] noticed that a WE43 (Mg-Y-Nd-Zr) alloy underwent rapid degradation, releasing a substantial amount of hydrogen. This degradation

process hindered the attachment of erythrocytes and multipotent mesenchymal stromal cells to the alloy surface after 5 days of cell culture. In a similar manner, Anisimova et al. [236] found decreased viability, adhesion, and proliferation of mouse bone marrow mesenchymal multipotent stromal cells when cultured on the surface of homogenized WE43 (Mg-Y-Nd-Zr) alloy for 5 days in supplemented DMEM. All these results can be attributed to the potential cathodic effect of the intermetallic phases and uneven dispersion of REE in the WE43 alloys, resulting in the increased degradation of the WE43 alloys *in vitro* [235,279]. The presence of these intermetallic phases in Mg alloys is recognized to increase the degradation rate with more intense hydrogen release, which may disturb the seeded cells [235].

In contrast, Byun et al. [274] found no disparities in the adhesion of MC3T3-E1 cells when they were directly cultured on pure Mg and WE43 alloy for 24h. Yamamoto et al. [243,280] also noticed cell spread and proliferation of L929 and SaOS-2 cells on pure Mg, AZ31, and Mg-Zn-Mn alloys. Zhang et al. [164] reported that macrophages (RAW267.7 cell line) exhibited good viability when cultured on a Mg-Nd-Zn-Zr alloy. Additionally, they observed that the alloy underwent uniform corrosion after being exposed to cell culture for 7 days. All these results indicate that the cell behavior differed depending on the Mg materials tested *in vitro* [99,226]. The hydrogen evolution and the released degradation products from the corroded Mg devices may have an ambivalent impact on cell adhesion and proliferation in direct contact with Mg substrates.

3.4.4. Influence of OB and OC cells on the composition of the corrosion layer of Mg substrates

Previous studies have indicated that cells could increase the thickness of the corrosion products/layer, influencing the corrosion behavior of Mg alloys [238]. Our results revealed that both Mg materials developed a corrosion layer thickness that progressively increased on both Mg materials. However, the corrosion layer formed on the WE43 groups, regardless of the presence of the cells, was thicker than those formed on the Mg group. Willumeit et al. [161] showed similar findings when cultured L929 cells on pure Mg. After 14 days, they observed comparable corrosion layer thicknesses with and without cells (~9 μm and ~7μm, respectively). In contrast, Zhang et al. [164] found that while RAW264.7 macrophage cell body did not affect the local thickness, the entire corrosion layer formed on JDBM alloy was almost 3-fold thicker when the cell density increased after 7 days of cell incubation. Bonyadi et al. [163] also noted a variety of corrosion layer thicknesses (ranging from 8 to 25 μm) on pure Mg, Mg-2Ag, and ultrahigh-purity Mg (XHP-Mg) after directly exposing them to MC3T3 cells for 12 days. Agha

et al. [162] described contrasting results regarding the influence of the cells at the degradation interface. The corrosion layer exhibited thinner thickness when human primary osteoblast cells (hOBs) were present on Mg-10Gd alloy (~13 µm), as compared to pure Mg and Mg-2Ag (~22 µm). This wide range of corrosion layer thicknesses can be ascribed to the various *in vitro* tested Mg substrates, their chemical composition, microstructures, and resulting degradation mechanisms of the Mg alloys. Additionally, the variation in thicknesses may be influenced by different cell lines and cell densities employed in prior studies.

The corrosion product layers formed on the Mg and WE43 specimens were mostly composed of O, P, Ca, and Mg with traces of the alloying elements present in the WE alloy. Carbon (C) was not considered for the EDX semiquantitative analysis because of the carbon-induced contamination during FIB/SEM/EDX [281,282]. However, the chemistry of these layers exhibited differences between monoculture, coculture, and Mg substrates. Our findings indicate that after 14 days, the coculture's outer part and middle zones of the corrosion layer were enriched in P and Ca on the Mg samples (Fig. 9). This suggests the presence of calcium phosphate compounds in these regions, which agrees with previous *in vitro* [162–164,254] and *in vivo* [175,179,180,183,283] studies. Unlike our findings, Agha et al. [162] observed a high concentration of Ca and P in the corrosion layer adjacent to the hOBs cells rather than beneath them. Bonyadi et al. [163] only noted this trend, particularly when MC3T3-E1 cells were cultured on an XHP-Mg substrate. In contrast, only the outermost part of the corrosion layer on WE43 alloy displayed this enrichment of Ca-P in the coculture group after 7 days. Interestingly, besides the presence of the alloying elements, traces of Na were found in the WE43 groups after 7 days. This suggests that additional new complex phases may be formed during the degradation of the WE43 alloy [254], where the alloying elements can contribute to forming a protective corrosion layer containing REE and Y [284,285].

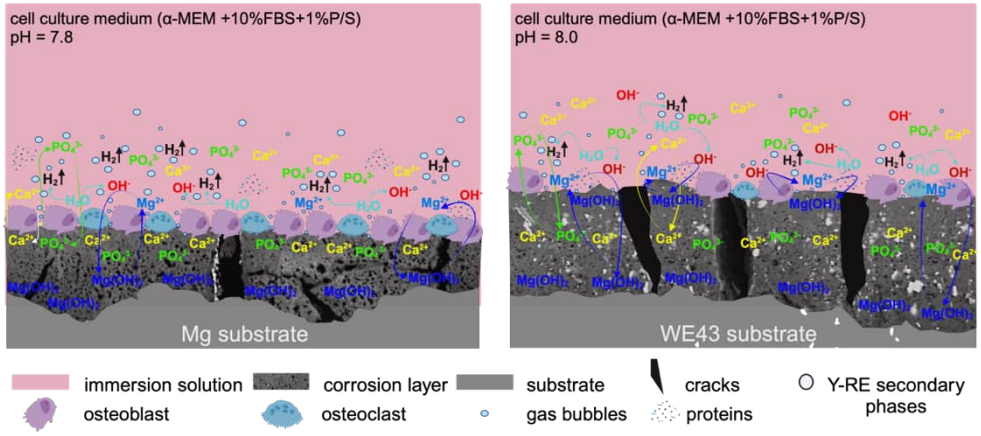

Figure 3.9. Schematic illustration of the *in vitro* degradation of Mg and WE43 samples after 14 days of OB-OC coculture.

Contrasting with the Mg coculture, the middle part of the corrosion layer in the coculture with the WE43 alloy showed increased Ca-P enrichment (Figure 3.9) after 14 days, consistent with a previous work [286]. This could be explained by the initial reactions between water molecules in the α-MEMc that react with the Mg surfaces, resulting in the formation of $Mg(OH)_2$ and H_2 release. Cl^- ions in the culture medium will form soluble $MgCl_2$ and OH^- ions, leading to continuous degradation. However, in the coculture, it can be speculated that the inherent tendency of the cell to secrete extracellular matrix may reduce the interaction at the interface between the culture medium and the Mg substrates [162]. Thus, as the degradation layer builds up, P and Ca ions gradually deposit from the α-MEMc onto the Mg surface. After 7 days of cell incubation, Mg and WE43 cocultures exhibited an uppermost corrosion layer rich in Ca-P. As corrosion proceeds and the incubation time increases, there is less diffusion of Ca-P ions toward the inner part of the corrosion layers, which are primarily composed of Mg/oxides and hydroxides. The well-spread OB and OC on the Mg surface form a physical barrier to the Mg samples. The regular medium changes also replenish the ionic compounds [284]. This provides nutrients for the cells and contributes to Ca and P ions, which precipitate on the Mg surface. Thus, the uppermost corrosion layer, which is rich in calcium phosphates, restricts mass transport, decreasing the corrosion of Mg specimens in the coculture group (Figure 3.9, left). In contrast, despite the precipitation of magnesium-calcium phosphate compounds on the WE43 alloy surface after 7 days in the coculture, the non-homogeneous cell attachment to the WE43 substrate caused a bigger surface area to be exposed to the culture medium (Figure 3.9, right). As a result, an increase of $Mg(OH)_2$ species occurs on the outermost surface. This could explain the accelerated degradation of the WE43 alloy after 14 days of exposure to α-MEMc. However, the presence of cells influenced the degradation of the WE43 alloy, resulting in its slow degradation, particularly evident in the coculture group. The Ca-P enrichment at the degradation interface noticed on the coculture of both Mg materials after 7 days of culture and on the Mg group after 14 days offers several benefits for bone applications such as enhanced biocompatibility [287], cell attachment [288], improved osseointegration [221,289], and enhanced corrosion resistance of the Mg implants [167,290]. Therefore, it can be inferred that the coculture of OB and OC cells influences the chemical nature of the corrosion layers that form on Mg materials, thereby modulating their cellular response at the degradation interface.

3.5. Conclusion

The comparison of pre-differentiated OB and OC in monoculture and coculture on two different Mg substrates revealed variations in cell spread and attachment, which differed depending on the Mg substrates. This study demonstrates a noticeable influence of coculturing OB and OC on the corrosion layer composition and corrosion rate compared to monoculture. Ca-P enrichment was observed in the outer-middle region of the corrosion layer but only in the coculture after 7 and 14 days on WE43 and Mg specimens, respectively. Further investigations in subsequent *in vitro* direct culture studies are required to elucidate how the OB-OC crosstalk alters the chemical composition of the corrosion interface, which is influenced by the different corrosion performance of the Mg materials. Although the WE43 alloy is recognized for its good corrosion resistance, the faster degradation performance observed *in vitro* may be attributed to the susceptibility of some Mg materials to medium changes performed in the *in vitro* tests [284]. Therefore, it is necessary to improve our *in vitro* coculture model by employing a continuous flow cell-culture system to closely mimic the biological environment. This could result in a more relevant correlation between the degradation performance of Mg alloys for biomedical applications *in vitro* and *in vivo*, thereby reducing the need for animal testing.

Supplementary materials

Table S3.1: Chemical composition of the Mg and WE43 alloy discs determined by optical spark emission spectrometry (OES)

Element (wt. %) / Material	Mg	Fe	Cu	Ni	Zn	RE	Y	Zr
Pure Mg	99.998	0.0021	0.0013	<0.0002	-	-	-	-
WE43	85.2 – 95.89	-	-	-	0.01-0.8	2.5 – 5	1.5 -5	0.1 – 2.5

Sample preparation for SEM imaging

Pure Mg specimens attempted two kinds of sample preparation for SEM observations: critical point drying (CPD) and freeze-drying (FD), while WE43 specimens were only prepared by CPD.

After the cell culture period of incubation, the Mg-cell specimens were chemically fixed in 2.5% glutaraldehyde solution, followed by a post-fixation in osmium tetroxide (OsO_4) and serial dehydration in 20%, 40%, 60%, 80%, and 100% isopropanol. Afterward, the samples were critically point-dried (Leica EM CPD030, Germany) and covered with a 10 nm gold layer (Leica AC200, Leica Microsystems, Austria).

The second sample preparation technique was based on freeze drying. This includes the Mg-cell specimens´ chemical fixation with 2.5% glutaraldehyde solution followed by freeze-drying with 0.01 mbar over 72h (alpha 1-2 LD plus, Martin Christ Gefriertrocknungsanlagen, Osterode, Germany).

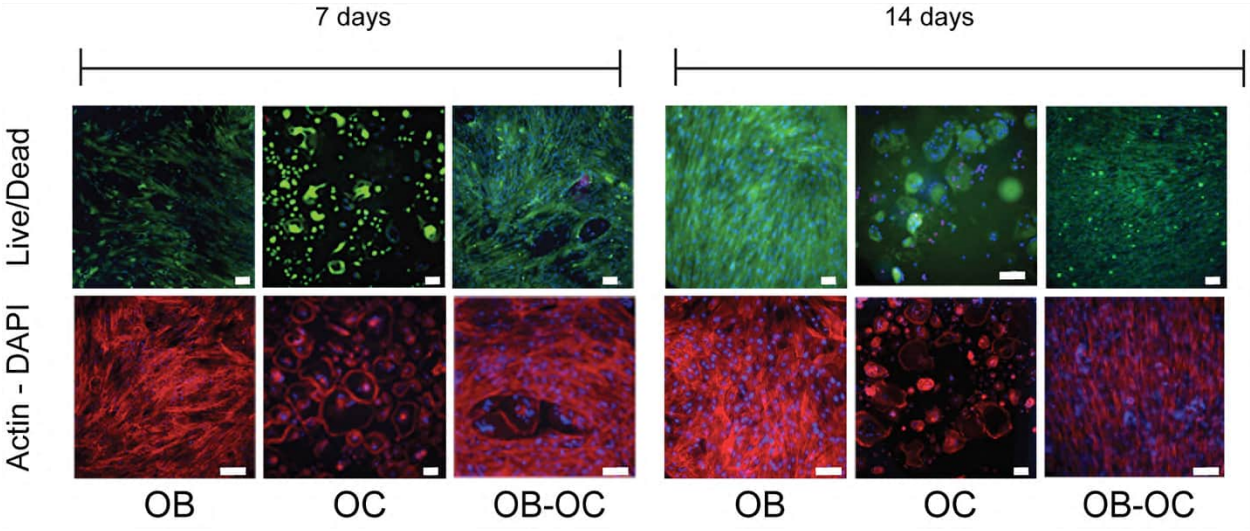

Figure S3.1. Fluorescence microscopy of the cell viability and morphology on glass substrates (after 7- and 14- days. In the Live/Dead panels, live cells are stained in green and dead cells in red. In the Actin-DAPI, the actin is stained in red, and cell nuclei are stained in blue. OB: osteoblast, OC: osteoclast, OB-OC: osteoblast-osteoclast coculture. Scale bar = 100 µm

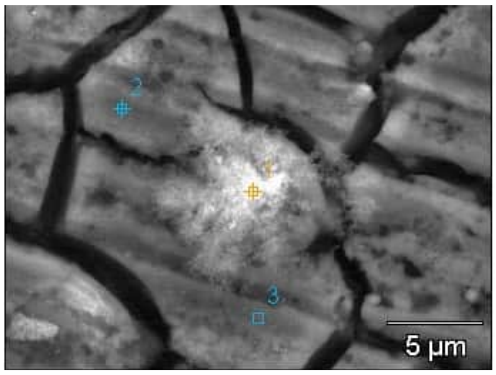

EDX (wt.%)

point	O	Mg	P	Ca	Os
pt1	45.3	8.5	10.6	12.0	23.7
pt2	45.2	17.8	19.5	17.5	-
pt3	52.2	10.9	17.7	19.2	-

Figure S3.2. EDX point analysis on the Mg specimen after 7 days of cell culture. It can be observed that the white porous particles on the Mg surface are osmium particles that remain after the sample preparation for SEM observations.

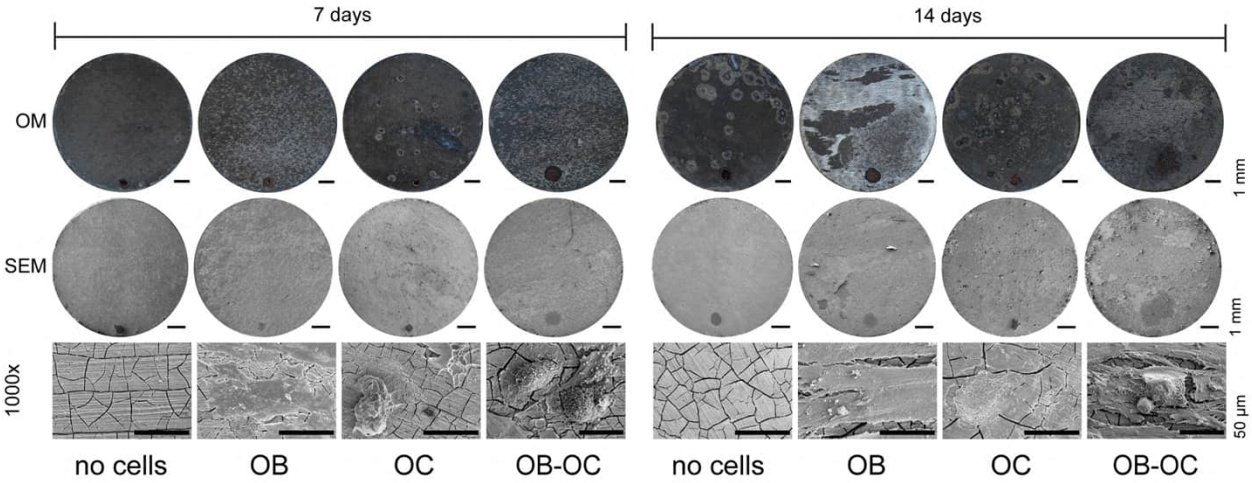

Figure S3.3. Representative stereomicroscope and SE-SEM images of the various cell culture conditions on the Mg samples after freeze-drying. *First row*: overall optical images of the Mg surface and the presence of cells denoted by white frames, *second row*: The overall SE-SEM image of the Mg specimens, and *third row*: higher magnification SE-SEM images displaying the cell morphology in monoculture and co-culture. The black spots in overall images in the first and second rows were marked to define a coordinated position. OB: osteoblast, OC: osteoclast, OB-OC: osteoblast-osteoclast coculture.

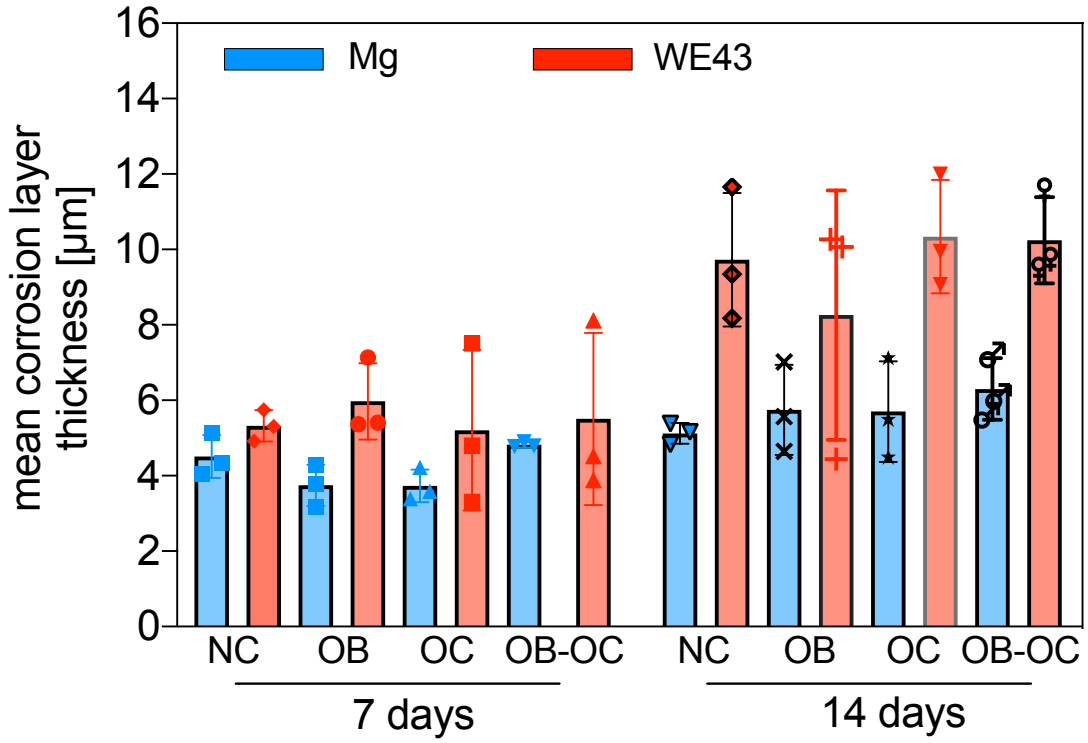

Figure S3.4. Changes in the corrosion layer thickness as a function of time without and with the presence of cells in monoculture and coculture. Data presented as mean ± standard deviation (n = 40 – 150 measurements/time point/cell culture condition from 3 independent samples). NC: No cells, OB: osteoblast, OC: osteoclast, OB-OC: osteoblast-osteoclast coculture.

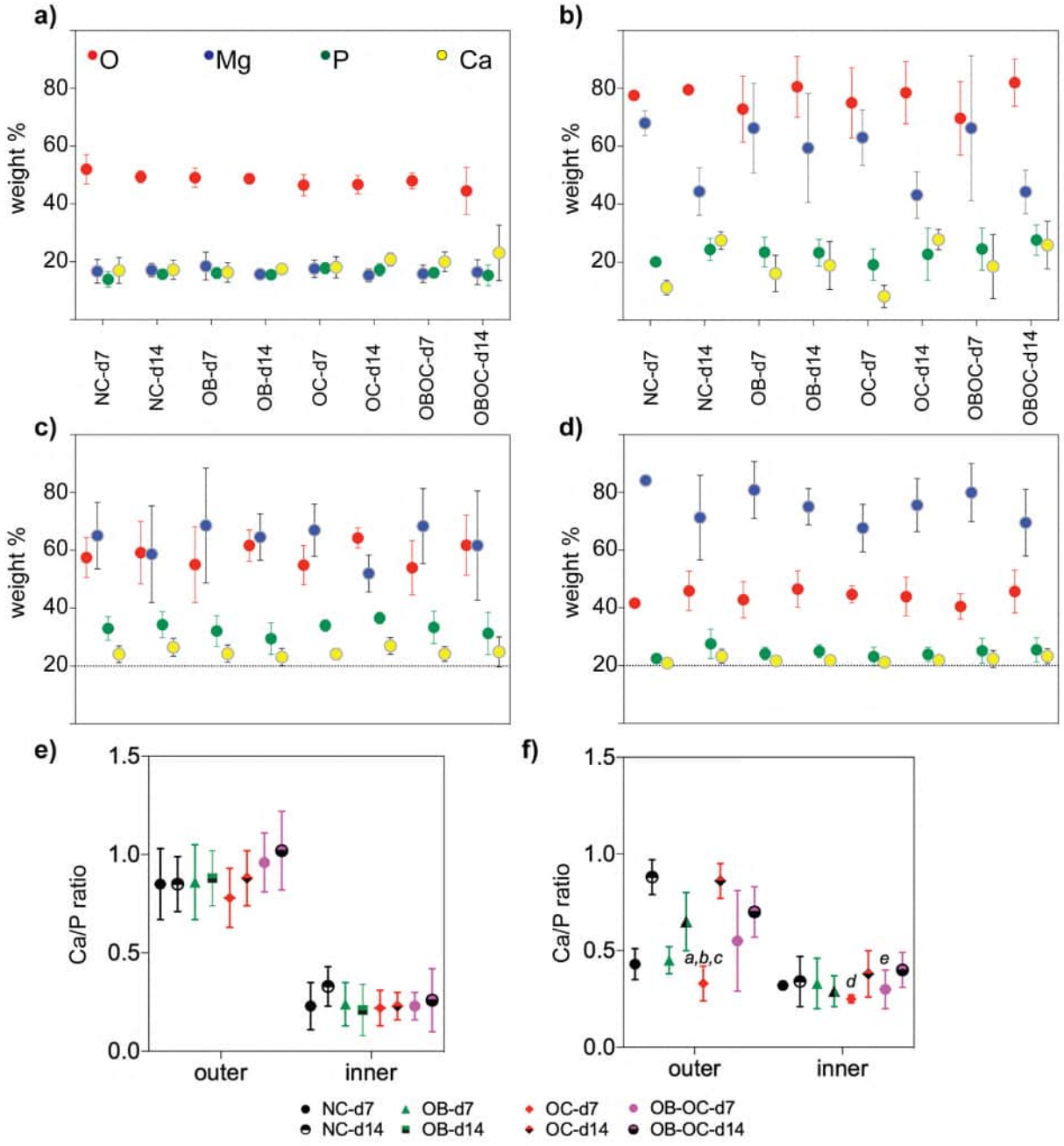

Figure S3.5. Semi-quantitative EDX analysis of the main elements composing the corrosion layers formed on Mg and WE43 substrates after 7- and 14- days of monoculture and coculture. The elemental composition of the outer region of the corrosion layers formed on Mg and WE43 alloy are depicted in a) and b), respectively. The corrosion layer inner layer´s composition is shown in c) and d) for Mg and WE43 alloy, respectively. The changes in the Ca/P ratio in the formed corrosion layers are depicted in e) and f), respectively. NC: No cells, OB: osteoblast, OC: osteoclast, OB-OC: osteoblast-osteoclast coculture.

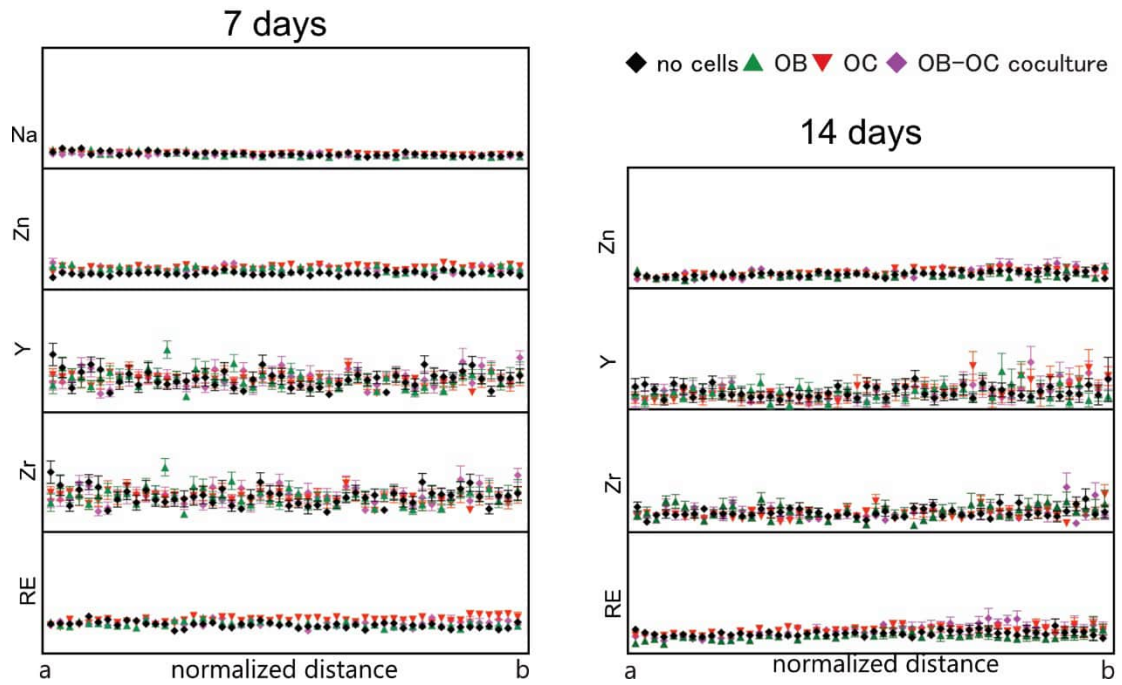

Figure S3.6. Changes in the concentration of elements in weight percent (wt.%) across the corrosion layers formed in the different cell culture conditions. The EDX line scan measurements were performed in the corrosion layer on the processed FIB cross-sections depicted in Fig.6 and are normalized by distance from the outer region (a) to the inner region (b). Osteoblasts (OB), osteoclasts (OC), sodium (Na), zinc (Zn), yttrium (Y), Zirconium (Zr), and rare earth (RE) elements. Lines scan data presented as mean ± standard error of the mean (SEM) (n = 5-line scans/sample/cell culture condition/timepoint from 3 independent samples).

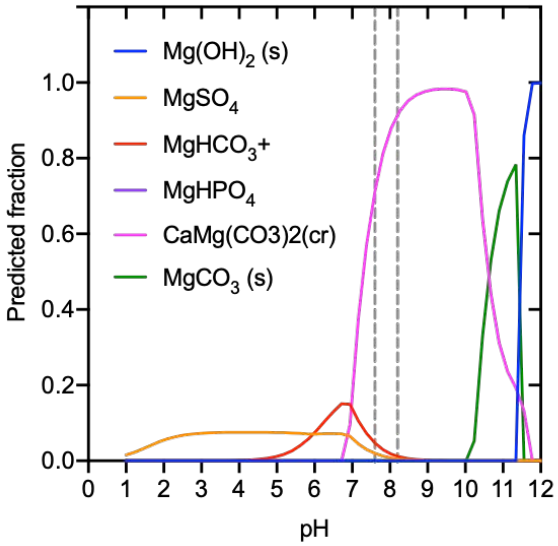

Figure S3.7. Hydra Medusa software calculated the total predicted fraction diagram of Mg chemical compounds as a pH function. Data from the Mg and WE43 samples immersed in an α – MEM + 10% FBS + 1% P/S. Vertical grey dashed lines denoted the pH range during the *in vitro* experiment after 14 days of immersion under physiological conditions (37oC, 5% CO_2, 95% relative humidity)**.** **(**s = unknown crystallinity, cr = crystalline**).**

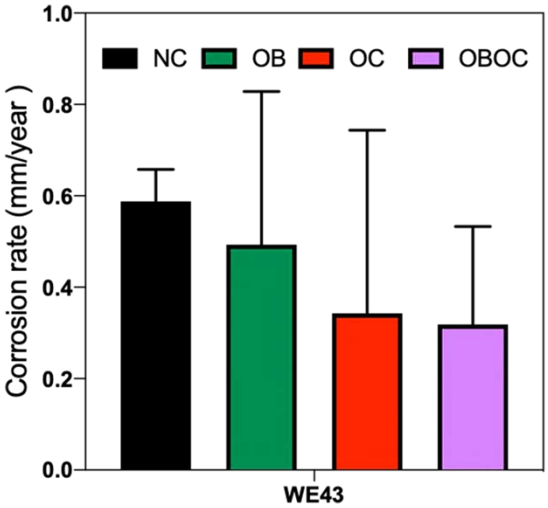

Figure S3.8. Calculated corrosion rate from the WE43 alloy based on mass loss after 14 days. Samples were incubated without and with osteoblast and osteoclasts in monoculture and coculture in α – MEM +105 FBS + 1% P/S. Data presented as mean ± standard deviation (n = 3/culture condition)

Bridging Chapter 3 and Chapters 4 to 7

The findings in Chapter 3 demonstrated that despite the variation in cell attachment, coculture of OB and OC cells influence the composition of the corrosion layers. These corrosion layers were enriched in Ca-P in the outermost layer at different time points between Mg substrates. The release of Ca and P ions from biomaterials have shown to promote the activation of OB and OC cells, thereby encouraging bone regeneration [291]. These findings are highly relevant, as one of the primary areas of interest for Mg implants is their use in orthopedics. However, the primary drawback of *in vitro* research is the challenge of replicating the complex biomaterial-cell-tissue interactions of *in vivo* organisms [203]. Therefore, it is imperative to conduct *in vivo* investigations on Mg-based devices to acquire a more comprehensive understanding of the degradation interface, the gas void formation, the local and systemic responses resulting from the presence of corrosion products [174]. Hence, in the following chapters, the corrosion performance of Mg-based devices was investigated with the aim of ***analyzing the bone-corrosion layer-implant interface to determine whether the Mg-based implants undergo uniform degradation in vivo. In addition, it is hypothesized that this degradation should be accompanied by proper cell and extracellular matrix attachment to the remaining implant, without interfering with the formation and remodeling of bone tissue.***

Chapter 4

Monitoring osseointegration and degradation of Mg-alloy implants through plasma biomarkers of inflammation and bone regeneration†

Eduarda Mota-Silva, **Diana C. Martinez***, *Giuseppina Basta, Serena Babboni, Serena del Turco, Davide Fragnito, Stefano Salvatore, Claudia Kusmic, Leon Riehakainen, Daniele Panetta, Beatrice Campanella, Massimo Onor, Tomasz Plocinski, Wojciech Swieszkowski, Luca Menichetti*

* *These authors contributed equally to this work.*

Manuscript submitted in ***Journal of Tissue Engineering***

(Under review)

† *To improve the readability of this chapter, some sections of the manuscript have been rearranged.*

ABSTRACT

Magnesium-degradable implants are ideal for temporary orthopedic applications due to their mechanical and osteogenic properties. However, they are underutilized because of insufficient methods to monitor implant osseointegration and tissue healing.

This study evaluated the use of circulatory biomarkers of inflammation and bone regeneration to monitor the bilateral implantation of an Mg-alloy in rats' femurs. Sixteen biomarkers were measured from plasma samples collected at multiple time points up to 90 days after implantation. All animals from the Mg-alloy group, and control groups (Ti-alloy, sham-non-critical bone defect) were monitored for pin placement using computed tomography. Bone regeneration and implant degradation were assessed through histological and EM-EDX analysis. The Sham group displayed higher DKK1, OPG, VEGF and KIM-1 plasma levels, indicating a stronger response in larger bone defects than the implanted groups. Mg-alloy group showed delayed bone regeneration compared to Ti-alloy group due to the release of H_2 gas. Active bone regeneration was observed in the Mg-alloy group up to day 180, and it was associated with significantly increased levels of G-CSF, OPG, and VEGF. The Mg-alloy group achieved direct bone-implant contact, suggesting superior osseointegration, and the elevated IL-10 and reduced FGF23 levels found at day 28 correlated with the accelerated implant degradation. Additionally, we revealed that Rare Earth Elements, released from Mg-alloy implants, accumulated in organs distant from the implantation site. In summary, these results underline the complex interactions between biomaterials and biological systems in orthopedic applications and encourage the utilization of circulating markers for enhanced follow-up monitoring.

Keywords: *Biomarkers, Magnesium-alloy, Titanium-alloy, bone-tissue regeneration, biodegradable*

GRAPHICAL ABSTRACT

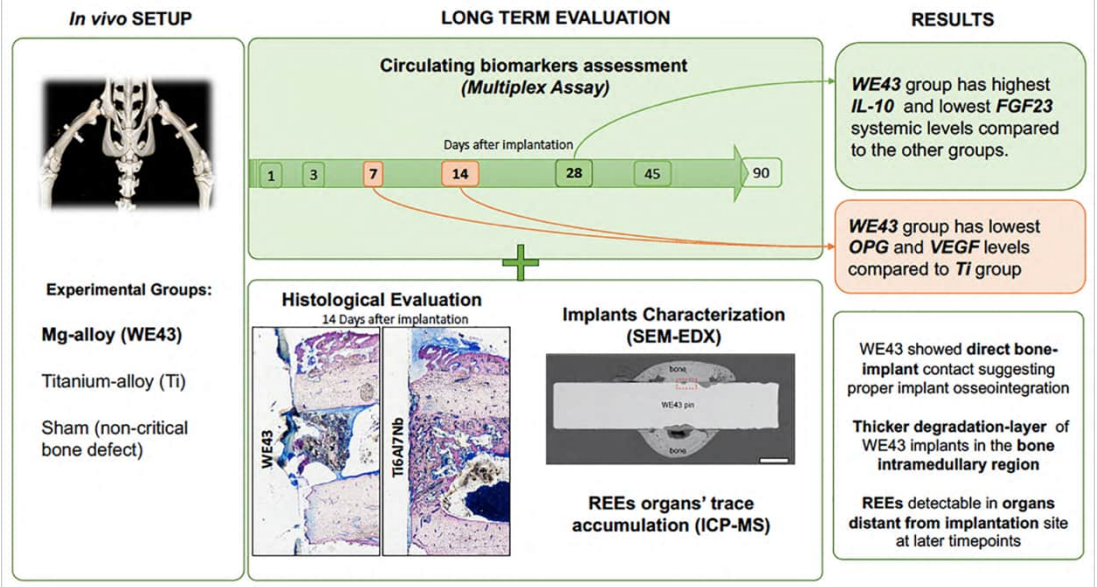

4.1. Introduction

Magnesium-degradable implants have been extensively investigated as an alternative to permanent metallic implants made of titanium (Ti) or cobalt-chromium (Co-Cr) alloys for orthopedic applications due to their adequate mechanical and osteogenic properties. While four orthopedic Mg devices have gained clinical approval and shown comparable results to conventional metallic implants, they are not yet widely used. [292]. Challenges in ensuring the predictable and consistent performance of biodegradable implants hinder their adoption, necessitating follow-up clinical studies for assessment of degradability and safety [293,294]. Traditional evaluation methods, like biomechanical testing and imaging (computed tomography (CT), X-ray), are not always adequate or sufficient for assessing Mg implant degradation and tissue regeneration [295,296]. Magnesium alloys (Mg-alloys) lead to a dynamic process of implant degradation and simultaneous tissue regeneration [297,298]. *In vitro* studies demonstrate that Mg^{2+} released from Mg-alloys modulates early inflammatory responses, shifting macrophage profile from pro- to anti-inflammatory status and inducing osteoblast differentiation from bone mesenchymal stem cells (BMSC) [190]. Furthermore, Mg^{2+} release inhibits osteoclast formation via osteoprotegerin (OPG) /receptor activator of the nuclear factor kappa-B ligand (RANK)/receptor activator of nuclear factor κ B (RANKL) pathway [237]. In vivo studies show heterogeneous bone-implant interfaces, indicating simultaneous bone regeneration and remodeling [123,299]. Mg-alloys promote direct bone-implant contact, guaranteeing proper osseointegration and implant stability, contrary to the fibrotic encapsulation frequently found with other metallic implants [221,300]. However, the release of H_2 from Mg implants leads to the formation of voids in the peri-implant tissue, which can initially delay cell adhesion [283,301]. Nonetheless, these voids do not hinder long-term tissue regeneration [221,300].

In situ evaluation of bone and inflammatory biomarkers in tissues surrounding Mg implants can provide insights into their biocompatibility [302–304]. Biomarkers of bone cell activity, such as osteopontin (OPN) and growth factors are frequently investigated through immunohistochemistry and gene expression analysis [305,306], which require animal sacrifice and limit evaluation to a single timepoint. This approach restricts longitudinal observation, confining the assessment to tissue and cellular responses at the implant site and neglecting broader systemic effects.

Beyond imaging techniques which provide localized observation of implants and surrounding tissues without animal sacrifice, blood biomarker analysis offers non-invasive approach for understanding the systemic impact of implants on the body, complementing the information obtained from imaging techniques. Most pre-clinical studies on Mg implants focus on early response, evaluating pro-inflammatory (tumor necrosis factor [TNF-α], interleukin [IL-6, IL- 1β, IL-2]) and anti-inflammatory markers (IL-10) [307,308]. Assessment of biomarkers is routinely performed in numerous clinical fields, including musculoskeletal diseases [190,309]. Furthermore, studies performed on patients with permanent metallic implants (i.e Ti and Co-Cr alloys) have revealed the effectiveness of biomarkers in detecting early signs of peri-implant osteolysis, a well-known and common complication associated to metallic implant usage [310,311]. Given their non-invasiveness, ease of use, and accuracy, we propose to test in blood a panel of inflammatory and bone metabolism biomarkers, using a multiplex immunoassay approach, which allows simultaneous detection of multiple analytes from one single small sample and the longitudinal monitoring of the systemic response [312].

This study employed a rodent model of transcortical implantation in the rat femur for assessing implant osseointegration. For the Mg-alloy, we chose WE43, a slow degrading alloy with Yttrium, Zirconium and rare earth elements (REE) in its chemical composition. WE43 received CE approval for clinical orthopaedical use in 2013 and despite its commercialization and proven biocompatibility, certain aspects of alloy's degradation behavior and the impact of REE release remain unclear [289,313]. Therefore, we also investigate the systemic distribution of Yttrium and rare earth elements (REE) in the liver, kidney, and spleen. The experimental design included three groups of animals: the sham group, animals with a non- critical bone defect, the WE43-implanted group and the titanium (Ti)-implanted group.

A list of 16 soluble proteins including biomarkers of both inflammatory and bone metabolism was selected. Additionally, the morphology of peri-implant bone tissue and the bone-implant interface elemental composition were assessed through histology and scanning electron microscopy with energy dispersive X-ray spectroscopy (SEM-EDX), respectively.

We unveiled intriguing patterns and kinetic differences in the blood release of biomarkers between groups implanted with WE43 and Ti pins, compared to the natural bone

regeneration process observed in the sham group. Additionally, we established correlations between biomarkers and various aspects of tissue regeneration and implant degradation in the WE43- implanted group.

4.2. Materials and Methods

4.2.1. Implants

Cylindrical pins of 8mm length and 1.6mm diameter were made of WE43-based material manufactured by Syntellix AG (Hannover, Germany) and produced using a turning method. The chemical composition of WE43 is Yttrium (3.7–4.3%), REE (2.4–4.4%), zirconium (0.4%) and the residual percentage of Mg. A Ti alloy – (Ti6Al7Nb) – manufactured by Acnis International (Chassieu, France) with equivalent geometry was used as control. The material was annealed and centerless grounded and then deflected, finally, it was grounded and polished. Both implant materials were then individually packaged, and gamma sterilized at a 25 kGy dose.

4.2.2. Preimplantation characterization

The surface of the WE43 (n=3) and Ti (n=2) pin was evaluated before implantation by stereomicroscope and SEM-EDX. Optical images were taken with an SZ61 stereomicroscope (Olympus, Japan) coupled with an OPTA-Tech HDMI camera. To qualitatively evaluate the surface morphology of the pins, random areas were analyzed using an SEM microscope (Hitachi, SU-8000, Japan) in high vacuum mode. Each sample was observed at magnifications from 30x to 5000x with secondary (SE) and backscattered (BSE) detectors. Elemental semiquantitative analysis of the pin surfaces was performed with energy-dispersive X-ray spectroscopy (EDX) using an UltraDry EDS detector (Thermo Scientific™, USA) coupled to the SEM, at 15 mm working distance and accelerating voltage of 15kV and 30kV for Ti and WE43, respectively.

4.2.3. Animal surgery and study design

We used wistar female rats (n = 60; 9-12 weeks old; 200-250g; Envigo), housed communally (maximum 4 rats/cage) on a 12-12 h dark-light cycle with unrestricted access to water and standard rodent diet. The animals were anesthetized with an intraperitoneal injection of 5 mg/kg of Xylazine (Rompum Elanco, Italy) and 10 mg/kg of Zoletil

(zolazepam + tiletamine) (Virbac, Switzerland). The surgical procedures are following a previously published method [31]. The experimental sites were implanted with cylindrical pins composed of either WE43 or Ti or were left without implants (sham). After surgery, the animals were injected intraperitonially with 0.1 mL of Ketorolac for analgesia and put back in their cages. Antibiotics (Baytril 5mg/100mL) and analgesics (Tramadol 3mg/100mL) were administered in water and standard rodent food was presented *ad libitum*. All animal procedures were carried out in accordance with the National Ethical Guidelines (Italian Ministry of Health; D.L. vo 26/2014) and the protocol was approved by the Instituto Superiore di Sanità on behalf of the Italian Ministry of Health and Ethics Panel (Prot. n° 299/2020-PR). The samples collected from the animals and samples distribution is represented in Figure 4.1.

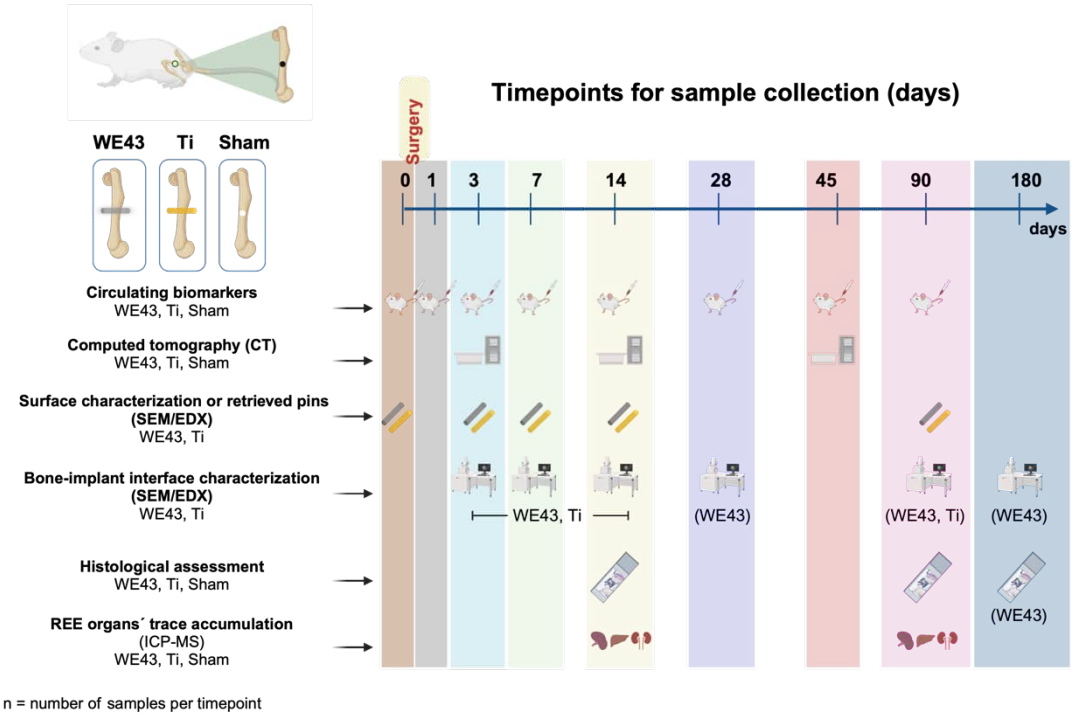

Figure 4.1. Schematic representation of experimental groups (WE43, Ti and Sham), methods used for samples analysis and time points of evaluation. *Image created with Biorender.com*

4.2.4. Computed Tomography

Animals with implants and sham animals were imaged on days 3,14 and 45 after surgery for assessment of pin fitting with a IRIS PET/CT scanners (Inviscan Imaging System, Strasbourg, France), hardware specifications are detailed on a previously published work. [1] The acquisition settings were 120 µm voxel size, 80kV voltage, 800 projections and 50 ms integration time. The 3D renders were done using a A Medical Image Data Examiner [314].

4.2.5. Preservation of serum samples

A volume of 0.5mL of blood was collected from animals' tail vein and immediately transferred to EDTA treated tubes which were left at room temperature for 30 minutes. The blood samples were then centrifuged at 4 ° C for 10 min at 3000 rpm, aliquoted into volumes of 100 mL and stored at -80 ° C until analysis.

4.2.6. Assessment of circulating biomarkers

16 plasma biomarkers related to inflammation and bone regeneration were assessed using custom-designed immunoassays based on Luminex xMAP Technology (MILLIPLEX, EMD Millipore Corporation, Billerica, MA). Three panels were utilized: Rat Cytokine/Chemokine Magnetic Bead Panel (G-CSF, GRO-KC/ CXCL-1, TNF-*a*, IL-6, IL- 1*a*, IL-10, IL-4; IFNγ, MCP-1); Rat Bone Magnetic Bead Panel (DKK1, FGF23, OPG); Rat Kidney Magnetic Bead Panel (OPN, VEGF, KIM-1, TIMP-1). A detailed description of this methodology can be found on Supplementary materials.

4.2.7. Histology

After implantation, animals were euthanized with an overdose of isoflurane and the femurs with implanted pins were retrieved and fixed in 10% PBS buffered formalin. Then, samples were dehydrated in a series of alcohol grades and embedded in methylmethacrylate. Subsequently, longitudinal sectioning was performed using a laser microtome (TissueSurgeon, LLS ROWIAK LaserLabSolutions, Hannover, Germany) to a thickness of approximately 10 μm. Finally, the histological slides were stained with Levai & Laczko staining as previously described [315]. Sham samples were processed through decalcified histology. The bones were formalin-fixed for a minimum of 72 h. Afterwards, they were rinsed in running tap water (10-15 minutes) and transferred to 12% EDTA (pH 7.4) for 4 weeks. Subsequently, samples were rinsed in running tap water (15 minutes), dehydrated in a graded series of ethanol solutions, and embedded in paraffin. A 5μm thickness slides were stained with Mayer's hematoxylin and eosin Y. Histological images were acquired with a light microscope (Olympus BX43, Japan) coupled with an RGB video camera (Olympus DP 20, Japan).

4.2.8. Surface Characterization of extracted implants

Implants were removed from the bone using a disc saw, fixed in 99.9% ethanol for 2 h and dried in air for 2 h, then, vacuum-stored until analysis. Optical images of the retrieved pins were captured with an SZ61 stereomicroscope (Olympus, Japan) coupled with an OPTA-Tech

HDMI camera. A gold layer of 7 nm was sputtered onto samples surface ((Leica EM ACE200, Leica Microsystems, Austria). Implants were examined using an SEM microscope (SU-8000, Hitachi, Japan) and elemental composition was assessed using energy-dispersive X-ray spectroscopy (EDX, UltraDry EDS detector (Thermo Scientific™) coupled to the SEM device) at 15 mm working distance, and at 15kV and 30kV accelerating voltage for Ti and WE43, respectively.

4.2.9. Cross-sectional characterization of bone-implant interface

The femurs collected from WE43, and Ti groups were sectioned at the epiphysis and fixed in 10% neutral buffered formalin. Afterward, the specimens were dehydrated using ethanol series and subsequently embedded in methylmethacrylate (Technovit® 9100 neu, Kulzer, Germany). Then, the embedded specimens were sectioned parallel to the longitudinal axis of the pin using a laser microtome (TissueSurgeon, LLS ROWIAK LaserLabSolutions, Hannover, Germany). The morphology and chemical composition of the bone-implant interface and the peri- implant bone was examined by SEM/EDX (SU8000, Hitachi, Japan).

4.2.10. Inductively Coupled Plasma-Mass Spectrometer

Concentrations of Yttrium and REE were measured from liver, kidneys and spleen samples collected at 14, 90 and 180 days after surgery from all groups. Lyophilized samples of 100mg were put in a mixture of HNO_3(6 mL, 69 % w/w) and water (2 mL, 30 % w/w) for 1h and then digested in a microwave oven, slowly increasing temperature to 200°C and maintaining it for 20 minutes. An Agilent7700x inductively coupled plasma mass spectrometer (Agilent Technologies, Tokyo, Japan) with a MicroMist nebulizer and cooled (2°C) quartz Scott-type double-pass glass spray chamber was used for the quantification of Y and REE. A solution of 10 µg/L iridium in 2% HNO_3 was used as internal standard.

4.2.11. Statistical analysis

The immunoassay results are presented as the logarithmic transformation of concentration (pg/mL) values and plotted as mean ± SEM or percentage. Pairwise comparison tests were carried out to find differences between the experimental groups at each time point and for each biomarker, and pairwise longitudinal tests were performed to investigate differences in biomarker concentration between time points. To reduce type I error, all tests were

adjusted following the false discovery rate procedure (FDR), according to Benjamin-Hochberg et al. [316], where only *P*-values adjusted to FDR <0.05 were considered statistically significant. We used the open-source statistical software R (Core Team (2018), R foundation for Statistical Computing, Vienna, Austria) with the mgcv package and the bam function. Additionally, considering the variability associated with the chosen experimental design, the suitability of a generalized additive model (GAM) was explored to modulate the results of circulating biomarkers.

4.3. Results

4.3.1. Pin pre-implantation characterization

The pre-implantation characterization of both pins (WE43, Ti) was performed using SEM/EDX (Figure 4.2). The geometry of the pins differed slightly, with Ti pins presenting rounded edges, grooves, and rounded Nb-enriched particles, whereas the characteristic of WE43 pins were uniform vertical lines from manufacturing. Elemental analysis of the pins confirmed their chemical composition and the content of oxygen, suggesting the formation of a thin oxide layer in both materials, possibly the result of the contact with air and moisture during manufacturing and cleaning procedures, as well as the natural aging process during storage before *in vivo* implantation [317].

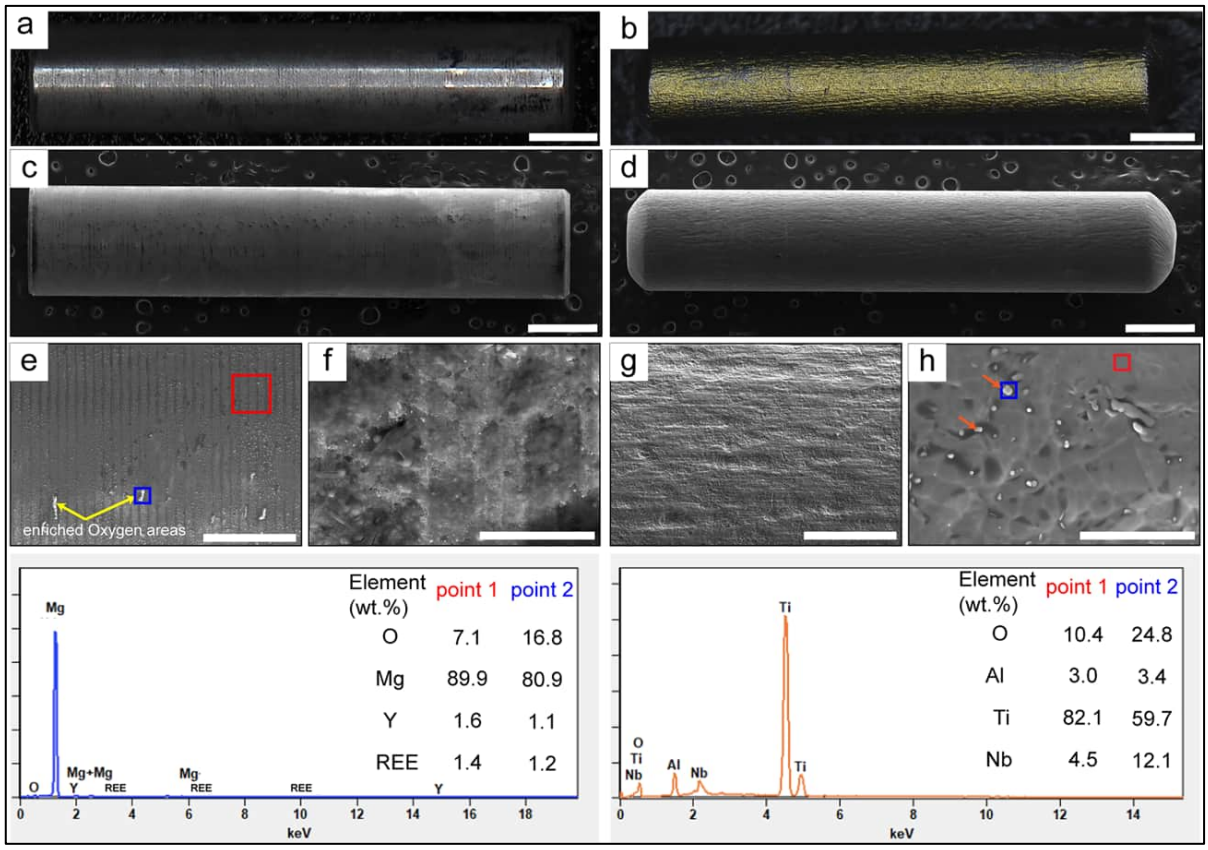

Figure 4.2. Stereomicroscope and SEM image of pins prior to implantation. Overall optical and SEM images of the WE43 (a, c) and Ti6Al7Nb (b, d) pins. Low-magnification images of the WE43 (e) and Ti (g) pin. The enriched oxygen areas on the WE43 pin surface are denoted by yellow arrows. f, high-magnification image of WE43 pin (f). h, high-magnification high magnification of the Ti pin surface. The rounded articles denoted by orange arrows have a high weight percent Nb content. Elemental composition (in weight percent (wt%) of the WE43 (bottom left table) and Ti (bottom right table) pin surfaces is presented. Scale bars in (a, b, c, d) = 1 mm, (e, g) = 200 µm, and (f, h) = 10 µm.

4.3.2. Post-Surgical observation - Computed tomography imaging

Following surgery, animals were closely monitored, included animals exhibited normal weight gain recovery and gait. In addition, CT scan results were used to confirm the pin placement and fitting. Figure 2 demonstrates the placement of the pin in the mid-diaphyseal region of the femur on days 3,14, and 45 using 3D CT renders. Three days after implantation, small bone debris was visible in the vicinity of the implants, but these disappeared by day 14. The images taken on days 3,14, and 45 are from the same animal (Figure 4.3a-c), confirming the initial placement of the WE43 pins was maintained throughout the experimental period. The sham animal showed bone defect closure by day 14 and at day 45 the surgical bone defects were imperceptible (Figure 4.3e-f). Due to the streak artifacts caused by the presence of Ti implants [318], 3D reconstructions of the Ti implanted group were not included. Nevertheless, CT images were still used to validate the alignment of implants within the bone.

4.3.3. Exclusion of undetectable circulating biomarkers

Among the sixteen biomarkers assessed, concentrations of four inflammatory cytokines/chemokines (interleukin [IL-4, IL-6], interferon γ [IFN-γ], growth-regulated oncogene (GRO) -keratinocyte chemoattractant (KC) / chemokine (C-X-C motif) ligand [GRO-KC/ CXCL1]) were undetectable in over 50% of the animal/time points within each experimental group. Consequently, they were considered nonsignificant and excluded from further analysis. The rest of the biomarkers namely, TNFα, kidney injury molecule 1 (KIM-1), fibroblast growth factor 23 (FGF23), osteoprotegerin (OPG), growth colony stimulating factor (G-CSF), IL-10, vascular endothelial growth factor (VEGF), tissue inhibitor of metalloproteinases 1 (TIMP-1), OPN, monocyte chemoattractant protein-1 (MCP-1), IL-1α and dickkopf WNT signaling pathway inhibitor (DKK1) were analyzed. The undetectable concentration values, i.e. outside of equipment's detection range, were excluded from the mean calculations at each timepoint.

4.3.4. Differential expression of bone regeneration and angiogenic biomarkers between the Sham group and implanted animals

4 of the 12 examined biomarkers, including DKK1, OPG, VEGF and KIM-1, exhibited a similar expression pattern, particularly within the sham group (Figure 3A-D). The highest concentration values were consistently observed in the sham group between days 7 and 45 after implant placement, with distinct peaks at days 14 and 45. In contrast, the WE43 group showed the lowest concentration values, notably between days 3 and days 28 or 45.

OPG, an inhibitor of osteoclastic activity, consistently showed higher levels ($p<0.001$) in sham group at all experimental timepoints compared to Ti implanted group. Instead, OPG levels of sham group were significantly higher compared to WE43 group on day 0 ($p<0.001$) and on days 3, 7, 14 and 28 ($p<0.001$) (Figure 4.4a). We do not know the reason of this baseline variation among groups.

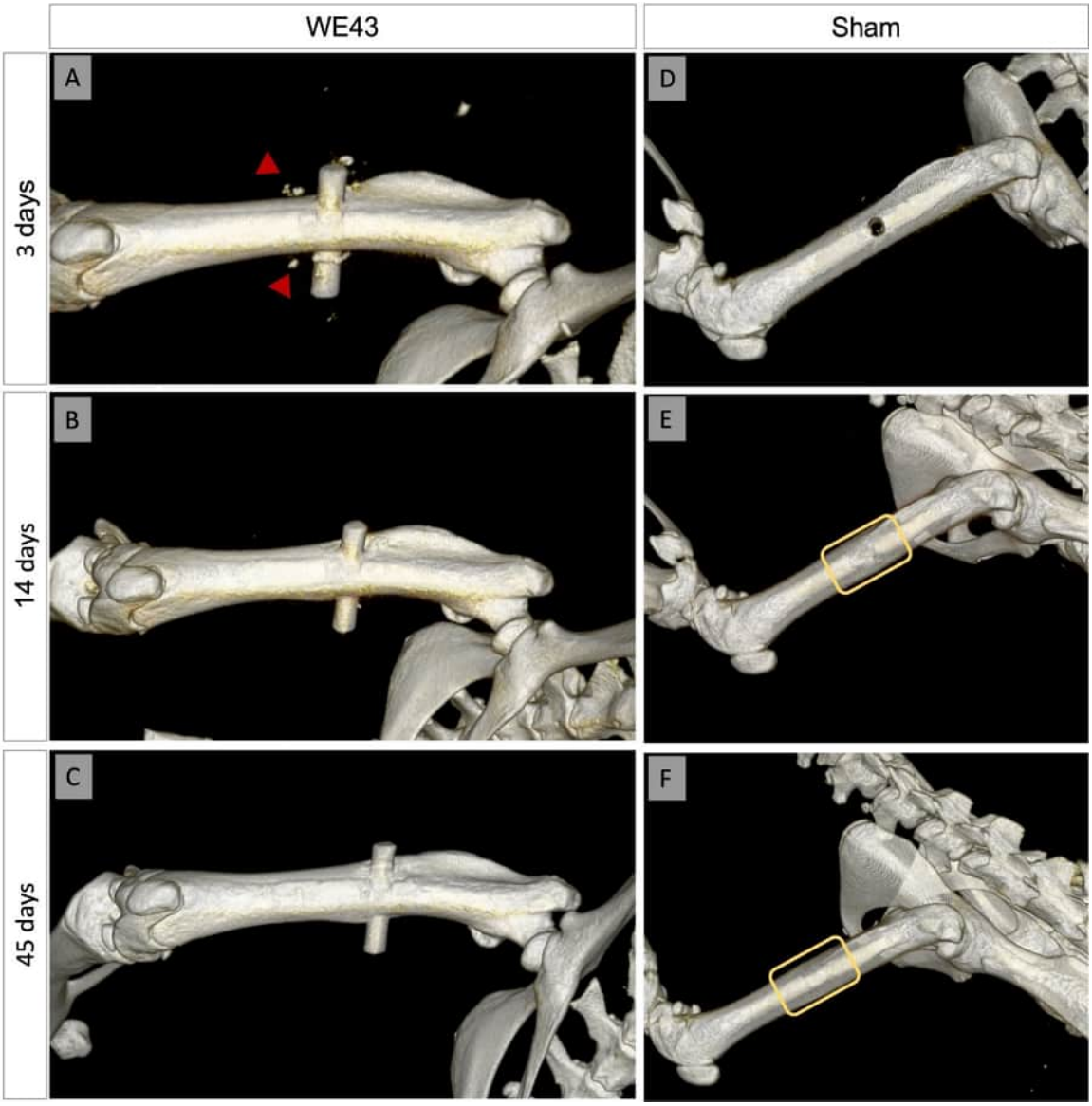

Figure 4.3. 3D CT renders of WE43 implanted animals (A-C) and a sham (D-F) surgically placed at 3, 14, and 45 days after surgery. Red arrows in A indicate bone debris caused by surgical procedure and press-fit during pins' implantation. The yellow rectangles in E and F show the region where the bone defect was created after 14 and 45 days.

DKK1, an inhibitor of osteoblastic activity, displayed peak concentrations between days 7 and 45 in the sham group. These concentrations were significantly elevated compared to Ti group on days 14 ($p < 0.001$), 28 ($p < 0.05$) and 45 ($p < 0.001$). Compared to the WE43 implanted group, the sham group showed significantly higher concentrations between days 3 and 45. (day 3 and 7 with $p < 0.05$ and days 14, 28, and 45 with $p < 0.001$) (Figure 4.4b). VEGF, critical in various fracture healing stages, showed significantly higher concentration in sham injury samples compared to WE43, between days 7 and 28 ($p < 0.001$). While not significantly different from Titanium, an elevated concentration between the same timepoints is observable (Figure 4.4c).

Finally, KIM-1 levels varied significantly between groups. Notably, the sham group

showed higher KIM-1 levels than the WE43 implanted animals on days 3, 7, 14, 28 ($p<0.001$), and 45 ($p<0.05$) (Figure 4.4d).

Interestingly, OPG, DKK1, VEGF, and KIM-1 displayed an upward trend in circulating concentration by day 90 in the WE43 group, a pattern not observed in the Ti or sham groups. Furthermore, the biomarkers G-CSF, TNFα, TIMP-1, MCP-1, OPN, and IL-1α, did not display statistically significant differences between the experimental groups (Figure S4.1).

4.3.5. Longitudinal variations within WE43 group

In the WE43 group, several biomarkers exhibited significant differences over time (Figure 4.5). OPG levels were elevated on days 1 and 90 post-implantation, compared to days 7 and 28 ($p<0.05$). Similarly, VEGF displayed increased concentration on day 1 compared to day 7 ($p<0.05$) and on day 90 compared to days 7, 14, and 28 ($p<0.05$). TIMP-1 showed its peak concentration on day 1, significantly surpassing on days 3, 7, 14, 28, and 45 ($p<0.001$). The baseline value (day 0) was also considerably higher than those on days 14 and 45 ($p<0.001$). Additionally, G-CSF levels were significantly higher on day 3 post-surgery compared to baseline ($p<0.001$). The elevated levels of OPG and VEGF at 90 days in respect to intermediate timepoints, confirm the upward trend visible in WE43 group at later timepoints when compared to the other groups (Ti, sham). In contrast, Sham group showed longitudinal differences only in G-CSF (Figure S4.2) while Ti group did not show temporal differences for any marker. The increased concentration in plasma of the biomarkers at early time points (3 and 7 days) could be associated to the higher corrosion rate observed in the WE43 pins (Figure S4.3). After 7 days the degradation of the pin slowed down due to the formation of the corrosion layers on the pins.

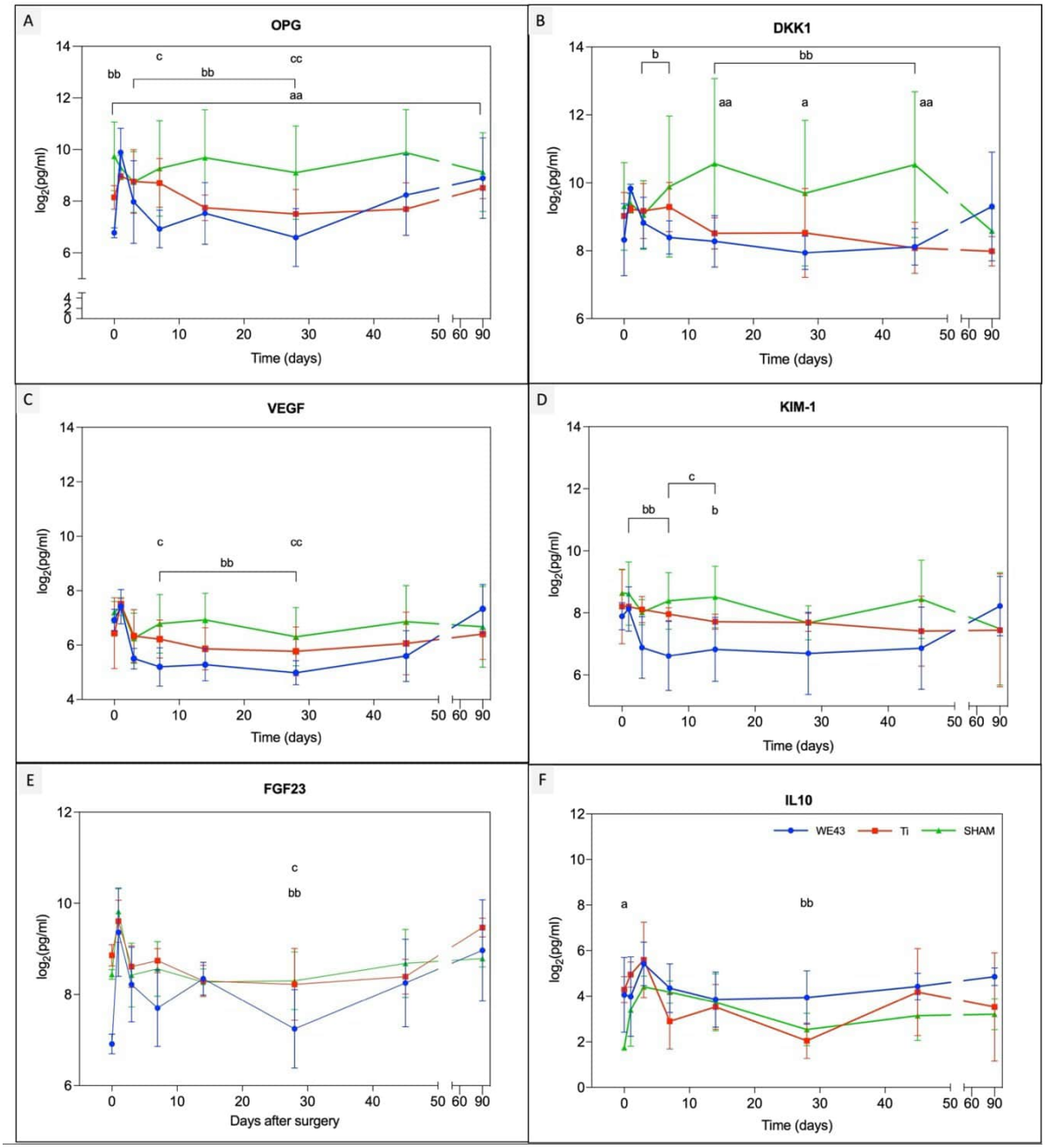

Figure 4.4. Differential concentrations of circulating biomarkers in different implant materials (WE43, Ti). Furthermore, statistical analysis revealed significant differences in circulating biomarker concentration between the implanted materials. In the Ti implant group, OPG and VEGF concentrations were notably higher on days 7 ($p < 0.05$) and 28 ($p < 0.001$) while KIM-1 levels were elevated on days 7 ($p < 0.05$) and 14 ($p < 0.05$) compared to WE43 implanted group (Fig 3A,C,D). The circulating concentration of FGF23 was significantly lower in the WE43 group on day 28 ($p < 0.05$) compared to both the sham and the Ti groups (Fig 3E). Regarding inflammatory markers, only IL10 displayed statistically significant differences: its concentration was higher in the Ti group on day 3 ($p < 0.05$) compared to sham, and significantly higher in the WE43 group on day 28 ($p < 0.001$) compared to Ti group (Fig.3F). Although without presenting a statistically significant difference, IL10 levels are still considerably higher on WE43 than on sham group at day 28. Finally, at day 90, G-CSF was significantly higher in WE43 when compared to Ti ($p<0.001$).

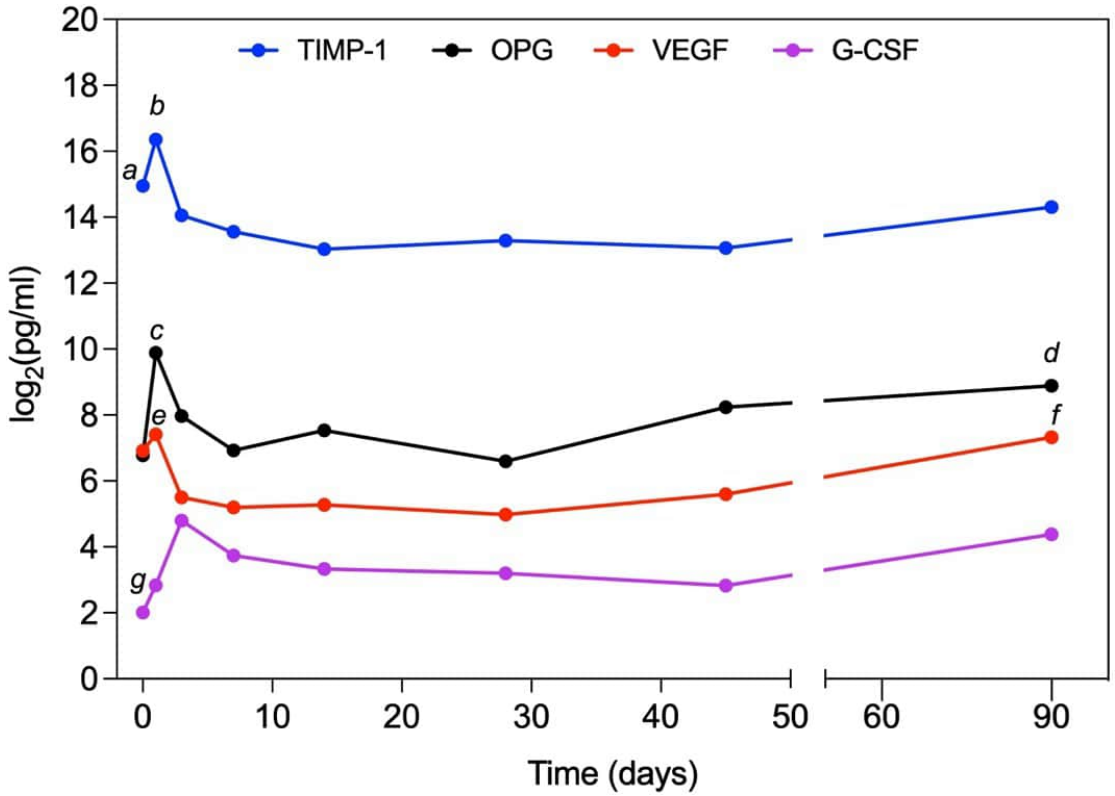

Figure 4.5. Longitudinal representation of TIMP-1, OPG, VEGF, and G-CSF for WE43 implanted animals. Mean ± SEM. **a**: *P*<0.001 day 0 *versus* days 14 and 45, **b**: *P* <0.001 day 1 *versus* day 3,7,14,28, and 45; **c**: *P* <0.05 day 1 *versus* days 7 and 28; **d**: *P* <0.05 day 90 *versus* days 7 and 28; **e**: *P* <0.05 day 1 *versus* day 7; **f** : *P* <0.05 day 90 *versus* day 7,14, and 28; **g**: *P* <0.001 day 0 *versus* day 3.

4.3.6. Peri-Implant bone morphology and implant osseointegration of WE43 and Ti

Qualitative histological analysis, displayed in Figure 5, was conducted on sham, WE43 samples at 14, 90, and 180 days after implantation and on the Ti specimens at 14 and 90 days. In the sham group, on day 14, a substantial amount of newly formed immature woven bone was observed filling the defect in the intramedullary region, which later progressed to fill the defect in the cortical areas (Figure 4.6a). By day 90 the cortical bone remodeling was still incomplete, with some areas showing disorganized new bone formation (Figure 4.6b).

For WE43, the peripheral bone around the implant exhibited progressive regeneration from day 14 to day 180. At day 14, newly formed periosteal bone was observed near the pin's surface. Notably, the pin's degradation was more evident in the intramedullary region, where degradation products were visible (Figure 4.6c). Large void areas noted on day 14, attributed to gas release, remain visible by days 90 and 180 (Figure 4.6d-e). However, direct contact between the bone and the degradation layer/pin is seen on later timepoints and darker pink bone areas, indicate ongoing new bone formation (Figure 4.6e). The Ti implant on day 14 displayed periosteal bone formation and tissue rearrangement in

the intramedullary region. However, a layer of fibrotic tissue was visible near the implant on day 14 and 90 (Figure 4.6f) indicating poor bone-Ti implant surface contact (Figure 4.6g) Both types of implants exhibited periosteal bone growth 14 days after implantation. Nevertheless, Ti implants showed a more advanced stage of tissue rearrangement in the intramedullary region compared to the WE43 group. On day 90, Ti implants displayed complete bone regeneration despite fibrotic encapsulation, while WE43 implants were still undergoing pin degradation and continuous regeneration.

4.3.7. Post-implantation characterization of WE43 and Ti Implants

Surface evaluation of explanted WE43 implants showed that implants kept their integrity up to 90 days and presented a progressive but non-uniform degradation pattern (Figure 4.7a-e). Intramedullary regions showed higher degradation with the surface becoming more cracked and rougher while compared to regions of the pin in contact with cortical bone and soft tissue. EDX revealed corrosion products formed on the surface of the WE43 pins were mainly composed of carbon (C), nitrogen (N), oxygen (O), Mg, phosphorus (P) and calcium (Ca), with traces of the alloying elements yttrium (Y), zirconium (Zr) and REEs (Figure 4.7e). Mg concentration in the corrosion layer decreased with implantation time, but C, N, and P concentration was consistent at all time points. O and Ca gradually increased up to day 90. The nitrogen content is a result of cell adhesion and the organic material remaining attached to the implant surface [319]. With respect to Ti pins (Figure 4.7f-j), EDX showed C, N, O, and Ti were the most abundant elements on Ti pin surfaces after implantation, along with traces of P, Ca, and the alloying elements Al and Nb. After 3 and 90 days, higher concentrations of C were depicted on Ti pins, with evidence of more biological tissues attached to the implant surface compared to 7 and 14 days when a higher concentration of O was observed.

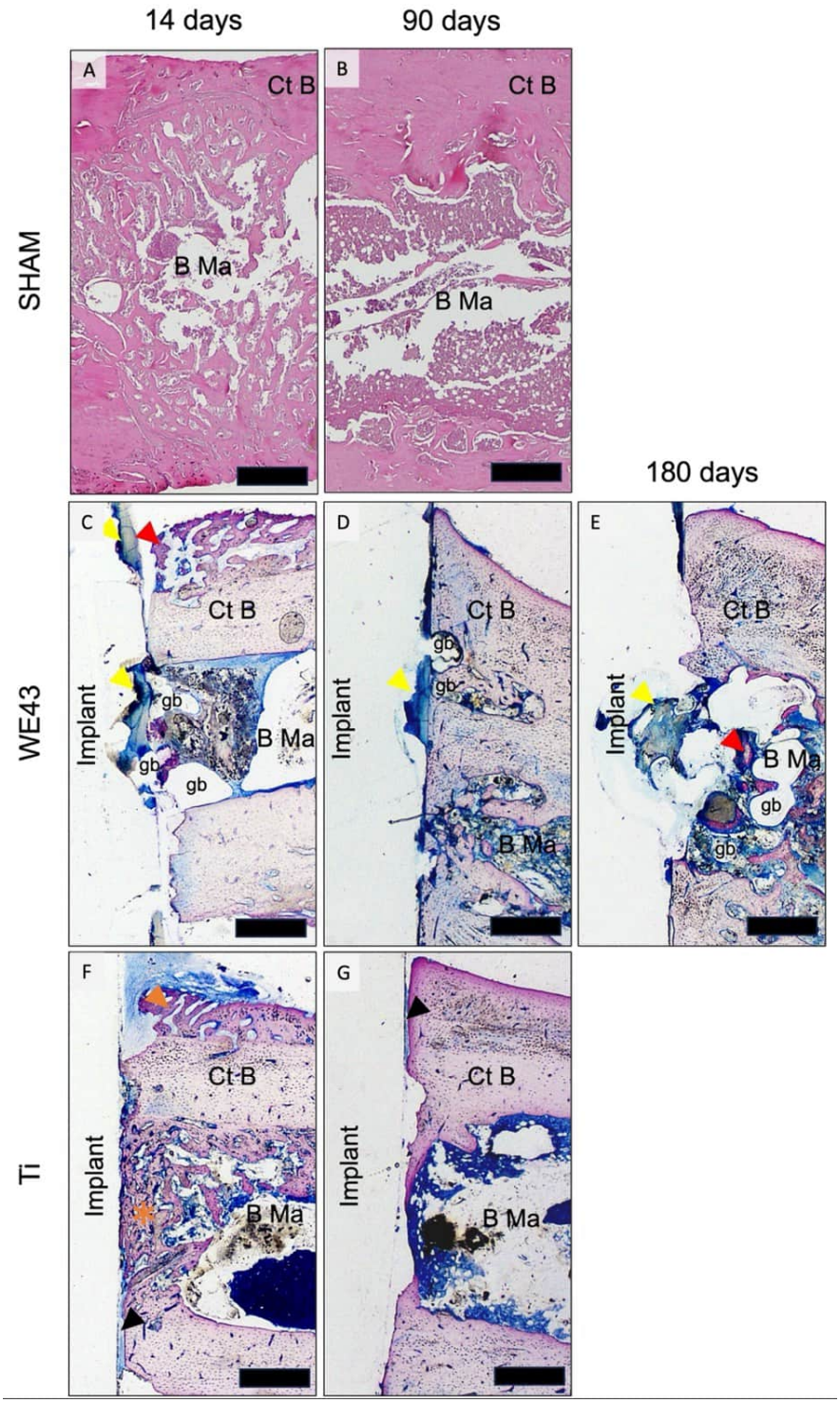

Figure 4.6. (A-B) Representative histological images of H&E-stained sham samples for days 14 and 90; (C-D-E) representative images of Levai-Lacsko-stained bone sections of WE43 at 14,90 and 180 days; (F,G) representative images Levai-Lacsko-stained bone sections of Titanium at 14 and 90 days after implantation. Ct B: cortical Bone; B Ma: Bone marrow; Gb: gas bubbles; Red arrow: new bone formation; Yellow arrow: corrosion products; Orange arrow and asterisks: new periosteal bone and bone in the medullary cavity; Black arrow: fibrotic tissue; Scale bar: 500 μm.

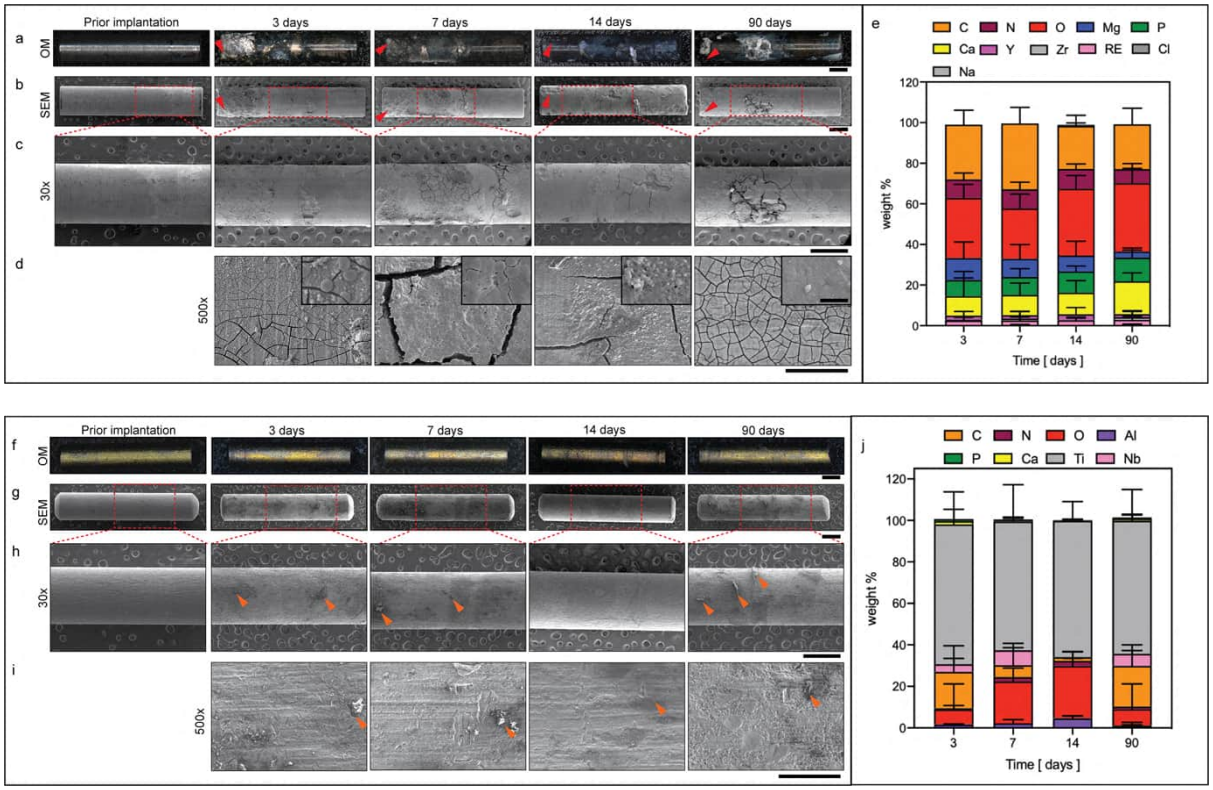

Figure 4.7. Surface morphology of explanted WE43 and Ti pins at 3,7,14 and 90 days post-implantation. Overall optical (a, f) and SEM (b-d, g-i) images of WE43 and Ti pins at different implantation times. Red arrows (a-b) depict damage caused by tweezer use while pinning implantation (e, j) Elemental composition in weight percentage (wt.%) of the pins' surfaces at all time points. Data presented as mean ± standard deviation. Scale bar = 1 mm in a-c and f-h; 500x scale bar = 100 µm; inset image in d, scale bar = 10 µm.

4.3.8. Characterization of the bone-implant interface

SEM-EDX analysis revealed that at the bone-implant interface, the WE43 pin degraded over time (Figure 4.8, Figure S4.3) with direct bone-implant contact observed since day 3. The main body of the implant was still present after 180 days of implantation. Regions of the pins were in contact with cortical bone, intramedullary cavity, or soft tissues, resulting in the formation of corrosion layers of varying thicknesses (from 1 to 155 µm) and composition. Thicker corrosion layers were formed within the intramedullary cavity (18-155 µm), and at the interface between the soft tissue and the cortical bone (30-89 µm), while thinner corrosion layers formed in the cortical bone compartment (2-18 µm) (Figure 4.9).

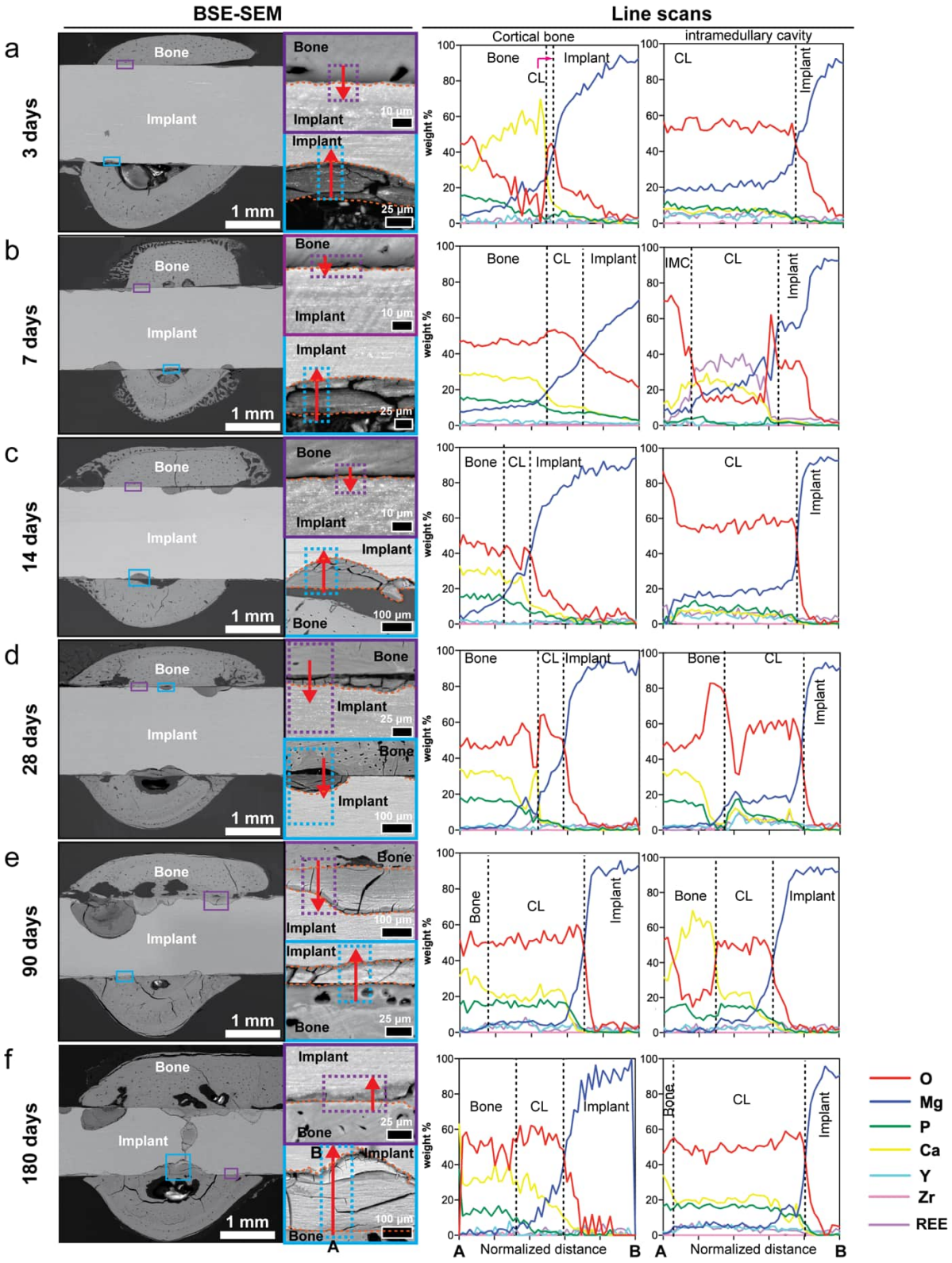

Figure 4.8. Characterization of the bone-implant interface of WE43 pins at 3, 7, 14, 28, 90, and 180 days after in vivo implantation by SEM/EDX. EDX line scans were performed in the selected purple- and blue-denoted areas. Line scans were performed from bone (A) to the residual implant side (B) as denoted by the red arrows. Line scans were plotted as element weight percentage over normalized distance from the bone to the residual implant. Corrosion layer thickness changes over time in three different compartments: in the interface between soft- tissue and cortical bone, in the cortical bone, and in the intramedullary cavity3.10 Yttrium and REE trace accumulation in the liver, kidney, and spleen.

On days 14 and 28, the corrosion layer on intramedullary regions (Figure 4.8, light blue squares) was thicker than on the pin surface in contact with cortical bone (Figure 4.8, purple squares) or other soft tissues. In the intramedullary cavity, corrosion layers formed without bone contact for up to 14 days, then exhibited bone formation from day 28 to 180. These layers comprised O, Mg, P, Ca, and trace alloying elements. Although thicker corrosion layers formed at 90 and 180 days, O remained unchanged, while P and Ca enrichment continued in both bone compartments. Interestingly, higher REE concentration was noted in the corrosion layer within the intramedullary region at day 7 (Figure S4.4). Ti group's bone-implant interface was also characterized (Figure 4.10) and pin integrity over time was confirmed. However, some gaps between bone and implant were noted by day 28. EDX elemental maps showed predominant O, P, Ca in the bone and Ti, Al and Nb in implant alloying elements. EDX elemental maps revealed O, P, and Ca as predominant elements in the bone with traces of the alloying elements (Al, Nb) as implant alloying elements. Interestingly on day 90, Nb has been incorporated into bone near the implant.

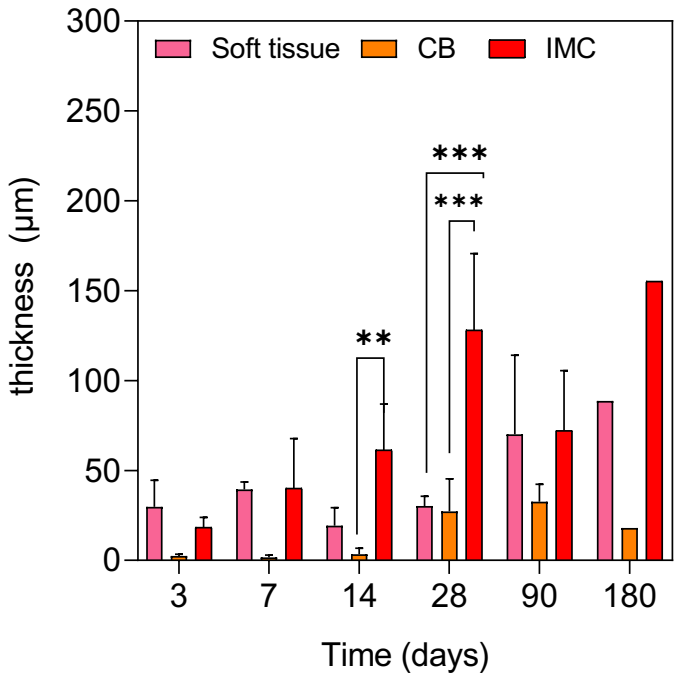

Figure 4.9. WE43 corrosion layer thickness, At different tissue compartments: Soft tissue, Cortical Bone (CB), and Intramedullary Cavity (IMC). Data presented as mean ± standard deviation. **: P<0.01; ***: P <0.001.

The investigation of trace accumulation of Yttrium and REE through ICP-MS analysis of spleen, liver, and kidney samples at 14, 90 and 180 days after implantation are shown in Figure 4.11. All organs showed trace amounts although no significant differences between timepoints were found. However, yttrium presented higher concentration in the spleen at

later timepoints (90 and 180 days), while REE showed increased levels in the spleen and liver (90 and 180 days). The kidney seems to have low affinity for these elements. Yttrium and REE analysis were also performed on sham and Ti implanted animals displaying a residual concentration of elements (Figure S4.5).

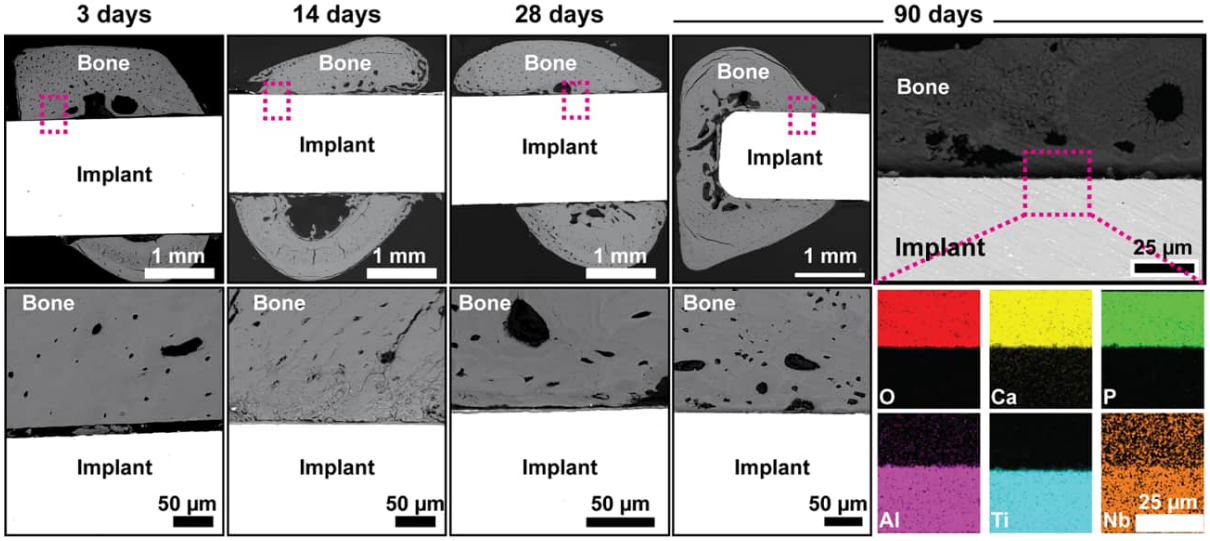

Figure 4.10. Characterization of the bone-implant interface of Ti6Al7Nb pins at 3, 14, 28 and 90 days after implantation by SEM/EDX. *First row*: Overall BSE-SEM image of the Ti-bone specimens from 3 to 28 days after implantation; *Second row*: Bone-implant interface of selected pin areas denoted by pink dotted lines in the first row. On the right, the elemental mapping of oxygen (O), calcium (Ca), phosphorus (), and the implant elements aluminum (Al), Titanium (Ti), and Niobium (Nb) at the bone-implant interface.

4.4. Discussion

The application of Mg alloys as orthopedic implants faces challenges that limit their widespread use. Information on the long-term behavior of Mg alloys is crucial for assessing their safety, efficacy, and performance in clinical applications. We investigate the expression pattern of selected biomarkers in a non-critical defect model, sham group, which presented the highest concentrations of DKK1, OPG, VEGF, and KIM-1, particularly on day 14 and day 45 post-surgery compared to the implanted groups (WE43, Ti). This result was expected since the larger bone defect would have triggered a significant response from the body, measured by higher circulating concentration of biomarkers associated with bone regrowth. Although information on the expression of OPG, DKK1 and VEGF is limited, their expression has been associated with bone healing events. OPG regulates osteoclastic activity by downregulating the OPG/RANK/RANKL system. It is constitutively expressed in unfractured bones and significantly increased throughout the repair process [320]. DKK1, a decoy in the Wnt signaling pathway and a mediator of

osteoblastic activity downregulation, has demonstrated increased expression 14 days post-femoral fracture in skeletally mature rats, coinciding with the phase of soft callus formation [321]. VEGF is recognized for its involvement in numerous steps of the fracture healing cascade, ranging from the initial stage of hematoma at the site of bone fracture to the promotion of bone turnover during the final remodeling phase [322,323].

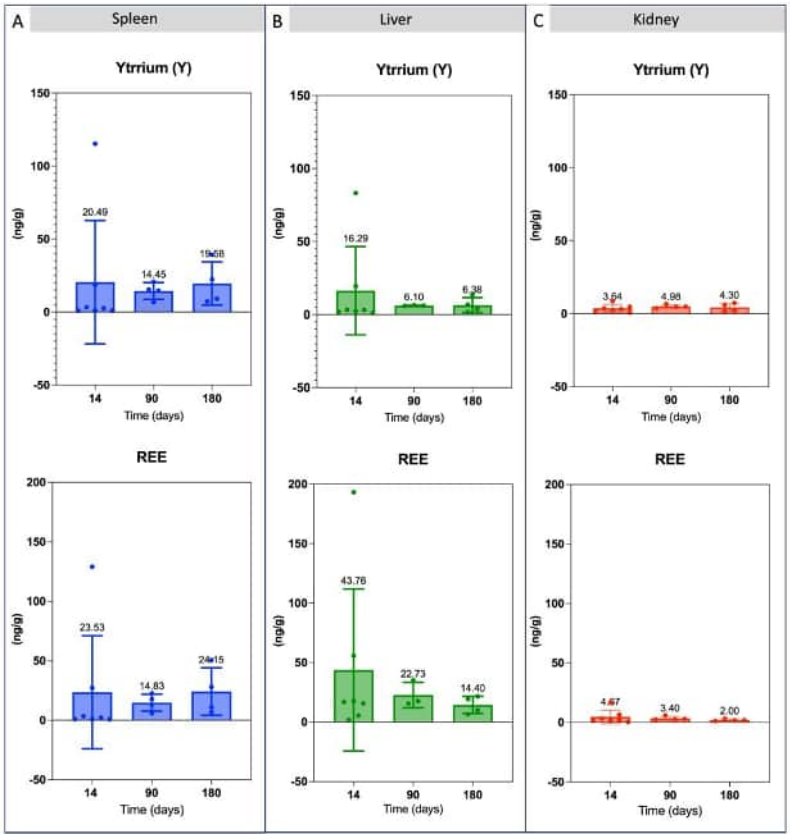

Figure 4.11. Yttrium and REE concentration values (ng/g) in the (A) Spleen; (B) Liver. and (C) Kidney at 14,90 and 180 days after surgery. Day 14 n = 7; day 90 n = 4; day 180 n = 4. Data presented as mean ± SEM.

According to clinical studies, both plasma and local VEGF concentrations correlated with greater *in situ* angiogenesis [324]. Furthermore, a study conducted on dogs demonstrated higher serum levels of VEGF in the group with a bone defect than in the group with implanted biomaterials [325]. More interestingly, a recent study by Begum et al. [221], utilizing a rodent model equivalent to the one used in the present study, has demonstrated that day 14 post-injury represents a critical time point of early bone regeneration. Furthermore, their research revealed woven bone formation in the cortical bone region at day 42, suggesting that bone regeneration processes are still ongoing at this later stage. [190,300]. Hence, the elevated circulating levels of OPG, DKK1, and VEGF observed on day 45 could be associated with a more advanced stage of the regeneration process. In our study, CT results confirm the closure of the bone gap by day 14 in the sham group.

Correspondingly, histological findings at this time point reveal the presence of woven bone formation.

Our study revealed elevated levels of KIM-1 on days 14 and 45 in animals with bone defects (sham). Although KIM-1 is primarily known as a kidney toxicity biomarker [326], this finding is particularly noteworthy given the intricate bone-kidney axis which is closely interconnected through shared regulatory pathways [327]. Discovering the circulating expression of KIM-1 associated to bone healing, rather than primarily related to the toxicity of implants, offers a new perspective, and warrants further investigation.

Regarding the implanted animals, where the bone defect requiring repair is smaller compared to the sham group, the circulating concentration of biomarkers is anticipated to be lower. However, significant differences remain between WE43 and Ti implants. The histological results of day 14 revealed that Ti-implanted animals underwent an earlier rearrangement of the soft tissue compared to WE43. Both types of implants exhibited new periosteal bone formation in proximity to the implant and extending towards the bone edges. However, within the intramedullary region, the Ti samples showed more pronounced tissue rearrangement and a large bone-implant contact surface. Instead, WE43 group showed large voids due to the release of H_2 gas that prevented tissue adhesion to the pin's surface. These voids were still visible in WE43 group on days 90 and 180. Other studies performed on rats showed similar slow degrading Mg-alloys to release gas up to 1 year after implantation in the femur diaphysis [300,301]. The gradual degradation of WE43 and gas void formation that delay bone regeneration, could explain the lower circulating concentration of bone biomarkers such as OPG, VEGF and KIM-1 on days 7 and 28 in the WE43 group compared to Ti group.

Corroborating the delayed bone regeneration hypothesis in the WE43 group, our findings show a significant elevation in G-CSF levels at day 90 post-implantation compared to Ti group, aligning with prior research that highlights G-CSF's pivotal role in bone regeneration in rats with bone defects [328,329]. Longitudinal biomarker analysis in the WE43 group revealed a substantial rise in OPG and VEGF levels at day 90, exceeding earlier measurements at days 7 and 28, indicating continuous bone regeneration. Histological results further support this, showing persistent bone regeneration at the bone-implant interface in the WE43 group up to day 180, confirming an active bone regeneration stage on animals implanted with WE43 at a later time-point compared to Ti and sham groups.

A notable finding in the Ti group was the presence of a fibrotic lining at the interface between the implant and bone on days 14 and 90. This fibrotic encapsulation of Ti implants,

indicative of a foreign body reaction to metallic alloys, is well-documented in the literature and associated with suboptimal implant osseointegration [330].On the other hand, the WE43 group exhibited direct bone-implant contact without fibrotic tissue development, confirming previous results found in the literature [289] and suggesting a more favorable osseointegration.

Relevant findings in the WE43 group seem to converge at 28 days after implantation, especially in relation to the biomarkers FGF23 and IL-10. FGF23 is crucial in the regulation of mineral ions and previous pre-clinical research suggest its expression is associated with mineralized tissue-forming cells like osteoblasts, mainly during the stage of new bone and soft callus formation. [331,332]. We found the lowest circulating concentration of FGF23 on day 28 in WE43 group. Coincidently, SEM-EDX analysis on day 28 revealed an enhanced degradation layer in the intramedullary region of the pin, accompanied by the presence of new compact bone in direct contact with the implant. Furthermore, EDX elemental mapping of the intramedullary region demonstrated that the degradation layer contained a higher phosphorus content than other time points. Accordantly, the WE43 group presented a significantly higher concentration of IL-10 on day 28 than the Ti and sham groups, maintaining this elevated cytokine level from days 28 to 90. IL-10, a potent anti-inflammatory cytokine, is known for its inhibitory effect on osteoclastogenesis and its role in promoting osteogenesis [333]. *In vitro* studies have shown that Mg^{2+} increases IL-10 expression [307,334]. An *in vivo* study further supports the osteogenic property of IL-10 by correlating elevated IL-10 levels to successful osseointegration and bone formation after Mg-alloy implantation [307]. As previously mentioned, WE43 pins presented a ticker corrosion layer in the intramedullary region at day 28, suggesting an accelerated degradation of the implant at this specific time point, possibly leading to a higher release of Mg^{2+}. This phenomenon could plausibly explain the increased serum concentration of IL-10 at the same time point.

Finally, our results confirm the trace accumulation of Yttrium and REE in organs farther from the implantation site, with the spleen and liver showing the highest concentrations after 90 days of implantation. REEs are commonly incorporated into Mg alloys to enhance corrosion resistance and mechanical properties. However, their long-term biological impact is poorly understood [335]. Although existent research has predominantly focused on the distribution of Mg and alloying elements near the implant, with some studies reporting an increased Mg concentration in peri-implant tissues [300,336], there have been few investigations into the systemic accumulation of REE in organs remote from the

implant site [337]. Therefore, although we are far from being able to apply biodegradable WE43 implants in significant human long bones, such as the femur, the prospect of employing multiple smaller WE43 implants for fracture repair emphasizes the urgency of comprehensively examining the long-term systemic consequences of REE.

4.5.- Conclusions

We highlight the effectiveness of circulating biomarkers as a detection tool for monitoring physiological changes after implantation of Mg-alloy in rat's femurs. A specific pattern of expression of bone biomarkers, including OPG, VEGF, DKK1, and KIM-1, appears to be correlated to phases of active bone regeneration, as demonstrated by the higher levels of these biomarkers in the Sham group. Furthermore, differential biomarker levels, specifically OPG and VEGF, were observed between WE43 and Ti groups. The WE43 group displayed an ongoing bone regeneration, where the gradual degradation of the alloy and hydrogen gas release seemed to prolong the bone regeneration timeline compared to the Ti group. Interesting findings specific to the WE43 group are the reduced FGF23 and elevated IL-10 plasma levels on day 28. Finally, we demonstrate the accumulation of Y and REE in organs distant from the implantation site after 90 days of WE43 implantation. These results emphasize the necessity for comprehensive research on the long-term systemic impact of REE released from Mg alloys. Finally, we draw attention to the potential utilization of biomarkers such as FGF23 and KIM-1, which, despite their established application in other clinical domains, remain relatively unexplored in the realm of bone regeneration or orthopedic implantation. Our results bring new hypotheses for further exploration in specific circulating biomarkers to monitor implant osseointegration and the effects of Mg alloys degradation products.

Supplementary materials

Assessment of Circulating Biomarkers

Plasma samples collected from the same animals of each experimental group at specific time points (Figure 4.1) and they were analyzed using the three different kits in accordance with manufacturer instructions [312]. Data acquisition was performed on MAGPIX Luminex xMAP technology for Median Fluorescence Intensity and analyzed using Belysa Immunoassay Curve Fitting software (Sigma-Aldrich, St. Louis, MO), with a 5-parameter model as described in [312].

The list of analyzed biomarkers' range, sensitivity and unit of measure can be found on the following links:

- Rat Cytokine/Chemokine Magnetic Bead Panel (G-CSF, GRO-KC/ CXCL-1, TNF-α, IL-6, IL-1α, IL-10, IL-4; IFNγ, MCP-1): https://www.sigmaaldrich.com/IT/it/product/mm/recytmag65k#product-documentation
- Rat Bone Magnetic Bead Panel (DKK1, FGF23, OPG):

https://www.sigmaaldrich.com/IT/it/product/mm/rbn1mag31k.

- Rat Kidney Magnetic Bead Panel (OPN, VEGF, KIM-1, TIMP-1):

https://www.sigmaaldrich.com/IT/it/product/mm/rktx1mag37k.

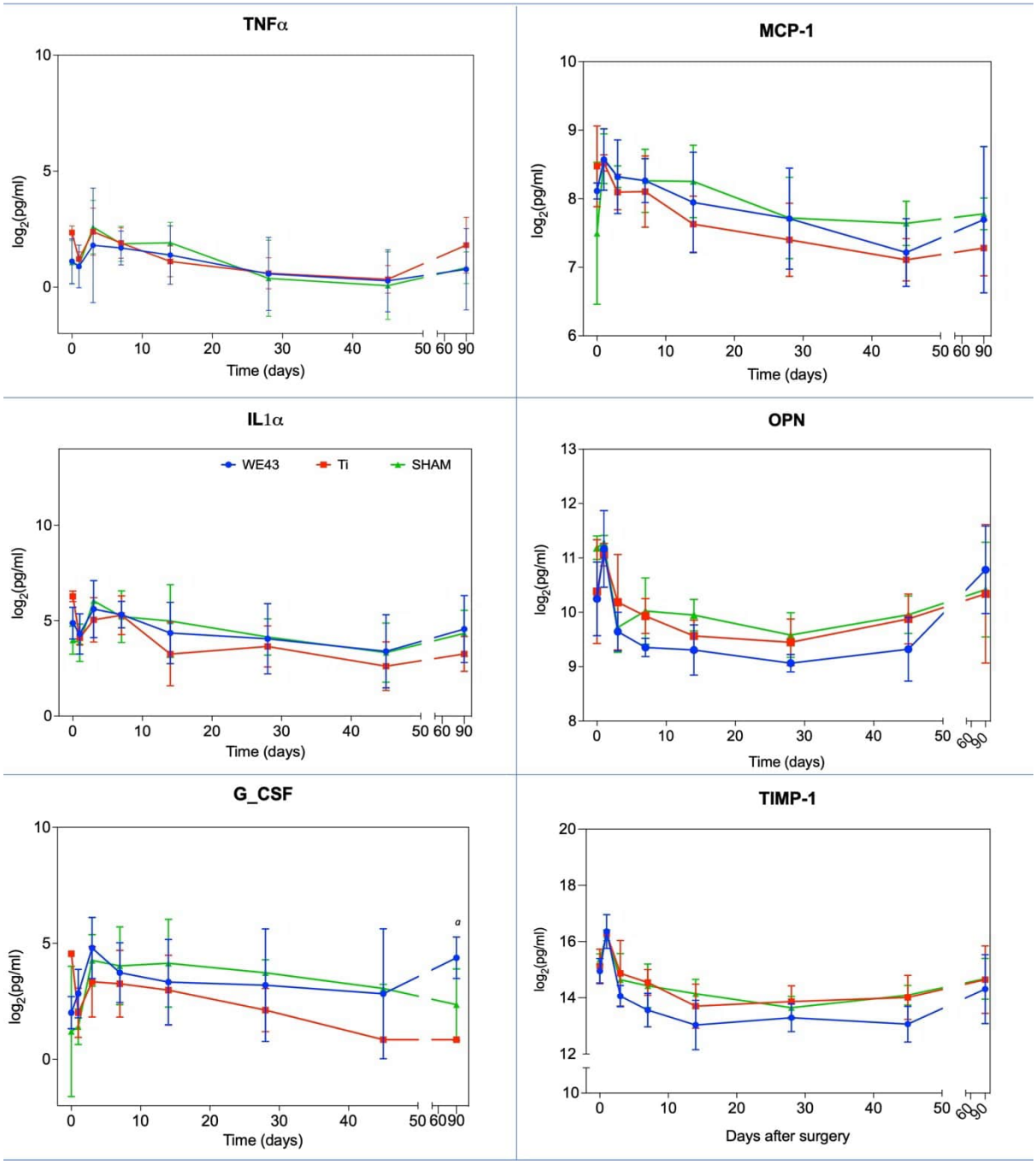

Figure S4.1.- Longitudinal profiling of circulating levels of G_CSF, TNFα, TIMP-1, MCP-1, OPN, and IL1α for the three experimental groups: WE43 (blue), Ti (red), sham (green). a: $P<0.001$. Data presented as mean ± SEM.

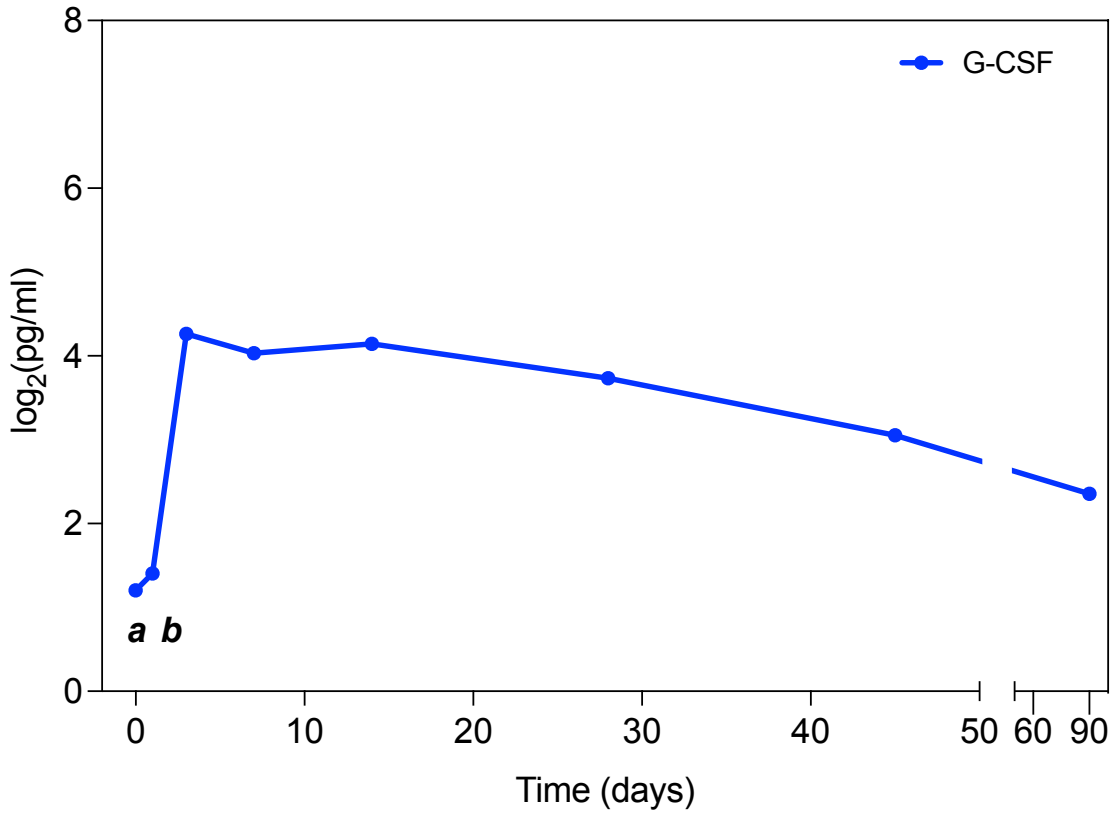

Figure S4.2. Longitudinal representation of G-CSF for Sham group. Mean± SEM. a: *P*<0.001 day 0 *versus* day 14; b: *P* <0.001 day 0 *versus* days 3,7 and 14.

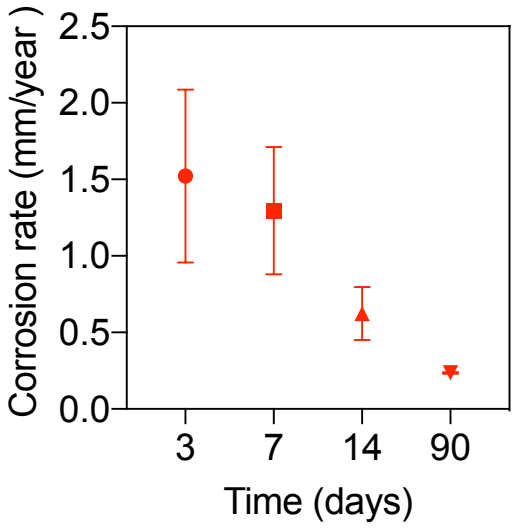

Figure S4.3. *In vivo* corrosion rate calculated by the mass loss method (n = 3 samples7 time point). Data presented as mean ± standard deviation.

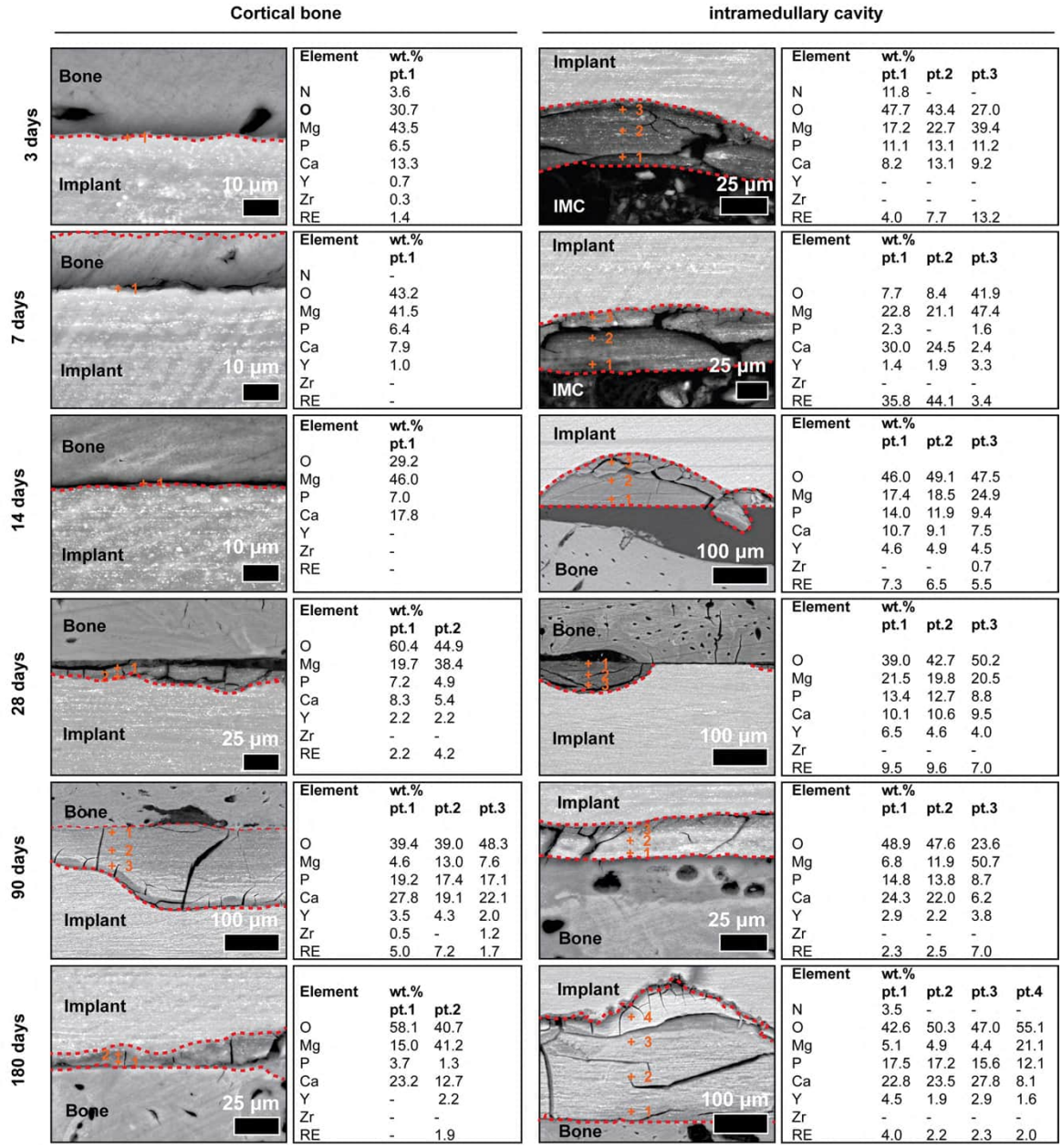

Figure S4.4. Cross-sectional SEM images and corresponding EDX point analysis of the corrosion layers formed on WE43 pins after 3,7,14,28,90, and 180 days of implantation**.**

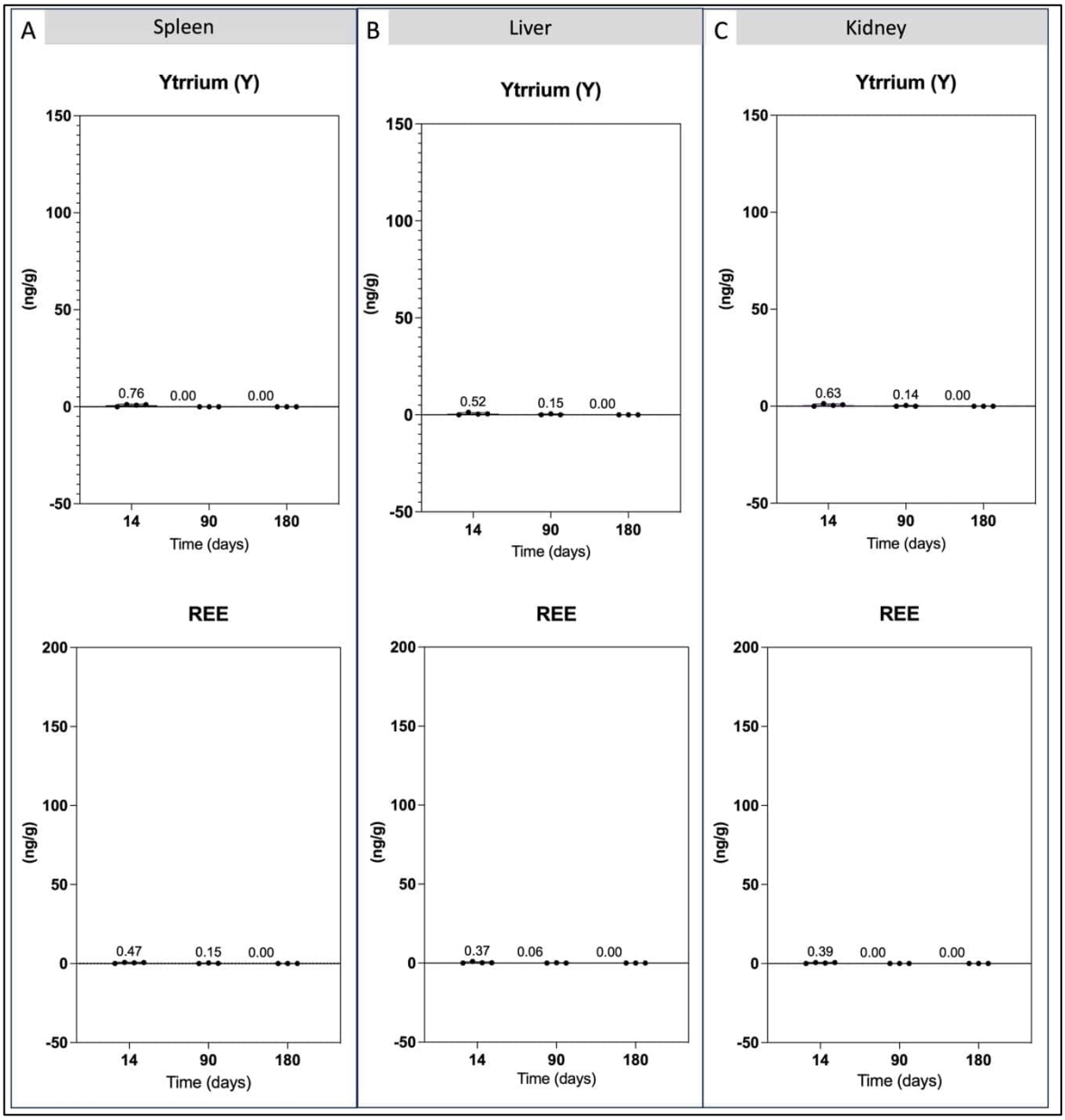

Figure S4.5. Yttrium and REE concentration values (ng/g) in the (A) Spleen; (B) Liver and (C) Kidney at 14, 90, and 180 days after implantation; Data presented as mean ± SEM.

Bridging the chapter 4 and 5

Several research has found increased Mg concentration in the peri-implant tissues [300,336], but only a few investigations have observed the accumulation of REE in organs distant from the implant site [338,339]. The presence of REE and Y in the liver, kidney, and spleen is something for further investigation due to limited research on REE. According to Waisy et al. [313], liver and spleen hyperplasia was observed in rabbits when implanting Mg-Y-REE-Zr screws. However, Zhang et al. [340,341] did not detect any changes in the liver and kidney functions when Mg-Nd-Zn-Zr screws were implanted in a goat femoral condyle fracture model for 18 months. Zhang et al. [342] surgically implanted Mg-Nd-Zn-Zr stents into the common

carotid artery of rabbits for up to 20 months. The authors observed Nd accumulation in the lung, liver, and spleen tissues. These contrasting results highlight the insufficient research on the short and long-term effects of released REE ions, both in the peri-implant environment during the degradation of Mg-REE-containing implants, as well as the effects of their accumulation at distant organs. Therefore, additional investigations over an extended period of time *in vivo* are required to elucidate the impact that Mg-REE-containing alloys could have on providing safety information for their commercialization and use in humans.

To address the biosafety concern associated with Mg-REE-containing alloys, alternative strategies to manufacture Mg alloying with essential elements for the human body such as Zn and Ca, have been an advised approach to develop Mg implantable devices [221]. In addition, when studying mechanisms related to body size or bone healing efficiency, it is important to select an animal model (size and anatomy) that closely resemble the human scenario [343], which is vital for translational research purposes. Sheep models are valuable for studying the biomechanical, biochemical and histological aspects of bone biology, due to similarities with humans in terms of weight, size, bone and joint structure, and bone remodeling process [344]. Therefore, in Chapter 5, human-sized screws made of ZX00 (Mg–Zn–Ca; <0.5 wt% Zn and <0.5 wt% Ca, in wt%; Fe-content <1 ppm) alloy were implanted into the diaphysis of sheep to assess the degradation and biocompatibility of the screws. The focus was on ***understanding how the manufacturing process may influence the corrosion performance at various regions of the implant***.

Chapter 5

In vitro and in vivo degradation behavior of Mg-0.45Zn-0.45Ca (ZX00) screws for orthopedic applications

Diana C. Martinez, Anna Dobkowska, Romy Marek, Hanna Ćwieka, Jakub Jaroszewicz, Tomasz Płociński, Črtomir Donik, Heike Helmholz, Bérengère Luthringer-Feyerabend, Berit Zeller-Plumhoff, Regine Willumeit-Römer, Wojciech Święszkowski

Published in ***Bioactive Materials*** *2023 (28): 132-154. doi: 10.1016/j.bioactmat.2023.05.004*

ABSTRACT

Magnesium (Mg) alloys have become a potential material for orthopedic implants due to their unnecessary implant removal, biocompatibility, and mechanical integrity until fracture healing. This study examined the *in vitro* and *in vivo* degradation of an Mg fixation screw composed of Mg-0.45Zn-0.45Ca (ZX00, in wt.%). With ZX00 human-sized implants, *in vitro* immersion tests up to 28 days under physiological conditions, along with electrochemical measurements were performed for the first time. In addition, ZX00 screws were implanted in the diaphysis of sheep for 6, 12, and 24 weeks to assess the degradation and biocompatibility of the screws *in vivo*. Using scanning electron microscopy (SEM) coupled with energy dispersive X-ray spectroscopy (EDX), micro-computed tomography (μCT), X-ray photoelectron spectroscopy (XPS), and histology, the surface and cross-sectional morphologies of the corrosion layers formed, as well as the bone-corrosion-layer-implant interfaces, were analyzed. Our findings from *in vivo* testing demonstrated that ZX00 alloy promotes bone healing and the formation of new bone in direct contact with the corrosion products. In addition, the same elemental composition of corrosion products was observed for *in vitro* and *in vivo* experiments; however, their elemental distribution and thicknesses differ depending on the implant location. Our findings suggest that the corrosion resistance was microstructure-dependent. The head zone was the least corrosion-resistant, indicating that the production procedure could impact the corrosion performance of the implant. In spite of this, the formation of new bone and no adverse effects on the surrounding tissues demonstrated that the ZX00 is a suitable Mg-based alloy for temporary bone implants.

Keywords: *magnesium alloys, biodegradable implants, microstructure, electron microscopy, corrosion layers*

Graphical abstract

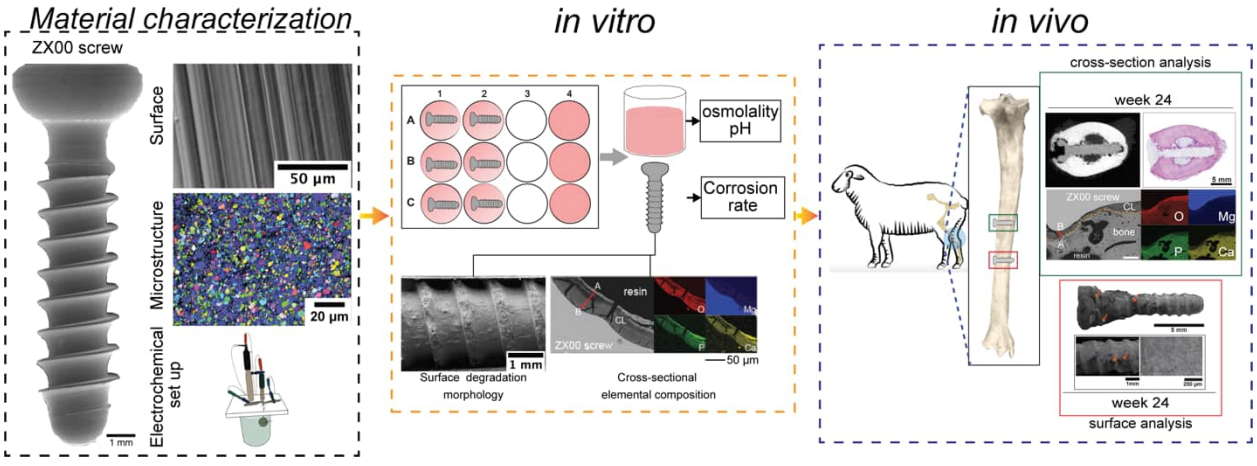

5.1. Introduction

In orthopedic surgery, permanent or temporary implants are used for realignment and fixation to ensure adequate bone healing. Permanent implants, such as the ankle, knee, wrist, or hip implants, will ideally function in the human body for the patient's life [8]. Temporary orthopedic implants, such as pins, wires, screws, or plates, are used to repair fractured bones and are only meant to be used for an adequate time [345]. Usually, metallic orthopedic implants made from Co-based alloys, stainless steel, and Ti and its alloys are considered the gold standard metals for the internal fixation [9]. However, toxic metallic ion release, periprosthetic infection, and stress shielding effects are permanent metallic implant-related complications [9,11,12,346].

These drawbacks of permanent implants could inhibit the bone formation or bone resorption processes and necessitate a second surgery to retrieve or remove them after the bone has healed [347]. On the other hand, due to its similar mechanical properties close to the bone, such as elastic modulus and density, Mg and its alloys are promising biodegradable materials [9,14,23,25,64,197,348–351]. Furthermore, as a material for orthopedic applications, Mg-based devices have shown osteoinductive and osteoconductive effects, substantially high mineral apposition rates, and enhanced bone mass around Mg-implants [185,352]. Nevertheless, one major obstacle that limits the application of Mg-based implants is its high corrosion rate, often leading to premature implant failure before bone tissue healing is completed [9,14,353–359].

Improving the corrosion resistance of Mg-based alloys is commonly considered an issue by researchers investigating biomaterials [360,361]. Purifying, alloying, coating, and surface treatments are different approaches that can decrease the corrosion activity of Mg-based materials [59]. It is worth noting that alloying elements not only improve biocompatibility and control of the degradation behavior but can also improve the mechanical properties of the material and introduce another biological function such as antibacterial effects (Ag) or further cellular processes (Zn, Ca) [48,187,289,358,362]. Studies show that resistance to general and pitting corrosion of Mg alloys is improved by adding Ca [13,64,76,357]. Zn also enhances the corrosion resistance of Mg alloys via a solid hardening mechanism and may reduce hydrogen evolution during the degradation [48,59,76,348,363]. Moreover, Zn is essential for numerous biological functions in the human body, such as stimulation of new bone formation, preservation of bone mass, signal transmission, apoptosis regulation, and gene expression

[364]. However, the high concentration of Zn can cause microporosity during solidification and increase the susceptibility to corrosion attack [358,365,366].

Recent preclinical studies [133,185,187,367,368] have demonstrated that the alloying system Mg-Zn-Ca (ZX alloys) is biologically safe and promotes osseointegration. Jang et al. [369] examined the corrosion behavior of Mg-Zn-Ca alloys in subcutaneous mouse models for 60 days. They observed that with the increasing Zn concentration, the degradation rate of the materials accelerated. Using micro-computed tomography (μCT) analysis, Kraus et al. [185] investigated the degradation behavior of ZX50 (Mg-5Zn-0.25Ca in wt.%) and WZ21 (Mg-1Zn-2Y in wt.%) pins. Although the results demonstrated that ZX50 degrades more rapidly with high hydrogen gas formation, an improvement in bone formation around the implant was observed. Grün et al. [187] studied the degradation behavior of ZX00 (Mg-0.45Zn-0.45Ca in wt.%) alloy using models of both small and large animals. After 6, 12 and 24 weeks of *in vivo* implantation the alloy degraded slowly and uniformly, with no adverse effect on bone formation and in-growth. Holweg et al. [133] examined the degradation performance of ZX00 screws for fracture stabilization in a sheep model, and they demonstrated that the osteotomies completely consolidated after 12 weeks. In the femur of juvenile rats, Cihova et al. [367] implanted ZX10 (Mg-1Zn-0.3Ca in wt.%) and ZX20 Mg-1.5Zn-0.25Ca in wt.%) pins, and it demonstrated that ZX10 degraded at a slower rate when compared to ZX20. Mao et al. [368] observed a slow degradation rate after 12 weeks when Mg-2Zn-0.05Ca rods were implanted in femoral condyles of rabbits with severe localized corrosion between 12 and 16 weeks, without accumulation of corrosion products in the surrounding tissues. Sommer et al. [370] studied the degradation of ZX00 pins after 4, 8 and 12 weeks of implantation in juvenile, old, and osteoporotic rats. Compared to young and aged rats, the osteoporotic rats exhibited accelerated degradation and increased gas evolution. After 24 weeks of implantation of ZX00 pins in rats, Okutan et al. [221], observed homogeneous degradation along with increased gas accumulation and superior new bone tissue formation. Marek et al. [371] also investigated the degradation behavior of ZX00 screws at various implant locations. According to their findings, the cortical bone thickness was greater around ZX00 screws than Ti screws, which showed low bone-to-implant contact (BIC) values. Similarly, they implanted trans-epiphyseal ZX00 nails in juvenile sheep, demonstrating no deleterious influence on the longitudinal bone growth, despite bone-structure alterations observed in the initial phase of ZX00 nail degradation [372]. Han et al. [373] implanted Mg5Ca1Zn pins in the femoral condyle of rats and observed accelerated bone healing due to the release of anabolic metallic ions into the adjacent tissues, which stimulated the growth of blood vessels and actively recruit osteoprogenitors cells.

One of the most critical problems regarding Mg-Zn-Ca alloys used in biomedicine is the precipitation-dependent corrosion of those alloys. Hofstetter et al. [358] investigated *in vitro* and *in vivo* corrosion behavior of conventional purity and ultrahigh-purity Mg-5Zn-0.3Ca (ZX50) Mg pins and found that a reduction in the impurity level to trace amounts decreased the alloy's degradation rate. Cihova et al. [367] compared Mg-1Zn-0.3Ca (ZX10) and Mg-1.5Zn-0.25Ca (ZX20) in terms of micro-galvanic corrosion, where various phases formed micro- or nano-galvanic couple with Mg matrix. They stated that the large cathode-to-anode ratio of μm-sized Mg-matrix grains and nanometric Mg_2Ca-type intermetallic particles (IMPs) expectedly caused the rapid dissolution of the latter in the ZX10 alloy. Nevertheless, the corrosion of ZX10 screws can be controlled, and the continuous degradation of the biomimicking calcification matrix initiates the bone formation process [183].

The extensive research on Mg as an absorbable metal has evolved into translational research. There have been clinical trials with Mg-based implants for orthopedic applications, and pure Mg, Mg-Ca-Zn, and Mg-RE screws are currently in clinical use [18,183,197,216,293,374–377]. Nevertheless, despite the fact that Mg implants can be used as absorbable metals for orthopedic applications, a 13% complicate rate [294] has been reported, including swelling and moderate hyperemia [378,379], femoral head collapse [374], resorption cysts [380], postoperative infection and pain [294]. Hence, it is meaningful to explore the causes of such clinical complications and how tailor de corrosion resistance of Mg implant to overcome these challenges.

Although the behavior of ZX alloys has been several times investigated under *in vitro* and *in vivo* conditions, there is a significant lack of information on the corrosion processes and changes in thickness and composition of the corrosion products resulting in degradation of Mg-0.45Zn-0.45Ca (ZX00) screws under physiological conditions. It is crucial to investigate the corrosion layer formed during Mg degradation as the formation of this layer might be modified and change during the implant degradation with some ions released and absorbed earlier than others [381], and as a consequence, various degradation could be observed. [382].

Previous studies of the ZX00 alloy have examined the microstructure and estimated the corrosion rate *in vitro* using simple samples (i.e. rods), while *in vivo* studies have been conducted using screw-shaped implants [133,367,383]. The fabrication procedures used for Mg-based implants have a direct influence on their properties and performance in the biological environment [292,384]. Marco et al. [175] observed distinct degradation of pure Mg, Mg-10Gd and Mg-2Ag alloys *in vitro and in vivo*. According to their findings, the increased corrosion rate observed *in vitro* may be due to different immersion solutions employed or the presence

of impurities in the alloys, but it may also be the result of different processing routes, as *in vitro* specimens were disc-shaped while *in vivo* specimens were pin-shaped, with larger grain size in the discs compared to the pins. Similarly, Liu et al. [385] found that differences in grain size and texture of pure Mg and AZ31 formed during different manufacturing processes may result in different local interactions with biomolecules such as proteins under physiological conditions, further contributing to the different immune responses. This was observed when pure Mg and AZ31 pins were implanted in the femoral shaft of rats.

In addition to the manufacturing procedures, the local tissue metabolism at the implantation site also influences the corrosion of Mg implants. The interface between a surgical implant and the adjacent tissues is characterized by complex and dynamic mechanical and biological interactions (immune and inflammatory response as well as bone healing processes [386]) between the implant and surrounding tissues [387,388]. These interfaces between tissues (bone, cartilage, tendon, ligament, muscle and soft tissues) and Mg implants are of crucial importance; and influence the corrosion performance of Mg-based devices and the healing and remodeling potential of tissues [389]. Understanding the complex biological interactions between Mg implants and adjacent tissues is essential for the target-oriented implant development processes of Mg-based devices taking into account the implantation sites used in clinics [390]. Consequently, it is still necessary to investigate the corrosion performance of Mg-Zn-Ca alloys and the influence of the processing routes in order to comprehend their degradation and interactions with the physiological environments to which the alloy is exposed. Hence, this study investigates the degradation behavior of low-alloyed ZX00 screws with the same geometry and dimensions under physiological conditions (*in vitro* and *in vivo*) and, for the first time, characterizes the subsequent corrosion products at different screw zones, with an emphasis on the impact that the manufacturing process may have on the corrosion performance at various regions of the screw: the head, the valley, and the tip.

5.2. Material and Methods

5.2.1. The fabrication process of the screw

Custom-made (not commercially available) screws were manufactured by Ernst Wittner GmbH, Wien, Austria, from extruded rods fabricated from rods produced at ETH Zürich in collaboration with Cavus AG. Briefly, the screws were fabricated from the ZX00 alloy (Mg-0.45Zn-0.45Ca) which was made from pure Mg (99.9999 wt.%) alloyed with Ca (99.95 wt.%) and Zn (99.9999 wt.%), and subsequently extruded to the shape of rods with 6 mm in diameter. The extrusion and homogenization process is further described in [133]. The thread and the head of the screws were computer-turned (using a computer numerical control machine, CNC), and the head's Torx was drily milled without using cooling oil to reduce the risk of corrosion attack and contamination. The screws were ultrasonically cleaned in acetone, air-dried and gamma sterilized at 25 kGy γ-radiation dose. As shown in Figure S7.1, the screws were fabricated with a length of 16 mm, an outer diameter of 3.5 mm, and a head diameter of 5.7 mm.

5.2.2. Microstructure characterization

The surface morphology of the as-received sterilized ZX00 screws was analyzed using a stereomicroscope (Olympus SZ61, Japan) and scanning electron microscopy (SEM, Hitachi, SU-8000, Japan) equipped with an energy dispersive X-ray detector (EDX, UltraDry EDS Detector, Thermo Scientific™). The chemical composition of the as-manufactured screw determined by EDX is presented in Table S5.1. The surface roughness was determined by analyzing three random areas of 100 µm × 100 µm per screw using a confocal laser scanning microscope (CLSM, Keyence, VK-1000, Japan). The phase composition of the screws was determined using X-ray diffraction (XRD, Bruker D8 Advance) operated at 40kV and 40mA with Cu-Kα radiation. The results were recorded by stepwise scanning 2θ from 10° to 120°, with a step size of 0.02° and a count time of 10 s per step. The microstructures on the surface perpendicular to the extrusion direction were observed using an SEM (Hitachi, SU70, Japan) after ion milling in an Ar+ beam (Hitachi, IM 4000, Japan). Crystallographic orientations and distribution of grain sizes were calculated based on the results obtained from the electron backscattered diffraction (EBSD) performed on the SEM SU70 equipped with a Bruker EBSD detector. The EBSD scans were conducted with a step size of 0.1 µm. The crystallographic orientations of grains are shown as inverse pole figure (IPF) maps where various colors

distinguish an orientation of a given sample direction in a crystal frame. Grain boundary characterizations are also shown. If the angle between two neighboring grains was distorted by more than 15°, then the angle between those grains was described as a high-angle grain boundary (HAGB). When the grains were misoriented by less than 15°, a low-angle grain boundary (LAGB) was created between those grains. Additionally, Kernel average misorientation maps calculated for 5th nearest neighbors are depicted.

5.2.3. In vitro studies

5.2.3.1. Immersion tests

Thirty screws were entirely immersed in α-minimum essential medium (α-MEM; Life Technologies, Germany), supplemented with 10% fetal bovine serum (FBS) (Gibco, Life Technologies, Germany) and 1% penicillin/streptomycin (100 units/ mL penicillin and 100 µg/mL streptomycin P/S; Invitrogen, Germany) for 3, 6, 14, 21, and 28 days, respectively (n=6/time point). Sterilized 12-well culture plates (Greiner Bio-One, Germany) were used to place one ZX00 screw per well. Each sample was immersed in 2 mL of immersion medium and incubated under cell culture conditions (37 ºC, 5% CO_2, 20% O_2 and 95% controlled humidity). Three empty wells filled with immersion medium were used as the control. The immersion medium was changed every 2-3 days. The pH and osmolality of the initial culture medium were recorded using a pH meter (Sentron® SI600, Sentrom Europe BV, Netherlands) with a MiniFET probe and a cryoscopic osmometer (OSMOMAT® auto, Gonotec GmbH, Germany), respectively. The pH and osmolality of the supernatant with and without samples were measured after each cell culture medium change. At the determined time of immersion (3, 6, 14, 21 and 28 days), samples were rinsed with deionized water and ethanol and finally air-dried.

Hydra Medusa Software [258] was used to calculate the fraction of the chemical equilibrium diagrams for each immersion time point based on the ionic concentration of the immersion medium composition (Table S5.2). The Mg concentration was determined using the calculated CR based on the mass loss measurements to understand the various compounds that could form during the immersion in the solution used for this research throughout the entire pH range.

5.2.3.2. Corrosion rate calculations after in vitro immersion

To calculate CR based on mass loss measurements, after immersion in the α-MEM medium for the defined time, the corrosion products from the samples (n = 3screws/time point)

were chemically removed by samples treatment in fresh chromic acid (180g/L in distilled water, VWR International, Germany). Equation 5.1 was used to calculate the CR [255]:

$$CR = (K \times W) / (A \times T \times D) \quad \text{(Eq. 5.1)}$$

where: K is a constant (8. 76 × 10^4 mm×y^{-1}), W is the mass loss change (g), A is the exposed surface area (cm^2), T is the time of exposure (h), and D is the material density (g×cm^{-3}).

All 3 to 28 days of data were fitted with linear regression and inserted into an empirical two-parameter Equation 5.2 [391].

$$h = h_\infty . t + h_0 \quad \text{(Eq. 5.2)}$$

where h is the mean degradation depth in µm, h_∞ describes the CR of the alloy at higher immersion times, t is the total incubation time in days, and h_0 is the y-intercept describing the degradation depth to initial reactions.

The CR calculated based on the mass loss measurements were compared with CR calculated using microcomputed tomography (µCT, Poenix Nanotom®, GE, Germany). To quantify CR, µCT scans were conducted at 100 keV, 1000 ms exposure time, and 7.5 µm voxel size on three immersed specimens for each designated time.. X-AID 2021.2.0. (MITOS, GmbH, Garching, Germany) and Amira-Avizo 9.4.0 (FEI SAS, ThermoScientific, France) software were used for reconstruction and segmentation, respectively. The corrosion rate of the screws was determined using the Equation 5.3 [392]:

$$CR = \frac{V_i - V_r}{A * t} \quad \text{(Eq. 5.3)}$$

where V_i is the volume of the as-received screw before immersion (mm^3), V_r is the residual volume (mm^3), A is the surface area of the as-received screw before immersion (mm^2), and t is the immersion time (years). Before immersion tests, the initial volume and surface, the volume and surface area of the original screw were calculated and it was found to be 114.54 mm^3 and 229.53 mm^2, respectively.

5.2.3.3. Characterization of the screws after in vitro immersion tests

After immersion tests, the macro images of the specimens were taken using an Olympus SZ61 stereomicroscope. Further observations of the corroded screws were done using SEM (Hitachi S3500N, Japan) in low vacuum mode at 70 Pa. The chemical analyses of the corrosion products were done using an energy-dispersive X-ray spectrometer (EDX, UltraDry EDS Detector, Thermo Scientific™). After each immersion period, changes in the surface area (S_A, mm^2) recorded using µCT were calculated using Equation 5.4:

$$S_A = A_i - A_d \quad \text{(Eq. 5.4)}$$

where A_i is the surface area calculated for the specimen after immersion, and A_d is the surface area of the corroded screw after removal of the corrosion layer. Additionally, the reconstructed 3D images of *in vitro* samples with and without corrosion products were shown and compared.

To determine the thickness and chemical composition of the corrosion layers, cross-sectional observations of *in vitro* specimens were performed. the samples were ion milled using IM4000 Hitachi Ion Milling System and subsequently coated with carbon. Then, measurements of the thickness of the corrosion layer were performed using Fiji software [257]. XRD measurements were performed on the immersed screws. However, except for peaks from the substrate phases and strong background noise, no information was obtained from the corroded surfaces. Similar challenges in identifying the phase constituents of the corrosion products have been reported previously [393–395]. Therefore, the chemical composition of the corrosion products formed on the three zones of the screw (head, valleys, tip) after 3 days of *in vitro* immersion were characterized using Versa Probe III AD photoelectron spectroscopy (XPS, PHI, USA) with a monochromatic Al K_α (1486.3 eV) X-ray source. For each measurement, spectra were acquired on a 200 µm analysis spot size with a charge neutralizer turned since the thick, unconducive oxides were present on the surface after the immersion. Survey spectra were measured at a pass energy of 224 eV and a step of 1 eV, while high-resolution XPS spectra were measured at a pass energy of 55 eV and a step of 0.05 eV. For survey spectra, 10 cycles were performed, and for all the HR spectra measurements, at least 15 cycles were done. The XPS spectra were corrected for the possible charging effect using carbon C 1s peak with the binding energy of 284.7 eV. After acquiring the spectra, the data were processed with the CasaXPS with Shirley background subtraction. The accuracy of the binding energy (BE) scale is estimated to be 0.2 eV. High-resolution spectra for Mg 1s, O 1s, C 1s and Ca 2p were analyzed. To remove the top layer of the sample, Ar^+ ion sputtering of the sample was performed. Sputter time was 2 minutes at 2 kV over a 2 mm × 2 mm area that was centered in the middle of the sample. Zalar rotation was turned on to sputter the sample evenly and to eliminate the ripening effect of the sputtering. Right after sputtering, high-resolution spectra for C 1s, O 1s, Mg 1s and Ca 2p were acquired on a spot area centered in the middle of the sample.

5.2.3.4. Electrochemical measurements

The corrosion resistance of the tip, the thread and the head of the screws was analyzed using electrochemical methods (open circuit potential, electrochemical impedance spectroscopy (EIS) and potentiodynamic polarization) in phosphate-buffered saline solution (PBS, tablets purchased from Sigma Aldrich). One tablet dissolved in 200 mL of deionized water yields 10 mM phosphate buffer, 2.7 mM potassium chloride, 137 mM sodium chloride, and a pH of 7.4. The electrochemical setup was composed of a platinum (Pt) wire as a counter electrode, silver chloride (Ag/AgCl) as a reference electrode, and the measured sample as the working electrode. Testing was done using potentiostat Gamry Instruments Reference 600+ at 37°C. First, the open circuit measurements were carried out for 1 h. Afterwards, EIS and potentiodynamic tests were recorded. EIS was carried out at open circuit potential with an AC amplitude of 10 mV over a frequency range from 0.01 Hz to 10 kHz. The potentiodynamic polarization tests were registered from the 0.5 V below open circuit potential (E_{OCP}) to 1.5 V vs E_{OCP} with a scan rate of 1 mV/s. The results were fitted using Gamry Framework™ software 7.8.2. For the electrochemical testing, samples were molded in acrylic resin. The exposed area of the samples was ground using 600-4000-grit SiC papers and subsequently polished with 3 and 1 μm water-free diamond suspensions (glycol-based lubricant was used). To ensure the reproducibility of the results, at least three measurements for each sample were made.

5.2.4. In vivo animal model

5.2.4.1. Ethical statement

The large animal trial (Permit number: BMBWF-66.010-0107-V-3b-2019) was approved by the Austrian Federal Ministry for Science and Research and followed the guidelines for the accommodation and care of animals formulated by the European Convention for the protection of vertebrate animals used for experimental and other scientific purposes. The experiment was performed according to the 3R principles (replace, reduce, and refine).

5.2.4.2. Animal surgical procedure

The *in vivo* degradation behavior of ZX00 screws was evaluated after implantation into the diaphysis of sheep (Ovis aries) over 24 weeks. 3-month-old female lambs were randomly assigned to three groups for observation periods of 6, 12 or 24 weeks (n=3 per group). The sheep were group-housed at the testing facility (Medical University of Graz) in a sheep-shed with access to the outdoor meadows for one week prior to surgery, to reduce stress and enable environmental acclimation. Food and water were always provided *ad libitum*. All lambs underwent surgeries under sterile clinical conditions and general anesthesia. After shaving and disinfection of the tibiae, three ~2 cm long incisions were made at 3–5 cm distances in the medial diaphyseal area, followed by periosteal dissection down to the bone. Bicortical drilling was performed at each dissected area, using a 2.7 mm drill bit and a 3.5 mm tapper. 18 screws were implanted into the right diaphysis of the animals in a strictly lateral direction to the tibial shaft (Figure S5.2). Wounds were closed in layers and disinfected using an iodine solution. Carprofen and buprenorphine were used as postoperative analgesia for four days, while gentamicin and penicillin were administered for infection prophylaxis reasons for five days. Wound checking was performed daily by trained employees for two weeks. Following, the sheep were transferred to an external housing facility, where they were kept on meadows with a shelter with access to hay, food, and water *ad libitum*. Daily inspection concerning behavioral peculiarities (e.g., eating, moving, etc.) was performed by the farmer and at least weekly by a vet. The animals were transferred back to the animal facility for the sacrification which was done by intravenous overdose injection of propofol, ketamine and potassium chloride after 6, 12 or 24 weeks. Finally, one tibia per animal was harvested for further use. Titanium (Ti) screws with similar dimensions were implanted in the left diaphysis of sheep as a control. The comparative analysis between ZX00 and Ti screws has been described in [371,396]. Therefore, these data are not presented here.

5.2.4.3. Ex vivo micro-computed tomography data acquisition and analyses

Ex vivo μCT imaging was performed on all harvested tibiae using a Bruker SkyScan 1276 scanning device (Bruker, Germany). An aluminum-copper filter was used with operating voltage and current of 100 kV and 200 mA, respectively. The rotation step size was set to 0.4 degrees at a binned pixel size of 80.2 μm. Nine explants were scanned, three explants per time point. The scanned data was converted into DICOM format and imported to Avizo Fire

Software (version 2020.2). For descriptive analysis, two-dimensional (2D) planes and three-dimensional (3D) reconstructions were assessed using Avizo Fire Software. The radiolucent zones adjacent to the screws were defined as gas bubbles caused by the corrosion of the screws.

5.2.4.4. Characterization of the corroded surfaces

Following µCT imaging, the diaphysis was cut in the transverse plane with a minimum of 2 cm from the screws. One-half of the screws (n = 9) were used for the characterization of the corroded surfaces, while the other half (n = 9) was used for the SEM/EDX and histological examination of the implant-tissue interface. For the corrosion layers characterization, three ZX00 screws were investigated after 6, 12, and 24 weeks of implantation. To extract the screws from the bone, the cortex of the diaphyses were cut using a Dremel rotatory cutter with a wood blade (SC544). Special care was taken to not cut into the screw or the corrosion layers. Then, the screw implants were carefully removed and fixed in 100% ethanol for 2 h and air-dried for 2h. Specimens were stored under vacuum conditions until microscope analysis. Stereomicroscope, SEM/EDX analysis in a low-vacuum mode (70 Pa) was performed to determine the surface morphology and the chemical composition of the corrosion layers at the head, shaft, and valley regions of the screw. For corrosion morphology analysis at the bone-implant interface, three bone-implant specimens per time point were retrieved and fixed in 70% ethanol at 4°C for at least five days. Afterwards, bone-implant tissue blocks were dehydrated in ascending grades of alcohol (80%, 96%, and 100%), infiltrated, and embedded in Technovit® 9100 New (Heraeus Kulzer) as described by Willbold et al. [397]. Then, embedded blocks were cut parallel to the longitudinal axis of the screws. The specimens were ground using up to 4000-grit SiC paper and ion milled in an Ar+ beam (Hitachi System IM4000). The samples were coated with a 10nm carbon layer using the Gatan precision etching coating system (PECS, Gatan 682). To determine the thickness and composition of the corrosion layer at different zones of the screws in the cortical bone and intra medullary cavity compartments, cross-sections were observed under SEM equipped with EDX. The distribution of O, Mg, P, and Ca on the cross sections of the corrosion layers were analyzed based on SEM-EDX maps and line scans. EDX point analysis was performed to semi-quantitatively analyze the elemental composition of the corrosion layer on the surface of ZX00 screws and to investigate the atomic ratio of Ca/P in the peri-implant bone regions. Image processing and bone-implant contact (BIC) determination were performed using Fiji image processing software. Mosaic J plugin [398] was used to stitch together backscattered electron (BSE) images to have an overall image of the cross-section of the resin bone-ZX00 screws blocks.

5.2.4.5. Histological evaluation

After SEM observations and before histological staining**,** one ZX00 bone-implant embedded block per time point was prepared by cutting along the longitudinal axis of the implant using a laser microtome (TissueSurgeon, LLS ROWIAK LaserLabSolutions) [315]. 10-15 µm sections fixed on glass slides were stained using McNeal staining (Tetrachrome, Toluidine Blue and Basic Fuchsin). The mounted slides were examined under transmitted light using an optical microscope (Nikon Eclipse E600) coupled with a Nikon DS-Fi3 Camera. Whole slide imaging was acquired at 4x/0.45 and 20x/0.75 objectives. The dyes stained older bone matrix in light pink, whereas younger bone stained dark pink. Cell nuclei, fibrous and adipose tissue were stained blue. Descriptive histological evaluation was performed on a selected region of interest in the cortical and bone marrow cavity at the bone-implant interface.

5.2.5. Statistical Analysis

Prism software (GraphPad Prism version 8.2.1.) was used for the statistical analysis. Statistically significant differences and comparisons of nonparametric independent samples were performed using Kruskal-Wallis tests with Dunn's multiple comparisons post hoc tests. Statistical significance was considered when $p \leq 0.05$.

5.3. Results

5.3.1. Characterization and microstructure description of the as-received screw

To characterize the ZX00 screw surface in terms of its topographical and physicochemical properties, SEM and CLSM were used to visualize and quantitatively analyze the surface topography on three regions of interest (the head, the valley, and the tip, Figure 5.1a). SEM images in Fig. 1b-d depicted the cutting tool-induced periodic hierarchical patterns perpendicular to the long implant axis dominated the surface topography. The initial surface roughness was uniform on the entire screw with an average surface roughness (R_a) of 0.3 µm in the head and the tip, and R_a of 0.4 µm in the valley, which according to Albrektson and Wennerberg [399] classifies the ZX00 screw investigated in this work as the presence of Mg, Zn, Ca and a trace amount of O suggesting the formation of a thin oxide layer on the surface of an implant with smooth surface roughness. EDX measurements at the different parts of the screw (Table S5.1) revealed the screw due to contact with air and moisture occurring during manufacturing or cleaning procedures.

Backscattered electron (BSE) SEM images revealed nonuniformly distributed course intermetallic particles (IMPs) enriched in Ca (marked by the red arrows in Figure 5.2a-c) in the ZX00 alloy. The Zn/Ca atomic ratio of the representative EDX point analyses performed on IMPs was much less than 1.23 suggesting that the Mg_2Ca forms in the alloy [133,400]. The presence of Mg_2Ca is also confirmed by XRD (Figure 5.2m). IPF maps of the cross-sections that are perpendicular to the extrusion direction clearly indicated that the microstructure of the different screw zones varied in terms of grain size and crystallographic orientation (Figure 5.2d-f). The average grain size calculated based on the equivalent dimension (d_{avg}) is the highest for the head zone (2.15 ± 0.10 μm), while the average grain sizes in the valley and tip regions are found to be 1.90 μm ± 0.06 μm and 1.91 μm ± 0.07 μm, respectively. Nevertheless, it must be underlined that the microstructure of the screw head is composed of elongated grains which are surrounded by very fine grains (Figure 5.2d). This is a typical microstructure with non-recrystallized areas (the elongated primary grains) and the small grains which were refined continuously by the dynamic recrystallization (DRX) [401–403]. It is clearly shown that the recrystallization processes in the valley and the tip of the screw were more intense which is, in our opinion, most likely related to the turning procedure. The microstructure of the valley and the tip of the screw is composed of randomly distributed greater grains surrounded by very fine equiaxed grains (Figure 5.2e,f). Grains formed in the head of the screw also have a random crystallographic orientation with the prevalence of the grains oriented to {2-1-10} (blue color) (Figure 5.2e,f). Importantly, the average grain size for each screw zone is different. The largest average grain size was observed in the screw head (with an average equivalent diameter d_{avg} of 5.4 μm). Due to the different recrystallization stages, the screw valley and tip displayed decreased grain sizes of 2.3 μm, and 3.7 μm, respectively). The Kernel average misorientation (KAM) maps imply a strong heterogeneous distribution of dislocations in the elongated grains observed in the head zone of the screw. The accumulation of dislocations in both the valley and tip regions was also observed. They were accumulated along the grain boundaries and their higher intensity is observed in the tip of the screw (Figure 5.2j-l).

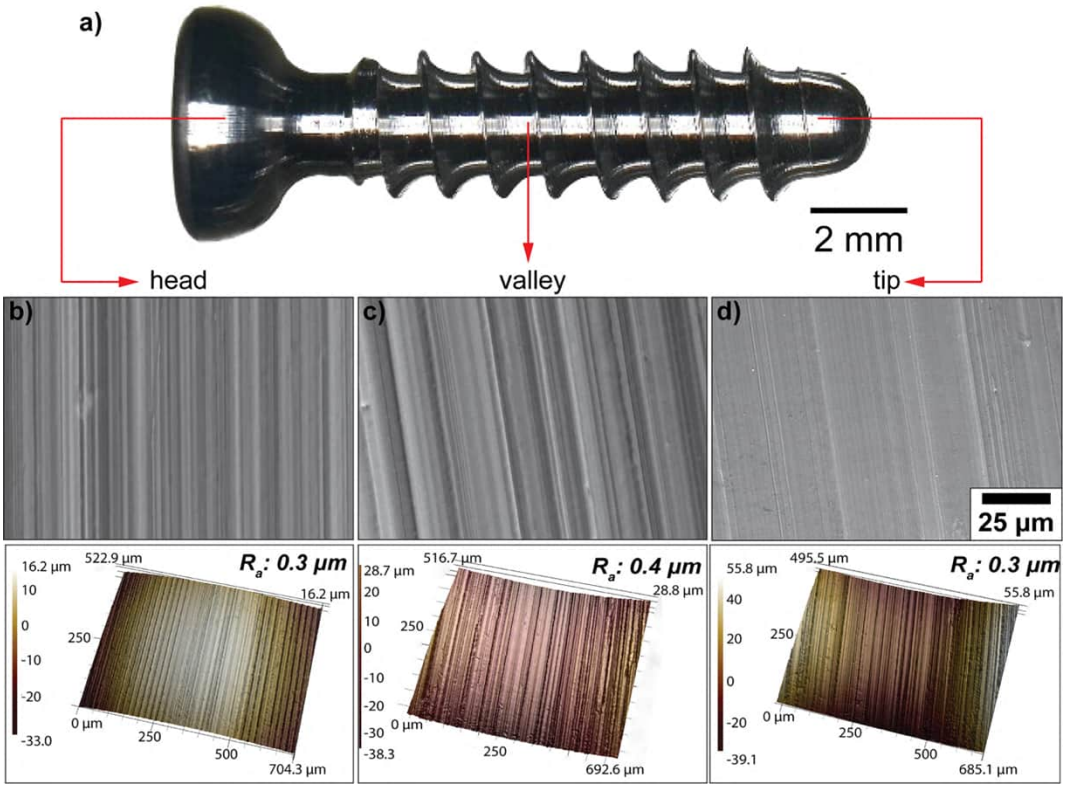

Figure 5.1. **Surface characterization of the ZX00 screw**. **a)** Stereomicrograph of the overall screw. Representative SEM images of **b)** the head, **c)** the valley and **d)** the tip zones with the corresponding surface roughness before *in vitro* and *in vivo* testing.

5.3.2. In vitro testing

5.3.2.1. Immersion tests

The corrosion rate (CR) of the entire screws was measured based on the immersion tests in α-MEM solution supplemented with 10% FBS and 1% P/S. The ZX00 screws were exposed for 3, 6, 14, 21, and 28 days. Figure 5.3a displays the calculated CR based on mass loss measurements and µCT data. Both methods of CR calculation demonstrated the same tendency for the CR to increase as immersion time increased. A near-linear increase in CR is observed as immersion time increases (Figure 5.3b). The largest variability between CR measurements calculated based on the mass loss measurements is observed at the beginning of immersion. After 3 days of testing the CR was found to be 0.74 mm×year^{-1}. The pH of the solution increased abruptly during this short time of immersion, indicated by the color change of the immersion solution from light to intense pink (Figure S5.3). After 3 days, the pH did not change markedly and stabilized after longer immersion times (Figure 5.3c). The evident increase in the pH of the solution with the immersed screws is a result of the screw's degradation and the formation of hydroxide ions during the initial degradation of the ZX00 screw.

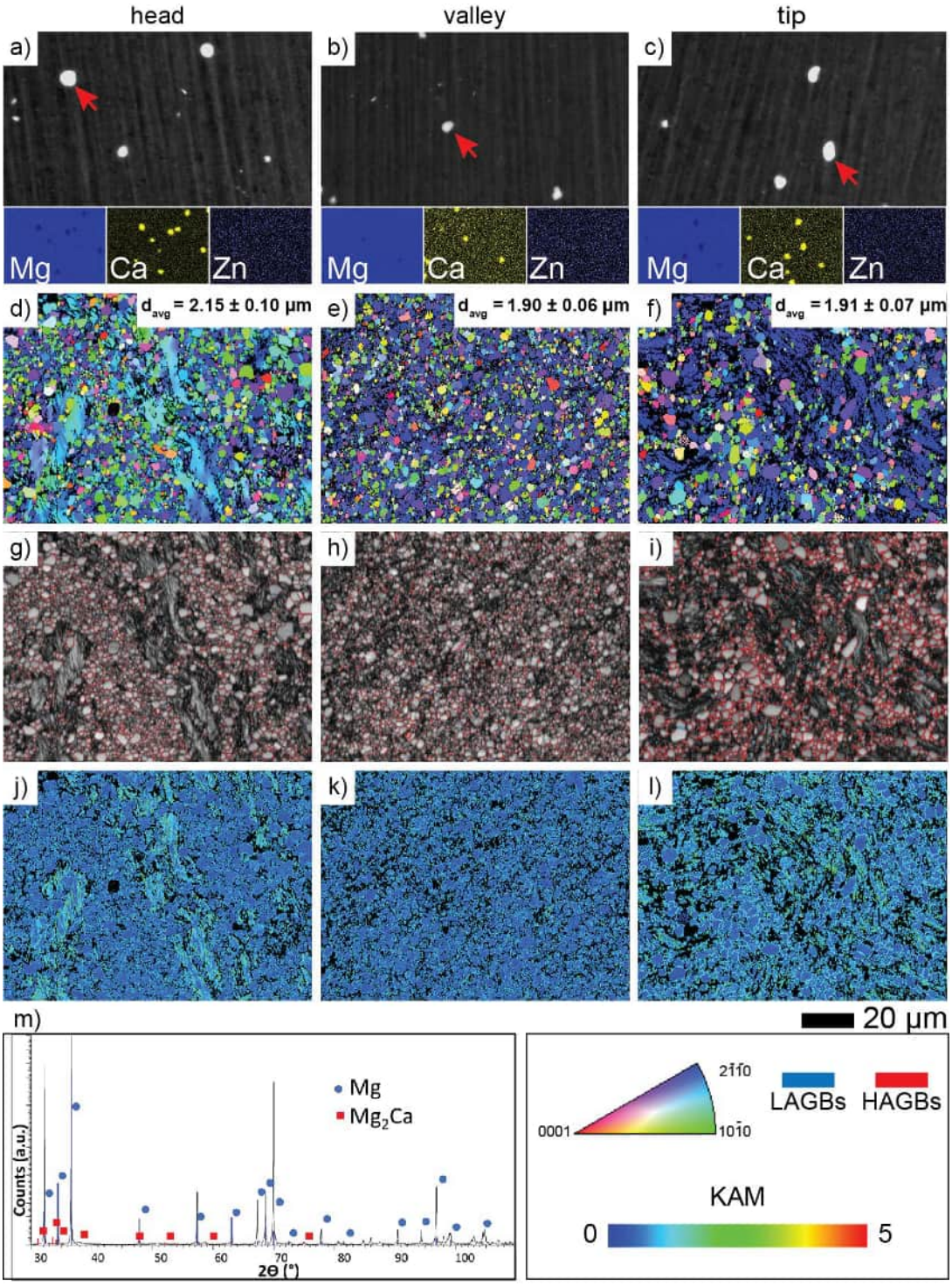

Figure 5.2. Microstructural characterization of various regions of ZX00 screws before *in vitro* immersion and *in vivo* implantation. SEM images with the corresponding EDX maps and the equivalent dimensions for grains (**a–c**), inverse pole figure (IPF) maps with the average grain size (**d–f**), grain boundary (GB) distributions (**g–i**), Kernel average misorientation (KAM) maps (**j–l**), and X-ray diffraction patterns of the ZX00 alloy (**m**).

After 6 days of immersion, the CR increased to 1.18 mm×year^{-1}. Afterwards, the CR slightly decreased to 0.93 and 0.97 mm×year^{-1} after 14 and 21 days of immersion, respectively. During the remainder of the experiment, the corrosion processes slowed down, and the calculated CR was found to be 1.04 mm×year^{-1}. Based on the validity of the linear regression of the CR plot, one can assume that the corrosion rate increases after 25 days of the immersion when the real values of CR increase are located above the red line (Figure 5.3b). The increased osmolality of the immersed samples compared with the control α-MEM solution indicates that the cell culture conditions accelerated the degradation rate of the analyzed material (Figure 5.3d) [98,162].

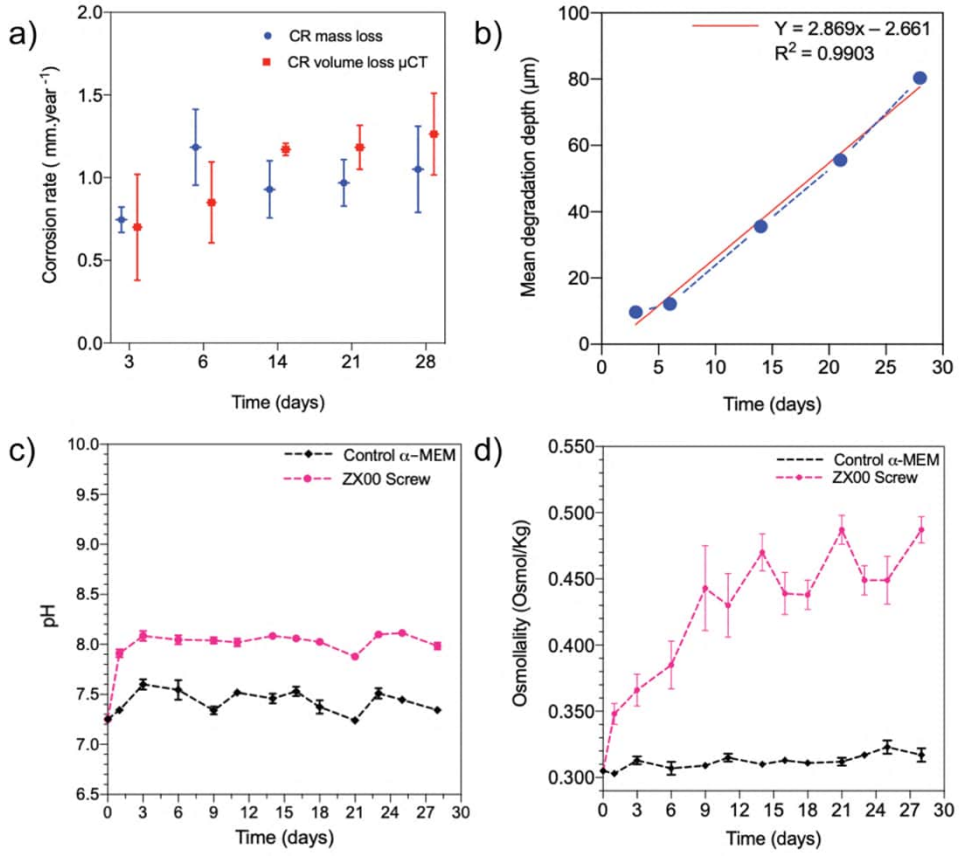

Figure 5.3. Degradation parameters for ZX00 screws during immersion in *α*-MEM culture medium supplemented with 10% FBS and 1% P/S under cell culture conditions: a) CR calculated based on mass loss (denoted in blue) and volume loss obtained from µCT measurements (denoted in red), **b)** mean degradation depth as a function of the immersion time with the linear approximation of the measured data, **c)** pH and **d)** osmolality measurements during 28 days of immersion. (a) and (b) (n = 3/time point); (c) and (d) (n = 6/time point). Data presented as mean ± standard deviation.

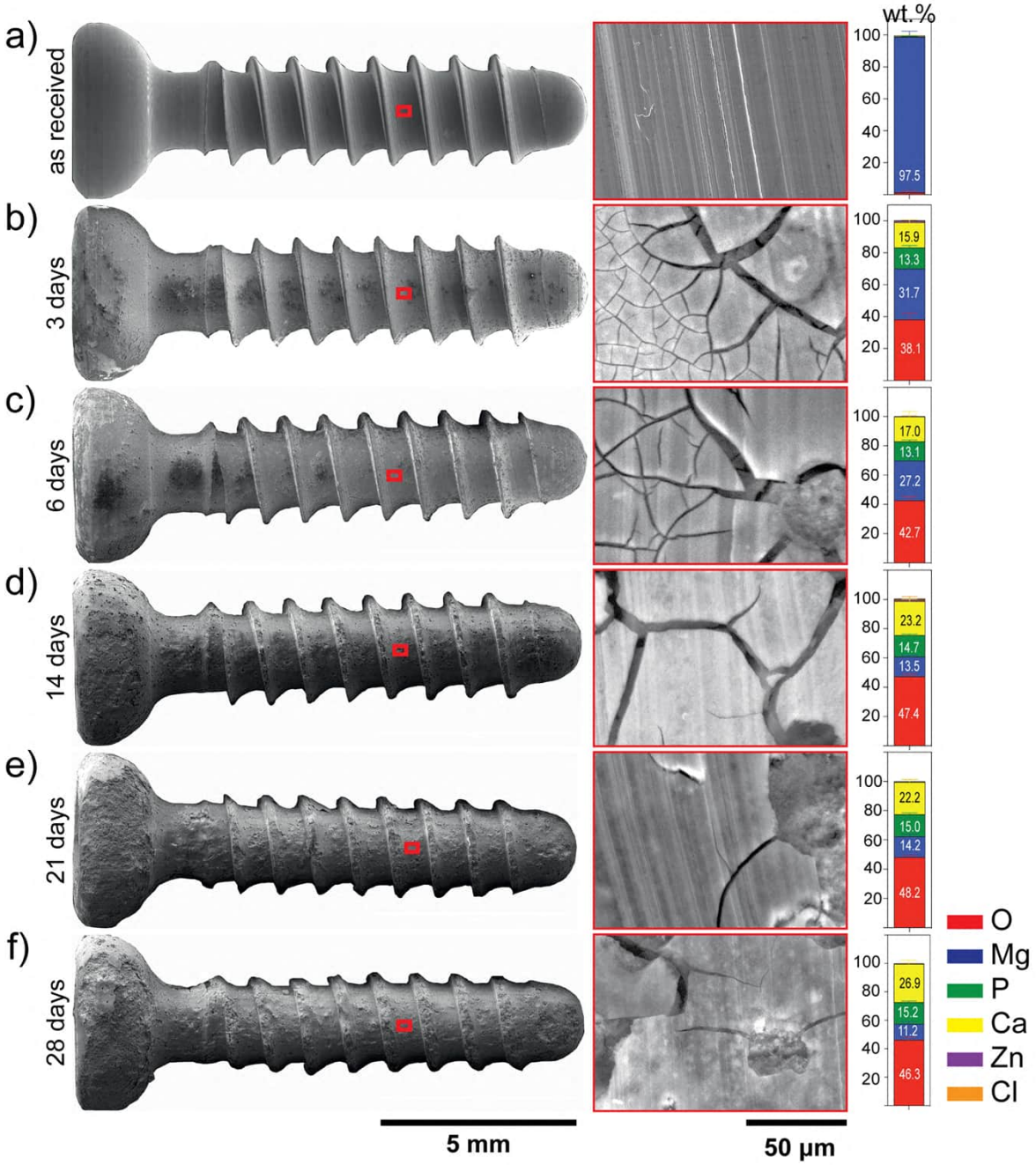

Figure 5.4. Surface characterization of the corroded screws under cell culture conditions exposed to *α*-MEM culture medium supplemented with 10% FBS and 1% P/S. SEM images of the screw and a representative image of the surface and EDX analysis of the corrosion products performed after each period of immersion: **a)** before immersion, **b)** after 3-, **c)** 6-, **d)** 14-, **e)** 21-, and **f)** 28- days of immersion. EDX data presented as mean ± standard deviation (n = 54 EDX point measurements/time point from 3 independent samples/time point).

To have a greater understanding of the degradation parameters of the screws, stereomicroscope, and SEM observations (from surface and cross-sections) were taken after 3-, 6-, 14-, 21-, and 28- days of immersion. As depicted in Figure 5.4a, the as-received surface of the screw was smooth and sharp threads were well-defined. With the increasing immersion time, the surface of the screw starts to become rough, more irregular, and uneven. Further, the

entire screw surface turned black and was covered with white corrosion products (Figure S5.4), which appeared as cracked corrosion films under SEM (Figure 5.4b-f-). After 14 days of immersion, the corrosion products tended to peel off and the screws progressively lost their sharp contours due to the substantial dissolution of the threads, which was particularly noticeable after 28 days. After immersion, the corroded surfaces were mainly composed of O, Mg, P, Ca and a trace amount of Zn and Cl (Figure 5.4). A slight increase in the concentration of O and Ca, homogeneous distribution of P and a decrease in Mg content was observed as the immersion time increased.

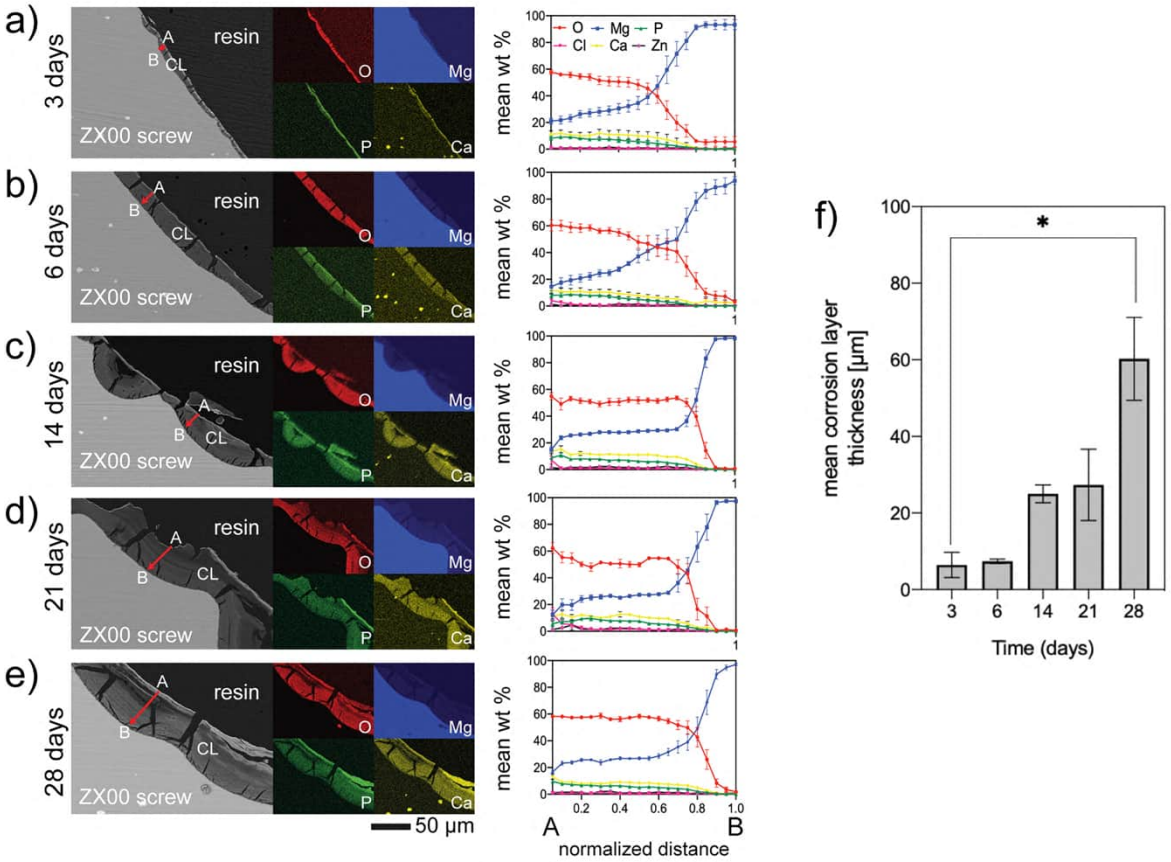

Figure 5.5. Cross-sectional characterization of the corrosion layers after *in vitro* degradation. Representative SEM images of the corrosion layers (CL) and corresponding EDX mapping, and line scans following the direction marked by the red arrows (from the outer layer (A) to the inner layer (B) of the corrosion products formed on the ZX00 screw: **a)** after 3-, **b)** 6-, **c)** 14-, **d)** 21-, and **e)** 28- days of immersion. Data presented as mean ± standard error of the mean (SEM) (n = 7–9-line scans/time point from 3 independent samples). **f)** Changes in the corrosion layer thickness as a function of time. Data presented as mean ± standard deviation (n = 150-300 measurements/time point from 3 independent samples); *$p < 0.05$ versus day 3 and 28. The Kruskal-Wallis test was used for comparison between time point.

The thickness and the chemical composition of the corrosion layer were also assessed on the cross-sections using EDX line scans and elemental distribution maps for O, Mg, P, and Ca (Figure 5.5a-e), and EDX point analysis (Figure S5.5). C was not considered for the

semiquantitative analysis since cross-sections were sputtered with it and because of the C contamination built up during SEM energy-dispersive X-ray spectroscopy (EDX) [281]. The EDX elemental mapping and line scan analysis revealed that the corrosion layers consisted primarily of O, Mg, P, and Ca with traces of Zn. O and Mg concentrations were consistently higher than P and Ca concentrations at all immersion times. The ratio of Mg/O and Ca/P ratios were approximately 0.5 and 1.40, respectively. As observed in Figure 5.5f, the corrosion layer thickness increased from 6.2 ± 6.1 μm after 3 days of immersion to 56.8 ± 29.3 μm after 28 days.

For further comparison with EDX analysis, Figure S5.6 depicted the total prediction fraction diagram of Mg chemical compounds as a function of pH. According to the fraction equilibrium diagrams, in α-MEM solution supplemented with 10% FBS and 1% P/S, the corrosion products may be composed of $Mg(OH)_2$, $MgHCO^{3+}$, $MgHPO_4$, $CaMg(CO_3)_2$, and $MgCO_3$, while $MgSO_4$ is one of the inorganic salts in the medium composition. Between the pH range throughout the immersion test, higher calcium magnesium carbonate compounds formed up to 14 days of immersion and then began to decrease, while magnesium carbonate compounds increased in the experimental pH range.

High-resolution XPS spectra for the head and the valley after 3 days of *in vitro* immersion shown in Figure 5.6 also agree with EDX analysis. The O 1s peak was deconvoluted and fitted with OH^- at 532.7 eV, O^{2-} at 530.9 eV, and H_2O at 534.4 eV, O-Mg at 528.9 eV (Figure 5.6a). The Mg 1s peak was used to identify Mg compounds, as it is depicted in Figure 5.6b. The spectrum from 1299 eV to 1318 eV was deconvoluted and fitted with $Mg(OH)_2$ at 1303.0 eV, $MgCO_3$ at1305.3 eV and $Mg(CO_3)_4(OH)_2$ at 1306.8 eV [404–407]. The signals obtained in the valley and the tip were fitted with the same peaks, therefore, high-resolution spectra for one of them are shown (for the valley, Figure 5.6c-d). The shape of the peaks of the head and the valley are different since the number of components in the corrosion products varied. The corrosion products formed on the valley and tip were composed of Mg 1s, O 1s, Ca 2p and P 1s [408]. We observed also Ca 2p high-resolution spectra with the binding energy best fit $CaMg(CO_3)_2$.

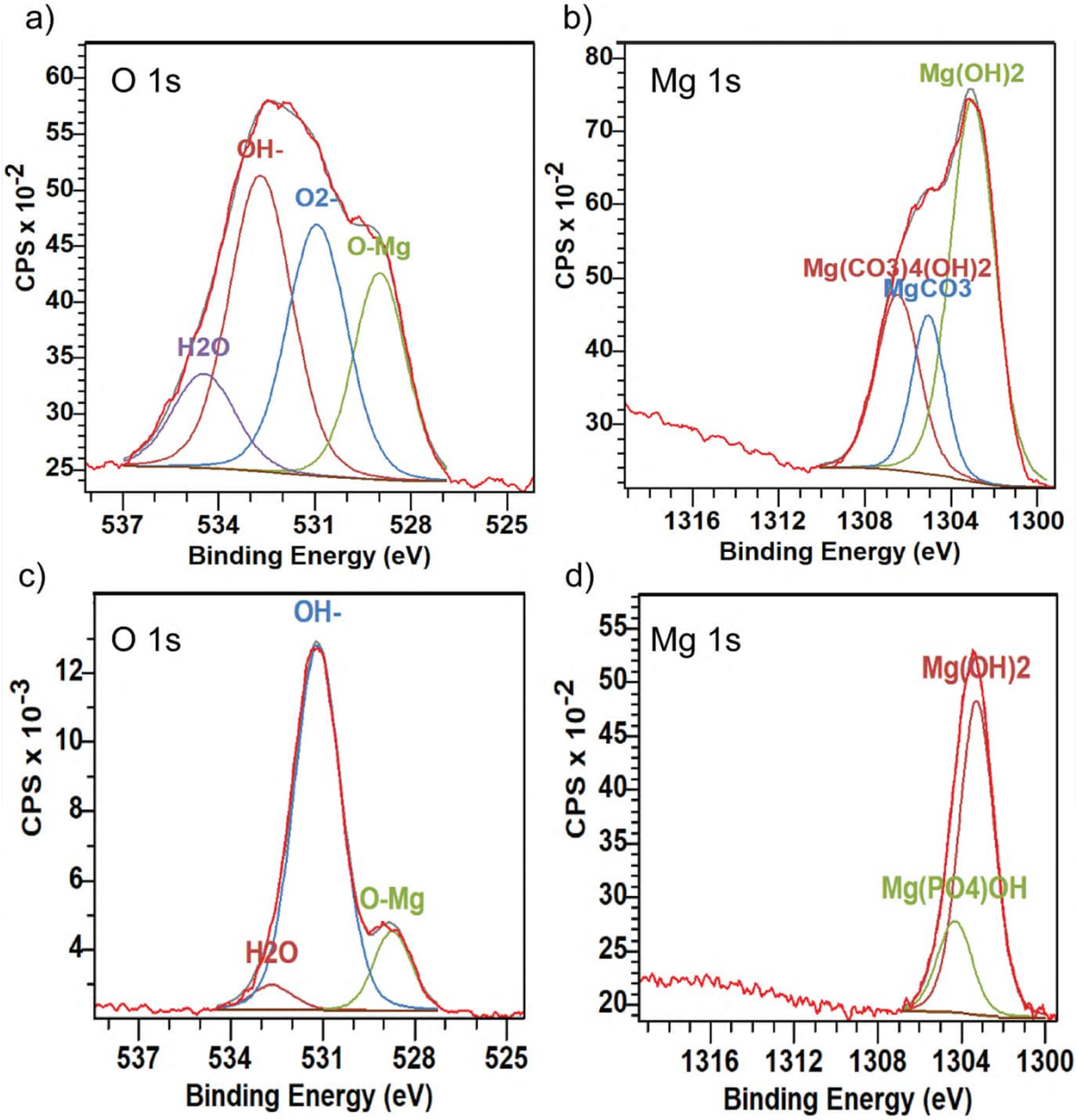

Figure 5.6. High-resolution XPS spectra on various regions of a ZX00 screw performed after 3 days of *in vitro* immersion in α-MEM solution supplemented with 10% FBS and 1% P/S. a) and b) O 1s and Mg 1s spectra for the head, respectively. c) and d) O 1s and Mg 1s spectra for the valley.

To analyze the surface and corrosion layer formed after the specific immersion times, µCT images of the screws were reconstructed before and after the removal of the corrosion layers. Figure 5.7 depicts the reconstructed µCT images and calculated surface area values of the screws after immersion (A_i) and after the removal of the corrosion layer (A_d) are depicted in Fig 7. The µCT reconstruction of the as-received screw and after 3 days of immersion is shown in Figure 5.7a. Due to the limitations of µCT resolution, it was not possible to

distinguish the degradation layer after 3 days of immersion. After 6 days of immersion, only a few pits are observed on the screw after corrosion product removal (Figure 5.7b). More intense corrosion damage was visible after 14 and 21 days of immersion (Figure 5.7c-d), and the well-developed surface of the screw resulting from the intense corrosion processes could be observed. The greatest difference between A_i and A_d was found after 28 days of immersion (Figure 5.7e). The significant difference between A_i and A_d indicates that, due to the intense corrosion processes, thick corrosion products were formed as the immersion time increased, confirming the corrosion thicknesses measurements performed on BSE images (Figure 5.5f). However, these corrosion products were porous and therefore cannot protect the surface of the screw.

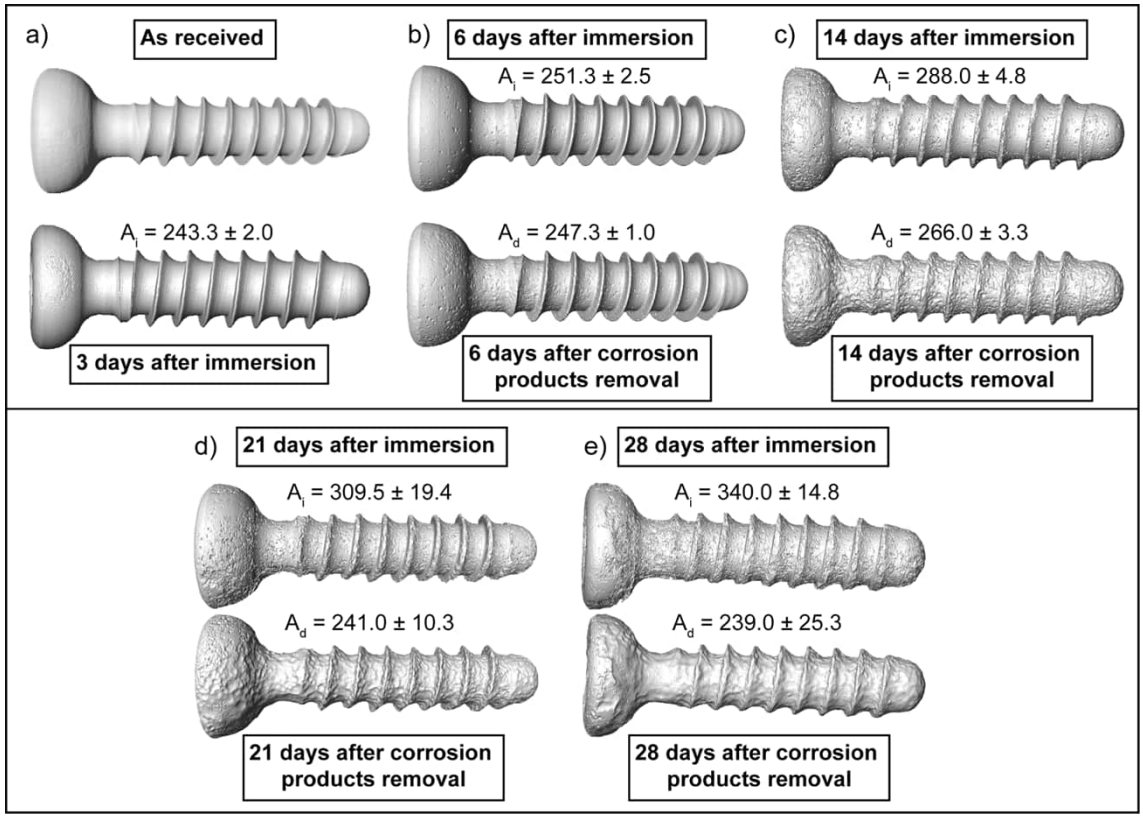

Figure 5.7. Characterization of the corroded ZX00 screws reconstructed based on the µCT data µCT reconstructed images are displayed after immersion in α-MEM culture medium supplemented with 10% FBS and 1% P/S under cell culture conditions and with subtracted corrosion layers: a) as received screw and after 3 days of immersion, b) after 6-, c) 14-, d) 21-, and e) 28 -days of immersion with the corresponding surface area after immersion (Ai) and after corrosion layer removal (Ad). Data presented as mean ± standard deviation (n = 3/time point).

5.3.2.2. Electrochemical response of various regions of the screw

The CR calculations are the most appropriate method for analyzing the overall corrosion propagation of various materials. However, in this work, we would like to focus on the

variables in the kinetics of the corrosion processes on the different zones of the screw, which is extremely important from the biomedical point of view. The electrochemical measurements were performed in a PBS solution. Figure 5.8a shows the evolution of the corrosion potential (E_{corr}) of the samples exposed to PBS solution under open circuit conditions for 1 h. The E_{corr} recorded for the head and tip of the screws did not change significantly during the experimental time. The lowest value of E_{corr} was recorded for the screw head (~-1.92 V/Ref). The tip of the screw had an E_{corr} value of ~-1.90 V/Ref). The screw valley had the greatest E_{corr} value, with some fluctuations visible over the time of immersion which is characteristic of the valley. The E_{corr} of the screw valley was initially -1.85 V/Ref, decreased to ~-1.87 V/Ref, and approached -1.80 V/Ref at the end of the immersion. The polarization curves obtained for the samples are given in Figure 5.8b. For Mg-based alloys, the cathodic range of the curves represents the cathodic hydrogen evolution, and the anodic side of the curves represents the dissolution of Mg [409–411]. The shape of the recorded polarization curves was similar. However, the curves were recorded over various ranges of current density and potential. Noticeably, all the curves exhibited a breakdown potential (E_b), which for the head was found to be -1.70 V/Ref. For the screw valley and the tip, the E_b values were -1.65 V/Ref and -1.71 V/Ref, respectively (Table 5.1). The corrosion potential (E_{corr}) and corrosion current density (i_{corr}) were derived directly from the polarization curves, and they are listed in Table 5.1. The results show that the highest i_{corr} of 32 μA/cm^2 and the most positive E_{corr} of -1.82 V/Ref values were characteristic for the head of the screw. Also, the passivation region recorded for the screw head sample was the narrowest among all analyzed specimens. Such a small difference between E_b and E_{corr} indicates that passivation processes are limited. The E_{corr} and i_{corr} calculated for the valley and the tip zones were similar (E_{corr} of -1.86 V/Ref and E_{corr} of-1.85 V/Ref, and i_{corr} of 21 μA/cm^2 and i_{corr} of 24 μA/cm^2, for the valley and the tip, respectively). Generally, the highest i_{corr} values were exhibited by materials with the highest CR values [355,412,413].

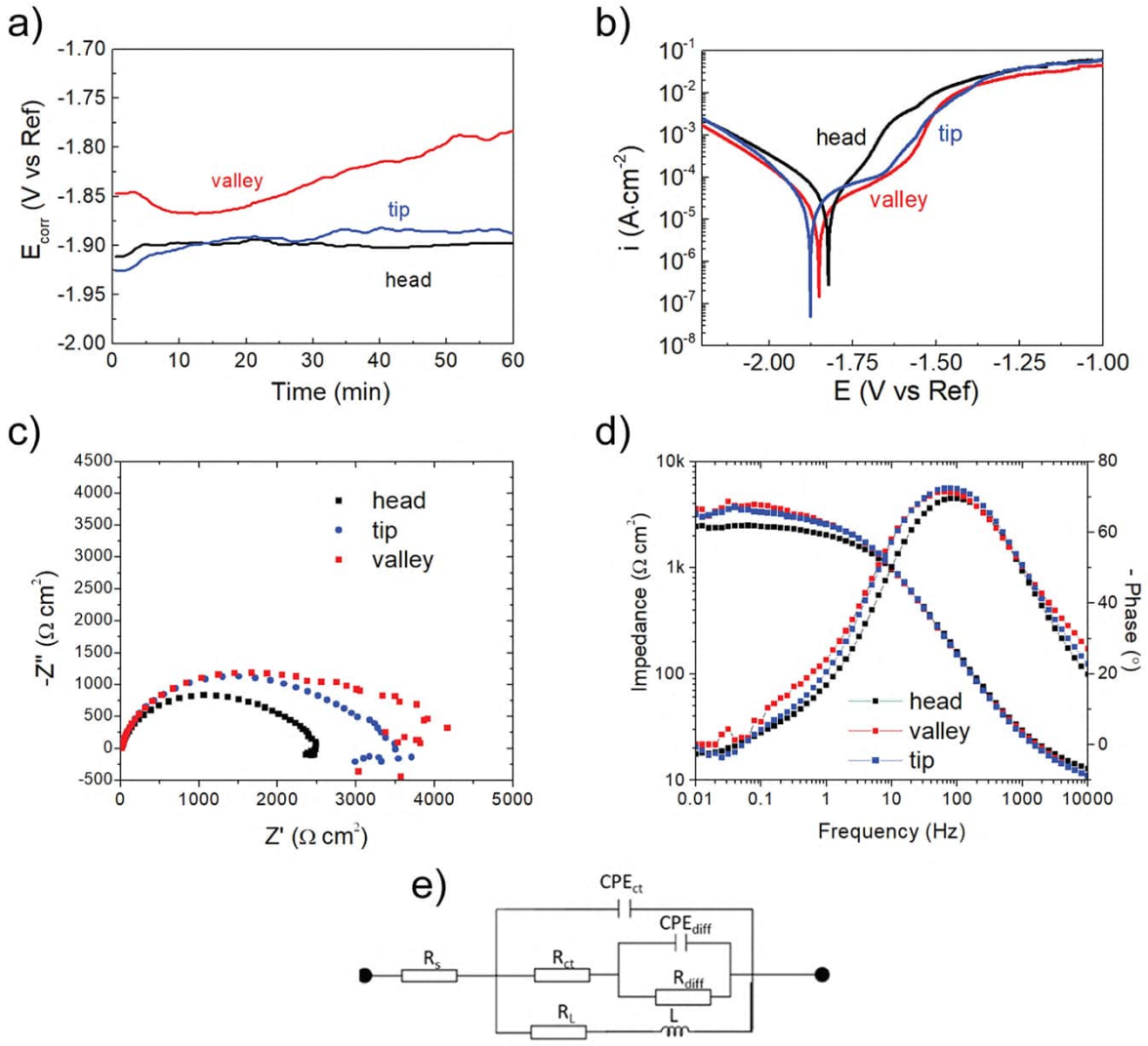

Figure 5 8. Electrochemical corrosion data obtained for the various zones of the ZX00 screw after 1 h of immersion in PBS solution: a) E_{corr} evaluation, b) potentiodynamic curves, c) EIS Nyquist plots, d) EIS Body plots.

However, in the case of Mg-based alloys, corrosion resistivity cannot be simply described based on the potentiodynamic results because of the negative difference effect [262]. To confirm the differences in the corrosion behavior of the various zones of the screw, EIS was performed (Figure 5.8c-d). The obtained data were fitted with the equivalent electrical circuit (Figure 5.8e). Two capacitive loops and one inductive loop in a low frequency can be recognized in the Nyquist plots recorded for all areas of the screw. The proposed circuit includes solution resistance (R_s), a constant phase element (CPE_{ct}), and a resistance (R_{ct}) which are associated with the double layer and charge transfer resistance. The diffusion of the ions through the porous corrosion layer is described by the R_{diff} and CPE_{diff}. The inductance (L) in series with the resistance (R_L) characterizes the inductive behavior at low frequencies (Table 5.2) [414,415].

Table 5.1. The electrochemical parameters of various zones of the ZX00 screw were extrapolated using the Tafel method

Zone of the screw	E_{corr} (V/Ref)	i_{corr} (μA/cm^2)	E_b (V/Ref)
head	-1.82	32	-1.70
valley	-1.86	21	-1.65
tip	-1.85	24	-1.71

Table 5.2. Characteristic values were deduced from the measured impedance spectra by means of fitting the equivalent electrical circuit (EEC) shown in Figure 5.3.

Zone	R_s (Ω cm^2)	R_{diff} (Ω cm^2)	CPE_{diff} (S·s^{a}cm^{-2})	a_1	R_{ct} (Ω cm^2)	CPE_{dl} (μS·s^{a}cm^{-2})	n_2	L (kH·cm^2)	R_L (Ω cm^2)
head	12	501	$1.6\cdot10^{-3}$	0.82	2196	26	0.84	67	19000
valley	10	1154	$0.8\cdot10^{-6}$	0.99	3189	30	0.83	63	18000
Tip	10	1040	$1.3\cdot10^{-3}$	0.81	2928	25	0.85	81	12000

The data presented in the form of Nyquist plots and Body graphs (Figure 5.8c-d) show that the order of the corrosion resistance for the various zones of the screw is: the valley > the tip > the head. This conclusion keeps highly consistent with the results of the potentiodynamic curves. Generally, the CR inversely scales with the polarization resistance (~R_p^{-1}). R_p, in turn, correlates with the impedance at zero frequency [262]:

$$\frac{1}{R_p} = \frac{1}{R_1+R_2} + \frac{1}{R_3} \qquad \text{(Eq. 5.5)}$$

Based on the equivalent electronic circuit given in Figure 5.8, the total calculation of R_p can be estimated by:

$$\frac{1}{R_p} = \frac{1}{R_{ct}+R_{diff}} + \frac{1}{R_L} \qquad \text{(Eq. 5.6)}$$

Therefore, the apparent differences between the corrosion performance of various zones of the screw are confirmed by the values of R_p (Table 5.3). The most corrosion-resistant zone is the valley of the screw. The screw tip is less corrosion-resistant, and the head of the screw is the least resistive.

Table 5.3. Polarization resistance is calculated according to equation (6) from the values given in Table 5.2.

Zone of the screw	**R_p (Ω cm^2)**
head	2361
valley	3498
tip	2981

5.3.3. In vivo testing

The surface morphology of the retrieved ZX00 screws without the surrounding bone tissue after 6-, 12-, and 24- weeks of *in vivo* implantation were characterized by SEM/EDX (Figure 5.9). The surface of the screw before implantation is uniformly smooth with sharp threads (Figure 5.9a). After 6 weeks of implantation, the surface morphology of the screw became rough. The threads began to lose their sharp contours, and a cracked corrosion layer formed on the implant surface (Figure 5.9b). With increasing implantation time (after 12 weeks), the threads and valleys beneath the head (shaft zone) became more corroded than those in the tip zone (Figure 5.9c). After 24 weeks, the implants maintained their screw shape with an uneven, corroded, cracked surface. However, the threads were worn away (Figure 5.9d). At 24 weeks of implantation, a tight bone-implant contact was observed below the head, in the shaft zone. This tight contact at this advanced state of bone integration did not allow bone tissue removal without damaging the corrosion layer and the screw implant. In addition, the cracks visible on the corrosion layer presumably resulted from the dehydration of the corrosion products during the sample preparation [95,158,163,416–419]. The EDX examination of the retrieved screws at the head, the shaft and the valley zones revealed a homogeneous distribution of P and Mg, a slightly higher concentration of O with the increasing implantation time, and a high Ca concentration in the shaft and head zone at 6 and 24 weeks, respectively (Figure 5.9e). Some bone tissue remained attached to the surface of the implant as observed in Figure S5.7. The tip zone of the screws was sometimes in contact with cortical bone and other times were within the intramedullary cavity in different samples at the different time points in the different retrieved screws analyzed. As a result, the chemical composition of the corrosion products formed in this screw region was performed on cross-sections of the bone-implant resin-embedded specimens.

To further understand the degradation of the ZX00 screws, the corrosion layers at the bone-implant interface were analyzed in detail. Figure 5.10, the thickness, distribution, and extent of the corrosion layers formed on the screws during implantation as well as their chemical compositions was implantation-site-dependent. Therefore, two distinct screw zones were characterized: those in contact with cortical bone and those within the intramedullary cavity. In regions where the implanted screw was in early direct contact with the cortical bone, a non-uniform corrosion layer formed at 6 weeks with a mean thickness of 19.8 ± 17.3 µm. A two-fold and three-fold increase in the thickness of the corrosion layer formed in the cortical bone compartment were observed after 12- and 24- weeks, respectively (39.8 ± 27.4 µm after

12- weeks, and 61.9 ± 34 µm after 24 weeks of implant placement) (Figure 5.10a,c). The formation of thick corrosion layers in the intramedullary cavity was observed at all-time points, with a mean ranging from 51.9 to 65.3 µm (Figure 5.10b-c). However, the larger standard deviation shown in Figure 5.10c was a result of the irregular thicknesses of the corrosion layer observed in the intramedullary cavity from sample to sample, with zones reaching thicknesses up to ~174 µm. Figure 5.10b). Similar to what was observed in the cortical bone, the corrosion layer that formed in the head zone increased in thickness from 18.2 µm after 6 weeks to 63.2 µm after 24 weeks (Figure S5.8a). Corrosion layers with non-uniform thickness were also observed in the tip zone because this region of the screw was sometimes in contact with cortical bone and sometimes within the intramedullary cavity (Figure S5.8b).

Figure 5.10 also summarizes the results of the elemental mapping and line scan investigations as well as BIC data obtained by BSE images of the dissected diaphysis of the sheep tibia cross sections. At all implantation times, the corrosion products were composed of O, Mg, P, Ca, and traces of Zn. The detected amount of Zn was negligible for all samples. Therefore, the corresponding mapping is not depicted. Ca and P elemental maps reveal the deposition of Ca and P in the newly formed bone in the peri-implant region. The line scans performed from the outer part of the corrosion layer to the residual implant revealed compositional changes within the degradation layers. After 6 weeks of implantation, O and Mg were homogeneously distributed within the corrosion layers while higher concentrations of Ca and P were detected in the outer part of the corrosion layers in the intramedullary cavity. After 12 and 24 weeks, Mg, O, P, and Ca were steadily distributed within the corrosion layer, with slightly higher Ca and P content detected at the outer part of the corrosion products in the head zone after 24 weeks (Figure S5.8a). Interestingly, after 6 and 12 weeks of implantation, only trace amounts of Ca, P, and Zn were observed in the thin degradation layer formed in the areas in contact with the cortical bone (Line scans in Figure 5.10a). O and Mg were present at higher concentrations, indicating that Mg hydroxide $Mg(OH)_2$ was the main corrosion product formed in this bone

compartment. Similarly, lower amounts of Ca and P were uniformly distributed in the corrosion layer formed in the intramedullary cavity after 24 weeks (Figure 5.10b).

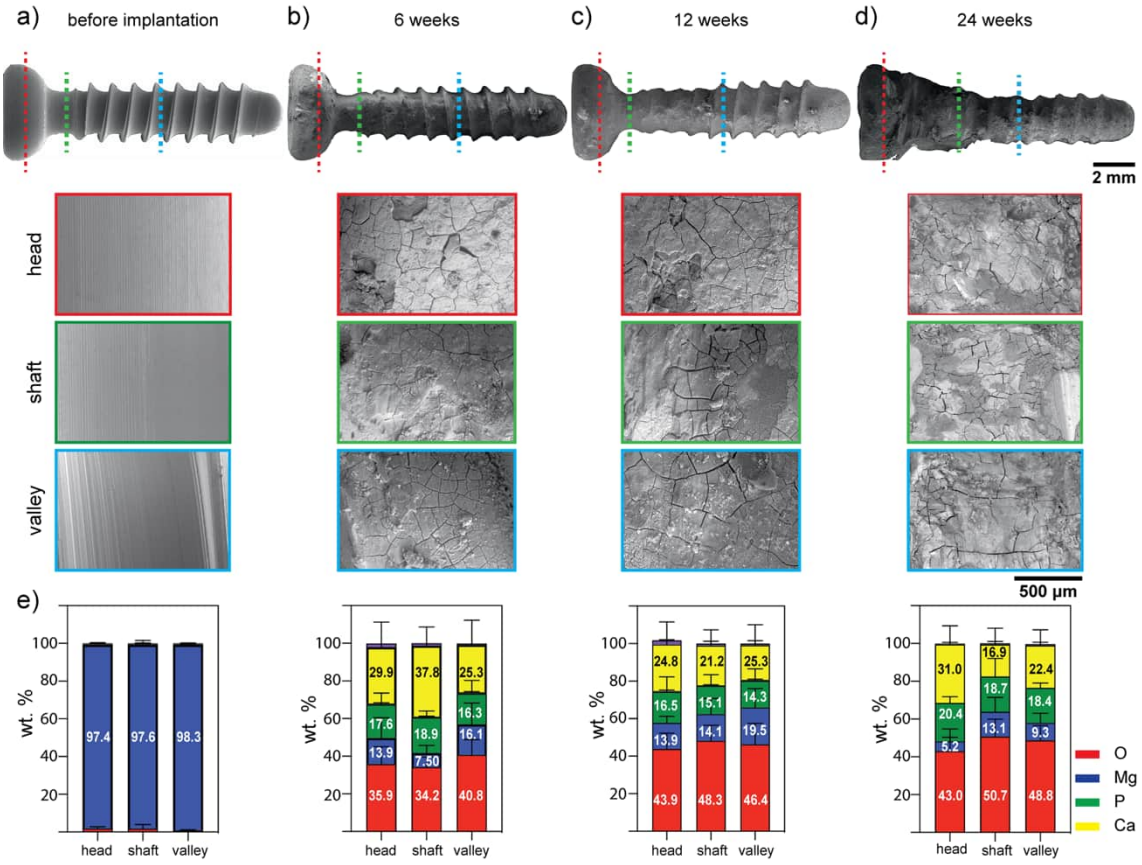

Figure 5.9. Surface characterization of retrieved ZX00 implants after 6-, 12-, and 24- weeks of in vivo implantation. **a)** before implantation, **b)** after 6-, **c)** 12- weeks, and **d)** 24- weeks of implantation, **e)** corresponding EDX analyses of the corrosion products formed on the different screw zones: head – red dotted line, shaft –green dotted line, valley – blue dotted line. Data presented as mean ± standard deviation (n = 47-50 EDX point measurements/time point from 3 independent samples).

In addition, EDX point analyses were conducted in randomly selected cortical bone zones adjacent to the corrosion layer at each time point. O concentration was high at all implantation times, P and Ca content were steadily distributed, and traces of Mg were found at all time points. The Ca/P ratios of bone in the vicinity of the corrosion layer were 1.63 ± 0.02, 1.63 ± 0.13, and 1.50 ± 0.04, after 6, 12, and 24 weeks after implant placement, respectively, with no statistically significant differences between time points (Figure 5.10d). With the extension of implantation time, an increase in BIC %, in the cortical bone and the intramedullary cavity was observed without significant differences between all three different implantation periods (Figure 5.10e).

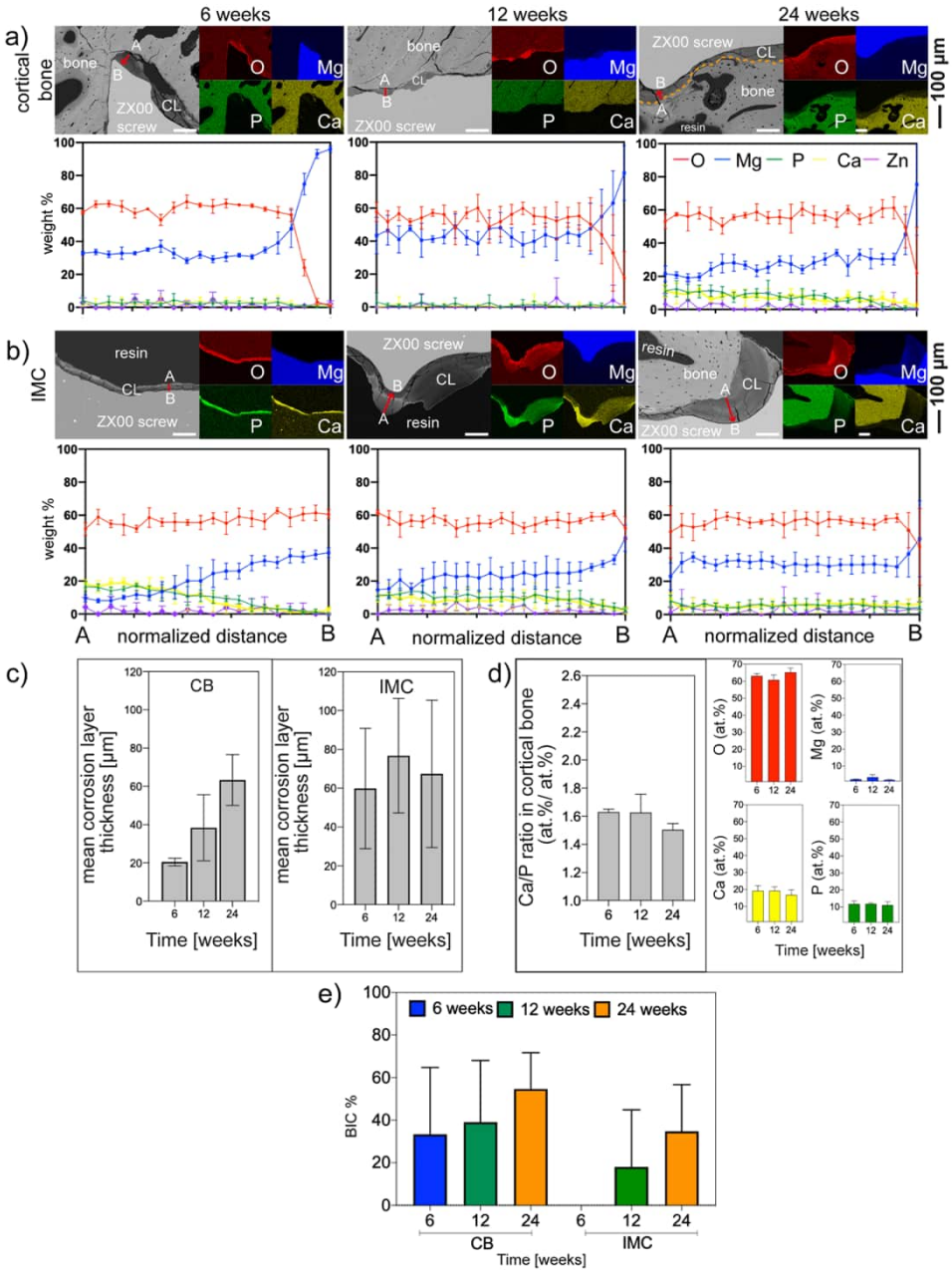

Figure 5.10. Characterization of the bone-implant interface. SEM images of the ZX00-implant interface with its corresponding elemental distribution maps and line scans of the corrosion layers after 6-, 12-, and 24- weeks of *in vivo* implantation performed at **a)** cortical bone (CB), and **b)** intramedullary cavity (IMC). Lines scans were performed from the outer part (A) to the inner part (B) of the corrosion layer, as depicted by red arrows. (n = 5 line scans/bone compartment/timepoint from 3 independent samples). **c)** corrosion layer thickness measurements from selected CB and IMC zones. **d)** semi-quantitative analyses of the changes of the Ca/P ratio, O, Mg, P, and Ca concentrations (at.%) at bone regions in immediate contact with the corrosion layer at different time points. **e)** The bone-implant contact (BIC) was determined at the cortical bone and intramedullary cavity compartments. Data presented as mean ± standard deviation. (c) n = 110-230 measurements/time point on three independent samples, d) n = 62-85 measurements/time point on three independent samples. (n = 6 regions/time points from 3 independent samples). The Orange dotted line in image a) at 24 weeks denoted the corrosion layer-bone interface.

The BIC for the cortical bone zone were measured at the shaft and the first thread below the head while the BIC measurements for the intramedullary cavity were performed at the middle section of the screw since this section was always located within the intramedullary cavity in

all explants. (As illustrated in Figure 5.12 (a-c), yellow and green dotted rectangles for cortical and intramedullary cavity regions, respectively).

Figure 5.11 depicts μCT reconstructions (2D and 3D) of the degradation performance for the implanted ZX00 screws, in which continuous and uniform degradation of the ZX00 is observed. After 24 weeks, the implanted screws were well preserved. Different regions of the implant were exposed to distinct bone compartments. Some screw threads below the head and some tip regions of the inserted screws were embedded in the cortical bone, while the middle section was exposed to the bone marrow cavity. After 6 weeks, the μCT scan images showed that significant gas was released around the implant and gas voids were primarily identified within the medullary cavity (Figure 5.11, red asterisks). After 12 weeks, the gas voids were still detectable, while at 24 weeks, they were barely apparent on μCT. In addition, the threads maintained their sharp shape until 12 weeks post-surgery. After 24 weeks of implantation, reduced and smoothed thread crests were observed, consistent with our *in vitro* findings.

Histological analysis was performed on selected zones in the cortical bone and the intramedullary cavity compartments to obtain information about the bone tissue response. At all-time points, cortico-periosteal reactions, appositional growth, and new bone formation in the endosteum zone were observed (Figure 5.12a-c, red arrows). In regions where the implanted screw made early contact with the cortical bone, a thin layer of corrosion products was observed (Figure 5.12d, black arrows) while in the medullary cavity, thicker corrosion products were seen (Figure 5.12e, black arrows). In some cases, osteoblasts (Ob) were connected to the newly formed bone (Figure 5.12d, small inset square). Gas voids (gb) were surrounded by thin fibrous tissue in the cortical and intramedullary cavity compartments (Figure 5.12d-e). New bone (nb) formation was observed in the cortical bone adjacent to the medullary cavity and around the gas voids. A cement line (Cm Ln) can be seen between new and pre-existing bone (Figure 5.12e). In the cortical bone, after 12 weeks of implantation, along with the degradation, new woven bone formed in direct contact with the corrosion layer (Figure 5.12f, yellow arrows).

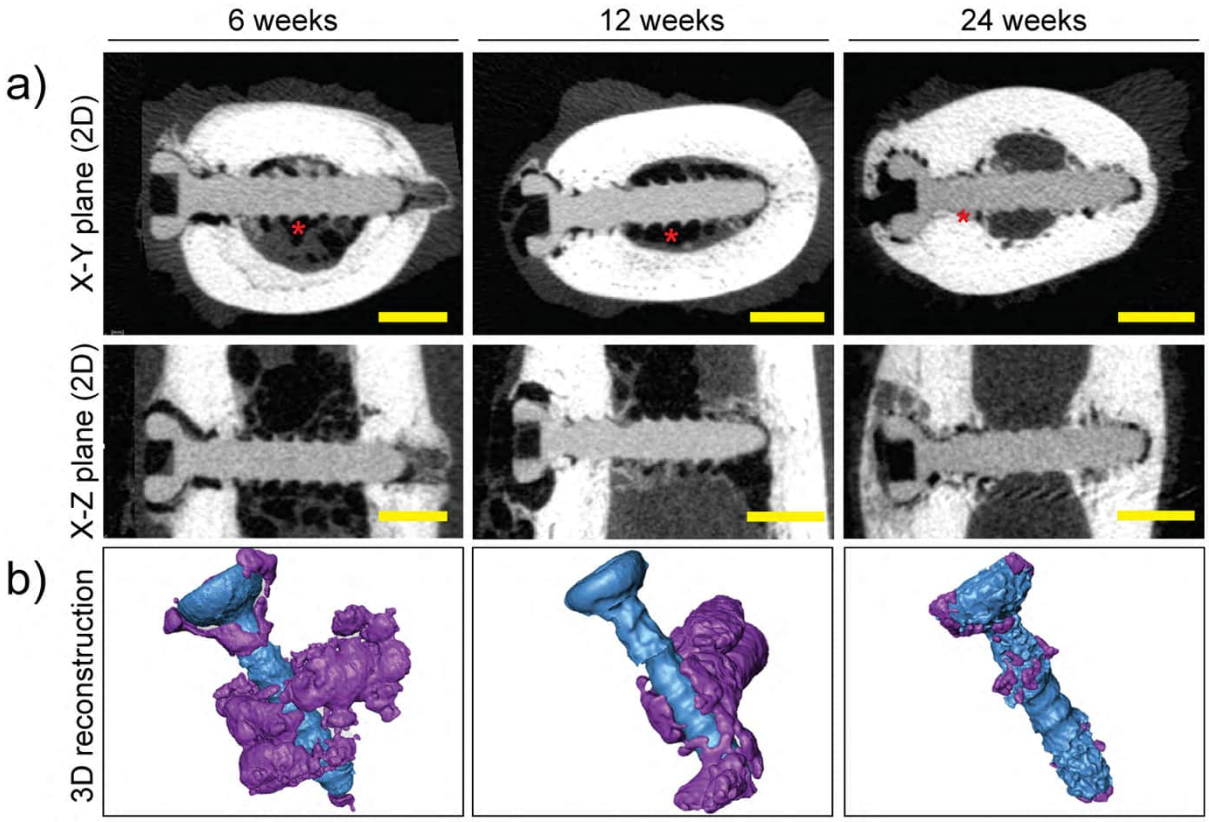

Figure 5.11. µCT reconstructions of ZX00 screws after 6-, 12-, and 24- weeks of *in vivo* implantation. **a)** µCT reconstructions (2D slices) in the X-Y plane (first row) and the X-Z plane (second row). The radiolucent zones adjacent to the implant screw were gas voids (red asterisks). **b)** 3D model reconstructions of the ZX00 screw (blue color) after 6, 12, and 24 weeks of implantation with surrounding gas cavities (purple color). Scale bar in panel a) is 2 mm.

The irregular Haversian tissue and additional Cm Lns were also observed. Moreover, some newly formed osteoid tissue was observed in the cortical bone that surrounded the medullary cavity. (Figure 5.12g, orange arrows). After 24 weeks, small gas voids remained surrounded by thin fibrous tissue in the cortical bone and medullary cavity compartments (Figure 5.12h-i). Tight direct bone contact with the degradation products and the formation of new bone next to the ZX00 screws was observed (Figure 5.12h-i, yellow arrows) which connected with the old, mature bone tissue. In the medullary cavity, new mineralized tissue in the form of parallel-fibered bone bridging the medullary cavity with thicker bone bridges formed on the corrosion products. Interestingly, the corrosion products formed on the 24 weeks inserted implants-stained pink, similar to the dark pink color of the newly formed mineralized tissue (Figure 5.12h-i).

5.4. Discussion

The purpose of the present study was to evaluate the corrosion performance of ZX00 screws under *in vitro* and *in vivo* physiological conditions. As the interaction between the implant surface and the surrounding tissues is crucial to the success of a medical implant, influencing its corrosion behavior [420] and the biological response [421], the surface of the ZX00 screw was characterized in terms of surface roughness and its chemical composition before implantation. Our results revealed that the initial surface of the ZX00 screws was smooth, anisotropic and free of contaminants, with a thin oxide layer resulting from contact with air and moisture during the manufacturing and cleaning process. In addition, no surface degradation was observed concerning packing and storage, as evidenced by the absence of O-enriched regions and adequate *in vivo* biocompatibility and degradation behavior. From the medical point of view, implants must withstand the standards of the cleaning and sterilization procedures without impairment of implant quality and safety. Specifically, the implants must be free of impurities that could embed into the surface of the screws during the different manufacturing stages, handling or packaging procedures prior to the surgical implantation [422–424]. It is essential to ensure that the surface properties of the implant remain unchanged during the storage [425] for the therapeutic use of Mg as biodegradable implants.

As proved based on EBSD data, the average grain size (d_{avg}) in the various regions of the screw changes: d_{avg} for the head was found to be the highest, while for the valley and the tip, it was lower and comparable to each other. Those results clearly confirm that the recrystallization and recovery processes in the case of the head, the tip and the valley, are various due to a long time of being in contact with the diamond tool during CNC processing. It is worth underlining that screws were manufactured using polycrystalline diamond tools without lubrication to avoid potential contamination and corrosive attack (ref 36). During turning, uncontrolled heat is generated as a r result of friction. For Mg alloys even such a slight local increase in temperature may cause microstructure reformation.

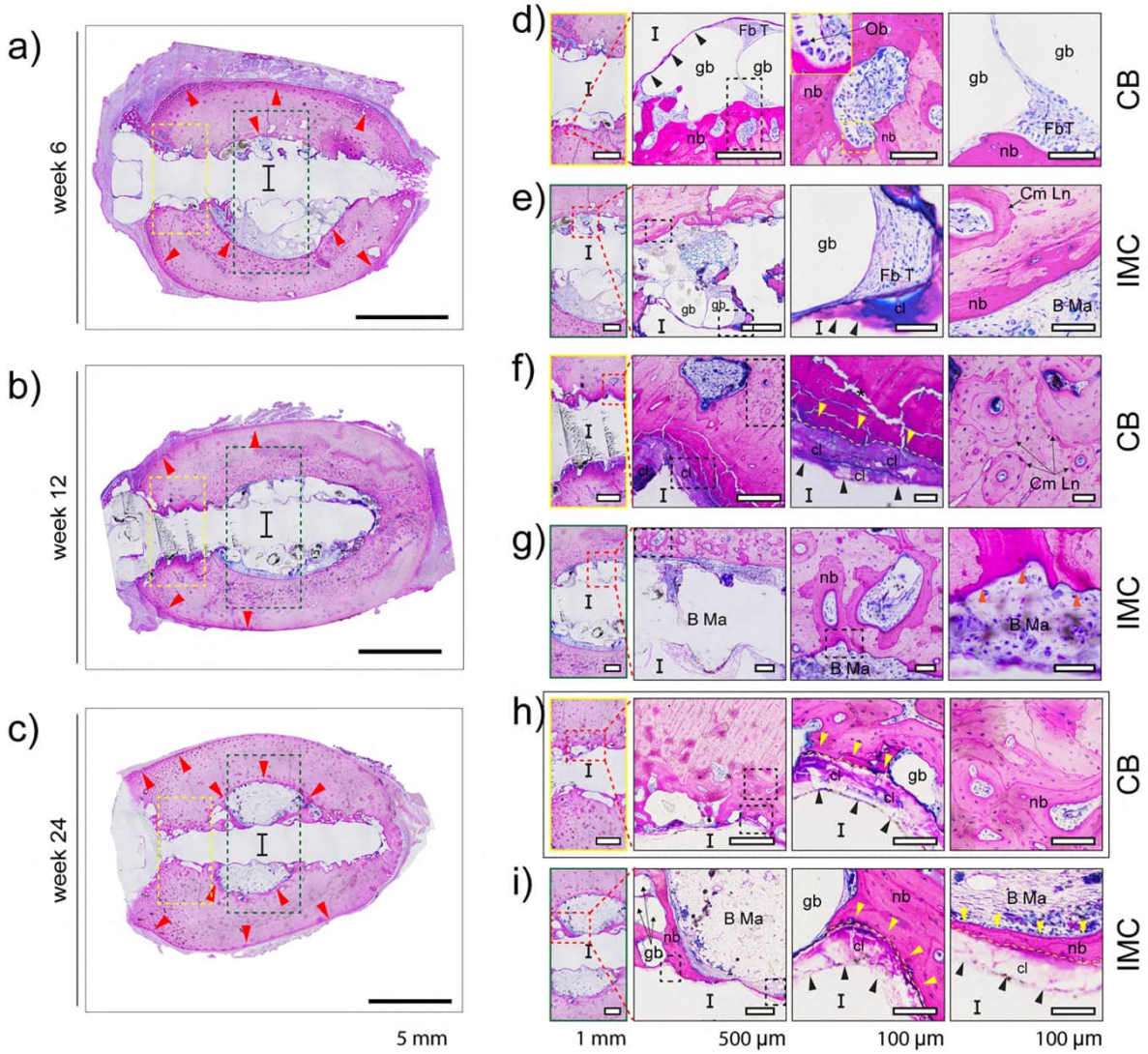

Figure 5.12. Representative images of McNeal-stained bone sections after 6- (a, d, e), 12- (b, f, g) and 24- (c, h, i) weeks of *in vivo* implantation. The first column provides an overview of the ZX00 screws after (**a**) 6-, (**b**) 12-, and (**c**) 24- weeks of implantation. CB and IMC compartments are magnified and denoted by yellow and green rectangles, respectively in (**d, e, f, g, h, i**). The red arrows in (**a, b, c**) point to the appositional growth in the periosteum and new bone formation in the endosteum zones. Corrosion products are indicated by black arrows. Tight direct bone contact with the degradation products and new bone formation next to the ZX00 screws is identified by yellow (**f, h, i**) and orange (g) arrows. (I) Site of implant and the following abbreviations used to describe various features: gb (gas bubbles), Ob (osteoblasts), nb (new bone), Fb T (fibrous tissue), Cm Ln (cement line), B Ma (bone marrow), cl (corrosion layer), and (*) sample preparation artifact.

As per the results of this work, the *in vitro* corrosion rates of the ZX00 screw were lower than those calculated by Cihova et al. [367] for the implants made from ZX10 and ZX20, by Hofstetter et al. [358] for the implants made from ZX50 and Ibrahim et al. [426] who immersed Mg-1.2Zn-0.5Ca alloy in simulated body fluids (SBF). This is due to the different experimental parameters and immersion solutions employed, as well as related to the alloying elements in the matrix of the material, where the Zn concentration is lower in ZX00 than the previously mentioned alloys. This is mostly related to alloying elements in the matrix of the material, where the Zn concentration is lower in ZX00 than in ZX10 or ZX20. As the number of

intermetallic phases containing Zn increases along with its concentration, a greater number of micro galvanic cells are formed. Our results also showed that there was a linear dependence on the corrosion rate even after 24 days of immersion. Similar results were shown by Zeller-Plumhoff et al. [427] where a computational model for pure Mg was utilized. However, our *in vitro* results revealed a higher corrosion rate than reported by Okutan et al. [221], who found a degradation rate of 0.29 ± 0.03 mm × $year^{-1}$ of ZX00 pins after three weeks of immersion in simulated body fluids (SBF). As stated by Gonzalez et al. [98], the differences may be due to the use of different immersion solutions, which results in the formation of different degradation products. Furthermore, when implanted into the distal metaphysis and epiphysis of three-month-old lambs, ZX00 alloy corroded at a rate between 0.2 and 0.75 mm × $year^{-1}$ [371], which is lower than our *in vitro* results where ZX00 screw corroded at a rate of 1.04 mm × $year^{-1}$. Consequently, identifying local *in vivo* environment parameters is essential for optimizing *in vitro* setups, leading to more accurate correlations between *in vitro* and *in vivo* data.

It is widely described in several publications that the kinetics of the corrosion process of Mg-based alloys in an aqueous environment is determined by the anodic and the cathodic reactions, resulting in a magnesium hydroxide $Mg(OH)_2$ formation, hydrogen gas release and local pH changes [98]. In a complex environment such as the human body, Cl^- ions make the protective layer soluble, and the presence of organic molecules can also influence the corrosion behavior [106] and the composition of corrosion products of the Mg-based devices. From our *in vitro* results, the ZX00 screw corroded nonuniformly with a corrosion layer forming on the surface of the screws composed of O, Mg, P, and Ca. As evidenced by the fluctuating *in vitro* osmolality, this corrosion layer did not cover the entire surface of the screws and did not compensate for the dissolution reactions. When released into the solution, soluble degradation products such as Mg^{2+}, Zn^{2+}, Ca^{2+}, and OH^- ions alter the pH and composition of the solution [428]. At the beginning of our immersion test (up to the 3rd day), a significant increase in pH of the corrosion medium and high corrosion rate indicated that intense corrosion occurred. However, after 3 days, our *in vitro* data indicated that the pH remained stable to reach 7.9 ± 0.03 at 28 days with the formation of Ca/Mg $(CO_3)_2$ as determined by XPS and the predicted fraction diagrams calculated by Hydra Medusa software. This is consistent with the findings of Lamaka et al. [429] who found a calcium-phosphate/carbonate corrosion layer stable at a pH lower of 8.5. They also highlighted different corrosion rates in immersion solutions containing Ca^{2+} compared to electrolytes solutions without Ca^{2+}, which could be the cause of discrepancies in corrosion rate between our results and previously described results from the ZX00 alloy [221,371].

Comparable to what was observed *in vitro*, the corrosion layers that formed on the ZX00 screws in our *in vivo* studies exhibited a similar composition. The corrosion products were composed of a Mg/O ratio of ~0.5, suggesting the presence of $Mg(OH)_2$, along with the presence of Ca and P indicating the formation of various Ca- and P-containing layers. This is consistent with *in vitro* results previously published investigating Mg-Ca-Zn and low-alloyed Mg-Ca-Zn alloys immersed in the artificial saliva [430], Kokubo´s solution [431,432], Hank´s solution [433], EBSS, MEM, and MEM supplemented with bovine serum albumin [434]. Similarly, Zhang et al. [428], who implanted Mg-2wt.%Zn-0.5wt.%Ca pins in a rat femoral defect model for 12 weeks, described corrosion products with a chemical composition comparable to our *in vivo* findings. Witte et al. [352] found corrosion layers containing calcium phosphates on 4 different magnesium alloys implanted within the medullary cavity of guinea pig femora. Lee et al. [183] observed changes in elemental composition and crystallinity within the degradation interface when implanted Mg-5Ca-1Zn rods in the femoral condyle of rabbits. According to their findings, a biomimicking calcification matrix was formed at the degrading interface which initiate the bone formation. Additionally, our histology revealed the staining of the corrosion products that resembled bone (dark pink) after 24 weeks of *in vivo* implantation. As previously reported, this pattern is consistent with the Ca- and P-rich degradation layers [133,352,370]. However, although the corrosion layers of ZX00 screws formed during our *in vitro* and *in vivo* tests were composed of the same elements, the corrosion layer thickness and the elemental distribution were different *in vivo*, consistent with some previous studies [175,177,367]. This might be because various screw zones in our *in vivo* study were surrounded by different local environments. The screw´s head was often enclosed by the soft tissues (overlying muscle/connective tissue), the shaft was in contact with the cortical bone, and the implant´s middle region was exposed to the bone marrow. These distinct tissue compartments (soft tissues, periosteal layer, cortical bone, and medullar cavity) play a role not only in bone fracture repair but also causes different degradation at various screw´s regions strongly influenced by the environment in which the implant was placed [373,390]. The amplified early inflammatory response in soft tissues [435] combined with hematoma formation and a local decrease in pH [352,436–438] results in a hypoxic and acidic environment when implanting an Mg orthopedic device with a faster degradation of the Mg implant region in contact with soft tissues [185,390,438,439]. However, the accelerated degradation of screw implant´s heads observed in soft tissues could be an advantage as faster degradation could avoid soft-tissue irritation. Herber et al. [215] demonstrated that the ZX00 screw's head located in the soft tissue area was predominantly resorbed avoiding shoe conflict

for the patients. Moreover, It has described the faster corrosion of Mg-based devices at the medullary cavity, assuming that the accelerated implant degradation is caused by the high blood vessel content and rich supply of body fluids promoting ion exchange between the surrounding tissue and the Mg implant surface [176,300,371,382,440,441]. In contrast, the dense mineralized structure of the cortical bone slows down the degradation of Mg implant regions placed in this compartment [185,390]. All factors influencing degradation, including implant location, must be considered when analyzing the degradation layer composition and degradation rate of implants, which makes it difficult to precisely estimate the corrosion rate of Mg implants. Furthermore, the relatively high standard deviation of the plotted corrosion layer thicknesses in our study, which ranged from ~20 µm to 62 µm in the cortical bone and from ~52 to 60µm in the medullary cavity with regions reaching up to ~174 µm, could be attributed to several factors, including the nature of each sheep (weight, growth, variation in feeding patterns and movement activity) [358,442], which may have influenced differences in their bone healing process, metabolism, and implant degradation.

Previous animal experiments that provide quantitative data revealed that the corrosion layer thicknesses range from 10 to 250 µm [133,176–180,182,183,187,443,444]. This broad range is a result of the various Mg-based biomaterials implanted, the different animal models and implantation sites, and the various experimental points for observations. In large animal models, Imwinkelried et al. [444] observed a ~30 µm corrosion products/layer on uncoated WE43 plates implanted subcutaneously on the nasal bones of minipigs for 24 weeks. Grün et al. [187] and Holweg et al. [133] investigated the corrosion behavior of ZX00 screws implanted in lamb tibia bones. After 12 weeks of implantation, histological analysis revealed similar thicknesses (~50 µm and ~43 µm, respectively) of corrosion layers formed on the screw surfaces. This broad range of corrosion layer thickness demonstrated the dependence of Mg corrosion on implant location, making it difficult to precisely estimate the corrosion rate of Mg implant materials. However, our *in vivo* results are of great clinical significance because they resemble real clinical scenarios in which implanted Mg devices are in contact with different tissue compartments that influence each other during Mg-implant degradation. In addition, it is important to consider that although the mechanisms of bone healing with implants are similar to those of bone healing without implants [8], in the *in vivo* environment, the corrosion of Mg-based implants is influenced by a continuous and time-dependent body-response phenomenon involving protein absorption, coagulation and inflammation [197]. This body response varies in each tissue in normal fracture healing where different cellular response evolves. It has been described as a lymphocyte- and granulocyte-rich inflammation in cortical and cancellous bone

healing, respectively [445]. Also, Liu et al. [385] found a different modulation of inflammation signaling pathways when pure Mg and AZ31 implants with varied manufacturing processes were implanted for 9 days in the femur of male rats. Hence, further investigations in subsequent *in vivo* studies are required to elucidate the corrosion environment at the cortico-cancellous bone transitional zone and ascertain the influence of Mg-implant degradation in the cellular response of both bone compartments.

As mentioned, our findings show that the screw does not corrode uniformly. The results from the electrochemical measurements proved that the least corrosion-resistant zone of the screw is the head. In this region, the grain size and the distribution of the dislocations were different from those observed in the valley and tip zones. As shown in our previous works [402,409], the Mg's dissolution rate strongly depends on the spatial distribution of the potential on the surface of materials. Mg´s dissolution rate is related to the anodic/cathodic sites of corrosion where cathodic reactions must be compensated by anodic reactions. In the case of the screw head, the large primary grains are the cathodic areas surrounded by the small anodic grains. The large cathodic areas drive small grains to dissolve quickly. Considering the screw valley and the tip, the spatial distribution of the half-reactions was more uniform due to more uniform grain size distribution in these screw regions. Also, the higher accumulation of the dislocation density in the head of the screw will promote corrosion reactions. We presumed that the microstructural differences in the screw head compared to the screw valley and tip regions resulted from the manufacturing process. Controlling the microstructure is a key component for modification of the dissolution of Mg screws for potential clinical use. Therefore, the manufacturing process must be carried out with the utmost accuracy. However, it is important to consider also that variations in implantation in our *in vivo* model make it difficult to compare the degradation performance of the screw head and tip. The anatomical variability [446,447] may also contribute to surgical inaccuracies in real-world clinical scenarios. Similar challenges in identifying a representative area for the entire degradation of Mg-based implants *in vivo* have been highlighted previously [175]. Therefore, future *in vivo* animal studies should undertake medical image-based analysis before implantation with the additional support of implant surgical guides, in order to precisely implant a ZX00 screw in the same position, thereby enabling a corrosion performance comparison of the head and tip region of the screw at different time points to determine whether the difference in corrosion observed *in vitro* occurs *in vivo* in these screw zones.

Previous *in vivo* studies have revealed that hydrogen gas evolution is primarily found adjacent to Mg-Zn-Ca implants investigated [133,185,187,221,370,448,449]. Although the

composition and volume of the released gas during ZX00 alloy degradation were not investigated in this study, our μCT and histology findings after 6 weeks of implantation revealed numerous gas voids mainly in the intramedullary cavity. These gas cavities were visible up to 12 weeks post-implantation, supporting previous findings [187,371]. After 24 weeks of implantation, corrosion reactions were not as intense. At this time point, the gas cavities in the cortical bone compartment were considerably smaller, suggesting that ZX00 alloy corrosion slowed over this period. Depending on the local gas saturation, this gas may cause irritation, cell and tissue displacement [300], accumulation in tissue cavities [440,450], mechanical disturbance that may disrupt the initial cortical bone healing process, resulting in callus formation [185], or altering the trabecular bone structure [372]. In the case of H_2 released in soft tissues, large gas voids can be formed, and the H_2 concentration can be permeated through the skin [451], eliminated by the local blood flow [300] or removed by puncture with a syringe as reported in small [352] and large animal studies [452]. When pure Mg was subcutaneously implanted in Sprague-Dawley® (SD) rats, Ben Amara et al. [435] observed that the H_2 accumulation accompanied the amplified early inflammatory response. In contrast, Zhang et al. [176], who implanted Mg-Zn-Mn pins did not observe gas voids in soft tissues 5 weeks after implantation owing to the alloy´s gradual degradation. However, gas voids probably dissipated through absorption in the surrounding tissue [438] and were not visible at the time point of experimental observation.

Similarly, gas cavities have been observed in Mg implants exposed to the intramedullary cavity in small and large animal models. Transcortical implantation of XHP-Mg pins versus ZX00 pins in the diaphysis of SD rats resulted in moderate gas evolution that was more pronounced for XHP Mg pins already at 2 weeks [221], whereas increased gas formation and enhanced implant volume loss due to faster degradation was observed around ZX00 pins also transcortical implanted in the tibia of ovariectomy-induced osteoporotic rats. Osteoporotic bone has decreased mineralization [370] and deteriorated bone microarchitecture [453,454]. Marek et al. [372] observed gas surrounding ZX00 intramedullary nails at the proximal epiphysis with an increased gas volume at 2 weeks which decreased up to 76 weeks causing bone-structure alterations in the initial phase of ZX00 degradation. As the bone marrow cavity is highly perfused by blood vessels, the water content and local blood flow around the implants influenced not only the accelerated corrosion of Mg implants at this bone compartment but also the local diffusion and solubility of H_2, which contributed to the gas transport and absorption by the vascular system, reducing the size of the gas pockets [185,371,455,456].

In contrast to what has been reported regarding the gradual disappearance of gas bubbles as the implantation time increases as observed in our study, Wang et al. [457] observed an increased density of the gas bubbles after 24 weeks around the Mg-Zn-Zr pins implanted into the femoral condyles of Japanese white rabbits. The femoral condyle is composed of bone marrow, spongy bone, compact bone and cartilage [390] is a region of high blood flow that could contribute to rapid corrosion of the alloy, which would explain the number of gas cavities the authors observed at the experimental time point. According to their findings, the degradation of Mg-Zn-Zr alloy caused gas cavitation within the cancellous bone, which was progressively filled with newly regenerated bone, cartilage, and fibrous connective tissues. Han et al. [373] (2020), who implanted Mg5Ca pins in the femoral condyle of SD rats, observed insufficient bone healing and low-density tissue adjacent to the implants, indicating the possible fibrotic tissue formation due to the alloy´s rapid degradation accompanied by metallic ions and hydrogen gas release. With W4 interferences screws implanted in the femoral condyle of sheep, Thormann et al. [458] also observed implant loosening, delayed osseointegration, and a significant amount of gas evolution. After 6 weeks, gas voids were observed surrounding the entire implant and spreading in the trabecular bone; after 12 weeks, the voids were surrounded by soft tissue. In addition, they observed a large number of multinuclear cells and blood vessels in close proximity to the gas cavities, indicating an endeavor by the tissue to control the gas evolution. However, after 12 weeks the number of vessels decreased, indicating a reduced effort by tissue to regulate the gas released. Thus, this gas formation ascribed to the hydrogen evolution during Mg corrosion [459] is proportional to the Mg alloy`s rate of degradation, the implant location, and the selected animal model [455,460]. Nevertheless, H_2 may not be the sole gas present in the gas cavities. Before implantation, the body fluid contains dissolved nitrogen (N_2), oxygen (O_2) and carbon dioxide (CO_2) in proportion to their partial pressure. When an Mg device is implanted, corrosion reactions generate H_2 with a proportionate increase in H_2 pressure. As previously demonstrated [456], this H_2 is dissolved and/or diffused through the vascular system while being exchanged with the undissolved N_2, O_2 and CO_2 gases present in the voids [459]. Hence, the chemical composition of the Mg-based alloy, the implant location in the body, and the time points selected for observations may account for differences in the generation and dissolution of the gas voids. However, in our study, despite the degradation reactions and gas formation, new bone in direct contact with corrosion products was formed demonstrating that the ZX00 alloy did not cause adverse effects in the surrounding tissues, promoting osteogenesis and bone healing consistent with previously reported studies [133,185,187,367,371,457]. Nevertheless, the specific composition and effects of the gas

produced by the degradation of the ZX00 alloy are still not fully understood and need to be clarified in future studies.

Additionally, implant integrity is crucial during the initial fracture-healing stage to provide sufficient stability for the reduction and fixation of bone fracture fragments [8,367]. To provide sufficient primary fracture stabilization, the corrosion behavior of Mg-based implants should match the healing time of a bone fracture. This mechanical integrity must be maintained for 4 to 6 weeks in children and 12 to 18 weeks in adults [221,300]. The majority of fractures involving the clavicle, hand, wrist and distal radius fractures require 4-8 weeks of mechanical support, whereas femur fractures and femoral neck fractures required 8-14 and 12-24 weeks of healing time, respectively [368]. Our results found that the main body of the ZX00 screw slowly degraded and still was present after 24 weeks of implantation. Lee et al. [183] demonstrated that 4 to 6 weeks of mechanical support for bone-healing was required when Mg-5wt.% Ca-1wt.% Zn was implanted to treat wrist and hand fractures. Castellani et al. [289] observed a similar outcome after implanting Mg-RE alloy rods in the femoral bone of Sprague-Dawley rats for up to 24 weeks. Holweg et al. [133] also found fracture consolidation without impairment in a juvenile sheep model using ZX00 osteosynthesis screws which still were discernible after 12 weeks. In contrast, Bian et al. [223] observed that Mg-1.8Zn-0.2Gd pins implanted in the tibia of rats, the pins maintained their shape for the first 2 months before degrading nearly completely after 6 months of implantation. In the cortical zone, the implant was directly integrated with the bone, whereas in the medullary cavity, some trabecular bones were in contact with the implant and some trabecular bones were found at a certain distance to the implant. They attributed the accelerated degradation to the mildly localized corrosion observed *in vivo*, which was ascribed to the alloy´s inhomogeneous composition and impurities introduced during the production processes. This demonstrates how crucial is to have consistent manufacturing methods to prevent the introduction of impurities and the continuous monitoring of the microstructure of Mg implants to ensure homogeneous composition throughout the entire Mg implant geometry for those intended for biomedical applications. Based on our SEM, histology and BIC findings, ZX00 screws provide sufficient long-term fixation for adequate bone healing and mechanical strength.

5.5. Conclusion

Based on the results presented in this study the following conclusions can be drawn:

- The corrosion performance of the screws produced from ZX00 alloys was investigated under *in vitro* and *in vivo* conditions, and the results from both methods were complementary. Although the corrosion layers formed under *in vitro* and *in vivo* conditions had the same elemental composition, the elemental distribution and thickness of the corrosion layers varied. This indicated that the degradation mechanisms occurring under physiological conditions are highly dependent on the surrounding environment to which the implants are exposed. Consequently, *in vitro* tests must be further improved. This confirms that replicating the exact conditions of *in vivo* testing is difficult to achieve through *in vitro* testing. Therefore, improving *in vitro* experimental design is of critical importance to reduce *in vivo* trials.
- Until 28 days of immersion under physiological conditions, the corrosion rate calculated based on *in vitro* methods increased continuously.
- The corrosion rate of ZX00 after *in vitro* testing was slower (1.04 $mm \times year^{-1}$) when compared to the alloys with higher Zn concentration (ZX10, ZX20, and ZX50).
- The technological aspect of screw manufacturing is important from a materials design point of view. Our results clearly indicate that the ZX00 screw corroded nonuniformly, and the zones of the screw with the uniform grain size distribution had the lowest degradation rate. Therefore, controlling microstructure is a key parameter that can be used to tune the dissolution of Mg screws under physiological conditions.
- The vast number of voids observed i*n vivo* 6 weeks after implantation was indicative of gas produced by the degradation of the ZX00 screw, predominantly within the intramedullary cavity. As the implantation time increased, the observed voids were smaller in size. This size reduction over time may be due to the exchange mechanism of water content and blood flow in the surrounding tissues and does not necessarily indicate the deceleration of the corrosion mechanisms.
- Despite the corrosion reactions and gas release during the ZX00 screw degradation, new bone formed in direct contact with corrosion products without any adverse effects in the surrounding tissues. Therefore, ZX00 alloy is a potential Mg-based alloy to consider for temporary bone implants.

Supplementary materials

Table S5.1: Chemical composition of different screw zones performed via EDX (Data presented as mean ± standard deviation from 3 independent samples)

Screw Zone/Element (wt.%)	O	Mg	Ca	Zn
Head	1.9 ± 0.9	97.4 ± 1.2	0.4 ± 0.3	0.4 ± 0.2
Valley	0.9 ± 0.3	98.3 ± 0.5	0.3 ± 0.1	0.4 ± 0.2
Tip	2.2 ± 1.7	97.0 ± 1.7	0.4 ± 0.2	0.5 ± 0.3

Table S5.2: The composition of the α-MEM [461]

Ingredient	**α-MEM**	
	mg/L	mM
Aminoacids (21 kinds)	1193.4	8.33
Vitamins (12 kinds)	59.56	2.9
Inorganic salts		
Calcium Chloride $CaCl_2.2H_2O$)	264	1.80
Magnesium Sulfate ($MgSO_4.7H_2O$)	97.67	0.81
Potassium Chloride (KCl)	400	5.33
Sodium Bicarbonate ($NaHCO_3$)	2200	26.19
Sodium Chloride (NaCl)	6800	117.24
Sodium Phosphate monobasic ($NaH_2PO_4.H2O$)	140	1.01
Other components		
D-Glucose (Dextrose)	1000	5.56
Lipoic Acid	0.2	0.000097
Phenol Red	10	0.03
Sodium Pyruvate	110	1.00

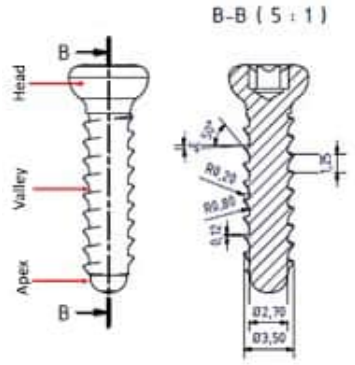

Figure S5.1. Schematic of the ZX00 screw. Head, valley, and apex zones are shown in the diagram on the left. On the right: thread angle (50°), pitch distance (1.25), and outer and inner diameter (3.50 and 2.70 mm) are shown.

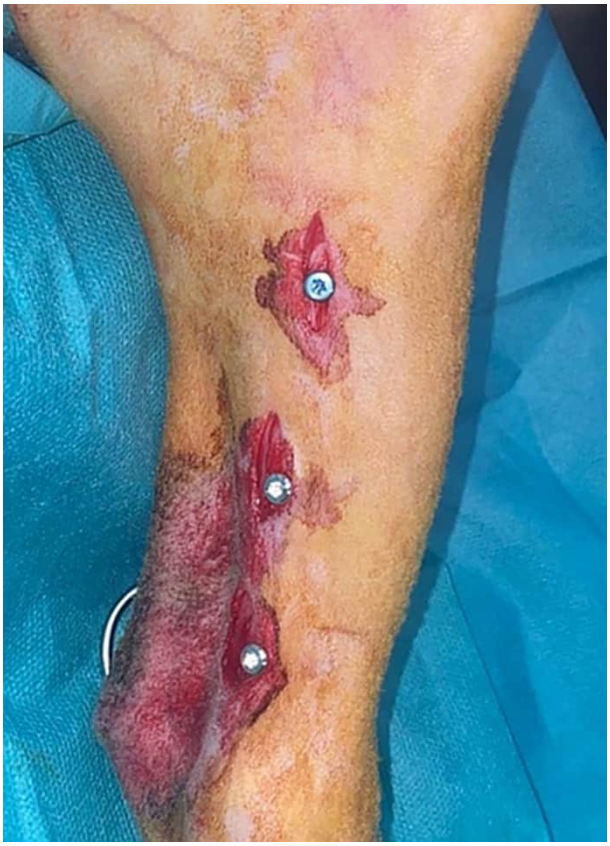

Figure S5.2. Operative site of implant insertion. ZX00 screws were implanted in the diaphysis of sheep.

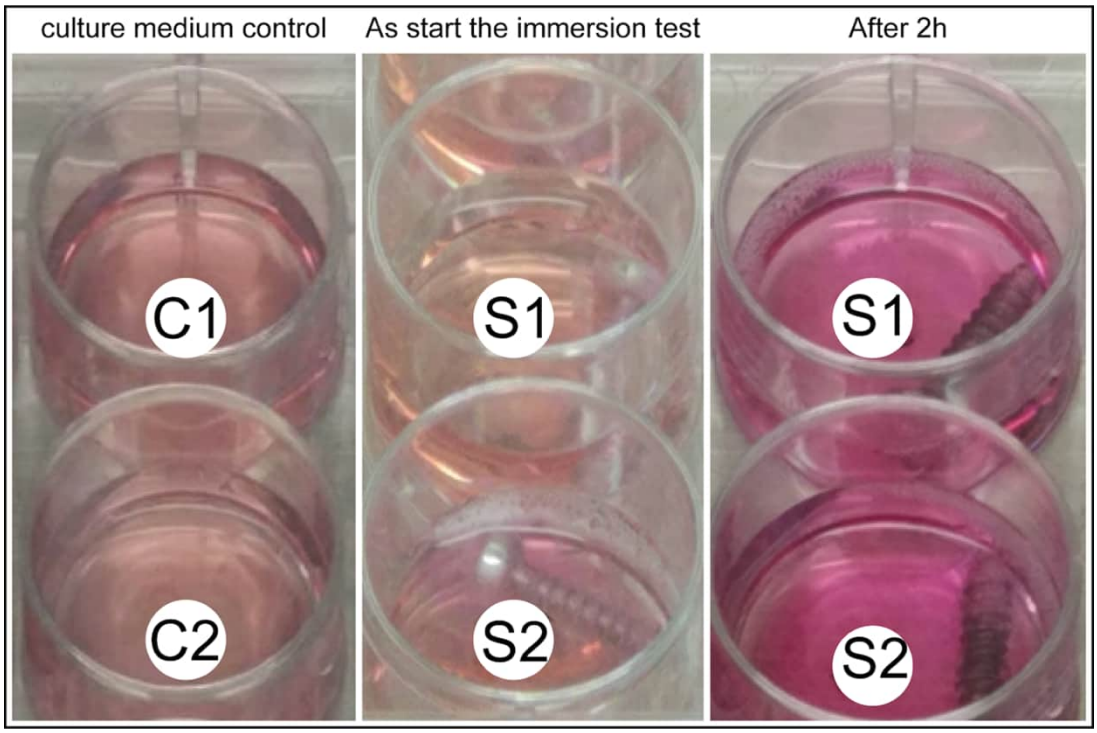

Figure S5.3: pH variation in the immersion medium during the ZX00 immersion test under cell culture conditions. ZX00 screws were placed in 12-well plates and 2mL of immersion medium was added per well. The strong initial corrosion of ZX00 screws leads to a change in the pH visible in the culture medium from light pink (control medium) to dark pink. Immersion medium: α-MEM supplemented with 10% FBS and 1% penicillin/streptomycin.

Figure S5.4: Stereomicroscopy images of ZX00 screws after 3-, 6-, 14-, 21-, and 28-days of immersion. Screws were exposed to α-MEM culture medium supplemented with 10% FBS and 1% penicillin/streptomycin under cell culture conditions (37ºC, 20% O_2, 5%CO_2, and 95% relative humidity).

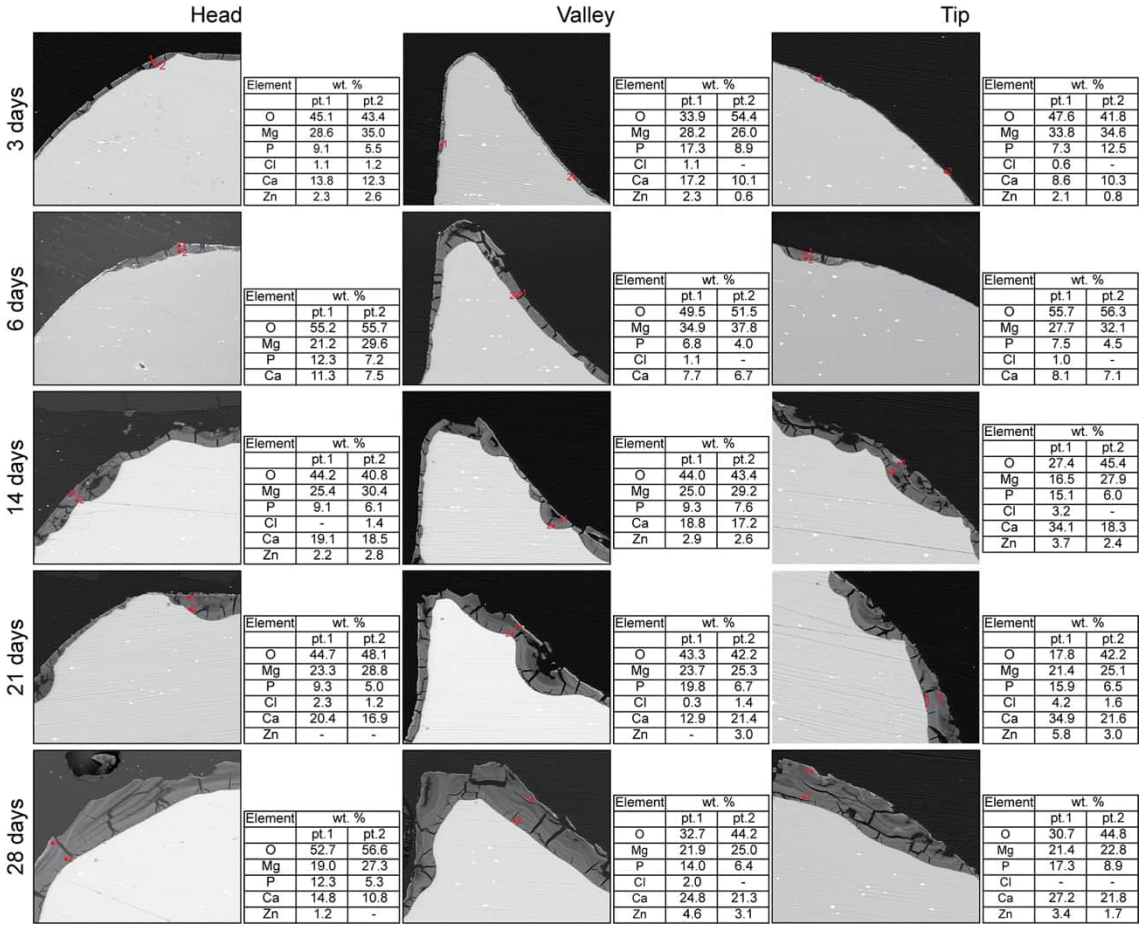

3 days – Head	wt. %	
Element	pt.1	pt.2
O	45.1	43.4
Mg	28.6	35.0
P	9.1	5.5
Cl	1.1	1.2
Ca	13.8	12.3
Zn	2.3	2.6

3 days – Valley	wt. %	
Element	pt.1	pt.2
O	33.9	54.4
Mg	28.2	26.0
P	17.3	8.9
Cl	1.1	-
Ca	17.2	10.1
Zn	2.3	0.6

3 days – Tip	wt. %	
Element	pt.1	pt.2
O	47.6	41.8
Mg	33.8	34.6
P	7.3	12.5
Cl	0.6	-
Ca	8.6	10.3
Zn	2.1	0.8

6 days – Head	wt. %	
Element	pt.1	pt.2
O	55.2	55.7
Mg	21.2	29.6
P	12.3	7.2
Ca	11.3	7.5

6 days – Valley	wt. %	
Element	pt.1	pt.2
O	49.5	51.5
Mg	34.9	37.8
P	6.8	4.0
Cl	1.1	-
Ca	7.7	6.7

6 days – Tip	wt. %	
Element	pt.1	pt.2
O	55.7	56.3
Mg	27.7	32.1
P	7.5	4.5
Cl	1.0	-
Ca	8.1	7.1

14 days – Head	wt. %	
Element	pt.1	pt.2
O	44.2	40.8
Mg	25.4	30.4
P	9.1	6.1
Cl	-	1.4
Ca	19.1	18.5
Zn	2.2	2.8

14 days – Valley	wt. %	
Element	pt.1	pt.2
O	44.0	43.4
Mg	25.0	29.2
P	9.3	7.6
Ca	18.8	17.2
Zn	2.9	2.6

14 days – Tip	wt. %	
Element	pt.1	pt.2
O	27.4	45.4
Mg	16.5	27.9
P	15.1	6.0
Cl	3.2	-
Ca	34.1	18.3
Zn	3.7	2.4

21 days – Head	wt. %	
Element	pt.1	pt.2
O	44.7	48.1
Mg	23.3	28.8
P	9.3	5.0
Cl	2.3	1.2
Ca	20.4	16.9
Zn	-	-

21 days – Valley	wt. %	
Element	pt.1	pt.2
O	43.3	42.2
Mg	23.7	25.3
P	19.8	6.7
Cl	0.3	1.4
Ca	12.9	21.4
Zn	-	3.0

21 days – Tip	wt. %	
Element	pt.1	pt.2
O	17.8	42.2
Mg	21.4	25.1
P	15.9	6.5
Cl	4.2	1.6
Ca	34.9	21.6
Zn	5.8	3.0

28 days – Head	wt. %	
Element	pt.1	pt.2
O	52.7	56.6
Mg	19.0	27.3
P	12.3	5.3
Ca	14.8	10.8
Zn	1.2	-

28 days – Valley	wt. %	
Element	pt.1	pt.2
O	32.7	44.2
Mg	21.9	25.0
P	14.0	6.4
Cl	2.0	-
Ca	24.8	21.3
Zn	4.6	3.1

28 days – Tip	wt. %	
Element	pt.1	pt.2
O	30.7	44.8
Mg	21.4	22.8
P	17.3	8.9
Cl	-	-
Ca	27.2	21.8
Zn	3.4	1.7

Figure S5.5. In vitro corrosion behaviour of ZX00 screws after immersion. Cross-sectional backscattered electron (BSE) micrographs with EDX point analysis performed on corrosion layers formed at the head, valley and tip zones of the ZX00 screw after 3-, 6-, 14-, 21-, and 28-days of immersion in α-MEM culture medium supplemented with 10% FBS and 1% penicillin/streptomycin.

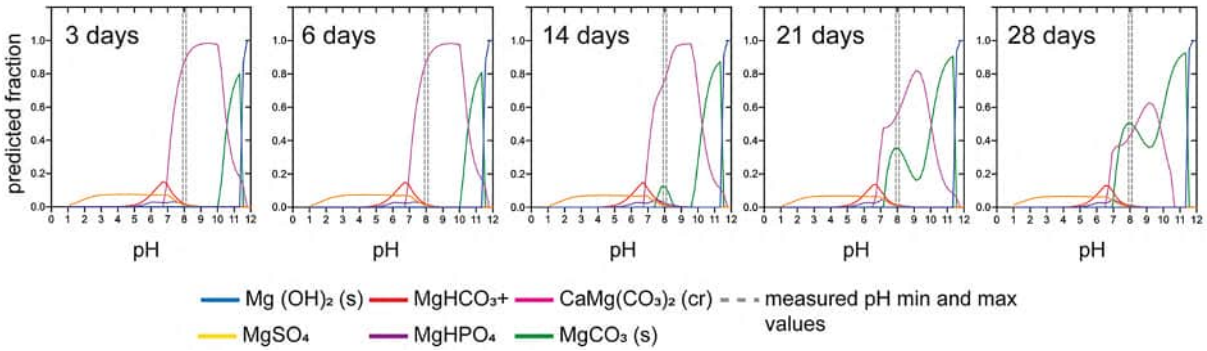

Figure S5.6. Total predicted fraction diagram of Mg chemical compounds as a function of pH calculated by Hydra Medusa software at 25ºC. Data from screw samples immersed in a α-MEM supplemented with 10% FBS and 1% P/S. Grey vertical dashed lines indicated the experimental pH range.

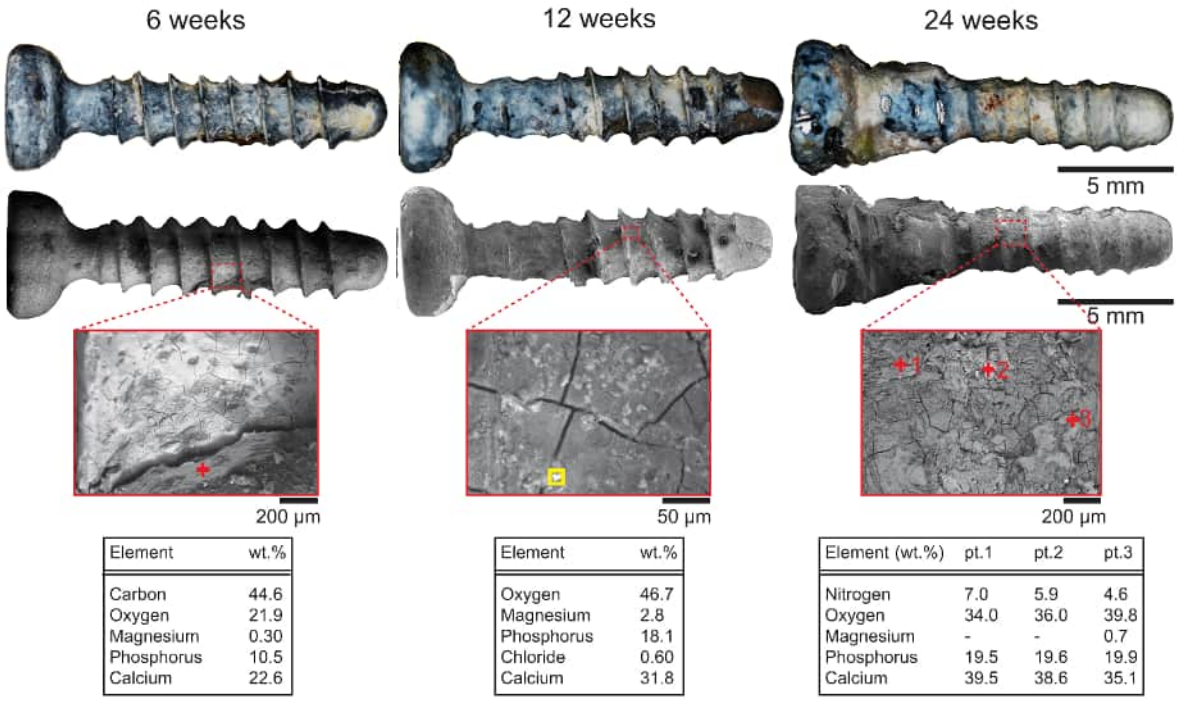

Element	wt.%
Carbon	44.6
Oxygen	21.9
Magnesium	0.30
Phosphorus	10.5
Calcium	22.6

Element	wt.%
Oxygen	46.7
Magnesium	2.8
Phosphorus	18.1
Chloride	0.60
Calcium	31.8

Element (wt.%)	pt.1	pt.2	pt.3
Nitrogen	7.0	5.9	4.6
Oxygen	34.0	36.0	39.8
Magnesium	-	-	0.7
Phosphorus	19.5	19.6	19.9
Calcium	39.5	38.6	35.1

Figure S5.7: Stereomicroscopy and SEM images of ZX00 screws after 6-, 12-, and 24- weeks of *in vivo* implantation. *First and second rows*: Representative stereomicrographs and SEM images of the retrieved ZX00 implants. Third *and four rows*: Representative SEM images and their respective EDX point analysis show some organic material (observed in yellow-brown color in the stereomicrographs) that remains attached to the implant surface after implant retrieval.

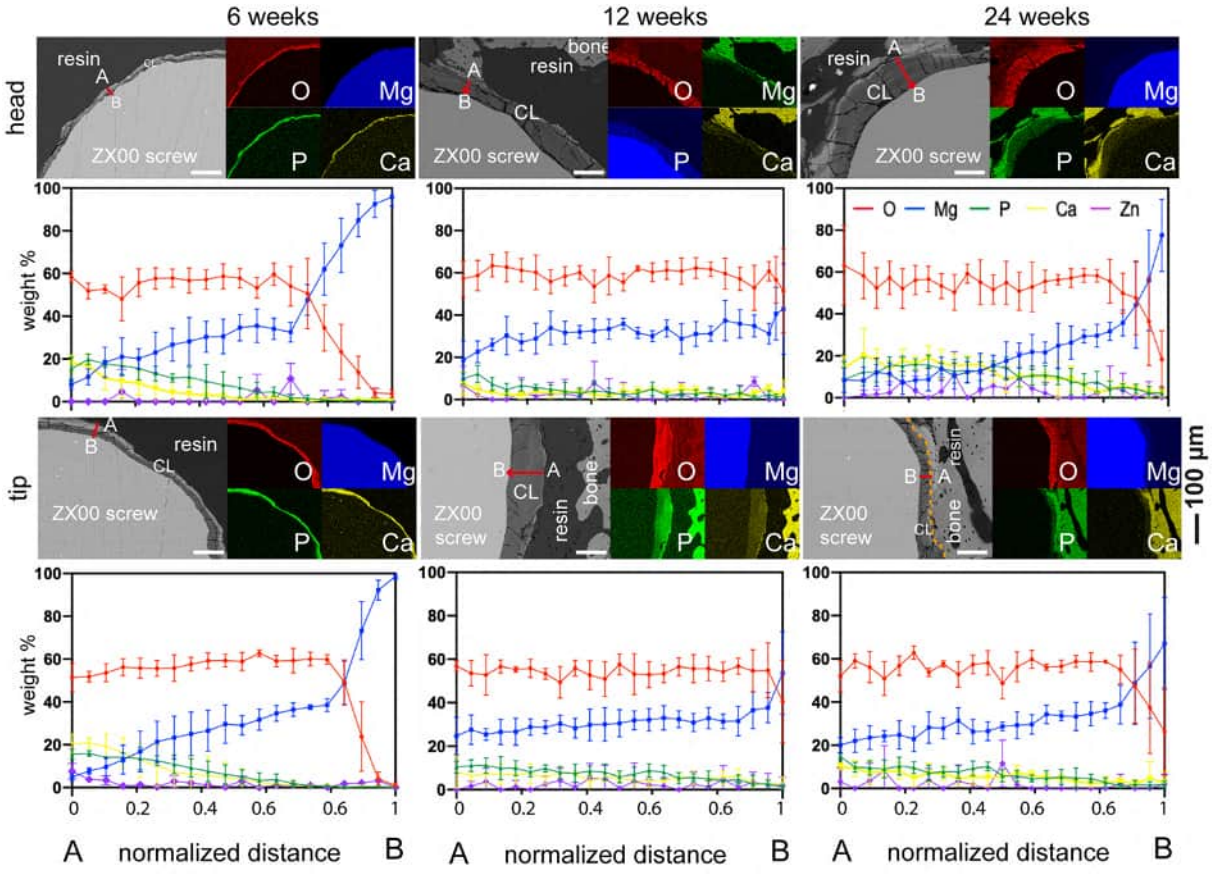

Figure S5.8: Characterization of the bone-implant interface of a) head and b) tip regions of ZX00 screws after 6-, 12-, and 24- weeks of implantation. SEM images and their corresponding EDX maps and line scans performed from the outer part (A) to the inner part of the corrosion layers denoted by red arrows. The dotted orange line in (b) at 24 weeks indicated the interface between the corrosion layer and bone. Data presented as mean ± standard deviation (n = 5 line scans/zone/time point from 3 independent samples).

Bridging chapter 5 and 6

Findings in chapter 5 clearly demonstrated that the degradation of Mg based devices was implant-site dependent. This highlights the challenge in estimating the corrosion rate from *in vivo* studies, primarily because of complex biological processes involved during the degradation of Mg implants. When a biomaterial is implanted within the human body, there is also an initial inflammatory response in the host tissue [462]. Therefore, in the following Chapter 6, the corrosion performance of pure Mg implants was investigated *in vitro*, and in an *in vivo* soft tissue model. The aim of the soft tissue model was ***to determine the kinetic changes that take place on pure Mg implants when implanted in soft tissue and evaluate the inflammatory response associated to the corrosion of the Mg material***.

Chapter 6

Magnesium implant degradation provides immunomodulatory and proangiogenic effects and attenuates peri-implant fibrosis in soft tissues

*Heithem Ben Amara, **Diana C. Martinez**, Furqan A. Shah, Anna Johansson Loo, Lena Emanuelsson, Birgitta Norlindh, Regine Willumeit-Römer, Tomasz Plocinski, Wojciech Swieszkowski, Anders Palmquist, Omar Omar, Peter Thomsen*

*Published in **Bioactive Materials** 2023 (26): 353-369.* doi: 10.1016/j.bioactmat.2023.02.014.

ABSTRACT

Implants made of magnesium (Mg) are increasingly employed in patients to achieve osteosynthesis while degrading in situ. Since Mg implants and Mg^{2+} have been suggested to possess anti-inflammatory properties, the clinically observed soft tissue inflammation around Mg implants is enigmatic. Here, using a rat soft tissue model and a 1-28 d observation period, we determined the temporo-spatial cell distribution and behavior in relation to sequential changes of pure Mg implant surface properties and Mg^{2+} release. Compared to nondegradable titanium (Ti) implants, Mg degradation exacerbated initial inflammation. Release of Mg degradation products at the tissue-implant interface, culminating at 3 d, actively initiated chemotaxis and upregulated mRNA and protein immunomodulatory markers, particularly inducible nitric oxide synthase and toll-like receptor-4 up to 6 d, yet without a cytotoxic effect. Increased vascularization was demonstrated morphologically, preceded by high expression of vascular endothelial growth factor. The transition to appropriate tissue repair coincided with implant surface enrichment of Ca and P and reduced peri-implant Mg^{2+} concentration. Mg implants revealed a thinner fibrous encapsulation compared with Ti. The detailed understanding of the relationship between Mg material properties and the spatial and time-resolved cellular processes provides a basis for the interpretation of clinical observations and future tailoring of Mg implants.

Keywords: Magnesium; Biodegradable Implants; Inflammation; Foreign-Body Reaction; Gene expression, Neovascularization

GRAPHICAL ABSTRACT

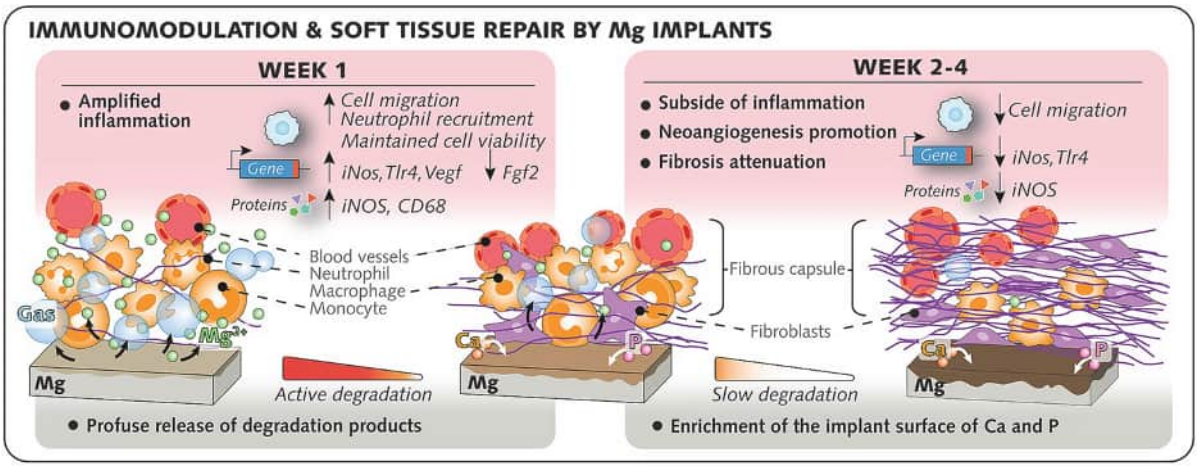

6.1. Introduction

In ever-increasing numbers, patients are being treated with implants made of magnesium (Mg), a metallic biomaterial designed to be eliminated from the body while fulfilling its function in situ [463]. The century-old concept of using Mg implants regained interest during the last two decades, simultaneously with the increased sophistication in controlling their degradation and in improving their mechanical properties [78,106,352]. Today, Mg-based implants are implemented in routine clinical practice within two primary applications: vascular [464] and orthopedic [18]. The former application refers to Mg biodegradable vascular stents which, in conjunction with angioplasty, enable geometry restoration and vasomotion of diseased vessels beyond complete implant degradation [465]. The latter set of implants (i.e., orthopedic implants) denotes Mg-based osteosynthesis systems that hold fractured bone in place to secure repair before full degradation of the implant [8]. For both applications, long term-studies [183,293,466] concur that Mg implants meet the need to overcome the flaws of their conventional permanent analogs: the unwanted re-narrowing of the stented vessel due to a reactive fibrotic proliferation [467], and the inevitable surgical removal of the orthopedic implant after healing of fractured bone [468].

However, a suboptimal outcome or failure is also reported to occur in patients treated with Mg implants. A recent systematic review and meta-analysis reported a complication rate of ~13% with Mg-based osteosynthesis implants, although not different from the complication rate with state-of-the-art implants made of titanium (Ti) [294]. While such complications are manifold ranging from events such as pain and infection to osteosynthesis failure [379,469], poor healing around Mg implants has been reportedly linked to an uncontrolled initial response [470]. When implanted in the body, Mg is reactive: it starts degrading immediately upon implantation and resorbs at the fastest rate during the initial postoperative period [471,472]. Thus, the early days after which a Mg-based osteosynthesis implant makes contact with the body involve the greatest release of degradation products [473] into the tissue environment, including bone and the overlying soft tissues alike.

Inflammation of soft tissues in the vicinity of Mg-based osteosynthesis implants is a clinical event documented during the early post-implantation period [470,474]. This inflammation is typically accompanied by subcutaneous radiolucent cavities resulting from the gaseous accumulation generated by the degradation of the nearby Mg implant [377,474–476]. In most instances where the Mg implant successfully integrates to the recipient bone, the initial

inflammation of the peri-implant soft tissues is reported to fully subside together with the gaseous voids a few weeks following implantation [377,470,475,476]. In contrast, when a Mg implant failure occurs, an exacerbated and persistent soft tissue reaction is described [379]. A soft tissue-damaging inflammation has been linked to the failure of other metallic orthopedic implants, such as cobalt-chromium implants for hip and knee replacement, which release micrometer-sized metallic wear particles and ions [477,478]. By eliciting a persistent inflammation involving a central role of macrophage cytotoxicity, metallic wear byproducts lead to an excessive foreign body response (FBR) in soft tissues [479]. These unanticipated complications raised questions on the safety and biocompatibility of metallic implants in the context of particles and ions deposited in the adjacent tissues.

Mg implants are traditionally assigned anti-inflammatory properties [480,481]; the underlying assumption being the widely reported potency of Mg^{2+} administration to attenuate inflammation [481–483]. This however contradicts the reported soft tissue inflammation at the postoperative stage in humans and animals receiving Mg osteosynthesis implants [274,474]. Further, the fast delivery of degradation products from Mg implants to the adjacent tissues might favor fibrosis [484]. The lack of *in vivo* information on the cellular and molecular response in relation to the degradation of Mg implant has hampered the understanding of the immune response in soft tissues to Mg implants.

Here, we hypothesize that the degradation of Mg implants amplifies the foreign body response (FBR) by promoting the initial inflammation and the subsequent fibrotic encapsulation. To test this assumption, we sequentially monitored the degradation of Mg implants and the linked cellular response from days 1 to 28 upon implantation in soft tissues in comparison to nondegradable Ti implants. We employed a rat subcutaneous model [485–487] previously used to scrutinize the cellular response at three topographically distinct compartments of the soft tissue interface with implants (Figure 6.1): the cells adherent to the implant surface, the inflammatory fluid around the implant (*exudate*), and the soft tissue *per se*. The results reveal that the initial *in situ* local release of degradation products from Mg implants, which culminates at 3 d *in vivo* and *in vitro*, triggers a robust proinflammatory response in soft tissue during the first postoperative week, yet without a cytotoxic effect in comparison to the response to Ti implants. Thereafter, the inflammation around Mg implants markedly subsides when the release of degradation products declines in the peri-implant exudate simultaneously with the development of a protective layer rich in calcium and phosphorus at the surface of Mg implants. This allows the assembly of a more vascularized

and thinner fibrous capsule around Mg implants in comparison to Ti implants. An amplified inflammation of the soft tissue initially in response to Mg implants is demonstrated, but is tuned by the degradation dynamics to improve vascularization and to attenuate fibrosis, with implications expanding to other tissue types.

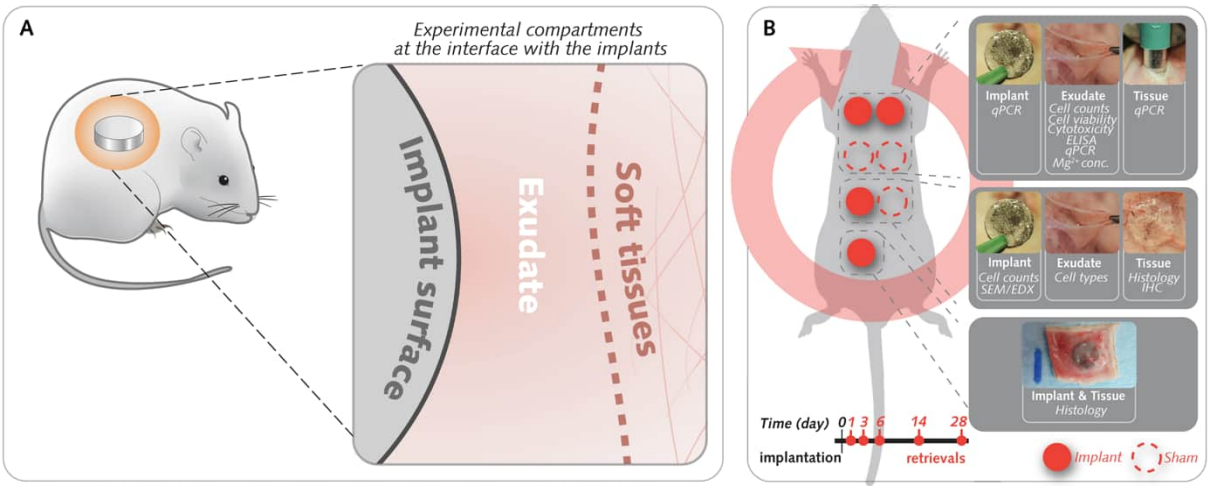

Figure 6.1: The rat subcutaneous model allows the compartmentalization of the interface with the implants. (**A**)**,** The cellular response was characterized at three topographically distinct compartments of the soft tissue-implant interface: the cells adherent to the implant surface, the inflammatory fluid around the implant (*exudate*), and the soft tissue *per se*. (**B**)**,** Four implants were inserted in each rat in addition to three sham wounds without implants. At 1-, 3-, 6-, 14-, and 28-days following implantation, the separate retrieval of implants, exudates, and tissues allowed the monitoring of Mg^{2+} concentration at the interface along with cellular (cell counts, cell viability, and cytotoxicity) and molecular analyses (gene expression with qPCR analysis; protein analyses with enzyme-linked immunosorbent assay [ELISA] and immunohistochemistry [IHC]). In addition, implants and tissues that were collected *en bloc* were allocated for morphometric analyses of tissues (histology and histomorphometry) and the Mg-degradation layer (SEM, secondary electron microscopy; EDX: energy dispersive X-ray spectroscopy). Random allocation of pockets to the different retrieval groups was achieved through a clockwise rotation scheme, as shown by the red circular arrow

6.2. Materials and methods

6.2.1. Implants

High-purity Mg (99.995%) discs (thickness = 1.4 mm, diameter = 9 mm) were fabricated as described previously [488]. Discs of identical dimensions were machined from commercially pure titanium grade IV. Chemical compositions of the as-manufactured discs were determined using spark emission spectroscopy (Table S6.1). Manufactured Mg implants were polished using 2500 grit SiC grinding paper, then cleaned by ultrasonic bathing in *n*-hexane, acetone, and ethanol (100%) successively, followed by air-drying in a vacuum. Individually packed Mg implants were then sterilized by gamma irradiation at a dose of 30.2 kGy (BBF GmbH, Stuttgart). Manufactured Ti implants were cleaned by ultrasonic bathing in extran® and ethanol

(70%), successively, followed by air-drying. Individually packed Ti implants were then steam-sterilized by autoclaving at 121 °C for 20 min.

6.2.2. Preimplantation characterization

6.2.2.1. Surface characterization

Mg and Ti implants (n = 3 each), that were cleaned and sterilized, were used for scanning electron microscopy (SEM; SU-8000, Hitachi) performed in the backscattered electron (BS-SEM) and secondary electron (SE-SEM) modes at 15 kV accelerating voltage. Chemical composition of the Mg implants was evaluated by energy-dispersive X-ray spectroscopy (EDX; UltraDry EDS Detector, NSS software v. 3.2, Thermo Fisher Scientific) at 15 kV and 15 mm working distances. Surface roughness (S_a) was determined using confocal laser-scanning microscopy (VK-1000, Keyence) equipped with a 20x objective. Nine 100 x 100 μm^2 regions on each of Mg and Ti implant surface (n = 3 each), were analyzed.

6.2.2.2. Microstructure analyses

Cross-sections were prepared using metallographic cutting equipment (MICRACUT 151, Metkon). For Mg implants, glycerol in ethanol, 1:3 (v/v), was used as the coolant. Ti and Mg implants were polished, followed by ion milling (IM 4000, Hitachi). SEM (SU-8000, Hitachi) and elemental analysis using EDX (UltraDry EDS Detector, NSS software v. 3.2, Thermo Fisher Scientific) were performed at accelerating voltages of 5 kV (imaging) and 15 kV (EDX), a 15 mm working distance, and a 20 µA beam current. In addition, electron backscattered diffraction (EBSD) was performed by SEM (SU-70, Hitachi) equipped with an e$^-$Flash^{HD} detector (Bruker Microanalysis System) at 20 kV and at step sizes of 0.2 µm and 1.5 µm for Ti and Mg implants, respectively, followed by data processing with HKL Channel 5 software v. 5.0.

6.2.2.3. Natural oxidation study

Mg implants from the same batch used *in vivo* were randomly selected and characterized. On each day scheduled for surgical implantation in animals, the entire surface of n = 3 Mg implants was examined under an Olympus SZ61 stereomicroscope coupled with an OPTA-Tech HDMI camera, and images of the entire surface were taken at 2x magnification. SEM observations of the surface of the discs were also performed at 30x, 500x and 5000x magnification and at a 5 kV acceleration voltage (Hitachi, SU-8000). To identify oxygen-rich regions, point measurements using EDX were performed at selected areas at 15 kV.

6.2.3. In vitro immersion test of Mg implants

Cleaned and sterilized Mg implants (n = 54) were individually immersed in 2 mL of alpha-minimum essential medium (α-MEM; Life Technologies) supplemented with 10% fetal bovine serum (Gibco, Life Technologies) and 1% penicillin/streptomycin (P/S; Invitrogen) under sterile cell culture conditions (37°C, 5% CO_2, and 95% controlled humidity) in an incubator (Heraeus BBD 6620, Fisher Scientific). Immersion times were 1, 3, 6, 14, 21, and 28 d (n = 9/time point). Control medium samples (n = 3/time-point) did not receive Mg implants. All media were changed every 2-3 days to maintain semistatic immersion conditions [98]. The pH and osmolality were recorded prior to implant immersion and in each collected medium postimmersion. The pH of the initial culture medium was measured using a pH meter (Sentron® SI600, Sentrom Europe BV) with a MiniFET probe. Similarly, the initial osmolality of the immersion medium was recorded by a cryoscopic osmometer (OSMOMAT® auto, Gonotec GmbH). The pH and osmolality of the supernatant were measured at each change in the implant-containing medium or control medium.

In addition, to calculate the degradation rate and depth, all implants were retrieved and weighed before and after removal of degradation products with chromic acid (180 g/L in distilled water, VWR International). The weight of each treated disc was measured to calculate the degradation rate (*DR*; mm/year) based upon the following formula (ASTM G1-03 2017):

$$DR = \frac{\Delta g.\ (8.76 \times 10^4)}{A.t.\rho} \quad (4.1)$$

where Δg is the difference in implant weight prior to immersion and after chromic acid treatment (g), A is the implant surface area (cm^2), t is the immersion time (h) and $\boldsymbol{\rho}$ is the density of the disc (g/cm^3).

The degradation depth (h; μm/day) was estimated by the following linear regression line equation [391]:

$$h = h_\infty . t + h_0 \quad (4.2)$$

where t is the total time of incubation (days), h_0 is the y-intercept describing the initial reactions during the immersion test, and h_∞ is the slope value representing the mean degradation rate.

6.2.4. Animal model and surgical procedure

Animal experiments were approved by the Local Ethical Committee for Laboratory Animals at the University of Gothenburg, Sweden (Dnr-02437/2018), and complied with the ARRIVE guidelines. Sprague-Dawley rats (n = 100; 250-350 g; Taconic Biosciences), housed together (maximum 4 rats/cage) on a 12-12-hour dark-light cycle with free access to water and standard rodent diet, were used. In brief, animals were anesthetized by administering 4% isoflurane by inhalation. The back of each rat was shaved and cleaned, and seven separate incisions were made to create subcutaneous pockets by blunt dissection. Experimental sites received implants (n = 4; Mg or Ti in each rat) or were left without implants (n = 3, Sham Ti or Sham Mg in each rat) before closure with nonresorbable sutures (Figure S6.1a-b). The back was cleaned, and rats were recovered from anesthesia before returning to animal house. For purpose of analgesia, Temgesic (Reckitt Benckiser; 0.03 mg/kg) was subcutaneously administrated at immediate- and at 8 h-postoperative. Animals were sacrificed with an overdose of pentobarbital after 1, 3, 6, 14, or 28 d (n = 20/time point). Four types of samples were retrieved from each rat according to a randomization scheme (Figure S6.1b):

1- *Implants (n = 8-9/group/time point):* collected following pocket re-entry for analyses of adherent cells (counting or gene expression) or for morphological and chemical analyses of implant surface.
2- *Peri-implant exudate (n = 8-9/group/time point):* obtained by lavage of the pockets with Mg^{2+}-free phosphate-buffered saline. Each retrieved volume was divided for analyses of cells (counting, viability, cytotoxicity, type, or gene expression) or for measurement of Mg^{2+} concentration.
3- *Peri-implant tissue (n = 8-9/group/time point):* retrieved for histology or gene expression analysis.
4- *Implant and peri-implant tissue (n = 8/group/time point)*: dissected *en bloc* for histology and for morphological analyses.

6.2.5. Quantitative polymerase chain reaction (qPCR)

qPCR was performed on cells in the different compartments: 1- *Exudate (n = 8-9/group/time point):* cells in the remaining volume after the deduction of samples used to determine cell counts were pelleted by centrifugation (400 × *g*, 5 min) and lysed in RNA preservation medium (RNA Shield, Zymo Research); 2- *Implant surface (n = 8-9/group/time point):* retrieved implants were placed in RNA Shield solution for the lysis of adherent cells. Cell lysates were then frozen (-80°C); and 3- *Soft tissue (n = 8/group/time point):* biopsies using 6 mm-diameter-

punches of experimental sites were homogenized in RNA Shield to an aqueous phase using a TissueLyser instrument (Qiagen GmbH), and frozen (-80°C).

RNA was extracted from the cells in all samples using RNeasy Micro Kit (Qiagen GmbH) following manufacturer's instructions. A pilot study representative of the present experiments allowed to verify RNA quality (Pico 6000 RNA Kit in Bioanalyzer 2100 electrophoresis system, Agilent Technologies) and RNA concentration (Nanophotometer P-36, Implen GmbH) in samples from all three compartments. Reverse transcription into cDNA was carried out using TATAA GrandMaster cDNA Synthesis Kit (TATAA Biocenter AB), following manufacturer's instructions. Predesigned and validated primers were purchased (Integrated DNA Technologies). The panel of genes of interest in all three compartments is provided in Table S6.2. Reference gene screening was performed using a rat reference gene panel (TATAA Biocenter AB) and determined with GeNorm and Normfinder (GenEx software, Multid). The most stable reference gene expression was achieved for GAPDH, which was used for normalization. Normalized relative quantities were calculated using the delta-delta-Cq method.

6.2.6. Histology, immunohistochemistry, and image analysis

Peri-implant tissues with implants dissected *en bloc* (n = 8-9/group/time point) were fixed in formalin, and dehydrated prior to embedding in plastic (LR White; London Resin Company Ltd.) [489], then cut transaxially (EXAKT Apparatebau GmbH & Co). Ground sections, 15-20 µm-thick, were stained with 1% toluidine blue. In addition, samples consisting of soft tissues from wounds without implants (n = 8-9/group/time point) were fixed in formalin, dehydrated and embedded in paraffin. Sections were cut at a thickness of 3-5 µm (Reichert-Jung), deparaffinized in xylene, and stained with hematoxylin and eosin.

Histology, and histomorphometry were blindly performed under an optical microscope (Nikon Eclipse E600, Nikon). Full-slide scans from all sections were acquired with a Plan Apo 20x/0.75 objective using imaging software (NIS-Elements, Nikon) and transferred to image analysis software using identical settings and thresholds applied to all slides.

Images of toluidine blue-stained sections (implant and peri-implant tissues) were transferred to Fiji software [257] to perform the following measurements in a standardized fashion using predefined regions of interest (Figure S6.1c): 1-*The thickness of the peri-implant fibrous capsule* was defined in each section at 16 equally distanced locations on the superficial side (implant surface facing panniculus carnosus muscle; 5 locations), on the deep side (implant surface facing the body interior; 5 locations), and on both lateral sides (3 locations for each

lateral side); 2-*Vessels in the fibrous capsule* were identified, and their number, lumen area and distance to the tissue/implant interface were measured on the superficial, deep and lateral sides of the implant as previously described [490]; 3-*Mast cells* were identified in the fascia underneath the panniculus carnosus on the superficial, deep, and lateral sides of the implants. The mast cell number was measured; 4-*Gas voids* were counted in the fascia underneath the panniculus carnosus at the superficial, deep, and lateral sides of Mg implants. The area of each void was measured.

To count total cells in tissues, full-slide images of hematoxylin and eosin-stained sections (tissues without implants or sham tissues) were imported into QuPath software (v0.3.2) [491]. Semi-automated cell counting, based upon the detection of hematoxylin-stained nuclei, was performed in regions of interest (ROIs) defined as the total tissue area underneath the panniculus carnosus and as the peri-implant fibrous capsule (Figure S6.1d). In addition, sections from the dorsum subcutis in unwounded animals were used as baseline controls to measure, in the subcutaneous fascia, the baseline total cellularity (in the respective ROIs of hematoxylin and eosin-stained slides; n = 6).

For immunohistochemistry, tissue sections (n = 5-6, at 3 d and 28 d in Mg and Ti-implanted sites) were deparaffinized, rehydrated, washed in PBS, incubated for 20 min at 90°C in water bath for antigen retrieval, prior to blocking with 5% goat serum in PBS for 30 min. Sections were then incubated with one of the following primary rabbit polyclonal antibodies: anti-rat iNOS (dilution:1:100; PA1036, ThermoFisher), anti-rat CD68 (dilution:1:3000; PA581594, ThermoFisher), anti-rat MRC1 (dilution:1:30; PA5101657, ThermoFisher), or anti-rat ARG1 (dilution:1:300; PA529645, ThermoFisher) for 2 h at room temperature. Immunoreactivity detection in all sections was obtained using horseradish peroxidase detection system (Pierce Horseradish PeroxidasE, ThermoFisher) with DAB (Metal Enhanced DAB Substrate Kit, ThermoFisher) as substrate following the manufacturer's instructions. Negative control sections were prepared following the same protocol but without the primary antibody (Figure S6.1e).

To quantify iNOS-, CD68-, MRC1-, and ARG1-positive cells, full-slide images of immunohistochemically stained sections were transferred to QuPath software (v0.3.2). In an ROI (Figure S6.1f) encompassing the peri-implant tissues within a distance of 200 µm from the interface with the implant, cells were counted using the automated 'positive cells detections' plugin (Figure S6.1g). The proportion of positive cells was measured in an average of ~10 000 cells/ROI in each section.

6.2.7. Surface characterization of the retrieved implant

Mg and Ti implants retrieved without tissues were observed using SE-SEM. Ti implants (n = 2/time point) were fixed in formalin (2 h) and stained with 1% OsO_4 (2 h). Mg implants (n = 2/time point) were fixed in 70% methanol (6 min at -20°C) to prevent inadvertent degradation. The Ti and Mg implants were then dehydrated in a graded ethanol series (70, 80, 90, 95, and 100% ethanol), allowed to air-dry overnight, and sputter-coated with Au. For chemical analysis of Mg degradation layer using EDX, retrieved Mg implants (n = 3/time point) were fixed in 100% ethanol and allowed to air-dry overnight. On each implant surface, 12 ± 3 randomly selected spots were measured. Complementary chemical analysis of Mg degradation layer (n = 1 implant/time point) with X-ray photoelectron spectroscopy (XPS) was conducted on a Thermo Electron™ Microlab 350™ spectrometer using a twin anode source (AlKα and MgKα) operated at 15 kV and an emission current intensity of 20 mA. All peaks were calibrated to the C1s peak binding energy at 285.0 eV.

6.2.8. Cross-sectional characterization of retrieved Mg implants

Cross-sections of halved specimens of implants with tissues in plastic (n = 5-6/group/time point) were polished up to 4000 grit SiC grinding paper, followed by ion milling (Hitachi, IM-4000). SEM and EDX analyses of selected regions of cross-sections were performed to analyze the degradation layer. BSE-SEM images were segmented using the WEKA plugin in ImageJ [492] for calculation of degradation layer thickness at three random locations per sample.

6.2.9. Cell number and cell viability assays

The number of cells adherent to the implant (n = 6-7/group/time point) or in the exudate (n = 8-9/group/time point), that were retrieved from animals, was measured using the NucleoCounter® system (ChemoMetec). To count cells adherent to the implants, the retrieved implants were immediately immersed in lysis buffer (100 µL, Reagent A100, ChemoMetec) in a 96-well plate and shaken for 2 min at 500 RPM to detach the cells from the implant surface. Implants were then removed from the lysate before adding the stabilization buffer (100 µL, Reagent B, ChemoMetec). The cell sample was then loaded in a NucleoCassette™ containing propidium iodide that stains nuclei for automatic counting of total cells. To count cells in exudate, an exudate fraction was directly loaded in NucleoCassette™ for dead cell quantification. An additional exudate faction was diluted 1:1:1 with lysis buffer and stabilization buffer and drawn into NucleoCassette™ as described above, to count total cells.

6.2.10. Cytotoxicity assay

Cytotoxicity was determined by analyzing the lactate dehydrogenase (LDH) content in supernatants that were centrifuged (400 × g, 5 min) from dedicated exudate volumes (125 µL; n = 8-9/group/time point) retrieved from animals. Spectrophotometric measurement of lactic acid due to LDH-mediated conversion of pyruvic acid was performed (C-laboratory, Sahlgrenska University Hospital, Gothenburg).

6.2.11. Cell type determination

The cell types in the exudate (100 µL; n = 8-9/group/time point) collected from animals were characterized by applying approximately 50,000 cells to a microscopic slide using cytospin centrifugation. Cells were stained with May-Grünewald-Giemsa, and the polymorphonuclear and mononuclear cells among at least 200 cells per slide were counted under a light microscope (Nikon Eclipse E600, Nikon).

6.2.12. Enzyme-linked immunosorbent assay

Fractions of exudate supernatants (100 µL; n = 8-9/group/time point) were allocated to enzyme-linked immunosorbent assay (ELISA) kits to quantify the concentrations of proteins iNOS (Abbexa), VEGF (Abcam), and FGF2 (R&D systems). In brief, undiluted samples were incubated with primary antibodies and washed followed by the addition of secondary antibody for immunoreactivity detection using horseradish peroxidase. Absorbance measurement at 450 nm (Omega BMG LUMIstar) allowed the quantification of protein concentrations in supernatants and standards.

6.2.13. Characterization of the magnesium content in exudates

Remaining volumes of exudate (n = 8-9/group/time point) sampled from animals were diluted in 1% Hydrochloric acid (dilution factor ∼1:500) to measure the Mg^{2+} concentration using inductively coupled plasma optical emission spectroscopy (ICP-OES; Agilent 5110 ICP-OES). The analysis was validated against interferences using standard addition, with recovery ranging between 90-110%. Spectral interferences were evaluated by comparing retrieved data at Mg wavelengths of 279.533 and 280.271 and were negligible.

6.2.14. Statistical analysis

Comparisons of independent samples (from different materials, compared with sham wounds, or retrieved at different time points) were performed using unpaired Kruskal-Wallis and Mann-Whitney U tests. Comparisons of paired samples (implanted wounds *vs.* sham wounds) were

performed using Wilcoxon signed-rank test. Spearman correlation and linear regression analyses were used to test statistical associations. Statistical analyses were performed in SPSS (v.27; IBM Corporation). Differences for which $P<0.05$ were considered statistically significant. Spearman correlation was considered statistically significant if $P<0.01$.

6.3. Results

6.3.1. Material characterization

After manufacturing, cleaning, and sterilization, the surface topography (roughness), microstructure, and chemical composition of disc-shaped pure magnesium (Mg) and titanium (Ti) implants were characterized prior to surgical insertion. Observation of the implant surfaces (Figure 6.2a-b; Figure S6.2a) using scanning electron microscopy with a secondary electron detector (SE-SEM) showed a unidirectional horizontal lay pattern at the surface of Mg implants and a circular lay pattern at the surface of Ti implants which was attributable to the manufacturing process.

Confocal laser scanning microscopy (Figure 6.2c-d) revealed that the surface roughness of Mg (0.22 µm ± 0.05 µm) and Ti implants (0.16 µm ± 0.05 µm) was similar. Energy-dispersive X-ray spectroscopy (EDX; Figure 6.2e) demonstrated low levels of oxygen, indicative of a thin superficial oxide film, on Mg implants but not on Ti implants (~99.8% titanium). This oxidation, consistently observed on the surface of Mg implants in this study (Figure S6.2b**)**, is generated by unavoidable exposure to moisture throughout the different steps of Mg implant preparation from manufacturing until storage [493]. In cross-sections of both Mg and Ti implants (Figure 6.2Ff), a hexagonal, closely packed structure with some twin deformation was revealed by scanning electron microscopy with an electron backscattered diffraction (EBSD) detector. Areas with a fine grain size featured a uniform and equiaxed grain shape, while in areas with a large grain size, the grain shape was less uniform (Figure S6.2c). The mean grain size was 16.87 µm for Mg and 2.45 µm for Ti (Figure S6.2d).

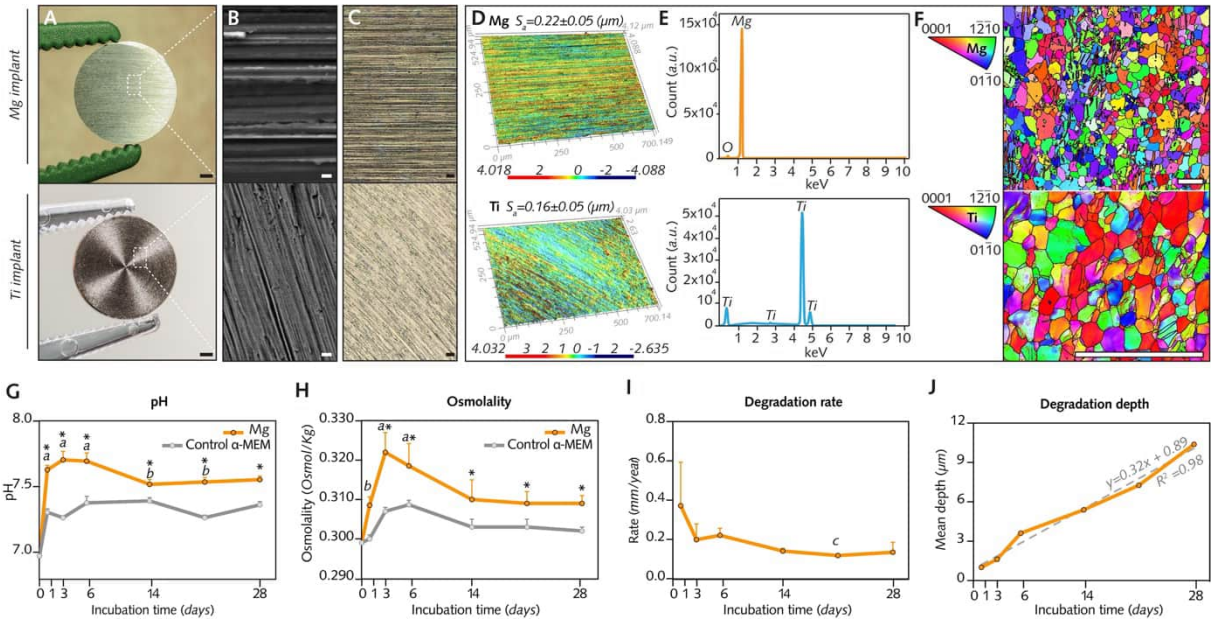

Figure 6.2: Preimplantation characterization and *in vitro* degradation. (**A**)**,** Disc-shaped pure Mg and pure Ti implants after cleaning and sterilization. (**B-C,** Implant surfaces imaged using secondary electron scanning electron microscopy (SE-SEM) and confocal laser-scanning microscopy (CLSM), respectively. (**D**)**,** Representative three-dimensional CLSM images of surface roughness and S_a mean measurements (n = 3 implants/group). (**E**)**,** Chemical composition of implant surfaces analyzed with energy-dispersive X-ray spectroscopy (EDX). (**F**)**,** Electron backscattered diffraction (EBSD) maps of implant cross-sections showing their microstructure. (**G-J**)**,** Degradation of Mg implants *in vitro* was monitored at days 1-28 following immersion in alpha minimum essential medium (α-MEM) supplemented with 10% fetal bovine serum and 1% penicillin/streptomycin (n = 9 implants/time point). Medium was retrieved to measure pH (**G**) and osmolality (**H**), while implants were collected and weighed following treatment with chromic acid to measure the degradation rate (**I**) and degradation depth (**J**). Identical cell culture media without implants served as controls (n = 3/time point). Data are means ± s.e.m.; * P<0.05 Mg media (α-MEM media with Mg implants) *versus* Control α-MEM media (without Mg implants). ***a****: P<0.05 versus* Control α-MEM at day 0; ***b****: P<0.05 versus* Mg media at day 3; ***c****: P<0.05 versus* Mg media at day 1. Unpaired Mann-Whitney *U* test. Scale **A**=1 mm; **B**=5 µm; **C**=50 µm; **F**=100 µm.

6.3.2. In vitro degradation of Mg implants

Mg implants were further characterized by monitoring their degradation *in vitro* from 1 to 28 days after immersion in alpha minimum essential medium (α-MEM) supplemented with 10% fetal bovine serum to simulate *in vivo* milieu [169]. To maintain semistatic immersion conditions [98], the medium was exchanged every 2-3 days. A sharp increase in the pH of the immersion medium (Figure 6.2g) was noted at 1 d and 3 d from a baseline pH of 6.9 before the pH stabilized in the range of 7.6-7.9. In parallel, osmolality records (Figure 6.2h), which indicate the concentration of dissolved particles in the immersion medium, also showed a clear increase at 1 d and 3 d, suggesting the rapid release of degradation products from Mg implants. This was followed by an overall decrease in osmolality up to 28 d, implying precipitation of

these soluble species over time. At all time points, both pH and osmolality remained consistently higher in media with Mg implants than in control media without implants.

Consistent with the changes in pH and osmolality over time, the degradation rate (Figure 6.2i), determined by estimating the degradation depth from the weight difference of Mg implants relative to baseline, was the highest at 1 d and then decreased until 28 d. The estimation of the mean degradation depth over time from weight records of Mg implants indicated a linear degradation rate of ~0.32 µm/day (Figure 6.2j).

6.3.3. Mg implants promote initial inflammation and attenuate subsequent fibrotic encapsulation

In dedicated groups of Sprague Dawley rats, Mg implants or Ti implants were implanted in the dorsum subcutis (Figure S6.1a). Pockets were surgically created by separating the panniculus carnosus muscle from the fat overlying the dorsal skeletal muscle (Figure S6.1b). In accordance with a predetermined randomization scheme (Figure 6.1b), each pocket either received an implant (Mg- or Ti-implanted sites) or was left without an implant (sham sites: Sham Mg or Sham Ti). Because the host response to biomaterials in this animal model typically engages an initial inflammation during the first post-operatory week followed by implant encapsulation [494], wounds were monitored from days 1 to 28 after surgery (Figure 6.3a).

Up to postoperative day 6, (Figure 6.3b) erythema and congestion, identified through dilation of the vascular arborescence in the tissue walls, remained visible in all wounded sites, particularly in those receiving Ti or Mg implants. Afterward (at 14 d and 28 d), these inflammatory signs dissipated, and tissues surrounding both implant types featured a cicatricial fibrous wall with a visible vasculature framework in close contact with the implant surface. Around Mg implants, multiple cavities, presumably related to gas evolution from Mg degradation as previously reported [451,495], were visible in the peri-implant tissue wall up to 6 d, but these cavities progressively decreased in number at 14 d and 28 d.

To further study the inflammatory response and the fibrotic encapsulation around both biomaterials, wounded tissues excised with or without associated implants were processed for histology by staining for hematoxylin and eosin (to study cellularity) and toluidine blue (to study the extracellular matrix (ECM)) (Figure 6.3c-e; Figure S6.3a-b). In agreement with the macroscopic observations, the initial response in tissues receiving Ti or Mg implants was marked by profuse cellular infiltration with vessel engorgement (Figure 6.3e). The cellular infiltrate measured in the loose connective tissue around Mg implants was consistently denser than that in the tissue around Ti and sham sites from 1 d to 14 d (Figure 6.3f). To verify the superior inflammation in tissues that received Mg implants, changes in gene levels of

inflammatory markers were monitored in punches from the tissue walls around both implant types and in sham sites (Figure 6.3g; Figure S.4). Between 1d and 6d, the qPCR analysis demonstrated in tissues around Mg implants a higher expression of pro-inflammatory genes (Inducible nitric oxide synthase, *iNos*; Tumor necrosis factor, *Tnf*; Toll-like receptor 2, *Tlr2*; and Toll-like receptor 4, *Tlr4*) and chemotaxis-related genes (Interleukin-8, *Il8*; and Monocyte chemoattractant protein-1, *Mcp1*) than in tissues around Ti implants, before decreasing afterward (Figure 6.3g; Figure S6.4). This difference in mRNA levels was in line with the amplified cellular infiltration in tissues around Mg implants, thus confirming that the initial response to Mg implants involved the heightened activation of proinflammatory pathways.

Because modulation of inflammation is known to influence the subsequent tissue repair around biomaterials [496], we sought to characterize the effects of Mg implant on the fibrosis of adjacent tissues. Fibrotic encapsulation of the implants, histologically identified through the presence of abundant collagenous ECM and a cell-rich infiltrate with giant cells at the implant interface [497], was evident as early as 6 d after surgery around both biomaterials (Figure 6.3e). To monitor the maturation of the fibrotic capsule over time, we quantified the cross-section thickness of peri-implant capsules (Figure 6.3h-i). The capsule thickness increased from 6 d to 28 d in both groups but remained consistently thinner over time around Mg implants than around Ti implants. Concomitantly, the cell density in peri-implant capsules was invariably higher in Mg group than Ti group (Figure 6.3j).

Mast cells are important actors in mediating the fibrotic reaction around implants by accumulating in adjacent tissues [498]. Thus, toluidine blue (purple)-positive mast cells (Figure S6.3b) were counted in sections of the loose connective tissue around Mg and Ti implants (Figure 6.3k). The number of mast cells around Mg implants was less than around Ti implants, with a significant difference at 6 d and 14 d, in line with the attenuated fibrotic encapsulation around Mg implants.

The organization of the neovascular bed at the implant interface holds a pivotal role in the healing of peri-implant tissues [499], and was therefore histomorphometrically compared between biomaterials. In comparison to Ti implants, a higher density of blood vessels was detected around Mg implants at 6 d (Figure 6.3l), with the vessels possessing a greater luminal area at 6 d and 28 d (Figure S6.3c) and exhibiting a smaller distance to the interface at 28 d (Figure 6.2l). These differences suggested an increased vascularity around Mg implants than Ti implants.

The presence of gas voids (Figure 6.3d; Figure S6.3a) was another morphological feature distinct to soft tissues around Mg implants. The number and the fractional area of these voids

(Figure 6.3m) culminated at 1 d and at 3 d, respectively, before decreasing afterward (at 14 d and 28 d).

Taken together, the inflammatory tissue environment around Mg implants, when compared to that around Ti implants, was concomitant with an elevated accumulation of gas in soft tissues and the development of a denser vascular network and reduced fibrotic encapsulation.

6.3.4. The degradation of Mg implants gradually elicits the enrichment of calcium and phosphorus on their surfaces

With the assumption that the degradation of Mg implants elicits a dissimilar response of soft tissue in comparison to Ti implants, we sought to characterize the degradation-induced changes of Mg implants that were excised without associated tissues from days 1 to 28 (Figure 6.4a-b). Observations of the surface of Mg implants with SE-SEM (Figure 6.4c) revealed areas with a high density of cells embedded in a three-dimensional complex ECM from 1 d to 6 d, in contrast to reduced numbers of cells and extracellular deposits at 14 d and 28 d. These morphological alterations were concomitant with changes in the chemical composition of the surface of Mg implants over time, as evidenced by measurements of the relative intensities of magnesium, oxygen, calcium, and phosphorous using EDX (Figure 6.4d). From days 1 to 28, the level of magnesium, the main element detected prior to surgery (Figure 6.4c, Figure S6.2b), decreased by 46%, while the level of oxygen showed a two-fold increase. This oxidation of the Mg implant surface occurred simultaneously with a distinct increase in calcium and phosphorous by 19% and 9%, respectively; these elements accounted for ~50% of the surface chemical composition between 6 d and 28 d. X-ray photoelectron spectroscopy (XPS; Figure S6.5a) confirmed the presence of the above-described elements together with nitrogen, which was steadily detected from 1 d to 28 d.

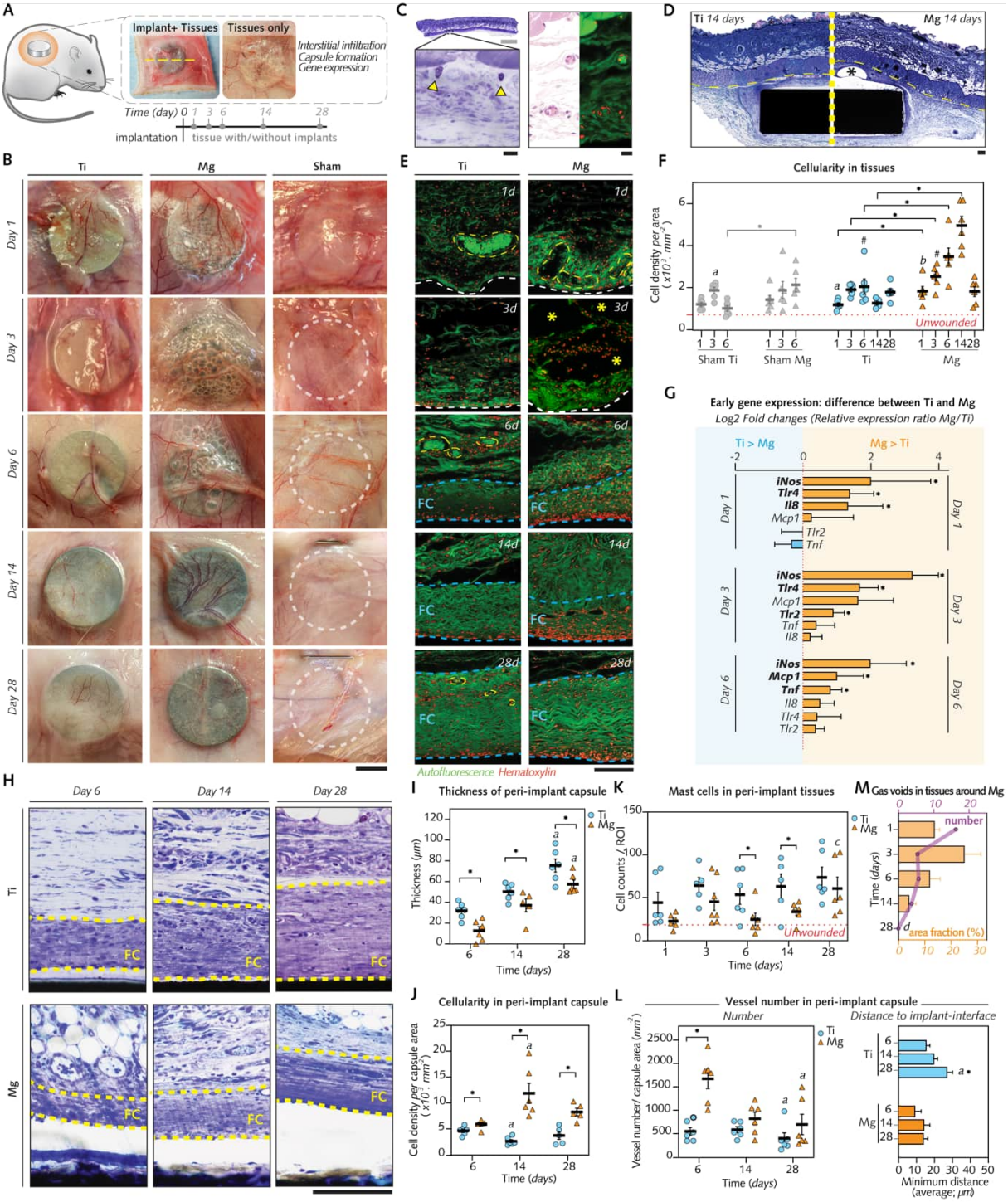

Figure 6.3. Mg implants promote early inflammation and angiogenesis but not fibrosis in tissues. **(A),** Wounded tissues retrieved after 1-28 d for histology/histomorphometry (n = 5-6/group/time-point; *line*: section orientation) and qPCR analysis (n = 5-8/group/time-point). **(B)**, Gross healing at re-entry of implanted and sham wounds (*line*). **(C),** Unwounded tissue histology featuring subcutaneous fascia underneath dorsal muscle (*left*: toluidine blue (TB) staining, *arrows*: mast cells; *right*: hematoxylin and eosin staining with autofluorescence micrograph, *red*: cells, *green*: extracellular matrix and vessels). **(D),** TB-stained sections of 14 d-implants with subcutaneous fascia and muscle (*line-separated*). Asterisk: gas void. **(E),** Autofluorescence micrographs of 1-28 d-interfacial tissues (*white*) showing: hematoxylin-detected cells, blood vessels (*yellow*), and fibrous capsule (FC; *blue*). Asterisk: 3 d-gas voids in tissues interfacing with Mg implant **(F),** Cellular density in fascia (unwounded tissues: n = 6). **(G),** Tissue gene expression after 1-6 d (log2 relative gene expression ratio Mg/Ti). **(H),** Micrographs of 6-28 d-fibrous capsule (FC). **(I-M),** Capsule histomorphometry:

thickness (**I**), cellular density (**J**), and vessel density and distance to implant-interface (**L**); mast cell density in fascia (**K**); Gas void number and relative area in Mg-implanted tissues (**M**). Data are means ± s.e.m.; * $P<0.05$ Mg *versus* Ti or Sham Mg *versus* Sham Ti; # $P<0.05$ Mg or Ti *versus* respective sham; ***a**: $P<0.05$ *versus* day 6; ***b**: $P<0.05$ *versus* day 14; ***c**: $P<0.05$ *versus* days 1 and 6; ***d***: $P<0.05$ *versus* day 3 (area). Unpaired Mann-Whitney *U* test or paired Wilcoxon signed-rank test. Scale **B**=4 mm; **C**: *gray*=500 µm; *black*=10 µm; **D**=200 µm; **E, H**=50 µm.

Observations of cross-sections with scanning electron microscopy using a backscattered electron detector (BS-SEM) revealed a superficial film consisting of degradation products at the interface with the metal bulk that increased in thickness from days 1 to 28 (Figure 6.4e). The thickness of this degradation layer steadily increased from 1.5 µm at 1 d to 13.6 µm at 28 d (Figure 6.4f). Simultaneously, the chemical composition of the degradation layer also changed over time, as revealed by EDX-elemental mapping (Figure 6.4e). In line with the results of Mg implant surface analysis, the incorporation of calcium and phosphorous in the degradation layer was visible as early as after 1 d. However, the preferential accumulation of calcium and phosphorous in the outer regions was clear starting from day 6 (Figure 6.4e; Figure S6.5a). These elements combined with oxygen, which was evenly distributed over the degradation layer cross-sections, resulting in an evident outer calcium-, phosphorus-, and oxygen-rich layer at 14 d and 28 d. In contrast, the inner regions of the degradation layer exhibited higher magnesium and oxygen contents at the expense of decreased calcium and phosphorous contents at 14 d and 28 d (Figure 6.4e; Figure S6.5a).

Together with the slower thickening after 14 d (Figure 6.4f), these findings demonstrate that the maturation of the degradation layer at the surface of Mg implants occurs simultaneously with changes in the topographical distribution of the chemical elements, whereby calcium and phosphorous are more concentrated at the tissue interface.

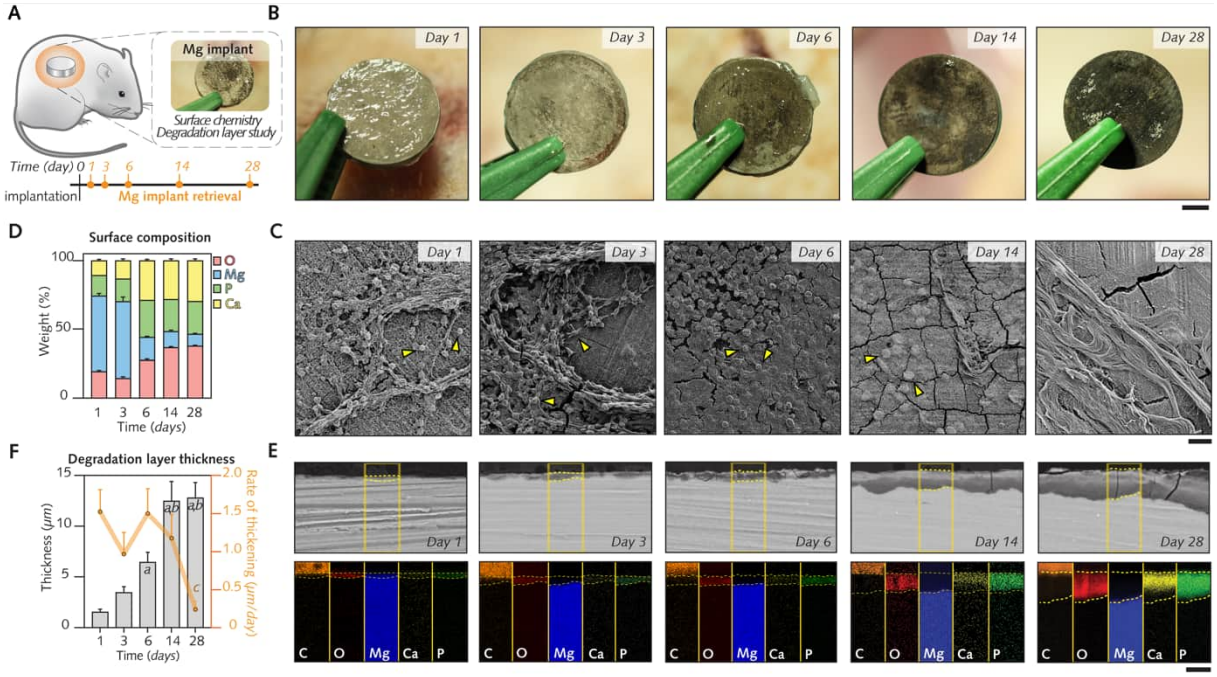

Figure 6.4. Interface magnified: Chemical fingerprint at the surface of Mg implants is altered over time by degradation. **(A),** Mg implants carefully retrieved from subcutaneous pockets for characterization of their surfaces. **(B),** Macroscopic observation of the Mg surface immediately following explantation after 1-28 d. **(C),** Scanning electron microscopy (SEM) images with a secondary electron detector showing the Mg surface with implant-adherent cells (*arrowheads*) and extracellular matrix. **(D),** Time survey of Mg surface chemical composition (Mg, O, Ca and P) using energy-dispersive X-ray spectroscopy (n = 3/time-point). **(E),** Top: Cross-sections of the degradation layer at the Mg surface observed with SEM using a backscattered electron detector (implant and tissues embedded in plastic). *Yellow dotted line*: degradation layer; bottom: Maps of Mg, O, C, Ca and P in the highlighted areas in **E** (C is generated from embedding medium). **(F),** Changes over time in degradation layer thickness and in the rate of thickening per day (n = 5-6/time-point).
Data are means ± s.e.m.; ***a****: P*<0.05 *versus* days 1 and 3; ***b****: P*<0.05 *versus* day 6. Unpaired Mann-Whitney *U* test. Scale **B**=2 mm; **C**=20 µm; **E**=10 µm.

6.3.5. Alteration of the Mg implant surface occurs with concomitant regulation of the number of implant-adherent cells and gene expression in these cells

The surface properties of implants are a pivotal factor that influences the host response [500]. The cells adherent to the implant surface, which have undergone migration, maturation and adhesion, directly sense these properties to mediate changes of their number, and of their gene expression [487,501].

We therefore harvested the implant-adherent cells to determine whether their counts and their mRNA levels are influenced by the degradation-induced changes on the surface of Mg implants in comparison to Ti implants from days to 1 to 28 (Figure 6.5a). While cytometry-counted cells (Figure 6.5b) on Ti implant surface remained comparable at all time points, the number of Mg implant-adherent cells sharply increased from 1 d to culminate at 6 d (~5-fold higher than cell number at the surface of Ti implants), thereafter decreasing toward 14 d and 28 d. These quantitative

differences were in agreement with morphological observations (Figure S6.6) showing, from 1 d to 6 d, the ECM- and cell-rich surface of Mg implants, in contrast with the inconsistent cellular presence and small amounts of extracellular material at the surface of Ti implants.

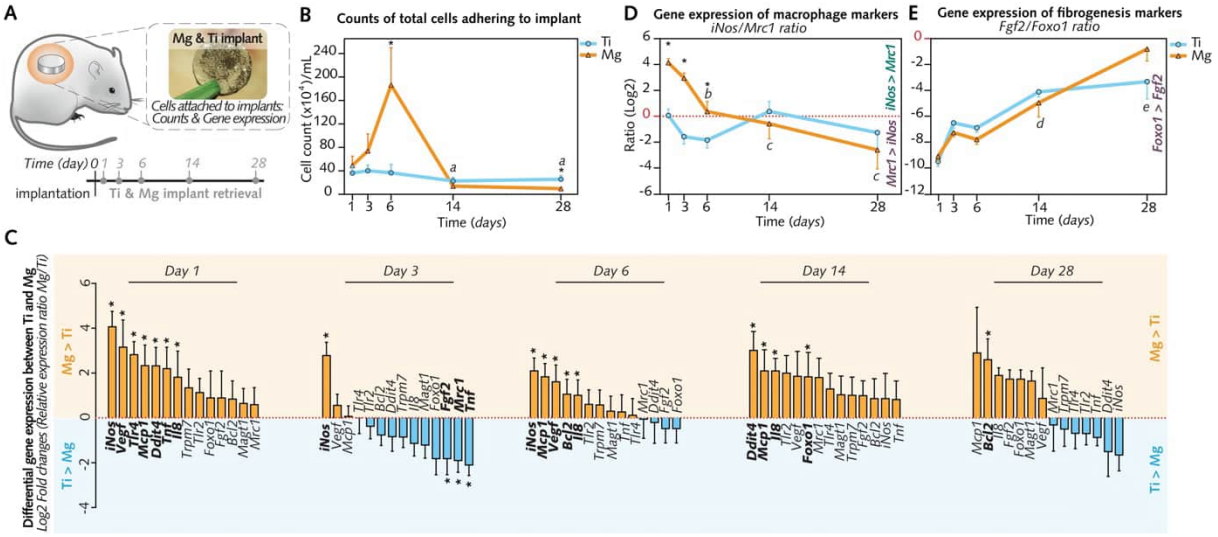

Figure 6.5: Interface magnified: Cells adherent to the implant surfaces, their enumeration and gene expression. (**A**)**,** Ti and Mg implants were collected from subcutaneous pockets to count cells adherent to their surface and to analyze their gene expression. (**B**)**,** Counts of total implant-adherent cells (n = 6-7/group/time-point). (**C**)**,** Differential gene expression between Mg and Ti (log2 of the relative gene expression ratio Mg/Ti; n = 8/group/time-point). (**D-E**)**,** Changes over time of the gene expression ratios: *iNos* (M1-macrophage marker) to *Mrc1* (M2-macrophage marker) (**D**), and *Fgf2* (fibrogenesis marker) to *Foxo1* (antifibrotic marker) (**E**). Log2 of relative gene expression ratios are shown (n = 8/group/time-point).
Data are means ± s.e.m.; * $P<0.05$ Mg *versus* Ti; ***a****: $P<0.05$ versus* days 1, 3, and 6 in Mg; ***b****: $P<0.05$ versus* day 1 in Mg; ***c:*** *$P<0.05$ versus* days 1 and 3 in Mg. ***d:*** $P<0.05$ *versus* day 1 in Mg and Ti. ***e:*** $P<0.05$ *versus* days 1 and 6 d in Mg and Ti. Unpaired Mann-Whitney *U* test.

qPCR analysis of implant-adherent cells was conducted using a panel of 14 genes of interest (Table S6.2) that mark for major events of the wound healing such as *Tnf*, *Il8*, *Mcp1, Tlr4* and *Tlr2* for inflammation, *iNos* (proinflammatory macrophages) and *Mrc1* (prohealing macrophages) for macrophage polarization, *Vegf* for angiogenesis, *Fgf2* for fibrogenesis, and *Foxo1* as an antifibrotic marker. Pro-apoptotic gene *Ddit4* and anti-apoptotic gene *Bcl2* were also included to explore cell death pathways, in addition to Mg^{2+} channel genes *Trpm7* and *Magt1,* suggested to be involved in the cellular response to Mg-based biomaterials [502].

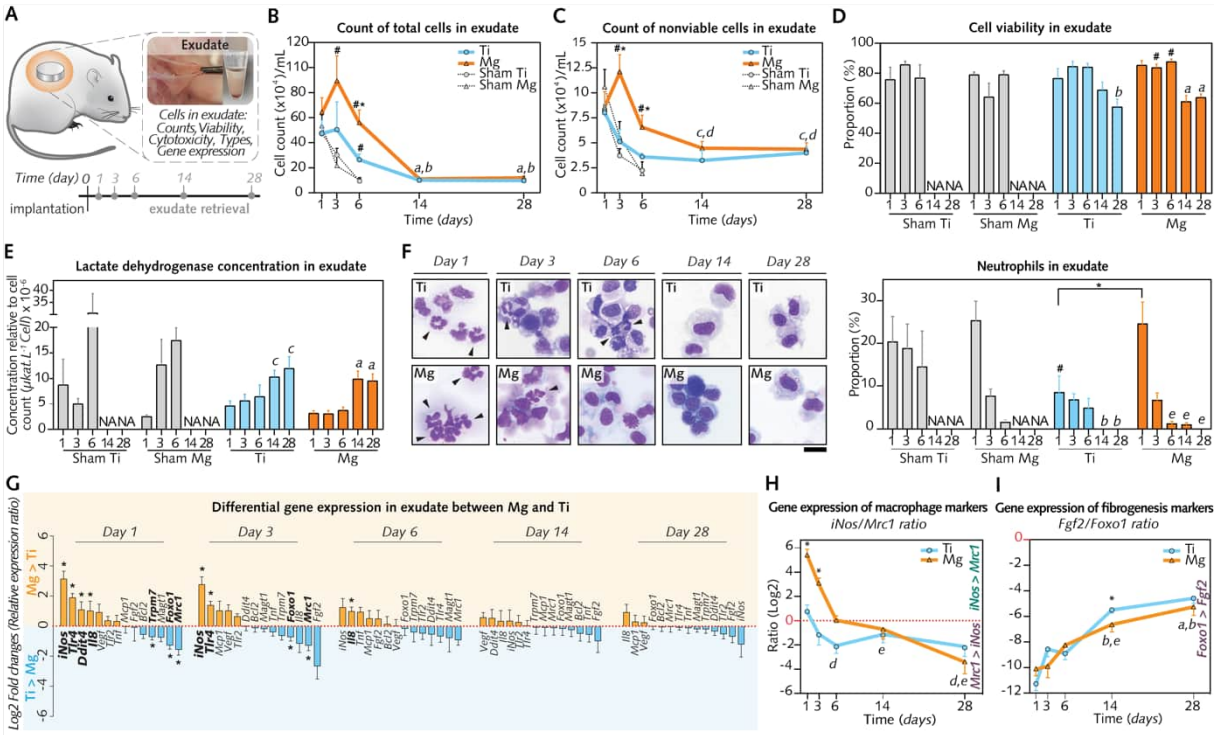

Figure 6.6: Interface magnified: Cells in the peri-implant exudate, their enumeration, types, viability and gene expression. (**A**)**,** The exudate was assigned to analyses of cells and their gene expression (n = 8/group/time-point). (**B**)**,** Counts of total cells. (**C**), Counts of nonviable cells. (**D**)**,** Proportions of viable cells. (**E**)**,** Relative cytotoxicity in exudate. (**F**)**,** Proportions of neutrophils (right; n = 5-7/group/time-point) and representative micrographs from cytospin preparations (left; *arrowheads:* neutrophils). (**G**)**,** Differential gene expression between Mg and Ti. (log2 of the relative gene expression ratio Mg/Ti; n = 8/group/time-point). (**H-I**)**,** Changes over time of the gene expression ratios: *iNos* (M1-macrophage marker) to *Mrc1* (M2-macrophage marker) (**H**), and *Fgf2* (fibrogenesis marker) to *Foxo1* (antifibrotic marker) (**I**). Log2 of relative gene expression ratios are shown (n = 8/group/time-point). Data are means ± s.e.m.; NA: Not analyzed. Exudates were not collected from Sham Ti and Sham Mg at days 14 and 28 (wounds were closed). * P<0.05 Mg *versus* Ti; # P<0.05 Mg or Ti versus respective sham; **a**: P<0.05 *versus* days 1, 3, and 6 in Mg; **b**: P<0.05 versus days 1, 3, and 6 in Ti; **c**: P<0.05 *versus* day 3 in Mg; **d**: P<0.05 *versus* day 1 in Ti; **e**: P<0.05 *versus* days 1 and 3 in Mg. Unpaired Mann-Whitney U test or paired Wilcoxon signed-rank test. Scale **F**=20 µm.

Between 1 d to 6 d, inflammatory signature genes (*iNos, Tnf*, *Il8*, *Mcp1* and *Tlr4*) remained highly expressed by cells adherent to Mg implants in comparison to cells adherent to Ti implants (Figure 6.5c; Figure S6.7), which is in agreement with the pronounced migration of cells to the Mg implant surface. For some chemotaxis genes (i.e., *Mcp1*, *Il8*), this upregulation of mRNA levels at the surface of Mg implants extended to 14 d. Cells adherent to Mg implants also featured a higher expression of *Vegf* up to 6 d in comparison to cells adherent to Ti implant surface (Figure 6.5c; Figure S6.7), in support of the superior vascular supply of the peri-implant fibrous capsule around Mg implants in comparison to Ti implants (Figure 6.3l; Figure S6.3c). Other genes that were upregulated on the surface of Mg implants in comparison to Ti implant

surface consisted of *Ddit4* (at 1d and 14 d) and *Bcl2* (at 6 d and 28 d) (Figure 6.5c; Figure S6.7), suggesting that the gene regulation of apoptotic pathways in Mg implant-adherent cells followed a sequence early proapoptosis–late antiapoptosis. Fibrosis-related genes also featured differences between Mg and Ti implants: antifibrotic marker *Foxo1* was upregulated at 14 d at the surface of Mg implants, whereas profibrotic marker *Fgf2* featured a superior expression at Ti implants as early as 3 d; however, the ratio *Fgf2* / *Foxo1* was not different between both biomaterials. Further supporting the early gene activation of fibrosis at the surface of Ti implants was the elevated expression of prohealing macrophage gene *Mrc1* at 3 d along with the ratio *iNos* / *Mrc1* (Figure 6.5d), that was shifted toward *Mrc1* gene from days 1 to 28. In contrast, *iNos* / *Mrc1* ratio for cells adherent to Mg implants was consistently shifted toward *iNos* gene between 1 d and 6 d, before decreasing and switching to a pattern similar to that of cells adherent at Ti implants (that is shifted toward *Mrc1* gene) at 14 d and 28 d. These trends indicated a differential gene regulation of macrophage polarization before and after 6 d in cells adherent to Mg implant but not Ti implants. No differences between Mg and Ti implants were observed for gene markers of Mg^{2+} channels *Trmp-7* and *Magt1* (Figure S6.7).

In summary, cytometry and qPCR findings suggested that the surface of Mg implants attracted higher number of cells and promoted the expression of inflammatory and neoangiogenesis genes between 1 d and 6 d in comparison to cells adherent to Ti implants. Afterward, the degradation-induced changes of Mg implants surface were accompanied by a reduced cellular migration and a downregulation of inflammatory genes together with an increased expression of antifibrotic gene *Foxo1*.

6.3.6. The inflammation in the exudate around Mg implants is amplified but transient and does not alter the cell viability

Having evidenced a pronounced proinflammatory response in cells directly adhering on the surface of Mg implants in comparison to Ti implants, we next turned to the adjacent exudate compartment and asked whether Mg implant degradation generates a cytotoxic effect. Cell death is pivotal to the initiation of the immune response to wear metallic particles and ions leading to peri-implant soft tissue damage [479,503]. Thus, we characterized the contents of the exudate surrounding both implant types, which was obtained by the lavage of the pockets (Figure 6.6a).

The total number of cells (Figure 6.6b) and nonviable cells (Figure 6.6c) were counted using cytometry in exudate samples to calculate the proportion of viable cells (Figure 6.6d). The total counts of cells (Figure 6.6b) in the exudate around Mg implants increased from 1 d to peak at 3 d before steadily decreasing until day 28. In comparison to the exudate around Ti implants

or in Sham Mg, a higher number of cells was detected in the exudate around Mg implants between 1 d and 6 d, in line with the counts of implant-adherent cells (Figure 6.6b). These changes over time in total cell counts were very similar to nonviable cell counts (Figure 6.6c) in exudate samples around both implant types from days 1 to 28. However, despite the increased number of nonviable cells around Mg implant, cell viability fractions in exudate around both biomaterials were comparable (Figure 6.6d). In exudate around Mg and Ti implants, the viable cell fraction ranged between 76% and 87% from 1 d to 6 d before decreasing at 14 d and 28 d to a range 69%-57%. To verify these cell viability results, the cytotoxicity in the same exudate specimens was also determined by measuring the concentrations of lactate dehydrogenase (LDH), an enzyme released from cells upon damage of their membrane [504]. Relative LDH concentration (Figure 6.6e) was similar from days 1 to 6 in exudate around Mg or Ti implants, before increasing at 14 d and 28 d without difference between the biomaterials. The agreement between cytotoxicity and cell viability findings was further confirmed by their significant association (Figure S6.8a), strengthening the conclusion that Mg implants did not preclude the viability of cells recruited to the interface.

Beyond their function as the first line of cells of innate immunity, prolonged recruitment of neutrophils is linked with a sustained inflammation in response to wear particles and ions from metallic implants [479]. Having observed an elevated expression of chemotaxis *Il8* at the surface of Mg implants, we visualized cell types recruited to the wounded sites using cytospin histological preparations from the exudate samples. While mononuclear cells predominated in both groups and at all time points (Figure 6.6f; Figure S6.8b), higher neutrophil counts were detected around Mg implants than around Ti implants at 1 d; though, neutrophils did not exceed 30% of the total cells. Noticeably, after 1 d, the fraction of neutrophils around Mg implants substantially decreased to levels comparable over time with those around Ti implants (Figure 6.6f).

mRNA levels of cells collected in exudate specimens (Figure 6.6g; Figure S6.9) were also measured using the same gene panel as for the implant-adherent cells (Table S6.2). Differences between biomaterials were observed only from days 1 to 6. On the one hand, cells in exudate around Mg implants featured the upregulation of only few inflammatory and chemotaxis genes in comparison to that around Ti implants: *Tlr4*, *Il8,* and most noticeably *iNos* (Figure 6.6g); overall, the elevated expression of the inflammatory signature genes at the interface with Mg implants was less evident in exudate cells than in implant-adherent cells (Figure 6.5c). Of note, *iNos* consistently featured at 1 d, at 3 d, and occasionally at 6 d, the highest difference between Mg and Ti implants at the 3 compartments: implant surface (Figure 6.5c), exudate (Figure

6.6g), and soft tissues proper (Figure 6.3g). Exudate around Mg implants also displayed an upregulation at 1 d of pro-apoptotic gene *Ddit4* in comparison to exudate around Ti implants. However, this expression difference between biomaterials was discrete compared to that for implant-adherent cells, and partially confirm the cell viability and cytotoxicity findings. On the other hand, cells in exudate around Ti implants featured a higher expression of *Trpm7* at 1 d in comparison to that around Mg implants, indicating a differential gene regulation of this Mg^{2+} channel. *Foxo1* and *Mrc1* gene expression were also higher in exudate around Ti implants than that around Mg implants at 1 d and 3 d. The first gene suggested a prompt antifibrotic modulation in exudate around Ti implants. The second gene reflected the early activation of prohealing macrophage in exudate around Ti implants as observed for implant-adherent cells. Most notably, the ratio *iNos* / *Mrc1* (Figure 6.6h) for both biomaterials featured kinetics very similar for exudate cells to that for implant-adherent cells, with an evident shift toward *iNos* from days 1 to 6 in exudate around Mg implants. *Fgf2* / *Foxo1* ratio (Figure 6.6i) was smaller at 14 d in exudate around Mg implants, confirming the 14 d- antifibrotic gene activation as observed for cells adherent to Mg implants.

To determine the expression of selected proteins, the concentrations of iNOS, VEGF, and FGF2 were measured in exudate supernatants at 3 d, 14 d and 28 d (Figure 6.7a).

While no differences existed between biomaterials in VEGF and FGF2 exudate concentrations, iNOS concentration was considerably higher at 3 d in exudate around Mg implants compared with Ti implants. Further supporting the major role of proinflammatory macrophages at 3 d in response to Mg implants, immunohistochemistry of peri-implant tissues (Figure 6.7b; Figure 6.7c) demonstrated a 3-fold and an 8-fold higher detection of cells with markers of macrophage subtype M1 iNOS and CD68, respectively, at the interface with Mg implants in comparison to Ti implants at 3 d. No differences between biomaterials were found at 3 d and 28 d in the detection of cells positive for MRC1 and Arginase-1 (ARG1) that mark for the macrophage subtype M2.

In conclusion, between days 1 and 6, vigorous cell recruitment, including neutrophils, and upregulation of inflammatory pathways, particularly through elevated gene levels and protein secretion of iNOS, were evident in the exudate and peri-implant tissue around Mg implants in comparison to that around Ti implants. However, Mg implants did not exert cytotoxic effects, and the amplified inflammation around these implants markedly subsided at 14 d and 28 d.

6.3.7. The temporal changes of Mg implant degradation modulate markers of early inflammation and subsequent tissue repair

To examine the relationship between the changes over time of Mg implant degradation and that of the cellular and molecular response, we monitored Mg^{2+} levels in the same exudate samples used to characterize the cell count, cell viability, cytotoxicity, and gene expression levels (Figure 6.8a).

First, Mg^{2+} concentration (Figure 6.8b) was measured with inductively coupled plasma optical emission spectroscopy (ICP-OES). The mean concentration in the exudate around Mg implants peaked at 3 d, was 1.7- and 2.5-fold higher than that around Ti implants at 1 d and 3 d, respectively, and was 1.8- to 3.4-fold higher than that around Sham Mg from days 1 to 6. Thereafter, this concentration in exudate around Mg implants markedly decreased until 14 d and 28 d. Noting that this pattern between days 1 and 28 of Mg^{2+} concentration was in line with that of total cell counts in exudate around Mg implants (Figure 6.6b), a regression analysis (Figure 6.8c) was performed to verify the relationship between the variables. We found a positive association [at early time points when the Mg^{2+} concentration was higher (i.e., 1 d, 3 d, and 6 d) (Figure 6.8c, *left*) as well as when data from all time points were pooled (Figure 6.8c, *right*), validating that the cell counts were linked to the Mg^{2+} concentrations in exudate around Mg implants, but not around Ti implants or in sham wounds (Figure S6.10a).

Furthermore, we questioned if a similar relationship existed in exudate around Mg implants between Mg^{2+} levels and cell viability (Figure 6.8d) or cytotoxicity (Figure 6.8e).

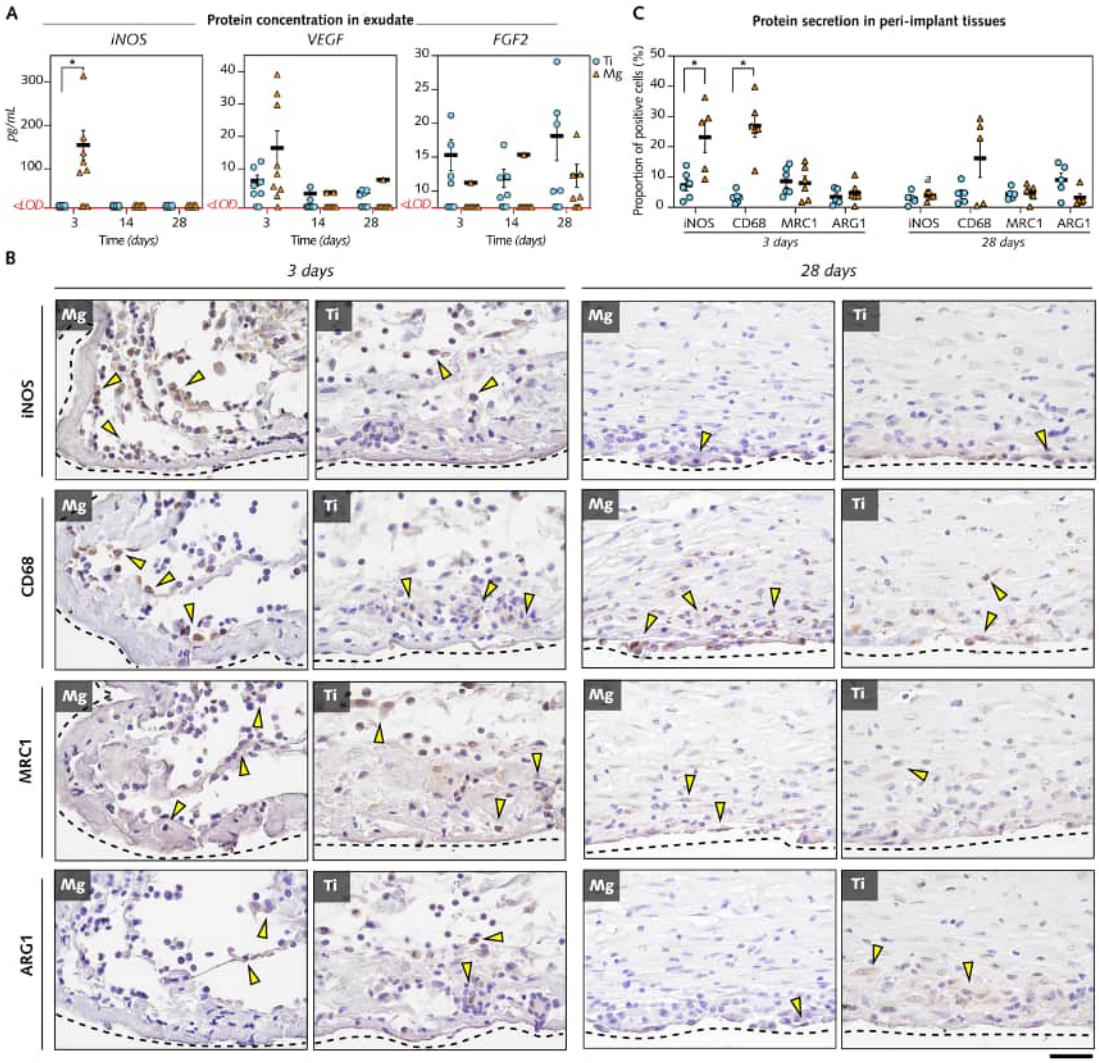

Figure 6.7: Interface magnified: Detection of protein secretion in exudates and immunoreactive cells in peri-implant tissues in response to Mg implants versus Ti implants. **(A),** The concentrations of iNOS, VEGF, and FGF2 were quantified using ELISA in exudate samples collected around Mg implants and Ti implants at 3 d, 14 d, and 28 d (n = 8-9/time point/group). *<LOD:* measurement below the limit of detection. **(B),** Immunohistochemistry to detect cells positive to M1 macrophage subtype markers (iNOS, CD68), and M2 macrophage subtype markers (MRC1, ARG1) in tissues interfacing with Mg and Ti implants at 3 d and 28 d. *Black-dotted lines:* interface with Mg and Ti implants. *Arrowheads*: indicate some of the positive cells. **(C),** Quantification of cells positive for iNOS, CD68, MRC1, and ARG1 at 3 d and 28 d in tissues within a distance of 200 µm from the interface with Mg implant and Ti implants (n = 5-6/time point/ group; proportion of positive cells in an average of ~10 000 cell/region of interest in each section). Data are mean ± s.e.m.; * $P<0.05$ Mg *versus* Ti; ***a****: $P<0.05$* day 3 *versus* day 28 in Mg. Unpaired Mann-Whitney *U* test. Scale **B**=20 µm.

Regression analyses (Figure 6.8d-e) showed, however, that such associations did not exist. Overall, these findings indicated that, at the interface with Mg implants, the early increase in the Mg^{2+} concentration was associated with an increase in the number of recruited cells; however, it did not affect the viability of these cells.

Last, we aimed to verify if a relationship existed between the changes over time of Mg^{2+} concentration and that of gene expression (Figure 6.6g, Figure S6.9) and of protein concentration

(Figure 6.7a) in exudate around Mg implants. Among all genes (Table S6.2), both correlation (Figure 6.8f, *left*) and regression analysis (Figure 6.8f, *right*) identified an association only for proinflammatory genes *iNos* (positive association), and *Tlr4* (positive association), and for profibrotic gene *Fgf2* (negative association). At the protein level (Figure 6.8g), Mg^{2+} concentration featured a strong positive association with iNOS concentration, and a positive association with VEGF. Together, these results suggest that the changes over time of Mg^{2+} sequentially modulate the initial acute yet transient and noncytotoxic reaction up to 6 d to enable the subsequent repair around Mg implants.

6.3.8. Mg implant degradation modulates the expression of markers of inflammation and tissue repair beyond the interfacial tissues

In this study, Sham Mg and Sham Ti sites consisted of pockets that were wounded at a distance of ~2 cm from Mg- and Ti-implanted pockets, respectively (Figure 6.9a).

We noticed from the histomorphometrical analysis of soft tissues (Figure 6.3f) that Sham Mg featured a higher cellular infiltration at 6 d than that in Sham Ti. We further compared the healing between these groups by examining the cell counts (Figure 6.6b) and mRNA levels (Figure 6.9b) in exudates retrieved by lavage of Sham Mg and Sham Ti pockets between 1 d and 6 d. While cell counts were statistically comparable between both groups, the qPCR analysis demonstrated that the Sham Mg group exhibited higher expression of the chemotaxis genes *Mcp1* (at 3 d) and *Il8* (at 3 d), the proinflammatory macrophage gene *iNos* (at 3 d), and the angiogenesis gene *Vegf* (at 1 d) in comparison to the Sham Ti group (Figure 6.9b). Importantly, this rise in gene expression was transient, ending at 6 d, and analogous to findings in exudates from sites receiving Mg implants. Thus, although not receiving Mg implants, Sham Mg group featured a gene expression different from that of Sham Ti group, but with notable similarities to the patterns of gene expression in Mg implant group.

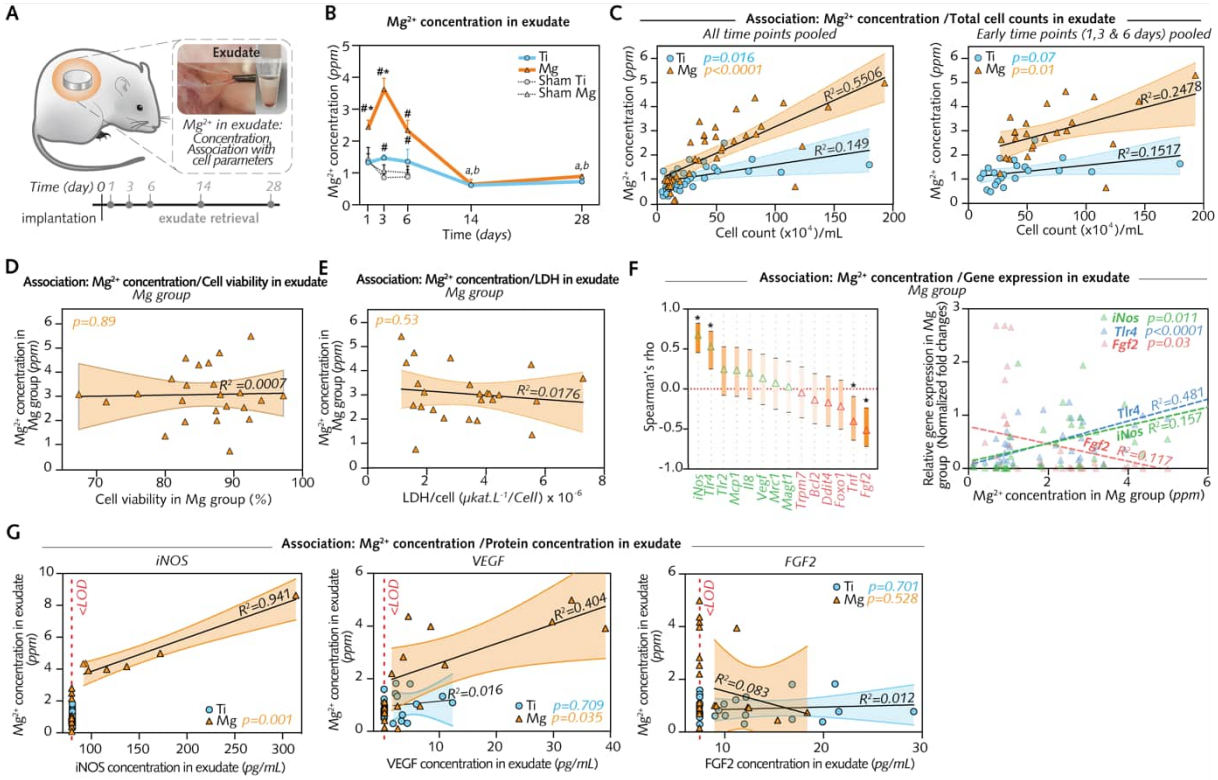

Figure 6.8: Interface magnified: Mg degradation sequentially tunes early inflammation and subsequent tissue repair. **(A),** Mg^{2+} concentration was measured and compared to cell counts, gene expression, and protein concentrations in the same samples (n = 7-8/group/time-point). **(B),** Mg^{2+} concentration measured using inductively coupled plasma optical emission spectroscopy (ICP-OES). **(C),** Linear regression of Mg^{2+} concentration and total cell counts (Left: Data from all time points pooled; Right: Data from 1 d, 3 d and 6 d pooled; 95% confidence intervals are shown). **(D),** Linear regression of Mg^{2+} concentration and cell viability in exudate around Mg at 1 d, 3 d and 6 d (data pooled; 95% confidence intervals). **(E)**, Linear regression of Mg^{2+} concentration and lactate dehydrogenase (LDH) in exudate around Mg at 1 d, 3 d and 6 d (data pooled; 95% confidence intervals). **(F),** Spearman correlation of Mg^{2+} concentration and gene expression (left; * $P<0.01$; 95% confidence intervals) and respective linear regression (right) confirming significant associations for genes *iNos*, *Tlr4*, and *Fgf2.* **(G),** Linear regression of Mg^{2+} concentration and protein concentration in exudate around Mg at 3 d, 14 d, and 28 d (data pooled; 95% confidence intervals) showing a significant association between Mg^{2+} concentration and iNOS and VEGF, respectively, at the protein level. *<LOD:* measurement below the limit of detection. Data are mean ± s.e.m.; * $P<0.05$ Mg *versus* Ti; # $P<0.05$ Mg or Ti *versus* respective sham wounds; ***a**: $P<0.05$ versus* days 1, 3, and 6 in Mg; ***b**: $P<0.05$ versus* days 1, 3, and 6 in Ti. Unpaired Mann-Whitney *U* test or paired Wilcoxon signed-rank test.

Next, in order to determine the relationship with the distinct gene expression in the distant Sham Mg pockets, we determined Mg^{2+} concentration in exudate from Sham Mg and Sham Ti groups (Figure 6.9c), yet without detecting a significant difference between both groups. Furthermore, Mg^{2+} concentration in the Sham Mg group did not reveal a significant association with the cell count (Figure S6.9a) or with mRNA levels (Figure 6.10b), thus assigning that a role of Mg^{2+} from Mg implant sites for cell behaviour in distant sham sites is less likely. However, macroscopic (Figure 6.9d) and microscopic observations (Figure 6.9e-f) provided evidence of voids in the tissues sampled in the Sham Mg group. In histological sections, the tissues surrounding these voids (Figure 6.9e) exhibited greater cellular infiltration, showing

similarities with the gas voids detected in tissues around Mg implants (Figure 6.9f). In summary, these findings inferred that the gas released from the Mg implant might contribute to the elevation of the initial inflammatory response in the distant Sham Mg pockets.

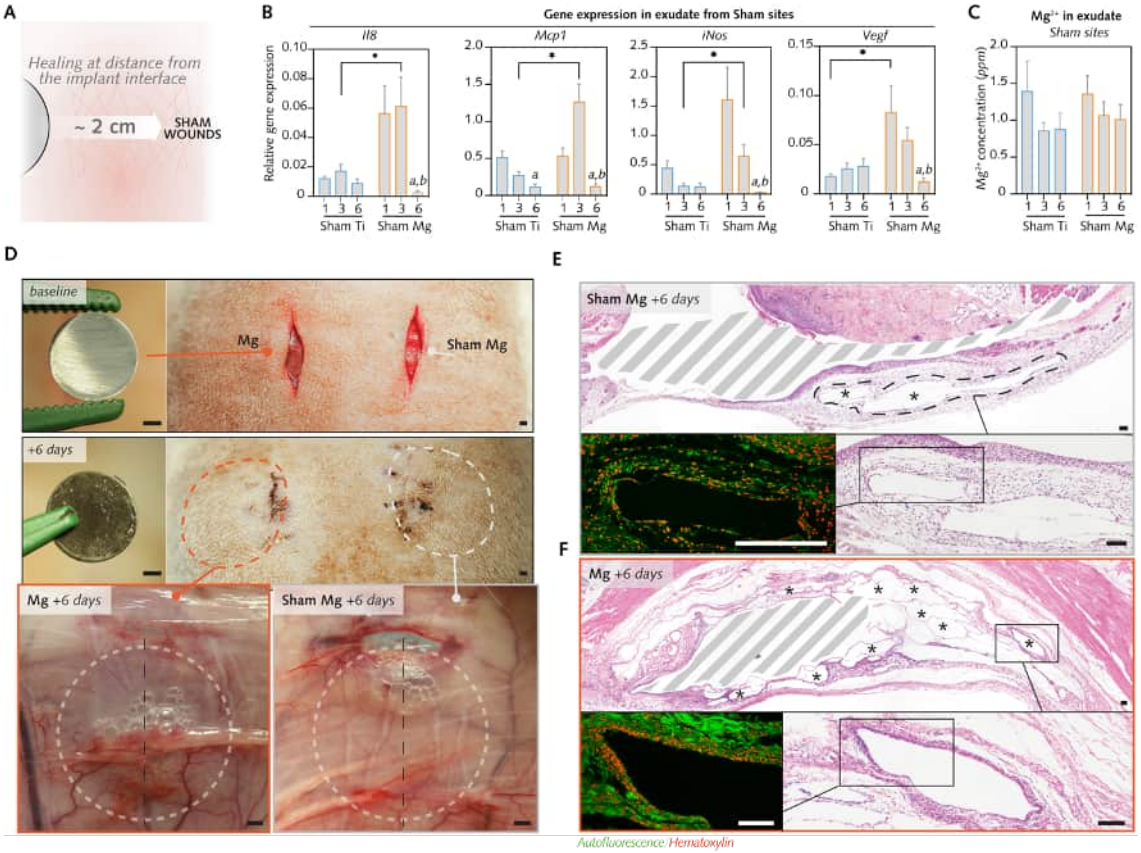

Figure 6.9: Changes over time of the cellular and molecular alterations in sham wounds. **(A),** To verify whether Mg degradation influences healing in Sham Mg, the cellular and molecular parameters in the exudate were compared between Sham Ti and Sham Mg after 1-6 d. **(B),** Relative gene expression in sham wounds (n = 8/group/time-point). **(C),** Mg^{2+} concentrations in exudate from sham wounds (n = 7-8/group/time-point). **(D),** Clinical photographs display the implantation of a Mg implant and sham wounding (top panel). At postsurgery day 6, wounds in the same rat were re-entered for retrieval of the implant (middle panel), the exudate and the tissues (*lower panel*). The fascia in Sham Mg wounds featured voids comparable to those in tissues around Mg implant. **(E-F),** Histological sections of wounds in **D** exhibiting voids in tissue walls in Sham Mg similar to gas voids around Mg implant in the same rat. Bottom panels in **E** and **F** (*hematoxylin and eosin staining with autofluorescence micrograph, red: cells, green: extracellular matrix and vessels*) show magnified areas of the voids (*Asterisks in upper panels of **E** and **F***) separated by thin walls of extracellular matrix and with a higher cellularity at their boundaries, similar to Mg-implanted tissues (**F,** *bottom left*). Dashed areas indicate surgically created pockets with or without implants. Data are means ± s.e.m.; * $P<0.05$ Mg *versus* Ti; ***a***: $P<0.05$ *versus* day 1; ***b***: $P<0.05$ *versus* day 3. Unpaired Mann-Whitney *U* test. Scale **D**=2 mm; **E, F**=100 µm.

6.4. Discussion

Magnesium is a prime example of a biodegradable material which has been introduced as an alternative to conventional non-degradable materials in orthopaedics and cardiovascular medicine. While Mg and biodegradable Mg implants are classically presented to hold anti-inflammatory properties, the inflammation of soft tissues around Mg orthopedic implants is an elusive clinical event and questions the safety and the biocompatibility of metallic degradation

byproducts deposited in the adjacent tissues. Using a soft tissue rat model, we demonstrate that an early amplified inflammation is inevitable and is initiated by the burst release of degradation products from Mg implants, yet without a cytotoxic effect. Thereafter, however, the slower degradation modulates the acute response and enables an improved vascular supply and reduced fibrosis of peri-implant soft tissues, therefore attenuating FBR in comparison to the state-of-art nondegradable implants made of Ti.

A pivotal feature of the initial response to Mg implants was the early and marked increase in inflammation in comparison to that upon implantation with Ti. Our findings are in opposition to the notion of anti-inflammatory properties assigned to Mg implants. This assumption mainly stems from the literature demonstrating the aptitude of Mg^{2+} supplementation to abrogate hypomagnesemia-related inflammation [505], or from previous *in vitro* studies reporting an anti-inflammatory effect in immune cells treated with Mg^{2+} [481,483]. The present study demonstrates *in vivo* that the initial profuse release of Mg^{2+} from Mg implants, culminating at 3 d, causes a pronounced cellular influx at the implant-interface. Such a marked chemotaxis in response to Mg degradation might be primarily ascribed to chemokines such as *Il8* and *Mcp1* which featured an upregulation of their gene expression. Moreover, Mg^{2+}, alike other divalent anions such as Ca^{2+}, can also potentiate chemotaxis in a dose-dependent-fashion [506]. Suggested mechanisms behind Mg^{2+}-induced cell migration include the activation of downstream pathways of receptors such as G-protein receptor [507] and calcium-sensing receptor CaSR [508], along with the disassembly of intercellular junction proteins, thus enabling cellular motility [509]. Chemotaxis promotion is also reported during the early response to Cu^{2+}-releasing implants in a soft tissue model identical to the animal model used in this study. Up to 3 d, the proinflammatory response at the interface with copper – mediated by: neutrophil recruitment [485], proinflammatory cytokine release [485,486], and activation of nuclear factor-kappaB (NF-κB) signaling pathway [510] – was sustained over time in contrast with a transient inflammation in control sites implanted with Ti. Our correlation and regression analyses, identifying a robust association linking Mg^{2+} release at the interface to chemotaxis, to the expression of genes *iNos* and *Tlr4* and to the secretion of iNOS protein, further supported that Mg implants elicit an initial proinflammatory reaction at the immediate tissue milieu. Such a response, however, should not be solely ascribed to Mg^{2+} and a role of other Mg degradation byproducts cannot be excluded.

Gas accumulation in soft tissues also accompanied the amplified inflammatory response to Mg implants in our study, and is presumed to result from hydrogen production by the corrosion reaction $Mg+2H_2O \rightarrow Mg^{2+}+2OH^{-}+H_2$ [106]. While an anti-inflammatory benefit is attributed to exogenous hydrogen administration [511], gas accumulation in tissues from Mg implants has been assumed to preclude the healing of Mg implants [134], advocating the removal of the gaseous voids by puncture procedure in some animal studies [352,452]. An explanation for this contradiction might be the gas composition inside tissue voids around Mg implants. In fact, hydrogen is believed to be only a minor component of these gaseous structures, due to its fast escape into the body fluid, at the expense of a higher concentration of other gases such as nitrogen, oxygen, and carbon dioxide [456]. Of importance is also the microscale alteration of pH near the Mg implant surface, resulting from hydroxide release. The initial and moderate alkalinization during Mg implant degradation, as suggested herein by the immersion tests, might also influence the cellular behavior including viability, proliferation, and differentiation [512,513]. In this study, Sham Mg wounds, which were at ~2 cm-distance from Mg implants, featured elevated levels of proinflammatory and angiogenesis genes. The macroscopic and histological evidence of voids resembling those detected around Mg implants, together with the comparable Mg^{2+} concentration with Sham Ti, evoked a plausible proinflammatory effect by gas in Sham Mg. This assumption is supported by the propagation capacity of the gas produced by Mg degradation which is reported in soft tissue [451,456]. Whether the gaseous composition or the mechanical cues by these voids might tune the response of nearby cells toward inflammation is yet to be elucidated.

The finding that the conspicuous inflammation in soft tissues around Mg implants was not associated with an amplified cellular death is of critical importance. Cytotoxicity triggered by wear particles and ions holds, indeed, a chief role in the immune cascade behind soft tissue damage in patients with e.g. cobalt-chromium implants [479]. Instead, the comparable cell viability and cytotoxicity that were demonstrated at the interface for Mg and Ti implants, and in sham wounds support the assumption that the increased inflammation by Mg implants does not detain the deleterious effects documented in the soft tissue reaction to wear byproducts from cobalt-chromium implants [503]. Although the mRNA levels of apoptotic marker *Ddit4* were elevated at the Mg implant-interface, the expression of this gene is also known to be regulated by hypoxia [514] – a condition typical of the degradation process at Mg implant surface [515].

From 6 d, the subside of the initial inflammation and the assembly of the fibrous capsule around Mg implants overlapped with noticeable alterations in Mg degradation dynamics. To recapitulate, the decrease in Mg^{2+} concentration at the interface, the reduction in gas voids in soft tissues, and the enrichment in calcium and phosphorus at Mg implant surface indicated the deceleration of Mg implant degradation. That a calcium-phosphorous-rich superficial layer conveys timely degradation protection to Mg implants, as we showed in soft tissues, corroborates similar observations in bone [183,352] and in vascular walls [516]. Upon contact with body fluids, Mg degrades via a series of anodic and cathodic reactions that consume dissolved oxygen and produce oxides and hydroxides along with hydrogen gas [106]. Although protective layers comprising Mg oxide [MgO] and Mg hydroxide [$Mg(OH_2)$] form on the implant surface, anions in body fluids break up the oxide phases of the covering layers, thus maintaining the degradation process [106]. As a consequence of the local alkalization that accompanies Mg degradation, Ca^{2+} and PO_4^{3-} in body fluids precipitate on the surface of the degrading metal. In turn, this calcium-phosphorous-rich layer, that was established at Mg implant surface after 6 d, would act as a barrier against oxygen transport, and stabilizes the degradation process.

Interestingly, the shift in degradation kinetics was intimately linked to the transition from a proinflammatory to a prohealing response. Illustrating this biphasic kinetic response at Mg implant microenvironment were the changes over time of iNOS both at the gene and the protein level. iNOS featured the strongest upregulation in mRNA levels between 1 d and 6 d, and a robust protein detection at 3 d in response to Mg implants, and implies the vigorous initial activation of proinflammatory macrophage [517], as supported by the elevated presence of CD68-positive cells in the tissue around Mg implants. Then, after 6 d, mRNA and protein levels of iNOS dramatically declined together with *iNos* / *Mrc1* gene expression ratio, suggesting a switch toward activation of prohealing macrophages. This behavioral switching of macrophages is an important milestone in the course of wound healing around biomaterials, and drives the progression from the initial proinflammatory step toward the reparative phase [518]. However, if persistent, the activation of proinflammatory macrophages due to the prolonged release of Mg^{2+} precludes tissue repair as reported in bone defects [519]. Therefore, the transient proinflammatory response, intimately linked to the kinetics of Mg implant degradation and to the production of reactive oxygen and nitrogen species at the implant microenvironment [520], is a key event for the subsequent proper tissue repair. Such a sequence in tissues around Mg implants fostered neovascularization and mitigated peri-implant

fibrosis. Both features were demonstrated in this study by the morphology of the cicatricial capsule and by the molecular regulation of markers of angiogenesis (*Vegf*), fibrogenesis (*Fgf2*) and antifibrosis (*Foxo1*) at the Mg implant-interface. A lack of vascularization and an excessive fibrotic encapsulation of biomaterials are two hallmark components of the FBR, both intricately tuned by inflammation [521]. The promotion of inflammation is a strategy that has shown merit in improving neovascularization in various wound healing models [522], mainly through proinflammatory macrophages that produce high amounts of pro-angiogenic factors [523]. Among these, VEGF, in particular, is a key factor in initiating and driving vessel sprouting during the initial inflammatory stage [524]. If sustained, however, an overt inflammatory state becomes deleterious and leads to an excessive fibrotic response [521], as observed around Cu^{2+}-releasing implants that sustained soft tissue inflammation in the same rat model as herein [490]. At Mg implant surface, the 14 d-upregulation of *Foxo1* gene expression, key to the apoptosis of profibrogenic myofibroblasts [525], further testifies in favor of the subsequent antifibrotic effect. The attenuation of fibrous encapsulation was also reported in mice 28 d following implantation with Mg particles-embedded polymer nano-fiber meshes subsequent to an initial inflammatory response [526]. Collectively, the timely subside of inflammation is postulated to account for the lack of aberrant fibrosis around Mg implants and underpins the translational potential of their immunomodulatory effect.

From a clinical perspective, an improved vascularization without excessive fibrosis is coveted not only in soft tissues that overlay Mg osteosynthesis systems but also for other clinical applications of Mg-based biomaterials. Prime among these are clinically approved Mg-based vascular stents. Due to their fast degradation, these implants only partially succeed in preventing long-term re-narrowing (i.e., restenosis) of diseased vessels in patients [527], although being the main incentive behind using bioresorbable stents instead of their non-resorbable analogs. Translating the antifibrotic effect demonstrated herein in soft tissue, Mg-based vascular stents that are tailored to degrade slower might mitigate the unwanted fibrosis-linked restenosis in treated vessels, although a response discrepancy inherent to differences between tissues remains plausible.

The information conveyed by this study does not expand to time points beyond 28 d. This is a limitation when considering that Mg implants are designed to ultimately result in a full degradation in the body, while Mg implants remained unresorbed in large portions by 28 d in our study. Further studies are needed to address unanswered questions on the fate of Mg degradation and the associated long-term soft tissue response, notably inflammation and

fibrotic encapsulation. Moreover, in patients with diseased tissues, it remains to be elucidated how a pre-existing inflammatory environment would influence the kinetics and magnitude of the combined host- and Mg-material-elicited inflammation and tissue response.

6.5. Conclusion

In summary, the present study demonstrates that, upon Mg implantation in soft tissue, an early inflammatory cell recruitment and adhesion together with a proinflammatory and proangiogenic gene expression and protein secretion are triggered by a rapid initial release of Mg^{2+}. The transition to an appropriate tissue repair coincided with the enrichment of Mg implant surface in Ca and P, an attenuated Mg^{2+} concentration in the peri-implant environment, and the morphological detection of reduced number and area of gas voids. From a translational perspective, the results suggest that the inflammation clinically reported in soft tissues early following Mg implant insertion is associated with a rapid implant degradation. Taken together, the detailed understanding of the relationship between Mg material properties and the spatial and time-resolved cellular processes will be important for the development of novel, disease-specific, i.e., personalized implant therapies.

Supplementary materials

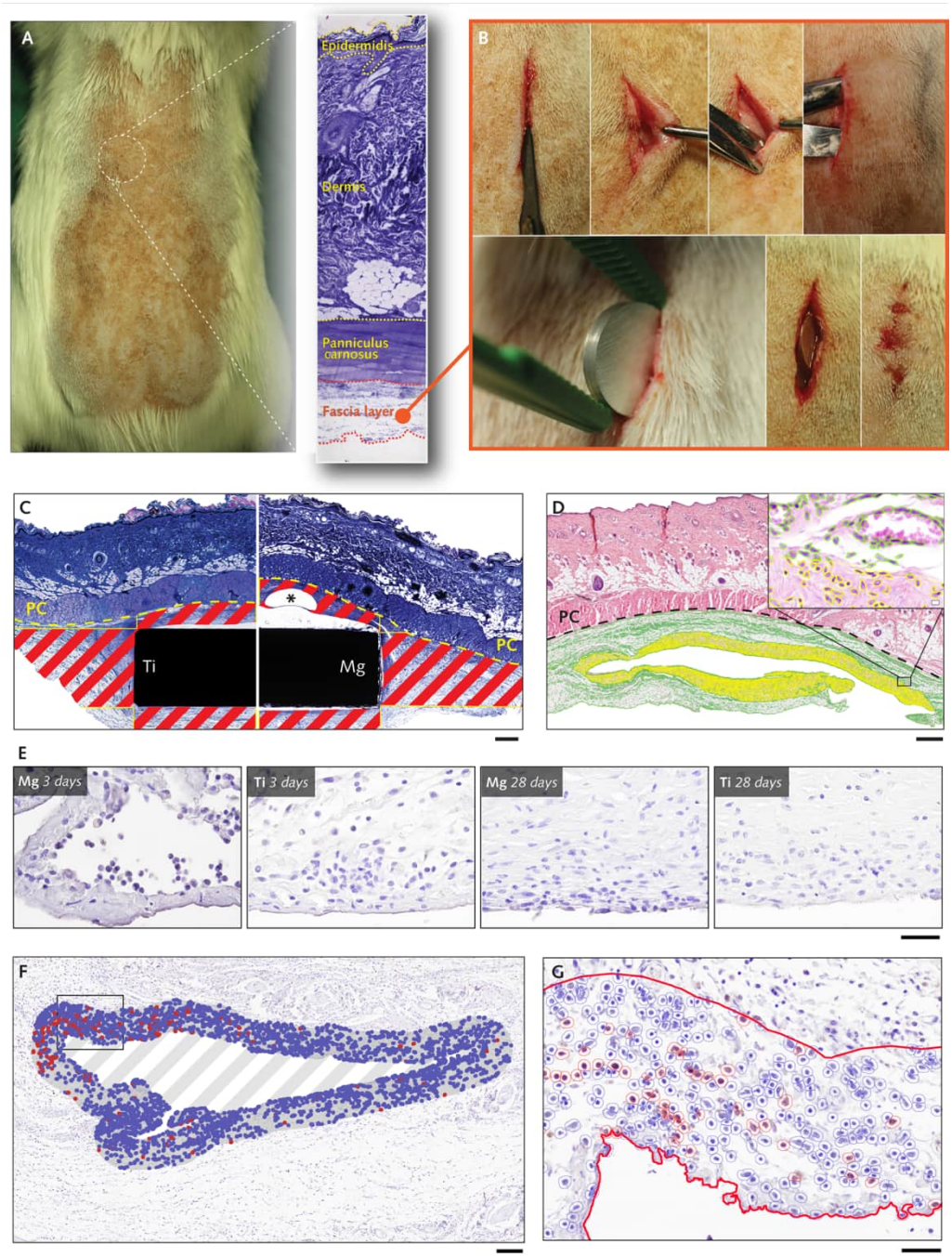

Figure S6.1. Implant insertion into animals, histology, immunohistochemistry, and regions of interest for histomorphometric analyses. (**A-B**)**,** The implantation site consisted of the back skin of Sprague–Dawley rats (**A**). Incision and blunt dissection of the subcutis allowed the insertion of implants in surgical pockets (**B**) created in the loose tissue layer underneath the panniculus carnosus. (**C**)**,** Regions of interest (ROIs) in toluidine blue-stained peri-implant [n = 4 hashed red areas of the subcutaneous fascia extending to each side of the implant cross-section underneath the panniculus carnosus muscle (PC)]) where the following parameters were histomorphometrically measured: 1-*Thickness of the fibrous capsule;* 2-*Vessels inside the capsule: number, lumen area, and distance to the interface;* 3-*Mast cells: number;* 4-*Gas voids (asterisk) around Mg implants: number and area*. (**D**)**,** Hematoxylin and eosin-stained tissues were used for the calculation of cellular density. Detected cells are highlighted in the subcutaneous fascia (green) underneath the panniculus carnosus muscle (PC) and in the fibrous capsule (yellow) and magnified in the inset. (**E**)**,** Micrographs exemplifying negative control sections. (**F**,**G**)**,** ROI to analyze immunostained sections encompassed tissues within a distance of 200 µm from the interface with the implants (hashed grey area; **F**). Cells positive (outlined in red) to proteins iNOS, or CD68, or MRC1, or

ARG1, and cells negative (outlined in blue) to the respective antibodies were automatically detected (**G**) and counted in the ROI (depicted by the red lines).
Scale **C**=200 µm*;* **D**: *black*=200 µm*, white (inset)*=50 µm; **E**=20 µm; **F**=200 µm; **G**=50 µm.

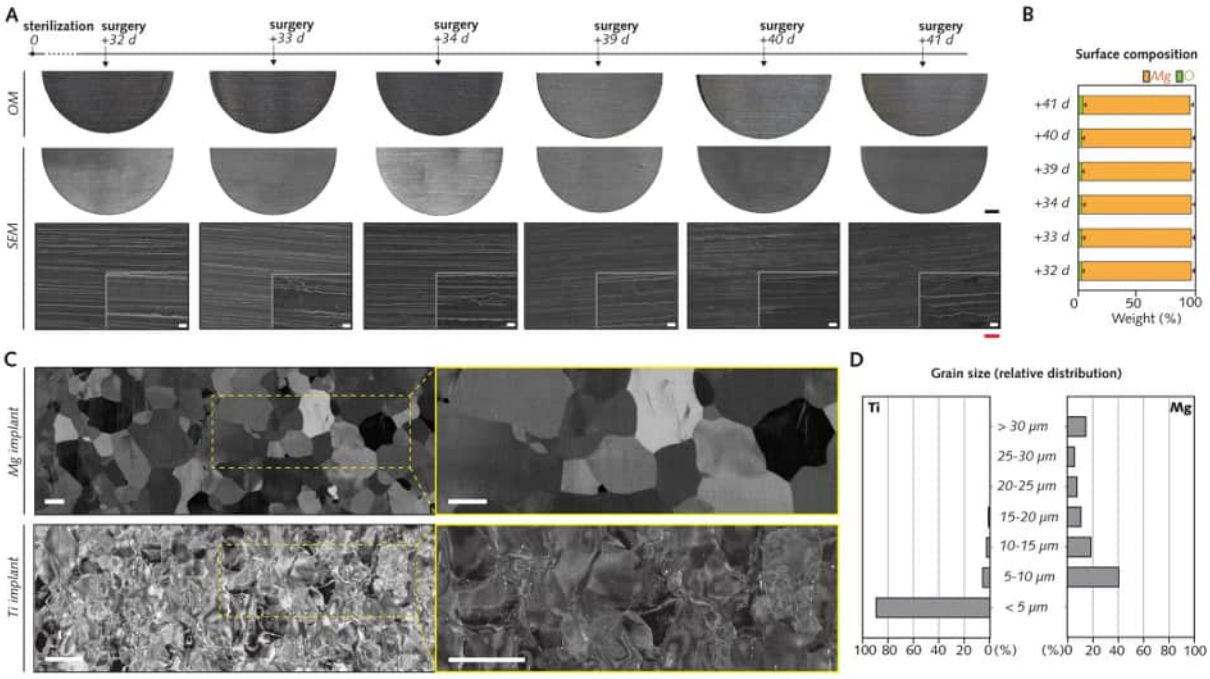

Figure S6.2. Implant microstructure and surface oxidation of Mg implants prior to implantation. (**A**)**,** Representative images of the Mg implant surface at each day of surgery (between 32 days to 41 days after sterilization of Mg implants) using optical microscopy (OM; *Top panel*) and scanning electron microscopy with a secondary electron detector (SEM; *Lower panel;* x10 magnification in inset). (**B**)**,** Chemical composition of the Mg implant surface on each day of surgical insertion (between 32 days and 41 days after sterilization) showing minor and comparable oxidation of the discs (n = 3 implants at each time point). (**C**)**,** Backscattered electron images of disc cross-sections showing a microstructure characterized by an array of equiaxed grains with different grain sizes and some twin deformation. (**D**)**,** Scanning electron microscopy using an electron backscattered diffraction detector allowed the measurement of the grain size on implant cross-sections using inverse pole figures (as shown in **Fig. 1F** of the main document) with crystallographic orientations and calculation by the linear intercept method. Data are means ± s.e.m. Scale **A**: *black*=2 mm, *red*=50 µm, *white (inset)*=5 µm, **C**=50 µm.

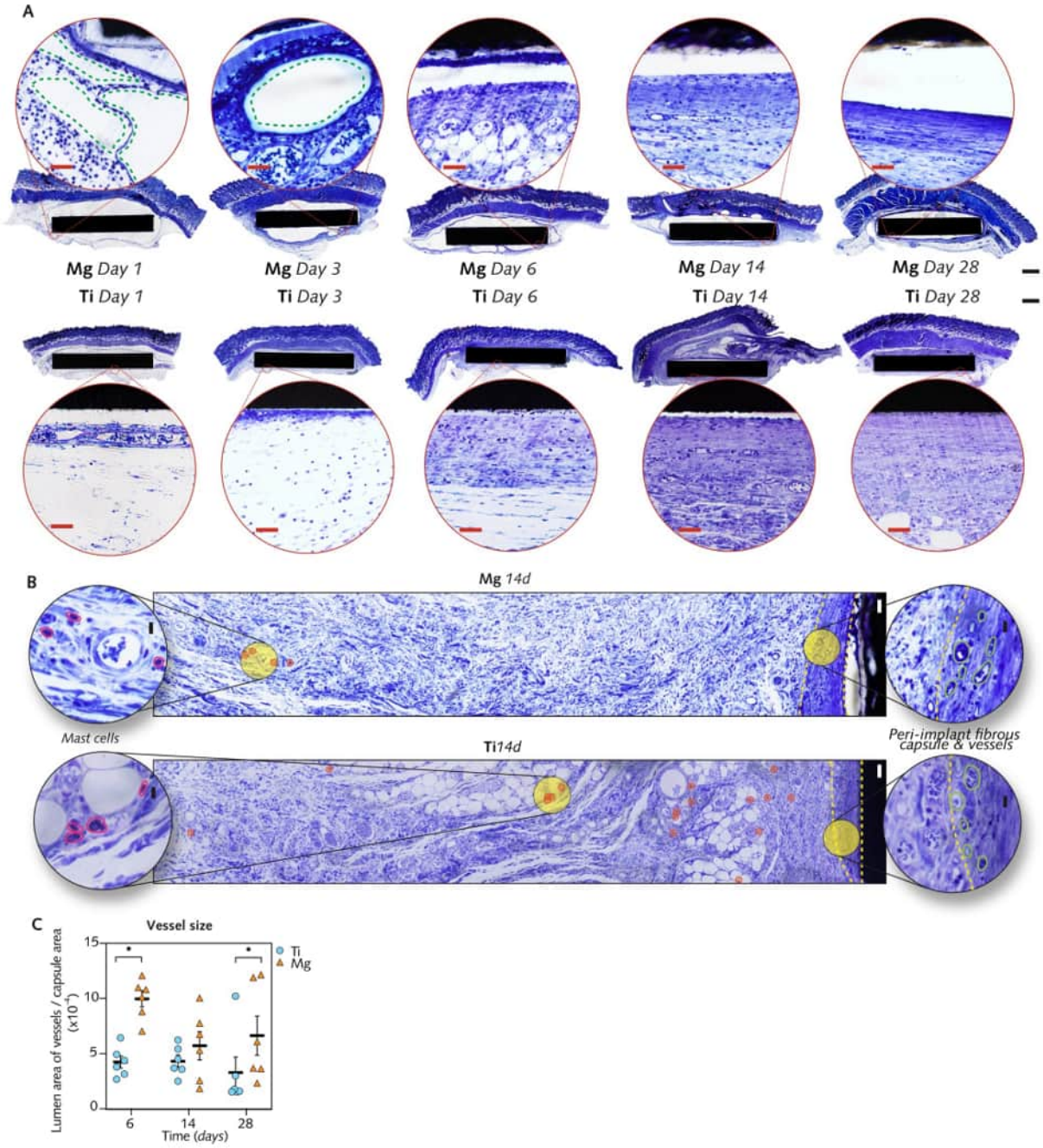

Figure S6.3. Histological analyses of peri-implant tissues. (**A**)**,** Cross-sections of Ti or Mg implants and surrounding tissues stained with toluidine blue (TB). Insets show magnified regions of the tissue-implant interface. Gas voids in tissues interfacing with Mg implants are highlighted in insets with green dotted lines. (**B**)**,** Magnified regions of peri-implant tissues stained with TB highlighting the fibrous capsule (yellow dotted lines), vessels in the capsule (green lines), and mast cells (red lines). (**C**)**,** Lumen area of vessels inside the fibrous capsule measured between 6 d and 28 d. Data are means ± s.e.m.; * $P<0.05$ Mg *versus* Ti. Unpaired Mann–Whitney *U* test. Scale **A:** *black*=2 mm, *red (inset)*=200 µm*;* **B:** *white*=50 µm*, black (inset)*=20 µm;

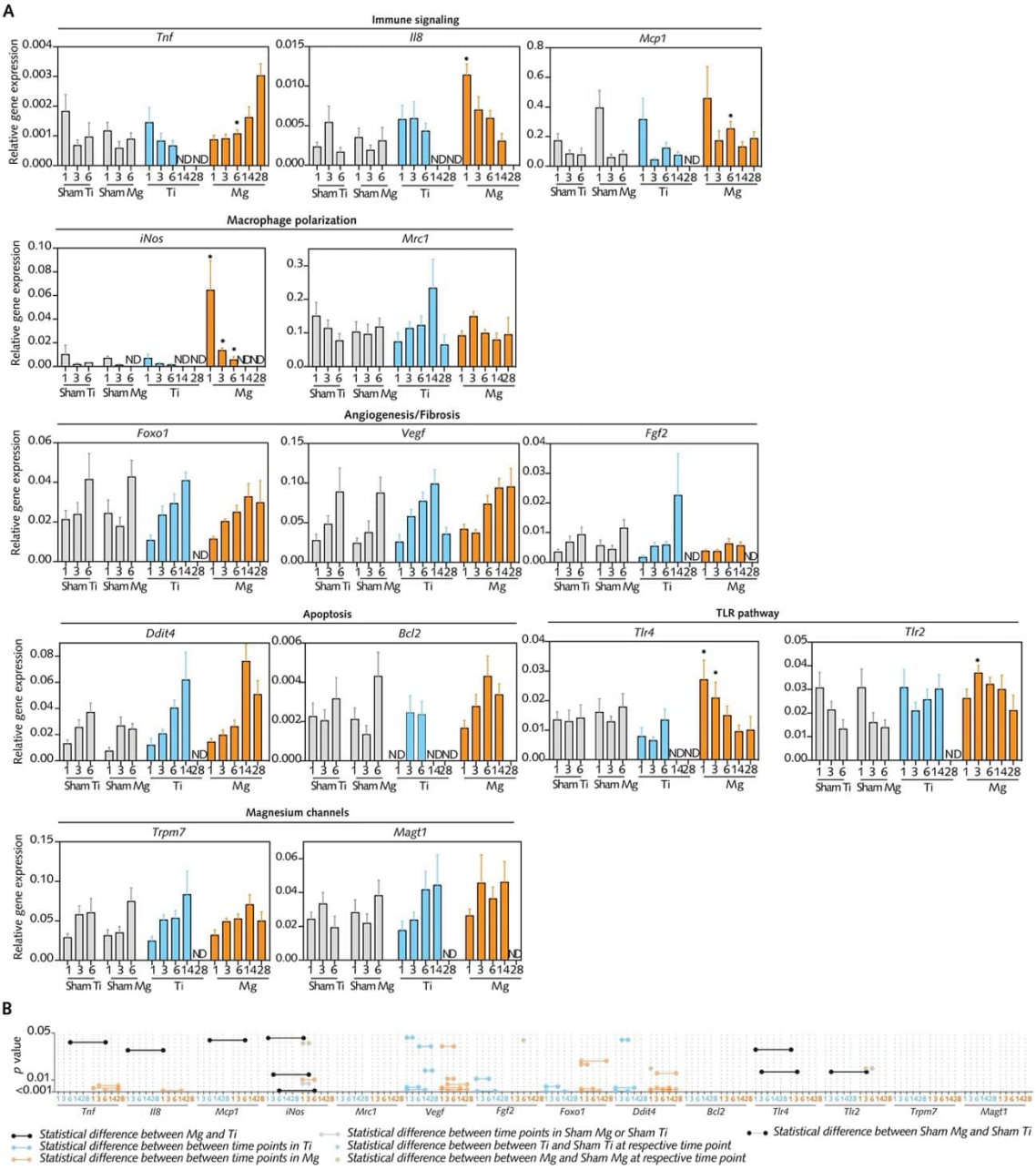

Figure S6.4. Gene expression analysis of peri-implant tissues. Punches of tissues from sites implanted (Ti and Mg) or not (Sham Ti and Sham Mg) were retrieved at each time point (n = 5-8/group/time point) and were assigned for qPCR analysis. Relative gene expression (n = 5-8/group/time-point) is shown for each gene in (**A**), and statistically significant differences between biomaterials, between time points, or between implanted sites and respective shams are provided in (**B**).Data are means ± s.e.m.; *ND*: No detectable gene expression. Sham Ti and Sham Mg wounds were fully closed at 14 d and 28 d and were not analyzed with qPCR at these time points. * $P<0.05$ Mg *versus* Ti. Unpaired Mann–Whitney *U* test or paired Wilcoxon signed-rank test.

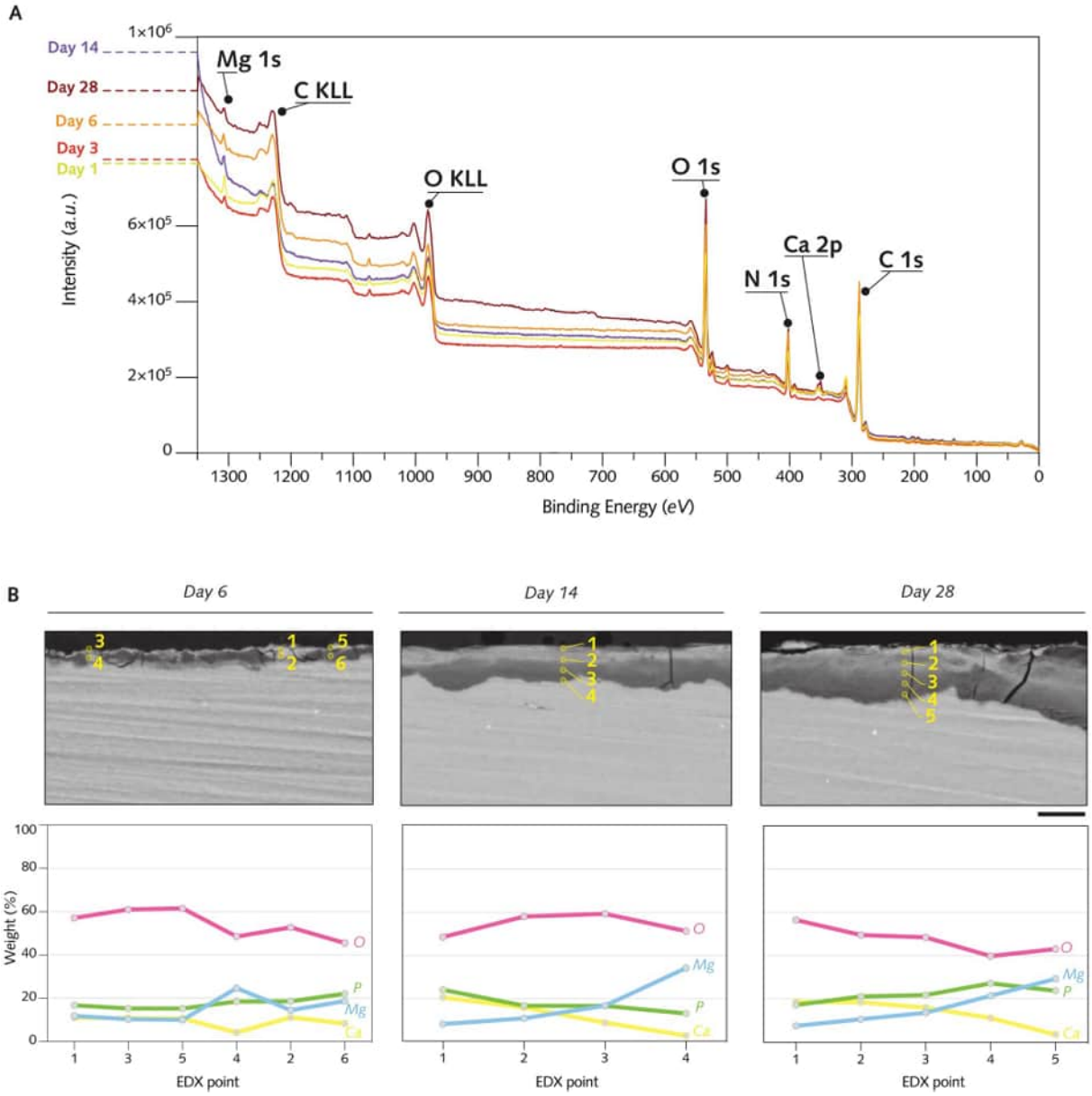

Figure S6.5. Surface chemistry and cross-sections of retrieved Mg implants. (**A**), X-ray photoelectron spectroscopy (XPS) survey scan spectrum of the surface of retrieved Mg implants. Discs were collected from peri-implant pockets and fixed in 100% ethanol. XPS was run on an n = 1 Mg implant/time point following scanning electron microscopy (SEM) and energy-dispersive X-ray spectroscopy (EDX) analysis. (**B**), EDX point measurements at cross-sections of the superficial degradation layer on Mg implants collected at 6, 14, and 28 days. The upper panel shows SEM with backscattered electron detector images of implant cross-sections. The lower panel provides the elemental composition at each point as indicated in the respective images of the upper panel. Scale **B**=10 μm.

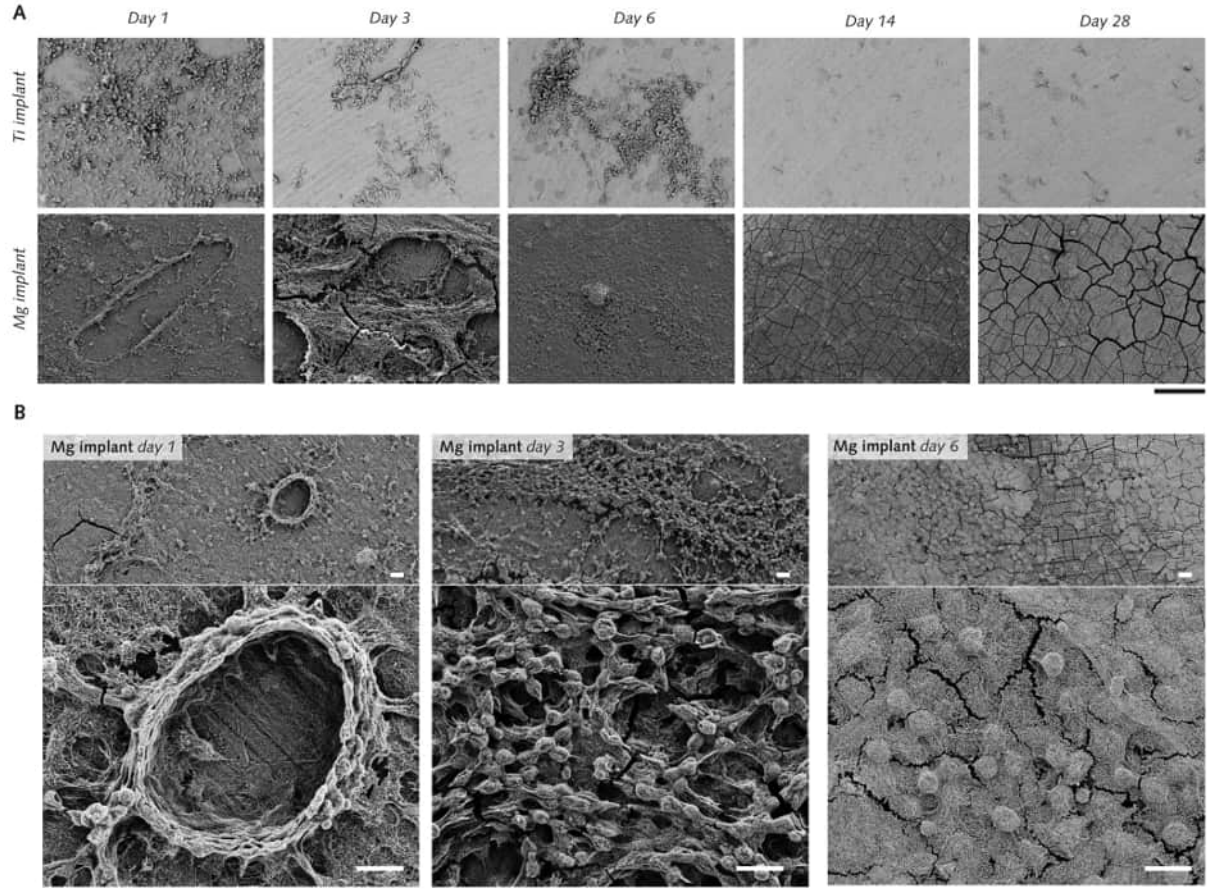

Figure S6.6. Electron microscopy observations of the implant surface. (**A**)**,** Images from scanning electron microscopy, using a secondary electron detector, of the surface of Ti and Mg implants retrieved at 1–28 days. (**B**)**,** Areas of the Mg implant surface showed a high cellular presence with a dense extracellular matrix (ECM) between 1 d and 6 d. The organization of cells and ECM featured a characteristic circular pattern at the micron scale. Images in the bottom panel are magnifications of the images in the upper panel. Scale **A:** *black*=100 μm*;* **B:** *white*=20 μm.

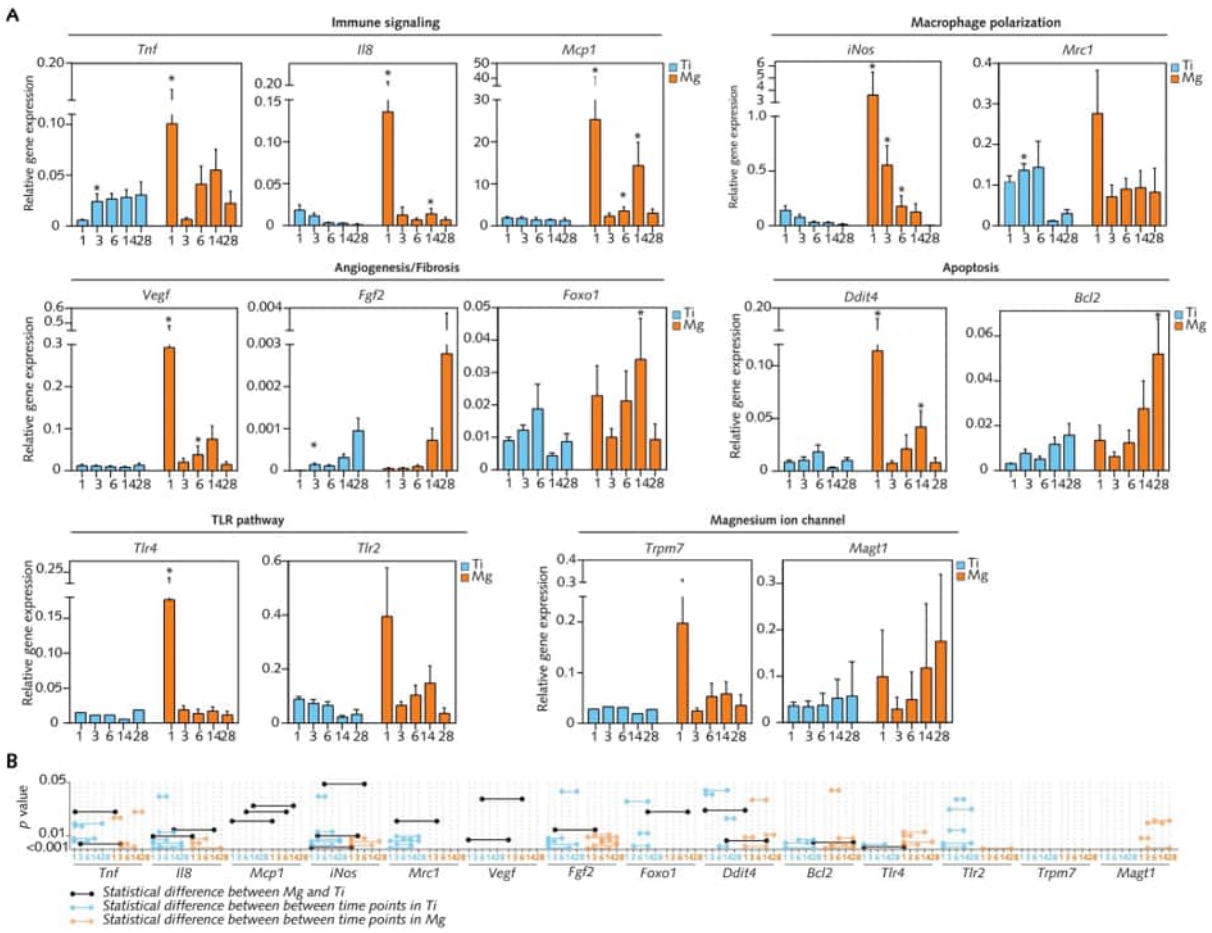

Figure S6.7. Gene expression analysis of implant-adherent cells. Cells adherent to the surface of implants were retrieved (n = 8/group/time-point) and subjected to qPCR analysis. (**A),** Relative gene expression (n = 8/group/time-point) is shown for each gene, and statistically significant differences between biomaterials and between time points are provided in (**B**). Data are means ± s.e.m.; * P<0.05 Mg *versus* Ti. Unpaired Mann–Whitney *U* test.

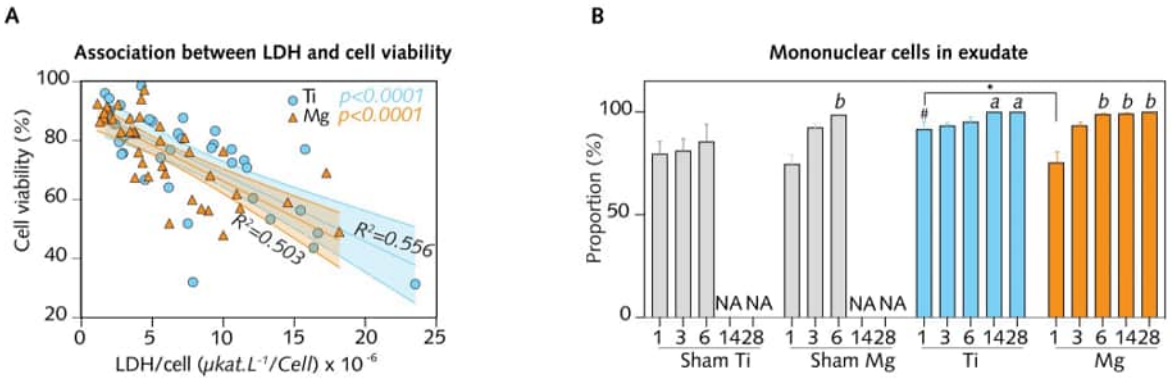

Figure S6.8. Cellular analyses of exudate samples. **(A),** Linear regression analysis confirming the comparable results between relative lactate dehydrogenase concentration (LDH; based upon spectroscopic analysis) and cell viability (based upon cell counting with Nucleocounter® analysis) in the Mg and Ti groups. Samples taken at all time points were pooled in each group (all time points pooled; 95% confidence intervals and *P* values shown). **(B),** Mononuclear cell proportion in the exudate (n = 6-7/group/time-point). Data are mean ± s.e.m.; *NA*: Not analyzed. Exudates were not collected from Sham Ti and Sham Mg groups at 14 d and 28 d (wounds were closed). * $P<0.05$ Mg *versus* Ti groups; # $P<0.05$ Mg or Ti *versus* respective sham; ***a****: $P<0.05$ versus* days 1–6 d in Ti; ***b****: $P<0.05$ versus* days 1–3 in Mg and Sham Mg. Unpaired Mann–Whitney *U* test or paired Wilcoxon signed-rank test.

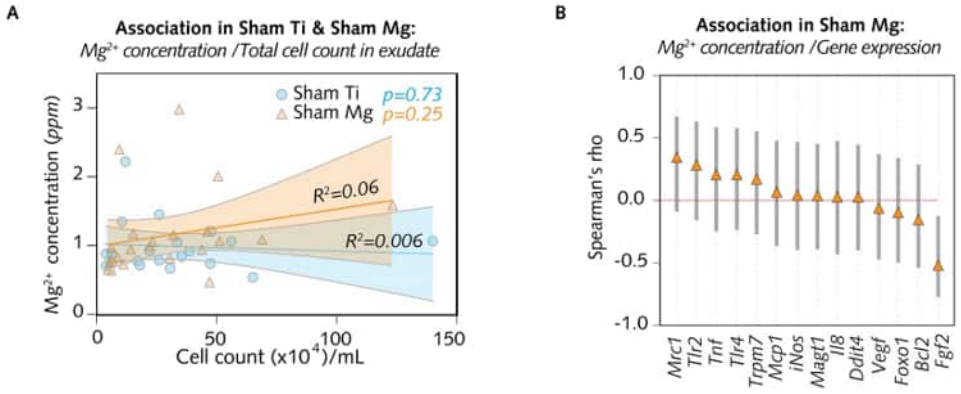

Figure S 6.9. Mg^{2+} concentration is not associated with cell count or gene expression in exudates from sham sites. (**A**), Linear regression of Mg^{2+} concentration and cell viability in exudate from the Sham Ti and Sham Mg groups at 1 d, 3 d and 6 d did not show a significant association (data pooled; 95% confidence intervals; statistical significance if $P<0.05$). (**B**), No correlation was found between Mg^{2+} concentration and gene expression in the Sham Mg group at 1 d, 3 d and 6 d (Spearman correlation; data pooled; 95% confidence intervals; statistical significance if $P<0.01$).

Supplementary tables

Table S6.1. Chemical composition of magnesium implants (*upper table*) and titanium implants (*lower table*).

Mg	Fe	Cu	Ni
99.995 %	0.0048 %	0.0003 %	<0.0002 %

Ti	O	Fe	C	N	Ni
99.55 %	0.34 %	0.08 %	0.01 %	0.01 %	0.006 %

Table S6.2. List of genes of interest.

Gene name	**Gene abbreviation**
Tumor necrosis factor-alpha	*Tnf*
Interleukin-8	*Il8*
Monocyte chemoattractant protein-1	*Mcp1*
Inducible nitric oxide synthase	*iNos*
Macrophage mannose receptor C type-1	*Mrc1*
Vascular endothelial growth factor	*Vegf*
Fibroblast growth factor 2	*Fgf2*
Forkhead box O-1	*Foxo1*
DNA-damage inducible transcript 4	*Ddit4*
B-cell lymphoma 2	*Bcl2*
Toll-like receptor 2	*Tlr2*
Toll-like receptor 4	*Tlr4*
Transient receptor potential melastatin 7	*Trpm7*
Magnesium transporter 1	*Magt1*

Bridging Chapter 6 and the following chapter 7

Investigating the degradation of Mg implants in soft tissues is relevant for clinical applications, such as using Mg wires for repairing blood vessels or nerves. The findings of Chapter 6 obtained from *in vitro* experiments offer a baseline information regarding the degradation mechanisms of pure Mg. The *in vivo* environmental conditions within the soft tissue model demonstrated that the strong initial reactions of Mg degradation, resulted in an early amplified inflammatory response. However, with longer implantation time, the formation of a corrosion layer on the Mg implant slowed down the degradation of the Mg device, leading to a tissue repair process.

Another approach for Mg medical implants is to exhibit exceptionally high purity magnesium implants to reduce the number of impurities that may trigger adverse reactions, thereby compromising their biocompatibility and regulatory approval for clinical use. It is crucial to emphasize that even small amount of impurities in pure Mg can drastically influence its corrosion resistance. Therefore, in Chapter 7, the corrosion performance of ultrahigh-purity Mg (XHP-Mg, >99.999 wt% Mg; Fe-content <1 ppm) and ZX00 (Mg–Zn–Ca; <0.5 wt% Zn and <0.5 wt% Ca, in wt%; Fe-content <1 ppm) pins was assessed in a small animal model.

Chapter 7

The combined effect of zinc and calcium on the biodegradation of ultrahigh-purity magnesium implants†

Begüm Okutan, Uwe Y. Schwarze, Leopold Berger, ***Diana C. Martinez***, Valentin Herber, Omer Suljevic, Tomasz Plocinski, Wojciech Swieszkowski, Susana G. Santos, Rainer Schindl, Jörg F. Löffler, Annelie M. Weinberg, Nicole G. Sommer

Published in ***Biomaterials Advances*** *2023 (146): 1-16. doi: 10.1016/j.bioadv.2023.213287*

† *To improve the readability of this chapter, some sections of the publication have been rearranged.*

ABSTRACT

Magnesium (Mg)-based implants are promising candidates for orthopedic interventions, because of their biocompatibility, and good mechanical features, and ability to degrade completely in the body, eliminating the need for an additional removal surgery. In the present study, we synthesized and investigated two Mg-based materials, ultrahigh-purity ZX00 (Mg<0.5Zn<0.5Ca, in wt.%; Fe-content < 1 ppm) and ultrahigh-purity Mg (XHP-Mg, >99.999 wt.% Mg; Fe-content < 1 ppm), in vitro and in vivo in juvenile healthy rats to clarify the effect of the alloying elements Zn and Ca on mechanical properties, microstructure, cytocompatibility and degradation rates. Potential differences in bone formation and bone in-growth were also assessed and compared with state-of-the-art non-degradable titanium (Ti)-implanted, sham-operated, and control (non-intervention) groups, using micro-computed tomography, histology and scanning electron microscopy. At 6 and 24 weeks after implantation, serum alkaline phosphatase (ALP), calcium (Ca), and Mg level were measured and bone marrow stromal cells (BMSCs) were isolated for real-time PCR analysis. Results show that ZX00 implants have smaller grain size and superior mechanical properties than XHP-Mg, and that both reveal good biocompatibility in cytocompatibilty tests. ZX00 homogenously degraded with an increased gas accumulation 12 and 24 weeks after implantation, whereas XHP-Mg exhibited higher gas accumulation already at 2 weeks. Serum ALP, Ca, and Mg levels were comparable among all groups and both Mg-based implants led to similar relative expression levels of Alp, Runx2, and Bmp-2 genes at weeks 6 and 24. Histologically, Mg-based implants are superior for new bone tissue formation and bone in-growth compared to Ti implants. Furthermore, by tracking the sequence of multicolor fluorochrome labels, we observed higher mineral apposition rate at week 2 in both Mg-based implants compared to the control groups.

Our findings suggest that (i) ZX00 and XHP-Mg support bone formation and remodeling, (ii) both Mg-based implants are superior to Ti implants in terms of new bone tissue formation and osseointegration, and (iii) ZX00 is more favorable due to its lower degradation rate and moderate gas accumulation.

Keywords: Magnesium-based biomaterials, degradation, femoral bone, fluorochromes, micro-computed tomography

7.1. Introduction

Conventional titanium alloys (Ti) and surgical stainless steel implants are commonly used in orthopedics and traumatology. These permanent metals have many limitations: (i) due to their high Young's modulus, they can induce stress shielding [528]; (ii) although assumed to be inert, they can still release metallic ions that are associated with a potential toxicological risk in long-term [529–531]; and (iii) implant removal, especially in children, is frequent [532–534], generating a second anesthesia, hospitalization and higher economic costs [535].

Only recently, there has been a growing interest in resorbable magnesium (Mg)-based implants in the orthopedic field due to Mg's good biocompatibility and desirable mechanical properties. Since Mg's Young modulus is similar to that of cortical bone, stress shielding is largely avoided, making them a promising candidate for fracture stabilization [80,536]. Moreover, these resorbable implants can be replaced by new bone, demonstrating their potential for pediatric cases [18]. Besides all of these features, Mg^{2+} ions are the fourth-most abundant cations found within the human body and are involved in many metabolic reactions such as protein and nucleic acid synthesis, ion channel modulation, and mitochondrial activity [537].

The mechanical integrity of implants should maintain at least 12 to 18 weeks in adults and 6 weeks in children [352,538,539]. This requires sufficient mechanical strength and low and homogenous degradation speed. Since Mg in pure form is mechanically very soft, alloying and proper processing is necessary to increase its strength to a sufficient level. However, the alloying of almost any element increases the risk of the formation of electrochemical noble precipitates, which would lead to galvanic corrosion and thus to more uneven and rapid degradation. Therefore, poor corrosion resistance of Mg and Mg-based implants is the main limitation in the use of these materials, initiating rapid degradation with gas accumulation in the surrounding tissue [352,540]. To overcome this issue, material scientists favor the synthesis of Mg with alloying elements that ideally benefit corrosion resistance or only moderately decrease it. Most prominently, alloying Mg with rare-earth elements (REEs) can improve strength as well as corrosion and creep resistance [541]. Mg–REE-based alloys, such as Mg–Y, Mg–Gd and Mg–Y–RE–Zr, are currently investigated in preclinical and clinical trials [469,474,476,542]. For instance, May et al. [377] investigated Mg–Y–RE–Zr and Ti screws in a cohort of 48 patients for the treatment of medial malleolar fractures, retrospectively. Results demonstrated that Mg–Y–RE–Zr and Ti screws had similar functional and radiological outcomes but the rate of implant removal was higher with Ti screws [377]. However, the biosafety of REEs is still under concern since higher concentrations are considered mildly toxic

[543,544] and recent studies reported accumulation of REEs in organs of study animals with unknown long-term effects [338,339]. Therefore, synthesis of Mg with only endogenous elements to overcome the biosafety risks associated with REEs may be advised.

Another approach to reduce the degradation rate of Mg is the reduction of impurities. High amounts of impurities are correlated with higher degradation rates since some impurities have exceptionally low solid-solubility in Mg (Co, Cu, Ni, but most notable Fe) and can form cathodic sites, causing microgalvanic corrosion in corrosive media [545]. It was found that the threshold of Fe-content in wrought Mg alloys is as low as 5 ppm [546]. At impurity levels above this tolerance limit, an Fe-rich phase of BCC crystal structure can precipitate, which is significantly more noble than the magnesium matrix, leading to the above-mentioned microgalvanic corrosion.

The purest commercially available Mg (HP-Mg, 99.99 wt.%) comprises typically about 20 – 40 ppm Fe. Even above the threshold of 5 ppm, this shows already improved corrosion resistance with the corrosion rate of HP-Mg found to be lower than that of many Mg alloys [547,548]. From the perspective of application as implant material, however, pure Mg shows low compressive yield strength (65–100 MPa), even after processing, when compared to bone (130–180 MPa). Thus its poor mechanical properties are a major concern and therefore non-alloyed Mg is primarily investigated for non-load-bearing to low-load-bearing indications [80]. For example, Han et al. conducted *in vitro* and *in vivo* studies on high-purity (HP) Mg that shows potential as internal fixation devices for femoral intracondylar fractures [549]. Chen et al. used pure Mg screws to treat trauma-induced femoral head necrosis [550]. Imaging examinations showed that the screw degraded 69.5% at 1 year post-operation and the hip function was significantly improved, with almost completely merged bone flaps [550]. In another clinical study, pure Mg screws (99.99 wt.%) were used for the fixation of vascularized bone grafts in patients with osteonecrosis of the femoral head. After a 1 year follow-up period, results demonstrated that pure Mg screws had better bone-flap stabilization without any adverse effects when compared to the control group (vascularized bone grafting without fixation) [374].

Primarily because of the mechanical limitations of pure Mg and the associated risks of alloying with REEs or other typical alloying elements such as Al, our research focused on Zn and Ca as alloying elements. Previous studies investigated the *in vivo* degradation of ZX00 (Mg–Zn–Ca; <0.5 wt.% Zn and <0.5 wt.% Ca) in small- and large-animal models. Grün et al. demonstrated homogenously degrading ZX00 pins and new bone formation around ZX00 after 24 weeks in rat femurs [187]. Holweg et al. [133] highlighted fracture consolidation without adverse effects

upon implantation of ZX00 screws in a sheep fracture model. Furthermore, in a prospective non-randomized clinical study, Holweg et al. [188] investigated ZX00 screws for the treatment of fractures of the medial malleolus. All ankle fractures were reduced and stabilized sufficiently by two ZX00 screws without any screw loosening or breakage. Additionally, several other studies reported that Mg–Zn–Ca alloys show good biocompatibility and satisfactory antibacterial properties [14,238,551–553].

Ca is the most essential mineral in the human body and plays a significant role in bone function, the vascular system, and many cellular signaling pathways [554]. Since Mg is necessary for the Ca uptake into bone, implanted Mg–Ca alloys can be beneficial for the bone-healing process [555]. Li et al. showed that Mg–Ca pins were not cytotoxic to L-929 cells and induced new bone tissue formation within rabbit femoral shafts [556]. Moreover, the addition of Ca typically improves the mechanical properties of Mg alloys [557] and a recent in vitro study even suggested a strongly improved corrosion resistance of Mg–Ca, attributed to micro-additions of Ca [558].

Similarly, Zn is an essential element for the human body as a co-factor for many enzymes, and plays a significant role in the immune system [559]. The solubility of Zn in Mg is up to 6.2 wt.%, which makes it a great candidate as an alloying element with an exceptionally high strengthening potential. Although Zn content increases the tensile strength of Mg-based biomaterials, more than 1 wt.% of Zn content can decrease the corrosion resistance of the alloy [367]. In small amounts, however, the combined addition of Zn and Ca was found to increase the corrosion resistance [560], similar to the above-mentioned effect of micro-alloying of Ca alone [558]. Both studies are rather novel and have been conducted using a simple NaCl solution as corrosive medium. It was not clear to date whether these effects would also be present in the complex environment of an *in vivo* situation.

In order to purify magnesium to levels below the Fe-tolerance limit of 5 ppm, a distillation device for magnesium was developed that allows to obtain ultrahigh-pure (XHP) magnesium with an Fe-content < 1 ppm [561].

In the present study, we directly compare the degradation of ZX00 implants with ultrahigh-purity Mg implants and the related bone response to these Mg alloys in juvenile healthy rats over a study period of 6 and 24 weeks. ZX00 was also synthesized in ultrahigh-purity quality to ensure that potential differences can purely be attributed to the alloying elements Zn and Ca. To the best of our knowledge this is the first time that Mg and a Mg alloy, both with an Fe content lower than 1 ppm, are directly compared in an in vivo situation and sequential fluorochrome tracking throughout a study period of 24 weeks. As a state-of-the-art control, Ti

implants were used. Additionally, we added a sham surgery model (same surgical intervention without implant) and control animals (without any intervention) to this study. Based on literature and preliminary data, we hypothesized that ZX00 implants are superior to XHP-Mg in regard of degradation, bone formation and remodeling.

7.2. Material and methods

7.2.1.Material Preparation

In a first step, commercially available magnesium was ultrahigh-purified with a custom distillation process [561]. Subsequently, one part of the material was alloyed with zinc (Zn, 99.9999%) and calcium (Ca, 99.95%) in a nominal composition of 0.45 wt.% Zn and 0.45 wt.% Ca, subjected to a solution heat-treatment and extruded to rods of 6 mm. This material is named "ZX00" according to the standardized nomenclature for magnesium alloys. The second part of the ultrahigh-purified magnesium was equally extruded to rods of 6 mm and is named "XHP-Mg". After extrusion, alloy composition and impurity content of ZX00 and XHP-Mg were determined by inductively coupled plasma optical emission spectrometry (ICP-OES, alloying elements Zn and Ca) and glow discharge mass spectrometry (trace elements).
Mechanical properties of ZX00 and XHP-Mg were determined by tensile tests according to ISO 6892-1 (strain rate = 0.001 $^{s-1}$, n = 6).

7.2.2. Microstructure characterization

Cross-sections orthogonal to the extrusion direction of ZX00 and XHP-Mg were used to characterize their microstructure. These surfaces were mechanically ground with P600, P1200, P2500, and P4000 SiC abrasive paper, and then were subjected to ion-beam milling with Ar-ions (Hitachi IM4000). Using scanning electron microscopy (SEM), the microstructure was examined with a Hitachi SU-8000 SEM coupled with an UltraDry EDS detector (ThermoScientificTM). Image J was used to analyze grain size by the intercept method according to ASTM E112-10.

7.2.3. In vitro degradation test

In vitro degradation rate was determined by immersion in simulated body fluid (composition: [133]) according to the weight-loss method. Discs of diameter 5.5 mm and thickness 0.5 mm (n=6/group) were prepared from ZX00 and XHP-Mg by cutting and subsequently grinding with P4000 SiC abrasive paper. The simulated body fluid was maintained at a controlled temperature of 37°C ± 0.5°C and at controlled pH of 7.4 ± 0.05 by the injection of CO_2. After

3 weeks, the specimens were extracted, degradation products chemically removed (50 g CrO_3, 2 g $AgNO_3$, 4 g $Bi(NO_3)_2$ in 250 mL deionized water), and the mass loss to the pre-immersed state measured. The degradation rate was then determined according to

$$DR = \frac{\Delta m}{t.\rho.A} \qquad (7.1)$$

where Δm is the mass loss, t is the immersion duration, ρ is the sample material's density and A is the sample surface.

7.2.4. In vitro cytocompatibility test

The CellTiter 96® AQueous One Solution Cell Proliferation Assay (Promega, Austria) was used to test the toxicity and proliferation of the osteoblast precursor cell line (MC3T3-E1, ECACC, Salisbury, UK) on ZX00 and XHP-Mg disc samples (10 mm in diameter and 1 mm thickness). Cells were cultured with Dulbecco's modified eagle medium (DMEM, Gibco) supplied with 10% fetal bovine serum, 100 U/mL penicillin, and 100 µg/mL streptomycin at humidified atmosphere of 5% CO_2 at 37 °C. Discs were immersed in DMEM to prepare the extracts of alloys at 37 °C for 24 h. The discs' area-to-solution volume ratio was 3 cm^2/mL according to ISO 10993-12 as previously described in [562]. MC3T3-E1 cells were seeded in 96-well plates with a cell density of 2×10^4 per well. After 24 hours, the culture media in each well was replaced with 100 µL of extracts, with a concentration at 100% and 50% of extracts, respectively. The negative control was selected as culture medium, and the positive control group was selected as culture medium with 10% dimethyl sulfoxide (DMSO, Sigma-Aldrich, Austria). After 1, 3, and 5 days of incubation, the extracts were replaced with new culture medium added with 20 µL MTS/PMS solution per well, then incubated for 2 h. The optical density (OD) of each well was detected at 490 nm using a microplate reader (CLARIOstar Plus, BMG Labtech).

7.2.5.Animal experiments

7.2.5.1.Ethical statement

All animal experiments were approved by the Austrian Federal Ministry of Science and Research (Permit Number: GZ 66.010/0066-V/3b/2019) and performed under established guidelines (European Convention for the Protection of Vertebrate Animals Used for Experimental and Other Scientific Purposes). The 3R principles were conducted during the entire animal study.

7.2.5.2.Surgery and experimental design

Cylindrical pins (1.6 mm in diameter and 8 mm in length) were manufactured from ZX00 and XHP-Mg and formed the main investigation groups. As a control group, Ti pins of 1.5 mm diameter and 8 mm length (Hofer GmbH & Co KG, Austria) were used. Further details on sample preparation and sterilization are published elsewhere [133]. Female Sprague–Dawley® (SD; Janvier Labs, Saint Berthevin, France) rats (n = 12) with a bodyweight of 200 g and 6 weeks of age were used in this study. All rats were kept on normal chow for the entire study and housed in a conventional facility (12-hour light/dark cycle with free access to food and water). Bodyweights of rats were recorded before operations and sacrifice. The rats were divided into two groups: the 6 weeks' short-term evaluation group (n = 6) and the 24 weeks' mid-term evaluation group (n = 6). Each rat in each group underwent bilateral, bicortical and diaphyseal implantation of cylindrical ZX00, XHP-Mg, or Ti pins into both femurs, respectively. Moreover, five SD® rats underwent the same surgical intervention without implant, thereby serving as sham controls. Additionally, five SD® rats were used as control group (no intervention) for the short-term evaluation group. The entire surgical and post-operative procedures were described in [185]. For general anesthesia, volatile isoflurane followed by a Fentanyl/Midazolam/Medetomidine mixture was administered. Anesthesia was antagonized by an intraperitoneal injection of Naloxone, Flumazenil and Atipamezole. Post-operatively, animals received Caprofen on the day of surgery and Piritramid several days post-surgery. The entire procedure for anesthesia and analgesia including dosage and administration has been previously published in [370]. Six and 24 weeks after surgery, rats were euthanized with 25 mg sodium thiopental (Thiopental® Sandoz, Sandoz GmbH, Kundl, Austria). All femoral bones were explanted; one femur was used for bone marrow isolation and another one was stored in isopropanol at 4°C for histological and SEM-EDX analyses.

7.2.5.3. Rat bone marrow stromal cell isolation

Rat bone marrow stromal cells (rBMSCs) were isolated from bone marrow as previously described [563,564]. Briefly, both epiphyses were cut off and bone marrow was flushed with alpha minimum essential medium (α-MEM, Gibco) supplemented with 10% fetal bovine serum, 100 U/mL penicillin, and 100 µg/mL streptomycin into centrifuge tubes using a sterile syringe. The extract was homogenized by pipetting and centrifuged at 2000 rpm for 5 min. The cell pellet was resuspended in complete α-MEM, seeded onto 75 cm^2 tissue culture flasks, and incubated at humidified atmosphere of 5% CO^2 at 37°C. The adherent cells grown to 70% confluence were defined as passage zero (P0) cells.

7.2.5.4. Real-time quantitative polymerase chain reaction (qRT-PCR) analysis

The relative expression level of osteogenic related genes such as alkaline phosphatase (*Alp*), runt-related transcription factor (*Runx2*), and bone morphogenic protein (*Bmp2*) were evaluated by quantitative real-time (qRT)-PCR. Briefly, isolated rBMSCs from each animal were cultured until P3. Total RNA was extracted using RNeasy Mini Kit (Qiagen, Germany) and quantified by nanodrop (NanoDrop 2000c, Thermo Scientific). Complementary DNA (cDNA) was synthesized with random hexamers (Life Technologies, Carlsbad, CA, USA) and dNTPs using SuperScript III Reverse Transcriptase (Life Technologies, Carlsbad, CA, USA). The qRT-PCR was performed in an iQ5 Real-Time PCR Detection System (Bio-Rad Laboratories, Irvine, CA, USA) using cDNA, gene specific primers for BMSCs (Table 1), and iTaq Universal SYBR Green Supermix (Bio-Rad Laboratories, Irvine, CA, USA). Relative gene expression was calculated using the $2^{-\Delta CT}$ method and normalized with the GAPDH reference gene, considering threshold cycles <35. The primer sequences are listed in Table S7.1.

7.2.5.5. Serum ALP-Ca-Mg level

End-blood was collected and serum was isolated by centrifugation at 13,000 rpm for 10 minutes. Collected serum samples were stored at -80°C for biochemical analysis. Serum alkaline phosphatase (ALP), Ca and Mg, which are biomarkers to monitor bone disorders, metabolic disorders, and liver toxicity conditions [565,566], were measured using a colorimetric method with an autoanalyzer (Dri-Chem-NX500, Fujifilm, Austria).

7.2.5.6.Micro-computed tomography

In vivo micro-computed tomography (µCT; SkyScan1276, Bruker µCT) scans were performed immediately after surgery and 2, 6, 12, 18, and 24 weeks after surgical intervention (n = 10) at a resolution of 35 µm voxel size. For these studies, animals were anaesthetized with volatile isoflurane (Forane©, Abbot AG, Baar, Switzerland). Ex vivo µCT imaging of extracted femoral bones was performed using a high-resolution protocol (80 kV voltage, 200 µA current, 10.1 µm voxel size). The scanned data were reconstructed and converted into DICOM and analyzed with the software Mimics, Version 23.0 (Materialise, Leuven, Belgium). The segmentation threshold was set at 850 to 3900 HU, 5514 to 13400 HU, and -1024 to 116 HU for the Mg-based pins, Ti pins, and gas volume, respectively. Implant surface, implant volume, and gas surface were evaluated and three-dimensional (3D) morphometric analysis was performed with Mimics. The values obtained for implant volume and implant surface area were subsequently

used to determine the degradation rate, DRi, as previously described [187], according the following equation:

$$\mathrm{DR}_i = \frac{\Delta V_i}{\bar{S}_i \, \Delta t}, \qquad (6.2)$$

with i the observation time point, ΔV_i the volume change, $\bar{S}_i$ the average surface area between two observation time points t_i and t_{i-1}, and Δt the difference between the two observation time points.

7.2.5.7. Fluorochrome application and visualization

Sequential fluorochrome markers (Sigma Aldrich, Austria) were administered to monitor the mineralization process of new bone formation. Subcutaneous administration with tetracycline (25 mg/kg), calcein green (10 mg/kg), xylenol orange (90 mg/kg), and alizarin red complexone (30 mg/kg) was performed 5 days prior and 3 days post-surgery as well as 2, 4, 6, 12, 18 weeks after surgery and 5 days prior to sacrifice, respectively. Alizarin red complexone was used for the mid-term animal group at week 18 because of its short plasma half-lives [567]. Tetracycline was dissolved in PBS (25 mg/mL), and calcein (20 mg/mL), xylenol orange (90 mg/mL), and alizarin red complexone (30 mg/mL) were dissolved in 1.4% isotonic $NaHCO_3$ (Sigma Aldrich, Austria). All fluorochromes were adjusted to pH 7.4 and filtered before injection. Explanted bone sections were visualized under a Nikon A1R+ confocal microscope (Nikon, Tokyo, Japan) before histological staining. Details of the fluorochromes are given in Table S7.2.

7.2.5.8. Histological and histomorphometric analysis

For histological examination, extracted femurs from each group were fixed in isopropanol, dehydrated by ethanol 100%, and embedded in Technovit 9100 New (Heraeus Kulzer, Wehrheim, Germany) as previously described [397]. The blocks were ground using a sequence of abrasive papers (P320, P1200, P4000 and polished with 0.3 µm aluminum oxide) under water with the cut and grinding equipment EXAKT (EXAKT Advanced Technologies GmbH, Norderstedt, Germany). The sections were stained with Levai & Laczko dye including methylene blue/azure II solution and basic fuchsin solution, as described in [568]. The bone tissues were imaged using a custom-made Olympus BX53 scanning system (OLYMPUS EUROPA SE & CO. KG, Hamburg, Germany).

Dynamic histomorphometry was performed with labeled fluorochromes and measured from visualized bone sections. Mineral apposition rate (MAR) was calculated by measuring the distance between two fluorochromes and dividing this by the number of weeks separated between the fluorochrome injections. Quantitative analysis was performed using a digital

image analysis program (Adobe Photoshop CC Software 2020, San Jose, CA, USA). For histology examinations and dynamic histomorphometry, one femur per animal was used (n=5/group).

7.2.5.9. SEM and EDX analysis

Embedded cross-section specimens for SEM examination (n=3-5/group) were fabricated as histological slides and mechanically polished with silicon carbide (SiC) paper P2500 and P4000, followed by broad argon ion-beam milling (IM4000, Hitachi, Japan). To reduce the effect of the embedding material´s charging, specimens were carbon sputtered (Leica AC200). Using a scanning electron microscope (SEM, SU8000, Hitachi, Japan), the degradation interface morphology of samples from Ti and each Mg group was analyzed. Applying EDX mapping, and point and line scans analyses, the elemental distribution on the sham, new bone, and corrosion layers was determined (UltraDry EDS Detector, Thermo Scientific).

7.2.6. Data Analysis

All data is presented as mean ± standard deviation (SD). Statistical analysis was performed using two-way ANOVA followed by Tukey's post-hoc test using the GraphPad Prism 9.0 software (GraphPad Software, San Diego, USA). Differences between bodyweights within groups were assessed by one-way ANOVA using Tukey's post-hoc test. One animal from the XHP-Mg group was excluded from the midterm evaluation group due to monocortical implantation, therefore the number of samples was eight for this group. The differences in implant volume, surface, gas volume, and qRT-PCR analysis were assessed via mixed-effect analysis followed by Sidak's multiple comparisons test. For SEM and EDX analyses, a Kruskal-Wallis test was used to compare nonparametric independent samples, followed by the Mann-Whitney test to determine the differences between groups applying the SPSS software (version 27, SPSS statistics, IBM®). Statistical significance was confirmed when the *p*-value was < 0.05.

7.3. Results

The synthesized XHP-Mg reached a purity level of >99.999 wt% (except Zn) and even after alloying with Zn and Ca (ZX00) the purity level could essentially be kept at this level. The Fe-content of XHP-Mg and ZX00 was found to be below 1 ppm by weight for both materials (Table 7.3).

Figure 7.1a shows characteristic stress-strain curves obtained for ZX00 and XHP-Mg. While XHP-Mg exhibits a rather low tensile yield strength of 35.6 ± 2.3 MPa followed by strain hardening up to an ultimate tensile strength of 159 ± 4.2 MPa, ZX00 shows a pronounced yield-point phenomenon with a significantly higher tensile yield strength of 253.0 ± 8.7 MPa and a significantly higher ultimate tensile strength of 271.9 ± 3.9 MPa compared to XHP-Mg. Elongation at fracture was also found to be higher for ZX00 than XHP-Mg with 20.9 ± 0.7% and 15.8 ± 0.5%, respectively. Figure 7.1b depicts SEM backscattered electron (BSE) images of the microstructures of ZX00 and XHP-Mg. In the recrystallized regions of the ZX00 alloy, uniformly equiaxed grains with an average grain size of 2.54 ± 0.21 µm and some non-recrystallized areas are observed (Figure 7.1b, left). In the ZX00 alloy, intermetallic particles (IMPs) were found, and elemental analysis of these IMPs was conducted using EDX analyses. EDX confirmed that these particles are rich in Mg and Ca (Figure S7.1). In contrast, Zn was found to be nearly uniformly distributed throughout the matrix. In comparison, XHP-Mg exhibited significantly coarser grains with several slips and twin deformations, as can be seen in the backscattered electron image in Figure 7.1b, right.

7.3.1. In vitro degradation and cytocompatibility

The *in vitro* degradation rate of ZX00 was determined with 0.29 ± 0.03 mm/yr versus 0.33 ± 0.05 mm/yr for XHP-Mg. Although the mean value was smaller for ZX00, statistical significance was not found (Figure 7.1c).

Cytocompatibility results of ZX00 and XHP-Mg (Figure 7.1d) show that at day 1 the proliferation of MC3T3-E1 cells cultured in 100% extracts of ZX00 and XHP-Mg, or 50% extract of ZX00, was significantly decreased compared with the negative control. However, at day 3, cells cultured in 50% concentration of both ZX00 and XHP-Mg, or 100% concentration of XHP-Mg, had similar proliferation as the negative control group. Nonetheless, the proliferation of MC3T3-E1 cells cultured in 50% XHP-Mg extract was significantly lower on day 5. The OD value of the positive control group (DMEM+10%DMSO) was negative on days 3 and 5, indicating no cell viability (data not shown).

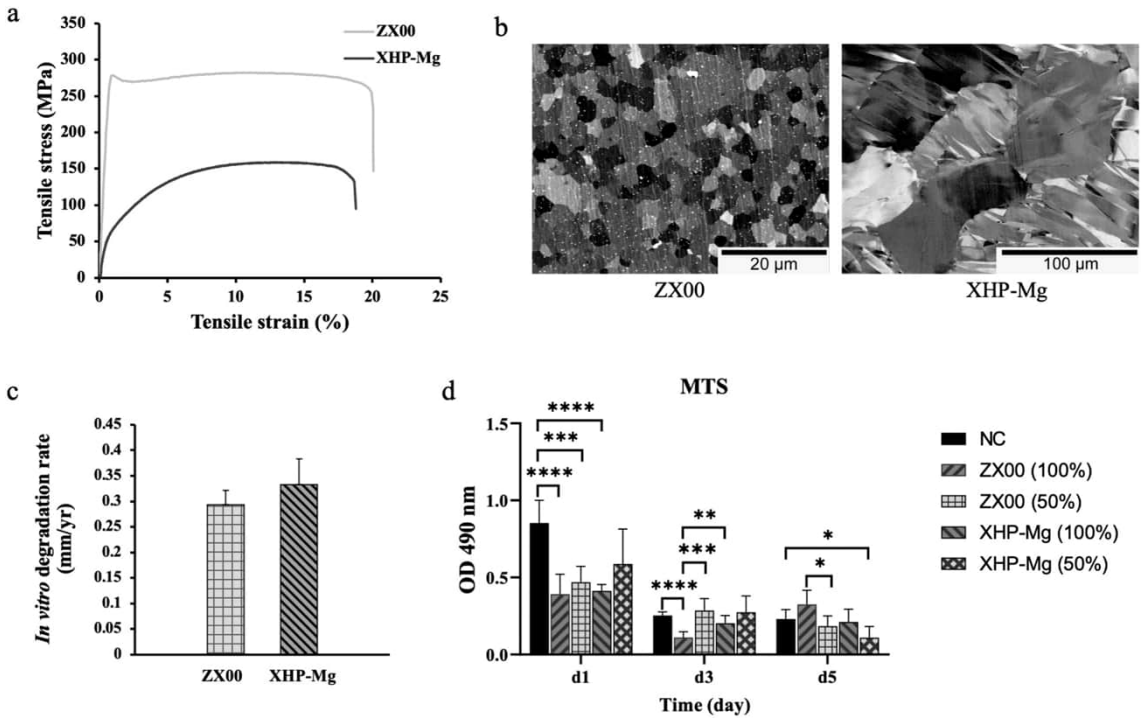

Figure 7.1. *In vitro* testing results. a) Typical stress-strain curves as obtained by tensile testing for ZX00 and XHP-Mg. b) Backscattered electron images of ZX00 and XHP-Mg revealing the materials' microstructure. c) Degradation rates as determined by immersion in simulated body fluid for 3 weeks; Kruskal-Wallis H test resulted in a *p*-value of 0.2. d) Cytocompatibility results of MC3T3-E1 cells cultured in 100 % and 50 % concentrations of ZX00 and XHP-Mg extracts on days 1, 3, and 5. Three independent measurements with three replicates were performed. Two-way ANOVA followed by Tukey's multiple comparisons test was applied (n = 9/group). *p < 0.05, **p < 0.01, ***p < 0.001, ****p < 0.0001.

7.3.2. Bodyweight records and biochemical analysis

Three different implant types (ZX00, XHP-Mg and Ti) were bicortically implanted into rat femurs. Moreover, one group underwent sham surgery, whereas another group did not undergo surgery and therefore served as control group. In order to investigate the effect of implantation and sham surgery, the bodyweight of all rats was recorded before (week 0) as well as after surgery (weeks 6 and 24). Animals gained weight throughout the entire study period and there was no statistical difference between the bodyweight of implanted animal groups and the sham

group (Figure S7.2a Figure 2a). We measured ALP, Ca, and Mg markers from collected end-blood samples at weeks 6 and 24. Serum ALP levels were significantly elevated in the Ti group compared to the sham group at week 6, which significantly leveled out at week 24 (Figure S7.2b). Although, there was no significant difference in Ca levels between the Mg-based implantation groups (XHP-Mg and ZX00), rats within the Ti group showed significantly higher Ca levels at week 6 compared to the control group, with the difference decreasing at week 24 (Figure S7.2c-d). At that time point, a significant difference between the Ti and XHP group was observed. Moreover, no significant difference was found in serum Mg levels at both time points (Figure S7.2c-d).

7.3.3. In vivo µCT scans

Figure 7.2. shows representative µCT images of one animal per group, providing examples of the bone response to the implants and sham surgery as well as the degradation process of the ZX00 and XHP-Mg implants, respectively. We observed osseointegration immediately after 2 weeks for all groups. The ZX00 group showed new bone tissue and callus formation already at week 2 (Figure 7.2, blue arrow). Moderate gas accumulation was mainly observed over the entire study period in the medullary cavity (Figure 7.2, yellow arrows). Moreover, gas accumulation was observed outside the bone in the surrounding tissue at weeks 18 and 24 (Figure 7.2, white arrows). Similarly, distinct callus formation was observed at week 2, representing new bone tissue formation around implants in the XHP-Mg group (Figure 7.2, blue arrow head). As expected, Ti pins maintained the original morphology, and osseointegration was observable after 2 weeks. For the sham group, new bone tissue formation was observed already after 2 weeks and the bone totally healed after 6 weeks (Figure 7.2, white arrow heads).

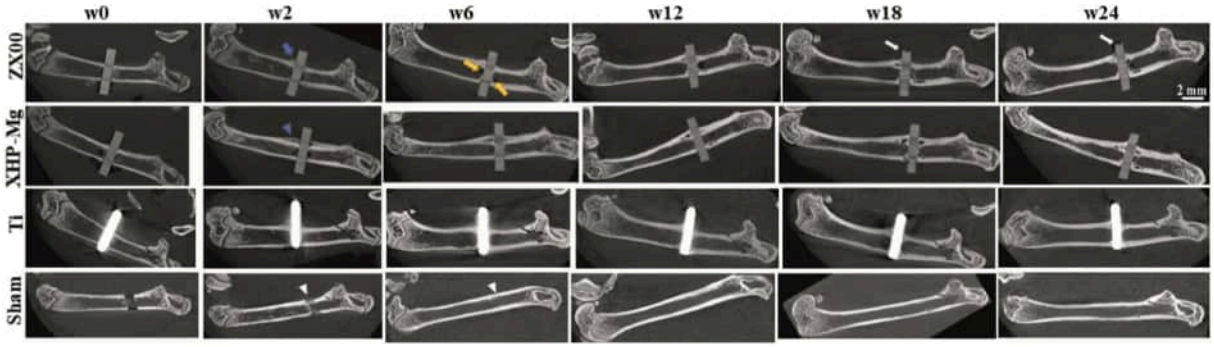

Figure 7.2. *In vivo* low-to-medium resolution µCT scans over the entire study period of 24 weeks. a) ZX00 group, b) XHP-Mg group, c) Ti group, and d) Sham group. µCT images at a resolution of 35 µm voxel size represent the bone response and degradation process of the pins. Osseointegration was observed in all groups after 6 weeks. The blue arrow and blue arrow head represent callus formation and new bone tissue formation around the implant, respectively. During ZX00 and XHP-Mg degradation, radiolucent zones appeared within the

medullary cavity, indicated by yellow arrows. The white arrows and white arrow heads represent gas accumulation in the surrounding tissue and bone healing for the sham group, respectively.

7.3.4. Implant volume and surface

To quantify the differences between ZX00 and XHP-Mg pins, *in vivo* µCT scans were reconstructed and implant volume and surface area were calculated with MIMICS software. The 3-D reconstructed µCT images indicated moderate volume loss and gas accumulation in both the ZX00 and XHP-Mg groups. As expected, there was no difference observable for the state-of-the-art control Ti (Figure 7.3). At the beginning, the average ZX00 and XHP-Mg implant volumes were 15.81 ± 0.43 mm³ and 15.46 ± 0.46 mm³, respectively. ZX00 pins showed a moderate increase in implant volume until week 6 (Figure 7.4a). However, after that time, the implant volume significantly decreased with time. On the other hand, XHP-Mg pins immediately started to degrade after implantation.

Quantification of XHP-Mg implant volume revealed markedly decreased values between week 18 and 24 (Figure 7.4b). However, implant volume loss was more pronounced in the XHP-Mg group and significantly differed between ZX00 and XHP-Mg at weeks 2, 6, 18, and 24. After 24 weeks, approximately 14.25% (ZX00) and 9.03% (XHP-Mg) of the respective initial implant volume was degraded. In parallel to implant-volume loss, we observed an increased implant surface area until week 6, which was more pronounced in the ZX00 group (Figure 7.4b). After 6 weeks, the implant surface markedly decreased in ZX00 and XHP-Mg until 18 weeks after implantation, which then leveled out until the end of the study. We additionally calculated the average degradation rate according to equation (1), considering the volume and surface of the time points at 0 and 24 weeks. The average degradation rates throughout the 24 weeks of implantation were higher in the XHP-Mg group (0.08 ±0.06 mm/year) than in the ZX00 group (0.06 ±0.04 mm/year).

7.3.5. Gas volume

Similarly, gas volume was quantified from 3-D reconstructed images of implants with MIMICS software. Both ZX00 and XHP-Mg pins showed moderate gas accumulation (Figure 7.4c). However, we observed more pronounced gas accumulation in the XHP-Mg group at week 2. The gas accumulation slightly increased over time and reached 2 mm3 at week 24 in the ZX00 group. The gas accumulation was faster in the XHP-Mg group and already increased to almost 2 mm3 at week 2 and peaked at 12 weeks. The degradation acceleration between weeks 6 and 12 was accompanied by a pronounced increase in gas volume in both groups. However, gas

accumulation did not exceed 2 mm^3 throughout the entire study period for both ZX00 and XHP-Mg.

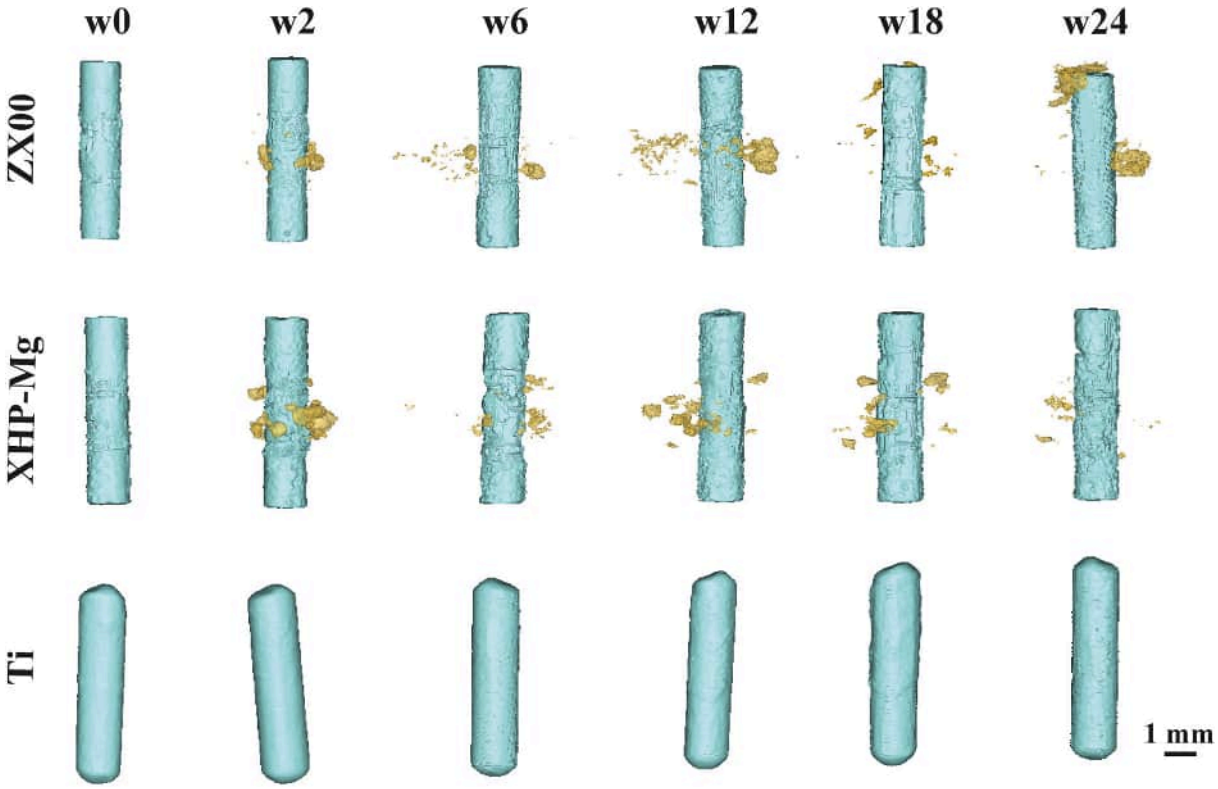

Figure 7.3. Three-dimensional reconstructions of µCT images of one representative animal followed over the entire study period of 24 weeks. a) ZX00, b) XHP-Mg, and c) Ti pins were 3D-reconstructed using MIMICS Software. Cyan indicates the implant, whereas yellowish-brown indicates gas accumulation.

7.3.6. Gene expression analysis of osteogenesis related genes

To understand the mechanisms by which Mg-based implants could promote higher bone formation, the expression of osteogenesis-related genes in rBMSC isolated from animals of the different groups was quantified. In general, the early osteogenic marker *Alp* showed the highest expression levels in rBMSCs among all other markers (Figure S7.3a). In detail, *Alp* expression levels were significantly upregulated in the Ti group at week 24 compared to week 6. However, gene expression level of *Runx2* was significantly downregulated, compared to the control group at week 6 (Figure S7.3b). *Bmp-2* expression levels did not differ significantly between the different groups and time points (Figure S7.3c). In summary, there was no significant difference in osteogenic gene expression between Mg-based implants and control groups at any time point.

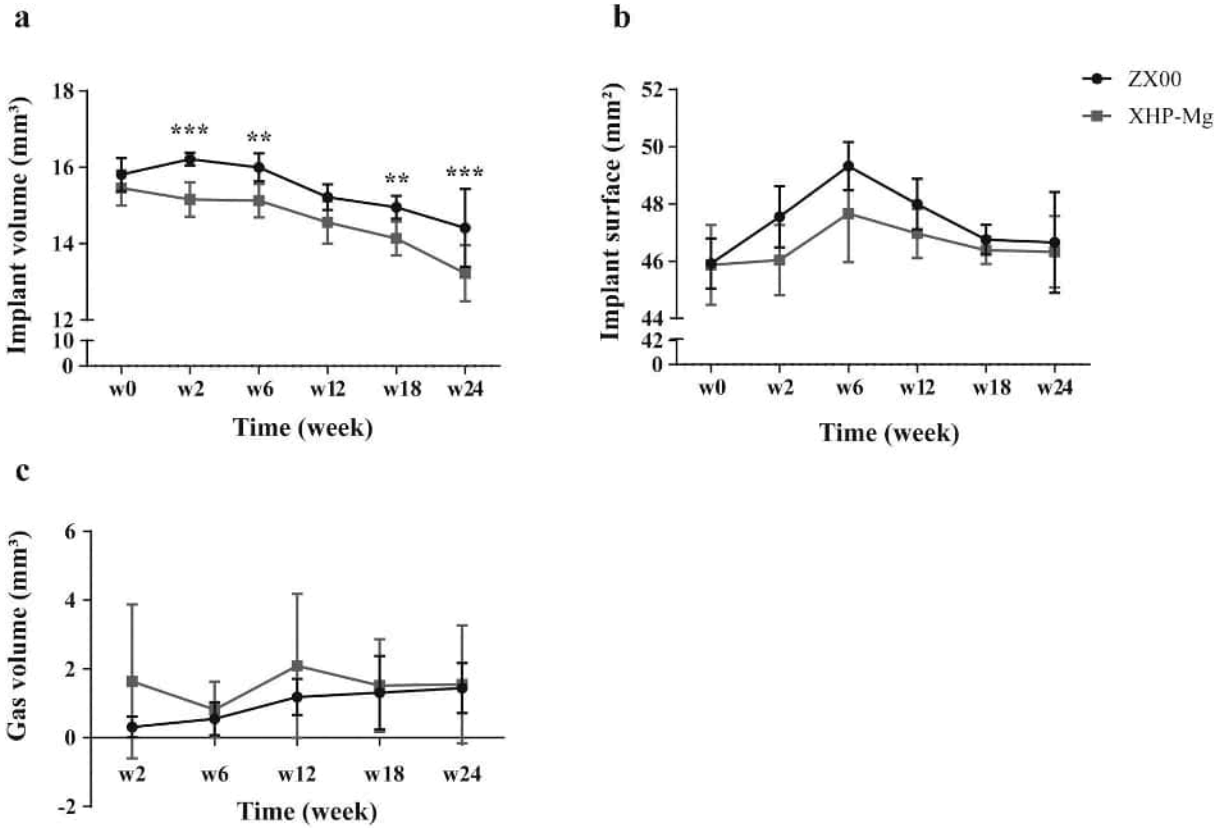

Figure 7.4. Quantification of the degradation performance of implanted ZX00 and XHP-Mg over 24 weeks. a) Implant volume, b) implant surface, and c) gas volume. Mixed-effect analysis followed by Sidak's multiple comparisons test was performed (ZX00, n=10; XHP-Mg, n=8). $**p<0.001$, $***p<0.0001$.

7.3.7. Histology and histomorphometry

Histological images showed that there was progressive bone remodeling at the operation site for all groups (Figure 7.5). ZX00 and XHP-Mg revealed a histologically similar appearance, i.e. a homogeneous and occasionally lacuna-shaped degradation. Both Mg alloys were still preserved to a large extent after 24 weeks and surrounded by corrosion products with newly formed bone in direct contact to the degradation layer. These newly formed bone clusters grew and formed tapestry-like or thicker bone bridges on the corrosion layer to span the medullary cavity. The bone-degradation layer contact was more pronounced in the ZX00 group (Figure 7.5a,f). Furthermore, we observed a direct bone-to-implant contact for ZX00 at week 6 (Figure 7.5a). The gas voids were more pronounced in the XHP-Mg group (Figure 7.5g-l). Ti implants especially from week 6 fell out during the histology procedures. Histological images indicated partly soft tissue between the Ti surfaces and newly formed bone, confirming poor bone-to-implant attachment, especially from week 24 (Figure 7.5m-r, Figure S7.4,orange arrowheads). Newly formed bone also bridged the medullary cavity often with thicker bone bridges than in the Mg groups (Figure S7.4).

We observed remnants of drilled holes for the sham group at week 6 (Figure S7.5, blue arrow). At week 24, the newly formed bone was mainly built as laminar bone for the sham group, but at week 6 the new bone of the sham group was woven bone especially on the periosteal side. Control groups kept the normal bone morphology with woven bone in areas of chondral growth and lamellar bone in areas of appositional growth (Figure S7.5). Overall, we did not observe direct bone-to-implant contact (except for the ZX00 implants) and any sclerotic areas or fibrous capsules for all groups.

Newly formed bone tissue was analyzed via sequential fluorochrome labeling throughout the study periods of 6 and 24 weeks. The yellow (tetracycline), green (calcein), orange (xylenol orange), and red (alizarin complexone) bands represent regions of Ca precipitation labeled by fluorochromes at different time points of tissue mineralization (Figure S7.6a). The mineral apposition rate (MAR) was quantitively analyzed for all implants for the study periods of 6 weeks (Figure S7.6b) and 24 weeks (Figure 76.6c). Calcein was observed on a wider area surrounding the ZX00 and XHP-Mg implants compared to the other groups, indicating more extended new bone tissue formation at the first 2 weeks post-operation (Figure S7.6a, white arrow). However, there was no significant difference between the groups in terms of MAR due to the resulting high standard deviations (Figure S7.6b). At later time points all groups showed similar or reduced MAR. The MAR was significantly decreased from week 2 to week 18 for the ZX00 group and from week 6 to week 24 for the Ti group (Figure 8c, $p<0.05$).

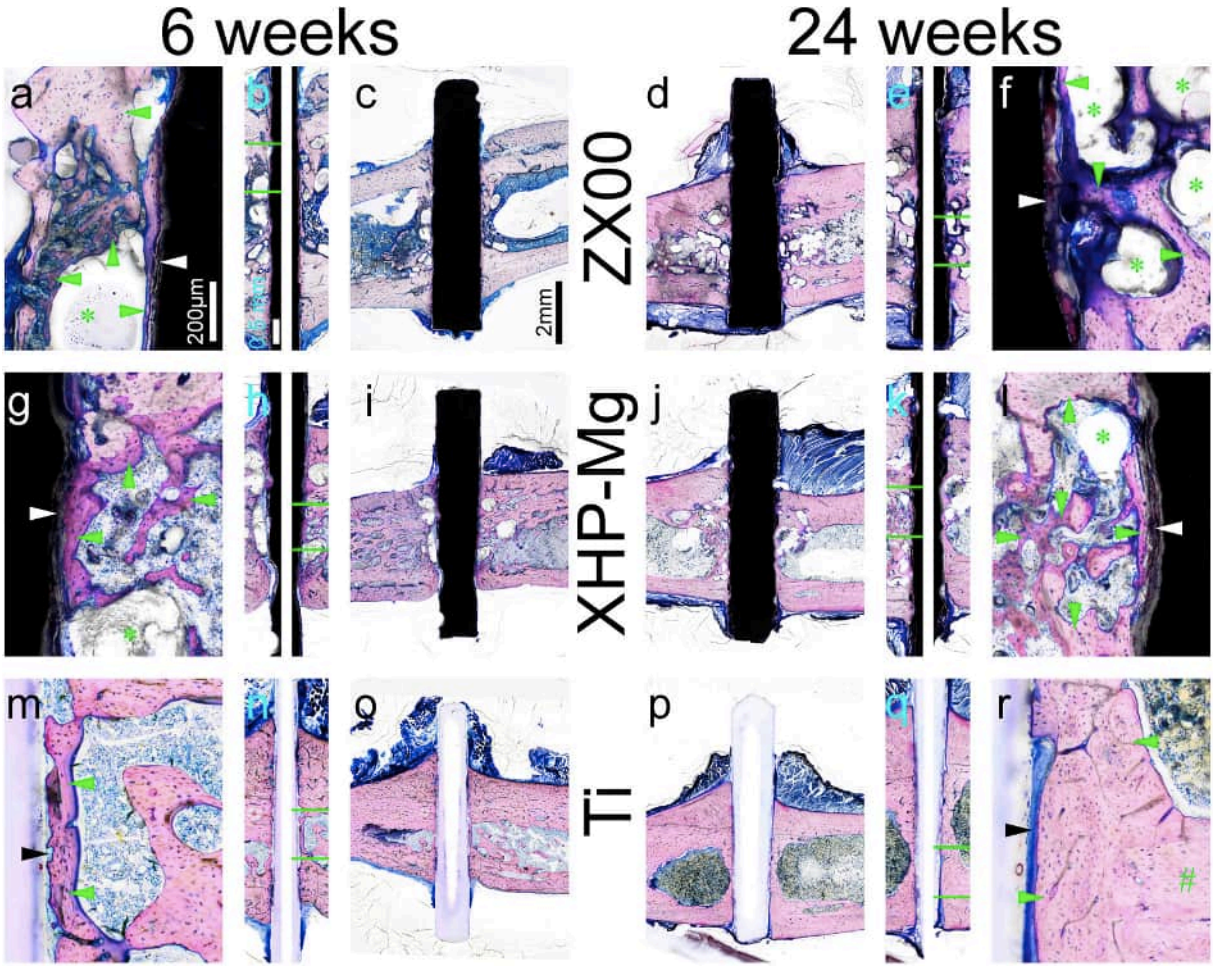

Figure 7.5. Representative images of Levai-Laczko-stained bone sections at 6 and 24 weeks post-operation. ZX00 (a-f), XHP-Mg (g-l), and Ti (m-r). Overviews (c, d, i, j, o, p) and magnifications of whole bone area to implant contact (b, e, h, k, n, q) with green markings for areas of details forof bone-to-implant contact (a, f, g, l, m, r). Histological morphology at the bone-implant interfaces indicates good osseointegration for the Mg-based implants. Ti shows a large amount of new bone formation (green arrowheads), but the attachment to the implant seems weak, as revealed by the soft tissue between bone and implant (black arrowhead) and the detachment of the implant during histological processing. Old bone is still visible as pale pink (labeled with octothorpe in r). In the Mg alloys (a-l) new bone formation (intense pink, marked with green arrowheads) is often separated from the metal (black) by a degradation layer (white arrowheads). Void areas indicate gas formation in white (marked with green asterisks) in contrast to soft tissue, such as connective tissue and muscle, and uncalcified bone matrix (shown in blue).

7.3.8. SEM and EDX analysis

To determine the bone-implant interface morphologies of the ZX00, XHP-Mg, and Ti groups as well as bone morphologies of the sham and control groups, SEM-EDX analysis was performed 6 and 24 weeks after implantation. At both designated time points a corrosion layer formed on the surface of the Mg-based implants (Figure 7.6.a, b, f, and g). The ZX00 group exhibited a thinner corrosion layer after 6 weeks and a thicker degradation layer after 24 weeks in both cortical bone (CB) and intramedullary cavity (IMC) compartments compared to the XHP-Mg group (Table 7.1).

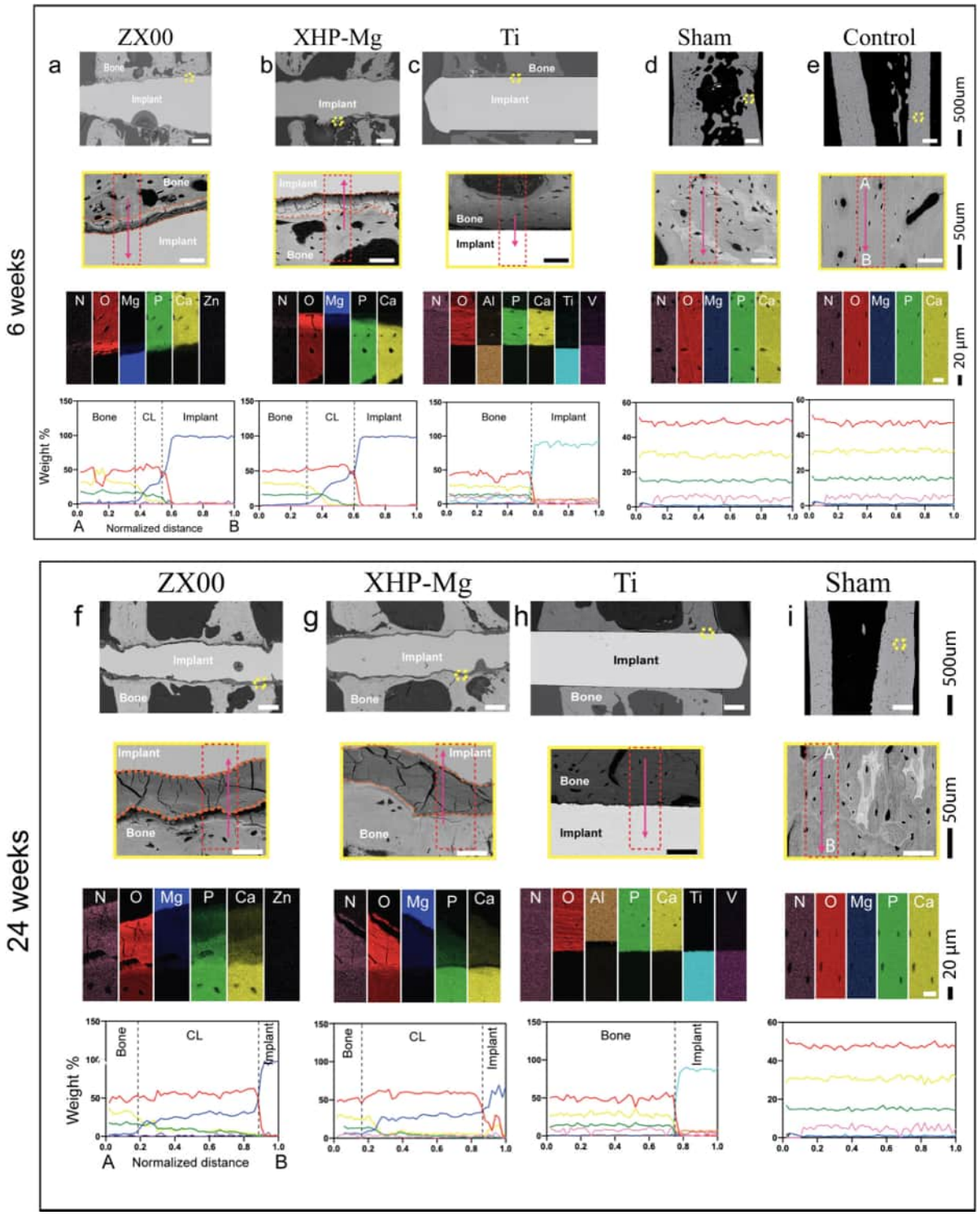

Figure 7.6. Characterization of bone-implant interface in ZX00 (a, f), XHP-Mg (b, g), and Ti groups (c, h), as well as bone in the sham (d, i) and control groups (e), after 6 and 24 weeks of *in vivo* implantation. *First and second rows*: backscattered electron images (BSE), third row: X-ray elemental mapping, and fourth row: EDX line scans. The yellow dotted squares in the first row denote randomly selected regions for higher-magnification analysis (second row). The orange dashed lines indicate the formed corrosion layers in the Mg materials. *Third row*: nitrogen (N) in pink, oxygen (O) in red, Mg in blue, phosphorus (P) in green, Ca in yellow, Zn in purple, aluminum (Al) in orange, titanium (Ti) in light blue, and vanadium (V) in violet represent the distribution of elements in the bone-implant interface, as determined by X-ray elemental mapping in the red-dashed box regions of the second row. *Fourth row*: EDX line scans following the direction of the pink arrows displayed in the second row. Three regions are detected at the bone-implant interface in the XHP-Mg and ZX00 groups (see black dashed lines): bone, corrosion layer (CL) and residual implant zones, whereas no CL and only traces of Ti were visible in the bone adjacent to the Ti implants.

The corrosion layers were not dense and contained numerous cracks (Figure 7.6.a, b, f, and g). After 6 and 24 weeks, new bone formed in direct contact with the degradation layers in the Mg groups (Figure 7.6.a, b, f, and g) as also observed by histology (Figure 7.5. a, g, f, l). In the Ti group, regions of the pin implant surfaces were surrounded by new bone anchored to the metal surface (Figure 7.6c, h) after 6 and 24 weeks. The sham groups exhibited a disorganized, bone-like structure with a woven appearance (Figure 7.6d, i), whereas the control group exhibited a well-organized lamellar bone (Figure 7.6e).

The chemical composition of new bone adjacent to the pin implants was determined using EDX analysis. Nitrogen (N), oxygen (O), phosphorus (P), Ca, and traces of Mg were the main components in the bone tissue of the Mg-alloy groups, sham, and control, whereas only traces of Ti were found in the surrounding bone of the Ti group (Figure 7.7a).

In addition, various grey levels were observed in the BSE images of the sham groups, where bright zones (indicated by red arrows) exhibited slightly higher Ca concentrations at 6 and 24 weeks post-operation, indicating varying degrees of mineralization (Figure S7.7). Furthermore, after 6 and 24 weeks, the weight-percentage elemental distribution of N, Mg, O, P, Na and Ca in the bone was comparable in all groups, with minor increases in Ca and P and a decrease in O in the surrounding bone of the Ti group after 24 weeks (Figure 7.7a) (Figure 7.6, *fourth row*).

The corrosion layer formed on both Mg alloys consists primarily of O, Mg, P and Ca with traces of Cl, K, and Zn present only in the ZX00 group. However, as shown by the line scans in Figure 7.6 (*fourth row*) and the EDX point analysis in Figure 7.7c, the chemical distribution of each element within the Mg groups is not uniform throughout the entire corrosion layer. Whereas the outer portion of the degradation layer of both Mg groups tends to be rich in Ca and P, the XHP-Mg group exhibits higher Ca and lower P concentrations than the ZX00 group. The Ca/P atomic ratio of the corrosion layers determined by EDX was 0.3 in the inner part for both Mg groups whereas the outer region of the corrosion layer in the XHP group was higher than in the ZX00 group (1.4 ± 0.4 and 0.7 ± 0.1, respectively). Nitrogen was only detected in the corrosion layer formed on the XHP-Mg group after 6 weeks, which may be from organic matter of the surrounding tissues. In addition, the Mg-Ca/P atomic ratio of the bone adjacent to the corrosion layers is comparable in the control and sham groups, but slightly higher compared to these groups in the ZX00 group at 6 weeks and the XHP-Mg group after 6 and 24 weeks (1.74 ± 0.09, 1.78 ± 0.03 and 1.79 ± 0.04, respectively). In contrast, the Mg-Ca/P atomic

ratio in the Ti group was significantly lower after 6 weeks (1.48 ± 0.02) than in the XHP Mg group after 6 and 24 weeks (Figure 7.7c).

Table 7.1. Corrosion layer thickness in the XHP-Mg and ZX00 groups in the cortical bone (CB) and in the intramedullary cavity (IMC) compartments after 6 and 24 weeks of *in vivo* implantation.

Alloy/time point	XHP-Mg		ZX00	
Week 6	CB	IMC CB	CB	IMC
	32.6 ± 15.4 µm	38.5 ± 14.5 µm	16.8 ± 7.4 µm	16.9 ± 6.0 µm
Week 24	CB	IMC	CB	IMC
	74.1 ± 34.3 µm	51.57 ± 15.13 µm	86 ± 35 µm	82.4 ± 37.6 µm

7.4. Discussion

The objective of this study was to investigate the effect of the alloying elements Zn and Ca on biocompatibility and degradation rate of magnesium-based implants. While Zn and Ca are a deliberate and crucial addition for the strengthening of the material (Figure 7.1 and [133,569]), the data demonstrates that the two alloying elements lead additionally to a reduction in degradation rate *in vitro* and *in vivo*.

It is known that impurities influence the degradation of Mg in corrosive media significantly. Especially elements of relatively high electrochemical potential and at the same time low solubility in Mg are detrimental and can lead to a strong increase in degradation rate [358]. When present above the solubility limit those elements form intermetallic compounds that are generally electrochemically cathodic to the Mg matrix and thereby cause microgalvanic corrosion [111,547]. The most relevant examples for such behavior are Fe, Co, Cu and Ni, whose solubility limit in Mg is in the order of 5 ppm. Therefore, for the present study, Mg was purified to such an extraordinary extent that all those elements are in solid solution (concentration of each element below 1 ppm by weight). This minimizes all other effects on degradation and biocompatibility, except for the alloying elements.

In order to evaluate the degradation behavior of Mg alloyed with Zn and Ca in comparison to unalloyed Mg and the corresponding bone response, we first investigated the microstructure, *in vitro* degradation, and cytocompatibility of ZX00 and XHP-Mg implants. Then, we bicortically implanted cylindrical ZX00 (ultrahigh-purified Mg–Zn–Ca), XHP-Mg (ultrahigh-purified Mg), and Ti pins into both femurs of juvenile, healthy Sprague–Dawley® rats.

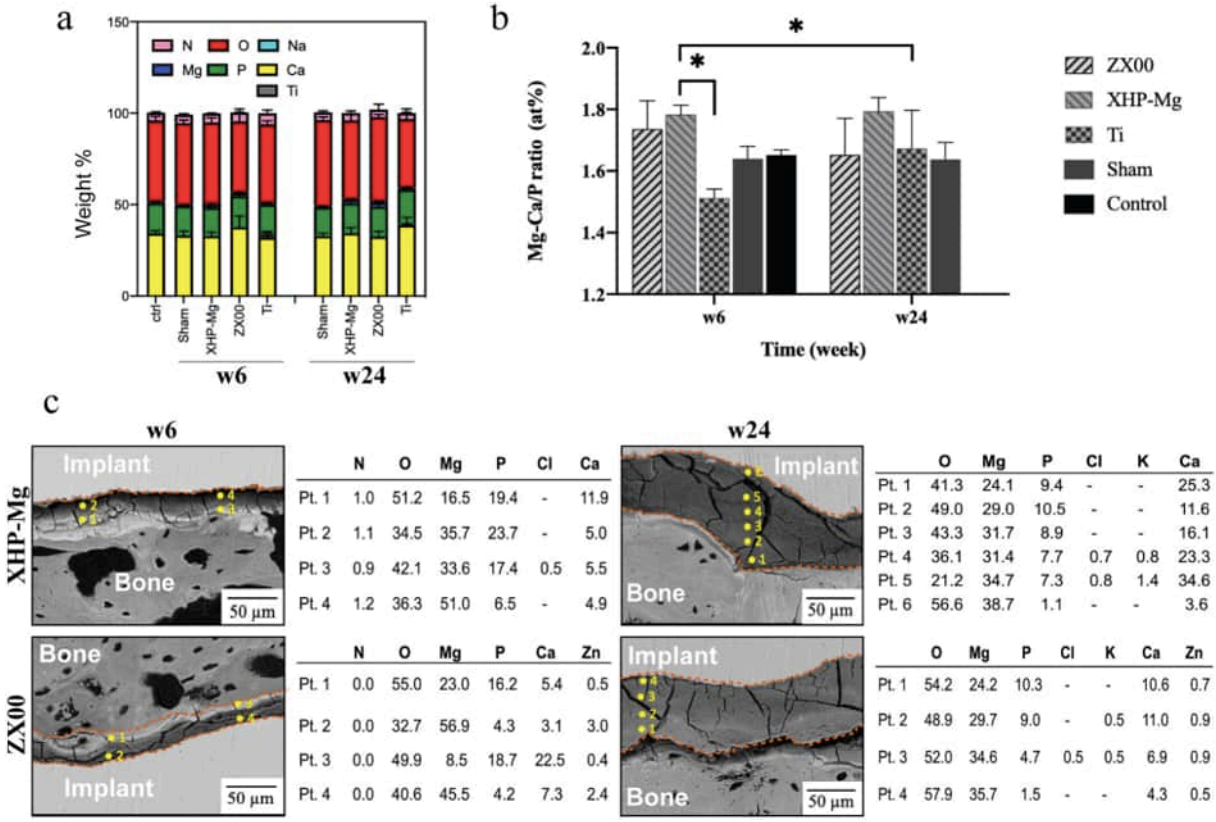

w6	N	O	Mg	P	Cl	Ca
Pt. 1	1.0	51.2	16.5	19.4	-	11.9
Pt. 2	1.1	34.5	35.7	23.7	-	5.0
Pt. 3	0.9	42.1	33.6	17.4	0.5	5.5
Pt. 4	1.2	36.3	51.0	6.5	-	4.9

w24	O	Mg	P	Cl	K	Ca
Pt. 1	41.3	24.1	9.4	-	-	25.3
Pt. 2	49.0	29.0	10.5	-	-	11.6
Pt. 3	43.3	31.7	8.9	-	-	16.1
Pt. 4	36.1	31.4	7.7	0.7	0.8	23.3
Pt. 5	21.2	34.7	7.3	0.8	1.4	34.6
Pt. 6	56.6	38.7	1.1	-	-	3.6

w6	N	O	Mg	P	Ca	Zn
Pt. 1	0.0	55.0	23.0	16.2	5.4	0.5
Pt. 2	0.0	32.7	56.9	4.3	3.1	3.0
Pt. 3	0.0	49.9	8.5	18.7	22.5	0.4
Pt. 4	0.0	40.6	45.5	4.2	7.3	2.4

w24	O	Mg	P	Cl	K	Ca	Zn
Pt. 1	54.2	24.2	10.3	-	-	10.6	0.7
Pt. 2	48.9	29.7	9.0	-	0.5	11.0	0.9
Pt. 3	52.0	34.6	4.7	0.5	0.5	6.9	0.9
Pt. 4	57.9	35.7	1.5	-	-	4.3	0.5

Figure 7.7. Energy dispersive X-ray (EDX) analysis of embedded cross-sections. a) Weight percentage (wt%) of nitrogen (N) in pink, oxygen (O) in red, magnesium (Mg) in blue, phosphorus (P) in green, sodium (Na) in light blue, calcium (Ca) in yellow, and titanium (Ti) in grey as mean ± standard deviation of bone in the control and sham groups as well as bone in the vicinity of the ZX00, XHP-Mg, and Ti implants after 6 and 24 weeks of implant placement. b) Cross-sectional morphology and EDX point analysis of the corrosion layers following implantation of the XHP-Mg and ZX00 groups for 6 and 24 weeks, indicating different elemental distributions within the degradation layers. c) Changes in the Mg–Ca/P ratio in the bone regions of the control and sham groups as well as the bone regions in the vicinity of the XHP-Mg, ZX00 and Ti groups at 6 and 24 weeks post-implantation. ∗$p<0.05$.

Microstructure characterization showed that ZX00 has a smaller grain size than XHP-Mg and comprises Mg- and Ca-rich intermetallic particles. Additionally, we performed mechanical tests to prove the suitability of ZX00 as a load-bearing implant material. The results clearly demonstrate the superior mechanical properties of ZX00 compared to XHP-Mg. This can be attributed to the small grain size, which leads to grain-size strengthening according to the well-known Hall-Petch relationship, and is particularly efficient in Mg alloys that generally reveal a rather high Hall-Petch coefficient [569]. This grain refinement is achieved mainly by adding the alloying element Ca, facilitating precipitation of Ca-rich intermetallic particles (IMPs) of composition Mg_2Ca by appropriate thermal treatment, and subsequent hot extrusion. During the hot-extrusion process the Mg2Ca IMPs effectively pin grain boundaries and thus prevent otherwise unavoidable thermally-driven grain growth [569]. The result is ZX00 with an extraordinary fine microstructure and high strength, while XHP-Mg exhibits the expected coarse microstructure with lower strength.

The results of the *in vitro* cytocompatibility tests indicate a favorable performance of both ZX00 and XHP-Mg after 24 h. Although Mg and Ca ions are known to promote cell proliferation [252,570], the 50% extract of the ZX00 alloy supported cell proliferation better than the 100% extract on day 3. The significant reduction of MC3T3-E1 cell viability might be related to increased osmolarity of the cell media because of higher Ca and Mg-ion contents in the 100% extract. However, on day 5 both the ZX00 and XHP-Mg extracts with 100% concentration supported cell proliferation better than the 50% extracts. Our results thus also confirm that both ZX00 and XHP-Mg implants do not have toxic effects on cell proliferation and cell viability [224,240,571].

To evaluate the mid-term safety of the ZX00 and XHP-Mg implants, biochemical analysis of serum ALP, Ca, and Mg was assessed from the Sprague–Dawley rats at weeks 6 and 24 post-operation. We found for all implant groups a consistent ALP level with no significant differences to the control and sham groups. Although ALP occurs in several tissues, liver is the main source of ALP [572]. Consequently, we can demonstrate in this work that the implantation of Ti as well as the degradation of ZX00 and XHP-Mg does not cause any disturbances in the liver at designated time points. Similarly, implantation of Mg-based pins did not significantly affect the Mg concentration in serum for both time points, indicating normal liver and kidney function in all animals with Mg-based implants. Hence, we assume the excretion of excess Mg^{2+} ions from the kidneys. Other *in vivo* studies similarly demonstrated that serum ALP, Ca, and Mg levels were not affected by the degradation of Mg-based implants, thereby supporting our results [176,438,573]. However, we found a significant difference between the Ti and control groups in terms of serum ALP and Ca level at week 6. Since there was no direct bone-to-implant contact in the Ti group, we suggest that increased bone resorption as a result of foreign-body reaction at the beginning may be the reason of elevated ALP and Ca serum level at week 6. In line with this result, Kawamoto et al. observed remarkable bone resorption in the bone-marrow side of Ti-implanted rat femurs as a result of granulation tissue after 15 and 30 days of implantation [574].

We examined implant volume and surface changes as well as gas accumulation after ZX00 and XHP-Mg implantation via *in vivo* µCT analysis throughout the entire study period of 24 weeks. Accordingly, the degradation rate was computed for ZX00 and XHP-Mg pins over the entire study period. We found a slower degradation rate for ZX00 (0.06 ± 0.04 mm/year or 0.18 ± 0.12 µm/day) when compared to XHP-Mg (0.08 ± 0.06 mm/year or 0.23 ± 0.18 µm/day). It is important to note that gas accumulation was more pronounced in the XHP-Mg group at week 2, which supports the implant-volume loss results. Similarly, Grün et al. [187] demonstrated a

homogenous *in vivo* degradation performance and moderate gas release for ZX00 implants with a degradation rate of 0.21 ± 0.46 µm/day. The *in vivo* degradation rates of pure Mg pins (99.99 wt.%) reported in literature range from 0.15 mm/year [175] to 0.4 mm/year [575]. Furthermore, Hofstetter et al. [545] found an average *in vivo* degradation rate for XHP-Mg pins of 0.013 mm/year for a period of 3 months. Unexpectedly, implant volume of ZX00 apparently increased until week 6 (Figure 5a). However, since a small amount of gas was detected for ZX00 in weeks 2 and 6 (Figure 5c), magnesium degradation was also certainly existent during this period. The measured increase in implant volume may be explained by segmentation uncertainties from µCT images caused by the similar grey values of cortical bone and the magnesium implants (Figure 7.3). Likewise, implant surface was found to increase for both Mg-based materials until week 6. This phenomenon was reported before and can be sufficiently explained by an increased surface roughness caused by implant degradation [187].

It has already been demonstrated that the lower amount of Zn in ZX00 compared to well-known Mg–Zn–Ca alloys, such as ZX10 with 1 wt% Zn, leads to lower in vitro degradation rates [133]. Here, we show that the combined alloying of Zn and Ca in small amounts leads even to smaller degradation rates than the intrinsic degradation rate of magnesium. While this effect is indicated from our in vitro degradation tests, it is clearly visible *in vivo* where we found significantly lower degradation rates, reduced gas evolution and a denser corrosion layer of ZX00 compared to XHP-Mg. This is in accordance with results by Deng et al. [558], who demonstrated that micro-additions of Ca restrict the cathodic water reduction kinetics of Mg corrosion, and at the same time a protective surface film forms that reduces anodic oxidation. This can generate a degradation rate that is even lower than that of ultrahigh-purity Mg. While these results were obtained from measurements in NaCl solution, our data indicates the same in simulated body fluid *in vitro* and confirms it *in vivo*, suggesting that the described mechanisms are still present and dominating in the highly complex and dynamic *in vivo* environment.

Besides implant degradation the response of surrounding bone tissue is of particular interest. Only sufficient osseointegration allows the necessary transfer of mechanical loads that is needed to stabilize bone fracture. Osseointegration is a dynamic process where different types of cells and cytokines are involved to promote osteoblast recruitment, osteogenesis, and eventually new bone tissue formation [576]. Failure in osseointegration results in fibrous tissue at the bone-implant interface, which may cause loosening of the implant and eventually implant failure [577]. Representative ex vivo images illustrated the remarkably good coherence between histological sections and also indicated good osseointegration for both Mg-based

implants (Figure S7.8). In general, we did not observe any sclerotic areas or multinucleated giant cells for all groups. Histological and SEM evaluations displayed new bone formation in direct contact to the degradation layer in ZX00 and XHP-Mg pins, whereas there was partially less direct bone-to-implant contact in the Ti groups, indicating poorer osseointegration. As a result of poorer osseointegration, all Ti implants fell out during histological procedures. In line with our results, Castellani et al. [289] revealed that Mg-based implants are superior to Ti implants with respect to both, bone-implant interface strength and osseointegration. Moreover, we observed pronounced bone bridges at week 24 in the Ti group as a result of encapsulation of the Ti implants. The immunological host reaction promoted bone-tissue formation on the Ti surface to isolate new foreign material from the bone-marrow space. Similarly, Trindade et al. revealed that bone resorption was suppressed around Ti implants compared to the sham group after 4 weeks of implantation due to foreign-body reaction. As a result, Ti implants are isolated from the bone marrow through surface sheath of bone build-up [578]. In line with our histological evaluations, relative *Runx2* expression levels were significantly decreased in the Ti group compared to the control group at week 6, which correlates with osteoblast differentiation, matrix production, and mineralization during bone formation [579]. As a result, the early osteogenic marker Alp was significantly increased between weeks 6 and 24 in the Ti group, which may indicate a maintenance of bone homeostasis.

Additionally, qualitative histological evaluation indicated new vessel formation together with bone bridges at the degradation layer of Mg-based implants at the time point of 24 weeks. This is attributed to enhanced vascularization of the bone marrow and can explain the more pronounced implant volume loss in the medullary cavity. Since gas bubbles at the bone-implant interface may greatly affect osseointegration [580], we did not observe direct bone-to-implant contact for XHP-Mg implants in contrast to ZX00. The bone bridging here was different to that of the Ti group in that it was thinner, grew in steps, and had spaces in between occupied by soft tissue or void. The SEM and EDX analyses revealed that the corrosion layers on both ZX00 and XHP-Mg groups are composed of O, Mg, Ca and P, with traces of Zn present only in the ZX00 group. While a Ca–P rich outer portion of the corrosion layer was observed in both Mg-based implants, the XHP-Mg group exhibited degradation layers with higher Ca content than the ZX00 group. In line with previous studies [175,179,183], the presence of Mg and O indicates the formation of $Mg(OH)_2$ while the presence of Ca and P suggests the formation of calcium phosphates in the corrosion products.

In order to monitor new bone formation over the study periods of 6 and 24 weeks, sequential fluorochrome markers were administered subcutaneously into the juvenile healthy rats.

Although there were no significant differences between the Mg-based implants and control groups on osteogenic gene expression level, we observed wider green bands (calcein) in the ZX00 and XHP-Mg groups, indicating enhanced new bone tissue formation at week 2 for the Mg implants. Quantification of MAR showed higher MAR at week 2, thereby confirming the qualitative fluorochrome examinations. Hence, better osseointegration and osteogenesis were achieved with the ZX00 and XHP-Mg groups 2 weeks after implantation. Similarly, Janning et al. [581] found the highest MAR at week 2 in $Mg(OH)_2$ cylinders implanted in rabbit femur condyles, and in other studies MAR was higher in the Mg-implant groups compared to stainless steel [582,583]. Since we have a growing-animal model, we observed reduced new bone tissue formation in all animals regardless of the experimental groups after 12 weeks. However, sequential fluorochrome labeling is a limited technique in terms of color discrimination using conventional image analysis and different filter sets [567]. Besides, labeling of mineralized regions depends on many factors such as Ca affinity, fluorochrome metabolization, and half-live in *in vivo* tests [584]. One limitation of this study was to discriminate the different fluorochrome markers over the entire study period. Therefore, MAR evaluations included less animal numbers than other evaluations, especially for the 24 weeks animal groups. Nevertheless, to the best of our knowledge, this study provides the first data on fluorochrome tracking in a long-term study of more than 8 weeks. We were able to visualize fluorochromes, which were injected 3 days after implantation, at the 24 weeks sacrifice time points. Thus, we suggest fluorochrome tracking to be a powerful tool to examine newly formed bone tissue and also to minimize the number of animals in mid-and long-term *in vivo* studies.

Taken together we demonstrated that implant degradation in juvenile healthy rats is comparable for both, ZX00 and XHP-Mg implants. Both implant types support new bone tissue formation and in-growth. Mg-based implants were superior to Ti in terms of osseointegration and new bone-tissue formation [577], especially within the first weeks after operation. Therefore, ZX00 and XHP-Mg implants have great potential to overcome the disadvantages of permanent implants, such as secondary surgery for implant removal, stress shielding, and toxicological risk. Nevertheless, the specific molecular and biochemical mechanisms underlying osteogenesis are still not fully elucidated and need to be clarifiedilluminated in future studies on Mg-based implants.

7.5. Conclusions

We demonstrate the safe *in vitro* and *in vivo* degradation performance of two different Mg implants (ZX00 and XHP-Mg) and the corresponding bone response in a healthy, juvenile

growing-rat model. Both Mg implants have great potential to overcome the disadvantages of conventional Ti implants because they do not only degrade but also reveal better osseointegration and promote new bone-tissue formation within the first weeks after operation. Similar to rare-earth elements, the addition of Zn and Ca was found to reduce the degradation rate of ultrahigh-purity Mg even further, however without the potential risk of biosafety. We therefore consider ZX00 as a very interesting material for biodegradable implant applications because of its lower degradation rate and moderate gas accumulation, which are closely related to osseointegration, long-term bone repairs, and biological safety. Furthermore, the excellent mechanical properties of ZX00 can provide a wide range of clinical applications, not only in the orthopedic field but also in other applications such as cardiovascular stenting, sports medicine, or absorbable surgical clips.

Supplementary materials

Table S7.1. Osteogenesis-related genes and primers.

Genes	**Forward primer (5'–3')**	**Reverse primer (5'–3')**
Gapdh	TGCCACTCAGAAGACTGTGG	TTCAGCTCTGGGATGACCTT
Alp	GACAAGAAGCCCTTCACAGC	CTGGGCCTGGTAGTTGTTGT
Runx2	CCGATGGACCGTGGTT	CAGCAGAGGCATTTCGTAGCT
Bmp-2	CACGAGAATGGACGTGCCC	GCAACACTAGAAGACAGCGG

Table S7.2. Details of the applied fluorochromes.

Fluorochromes	Dosage (mg/kg)	Fluorochrome Injection Time for short-term animals (6 w)	Fluorochrome Injection Time for mid-term animals (24 w)
Tetracycline	25	Pre-surgery (-day 5), post-surgery (+day 3), week 6	Pre-surgery(-day 5), post-surgery (+day 3), week 24
Calcein	20	Week 2	Week 2, week 12
Xylenol Orange	90	Week 4	Week 6
Alizarin Red	30	x	Week 18

Table S7.3. Concentration of alloying elements and impurities of ZX00 and XHP-Mg. Only elements >0.1 ppm wt. are listed. Trace elements entail a relative error of ≈20% (instrument uncertainty).

Element	Concentration in ppm wt.	
	ZX00	XHP-Mg
Zn	4140 ± 30	68
Ca	4840 ± 70	0.03
Na	0.22	<0.01
Al	0.91	0.22
Si	1	0.67
S	0.27	0.52
Cl	0.23	0.42
Cr	0.27	<0.05
Mn	0.87	0.94
Fe	0.79	0.36
Cu	0.54	0.08
Pb	7.8	5.7

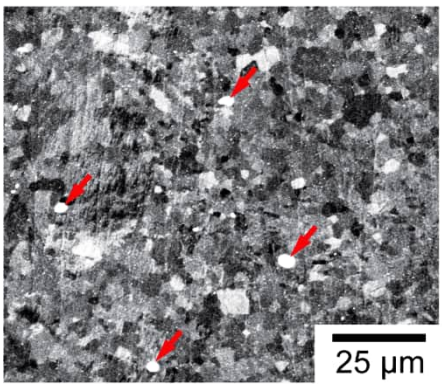

Element	wt.%
O	0.7 ± 0.2
Mg	71.4 ± 5.4
Ca	26.0 ± 5.1
Zn	1.9 ± 0.3

Figure S7.1. BSE image of ZX00 alloy illustrating the bright intermetallic particles (IMPs) denoted by red arrows and corresponding EDXs results of IMPs.

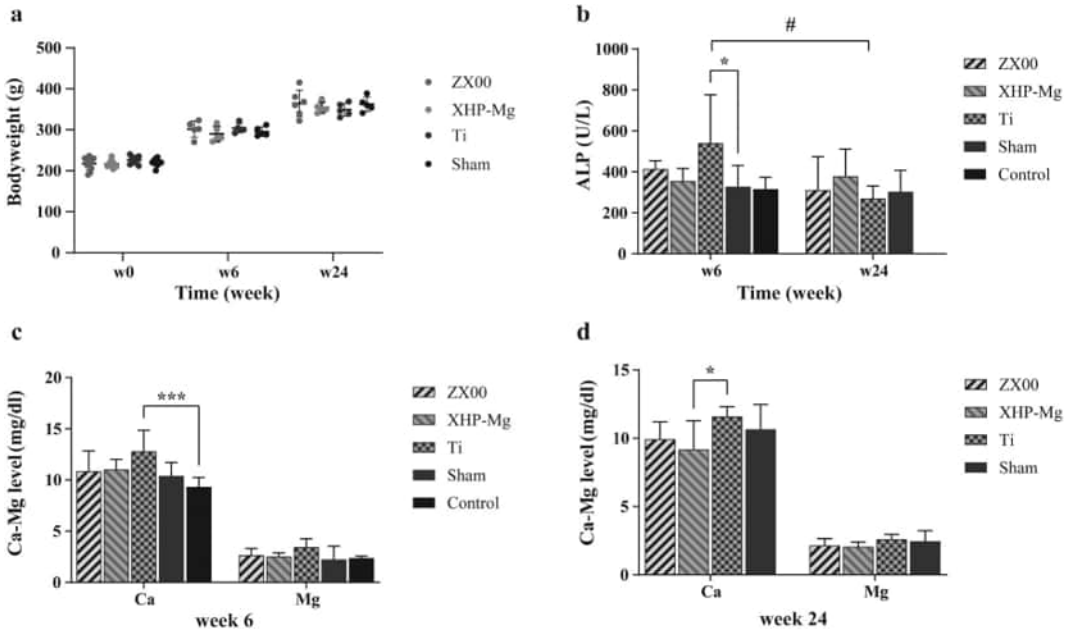

Figure S7.2. Bodyweight records and serum ALP, Ca, and Mg measurements. a) Bodyweight was recorded before as well as 6 and 24 weeks after surgery. b-d) Serum ALP, Ca and Mg levels were measured with colorimetric and potentiometric methods 6 and 24 weeks after surgery (week 0, n=10; weeks 6 and 24, n=5). Data represents the arithmetic mean ± standard deviation (SD). ∗p<0.05, ∗∗∗p<0.001, #p<0.05.

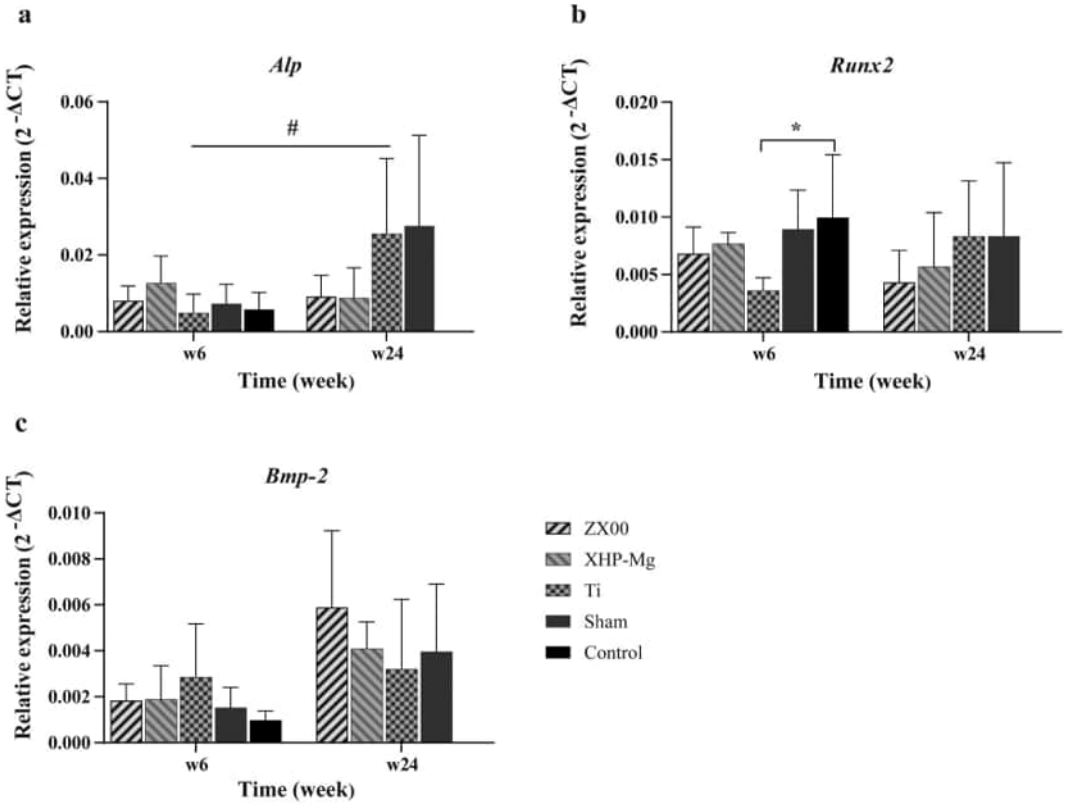

Figure S7.3. Relative gene expression levels of a) Alp, b) Runx2, and c) Bmp-2. Mixed-effect analysis followed by Sidak's multiple comparisons test was performed (ZX00, Ti, Sham, Control, n=5; XHP-Mg, n=4). ∗p<0.05.

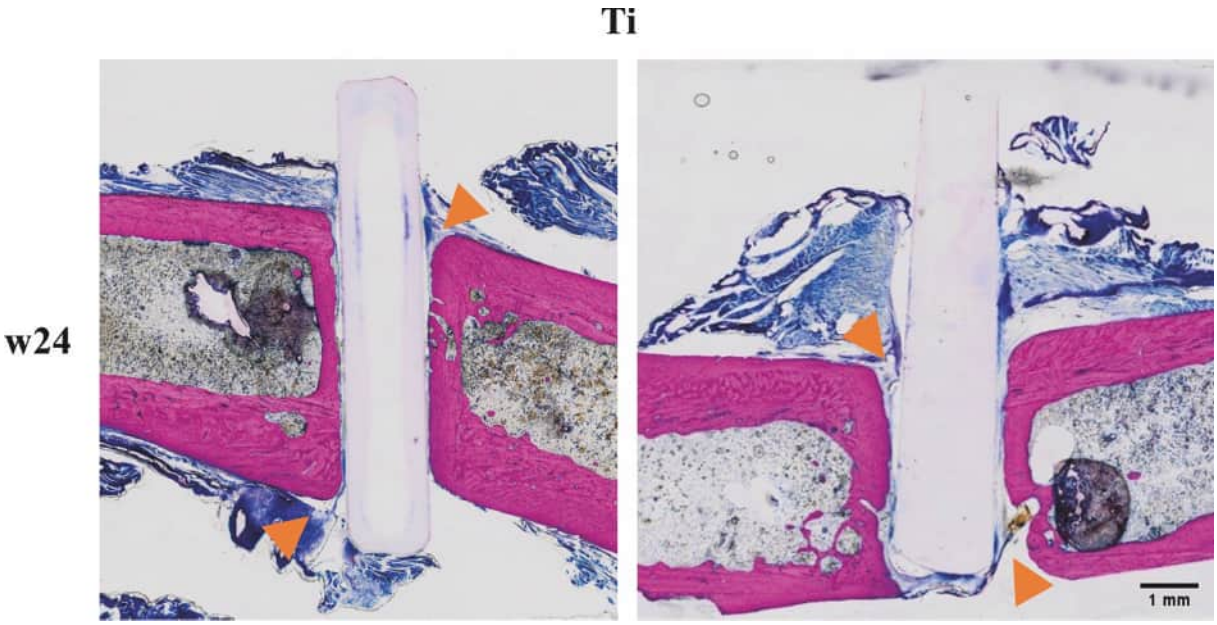

Figure S7.4. Levai-Laczko-stained Ti group bone sections at 24 weeks post-operation. Orange arrowheads indicate the poor bone-to-implant attachment at week 24. Scale bar = 1 mm.

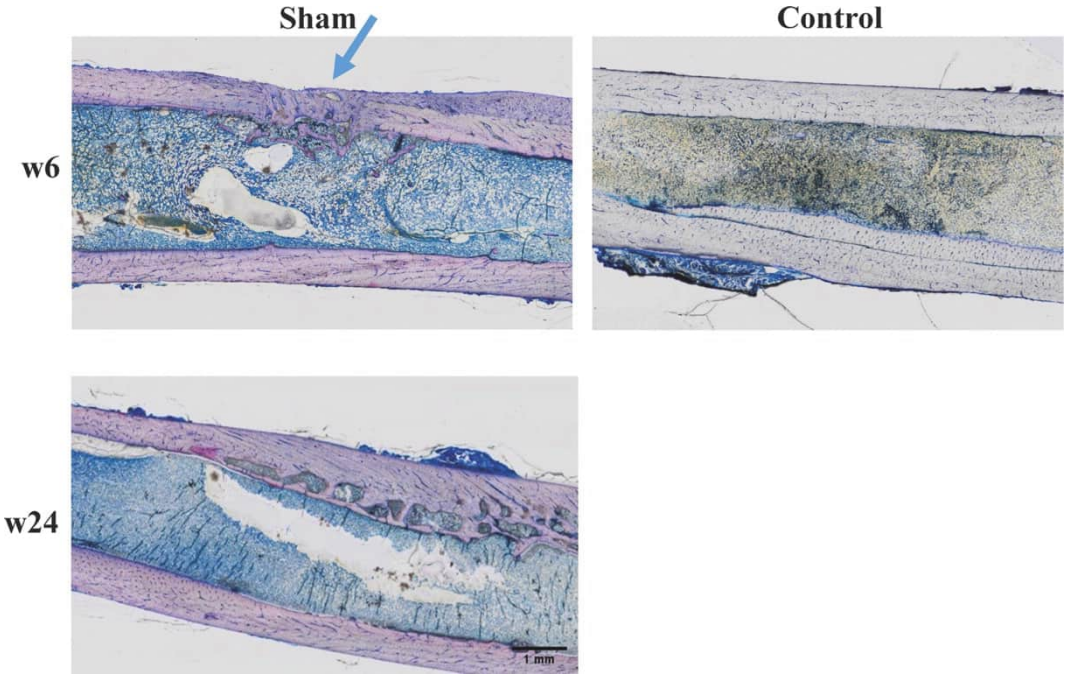

Figure S7.5. Representative image of Levai-Laczko-stained sham and control group bone sections at 6 and 24 weeks post-operation. The blue arrow indicates the remnants of drilled hole for the sham group at week 6. Scale bar = 1 mm

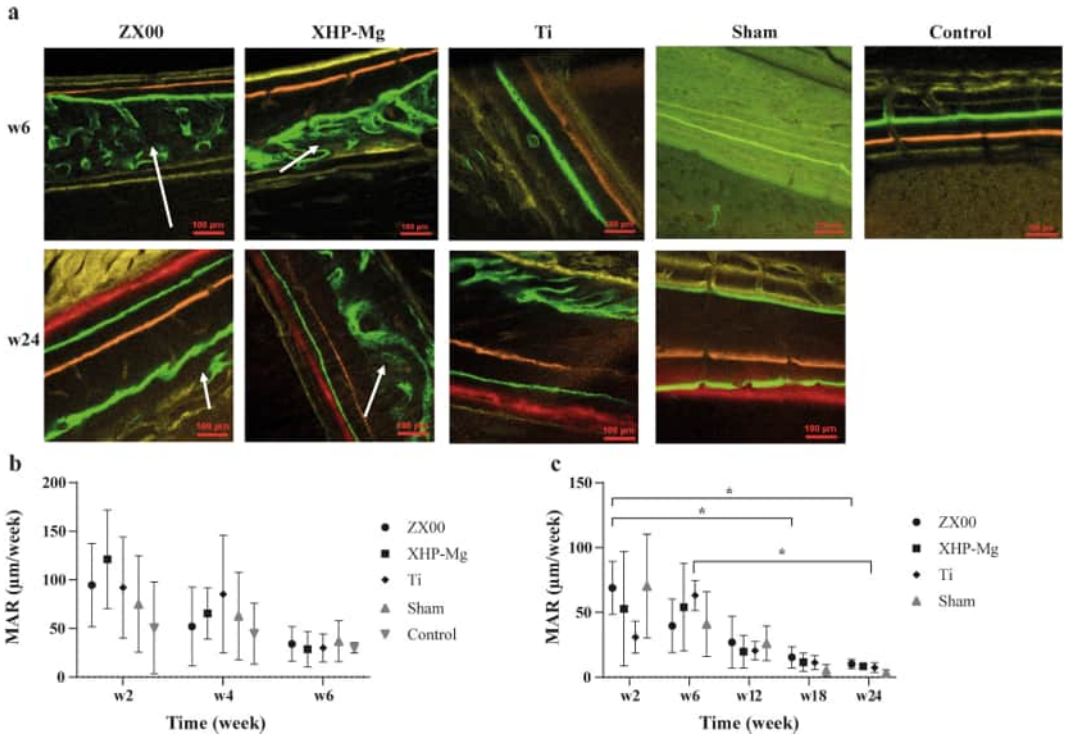

Figure S7.6. Dynamic process of bone formation extracted from representative images. a) Fluorochrome images after tetracycline (yellow), calcein (green), xylenol orange (orange), and alizarin red complexone (red) administration. The white arrows indicate the calcein labeling at week 2. The distances between the bands demonstrate the rate of bone growth over 6 and 24 weeks, respectively. b, c) Mineral apposition rate (MAR) of bone over designated time points for the study periods of 6 and 24 weeks. Two-way ANOVA followed by Tukey's multiple comparisons test was performed (ZX00, Ti, n=4; XHP-Mg, Sham, Control, n=3). Scale bar=100 μm, ∗p<0.05.

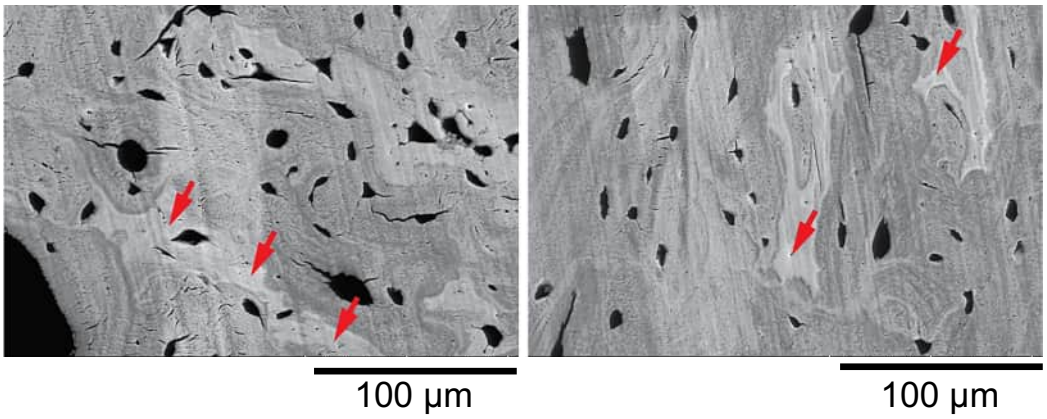

	N	O	Na	Mg	P	Ca
Mean	3.71	41.23	0.34	0.46	15.68	38.66
SD	0.38	5.76	0.05	0.11	1.78	5.81

	N	O	Na	Mg	P	Ca
Mean	3.25	46.32	0.41	0.54	16.21	33.43
SD	0.24	5.71	0.07	0.10	1.65	4.23

Figure S7.7. Cross-sectional morphology and EDX analysis (weight percentage wt.%) of the bone in the sham groups at 6 and 24 weeks. Various grey levels are observed. The red arrows point to bright areas where slightly higher calcium was observed at 6 weeks compared to 24 weeks post-operation, suggesting a difference in mineralization degree.

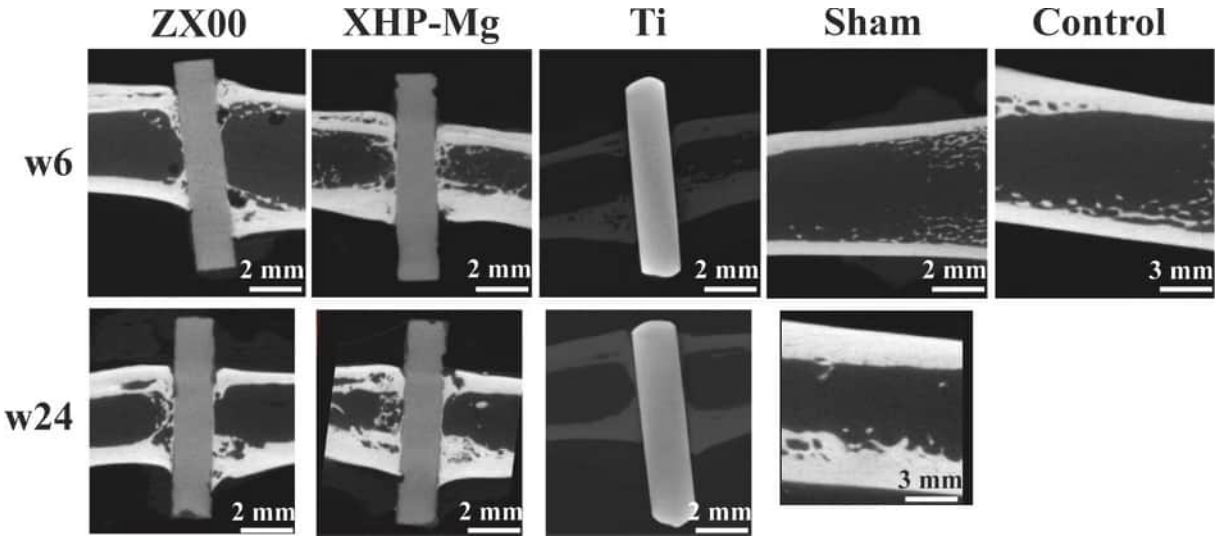

Figure S7.8. Ex vivo high-resolution μCT images (pixel size = 10.1 μm) at 6 and 24 weeks post-operation.

Chapter 8

Conclusion and future perspectives

In this thesis, the corrosion performance of various Mg materials, including pure Mg, XHP-Mg, MgYREZr (WE43), and ZX00(Mg-0.45Zn-0.45Ca) was studied with multimodal approaches *in vitro* and *in vivo*. Based on the findings, it can be concluded that:

1. The wide variation of contact angle across various Mg alloys highlights the influence of surface wettability, along with other surface properties, such as surface roughness, in determining the biological response at the cell/material interface. This emphasizes the importance of tailoring Mg material properties according to the intended clinical application.

2. *In vitro* testing of Mg-based devices using immersion solutions that closely mimic body fluids yields a baseline information regarding the corrosion performance and the composition of the corrosion products. However, it is crucial to acknowledge that while the corrosion layers have comparable elemental composition in both *in vitro* and *in vivo* conditions, the composition of the corrosion layer *in vivo* were implant-site dependence. This highlights the importance of taking into account specific aspects related to the implant location (bone quality, mechanical loading, vascularization, adjacent structures, infection risks, and functional/esthetic considerations) when assessing the corrosion behavior of Mg implants in clinical use.

3. Pure Mg, and WE43 alloy specimens exhibited non-cytotoxicity on pre-differentiated OB and OC cells. However, the comparison of pre-differentiated OB and OC in monoculture and coculture on two different Mg substrates revealed variations in cell spread and attachment, which differed depending on the Mg substrates. ***The results from the monoculture and coculture study demonstrates a noticeable influence of coculturing OB and OC on the corrosion layer composition and corrosion rate compared to monoculture***. Ca-P enrichment was observed in the outer-middle region of the corrosion layer but only in the coculture after 7 and 14 days on WE43 and Mg specimens, respectively.

4. The corrosion resistance of Mg alloys is microstructure-dependent, making the optimization of microstructure a crucial aspect of implant manufacture. As evidenced by our *in vivo* study using ZX00 screws, the ZX00 screws exhibited non-uniform corrosion, with lower corrosion rate in the regions of the screw that had a uniform grain size distribution. Therefore, by carefully tailoring the alloy´s composition and processing parameters, manufacturers can design Mg implants where their mechanical properties and biocompatibility can enhance their performance and biodegradability in physiological environments.

5. Mg-based implants exhibited favorable biocompatibility, promoting new bone formation and enabling ongoing remodeling. Moreover, these Mg implants do not induce

significant side effects during degradation. The corrosion of Mg-based implants in bone tissues is influenced by a continuous and time-dependent body-response phenomenon that involves a series of interconnected events, including the protein absorption, coagulation, inflammation, cellular recruitment, osteogenic differentiation, bone formation and remodeling. ***However, the varying corrosion rates and the wide range of corrosion layer thicknesses demonstrated the dependence of Mg corrosion on implant location***. This makes it challenging to precisely estimate the corrosion rate of Mg implant materials *in vivo*.

Therefore, in the scope of the performed research, the following hypotheses were verified:

- **Hypothesis 1**: The composition of the corrosion layer on Mg-based materials is significantly affected by cell viability, proliferation, and cell adhesion under *in vitro* conditions, suggesting that the biological interaction between cells and Mg implants plays a crucial role in the corrosion behavior of these materials.

  SUSTAINED

- **Hypothesis 2**: The composition of corrosion layers on implants varies according to their *in vivo* location, indicating that the local biological environment and mechanical stresses specific to the implantation site are key determinants in the degradation process of the material.

  SUSTAINED

This PhD research has provided the opportunity to explore and conduct investigations across most of the key areas on the path to development and clinical application of Mg-based implants. The essential steps include initial material characterization, *in vitro* and *in vivo* testing, developing standards and methods to analyze the corrosion layers and the implant-tissue interface from *in vivo* studies. Throughout the PhD research, a multimodal approach has been employed (using optical microscopy, SEM, FIB/SEM/EDX, electrochemical measurements, contact angle measurements, XPS, fluorescence microscopy) to thoroughly analyze the features of Mg-based implants. This allows to gain a comprehensive understanding of as-received material and extend their performance in biological environments through *in vitro* and *in vivo* implantation. Understanding the composition of the corrosion layers of Mg implants is essential since these layers are a dynamic interface that plays a crucial role in interacting with the surrounding tissues. The gained knowledge may contribute to predicting the implant´s long-term behavior to ensure its functions as intended.

In addition, as this PhD research focuses on clinical-grade commercially available Mg alloys, this work highlights its practical significance and potential relevance in real-world application. This research greatly benefits from the collaborative efforts of scientists, doctors, engineers, and business partners. The diversified knowledge and multidisciplinary work environment are valuable for developing Mg implants. Such interdisciplinary collaboration is crucial for ensuring innovation and providing high-quality scientific evidence, which is required for regulatory approvals and clinical acceptability. Therefore, this research not only provides knowledge in the biomaterials field by comprehensive investigating the Mg-based implant ‘properties but also provide a solid foundation for the continued development and optimization of absorbable Mg-based devices supporting their further widespread adoption in medical practice.

Further research should address:

- The existing gap in our understanding of the wettability properties of the current knowledge of the Mg-based implants requires further investigation in future studies.

- Additional research is needed to elucidate how the OB-OC cross talk influence the corrosion behavior and composition of the corrosion layers formed on Mg materials. For this, our co-culture model can be improved by employing a continuous flow cell-culture system to mimic the biological milleu. This could improve the correlation between *vitro* and *in vivo* corrosion rates.

- Further investigations of OC cells in direct contact with Mg substrates cells are required to provide knowledge regarding the impact of the degradation of Mg in the modulation of the actin cytoskeleton of OC. This could provide knowledge of how the surface chemistry and topography influence the behaviour of OC and may influence the resorbing or non-resorbing phase of OC cells.

- Numerous animal experiments have been undertaken to examine the effectiveness of Mg implants in fracture models. However, it is necessary for further research to design animal trials that more accurately mimic real clinical scenarios. These trials should use implant designs that closely resemble those intended for clinic use. Additionally, the selection of implant locations should correspond to regions in humans with a high frequency of fractures. This approach guarantees that the findings obtained are directly relevant to the safe and effective use of Mg implants in human patients.

- Although Mg-REE-containing alloys show potential for use in biomedical applications such as orthopedic and cardiovascular implants, it is crucial to assess their possible effects on patient health thoroughly. Further investigations are required to evaluate the long-term safety and effectiveness of Mg-REE alloys for clinical use. In addition, regulatory agencies play a vital role in assessing the safety of these Mg-RE alloys and verifying their compliance with rigorous quality and safety standards before their use in medical applications. Post-market surveillance of Mg-RE alloys necessitates a dynamic and collaborative approach involving data collecting, analysis, risk assessment, and communication. This is necessary to safeguard the health of those who have been implanted with Mg-RE devices.

- Additional research is required to examine the degradation of the Mg-based implants under loading conditions that replicate the mechanical stresses encountered in real clinical scenarios. Further studies should analyze the mechanical properties at the bone-corrosion layer-Mg implant interface to elucidate possible failure mechanisms of Mg implants.

Finally, although there are now commercially available Mg alloys for clinical use, it is crucial to explore the development of new Mg alloys to provide alternatives that can fulfill the increasing need for orthopedic implants. Sustained research efforts are necessary to cultivate novel alloys that can provide enhanced performance focused on real clinical needs. Furthermore, conducting continuous surveillance of commercial Mg alloys via clinical trials is imperative, as there are gaps in our understanding of the biological performance of Mg materials. It is also important to develop methods for monitoring the degradation of Mg-based devices in vivo. This should involve the use of improved imaging tools and the development of local methods, such as sensors. These sensors can provide real-time data on the degradation process of Mg implantable materials. Addressing these gaps through research can ensure that Mg materials used in medical applications are safe and effective for long-term patient use.

REFERENCES

[1] A.-M. Wu, C. Bisignano, S.L. James, G.G. Abady, A. Abedi, E. Abu-Gharbieh, R.K. Alhassan, V. Alipour, J. Arabloo, M. Asaad, W.N. Asmare, A.F. Awedew, M. Banach, S.K. Banerjee, A. Bijani, T.T.M. Birhanu, S.R. Bolla, L.A. Cámera, J.-C. Chang, D.Y. Cho, M.T. Chung, R.A.S. Couto, X. Dai, L. Dandona, R. Dandona, F. Farzadfar, I. Filip, F. Fischer, A.A. Fomenkov, T.K. Gill, B. Gupta, J.A. Haagsma, A. Haj-Mirzaian, S. Hamidi, S.I. Hay, I.M. Ilic, M.D. Ilic, R.Q. Ivers, M. Jürisson, R. Kalhor, T. Kanchan, T. Kavetskyy, R. Khalilov, E.A. Khan, M. Khan, C.J. Kneib, V. Krishnamoorthy, G.A. Kumar, N. Kumar, R. Lalloo, S. Lasrado, S.S. Lim, Z. Liu, A. Manafi, N. Manafi, R.G. Menezes, T.J. Meretoja, B. Miazgowski, T.R. Miller, Y. Mohammad, A. Mohammadian-Hafshejani, A.H. Mokdad, C.J.L. Murray, M. Naderi, M.D. Naimzada, V.C. Nayak, C.T. Nguyen, R. Nikbakhsh, A.T. Olagunju, N. Otstavnov, S.S. Otstavnov, J.R. Padubidri, J. Pereira, H.Q. Pham, M. Pinheiro, S. Polinder, H. Pourchamani, N. Rabiee, A. Radfar, M.H.U. Rahman, D.L. Rawaf, S. Rawaf, M.R. Saeb, A.M. Samy, L. Sanchez Riera, D.C. Schwebel, S. Shahabi, M.A. Shaikh, A. Soheili, R. Tabarés-Seisdedos, M.R. Tovani-Palone, B.X. Tran, R.S. Travillian, P.R. Valdez, T.J. Vasankari, D.Z. Velazquez, N. Venketasubramanian, G.T. Vu, Z.-J. Zhang, T. Vos, Global, regional, and national burden of bone fractures in 204 countries and territories, 1990–2019: a systematic analysis from the Global Burden of Disease Study 2019, Lancet Heal. Longev. 2 (2021) e580–e592. https://doi.org/10.1016/s2666-7568(21)00172-0.

[2] P. Wang, Y. Gong, G. Zhou, W. Ren, X. Wang, Biodegradable Implants for Internal Fixation of Fractures and Accelerated Bone Regeneration, ACS Omega. (2023). https://doi.org/10.1021/acsomega.3c02727.

[3] A. Ho-Shui-Ling, J. Bolander, L.E. Rustom, A.W. Johnson, F.P. Luyten, C. Picart, Bone regeneration strategies: Engineered scaffolds, bioactive molecules and stem cells current stage and future perspectives, Biomaterials. 180 (2018) 143–162. https://doi.org/10.1016/j.biomaterials.2018.07.017.

[4] C. Ye, W.D. Leslie, Fracture risk and assessment in adults with cancer, Osteoporos. Int. 34 (2023) 449–466. https://doi.org/10.1007/s00198-022-06631-4.

[5] U.S. Department of Health and Human Services, Bone Health and Osteoporosis A Report of the Surgeon General, Rockville, MD. Office of Surgeon General (US), 2004. https://doi.org/PMID: 20945569.

[6] F. Borgström, L. Karlsson, G. Ortsäter, N. Norton, P. Halbout, C. Cooper, M. Lorentzon, E. V. McCloskey, N.C. Harvey, M.K. Javaid, J.A. Kanis, J.Y. Reginster, S. Ferrari, Fragility fractures in Europe: burden, management and opportunities, Arch. Osteoporos. 15 (2020). https://doi.org/10.1007/s11657-020-0706-y.

[7] J.A. Kanis, N. Norton, N.C. Harvey, T. Jacobson, H. Johansson, M. Lorentzon, E. V. McCloskey, C. Willers, F. Borgström, SCOPE 2021: a new scorecard for osteoporosis in Europe, Arch. Osteoporos. 16 (2021). https://doi.org/10.1007/s11657-020-00871-9.

[8] T. Kim, C.W. See, X. Li, D. Zhu, Orthopedic implants and devices for bone fractures and defects: Past, present and perspective, Eng. Regen. 1 (2020) 6–18. https://doi.org/10.1016/j.engreg.2020.05.003.

[9] M. Chagnon, L.G. Guy, N. Jackson, Evaluation of Magnesium-based Medical Devices in Preclinical Studies: Challenges and Points to Consider, Toxicol. Pathol. 47 (2019) 390–400. https://doi.org/10.1177/0192623318816936.

[10] A. Goharian, M.R. Abdullah, 7 - Bioinert Metals (Stainless Steel, Titanium, Cobalt Chromium), in: A.B.T.-T.P.S. Goharian (Ed.), Trauma Plat. Syst. Biomech. Mater. Biol. Clin. Asp., Elsevier, 2017: pp. 115–142. https://doi.org/https://doi.org/10.1016/B978-0-12-804634-0.00007-0.

[11] N. Shayesteh Moghaddam, M. Taheri Andani, A. Amerinatanzi, C. Haberland, S. Huff, M. Miller, M. Elahinia, D. Dean, Metals for bone implants: safety, design, and efficacy, Biomanufacturing Rev. 1 (2016) 1–16. https://doi.org/10.1007/s40898-016-0001-2.

[12] O. Bazaka, K. Bazaka, P. Kingshott, R.J. Crawford, E.P. Ivanova, Chapter 1. Metallic Implants for Biomedical Applications, in: Christopher Spi (Ed.), Chem. Inorg. Biomater., 2021: pp. 1–98. https://doi.org/10.1039/9781788019828-00001.

[13] D.T. Chou, D. Hong, P. Saha, J. Ferrero, B. Lee, Z. Tan, Z. Dong, P.N. Kumta, In vitro and in vivo corrosion, cytocompatibility and mechanical properties of biodegradable Mg-Y-Ca-Zr alloys as implant materials, Acta Biomater. 9 (2013) 8518–8533. https://doi.org/10.1016/j.actbio.2013.06.025.

[14] P.-R. Cha, H.-S. Han, G.-F. Yang, Y.-Y.Y.-C. Kim, K.-H. Hong, S.-C. Lee, J.-Y. Jung, J.-P. Ahn, Y.-Y.Y.-C. Kim, S.-Y. Cho, J.Y. Byun, K.-S. Lee, S.-J. Yang, H.-K. Seok, Biodegradability engineering of biodegradable Mg alloys: Tailoring the electrochemical properties and microstructure of constituent phases, Sci. Rep. 3 (2013) 2367. https://doi.org/10.1038/srep02367.

[15] N.T. Kirkland, N. Birbilis, Influence of Environmental Variables on In vitro Performance, in: N.T. Kirkland, N. Birbilis (Eds.), Magnes. Biomater. Des. Testing, Best Pract., Springer, Cham, 2014: pp. 39–72. https://doi.org/10.1007/978-3-319-02123-2_3.

[16] B. Schaller, N. Saulacic, S. Beck, T. Imwinkelried, B.T. Goh, K. Nakahara, W. Hofstetter, T. Iizuka, In vivo degradation of a new concept of magnesium-based rivet-screws in the minipig mandibular bone, Mater. Sci. Eng. C. 69 (2016) 247–254. https://doi.org/10.1016/j.msec.2016.06.085.

[17] F. El-Taib Heakal, O.S. Shehata, N.S. Tantawy, Degradation behaviour of AZ80E magnesium alloy exposed to phosphate buffer saline medium, Corros. Sci. 86 (2014) 285–294. https://doi.org/10.1016/j.corsci.2014.06.008.

[18] J.L. Wang, J.K. Xu, C. Hopkins, D.H.K. Chow, L. Qin, Biodegradable Magnesium-Based Implants in Orthopedics—A General Review and Perspectives, Adv. Sci. 7 (2020). https://doi.org/10.1002/advs.201902443.

[19] H. Khan, B. Barkham, A. Trompeter, The use of bioabsorbable materials in orthopaedics, Orthop. Trauma. 35 (2021) 289–296. https://doi.org/10.1016/j.mporth.2021.07.005.

[20] D.S. Levi, A.L. Cheng, Biodegradable Implants BT - Pediatric and Congenital Cardiology, Cardiac Surgery and Intensive Care, in: E.M. Da Cruz, D. Ivy, J. Jaggers (Eds.), Springer London, London, 2014: pp. 1219–1235. https://doi.org/10.1007/978-1-4471-4619-3_128.

[21] G.M. Raghavendra, K. Varaprasad, T. Jayaramudu, Biomaterials: Design, Development and Biomedical Applications, Nanotechnol. Appl. Tissue Eng. (2015) 21–44. https://doi.org/10.1016/B978-0-323-32889-0.00002-9.

[22] Z. Sheikh, S. Najeeb, Z. Khurshid, V. Verma, H. Rashid, M. Glogauer, Biodegradable materials for bone repair and tissue engineering applications, Materials (Basel). 8 (2015) 5744–5794. https://doi.org/10.3390/ma8095273.

[23] S. Agarwal, J. Curtin, B. Duffy, S. Jaiswal, Biodegradable magnesium alloys for orthopaedic applications: A review on corrosion, biocompatibility and surface modifications, Mater. Sci. Eng. C. 68 (2016) 948–963. https://doi.org/10.1016/j.msec.2016.06.020.

[24] D. Pappalardo, T. Mathisen, A. Finne-Wistrand, Biocompatibility of Resorbable Polymers: A Historical Perspective and Framework for the Future, Biomacromolecules. 20 (2019) 1465–1477. https://doi.org/10.1021/acs.biomac.9b00159.

[25] S. Amukarimi, M. Mozafari, Biodegradable magnesium-based biomaterials: An overview of challenges and opportunities, MedComm. 2 (2021) 123–144. https://doi.org/10.1002/mco2.59.

[26] Y. Yang, X. Xiong, J. Chen, X. Peng, D. Chen, F. Pan, Research advances in magnesium and magnesium alloys worldwide in 2020, J. Magnes. Alloy. 9 (2021) 705–747. https://doi.org/10.1016/j.jma.2021.04.001.

[27] V. Tsakiris, C. Tardei, F.M. Clicinschi, Biodegradable Mg alloys for orthopedic implants – A review, J. Magnes. Alloy. (2021). https://doi.org/10.1016/j.jma.2021.06.024.

[28] G. Uppal, A. Thakur, A. Chauhan, S. Bala, Magnesium based implants for functional bone tissue regeneration – A review, J. Magnes. Alloy. 10 (2022) 356–386. https://doi.org/10.1016/j.jma.2021.08.017.

[29] L.C. Whitmore, J. Denk, G.A. Zickler, G.R. Bourret, O. Huber, N. Huesing, O. Diwald, Macro to nano: A microscopy study of a wrought magnesium alloy after deformation, Eur. J. Phys. 40 (2019). https://doi.org/10.1088/1361-6404/ab168a.

[30] S. Rahimpour Golroudbary, I. Makarava, A. Kraslawski, Environmental Assessment of Global Magnesium Production, Miner. Process. Extr. Metall. Rev. 44 (2023) 389–406. https://doi.org/10.1080/08827508.2022.2084734.

[31] B. Liu, J. Yang, X. Zhang, Q. Yang, J. Zhang, X. Li, Development and application of magnesium alloy parts for automotive OEMs: A review, J. Magnes. Alloy. 11 (2023) 15–47. https://doi.org/10.1016/j.jma.2022.12.015.

[32] S. Gautam, D. Bhatnagar, D. Bansal, H. Batra, N. Goyal, Recent advancements in nanomaterials for biomedical implants, Biomed. Eng. Adv. 3 (2022) 100029. https://doi.org/10.1016/j.bea.2022.100029.

[33] A.A. Kaya, Physical metallurgy of magnesium, in: M.O. Pekguleryuz, K.U. Kainer, A.B.T.-F. of M.A.M. Arslan Kaya (Eds.), Fundam. Magnes. Alloy Metall., Woodhead Publishing, 2013: pp. 33–84. https://doi.org/https://doi.org/10.1533/9780857097293.33.

[34] R.E. Schäublin, M. Becker, M. Cihova, S.S.A. Gerstl, D. Deiana, C. Hébert, S. Pogatscher, P.J. Uggowitzer, J.F. Löffler, Precipitation in lean Mg–Zn–Ca alloys, Acta Mater. 239 (2022) 118223. https://doi.org/10.1016/j.actamat.2022.118223.

[35] National Library of Medicine, PubChem, (n.d.). https://pubchem.ncbi.nlm.nih.gov/element/Magnesium (accessed February 29, 2024).

[36] G.L. Song, A. Atrens, Corrosion mechanisms of magnesium alloys, Adv. Eng. Mater. 1 (1999) 11–33. https://doi.org/10.1002/(SICI)1527-2648(199909)1:1<11::AID-ADEM11>3.0.CO;2-N.

[37] Y. Yang, C. He, Dianyu E, W. Yang, F. Qi, D. Xie, L. Shen, S. Peng, C. Shuai, Mg bone implant: Features, developments and perspectives, Mater. Des. (2020). https://doi.org/10.1016/j.matdes.2019.108259.

[38] R. Neelameggham, Primary production of magnesium, in: M.O. Pekguleryuz, K.U. Kainer, A.B.T.-F. of M.A.M. Arslan Kaya (Eds.), Fundam. Magnes. Alloy Metall., Woodhead Publishing, 2013: pp. 1–32. https://doi.org/https://doi.org/10.1533/9780857097293.1.

[39] F. Gao, Z. Nie, Z. Wang, X. Gong, T. Zuo, Life cycle assessment of primary magnesium production using the Pidgeon process in China, Int. J. Life Cycle Assess. 14 (2009) 480–489. https://doi.org/10.1007/s11367-009-0101-9.

[40] USGS, Mineral Cpmmodity Summaries, 2023. https://doi.org/https://doi.org/10.3133/mcs2023.

[41] International Magnesium Association, Magnesium Prices are Skyrocketing, (2021). https://www.intlmag.org/news/583048/Magnesium-Prices-are-Skyrocketing.htm (accessed February 29, 2024).

[42] M. Esmaily, J.E. Svensson, S. Fajardo, N. Birbilis, G.S. Frankel, S. Virtanen, R. Arrabal, S. Thomas, L.G. Johansson, Fundamentals and advances in magnesium alloy corrosion, Prog. Mater. Sci. 89 (2017) 92–193. https://doi.org/10.1016/j.pmatsci.2017.04.011.

[43] Q. Chen, G.A. Thouas, Metallic implant biomaterials, Mater. Sci. Eng. R Reports. 87 (2015) 1–57. https://doi.org/10.1016/j.mser.2014.10.001.

[44] M. Abdalla, A. Joplin, M. Elahinia, H. Ibrahim, Corrosion Modeling of Magnesium and Its Alloys for Biomedical Applications: Review, Corros. Mater. Degrad. 1 (2020) 219–248. https://doi.org/10.3390/cmd1020011.

[45] R. Chalisgaonkar, Insight in applications, manufacturing and corrosion behaviour of magnesium and its alloys – A review, Mater. Today Proc. (2020). https://doi.org/10.1016/j.matpr.2020.02.211.

[46] M. Pogorielov, E. Husak, A. Solodivnik, S. Zhdanov, Magnesium- based biodegradable alloys: Degradation, application, and alloying elements, Interv. Med. Appl. Sci. 9 (2017) 27–38. https://doi.org/10.1556/1646.9.2017.1.04.

[47] K. Gusieva, C.H.J. Davies, J.R. Scully, N. Birbilis, Corrosion of magnesium alloys: The role of alloying, Int. Mater. Rev. 60 (2015) 169–194. https://doi.org/10.1179/1743280414Y.0000000046.

[48] R. Radha, D. Sreekanth, Insight of magnesium alloys and composites for orthopedic implant applications – a review, J. Magnes. Alloy. 5 (2017) 286–312. https://doi.org/10.1016/j.jma.2017.08.003.

[49] R. Kumar, P. Katyal, Effects of alloying elements on performance of biodegradable magnesium alloy, Mater. Today Proc. 56 (2022) 2443–2450.

https://doi.org/10.1016/j.matpr.2021.08.233.

[50] ASTM International, ASTM B951-11: 2018 Standard Practice for Codification of Unalloyed Magnesium and Magnesium-Alloys, Cast and Wrought., (2018).

[51] L.M. Calado, M.J. Carmezim, M.F. Montemor, Rare Earth Based Magnesium Alloys—A Review on WE Series, Front. Mater. 8 (2022) 1–18. https://doi.org/10.3389/fmats.2021.804906.

[52] T.M. Sridhar, S.P. Vinodhini, U. Kamachi Mudali, B. Venkatachalapathy, K. Ravichandran, Load-bearing metallic implants: electrochemical characterisation of corrosion phenomena, Mater. Technol. 31 (2016) 705–718. https://doi.org/10.1080/10667857.2016.1220752.

[53] F. Witte, N. Hort, C. Vogt, S. Cohen, K.U. Kainer, R. Willumeit, F. Feyerabend, Degradable biomaterials based on magnesium corrosion, Curr. Opin. Solid State Mater. Sci. 12 (2008) 63–72. https://doi.org/10.1016/j.cossms.2009.04.001.

[54] U. Riaz, I. Shabib, W. Haider, The current trends of Mg alloys in biomedical applications—A review, J. Biomed. Mater. Res. Part B Appl. Biomater. 107 (2019) 1970–1996. https://doi.org/10.1002/jbm.b.34290.

[55] Y. Ding, C. Wen, P. Hodgson, Y. Li, Effects of alloying elements on the corrosion behavior and biocompatibility of biodegradable magnesium alloys: A review, J. Mater. Chem. B. 2 (2014) 1912–1933. https://doi.org/10.1039/c3tb21746a.

[56] A. Atrens, G.L. Song, F. Cao, Z. Shi, P.K. Bowen, Advances in Mg corrosion and research suggestions, J. Magnes. Alloy. 1 (2013) 177–200. https://doi.org/10.1016/j.jma.2013.09.003.

[57] M. Liu, G.L. Song, Impurity control and corrosion resistance of magnesium–aluminum alloy, Corros. Sci. 77 (2013) 143–150. https://doi.org/10.1016/J.CORSCI.2013.07.037.

[58] Y. Xin, T. Hu, P.K. Chu, In vitro studies of biomedical magnesium alloys in a simulated physiological environment: A review, Acta Biomater. 7 (2011) 1452–1459. https://doi.org/10.1016/j.actbio.2010.12.004.

[59] K. Chen, J. Dai, X. Zhang, Improvement of corrosion resistance of magnesium alloys for biomedical applications, Corros. Rev. 33 (2015) 101–117. https://doi.org/10.1515/corrrev-2015-0007.

[60] N. Sezer, Z. Evis, S.M. Kayhan, A. Tahmasebifar, M. Koç, M. Koc, Review of magnesium-based biomaterials and their applications, J. Magnes. Alloy. 6 (2018) 23–43. https://doi.org/10.1016/j.jma.2018.02.003.

[61] M. Wang, X. Yang, F. Wang, R. Li, H. Ning, L. Na, Y. Huang, Y. Song, L. Liu, H. Pan, Q. Zhang, L. Fan, Y. Li, C. Sun, Calcium-deficiency assessment and biomarker identification by an integrated urinary metabonomics analysis, BMC Med. 11 (2013). https://doi.org/10.1186/1741-7015-11-86.

[62] D. Bian, X. Chu, J. Xiao, Z. Tong, H. Huang, Q. Jia, J. Liu, W. Li, H. Yu, Y. He, L. Ma, X. Wang, M. Li, T. Yang, W. Huang, C. Zhang, M. Yao, Y. Zhang, Z. Xu, S. Guan, Y. Zheng, Design of single-phased magnesium alloys with typically high solubility rare earth elements for biomedical applications: Concept and proof, Bioact. Mater. 22 (2023) 180–200. https://doi.org/10.1016/j.bioactmat.2022.09.018.

[63] G. Cossellu, V. Motta, L. Dioni, L. Angelici, L. Vigna, G. Farronato, A.C. Pesatori, V. Bollati, Titanium and Zirconium levels are associated with changes in MicroRNAs expression: Results from a human cross-sectional study on obese population, PLoS One. 11 (2016) 1–12. https://doi.org/10.1371/journal.pone.0161916.

[64] Y. Li, C. Wen, D. Mushahary, R. Sravanthi, N. Harishankar, G. Pande, P. Hodgson, Mg-Zr-Sr alloys as biodegradable implant materials, Acta Biomater. 8 (2012) 3177–3188. https://doi.org/10.1016/j.actbio.2012.04.028.

[65] M. Razavi, Y. Huang, Assessment of magnesium-based biomaterials: From bench to clinic, Biomater. Sci. 7 (2019) 2241–2263. https://doi.org/10.1039/c9bm00289h.

[66] W. Jin, G. Wu, H. Feng, W. Wang, X. Zhang, P.K. Chu, Improvement of corrosion resistance and biocompatibility of rare-earth WE43 magnesium alloy by neodymium self-ion implantation, Corros. Sci. 94 (2015) 142–155. https://doi.org/10.1016/j.corsci.2015.01.049.

[67] I. Johnson, H. Liu, A Study on Factors Affecting the Degradation of Magnesium and a Magnesium-Yttrium Alloy for Biomedical Applications, PLoS One. 8 (2013). https://doi.org/10.1371/journal.pone.0065603.

[68] D. Drozdenko, M. Yamasaki, K. Máthis, P. Dobroň, P. Lukáč, N. Kizu, S. Inoue, Y. Kawamura, Optimization of mechanical properties of dilute Mg-Zn-Y alloys prepared by rapid solidification, Mater. Des. 181 (2019) 107984. https://doi.org/10.1016/j.matdes.2019.107984.

[69] D. Xu, E.H. Han, Y. Xu, Effect of long-period stacking ordered phase on microstructure, mechanical property and corrosion resistance of Mg alloys: A review, Prog. Nat. Sci. Mater. Int. 26 (2016) 117–128. https://doi.org/10.1016/J.PNSC.2016.03.006.

[70] E. Abe, A. Ono, T. Itoi, M. Yamasaki, Y. Kawamura, Polytypes of long-period stacking structures synchronized with chemical order in a dilute Mg-Zn-Y alloy, Philos. Mag. Lett. 91 (2011) 690–696. https://doi.org/10.1080/09500839.2011.609149.

[71] F. Lu, A. Ma, J. Jiang, D. Yang, Q. Zhou, Review on long-period stacking-ordered structures in Mg-Zn-RE alloys, Rare Met. 31 (2012) 303–310. https://doi.org/10.1007/s12598-012-0510-y.

[72] T. Tsumuraya, H. Momida, T. Oguchi, Electronic origin of phase stability in Mg-Zn-Y alloys with a long-period stacking order, Appl. Phys. Express. 15 (2022). https://doi.org/10.35848/1882-0786/ac7b68.

[73] M.A. Zoroddu, J. Aaseth, G. Crisponi, S. Medici, M. Peana, V.M. Nurchi, The essential metals for humans: a brief overview, J. Inorg. Biochem. 195 (2019) 120–129. https://doi.org/10.1016/J.JINORGBIO.2019.03.013.

[74] W.L. Yang, Y. Zhang, J.H. Yang, L.L. Tan, K. Yang, Potential antiosteoporosis effect of biodegradable magnesium implanted in STZ-induced diabetic rats, J. Biomed. Mater. Res. Part A. 99A (2011) 386–394. https://doi.org/10.1002/jbm.a.33201.

[75] H. Helmholz, B.J.C. Luthringer-Feyerabend, R. Willumeit-Römer, Elemental mapping of biodegradable magnesium-based implants in bone and soft tissue by means of μ X-ray fluorescence analysis, J. Anal. At. Spectrom. 34 (2019) 356–365. https://doi.org/10.1039/c8ja00377g.

[76] R.S. Park, Y.K. Kim, S.J. Lee, Y.S. Jang, I.S. Park, Y.H. Yun, T.S. Bae, M.H. Lee,

Corrosion behavior and cytotoxicity of Mg-35Zn-3Ca alloy for surface modified biodegradable implant material, J. Biomed. Mater. Res. Part B-Applied Biomater. 100B (2012) 911–923. https://doi.org/10.1002/jbm.b.32652.

[77] J.H.F. de Baaij, J.G.J. Hoenderop, R.J.M. Bindels, Magnesium in man: Implications for health and disease, Physiol. Rev. 95 (2015) 1–46. https://doi.org/10.1152/physrev.00012.2014.

[78] F. Witte, The history of biodegradable magnesium implants: A review, Acta Biomater. 6 (2010) 1680–1692. https://doi.org/10.1016/j.actbio.2010.02.028.

[79] Y. Sun, H. Wu, W. Wang, R. Zan, H. Peng, S. Zhang, X. Zhang, Translational status of biomedical Mg devices in China, Bioact. Mater. 4 (2019) 358–365. https://doi.org/10.1016/j.bioactmat.2019.11.001.

[80] H. Zhou, B. Liang, H. Jiang, Z. Deng, K. Yu, Magnesium-based biomaterials as emerging agents for bone repair and regeneration: from mechanism to application, J. Magnes. Alloy. 9 (2021) 779–804. https://doi.org/10.1016/j.jma.2021.03.004.

[81] V.D. Lespinasse, G.C. Fisher, J. Eisenstaedt, A practical mechanical method of end-to-end anastomosis of blood-vessels: Using Absorbable Magnesium Rings, J. Am. Med. Assoc. 55 (1910) 1785–1790. https://doi.org/10.1001/jama.1910.04330210013005.

[82] E.W. Andrews, Absorbable Metal Clips, J. Am. Med. Assoc. 69 (1917) 278–281. https://doi.org/doi:10.1001/jama.1917.02590310030008.

[83] M. Nasr Azadani, A. Zahedi, O.K. Bowoto, B.I. Oladapo, A review of current challenges and prospects of magnesium and its alloy for bone implant applications, Prog. Biomater. 11 (2022) 1–26. https://doi.org/10.1007/s40204-022-00182-x.

[84] D. Zhao, F. Witte, F. Lu, J. Wang, J. Li, L. Qin, Current status on clinical applications of magnesium-based orthopaedic implants: A review from clinical translational perspective, Biomaterials. 112 (2017) 287–302. https://doi.org/10.1016/j.biomaterials.2016.10.017.

[85] J. Song, J. Chen, X. Xiong, X. Peng, D. Chen, F. Pan, Research advances of magnesium and magnesium alloys worldwide in 2021, J. Magnes. Alloy. 10 (2022) 863–898. https://doi.org/10.1016/j.jma.2022.04.001.

[86] A.R. Khan, N.S. Grewal, C. Zhou, K. Yuan, H.J. Zhang, Z. Jun, Recent advances in biodegradable metals for implant applications: Exploring in vivo and in vitro responses, Results Eng. 20 (2023) 101526. https://doi.org/10.1016/j.rineng.2023.101526.

[87] U.S.F.& D. Aministration, FDA Roundup: March 31, 2023, (2023). https://www.fda.gov/news-events/press-announcements/fda-roundup-march-31-2023 (accessed March 1, 2024).

[88] S. Feliu, A. Samaniego, E.A. Bermudez, A.A. El-Hadad, I. Llorente, J.C. Galván, Effect of native oxide film on commercial magnesium alloys substrates and carbonate conversion coating growth and corrosion resistance, Materials (Basel). 7 (2014) 2534–2560. https://doi.org/10.3390/ma7042534.

[89] F. Cao, G.L. Song, A. Atrens, Corrosion and passivation of magnesium alloys, Corros. Sci. 111 (2016) 835–845. https://doi.org/10.1016/J.CORSCI.2016.05.041.

[90] Q. Tan, Y. Yin, N. Mo, M. Zhang, A. Atrens, Recent understanding of the oxidation and

burning of magnesium alloys, Surf. Innov. 7 (2019) 71–92. https://doi.org/10.1680/jsuin.18.00062.

[91] A. Samaniego, K. Gusieva, I. Llorente, S. Feliu, N. Birbilis, Exploring the possibility of protective surface oxides upon Mg alloy AZ31 via lutetium additions, Corros. Sci. 89 (2014) 101–110. https://doi.org/10.1016/J.CORSCI.2014.08.015.

[92] M. Echeverry-Rendon, J.P. Allain, S.M. Robledo, F. Echeverria, M.C. Harmsen, Coatings for biodegradable magnesium-based supports for therapy of vascular disease: A general view, Mater. Sci. Eng. C. 102 (2019) 150–163. https://doi.org/10.1016/j.msec.2019.04.032.

[93] M. Shahabi-Navid, Y. Cao, J.E. Svensson, A. Allanore, N. Birbilis, L.G. Johansson, M. Esmaily, On the early stages of localised atmospheric corrosion of magnesium–aluminium alloys, Sci. Rep. 10 (2020) 1–16. https://doi.org/10.1038/s41598-020-78030-w.

[94] C. McIntyre, N. S., Chen, Role of impurities on Mg surfaces unde r ambient exposure conditions, Corros. Sci. 40 (1998) 1697–1709. https://doi.org/https://doi.org/10.1016/S0010-938X(98)00072-9.

[95] M. Ascencio, M. Pekguleryuz, S. Omanovic, An investigation of the corrosion mechanisms of WE43 Mg alloy in a modified simulated body fluid solution: The influence of immersion time, Corros. Sci. 87 (2014) 489–503. https://doi.org/10.1016/j.corsci.2014.07.015.

[96] S. Leleu, B. Rives, J. Bour, N. Causse, N. Pébère, On the stability of the oxides film formed on a magnesium alloy containing rare-earth elements, Electrochim. Acta. 290 (2018) 586–594. https://doi.org/10.1016/j.electacta.2018.08.093.

[97] E. Ghali, Magnesium and Magnesium Alloys, in: R.W. Revie (Ed.), Uhlig's Corros. Handb., 3rd Ed, Wiley, 2011: pp. 809–836. https://doi.org/10.1002/9780470872864.ch58.

[98] J. Gonzalez, R.Q. Hou, E.P.S.S. Nidadavolu, R. Willumeit-Römer, F. Feyerabend, Magnesium degradation under physiological conditions – Best practice, Bioact. Mater. 3 (2018) 174–185. https://doi.org/10.1016/j.bioactmat.2018.01.003.

[99] R. Harrison, D. Maradze, S. Lyons, Y. Zheng, Y. Liu, Corrosion of magnesium and magnesium-calcium alloy in biologically-simulated environment, Prog. Nat. Sci. Mater. Int. 24 (2014) 539–546. https://doi.org/10.1016/j.pnsc.2014.08.010.

[100] J. Kim, H. Pan, Effects of magnesium alloy corrosion on biological response – Perspectives of metal-cell interaction, Prog. Mater. Sci. 133 (2023) 101039. https://doi.org/10.1016/j.pmatsci.2022.101039.

[101] M. Pourbaix, 12.2.3.2 Stability and Corrosion of Magnesium, in: Atlas Electrochem. Equilibria Aqueous Solut., NACE International, 1974. https://app.knovel.com/hotlink/khtml/id:kt0127WA11/atlas-electrochemical/stability-corrosion-magnesium.

[102] M.N. Sarian, N. Iqbal, P. Sotoudehbagha, M. Razavi, Q.U. Ahmed, C. Sukotjo, H. Hermawan, Potential bioactive coating system for high-performance absorbable magnesium bone implants, Bioact. Mater. 12 (2022) 42–63. https://doi.org/10.1016/j.bioactmat.2021.10.034.

[103] Y. Liu, Y. Zheng, X.H. Chen, J.A. Yang, H. Pan, D. Chen, L. Wang, J. Zhang, D. Zhu, S. Wu, K.W.K. Yeung, R.C. Zeng, Y. Han, S. Guan, Fundamental Theory of Biodegradable Metals—Definition, Criteria, and Design, Adv. Funct. Mater. 29 (2019) 1–21. https://doi.org/10.1002/adfm.201805402.

[104] R.Q. Hou, N. Scharnagl, F. Feyerabend, R. Willumeit-Römer, R. Willumeit-Romer, Exploring the effects of organic molecules on the degradation of magnesium under cell culture conditions, Corros. Sci. 132 (2018) 35–45. https://doi.org/10.1016/j.corsci.2017.12.023.

[105] Y. Xin, K. Huo, H. Tao, G. Tang, P.K. Chu, Influence of aggressive ions on the degradation behavior of biomedical magnesium alloy in physiological environment, Acta Biomater. 4 (2008) 2008–2015. https://doi.org/10.1016/j.actbio.2008.05.014.

[106] Y.F. Zheng, X.N. Gu, F. Witte, Biodegradable metals, Mater. Sci. Eng. R Reports. 77 (2014) 1–34. https://doi.org/10.1016/j.mser.2014.01.001.

[107] D. Mei, S. V. Lamaka, X. Lu, M.L. Zheludkevich, Selecting medium for corrosion testing of bioabsorbable magnesium and other metals – A critical review, Corros. Sci. 171 (2020) 108722. https://doi.org/10.1016/j.corsci.2020.108722.

[108] M. Abd Mutalib, M.A. Rahman, M.H.D. Othman, A.F. Ismail, J. Jaafar, Scanning Electron Microscopy (SEM) and Energy-Dispersive X-Ray (EDX) Spectroscopy, Elsevier B.V., 2017. https://doi.org/10.1016/B978-0-444-63776-5.00009-7.

[109] E. Ghali, W. Dietzel, K.U. Kainer, Testing of general and localized corrosion of magnesium alloys: A critical review, J. Mater. Eng. Perform. 13 (2004) 517–529. https://doi.org/10.1361/10599490420665.

[110] L. Wei, Z. Gao, Recent research advances on corrosion mechanism and protection, and novel coating materials of magnesium alloys: a review, RSC Adv. 13 (2023) 8427–8463. https://doi.org/10.1039/d2ra07829e.

[111] G. Song, A. Atrens, Understanding magnesium corrosion. A framework for improved alloy performance, Adv. Eng. Mater. 5 (2003) 837–858. https://doi.org/10.1002/adem.200310405.

[112] G. Eddy Jai Poinern, S. Brundavanam, D. Fawcett, Biomedical Magnesium Alloys: A Review of Material Properties, Surface Modifications and Potential as a Biodegradable Orthopaedic Implant, Am. J. Biomed. Eng. 2 (2012) 218–240. https://doi.org/10.5923/j.ajbe.20120206.02.

[113] X. Li, X. Liu, S. Wu, K.W.K. Yeung, Y. Zheng, P.K. Chu, Design of magnesium alloys with controllable degradation for biomedical implants: From bulk to surface, Acta Biomater. 45 (2016) 2–30. https://doi.org/10.1016/j.actbio.2016.09.005.

[114] S. Bauer, P. Schmuki, K. von der Mark, J. Park, Engineering biocompatible implant surfaces: Part I: Materials and surfaces, Prog. Mater. Sci. 58 (2013) 261–326. https://doi.org/10.1016/j.pmatsci.2012.09.001.

[115] H. Wu, C. Zhang, T. Lou, B. Chen, R. Yi, W. Wang, R. Zhang, M. Zuo, H. Xu, P. Han, S. Zhang, J. Ni, X. Zhang, Crevice corrosion – A newly observed mechanism of degradation in biomedical magnesium, Acta Biomater. 98 (2019) 152–159. https://doi.org/10.1016/j.actbio.2019.06.013.

[116] H. Wang, Y. Song, J. Yu, D. Shan, H. Han, Characterization of Filiform Corrosion of

Mg–3Zn Mg Alloy, J. Electrochem. Soc. 164 (2017) C574–C580. https://doi.org/10.1149/2.1221709jes.

[117] M. He, L. Chen, M. Yin, S. Xu, Z. Liang, Review on magnesium and magnesium-based alloys as biomaterials for bone immobilization, J. Mater. Res. Technol. 23 (2023) 4396–4419. https://doi.org/10.1016/j.jmrt.2023.02.037.

[118] C. Gao, S. Peng, P. Feng, C. Shuai, Bone biomaterials and interactions with stem cells, Bone Res. 5 (2017) 1–33. https://doi.org/10.1038/boneres.2017.59.

[119] C. Ma, T. Du, X. Niu, Y. Fan, Biomechanics and mechanobiology of the bone matrix, Bone Res. 10 (2022). https://doi.org/10.1038/s41413-022-00223-y.

[120] E.F. Morgan, G.U. Unnikrisnan, A.I. Hussein, Bone Mechanical Properties in Healthy and Diseased States, Annu. Rev. Biomed. Eng. 20 (2018) 119–143. https://doi.org/10.1146/annurev-bioeng-062117-121139.

[121] H. Qu, H. Fu, Z. Han, Y. Sun, Biomaterials for bone tissue engineering scaffolds: A review, RSC Adv. 9 (2019) 26252–26262. https://doi.org/10.1039/c9ra05214c.

[122] G.L. Koons, M. Diba, A.G. Mikos, Materials design for bone-tissue engineering, Nat. Rev. Mater. 5 (2020) 584–603. https://doi.org/10.1038/s41578-020-0204-2.

[123] F.A. Shah, P. Thomsen, A. Palmquist, Osseointegration and current interpretations of the bone-implant interface, Acta Biomater. 84 (2019) 1–15. https://doi.org/10.1016/j.actbio.2018.11.018.

[124] X. Wang, S. Xu, S. Zhou, W. Xu, M. Leary, P. Choong, M. Qian, M. Brandt, Y.M. Xie, Topological design and additive manufacturing of porous metals for bone scaffolds and orthopaedic implants: A review, Biomaterials. 83 (2016) 127–141. https://doi.org/10.1016/j.biomaterials.2016.01.012.

[125] K.M. Alghazali, Z.A. Nima, R.N. Hamzah, M.S. Dhar, D.E. Anderson, A.S. Biris, Bone-tissue engineering: Complex tunable structural and biological responses to injury, drug delivery, and cell-based therapies, Drug Metab. Rev. 47 (2015) 431–454. https://doi.org/10.3109/03602532.2015.1115871.

[126] C.M. Weaver, C.M. Gordon, K.F. Janz, H.J. Kalkwarf, J.M. Lappe, R. Lewis, M. O'Karma, T.C. Wallace, B.S. Zemel, The National Osteoporosis Foundation's position statement on peak bone mass development and lifestyle factors: a systematic review and implementation recommendations, Osteoporos. Int. 27 (2016) 1281–1386. https://doi.org/10.1007/s00198-015-3440-3.

[127] S. Salman, M. Gouda, Biodegradable Mg alloys for Orthopedic Implant Materials, in: G.A.M. Ali, A.S.H. Makhlouf (Eds.), Handb. Biodegrad. Mater., Springer, Cham, 2023: pp. 1–29. https://doi.org/10.1007/978-3-031-09710-2.

[128] G. Zhu, T. Zhang, M. Chen, K. Yao, X. Huang, B. Zhang, Y. Li, J. Liu, Y. Wang, Z. Zhao, Bone physiological microenvironment and healing mechanism: Basis for future bone-tissue engineering scaffolds, Bioact. Mater. 6 (2021) 4110–4140. https://doi.org/10.1016/j.bioactmat.2021.03.043.

[129] M.R. Reagan, C.J. Rosen, Navigating the bone marrow niche: Translational insights and cancer-driven dysfunction, Nat. Rev. Rheumatol. 12 (2016) 154–168. https://doi.org/10.1038/nrrheum.2015.160.

[130] M. Haghshenas, Mechanical characteristics of biodegradable magnesium matrix composites: A review, J. Magnes. Alloy. 5 (2017) 189–201. https://doi.org/10.1016/j.jma.2017.05.001.

[131] R. Havaldar, S. Pilli, B. Putti, Insights into the effects of tensile and compressive loadings on human femur bone, Adv. Biomed. Res. 3 (2014) 101. https://doi.org/10.4103/2277-9175.129375.

[132] A. Kemper, C. Mcnally, E. Kennedy, S. Manoogian, V. Tech, W. Forest, I. Biomechanics, The material properties of human tibia cortical bone, Proc. 20th Enhanc. Saf. Veh. Conf. (2007). http://www.ncbi.nlm.nih.gov/pubmed/19141952.

[133] P. Holweg, L. Berger, M. Cihova, N. Donohue, B. Clement, U. Schwarze, N.G. Sommer, G. Hohenberger, J.J.J.P. van den Beucken, F. Seibert, A. Leithner, J.F. Löffler, A.M. Weinberg, A lean magnesium–zinc–calcium alloy ZX00 used for bone fracture stabilization in a large growing-animal model, Acta Biomater. 113 (2020) 646–659. https://doi.org/10.1016/j.actbio.2020.06.013.

[134] B. Zberg, P.J. Uggowitzer, J.F. Löffler, MgZnCa glasses without clinically observable hydrogen evolution for biodegradable implants, Nat. Mater. 8 (2009) 887–891. https://doi.org/10.1038/nmat2542.

[135] Y. Kawamura, F. Shimada, K. Hamada, S. Ueno, S. Inoue, Development of Biomedical Mg–1.0Ca–0.5Zn–0.1Y–0.03Mn (at%) Alloy by Rapidly Solidified Powder Metallurgy Processing, Mater. Trans. 64 (2023) 2333–2336. https://doi.org/doi:10.2320/matertrans.MT-M2023066.

[136] J.N. Kim, J.Y. Lee, K.J. Shin, Y.C. Gil, K.S. Koh, W.C. Song, Haversian system of compact bone and comparison between endosteal and periostealsides using three-dimensional reconstructionin rat, Anat. Cell Biol. 48 (2015) 258–261. https://doi.org/10.5115/acb.2015.48.4.258.

[137] R. Florencio-Silva, G.R.D.S. Sasso, E. Sasso-Cerri, M.J. Simões, P.S. Cerri, Biology of Bone Tissue: Structure, Function, and Factors That Influence Bone Cells, Biomed Res. Int. 2015 (2015). https://doi.org/10.1155/2015/421746.

[138] K. Grandfield, V. Vuong, H.P. Schwarcz, Ultrastructure of Bone: Hierarchical Features from Nanometer to Micrometer Scale Revealed in Focused Ion Beam Sections in the TEM, Calcif. Tissue Int. 103 (2018) 606–616. https://doi.org/10.1007/s00223-018-0454-9.

[139] A. Salhotra, H.N. Shah, B. Levi, M.T. Longaker, Mechanisms of bone development and repair, Nat. Rev. Mol. Cell Biol. 21 (2020) 696–711. https://doi.org/10.1038/s41580-020-00279-w.

[140] C. Kleinhans, F.F. Schmid, F. V. Schmid, P.J. Kluger, Comparison of osteoclastogenesis and resorption activity of human osteoclasts on tissue culture polystyrene and on natural extracellular bone matrix in 2D and 3D, J. Biotechnol. 205 (2015) 101–110. https://doi.org/10.1016/j.jbiotec.2014.11.039.

[141] R.J. Miron, M. Bohner, Y. Zhang, D.D. Bosshardt, Osteoinduction and osteoimmunology: Emerging concepts, Periodontol. 2000. (2023) 1–18. https://doi.org/10.1111/prd.12519.

[142] Y. Nakamichi, N. Takahashi, N. Udagawa, T. Suda, Chapter 18 - Osteoclastogenesis

and Vitamin D, in: D.B.T.-V.D. (Fourth E. Feldman (Ed.), Vitam. D, 4th editio, Academic Press, 2018: pp. 309–317. https://doi.org/https://doi.org/10.1016/B978-0-12-809965-0.00018-5.

[143] M.M. McDonald, A.S. Kim, B.S. Mulholland, M. Rauner, New Insights Into Osteoclast Biology, JBMR Plus. 5 (2021) 1–10. https://doi.org/10.1002/jbm4.10539.

[144] G. Borciani, G. Montalbano, N. Baldini, G. Cerqueni, C. Vitale-Brovarone, G. Ciapetti, Co-culture systems of osteoblasts and osteoclasts: simulating in vitro bone remodeling in regenerative approaches., (2020). https://doi.org/10.1016/j.actbio.2020.03.043.

[145] Q. Wang, J. Yan, J. Yang, B. Li, Nanomaterials promise better bone repair, Mater. Today. 19 (2016) 451–463. https://doi.org/10.1016/j.mattod.2015.12.003.

[146] P. Andrzejowski, P. V. Giannoudis, The 'diamond concept' for long bone non-union management, J. Orthop. Traumatol. 20 (2019). https://doi.org/10.1186/s10195-019-0528-0.

[147] R. Marsell, T.A. Einhorn, The biology of fracture healing, Injury. 42 (2011) 551–555. https://doi.org/10.1016/j.injury.2011.03.031.

[148] P. V Giannoudis, T.A. Einhorn, D. Marsh, Fracture healing: the diamond concept., Injury. 38 Suppl 4 (2007) S3-6. https://doi.org/10.1016/s0020-1383(08)70003-2.

[149] C.J. Agnes, A. Karoichan, M. Tabrizian, The Diamond Concept Enigma: Recent Trends of Its Implementation in Cross-linked Chitosan-Based Scaffolds for Bone Tissue Engineering, ACS Appl. Bio Mater. (2023). https://doi.org/10.1021/acsabm.3c00108.

[150] T.A. Einhorn, L.C. Gerstenfeld, Fracture healing: Mechanisms and interventions, Nat. Rev. Rheumatol. 11 (2015) 45–54. https://doi.org/10.1038/nrrheum.2014.164.

[151] G. Chandra, A. Pandey, Biodegradable bone implants in orthopedic applications: a review, Biocybern. Biomed. Eng. 40 (2020) 596–610. https://doi.org/10.1016/j.bbe.2020.02.003.

[152] J.E. Davies, Understanding Peri-Implant Endosseous Healing, J. Dent. Educ. 67 (2003) 932–949. https://doi.org/10.1002/j.0022-0337.2003.67.8.tb03681.x.

[153] P. Sekar, N. S, V. Desai, S. Narendranath, V. Desai, N. S, V. Desai, S. Narendranath, V. Desai, Recent progress in in vivo studies and clinical applications of magnesium based biodegradable implants – A review, J. Magnes. Alloy. 9 (2020) 1147–1163. https://doi.org/10.1016/j.jma.2020.11.001.

[154] E. Jablonská, J. Kubásek, D. Vojtěch, T. Ruml, J. Lipov, Test conditions can significantly affect the results of in vitro cytotoxicity testing of degradable metallic biomaterials, Sci. Rep. 11 (2021) 1–9. https://doi.org/10.1038/s41598-021-85019-6.

[155] A.H.M. Sanchez, B.J.C. Luthringer, F. Feyerabend, R. Willumeit, Mg and Mg alloys: How comparable are in vitro and in vivo corrosion rates? A review, Acta Biomater. 13 (2015) 16–31. https://doi.org/10.1016/j.actbio.2014.11.048.

[156] ISO/TS 73137-1 Biological evaluation of absorbable medical devices Part 1: General requirements, (2021). https://www.iso.org/standard/73582.html.

[157] S. Johnston, M. Dargusch, A. Atrens, Building towards a standardised approach to biocorrosion studies: a review of factors influencing Mg corrosion in vitro pertinent to

in vivo corrosion, Sci. China-Materials. 61 (2018) 475–500. https://doi.org/10.1007/s40843-017-9173-7.

[158] N.I. Zainal Abidin, A.A.D. Atrens, D. Martin, A.A.D. Atrens, Corrosion of high purity Mg, Mg2Zn0.2Mn, ZE41 and AZ91 in Hank's solution at 37°C, Corros. Sci. 53 (2011) 3542–3556. https://doi.org/10.1016/j.corsci.2011.06.030.

[159] J.L. Gilbert, Corrosion in the human body: Metallic implants in the complex body environment, Corrosion. 73 (2017) 1478–1495. https://doi.org/10.5006/2563.

[160] F. Feyerabend, In vitro analysis of magnesium corrosion in orthopaedic biomaterials, Woodhead Publishing Limited, 2014. https://doi.org/10.1533/9780857098104.2.225.

[161] R. Willumeit-Römer, N. Ahmad Agha, B. Luthringer, Degradable magnesium implants—assessment of the current situation, Miner. Met. Mater. Ser. Part F7 (2018) 405–411. https://doi.org/10.1007/978-3-319-72332-7_63.

[162] N.A. Agha, R. Willumeit-Romer, D. Laipple, B. Luthringer, F. Feyerabend, The Degradation Interface of Magnesium Based Alloys in Direct Contact with Human Primary Osteoblast Cells, PLoS One. 11 (2016). https://doi.org/10.1371/journal.pone.0157874.

[163] E. Bonyadi Rad, S. Mostofi, M. Katschnig, P. Schmutz, M. Pawelkiewicz, R. Willumeit-Römer, U. Schäfer, A. Weinberg, Differential apoptotic response of MC3T3-E1 pre-osteoblasts to biodegradable magnesium alloys in an in vitro direct culture model, J. Mater. Sci. Mater. Med. 28 (2017). https://doi.org/10.1007/s10856-017-5969-5.

[164] J. Zhang, S. Hiromoto, T. Yamazaki, J. Niu, H. Huang, G. Jia, H. Li, W. Ding, G. Yuan, Effect of macrophages on in vitro corrosion behavior of magnesium alloy, J. Biomed. Mater. Res. - Part A. 104 (2016) 2476–2487. https://doi.org/10.1002/jbm.a.35788.

[165] H. Azzeddine, A. Hanna, A. Dakhouche, L. Rabahi, N. Scharnagl, M. Dopita, F. Brisset, A.L. Helbert, T. Baudin, Impact of rare-earth elements on the corrosion performance of binary magnesium alloys, J. Alloys Compd. 829 (2020) 154569. https://doi.org/10.1016/j.jallcom.2020.154569.

[166] M.I. Jamesh, G. Wu, Y. Zhao, D.R. McKenzie, M.M.M.M. Bilek, P.K. Chu, Electrochemical corrosion behavior of biodegradable Mg-Y-RE and Mg-Zn-Zr alloys in Ringer's solution and simulated body fluid, Corros. Sci. 91 (2015) 160–184. https://doi.org/10.1016/j.corsci.2014.11.015.

[167] Y.K. Kim, K.B. Lee, S.Y. Kim, K. Bode, Y.S. Jang, T.Y. Kwon, M.H. Jeon, M.H. Lee, Gas formation and biological effects of biodegradable magnesium in a preclinical and clinical observation, Sci. Technol. Adv. Mater. 19 (2018) 324–335. https://doi.org/10.1080/14686996.2018.1451717.

[168] K. Tesař, K. Balík, Nucleation of corrosion products on H2 bubbles: A problem for biodegradable magnesium implants?, Mater. Today. 35 (2020) 195–196. https://doi.org/10.1016/j.mattod.2020.04.001.

[169] R.Q. Hou, N. Scharnagl, R. Willumeit-Römer, F. Feyerabend, Different effects of single protein vs. protein mixtures on magnesium degradation under cell culture conditions, Acta Biomater. 98 (2019) 256–268. https://doi.org/10.1016/j.actbio.2019.02.013.

[170] M. Kieke, F. Feyerabend, J. Lemaitre, P. Behrens, R. Willumeit-Römer, Degradation rates and products of pure magnesium exposed to different aqueous media under

physiological conditions, BioNanoMaterials. 17 (2016) 131–143. https://doi.org/10.1515/bnm-2015-0020.

[171] T. Li, Y. He, J. Zhou, S. Tang, Y. Yang, X. Wang, Influence of albumin on in vitro degradation behavior of biodegradable Mg-1.5Zn-0.6Zr-0.2Sc alloy, Mater. Lett. 217 (2018) 227–230. https://doi.org/10.1016/j.matlet.2018.01.082.

[172] L.Y. Cui, X.T. Li, R.C. Zeng, S.Q. Li, E.H. Han, L. Song, In vitro corrosion of Mg–Ca alloy — The influence of glucose content, Front. Mater. Sci. 11 (2017) 284–295. https://doi.org/10.1007/s11706-017-0391-y.

[173] R.C. Zeng, X.T. Li, S.Q. Li, F. Zhang, E.H. Han, In vitro degradation of pure Mg in response to glucose, Sci. Rep. 5 (2015) 1–14. https://doi.org/10.1038/srep13026.

[174] Y. Sun, H. Helmholz, R. Willumeit-Römer, Preclinical in vivo research of magnesium-based implants for fracture treatment: A systematic review of animal model selection and study design, J. Magnes. Alloy. 9 (2020) 351–361. https://doi.org/10.1016/j.jma.2020.09.011.

[175] I. Marco, A. Myrissa, E. Martinelli, F. Feyerabend, R. Willumeit-Römer, A.M. Weinberg, O. Van der Biest, In vivo and in vitro degradation comparison of pure Mg, Mg-10Gd and Mg-2Ag: A short term study, Eur. Cells Mater. 33 (2017) 90–104. https://doi.org/10.22203/eCM.v033a07.

[176] E.L. Zhang, L.P. Xu, G.N. Yu, F. Pan, K. Yang, In vivo evaluation of biodegradable magnesium alloy bone implant in the first 6 months implantation, J. Biomed. Mater. Res. Part A. 90A (2009) 882–893. https://doi.org/10.1002/jbm.a.32132.

[177] R.A. Lindtner, C. Castellani, S. Tangl, G. Zanoni, P. Hausbrandt, E.K. Tschegg, S.E. Stanzl-Tschegg, A.M. Weinberg, Comparative biomechanical and radiological characterization of osseointegration of a biodegradable magnesium alloy pin and a copolymeric control for osteosynthesis, J. Mech. Behav. Biomed. Mater. 28 (2013) 232–243. https://doi.org/10.1016/j.jmbbm.2013.08.008.

[178] A. Krause, N. von der Hoh, D. Bormann, C. Krause, F.W. Bach, H. Windhagen, A. Meyer-Lindenberg, N. Von Der Höh, D. Bormann, C. Krause, F.W. Bach, H. Windhagen, A. Meyer-Lindenberg, Degradation behaviour and mechanical properties of magnesium implants in rabbit tibiae, J. Mater. Sci. 45 (2010) 624–632. https://doi.org/10.1007/s10853-009-3936-3.

[179] J. Niu, M. Xiong, X. Guan, J. Zhang, H. Huang, J. Pei, G. Yuan, The in vivo degradation and bone-implant interface of Mg-Nd-Zn-Zr alloy screws: 18 months post-operation results, Corros. Sci. 113 (2016) 183–187. https://doi.org/10.1016/J.CORSCI.2016.10.009.

[180] M. Ma, D.B. Pokharel, J. Dong, L. Wu, R. Zhao, Y. Zhu, J. Hou, J. Xie, S. Sui, C. Wang, W. Ke, In vivo corrosion behavior of pure magnesium in femur bone of rabbit, J. Alloys Compd. 848 (2020) 156506. https://doi.org/10.1016/j.jallcom.2020.156506.

[181] J.X. Yang, F.Z. Cui, I.S. Lee, Y. Zhang, Q.S. Yin, H. Xia, S.X. Yang, In vivo biocompatibility and degradation behavior of Mg alloy coated by calcium phosphate in a rabbit model, J. Biomater. Appl. 27 (2012) 153–164. https://doi.org/10.1177/0885328211398161.

[182] L.L. Tan, Q. Wang, X. Lin, P. Wan, G.D. Zhang, Q. Zhang, K. Yang, Loss of mechanical

properties in vivo and bone-implant interface strength of AZ31B magnesium alloy screws with Si-containing coating, Acta Biomater. 10 (2014) 2333–2340. https://doi.org/10.1016/j.actbio.2013.12.020.

[183] J.-W. Lee, H.-S. Han, K.-J. Han, J. Park, H. Jeon, M.-R. Ok, H.-K. Seok, J.-P. Ahn, K.E.K.-S. Lee, D.-H. Lee, S.-J. Yang, S.-Y. Cho, P.-R. Cha, H. Kwon, T.-H. Nam, J.H. Lo Han, H.-J. Rho, K.E.K.-S. Lee, Y.-C. Kim, D. Mantovani, Long-term clinical study and multiscale analysis of in vivo biodegradation mechanism of Mg alloy, Proc. Natl. Acad. Sci. 113 (2016) 716–721. https://doi.org/10.1073/PNAS.1518238113.

[184] A. Chaya, S. Yoshizawa, K. Verdelis, N. Myers, B.J. Costello, D.T. Chou, S. Pal, S. Maiti, P.N. Kumta, C. Sfeir, In vivo study of magnesium plate and screw degradation and bone fracture healing, Acta Biomater. 18 (2015) 262–269. https://doi.org/10.1016/j.actbio.2015.02.010.

[185] T. Kraus, S.F. Fischerauer, A.C. Hanzi, P.J. Uggowitzer, J.F. Loffler, A.M. Weinberg, A.C. Hänzi, P.J. Uggowitzer, J.F. Löffler, A.M. Weinberg, Magnesium alloys for temporary implants in osteosynthesis: In vivo studies of their degradation and interaction with bone, Acta Biomater. 8 (2012) 1230–1238. https://doi.org/10.1016/j.actbio.2011.11.008.

[186] T. Imwinkelried, S. Beck, B. Schaller, Pre-clinical testing of human size magnesium implants in miniature pigs: Implant degradation and bone fracture healing at multiple implantation sites, Mater. Sci. Eng. C. 108 (2020) 110389. https://doi.org/10.1016/j.msec.2019.110389.

[187] N.G. Grün, P. Holweg, S. Tangl, J. Eichler, L. Berger, J.J.J.P. van den Beucken, J.F. Löffler, T. Klestil, A.M. Weinberg, Comparison of a resorbable magnesium implant in small and large growing-animal models, Acta Biomater. 78 (2018) 378–386. https://doi.org/10.1016/j.actbio.2018.07.044.

[188] P. Holweg, V. Herber, M. Ornig, G. Hohenberger, N. Donohue, P. Puchwein, A. Leithner, F. Seibert, A lean bioabsorbable magnesium-zinc-calcium alloy ZX00 used for operative treatment of medial malleolus fractures, Bone Joint Res. 9 (2020) 477–483. https://doi.org/10.1302/2046-3758.98.BJR-2020-0017.R2.

[189] V. Herber, B. Okutan, G. Antonoglou, N.G. Sommer, M. Payer, Bioresorbable Magnesium-Based Alloys as Novel Biomaterials in Oral Bone Regeneration: General Review and Clinical Perspectives, J. Clin. Med. 10 (2021). https://doi.org/10.3390/jcm10091842.

[190] Y. Luo, J. Wang, M.T.Y. Ong, P.S.H. Yung, J. Wang, L. Qin, Update on the research and development of magnesium-based biodegradable implants and their clinical translation in orthopaedics, Biomater. Transl. 2 (2021) 188–196. https://doi.org/10.12336/biomatertransl.2021.03.003.

[191] K. Xie, L. Wang, Y. Guo, S. Zhao, Y. Yang, D. Dong, W. Ding, K. Dai, W. Gong, G. Yuan, Y. Hao, Effectiveness and safety of biodegradable Mg-Nd-Zn-Zr alloy screws for the treatment of medial malleolar fractures, J. Orthop. Transl. 27 (2021) 96–100. https://doi.org/10.1016/j.jot.2020.11.007.

[192] A. Srinivasan, K.S. Shin, N. Rajendran, Influence of bicarbonate concentration on the conversion layer formation onto AZ31 magnesium alloy and its electrochemical corrosion behaviour in simulated body fluid, RSC Adv. 6 (2016) 49910–49922.

https://doi.org/10.1039/C6RA08478H.

[193] ISO 25178-2:2021 Geometrical Product Specifications (GPS)—Surface Texture: Areal—Part 2: Terms, Definitions and Surface Texture Parameters., Int. Organ. Stand. (2021).

[194] F. Rupp, R.A. Gittens, L. Scheideler, A. Marmur, B.D. Boyan, Z. Schwartz, J. Geis-Gerstorfer, A review on the wettability of dental implant surfaces I: Theoretical and experimental aspects, Acta Biomater. 10 (2014) 2894–2906. https://doi.org/10.1016/j.actbio.2014.02.040.

[195] D.K. Owens, R.C. Wendt, Estimation of the surface free energy of polymers, J. Appl. Polym. Sci. 13 (1969) 1741–1747. https://doi.org/10.1002/app.1969.070130815.

[196] V. Neubert, R. Schavan, Patent US9402669B2: Method for producing a medical implant from a magnesium alloy, 2016.

[197] H. Hermawan, Updates on the research and development of absorbable metals for biomedical applications, Prog. Biomater. 7 (2018) 93–110. https://doi.org/10.1007/s40204-018-0091-4.

[198] A.C. Lazanas, M.I. Prodromidis, Electrochemical Impedance Spectroscopy─A Tutorial, ACS Meas. Sci. Au. 3 (2023) 162–193. https://doi.org/10.1021/acsmeasuresciau.2c00070.

[199] ThermoFischer Scientific, MEM α, (n.d.). https://www.thermofisher.com/order/catalog/product/12561056?SID=srch-srp-12561056 (accessed March 7, 2024).

[200] Z. Xu, F. Fang, G. Zeng, O. Engineering, N. District, A. Science, Handbook of Manufacturing Engineering and Technology, Handb. Manuf. Eng. Technol. (2013) 1–28. https://doi.org/10.1007/978-1-4471-4976-7.

[201] N.S. Rajput, X. Luo, FIB Micro-/Nano-fabrication, Second Edi, Yi Qin, 2015. https://doi.org/10.1016/B978-0-323-31149-6.00003-7.

[202] C.J. Kirkpatrick, V. Krump-Konvalinkova, R.E. Unger, F. Bittinger, M. Otto, K. Peters, Tissue response and biomaterial integration: The efficacy of in vitro methods, Biomol. Eng. 19 (2002) 211–217. https://doi.org/10.1016/S1389-0344(02)00019-9.

[203] M. Fini, R. Giardino, In Vitro and in VIVO Tests for the Biological Evaluation of Candidate Orthopedic Materials: Benefits and Limits, J. Appl. Biomater. Biomech. 1 (2003) 155–163. https://doi.org/10.1177/228080000300100301.

[204] A. Guney, F. Kara, O. Ozgen, E.A. Aksoy, V. Hasirci, N. Hasirci, Surface Modification of Polymeric Biomaterials, in: A. Taubert, J.F. Mano, J.C. Rodriguez-Cabello (Eds.), Biomater. Surf. Sci., Wiley-VCH, Singapour, 2013: pp. 89–158. https://doi.org/10.1002/9783527649600.ch5.

[205] R. Aqib, S. Kiani, S. Bano, A. Wadood, M.A. Ur Rehman, Ag–Sr doped mesoporous bioactive glass nanoparticles loaded chitosan/gelatin coating for orthopedic implants, Int. J. Appl. Ceram. Technol. 18 (2021) 544–562. https://doi.org/10.1111/ijac.13702.

[206] A. Cerqueira, I. García-Arnáez, F. Romero-Gavilán, M. Azkargorta, F. Elortza, J.J. Martín de Llanos, C. Carda, M. Gurruchaga, I. Goñi, J. Suay, Complex effects of Mg-biomaterials on the osteoblast cell machinery: A proteomic study, Biomater. Adv. 137

(2022). https://doi.org/10.1016/j.bioadv.2022.212826.

[207] T. Zhang, W. Wang, J. Liu, L. Wang, Y. Tang, K. Wang, A review on magnesium alloys for biomedical applications, Front. Bioeng. Biotechnol. 10 (2022) 1–25. https://doi.org/10.3389/fbioe.2022.953344.

[208] V. Bazhenov, A. Koltygin, A. Komissarov, A. Li, V. Bautin, R. Khasenova, A. Anishchenko, A. Seferyan, J. Komissarova, Y. Estrin, Gallium-containing magnesium alloy for potential use as temporary implants in osteosynthesis, J. Magnes. Alloy. 8 (2020) 352–363. https://doi.org/10.1016/j.jma.2020.02.009.

[209] F. Witte, J. Fischer, J. Nellesen, H.A. Crostack, V. Kaese, A. Pisch, F. Beckmann, H. Windhagen, In vitro and in vivo corrosion measurements of magnesium alloys, Biomaterials. 27 (2006) 1013–1018. https://doi.org/10.1016/j.biomaterials.2005.07.037.

[210] M. Ezechieli, J. Diekmann, A. Weizbauer, C. Becher, E. Willbold, P. Helmecke, A. Lucas, R. Schavan, H. Windhagen, Biodegradation of a magnesium alloy implant in the intercondylar femoral notch showed an appropriate response to the synovial membrane in a rabbit model in vivo, J. Biomater. Appl. 29 (2014) 291–302. https://doi.org/10.1177/0885328214523322.

[211] J. Liu, B. Liu, S. Min, B. Yin, B. Peng, Z. Yu, C. Wang, X. Ma, P. Wen, Y. Tian, Y. Zheng, Biodegradable magnesium alloy WE43 porous scaffolds fabricated by laser powder bed fusion for orthopedic applications: Process optimization, in vitro and in vivo investigation, Bioact. Mater. 16 (2022) 301–319. https://doi.org/10.1016/j.bioactmat.2022.02.020.

[212] J. Liu, B. Yin, F. Song, B. Liu, B. Peng, P. Wen, Y. Tian, Y. Zheng, X. Ma, C. Wang, Improving corrosion resistance of additively manufactured WE43 magnesium alloy by high temperature oxidation for biodegradable applications, J. Magnes. Alloy. (2022). https://doi.org/10.1016/j.jma.2022.08.009.

[213] J.T. Choo, S.H.S. Lai, C.Q.Y. Tang, G. Thevendran, Magnesium-based bioabsorbable screw fixation for hallux valgus surgery – A suitable alternative to metallic implants, Foot Ankle Surg. 25 (2019) 727–732. https://doi.org/10.1016/j.fas.2018.09.001.

[214] H. Atkinson, S. Khan, Y. Lashgari, A. Ziegler, Hallux valgus correction utilising a modified short scarf osteotomy with a magnesium biodegradable or titanium compression screws – a comparative study of clinical outcomes, BMC Musculoskelet. Disord. 20 (2019). https://doi.org/10.1186/s12891-019-2717-7.

[215] V. Herber, V. Labmayr, N.G. Sommer, R. Marek, U. Wittig, A. Leithner, F. Seibert, P. Holweg, Can Hardware Removal be Avoided Using Bioresorbable Mg-Zn-Ca Screws After Medial Malleolar Fracture Fixation? Mid-Term Results of a First-In-Human Study, Injury. 53 (2022) 1283–1288. https://doi.org/10.1016/j.injury.2021.10.025.

[216] A. Gigante, N. Setaro, M. Rotini, S.S. Finzi, M. Marinelli, Intercondylar eminence fracture treated by resorbable magnesium screws osteosynthesis: A case series, Injury. 49 (2018) S48–S53. https://doi.org/10.1016/j.injury.2018.09.055.

[217] W.-H. Lam, C.-Y. Tso, N. Tang, W.-H. Cheung, L. Qin, R.M.-Y. Wong, Biodegradable magnesium screws in elbow fracture fixation: Clinical case series, J. Orthop. Trauma Rehabil. (2021) 2210491720986983. https://doi.org/10.1177/2210491720986983.

[218] A. Turan, Y. alper Katı, B. Acar, O. Kose, Magnesium Bioabsorbable Screw Fixation

of Radial Styloid Fractures: Case Report., J. Wrist Surg. 9 2 (2020) 150–155. https://doi.org/10.1055/S-0039-1685489.

[219] H. Leonhardt, A. Franke, N.M.H.H. Mcleod, G. Lauer, A. Nowak, Fixation of fractures of the condylar head of the mandible with a new magnesium-alloy biodegradable cannulated headless bone screw, Br. J. Oral Maxillofac. Surg. 55 (2017) 623–625. https://doi.org/10.1016/j.bjoms.2017.04.007.

[220] E.K. Brooks, M.E. Tobias, S. Yang, L.B. Bone, M.T. Ehrensberger, Influence of MC3T3-E1 preosteoblast culture on the corrosion of a T6-treated AZ91 alloy, J. Biomed. Mater. Res. - Part B Appl. Biomater. 104 (2016) 253–262. https://doi.org/10.1002/jbm.b.33378.

[221] B. Okutan, U.Y. Schwarze, L. Berger, D.C. Martinez, V. Herber, O. Suljevic, T. Plocinski, W. Swieszkowski, S.G. Santos, A.M. Weinberg, N.G. Sommer, R. Schindl, The combined effect of zinc and calcium on the biodegradation of ultrahigh-purity magnesium implants, Biomater. Adv. 146 (2023). https://doi.org/https://doi.org/10.1016/j.bioadv.2023.213287.

[222] D. Li, D. Zhang, Q. Yuan, L. Liu, H. Li, L. Xiong, X. Guo, Y. Yan, K. Yu, Y. Dai, T. Xiao, Y. Li, C. Wen, In vitro and in vivo assessment of the effect of biodegradable magnesium alloys on osteogenesis, Acta Biomater. 141 (2022) 454–465. https://doi.org/10.1016/j.actbio.2021.12.032.

[223] D. Bian, J. Deng, N. Li, X. Chu, Y. Liu, W. Li, H. Cai, P. Xiu, Y. Zhang, Z. Guan, Y. Zheng, Y. Kou, B. Jiang, R. Chen, In Vitro and in Vivo Studies on Biomedical Magnesium Low-Alloying with Elements Gadolinium and Zinc for Orthopedic Implant Applications, ACS Appl. Mater. Interfaces. 10 (2018) 4394–4408. https://doi.org/10.1021/acsami.7b15498.

[224] S. Prasadh, M. Gupta, R. Wong, In vitro cytotoxicity and osteogenic potential of quaternary Mg-2Zn-1Ca/X-Mn alloys for craniofacial reconstruction, Sci. Rep. 12 (2022) 1–12. https://doi.org/10.1038/s41598-022-12490-0.

[225] S. Nie, J. Chen, C. Liu, C. Zhou, J. Zhao, Z. Wang, J. Sun, Y. Huang, Effects of extract solution from magnesium alloys supplemented with different compositions of rare earth elements on in vitro epithelial and osteoblast progenitor cells, Front. Bioeng. Biotechnol. 11 (2023) 1–10. https://doi.org/10.3389/fbioe.2023.1138675.

[226] X. Gu, Y. Zheng, Y. Cheng, S. Zhong, T. Xi, In vitro corrosion and biocompatibility of binary magnesium alloys., Biomaterials. 30 4 (2009) 484–498. https://doi.org/10.1016/j.biomaterials.2008.10.021.

[227] Y. Liao, Q. Xu, J. Zhang, J. Niu, G. Yuan, Y. Jiang, Y. He, X. Wang, Cellular response of chondrocytes to magnesium alloys for orthopedic applications, Int. J. Mol. Med. 36 (2015) 73–82. https://doi.org/10.3892/ijmm.2015.2211.

[228] L.L. Wu, F. Feyerabend, A.F. Schilling, R. Willumeit-Romer, B.J.C. Luthringer, Effects of extracellular magnesium extract on the proliferation and differentiation of human osteoblasts and osteoclasts in coculture, Acta Biomater. 27 (2015) 294–304. https://doi.org/10.1016/j.actbio.2015.08.042.

[229] L. Pompa, Z.U. Rahman, E. Munoz, W. Haider, Surface characterization and cytotoxicity response of biodegradable magnesium alloys, Mater. Sci. Eng. C-Materials Biol. Appl. 49 (2015) 761–768. https://doi.org/10.1016/j.msec.2015.01.017.

[230] D. Maradze, D. Musson, Y. Zheng, J. Cornish, M. Lewis, Y. Liu, High Magnesium Corrosion Rate has an Effect on Osteoclast and Mesenchymal Stem Cell Role during Bone Remodelling, Sci. Rep. 8 (2018) 1–15. https://doi.org/10.1038/s41598-018-28476-w.

[231] F. Cecchinato, N.A. Agha, A.H. Martinez-Sanchez, B.J.C. Luthringer, F. Feyerabend, R. Jimbo, R. Willumeit-Römer, A. Wennerberg, Influence of magnesium alloy degradation on undifferentiated human cells, PLoS One. 10 (2015) 1–18. https://doi.org/10.1371/journal.pone.0142117.

[232] J.D. Cao, P. Martens, K.J. Laws, P. Boughton, M. Ferry, Quantitative in vitro assessment of Mg65Zn30Ca 5 degradation and its effect on cell viability, J. Biomed. Mater. Res. - Part B Appl. Biomater. 101 B (2013) 43–49. https://doi.org/10.1002/jbm.b.32811.

[233] S. Mostofi, E.B. Rad, H. Wiltsche, U. Fasching, G. Szakacs, C. Ramskogler, S. Srinivasaiah, M. Ueçal, R. Willumeit, A.M. Weinberg, U. Schaefer, Effects of corroded and non-corroded biodegradable mg and mg alloys on viability, morphology and differentiation of MC3T3-E1 cells elicited by direct Cell/Material interaction, PLoS One. 11 (2016) 1–21. https://doi.org/10.1371/journal.pone.0159879.

[234] R. Unbehau, B.J.C. Luthringer-Feyerabend, R. Willumeit-Römer, The impact of brain cell metabolism and extracellular matrix on magnesium degradation, Acta Biomater. 116 (2020) 426–437. https://doi.org/10.1016/j.actbio.2020.08.043.

[235] D. Dvorsky, J. Kubasek, E. Jablonska, J. Kaufmanova, D. Vojtech, Mechanical, corrosion and biological properties of advanced biodegradable Mg–MgF2 and WE43-MgF2 composite materials prepared by spark plasma sintering, J. Alloys Compd. 825 (2020) 154016. https://doi.org/10.1016/j.jallcom.2020.154016.

[236] N. Anisimova, N. Martynenko, K. Novruzov, O. Rybalchenko, A. Mansharipova, A. Kabiyeva, M. Gabdullin, S. Dobatkin, Y. Estrin, Modification of Biocorrosion and Cellular Response of, Metals (Basel). 12 (2022) 1–16. https://doi.org/https://doi.org/10.3390/met12010105.

[237] A. Burmester, R. Willumeit-Römer, F. Feyerabend, Behavior of bone cells in contact with magnesium implant material, J. Biomed. Mater. Res. - Part B Appl. Biomater. 105 (2017) 165–179. https://doi.org/10.1002/jbm.b.33542.

[238] X. Gu, Y. Zheng, S. Zhong, T. Xi, J. Wang, W. Wang, Corrosion of, and cellular responses to Mg-Zn-Ca bulk metallic glasses, Biomaterials. 31 (2010) 1093–1103. https://doi.org/10.1016/j.biomaterials.2009.11.015.

[239] V. Wagener, A. Schilling, A. Mainka, D. Hennig, R. Gerum, M.L. Kelch, S. Keim, B. Fabry, S. Virtanen, Cell Adhesion on Surface-Functionalized Magnesium, ACS Appl. Mater. Interfaces. 8 (2016) 11998–12006. https://doi.org/10.1021/acsami.6b01747.

[240] O. Charyeva, O. Dakischew, U. Sommer, C. Heiss, R. Schnettler, K. Lips, Biocompatibility of magnesium implants in primary human reaming debris- derived cells stem cells in vitro, Off. J. Ital. Soc. Orthop. Traumatol. 17 (2016) 63–73. https://doi.org/10.1007/s10195-015-0364-9.

[241] Q. Wang, S. Jin, X. Lin, Y. Zhang, L. Ren, K. Yang, Cytotoxic Effects of Biodegradation of Pure Mg and MAO-Mg on Tumor Cells of MG63 and KB, J. Mater. Sci. Technol. 30 (2014) 487–492. https://doi.org/10.1016/j.jmst.2014.03.004.

[242] S. Zhang, J. Li, Y. Song, C. Zhao, X. Zhang, C. Xie, Y. Zhang, H. Tao, Y. He, Y. Jiang, Y. Bian, In vitro degradation, hemolysis and MC3T3-E1 cell adhesion of biodegradable Mg-Zn alloy, Mater. Sci. Eng. C. 29 (2009) 1907–1912. https://doi.org/10.1016/j.msec.2009.03.001.

[243] A. Yamamoto, Y. Kohyama, Cytocompatibility of Mg alloys and the effect of cells on their degradation in biological environment, Magnes. Technol. (2014) 381–385. https://doi.org/10.1002/9781118888179.ch72.

[244] M.B. Kannan, A. Yamamoto, H. Khakbaz, Influence of living cells (L929) on the biodegradation of magnesium-calcium alloy, Colloids Surfaces B Biointerfaces. 126 (2015) 603–606. https://doi.org/10.1016/j.colsurfb.2015.01.015.

[245] P. Globig, R. Willumeit-Römer, F. Martini, E. Mazzoni, B.J.C. Luthringer-Feyerabend, Slow degrading Mg-based materials induce tumor cell dormancy on an osteosarcoma-fibroblast coculture model, Bioact. Mater. 16 (2022) 320–333. https://doi.org/10.1016/j.bioactmat.2021.12.031.

[246] P. Globig, R. Willumeit-Römer, F. Martini, E. Mazzoni, B.J.C. Luthringer-Feyerabend, Optimizing an osteosarcoma-fibroblast coculture model to study antitumoral activity of magnesium-based biomaterials, Int. J. Mol. Sci. 21 (2020) 1–18. https://doi.org/10.3390/ijms21145099.

[247] F. Seuss, S. Seuss, M.C. Turhan, B. Fabry, S. Virtanen, Corrosion of Mg alloy AZ91D in the presence of living cells, J. Biomed. Mater. Res. - Part B Appl. Biomater. 99 B (2011) 276–281. https://doi.org/10.1002/jbm.b.31896.

[248] A. Bernhardt, H. Helmholz, D. Kilian, R. Willumeit-Römer, M. Gelinsky, Impact of degradable magnesium implants on osteocytes in single and triple cultures, Biomater. Adv. 134 (2022) 112692. https://doi.org/10.1016/j.msec.2022.112692.

[249] Magnesium Electron WE43 Alloy (UNS M18430), AZO materials, (2013). 0.1016/j.actbio.2020.08.043 (accessed February 1, 2024).

[250] ISO 25178-3:2012 Geometrical product specifications (GPS)—Surface texture: Areal—Part 3: Specification operators, Int. Organ. Stand. Stand. (2012).

[251] B.J.C. Luthringer, F. Ali, H. Akaichi, F. Feyerabend, T. Ebel, R. Willumeit, Production, characterisation, and cytocompatibility of porous titanium-based particulate scaffolds, J. Mater. Sci. Mater. Med. 24 (2013) 2337–2358. https://doi.org/10.1007/s10856-013-4989-z.

[252] B.J.C. Luthringer, R. Willumeit-Römer, Effects of magnesium degradation products on mesenchymal stem cell fate and osteoblastogenesis, Gene. 575 (2016) 9–20. https://doi.org/10.1016/j.gene.2015.08.028.

[253] Q. Wang, L. Xu, H. Helmholz, R. Willumeit-Römer, B.J.C. Luthringer-Feyerabend, Effects of degradable magnesium on paracrine signaling between human umbilical cord perivascular cells and peripheral blood mononuclear cells, Biomater. Sci. 8 (2020) 5969–5983. https://doi.org/10.1039/d0bm00834f.

[254] R. Willumeit, A. Mohring, F. Feyerabend, Optimization of Cell Adhesion on Mg Based Implant Materials by Pre-Incubation under Cell Culture Conditions, Int. J. Mol. Sci. 15 (2014) 7639–7650. https://doi.org/10.3390/ijms15057639.

[255] Anon, Standard Practice for Preparing, Cleaning, and Evaluating Corrosion Test

Specimens, ASTM Spec. Tech. Publ. i (2017) 505–510. https://doi.org/10.1520/G0001-03R17E01.2.

[256] E.R. Fischer, B.T. Hansen, V. Nair, F.H. Hoyt, D.W. Dorward, Scanning electron microscopy, Curr. Protoc. Microbiol. Chapter 2 (2012) Unit2B.2-2B.2. https://doi.org/10.1002/9780471729259.mc02b02s25.

[257] J. Schindelin, I. Arganda-Carreras, E. Frise, V. Kaynig, M. Longair, T. Pietzsch, S. Preibisch, C. Rueden, S. Saalfeld, B. Schmid, J.-Y. Tinevez, D.J. White, V. Hartenstein, K. Eliceiri, P. Tomancak, A. Cardona, Fiji: an open-source platform for biological-image analysis, Nat. Methods. 9 (2012) 676–682. https://doi.org/10.1038/nmeth.2019.

[258] I. Puigdomenech, Chemical Equilibrium Diagrams, 2020. (n.d.). https://www.kth.se/ch%0De/medusa/chemeq-1.369367.

[259] G.S. Pereira, G.Y. Koga, J.A. Avila, I.M. Bittencourt, F. Fernandez, M.H. Miyazaki, W.J. Botta, W.W. Bose Filho, Corrosion resistance of WE43 Mg alloy in sodium chloride solution, Mater. Chem. Phys. 272 (2021). https://doi.org/10.1016/j.matchemphys.2021.124930.

[260] A. Dobkowska, A. Zielińska, I. Paulin, Č. Donik, M. Koralnik, B. Adamczyk – Cieślak, M. Wieczorek-Czarnocka, D. Kuc, J. Kubasek, T. Mikuszewski, M. Godec, J. Mizera, Microstructural, corrosion and mechanical properties of a WE43 alloy: conventional extrusion versus SPD, J. Alloys Compd. 976 (2024) 173090. https://doi.org/10.1016/j.jallcom.2023.173090.

[261] A.S. Gnedenkov, S. V. Lamaka, S.L. Sinebryukhov, D. V. Mashtalyar, V.S. Egorkin, I.M. Imshinetskiy, A.G. Zavidnaya, M.L. Zheludkevich, S. V. Gnedenkov, Electrochemical behaviour of the MA8 Mg alloy in minimum essential medium, Corros. Sci. 168 (2020) 108552. https://doi.org/10.1016/j.corsci.2020.108552.

[262] A.D. King, N. Birbilis, J.R. Scully, Accurate electrochemical measurement of magnesium corrosion rates; A combined impedance, mass-loss and hydrogen collection study, Electrochim. Acta. 121 (2014) 394–406. https://doi.org/10.1016/j.electacta.2013.12.124.

[263] S. Johnston, Z. Shi, A. Atrens, The influence of pH on the corrosion rate of high-purity Mg, AZ91 and ZE41 in bicarbonate buffered Hanks' solution, Corros. Sci. 101 (2015) 182–192. https://doi.org/10.1016/j.corsci.2015.09.018.

[264] G. Song, A. Atrens, D. St. John, X. Wu, J. Nairn, The anodic dissolution of magnesium in chloride and sulphate solutions, Corros. Sci. 39 (1997) 1981–2004. https://doi.org/10.1016/S0010-938X(97)00090-5.

[265] R. K.R., S. Bontha, R. M.R., M. Das, V.K. Balla, Laser surface melting of Mg-Zn-Dy alloy for better wettability and corrosion resistance for biodegradable implant applications, Appl. Surf. Sci. 480 (2019) 70–82. https://doi.org/10.1016/j.apsusc.2019.02.167.

[266] Y.H. Ho, K. Man, S.S. Joshi, M. V. Pantawane, T.C. Wu, Y. Yang, N.B. Dahotre, In-vitro biomineralization and biocompatibility of friction stir additively manufactured AZ31B magnesium alloy-hydroxyapatite composites, Bioact. Mater. 5 (2020) 891–901. https://doi.org/10.1016/j.bioactmat.2020.06.009.

[267] H. Ben, D.C. Martinez, K. Iskhakova, L. Emanuelsson, B. Norlindh, A. Johansson,

D.C.F. Wieland, B. Zeller-Plumhoff, R. Willumeit-Römer, T. Plocinski, W. Swieszkowski, F.A. Shah, A. Palmquist, P. Thomsen, Multifaceted response to immunomodulatory magnesium implants: Osteopromotion at the interface and adipogenesis in the bone marrow, (n.d.).

[268] W. Ali, M. Echeverry-Rendón, G. Dominguez, K. van Gaalen, A. Kopp, C. González, J. LLorca, Bioabsorbable WE43 Mg alloy wires modified by continuous plasma electrolytic oxidation for implant applications. Part II: Degradation and biological performance, Biomater. Adv. 147 (2023). https://doi.org/10.1016/j.bioadv.2023.213325.

[269] K.-L. Chen, Y. Lu, H. Tang, Y. Gao, F. Zhao, X. Gu, Y. Fan, Effect of strain on degradation behaviors of WE43, Fe and Zn wires., Acta Biomater. (2020). https://doi.org/10.1016/j.actbio.2020.06.028.

[270] W. Ding, Opportunities and challenges for the biodegradable magnesium alloys as next-generation biomaterials, Regen. Biomater. 3 (2016) 79–86. https://doi.org/10.1093/RB/RBW003.

[271] M. Esmaily, Z. Zeng, A.N. Mortazavi, A. Gullino, S. Choudhary, T. Derra, F. Benn, F. D'Elia, M. Müther, S. Thomas, A. Huang, A. Allanore, A. Kopp, N. Birbilis, A detailed microstructural and corrosion analysis of magnesium alloy WE43 manufactured by selective laser melting, Addit. Manuf. 35 (2020) 101321. https://doi.org/10.1016/j.addma.2020.101321.

[272] D. He, H. Li, Biomaterials affect cell-cell interactions in vitro in tissue engineering, J. Mater. Sci. Technol. 63 (2021) 62–72. https://doi.org/10.1016/j.jmst.2020.03.022.

[273] S.Y. Lee, S. Shrestha, B.K. Shrestha, C.H. Park, C.S. Kim, Covalent surface functionalization of bovine serum albumin to magnesium surface to provide robust corrosion inhibition and enhance in vitro osteo-inductivity, Polymers (Basel). 12 (2020). https://doi.org/10.3390/polym12020439.

[274] S.H. Byun, H.K. Lim, K.H. Cheon, S.M. Lee, H.E. Kim, J.H. Lee, Biodegradable magnesium alloy (WE43) in bone-fixation plate and screw, J. Biomed. Mater. Res. - Part B Appl. Biomater. 108 (2020) 2505–2512. https://doi.org/10.1002/jbm.b.34582.

[275] L.L. Wu, B.J.C. Luthringer, F. Feyerabend, A.F. Schilling, R. Willumeit, Effects of extracellular magnesium on the differentiation and function of human osteoclasts, Acta Biomater. 10 (2014) 2843–2854. https://doi.org/10.1016/j.actbio.2014.02.010.

[276] M. Muzylak, T.R. Arnett, J.S. Price, M.A. Horton, The In Vitro Effect of pH on Osteoclasts and Bone Resorption in the Cat: Implications for the Pathogenesis of FORL, J. Cell. Physiol. 213 (2007) 140–150. https://doi.org/10.1002/jcp.21103.

[277] X. Wang, Y. Yu, L. Ji, Z. Geng, J. Wang, C. Liu, Calcium phosphate-based materials regulate osteoclast-mediated osseointegration, Bioact. Mater. 6 (2021) 4517–4530. https://doi.org/10.1016/j.bioactmat.2021.05.003.

[278] E. Lukyanova, N. Anisimova, N. Martynenko, M. Kiselevsky, S. Dobatkin, Y. Estrin, Features of in vitro and in vivo behaviour of magnesium alloy WE43, Mater. Lett. 215 (2018) 308–311. https://doi.org/10.1016/j.matlet.2017.12.125.

[279] M. Li, F. Benn, T. Derra, N. Kröger, M. Zinser, R. Smeets, J.M. Molina-Aldareguia, A. Kopp, J. LLorca, Microstructure, mechanical properties, corrosion resistance and

cytocompatibility of WE43 Mg alloy scaffolds fabricated by laser powder bed fusion for biomedical applications, Mater. Sci. Eng. C. 119 (2021) 111623. https://doi.org/10.1016/j.msec.2020.111623.

[280] A. Witecka, A. Yamamoto, W. Święszkowski, Influence of SaOS-2 cells on corrosion behavior of cast Mg-2.0Zn0.98Mn magnesium alloy, Colloids Surfaces B Biointerfaces. 150 (2017) 288–296. https://doi.org/10.1016/J.COLSURFB.2016.10.041.

[281] N.T.H. Farr, G.M. Hughes, C. Rodenburg, Monitoring carbon in electron and ion beam deposition within fib-sem, Materials (Basel). 14 (2021). https://doi.org/10.3390/ma14113034.

[282] A. Vladar, M. Postek, Electron Beam-Induced Sample Contamination in the SEM, Microsc. Microanal. 11 (2005) 764–765. https://doi.org/10.1017/s1431927605507785.

[283] D.C. Martinez, A. Dobkowska, R. Marek, H. Cwieka, W. Swi, In vitro and in vivo degradation behavior of Mg-0.45Zn-0.45Ca (ZX00) screws for orthopedic applications, Bioact. Mater. 28 (2023) 132–154. https://doi.org/10.1016/j.bioactmat.2023.05.004.

[284] M. Liu, Q. Zhang, X. Tang, C. Liu, D. Mei, L. Wang, S. Zhu, M.L. Zheludkevich, S. Lamaka, S. Guan, Effect of medium renewal mode on the degradation behavior of Mg alloys for biomedical applications during the long-term in vitro test, Corros. Sci. 229 (2024) 111851. https://doi.org/10.1016/j.corsci.2024.111851.

[285] Y. Zhang, Y. Huang, F. Feyerabend, C. Blawert, W. Gan, E. Maawad, S. You, S. Gavras, N. Scharnagl, J. Bode, C. Vogt, D. Zander, R. Willumeit-Römer, K.U. Kainer, N. Hort, Influence of the amount of intermetallics on the degradation of Mg-Nd alloys under physiological conditions, Acta Biomater. 121 (2021) 695–712. https://doi.org/10.1016/j.actbio.2020.11.050.

[286] J. Nachtsheim, J. Burja, S. Ma, B. Markert, Long-Term in Vitro Corrosion of Biodegradable WE43 Magnesium Alloy in DMEM, Metals (Basel). 12 (2022). https://doi.org/10.3390/met12122062.

[287] L.P. Xu, F. Pan, G.N. Yu, L. Yang, E.L. Zhang, K. Yang, In vitro and in vivo evaluation of the surface bioactivity of a calcium phosphate coated magnesium alloy, Biomaterials. 30 8 (2009) 1512–1523. https://doi.org/10.1016/j.biomaterials.2008.12.001.

[288] S. Jin, D. Zhang, X. Lu, Y. Zhang, L. Tan, Y. Liu, Q. Wang, Mechanical properties, biodegradability and cytocompatibility of biodegradable Mg-Zn-Zr-Nd/Y alloys, J. Mater. Sci. Technol. 47 (2020) 190–201. https://doi.org/10.1016/j.jmst.2020.02.017.

[289] C. Castellani, R.A. Lindtner, P. Hausbrandt, E. Tschegg, S.E. Stanzl-Tschegg, G. Zanoni, S. Beck, A.-M.M. Weinberg, Bone-implant interface strength and osseointegration: Biodegradable magnesium alloy versus standard titanium control, Acta Biomater. 7 (2011) 432–440. https://doi.org/10.1016/j.actbio.2010.08.020.

[290] X. Wei, P. Liu, S. Ma, Z. Li, X. Peng, R. Deng, Q. Zhao, Improvement on corrosion resistance and biocompability of ZK60 magnesium alloy by carboxyl ion implantation, Corros. Sci. 173 (2020) 108729. https://doi.org/10.1016/j.corsci.2020.108729.

[291] J. Jeong, J.H. Kim, J.H. Shim, N.S. Hwang, C.Y. Heo, Bioactive calcium phosphate materials and applications in bone regeneration, Biomater. Res. 23 (2019) 1–11. https://doi.org/10.1186/s40824-018-0149-3.

[292] I. Antoniac, M. Miculescu, V. Mănescu, A. Stere, P.H. Quan, G. Păltânea, A. Robu, K.

Earar, Magnesium-Based Alloys Used in Orthopedic Surgery, Materials (Basel). 15 (2022) 1–32. https://doi.org/10.3390/ma15031148.

[293] C. Plaass, C. von Falck, S. Ettinger, L. Sonnow, F. Calderone, A. Weizbauer, J. Reifenrath, L. Claassen, H. Waizy, K. Daniilidis, C. Stukenborg-Colsman, H. Windhagen, Bioabsorbable magnesium versus standard titanium compression screws for fixation of distal metatarsal osteotomies - 3 year results of a randomized clinical trial., J. Orthop. Sci. 23 2 (2018) 321–327. https://doi.org/10.1016/j.jos.2017.11.005.

[294] C. Sukotjo, T.J. Lima-Neto, J.F.S. Júnior, L. Faverani, M. Miloro, Is There a Role for Absorbable Metals in Surgery? A Systematic Review and Meta-Analysis of Mg/Mg Alloy Based Implants, Materials (Basel). 13 (2020). https://doi.org/10.3390/ma13183914.

[295] J. Espiritu, M. Meier, J.-M. Seitz, The current performance of biodegradable magnesium-based implants in magnetic resonance imaging: A review, Bioact. Mater. 6 (2021) 4360–4367. https://doi.org/https://doi.org/10.1016/j.bioactmat.2021.04.012.

[296] L. Riehakainen, C. Cavallini, P. Armanetti, D. Panetta, D. Caramella, L. Menichetti, In Vivo Imaging of Biodegradable Implants and Related Tissue Biomarkers., Polymers (Basel). 13 (2021). https://doi.org/10.3390/polym13142348.

[297] Z. Shan, X. Xie, X. Wu, S. Zhuang, C. Zhang, Development of degradable magnesium-based metal implants and their function in promoting bone metabolism (A review), J. Orthop. Transl. 36 (2022) 184–193. https://doi.org/10.1016/j.jot.2022.09.013.

[298] Y. Lu, S. Deshmukh, I. Jones, Y.-L. Chiu, Biodegradable magnesium alloys for orthopaedic applications., Biomater. Transl. 2 (2021) 214–235. https://doi.org/10.12336/biomatertransl.2021.03.005.

[299] L. Tian, N. Tang, T. Ngai, C. Wu, Y. Ruan, L. Huang, L. Qin, Hybrid fracture fixation systems developed for orthopaedic applications: A general review., J. Orthop. Transl. 16 (2019) 1–13. https://doi.org/10.1016/j.jot.2018.06.006.

[300] F. Amerstorfer, S.F. Fischerauer, L. Fischer, J. Eichler, J. Draxler, A. Zitek, M. Meischel, E. Martinelli, T. Kraus, S. Hann, S.E. Stanzl-Tschegg, P.J. Uggowitzer, J.F. Löffler, A.M. Weinberg, T. Prohaska, J.F. Loffler, A.M. Weinberg, T. Prohaska, Long-term in vivo degradation behavior and near-implant distribution of resorbed elements for magnesium alloys WZ21 and ZX50, Acta Biomater. 42 (2016) 440–450. https://doi.org/10.1016/j.actbio.2016.06.025.

[301] T. Kraus, S. Fischerauer, S. Treichler, E. Martinelli, J. Eichler, A. Myrissa, S. Zotsch, P.J. Uggowitzer, J.F. Loffler, A.M. Weinberg, The influence of biodegradable magnesium implants on the growth plate, Acta Biomater. 66 (2018) 109–117. https://doi.org/10.1016/j.actbio.2017.11.031.

[302] W. Zhao, J. Wang, J. Weiyang, B. Qiao, Y. Wang, Y. Li, D. Jiang, A novel biodegradable Mg-1Zn-0.5Sn alloy: Mechanical properties, corrosion behavior, biocompatibility, and antibacterial activity, J. Magnes. Alloy. 8 (2020) 374–386. https://doi.org/https://doi.org/10.1016/j.jma.2020.02.008.

[303] N. Kawamura, Y. Nakao, R. Ishikawa, D. Tsuchida, M. Iijima, Degradation and Biocompatibility of AZ31 Magnesium Alloy Implants In Vitro and In Vivo: A Micro-Computed Tomography Study in Rats, Materials (Basel). 13 (2020). https://doi.org/10.3390/ma13020473.

[304] C. Hampp, N. Angrisani, J. Reifenrath, D. Bormann, J.M. Seitz, A. Meyer-Lindenberg, Evaluation of the biocompatibility of two magnesium alloys as degradable implant materials in comparison to titanium as non-resorbable material in the rabbit, Mater. Sci. Eng. C-Materials Biol. Appl. 33 (2013) 317–326. https://doi.org/10.1016/j.msec.2012.08.046.

[305] M. Cheng, T. Wahafu, G. Jiang, W. Liu, Y. Qiao, X. Peng, T. Cheng, X. Zhang, G. He, X. Liu, A novel open-porous magnesium scaffold with controllable microstructures and properties for bone regeneration., Sci. Rep. 6 (2016) 24134. https://doi.org/10.1038/srep24134.

[306] J. Wang, J. Xu, B. Song, D.H. Chow, P. Shu-Hang Yung, L. Qin, Magnesium (Mg) based interference screws developed for promoting tendon graft incorporation in bone tunnel in rabbits., Acta Biomater. 63 (2017) 393–410. https://doi.org/10.1016/j.actbio.2017.09.018.

[307] B. Li, P. Gao, H. Zhang, Z. Guo, Y. Zheng, Y. Han, Osteoimmunomodulation, osseointegration, and in vivo mechanical integrity of pure Mg coated with HA nanorod/pore-sealed MgO bilayer, Biomater. Sci. 6 (2018) 3202–3218. https://doi.org/10.1039/C8BM00901E.

[308] A. Mahato, M. De, P. Bhattacharjee, V. Kumar, P. Mukherjee, G. Singh, B. Kundu, V.K. Balla, S.K. Nandi, Role of calcium phosphate and bioactive glass coating on in vivo bone healing of new Mg–Zn–Ca implant, J. Mater. Sci. Mater. Med. 32 (2021). https://doi.org/10.1007/s10856-021-06510-0.

[309] M. Zhou, S. Li, J.L. Pathak, Pro-inflammatory Cytokines and Osteocytes., Curr. Osteoporos. Rep. 17 (2019) 97–104. https://doi.org/10.1007/s11914-019-00507-z.

[310] J.P. Connors, J.W. Stelzer, P.M. Garvin, I.J. Wellington, O. Solovyova, The Role of the Innate Immune System in Wear Debris-Induced Inflammatory Peri-Implant Osteolysis in Total Joint Arthroplasty, Bioengineering. 9 (2022). https://doi.org/10.3390/bioengineering9120764.

[311] R.D. Ross, Y. Deng, R. Fang, N.B. Frisch, J.J. Jacobs, D.R. Sumner, Discovery of biomarkers to identify peri-implant osteolysis before radiographic diagnosis., J. Orthop. Res. Off. Publ. Orthop. Res. Soc. 36 (2018) 2754–2761. https://doi.org/10.1002/jor.24044.

[312] G. Basta, F. Melandro, S. Babboni, S. Del Turco, R. Ndreu, F. Torri, C. Martinelli, B. Silvestrini, A. Peris, C. Lazzeri, F. Guarracino, R. Morganti, P. Maremmani, P. Bertini, P. De Simone, D. Ghinolfi, An extensive evaluation of hepatic markers of damage and regeneration in controlled and uncontrolled donation after circulatory death., Liver Transplant. Off. Publ. Am. Assoc. Study Liver Dis. Int. Liver Transplant. Soc. 29 (2023) 813–826. https://doi.org/10.1097/LVT.0000000000000122.

[313] H. Waizy, J. Diekmann, A. Weizbauer, J. Reifenrath, I. Bartsch, V. Neubert, R. Schavan, H. Windhagen, In vivo study of a biodegradable orthopedic screw (MgYREZr-alloy) in a rabbit model for up to 12 months, J. Biomater. Appl. 28 (2014) 667–675. https://doi.org/10.1177/0885328212472215.

[314] A.M. Loening, S.S. Gambhir, AMIDE: a free software tool for multimodality medical image analysis., Mol. Imaging. 2 (2003) 131–137. https://doi.org/10.1162/15353500200303133.

[315] C. Kunert-Keil, H. Richter, I. Zeidler-Rentzsch, I. Bleeker, T. Gredes, Histological comparison between laser microtome sections and ground specimens of implant-containing tissues, Ann. Anat. 222 (2019) 153–157. https://doi.org/10.1016/j.aanat.2018.12.001.

[316] G.H. Green, P.J. Diggle, On the operational characteristics of the Benjamini and Hochberg False Discovery Rate procedure., Stat. Appl. Genet. Mol. Biol. 6 (2007) Article27. https://doi.org/10.2202/1544-6115.1302.

[317] K. Bracht, N. Angrisani, J.M. Seitz, R. Eifler, A. Weizbauer, J. Reifenrath, The influence of storage and heat treatment on a magnesium-based implant material: An in vitro and in vivo study, Biomed. Eng. Online. 14 (2015) 1–17. https://doi.org/10.1186/s12938-015-0091-8.

[318] P. Midthun, E. Kirkhus, B.H. Østerås, P.R. Høiness, A. England, S. Johansen, Metal artifact reduction on musculoskeletal CT: a phantom and clinical study., Eur. Radiol. Exp. 7 (2023) 46. https://doi.org/10.1186/s41747-023-00354-9.

[319] J.S. Dhaliwal, S.R.N. David, N.R. Zulhilmi, S.K. Sodhi Dhaliwal, J. Knights, R.F. de Albuquerque Junior, Contamination of titanium dental implants: a narrative review, SN Appl. Sci. 2 (2020) 1–10. https://doi.org/10.1007/s42452-020-2810-4.

[320] T. Kon, T.-J. Cho, T. Aizawa, M. Yamazaki, N. Nooh, D. Graves, L.C. Gerstenfeld, T.A. Einhorn, Expression of Osteoprotegerin, Receptor Activator of NF-κB Ligand (Osteoprotegerin Ligand) and Related Proinflammatory Cytokines During Fracture Healing, J. Bone Miner. Res. 16 (2001) 1004–1014. https://doi.org/https://doi.org/10.1359/jbmr.2001.16.6.1004.

[321] X. Li, M. Grisanti, W. Fan, F.J. Asuncion, H.-L. Tan, D. Dwyer, C.-Y. Han, L. Yu, J. Lee, E. Lee, M. Barrero, P. Kurimoto, Q.-T. Niu, Z. Geng, A. Winters, T. Horan, S. Steavenson, F. Jacobsen, Q. Chen, R. Haldankar, J. Lavallee, B. Tipton, M. Daris, J. Sheng, H.S. Lu, K. Daris, R. Deshpande, E.G. Valente, H. Salimi-Moosavi, P.J. Kostenuik, J. Li, M. Liu, C. Li, D.L. Lacey, W.S. Simonet, H.Z. Ke, P. Babij, M. Stolina, M.S. Ominsky, W.G. Richards, Dickkopf-1 regulates bone formation in young growing rodents and upon traumatic injury., J. Bone Miner. Res. Off. J. Am. Soc. Bone Miner. Res. 26 (2011) 2610–2621. https://doi.org/10.1002/jbmr.472.

[322] C.H. Dreyer, K. Kjaergaard, M. Ding, L. Qin, Vascular endothelial growth factor for in vivo bone formation: A systematic review., J. Orthop. Transl. 24 (2020) 46–57. https://doi.org/10.1016/j.jot.2020.05.005.

[323] C.S. Bahney, R.L. Zondervan, P. Allison, A. Theologis, J.W. Ashley, J. Ahn, T. Miclau, R.S. Marcucio, K.D. Hankenson, Cellular biology of fracture healing., J. Orthop. Res. Off. Publ. Orthop. Res. Soc. 37 (2019) 35–50. https://doi.org/10.1002/jor.24170.

[324] J.T. Street, J.H. Wang, Q.D. Wu, A. Wakai, A. McGuinness, H.P. Redmond, The angiogenic response to skeletal injury is preserved in the elderly., J. Orthop. Res. Off. Publ. Orthop. Res. Soc. 19 (2001) 1057–1066. https://doi.org/10.1016/S0736-0266(01)00048-1.

[325] A.A.M. Rady, S.M. Hamdy, M.A. Abdel-Hamid, M.G.A. Hegazy, S.A. Fathy, A.A. Mostafa, The role of VEGF and BMP-2 in stimulation of bone healing with using hybrid bio-composite scaffolds coated implants in animal model, Bull. Natl. Res. Cent. 44 (2020) 131. https://doi.org/10.1186/s42269-020-00369-x.

[326] D.M. Tanase, E.M. Gosav, S. Radu, C.F. Costea, M. Ciocoiu, A. Carauleanu, C.M. Lacatusu, M.A. Maranduca, M. Floria, C. Rezus, The Predictive Role of the Biomarker Kidney Molecule-1 (KIM-1) in Acute Kidney Injury (AKI) Cisplatin-Induced Nephrotoxicity., Int. J. Mol. Sci. 20 (2019). https://doi.org/10.3390/ijms20205238.

[327] M. Yang, S. Luo, J. Yang, W. Chen, L. He, D. Liu, L. Zhao, X. Wang, Bone-kidney axis: A potential therapeutic target for diabetic nephropathy., Front. Endocrinol. (Lausanne). 13 (2022) 996776. https://doi.org/10.3389/fendo.2022.996776.

[328] A. Kurniawan, E. Kodrat, Y.I. Gani, Effectiveness of granulocyte colony stimulating factor to enhance healing on delayed union fracture model Sprague-Dawley rat., Ann. Med. Surg. 61 (2021) 54–60. https://doi.org/10.1016/j.amsu.2020.12.005.

[329] F. Roseren, M. Pithioux, S. Robert, L. Balasse, B. Guillet, E. Lamy, S. Roffino, Systemic Administration of G-CSF Accelerates Bone Regeneration and Modulates Mobilization of Progenitor Cells in a Rat Model of Distraction Osteogenesis., Int. J. Mol. Sci. 22 (2021). https://doi.org/10.3390/ijms22073505.

[330] S. Capuani, G. Malgir, C.Y.X. Chua, A. Grattoni, Advanced strategies to thwart foreign body response to implantable devices., Bioeng. Transl. Med. 7 (2022) e10300. https://doi.org/10.1002/btm2.10300.

[331] Y. Yoshiko, H. Wang, T. Minamizaki, C. Ijuin, R. Yamamoto, S. Suemune, K. Kozai, K. Tanne, J.E. Aubin, N. Maeda, Mineralized tissue cells are a principal source of FGF23., Bone. 40 (2007) 1565–1573. https://doi.org/10.1016/j.bone.2007.01.017.

[332] S. Goebel, J. Lienau, U. Rammoser, L. Seefried, K.F. Wintgens, J. Seufert, G. Duda, F. Jakob, R. Ebert, FGF23 is a putative marker for bone healing and regeneration., J. Orthop. Res. Off. Publ. Orthop. Res. Soc. 27 (2009) 1141–1146. https://doi.org/10.1002/jor.20857.

[333] K.E. Evans, S.W. Fox, Interleukin-10 inhibits osteoclastogenesis by reducing NFATc1 expression and preventing its translocation to the nucleus., BMC Cell Biol. 8 (2007) 4. https://doi.org/10.1186/1471-2121-8-4.

[334] M.D. Costantino, A. Schuster, H. Helmholz, A. Meyer-Rachner, R. Willumeit-Römer, B.J.C. Luthringer-Feyerabend, Inflammatory response to magnesium-based biodegradable implant materials, Acta Biomater. 101 (2020) 598–608. https://doi.org/10.1016/j.actbio.2019.10.014.

[335] W. Weng, A. Biesiekierski, Y. Li, M. Dargusch, C. Wen, A review of the physiological impact of rare earth elements and their uses in biomedical Mg alloys, Acta Biomater. 130 (2021) 80–97. https://doi.org/10.1016/j.actbio.2021.06.004.

[336] M. Meischel, D. Hormann, J. Draxler, E.K. Tschegg, J. Eichler, T. Prohaska, S.E. Stanzl-Tscheg, Bone-implant degradation and mechanical response of bone surrounding Mg-alloy implants, J. Mech. Behav. Biomed. Mater. 71 (2017) 307–313. https://doi.org/10.1016/j.jmbbm.2017.03.025.

[337] K. ODASHIMA, Y. SHIMIZU, Y. SANO, A. YAMAMOTO, T. MUKAI, Y. TAKADA, Y. YANAGISAWA, Y. IMAI, T. TAKAHASHI, H. KUMAMOTO, Osteogenic response under the periosteum by magnesium implantation in rat tibia, Dent. Mater. J. 40 (2021) 498–507. https://doi.org/10.4012/dmj.2020-011.

[338] A. Myrissa, S. Braeuer, E. Martinelli, R. Willumeit-Romer, W. Goessler, A.M.

Weinberg, Gadolinium accumulation in organs of Sprague-Dawley (R) rats after implantation of a biodegradable magnesium-gadolinium alloy, Acta Biomater. 48 (2017) 521–529. https://doi.org/10.1016/j.actbio.2016.11.024.

[339] N. Angrisani, J. Reifenrath, F. Zimmermann, R. Eifler, A. Meyer-Lindenberg, K. Vano-Herrera, C. Vogt, Biocompatibility and degradation of LAE442-based magnesium alloys after implantation of up to 3.5 years in a rabbit model, Acta Biomater. 44 (2016) 355–365. https://doi.org/10.1016/j.actbio.2016.08.002.

[340] X. Zhang, G. Yuan, L. Mao, J. Niu, P. Fu, W. Ding, Effects of extrusion and heat treatment on the mechanical properties and biocorrosion behaviors of a Mg-Nd-Zn-Zr alloy, J. Mech. Behav. Biomed. Mater. 7 (2012) 77–86. https://doi.org/10.1016/j.jmbbm.2011.05.026.

[341] X. Zhang, G. Yuan, J. Niu, P. Fu, W. Ding, Microstructure, mechanical properties, biocorrosion behavior, and cytotoxicity of as-extruded Mg-Nd-Zn-Zr alloy with different extrusion ratios, J. Mech. Behav. Biomed. Mater. 9 (2012) 153–162. https://doi.org/10.1016/j.jmbbm.2012.02.002.

[342] J. Zhang, H. Li, W. Wang, H. Huang, J. Pei, H. Qu, G. Yuan, Y. Li, The degradation and transport mechanism of a Mg-Nd-Zn-Zr stent in rabbit common carotid artery: A 20-month study, Acta Biomater. 69 (2018) 372–384. https://doi.org/10.1016/j.actbio.2018.01.018.

[343] N. Gabriele Sommer, D. Hahn, B. Okutan, R. Marek, A.-M. Weinberg, N.G. Sommer, D. Hahn, B. Okutan, R. Marek, A.-M. Weinberg, Animal Models in Orthopedic Research: The Proper Animal Model to Answer Fundamental Questions on Bone Healing Depending on Pathology and Implant Material, in: E. Tvrdá, S.C. Yenisetti (Eds.), Anim. Model. Med. Biol., IntechOpen, Rijeka, 2019: pp. 1–20. https://doi.org/10.5772/intechopen.89137.

[344] M.L. Ali, S.P. Kumar, K. Bjornstad, C.M.G. Duran, The sheep as an animal model for heart valve research, Vascular. 4 (1996) 543–549. https://doi.org/10.1177/096721099600400426.

[345] W. Jin, P.K. Chu, Orthopedic Implants, in: R.B.T.-E. of B.E. Narayan (Ed.), Encycl. Biomed. Eng., Elsevier, Oxford, 2019: pp. 425–439. https://doi.org/https://doi.org/10.1016/B978-0-12-801238-3.10999-7.

[346] A. Goharian, M.R.A. Kadir, M.R. Abdullah, Biodegradable metals (Biodegradable magnesium alloys), Elsevier Inc., 2017. https://doi.org/10.1016/B978-0-12-804634-0.00008-2.

[347] J.M. Lane, J.E. Mait, A. Unnanuntana, B.P. Hirsch, A.D. Shaffer, O.A. Shonuga, 6.616 - Materials in Fracture Fixation, in: P.B.T.-C.B. Ducheyne (Ed.), Comprenhensive Biomater., Elsevier, Oxford, 2011: pp. 219–235. https://doi.org/https://doi.org/10.1016/B978-0-08-055294-1.00251-8.

[348] L. Elkaiam, O. Hakimi, G. Yosafovich-Doitch, S. Ovadia, E. Aghion, Correction to: In Vivo Evaluation of Mg–5%Zn–2%Nd Alloy as an Innovative Biodegradable Implant Material, Ann. Biomed. Eng. 47 (2019) 2515. https://doi.org/10.1007/s10439-019-02378-y.

[349] C. Liu, Z. Ren, Y.D. Xu, S. Pang, X.B. Zhao, Y. Zhao, Biodegradable Magnesium Alloys Developed as Bone Repair Materials: A Review, Scanning. 2018 (2018).

https://doi.org/10.1155/2018/9216314.

[350] Z. Zeng, N. Stanford, C.H.J. Davies, J.F. Nie, N. Birbilis, Magnesium extrusion alloys: a review of developments and prospects, Int. Mater. Rev. 64 (2019) 27–62. https://doi.org/10.1080/09506608.2017.1421439.

[351] J. Zhang, Y. Jiang, Z. Shang, B. Zhao, M. Jiao, W. Liu, M. Cheng, B. Zhai, Y. Guo, B. Liu, X. Shi, B. Ma, Biodegradable metals for bone defect repair: A systematic review and meta-analysis based on animal studies, Bioact. Mater. 6 (2021) 4027–4052. https://doi.org/10.1016/j.bioactmat.2021.03.035.

[352] F. Witte, V. Kaese, H. Haferkamp, E. Switzer, A. Meyer-Lindenberg, C.J. Wirth, H. Windhagen, In vivo corrosion of four magnesium alloys and the associated bone response, Biomaterials. 26 (2005) 3557–3563. https://doi.org/10.1016/j.biomaterials.2004.09.049.

[353] S. Chen, S.K. Guan, W. Li, H.T.X. Wang, J. Chen, Y.S. Wang, H.T.X. Wang, In vivo degradation and bone response of a composite coating on Mg-Zn-Ca alloy prepared by microarc oxidation and electrochemical deposition, J. Biomed. Mater. Res. Part B-Applied Biomater. 100B (2012) 533–543. https://doi.org/10.1002/jbm.b.31982.

[354] M. Razavi, M. Fathi, O. Savabi, D. Vashaee, L. Tayebi, In vivo biocompatibility of Mg implants surface modified by nanostructured merwinite/PEO, J. Mater. Sci. Med. 26 (2015). https://doi.org/10.1007/s10856-015-5514-3.

[355] S.A. Abdel-Gawad, M.A. Shoeib, Corrosion studies and microstructure of Mg - Zn - Ca alloys for biomedical applications, Surfaces and Interfaces. 14 (2019) 108–116. https://doi.org/10.1016/j.surfin.2018.11.011.

[356] Z.R. Qi, Q. Zhang, L.L. Tan, X. Lin, Y. Yin, X.L. Wang, K. Yang, Y. Wang, Comparison of degradation behavior and the associated bone response of ZK60 and PLLA in vivo, J. Biomed. Mater. Res. - Part A. 102 (2014) 1255–1263. https://doi.org/10.1002/jbm.a.34795.

[357] H.W. Chai, L. Guo, X.T. Wang, X.Y. Gao, K. Liu, Y.P. Fu, J.L. Guan, L.L. Tan, K. Yang, In vitro and in vivo evaluations on osteogenesis and biodegradability of a β-tricalcium phosphate coated magnesium alloy, J. Biomed. Mater. Res. - Part A. 100 A (2012) 293–304. https://doi.org/10.1002/jbm.a.33267.

[358] J. Hofstetter, E. Martinelli, S. Pogatscher, P. Schmutz, E. Povoden-Karadeniz, A.M. Weinberg, P.J. Uggowitzer, J.F. Löffler, Influence of trace impurities on the in vitro and in vivo degradation of biodegradable Mg-5Zn-0.3Ca alloys, Acta Biomater. 23 (2015) 347–353. https://doi.org/10.1016/j.actbio.2015.05.004.

[359] F. Rosalbino, S. De Negri, A. Saccone, E. Angelini, S. Delfino, Bio-corrosion characterization of Mg-Zn-X (X = Ca, Mn, Si) alloys for biomedical applications, J. Mater. Sci. Mater. Med. 21 (2010) 1091–1098. https://doi.org/10.1007/s10856-009-3956-1.

[360] W.D. Mueller, M. Lucia Nascimento, M.F. Lorenzo De Mele, Critical discussion of the results from different corrosion studies of Mg and Mg alloys for biomaterial applications, Acta Biomater. 6 (2010) 1749–1755. https://doi.org/10.1016/j.actbio.2009.12.048.

[361] N.T. Kirkland, J. Lespagnol, N. Birbilis, M.P. Staiger, A survey of bio-corrosion rates

of magnesium alloys, Corros. Sci. 52 (2010) 287–291. https://doi.org/10.1016/j.corsci.2009.09.033.

[362] T. Sato, Y. Shimizu, K. Odashima, Y. Sano, A. Yamamoto, T. Mukai, N. Ikeo, T. Takahashi, H. Kumamoto, In vitro and in vivo analysis of the biodegradable behavior of a magnesium alloy for biomedical applications, Dent. Mater. J. 38 (2019) 11–21. https://doi.org/10.4012/dmj.2017-324.

[363] H. Miao, D. Zhang, C. Chen, L. Zhang, J. Pei, Y. Su, H. Huang, Z. Wang, B. Kang, W. Ding, H. Zeng, G. Yuan, Research on Biodegradable Mg-Zn-Gd Alloys for Potential Orthopedic Implants: In Vitro and in Vivo Evaluations, ACS Biomater. Sci. Eng. 5 (2019) 1623–1634. https://doi.org/10.1021/acsbiomaterials.8b01563.

[364] H. Kabir, K. Munir, C. Wen, Y. Li, Recent research and progress of biodegradable zinc alloys and composites for biomedical applications: Biomechanical and biocorrosion perspectives, Bioact. Mater. 6 (2021) 836–879. https://doi.org/10.1016/j.bioactmat.2020.09.013.

[365] Y. Lu, A.R. Bradshaw, Y.L. Chiu, I.P. Jones, Effects of secondary phase and grain size on the corrosion of biodegradable Mg-Zn-Ca alloys, Mater. Sci. Eng. C-Materials Biol. Appl. 48 (2015) 480–486. https://doi.org/10.1016/j.msec.2014.12.049.

[366] L.H.C. Becerra, M.A.L.H. Rodríguez, H. Esquivel-Solís, R.L. Arroyo, A.T. Castro, Bio-inspired biomaterial Mg–Zn–Ca: a review of the main mechanical and biological properties of Mg-based alloys, Biomed. Phys. Eng. Express. 6 (2020) 42001. https://doi.org/10.1088/2057-1976/ab9426.

[367] M. Cihova, E. Martinelli, P. Schmutz, A. Myrissa, R. Schäublin, A.M. Weinberg, P.J. Uggowitzer, J.F. Löffler, The role of zinc in the biocorrosion behavior of resorbable Mg–Zn–Ca alloys, Acta Biomater. 100 (2019) 398–414. https://doi.org/10.1016/j.actbio.2019.09.021.

[368] G. Mao, X. Jin, J. Sun, X. Han, M. Zeng, Y. Qiu, W. Bian, Microalloying Design of Biodegradable Mg-2Zn-0.05Ca Promises Improved Bone-Implant Applications, ACS Biomater. Sci. Eng. 7 (2021) 2755–2766. https://doi.org/10.1021/acsbiomaterials.1c00218.

[369] Y. Jang, Z. Tan, C. Jurey, Z. Xu, Z. Dong, B. Collins, Y. Yun, J. Sankar, Understanding corrosion behavior of Mg-Zn-Ca alloys from subcutaneous mouse model: Effect of Zn element concentration and plasma electrolytic oxidation, Mater. Sci. Eng. C. 48 (2015) 28–40. https://doi.org/10.1016/j.msec.2014.11.029.

[370] N.G. Sommer, D. Hirzberger, L. Paar, L. Berger, H. Ćwieka, U.Y. Schwarze, V. Herber, B. Okutan, A.J. Bodey, R. Willumeit-Römer, B. Zeller-Plumhoff, J.F. Löffler, A.M. Weinberg, Implant degradation of low-alloyed Mg–Zn–Ca in osteoporotic, old and juvenile rats, Acta Biomater. 147 (2022) 427–438. https://doi.org/10.1016/j.actbio.2022.05.041.

[371] R. Marek, H. Ćwieka, N. Donohue, P. Holweg, J. Moosmann, F. Beckmann, I. Brcic, U.Y. Schwarze, K. Iskhakova, M. Chaabane, S. Sefa, B. Zeller-Plumhoff, A.M. Weinberg, R. Willumeit-Römer, N.G. Sommer, Degradation behavior and osseointegration of Mg-Zn-Ca screws in different bone regions of growing sheep—a pilot study, Regen. Biomater. (2022) rbac077. https://doi.org/10.1093/rb/rbac077.

[372] R. Marek, J. Eichler, U.Y. Schwarze, S. Fischerauer, O. Suljevic, L. Berger, J.F. Löffler,

P.J. Uggowitzer, A.-M. Weinberg, Long-term in vivo degradation of Mg–Zn–Ca elastic stable intramedullary nails and their influence on the physis of juvenile sheep, Biomater. Adv. (2023) 213417. https://doi.org/https://doi.org/10.1016/j.bioadv.2023.213417.

[373] H.S. Han, I. Jun, H.K. Seok, K.S. Lee, K. Lee, F. Witte, D. Mantovani, Y.C. Kim, S. Glyn-Jones, J.R. Edwards, Biodegradable Magnesium Alloys Promote Angio-Osteogenesis to Enhance Bone Repair, Adv. Sci. 7 (2020) 1–12. https://doi.org/10.1002/advs.202000800.

[374] D. Zhao, S. Huang, F. Lu, B. Wang, L. Yang, L. Qin, K. Yang, Y. Li, W. Li, W. Wang, S. Tian, X. Zhang, W. Gao, Z. Wang, Y. Zhang, X. Xie, J. Wang, J. Li, Vascularized bone grafting fixed by biodegradable magnesium screw for treating osteonecrosis of the femoral head, Biomaterials. 81 (2016) 84–92. https://doi.org/10.1016/j.biomaterials.2015.11.038.

[375] H. Windhagen, K. Radtke, A. Weizbauer, J. Diekmann, Y. Noll, U. Kreimeyer, R. Schavan, C. Stukenborg-Colsman, H. Waizy, Biodegradable magnesium-based screw clinically equivalent to titanium screw in hallux valgus surgery: short term results of the first prospective, randomized, controlled clinical pilot study, Biomed. Eng. Online. 12 (2013) 62. https://doi.org/10.1186/1475-925X-12-62.

[376] M. Baldini, V. Coppa, D. Falcioni, G. Cusano, D. Massetti, M. Marinelli, A.P. Gigante, Resorbable magnesium screws for fixation of medial epicondyle avulsion fractures in skeletally immature patients: A comparison with Kirschner wires, J. Child. Orthop. 16 (2022) 481–487. https://doi.org/10.1177/18632521221136100.

[377] H. May, Y.A. Katı, G. Gumussuyu, T.Y. Emre, M. Unal, O. Kose, Y. Alper Kati, G. Gumussuyu, T. Yunus Emre, M. Unal, O. Kose, Y.A. Katı, G. Gumussuyu, T.Y. Emre, M. Unal, O. Kose, Bioabsorbable magnesium screw versus conventional titanium screw fixation for medial malleolar fractures, J. Orthop. Traumatol. 21 (2020) 4–11. https://doi.org/10.1186/s10195-020-00547-7.

[378] B. Acar, O. Kose, A. Turan, M. Unal, Y. alper Katı, F. Guler, Comparison of Bioabsorbable Magnesium versus Titanium Screw Fixation for Modified Distal Chevron Osteotomy in Hallux Valgus, Biomed Res. Int. 2018 (2018). https://doi.org/10.1155/2018/5242806.

[379] A. Wichelhaus, J. Emmerich, T. Mittlmeier, A Case of Implant Failure in Partial Wrist Fusion Applying Magnesium-Based Headless Bone Screws, Case Rep. Orthop. 2016 (2016) 1–5. https://doi.org/10.1155/2016/7049130.

[380] R. Meier, M. Panzica, Erste Ergebnisse mit einer resorbierbaren MgYREZr-Kompressionsschraube bei der instabilen Kahnbeinfraktur zeigen eine massive Zystenbildung, Handchirurgie Mikrochirurgie Plast. Chir. 49 (2017) 37–41. https://doi.org/10.1055/S-0042-121416.

[381] D. Dziuba, A. Meyer-Lindenberg, J.M. Seitz, H. Waizy, N. Angrisani, J. Reifenrath, Long-term in vivo degradation behaviour and biocompatibility of the magnesium alloy ZEK100 for use as a biodegradable bone implant, Acta Biomater. 9 (2013) 8548–8560. https://doi.org/10.1016/j.actbio.2012.08.028.

[382] L.P. Xu, G.N. Yu, E. Zhang, F. Pan, K. Yang, In vivo corrosion behavior of Mg-Mn-Zn alloy for bone implant application, J. Biomed. Mater. Res. Part A. 83A (2007) 703–711. https://doi.org/10.1002/jbm.a.31273.

[383] A. Kopp, H. Fischer, A.P. Soares, K. Schmidt-Bleek, C. Leber, H. Kreiker, G. Duda, N. Kröger, K. van Gaalen, H. Hanken, O. Jung, R. Smeets, M. Heiland, C. Rendenbach, Long-term in vivo observations show biocompatibility and performance of ZX00 magnesium screws surface-modified by plasma-electrolytic oxidation in Göttingen miniature pigs, Acta Biomater. 157 (2023) 720–733. https://doi.org/10.1016/j.actbio.2022.11.052.

[384] S. Saha, W. Lestari, C. Dini, M.N. Sarian, H. Hermawan, V.A.R. Barão, C. Sukotjo, C. Takoudis, Corrosion in Mg-alloy biomedical implants- the strategies to reduce the impact of the corrosion inflammatory reaction and microbial activity, J. Magnes. Alloy. 10 (2022) 3306–3326. https://doi.org/10.1016/j.jma.2022.10.025.

[385] X. Liu, G. Chen, X. Zhong, T. Wang, X. He, W. Yuan, P. Zhang, Y. Liu, D. Cao, S. Chen, K. ichi Manabe, Z. Jiang, T. Furushima, D. Kent, Y. Chen, G. Ni, M. Gao, H. Li, Degradation of differently processed Mg-based implants leads to distinct foreign body reactions (FBRs) through dissimilar signaling pathways, J. Magnes. Alloy. (2022). https://doi.org/10.1016/j.jma.2022.03.017.

[386] O. Suljevic, S.F. Fischerauer, A.M. Weinberg, N.G. Sommer, Immunological reaction to magnesium-based implants for orthopedic applications. What do we know so far? A systematic review on in vivo studies, Mater. Today Bio. 15 (2022) 100315. https://doi.org/10.1016/j.mtbio.2022.100315.

[387] R.M. Grzeskowiak, J. Schumacher, M.S. Dhar, D.P. Harper, P.Y. Mulon, D.E. Anderson, Bone and Cartilage Interfaces With Orthopedic Implants: A Literature Review, Front. Surg. 7 (2020) 1–15. https://doi.org/10.3389/fsurg.2020.601244.

[388] P.J. Yang, J.S. Temenoff, Engineering orthopedic tissue interfaces, Tissue Eng. - Part B Rev. 15 (2009) 127–141. https://doi.org/10.1089/ten.teb.2008.0371.

[389] N.T. Tran, Y.K. Kim, S.Y. Kim, M.H. Lee, K.B. Lee, Comparative Osteogenesis and Degradation Behavior of Magnesium Implant in Epiphysis and Diaphysis of the Long Bone in the Rat Model, Materials (Basel). 15 (2022). https://doi.org/10.3390/ma15165630.

[390] P. Han, M. Tan, S. Zhang, W. Ji, J. Li, X. Zhang, C. Zhao, Y. Zheng, Y. Chai, Shape and site dependent in vivo degradation of Mg-Zn pins in rabbit femoral condyle, Int. J. Mol. Sci. 15 (2014) 2959–2970. https://doi.org/10.3390/ijms15022959.

[391] E.P. Shubhakar Nidadavolu, F. Feyerabend, T. Ebel, R. Willumeit-Römer, M. Dahms, On the determination of magnesium degradation rates under physiological conditions, Materials (Basel). 9 (2016) 1–10. https://doi.org/10.3390/ma9080627.

[392] B. Zeller-Plumhoff, M. Gile, M. Priebe, H. Slominska, B. Boll, B. Wiese, T. Würger, R. Willumeit-Römer, R.H. Meißner, Exploring key ionic interactions for magnesium degradation in simulated body fluid – A data-driven approach, Corros. Sci. 182 (2021). https://doi.org/10.1016/j.corsci.2021.109272.

[393] W.H. Ma, Y.J. Liu, W. Wang, Y.Z. Zhang, Improved biological performance of magnesium by micro-arc oxidation, Brazilian J. Med. Biol. Res. 48 (2015) 214–225. https://doi.org/10.1590/1414-431X20144171.

[394] Y. Xin, K. Huo, T. Hu, G. Tang, P.K. Chu, Corrosion products on biomedical magnesium alloy soaked in simulated body fluids, J. Mater. Res. 24 (2009) 2711–2719. https://doi.org/10.1557/jmr.2009.0323.

[395] J. Lévesque, H. Hermawan, D. Dubé, D. Mantovani, Design of a pseudo-physiological test bench specific to the development of biodegradable metallic biomaterials, Acta Biomater. 4 (2008) 284–295. https://doi.org/10.1016/j.actbio.2007.09.012.

[396] K. Iskhakova, D.C. Florian Wieland, R. Marek, U. Schwarze, A. Davydok, H. Cwieka, T. AlBaraghtheh, J. Reimers, B. Hindenlang, S. Sefa, R. Willumeit-Römer, B. Zeller-Plumhoff, Sheep bone ultrastructure analyses reveal differences in bone maturation around Mg-based and Ti implants, (n.d.).

[397] E. Willbold, F. Witte, Histology and research at the hard tissue-implant interface using Technovit 9100 New embedding technique, Acta Biomater. 6 (2010) 4447–4455. https://doi.org/10.1016/j.actbio.2010.06.022.

[398] P. Thévenaz, M. Unser, User-friendly semiautomated assembly of accurate image mosaics in microscopy, Microsc. Res. Tech. 70 (2007) 135–146. https://doi.org/10.1002/jemt.20393.

[399] T. Albrektsson, A. Wennerberg, Oral implant surfaces: Part 1--review focusing on topographic and chemical properties of different surfaces and in vivo responses to them., Int. J. Prosthodont. 17 (2004) 536–543.

[400] S. Farahany, H.R. Bakhsheshi-Rad, M.H. Idris, M.R. Abdul Kadir, A.F. Lotfabadi, A. Ourdjini, In-situ thermal analysis and macroscopical characterization of Mg-xCa and Mg-0.5Ca-xZn alloy systems, Thermochim. Acta. 527 (2012) 180–189. https://doi.org/10.1016/j.tca.2011.10.027.

[401] A. Dobkowska, B. Adamczyk-Cieślak, M. Chlewicka, A. Towarek, A. Zielińska, M. Koralnik, D. Kuc, J. Mizera, Evolution of microstructure dependent corrosion properties of ultrafine AZ31 under conditions of extrusion with a forward backward oscillating die, J. Mater. Res. Technol. 18 (2022) 4486–4496. https://doi.org/https://doi.org/10.1016/j.jmrt.2022.04.131.

[402] A. Dobkowska, B. Adamczyk – Cieślak, D. Kuc, E. Hadasik, T. Płociński, E. Ura-Bińczyk, J. Mizera, Influence of bimodal grain size distribution on the corrosion resistance of Mg–4Li–3Al–1Zn (LAZ431), J. Mater. Res. Technol. 13 (2021) 346–358. https://doi.org/https://doi.org/10.1016/j.jmrt.2021.04.078.

[403] A. Tripathi, S.V.S.N. Murty, P.R. Narayanan, Microstructure and texture evolution in AZ31 magnesium alloy during caliber rolling at different temperatures, J. Magnes. Alloy. 5 (2017) 340–347. https://doi.org/https://doi.org/10.1016/j.jma.2017.07.001.

[404] Z. Li, G.L. Song, S. Song, Effect of bicarbonate on biodegradation behaviour of pure magnesium in a simulated body fluid, Electrochim. Acta. 115 (2014) 56–65. https://doi.org/10.1016/J.ELECTACTA.2013.10.131.

[405] T.A. Mahmood, J.E. Davies, Incorporation of amino acids within the surface reactive layers of bioactive glass in vitro: An XPS study, J. Mater. Sci. Mater. Med. 11 (2000) 19–23. https://doi.org/10.1023/A:1008929500904/METRICS.

[406] A. Shchukarev, B.Ö. Malekzadeh, M. Ransjö, P. Tengvall, A. Westerlund, Surface characterization of insulin-coated Ti6Al4V medical implants conditioned in cell culture medium: An XPS study, J. Electron Spectros. Relat. Phenomena. 216 (2017) 33–38. https://doi.org/10.1016/J.ELSPEC.2017.03.001.

[407] F.X. Qin, C. Ji, Z.H. Dan, G.Q. Xie, H. Wang, S.I. Yamaura, M. Niinomi, Y. De Li,

Corrosion behavior of MgZnCa bulk amorphous alloys fabricated by spark plasma sintering, Acta Metall. Sin. (English Lett. 29 (2016) 793–799. https://doi.org/10.1007/S40195-016-0451-9/FIGURES/7.

[408] D.L. Felker, P.M.A. Sherwood, Magnesium Phosphate (Mg3(PO4) 2) by XPS, Surf. Sci. Spectra. 9 (2021) 83. https://doi.org/10.1116/11.20030104.

[409] A. Dobkowska, B. Adamczyk – Cieślak, J. Kubásek, D. Vojtěch, D. Kuc, E. Hadasik, J. Mizera, Microstructure and corrosion resistance of a duplex structured Mg–7.5Li–3Al–1Zn, J. Magnes. Alloy. 9 (2021) 467–477. https://doi.org/10.1016/j.jma.2020.07.007.

[410] A. Atrens, Z. Shi, S.U. Mehreen, S. Johnston, G.L. Song, X. Chen, F. Pan, Review of Mg alloy corrosion rates, J. Magnes. Alloy. 8 (2020) 989–998. https://doi.org/10.1016/j.jma.2020.08.002.

[411] Z. Shi, M. Liu, A. Atrens, Measurement of the corrosion rate of magnesium alloys using Tafel extrapolation, Corros. Sci. 52 (2010) 579–588. https://doi.org/10.1016/j.corsci.2009.10.016.

[412] H.R. Bakhsheshi-Rad, M.H. Idris, M.R. Abdul-Kadir, A. Ourdjini, M. Medraj, M. Daroonparvar, E. Hamzah, Mechanical and bio-corrosion properties of quaternary Mg-Ca-Mn-Zn alloys compared with binary Mg-Ca alloys, Mater. Des. 53 (2014) 283–292. https://doi.org/10.1016/j.matdes.2013.06.055.

[413] W.A. Badawy, N.H. Hilal, M. El-Rabiee, H. Nady, Electrochemical behavior of Mg and some Mg alloys in aqueous solutions of different pH, Electrochim. Acta. 55 (2010) 1880–1887. https://doi.org/10.1016/j.electacta.2009.10.083.

[414] S. Leleu, B. Rives, N. Causse, N. Pébère, Corrosion rate determination of rare-earth Mg alloys in a Na2SO4 solution by electrochemical measurements and inductive coupled plasma-optical emission spectroscopy, J. Magnes. Alloy. 7 (2019) 47–57. https://doi.org/10.1016/j.jma.2018.12.002.

[415] P. Brunner, F. Brumbauer, S. Eva-Maria, O. Renk, A.-Ma. Weinberg, H. Schroettner, R. Wurchum, Influence of high-pressure torsion deformation on the corrosion behaviour of a bioresorbable Mg-based alloy studied by positron annihilation, Biomater. Sci. 9 (2021) 4099–4109. https://doi.org/10.1039/D1BM00166C.

[416] I. Antoniac, R. Adam, A. Biță, M. Miculescu, O. Trante, I.M. Petrescu, M. Pogărășteanu, Comparative assessment of in vitro and in vivo biodegradation of Mg-1Ca magnesium alloys for orthopedic applications, Materials (Basel). 14 (2021) 1–20. https://doi.org/10.3390/ma14010084.

[417] Y. Wen, Q. Liu, J. Wang, Q. Yang, W. Zhao, B. Qiao, Y. Li, D. Jiang, Improving in vitro and in vivo corrosion resistance and biocompatibility of Mg–1Zn–1Sn alloys by microalloying with Sr, Bioact. Mater. 6 (2021) 4654–4669. https://doi.org/10.1016/j.bioactmat.2021.04.043.

[418] H. Xu, T. Hu, M. Wang, Y. Zheng, H. Qin, H. Cao, Z. An, Degradability and biocompatibility of magnesium-MAO: The consistency and contradiction between in-vitro and in-vivo outcomes, Arab. J. Chem. 13 (2020) 2795–2805. https://doi.org/10.1016/j.arabjc.2018.07.010.

[419] G. Baril, N. Pébère, Corrosion of pure magnesium in aerated and deaerated sodium sulphate solutions, Corros. Sci. 43 (2001) 471–484. https://doi.org/10.1016/S0010-

938X(00)00095-0.

[420] T.L. Nguyen, A. Blanquet, M.P. Staiger, G.J. Dias, T.B.F. Woodfield, On the role of surface roughness in the corrosion of pure magnesium in vitro, J. Biomed. Mater. Res. - Part B Appl. Biomater. 100 B (2012) 1310–1318. https://doi.org/10.1002/jbm.b.32697.

[421] N. Zhao, D. Zhu, Collagen self-assembly on orthopedic magnesium biomaterials surface and subsequent bone cell attachment, PLoS One. 9 (2014). https://doi.org/10.1371/journal.pone.0110420.

[422] S.A. Rowland, S.W. Shalaby, R.A. Latour, A.F. von Recum, Effectiveness of cleaning surgical implants: quantitative analysis of contaminant removal, J. Appl. Biomater. 6 (1995). https://doi.org/10.1002/jab.770060102.

[423] D.U. Duddeck, T. Albrektsson, A. Wennerberg, C. Larsson, F. Beuer, On the cleanliness of different oral implant systems: A pilot study, J. Clin. Med. 8 (2019). https://doi.org/10.3390/jcm8091280.

[424] ISO, Implants for surgery - Cleanliness of orthopedic implants - General requirements (ISO 19227:2018), (2018).

[425] H. Lu, L. Zhou, L. Wan, S. Li, M. Rong, Z. Guo, Effects of storage methods on time-related changes of titanium surface properties and cellular response, Biomed. Mater. 7 (2012). https://doi.org/10.1088/1748-6041/7/5/055002.

[426] H. Ibrahim, A.D. Klarner, B. Poorganji, D. Dean, A.A. Luo, M. Elahinia, Microstructural, mechanical and corrosion characteristics of heat-treated Mg-1.2Zn-0.5Ca (wt%) alloy for use as resorbable bone fixation material, J. Mech. Behav. Biomed. Mater. 69 (2017) 203–212. https://doi.org/10.1016/j.jmbbm.2017.01.005.

[427] B. Zeller-Plumhoff, T. AlBaraghtheh, D. Höche, R. Willumeit-Römer, Computational modelling of magnesium degradation in simulated body fluid under physiological conditions, J. Magnes. Alloy. 10 (2022) 965–978. https://doi.org/10.1016/j.jma.2021.11.014.

[428] C. Zhang, J. Lin, N.Y.T. Nguyen, Y. Guo, C. Xu, C. Seo, E. Villafana, H. Jimenez, Y. Chai, R. Guan, H. Liu, Antimicrobial Bioresorbable Mg-Zn-Ca Alloy for Bone Repair in a Comparison Study with Mg-Zn-Sr Alloy and Pure Mg, ACS Biomater. Sci. Eng. 6 (2020) 517–538. https://doi.org/10.1021/acsbiomaterials.9b00903.

[429] S. V. Lamaka, J. Gonzalez, D. Mei, F. Feyerabend, R. Willumeit-Römer, M.L. Zheludkevich, Local pH and Its Evolution Near Mg Alloy Surfaces Exposed to Simulated Body Fluids, Adv. Mater. Interfaces. 5 (2018) 1–6. https://doi.org/10.1002/admi.201800169.

[430] A. Modabber, D. Zander, N. Zumdick, D. Schick, K. Kniha, S.C. Möhlhenrich, F. Hölzle, E. Goloborodko, Impact of Wound Closure on the Corrosion Rate of Biodegradable Mg-Ca-Zn Alloys in the Oral Environment, Materials (Basel). 13 (2020) 1–11. https://doi.org/10.3390/ma13194226.

[431] H.R. Bakhsheshi-Rad, M.R. Abdul-Kadir, M.H. Idris, S. Farahany, Relationship between the corrosion behavior and the thermal characteristics and microstructure of Mg-0.5Ca-xZn alloys, Corros. Sci. 64 (2012) 184–197. https://doi.org/10.1016/j.corsci.2012.07.015.

[432] H.R. Bakhsheshi-Rad, E. Hamzah, A. Fereidouni-Lotfabadi, M. Daroonparvar, M.A.M.

Yajid, M. Mezbahul-Islam, M. Kasiri-Asgarani, M. Medraj, Microstructure and bio-corrosion behavior of Mg-Zn and Mg-Zn-Ca alloys for biomedical applications, Mater. Corros. 65 (2014) 1178–1187. https://doi.org/10.1002/maco.201307588.

[433] D. Zander, N.A. Zumdick, Influence of Ca and Zn on the microstructure and corrosion of biodegradable Mg-Ca-Zn alloys, Corros. Sci. 93 (2015) 222–233. https://doi.org/10.1016/j.corsci.2015.01.027.

[434] J. Walker, S. Shadanbaz, N.T. Kirkland, E. Stace, T. Woodfield, M.P. Staiger, G.J. Dias, Magnesium alloys: Predicting in vivo corrosion with in vitro immersion testing, J. Biomed. Mater. Res. Part B-Applied Biomater. 100B (2012) 1134–1141. https://doi.org/10.1002/jbm.b.32680.

[435] H. Ben, D.C. Martinez, F.A. Shah, A. Johansson, L. Emanuelsson, B. Norlindh, R. Willumeit-r, W. Swieszkowski, A. Palmquist, O. Omar, P. Thomsen, Magnesium implant degradation provides immunomodulatory and proangiogenic effects and attenuates peri-implant fibrosis in soft tissues, Bioact. Mater. 26 (2023) 353–369. https://doi.org/10.1016/j.bioactmat.2023.02.014.

[436] P. Kolar, K. Schmidt-Bleek, H. Schell, T. Gaber, D. Toben, G. Schmidmaier, C. Perka, F. Buttgereit, G.N. Duda, The early fracture hematoma and its potential role in fracture healing, Tissue Eng. - Part B Rev. 16 (2010) 427–434. https://doi.org/10.1089/ten.teb.2009.0687.

[437] H. Schell, G.N. Duda, A. Peters, S. Tsitsilonis, K.A. Johnson, K. Schmidt-Bleek, The haematoma and its role in bone healing, J. Exp. Orthop. 4 (2017). https://doi.org/10.1186/s40634-017-0079-3.

[438] D.T. Chou, D. Hong, S. Oksuz, R. Schweizer, A. Roy, B. Lee, P. Shridhar, V. Gorantla, P.N. Kumta, Corrosion and bone healing of Mg-Y-Zn-Zr-Ca alloy implants: Comparative in vivo study in a non-immobilized rat femoral fracture model, J. Biomater. Appl. 33 (2019) 1178–1194. https://doi.org/10.1177/0885328219825568.

[439] E. Willbold, A.A. Kaya, R.A. Kaya, F. Beckmann, F. Witte, Corrosion of magnesium alloy AZ31 screws is dependent on the implantation site, Mater. Sci. Eng. B Solid-State Mater. Adv. Technol. 176 (2011) 1835–1840. https://doi.org/10.1016/j.mseb.2011.02.010.

[440] N. Erdmann, N. Angrisani, J. Reifenrath, A. Lucas, F. Thorey, D. Bormann, A. Meyer-Lindenberg, Biomechanical testing and degradation analysis of MgCa0.8 alloy screws: A comparative in vivo study in rabbits, Acta Biomater. 7 (2011) 1421–1428. https://doi.org/10.1016/j.actbio.2010.10.031.

[441] X.N. Gu, X.H. Xie, N. Li, Y.F. Zheng, L. Qin, In vitro and in vivo studies on a Mg-Sr binary alloy system developed as a new kind of biodegradable metal, Acta Biomater. 8 (2012) 2360–2374. https://doi.org/10.1016/j.actbio.2012.02.018.

[442] A. Karacs, A. Joob Fancsaly, T. Divinyi, G. Peto, G. Kovách, Morphological and animal study of titanium dental implant surface induced by blasting and high intensity pulsed Nd-glass laser, Mater. Sci. Eng. C. 23 (2003) 431–435. https://doi.org/10.1016/S0928-4931(02)00316-8.

[443] X.M. Guan, M.P. Xiong, F.Y. Zeng, B. Xu, L.D. Yang, H. Guo, J.L. Niu, J. Zhang, C.X. Chen, J. Pei, H. Huang, G.Y. Yuan, Enhancement of Osteogenesis and Biodegradation Control by Brushite Coating on Mg-Nd-Zn-Zr Alloy for Mandibular Bone Repair, ACS

Appl. Mater. Interfaces. 6 (2014) 21525–21533. https://doi.org/10.1021/am506543a.

[444] T. Imwinkelried, S. Beck, T. Iizuka, B. Schaller, Effect of a plasmaelectrolytic coating on the strength retention of in vivo and in vitro degraded magnesium implants, Acta Biomater. 9 (2013) 8643–8649. https://doi.org/10.1016/j.actbio.2012.08.047.

[445] L. Tätting, O. Sandberg, M. Bernhardsson, J. Ernerudh, P. Aspenberg, Different composition of leucocytes in cortical and cancellous bone healing in a mouse model, Bone Jt. Res. 7 (2018) 620–628. https://doi.org/10.1302/2046-3758.712.BJR-2017-0366.R2.

[446] L. Quintens, M. Herteleer, S. Vancleef, Y. Carette, J. Duflou, S. Nijs, J. Vander Sloten, H. Hoekstra, Anatomical Variation of the Tibia – a Principal Component Analysis, Sci. Rep. 9 (2019) 1–10. https://doi.org/10.1038/s41598-019-44092-8.

[447] D. Dimitriou, T.Y. Tsai, B. Yue, H.E. Rubash, Y.M. Kwon, G. Li, Side-to-side variation in normal femoral morphology: 3D CT analysis of 122 femurs, Orthop. Traumatol. Surg. Res. 102 (2016) 91–97. https://doi.org/10.1016/j.otsr.2015.11.004.

[448] N.S. Martynenko, N.Y. Anisimova, O. V. Rybalchenko, M. V. Kiselevskiy, G. Rybalchenko, B. Straumal, D. Temralieva, A.T. Mansharipova, A.O. Kabiyeva, M.T. Gabdullin, S. Dobatkin, Y. Estrin, Rationale for processing of a mg-zn-ca alloy by equal-channel angular pressing for use in biodegradable implants for osteoreconstruction, Crystals. 11 (2021). https://doi.org/10.3390/cryst11111381.

[449] M.S. Dargusch, N. Balasubramani, N. Yang, S. Johnston, Y. Ali, G. Wang, J. Venezuela, J. Carluccio, C. Lau, R. Allavena, D. Liang, K. Mardon, Q. Ye, In vivo performance of a rare earth free Mg–Zn–Ca alloy manufactured using twin roll casting for potential applications in the cranial and maxillofacial fixation devices, Bioact. Mater. 12 (2022) 85–96. https://doi.org/10.1016/j.bioactmat.2021.10.026.

[450] F. Witte, J. Fischer, J. Nellesen, C. Vogt, J. Vogt, T. Donath, F. Beckmann, In vivo corrosion and corrosion protection of magnesium alloy LAE442, Acta Biomater. 6 (2010) 1792–1799. https://doi.org/10.1016/j.actbio.2009.10.012.

[451] D. Zhao, T. Wang, K. Nahan, X. Guo, Z. Zhang, Z. Dong, S. Chen, D.T. Chou, D. Hong, P.N. Kumta, W.R. Heineman, In vivo characterization of magnesium alloy biodegradation using electrochemical H2 monitoring, ICP-MS, and XPS, Acta Biomater. 50 (2017) 556–565. https://doi.org/10.1016/j.actbio.2017.01.024.

[452] R.A. Kaya, H. Cavusoglu, C. Tanik, A.A. Kaya, O. Duygulu, Z. Mutlu, E. Zengin, Y. Aydin, The effects of magnesium particles in posterolateral spinal fusion: an experimental in vivo study in a sheep model, J. Neurosurgery-Spine. 6 (2007) 141–149. https://doi.org/10.3171/spi.2007.6.2.141.

[453] P.P. Lelovas, T.T. Xanthos, S.E. Thorma, G.P. Lyritis, I.A. Dontas, The laboratory rat as an animal model for osteoporosis research, Comp. Med. 58 (2008) 424–430.

[454] G. Osterhoff, E.F. Morgan, S.J. Shefelbine, L. Karim, L.M. McNamara, P. Augat, Bone mechanical properties and changes with osteoporosis, Injury. 47 (2016) S11–S20. https://doi.org/10.1016/S0020-1383(16)47003-8.

[455] S.Y. Cho, S.W. Chae, K.W. Choi, H.K. Seok, H.S. Han, S.J. Yang, Y.Y. Kim, J.T. Kim, J.Y. Jung, M. Assad, Load-bearing capacity and biological allowable limit of biodegradable metal based on degradation rate in vivo, J. Biomed. Mater. Res. - Part B

Appl. Biomater. 100 B (2012) 1535–1544. https://doi.org/10.1002/jbm.b.32722.

[456] J. Kuhlmann, I. Bartsch, E. Willbold, S. Schuchardt, O. Holz, N. Hort, D. Höche, W.R. Heineman, F. Witte, Fast escape of hydrogen from gas cavities around corroding magnesium implants, Acta Biomater. 9 (2013) 8714–8721. https://doi.org/10.1016/j.actbio.2012.10.008.

[457] J. Wang, H. Jiang, Y. Bi, J.E. Sun, M. Chen, D. Liu, Effects of gas produced by degradation of Mg-Zn-Zr Alloy on cancellous bone tissue, Mater. Sci. Eng. C. 55 (2015) 556–561. https://doi.org/10.1016/j.msec.2015.05.082.

[458] U. Thormann, V. Alt, L. Heimann, C. Gasquere, C. Heiss, G. Szalay, J. Franke, R. Schnettler, K.S. Lips, The biocompatibility of degradable magnesium interference screws: An experimental study with sheep, Biomed Res. Int. 2015 (2015). https://doi.org/10.1155/2015/943603.

[459] A. Yamamoto, A. Kikuta, Development of a Model System for Gas Cavity Formation Behavior of Magnesium Alloy Implantation, ACS Biomater. Sci. Eng. 8 (2022) 2437–2444. https://doi.org/10.1021/acsbiomaterials.1c01429.

[460] M. Thomann, C. Krause, D. Bormann, N. Von Der Höh, H. Windhagen, A. Meyer-Lindenberg, N. von der Hoh, H. Windhagen, A. Meyer-Lindenberg, Comparison of the resorbable magnesium alloys LAE442 und MgCa0.8 concerning their mechanical properties, their progress of degradation and the bone-implant-contact after 12 months implantation duration in a rabbit model, Materwiss. Werksttech. 40 (2009) 82–87. https://doi.org/10.1002/mawe.200800412.

[461] ThermoFisher-Scientific, 22571-MEM alpha, (n.d.). https://www.thermofisher.com/pl/en/home/technical-resources/media-formulation.206.html (accessed October 12, 2022).

[462] M. Yanez, J. Blanchette, E. Jabbarzadeh, Modulation of Inflammatory Response to Implanted Biomaterials Using Natural Compounds., Curr. Pharm. Des. 23 (2017) 6347–6357. https://doi.org/10.2174/1381612823666170510124348.

[463] H.S. Han, S. Loffredo, I. Jun, J. Edwards, Y.C. Kim, H.K. Seok, F. Witte, D. Mantovani, S. Glyn-Jones, Current status and outlook on the clinical translation of biodegradable metals, Mater. Today. 23 (2019) 57–71. https://doi.org/10.1016/j.mattod.2018.05.018.

[464] Y. Sotomi, Y. Onuma, C. Collet, E. Tenekecioglu, R. Virmani, N.S. Kleiman, P.W. Serruys, Bioresorbable scaffold: The emerging reality and future directions, Circ. Res. 120 (2017) 1341–1352. https://doi.org/10.1161/CIRCRESAHA.117.310275.

[465] M. Sabaté, F. Alfonso, A. Cequier, S. Romaní, P. Bordes, A. Serra, A. Iñiguez, P. Salinas, B. García Del Blanco, J. Goicolea, R. Hernández-Antolín, J. Cuesta, J.A. Gómez-Hospital, L. Ortega-Paz, J. Gomez-Lara, S. Brugaletta, Magnesium-Based Resorbable Scaffold Versus Permanent Metallic Sirolimus-Eluting Stent in Patients With ST-Segment Elevation Myocardial Infarction: The MAGSTEMI Randomized Clinical Trial., Circulation. 140 (2019) 1904–1916. https://doi.org/10.1161/CIRCULATIONAHA.119.043467.

[466] M. Haude, R. Erbel, P. Erne, S. Verheye, H. Degen, P. Vermeersch, N. Weissman, F. Prati, N. Bruining, R. Waksman, J. Koolen, Safety and performance of the DRug-Eluting Absorbable Metal Scaffold (DREAMS) in patients with de novo coronary lesions: 3-year results of the prospective, multicentre, first-in-man BIOSOLVE-I trial.,

EuroIntervention J. Eur. Collab. with Work. Gr. Interv. Cardiol. Eur. Soc. Cardiol. 12 (2016) e160-6. https://doi.org/10.4244/EIJ-D-15-00371.

[467] M. V Madhavan, A.J. Kirtane, B. Redfors, P. Généreux, O. Ben-Yehuda, T. Palmerini, U. Benedetto, G. Biondi-Zoccai, P.C. Smits, C. von Birgelen, R. Mehran, T. McAndrew, P.W. Serruys, M.B. Leon, S.J. Pocock, G.W. Stone, Stent-Related Adverse Events >1 Year After Percutaneous Coronary Intervention., J. Am. Coll. Cardiol. 75 (2020) 590–604. https://doi.org/10.1016/j.jacc.2019.11.058.

[468] M.L. Busam, R.J. Esther, W.T. Obremskey, Hardware removal: indications and expectations., J. Am. Acad. Orthop. Surg. 14 (2006) 113–120. https://doi.org/10.5435/00124635-200602000-00006.

[469] R. Meier, M. Panzica, [First results with a resorbable MgYREZr compression screw in unstable scaphoid fractures show extensive bone cysts]., Handchirurgie, Mikrochirurgie, Plast. Chir. Organ der Deutschsprachigen Arbeitsgemeinschaft fur Handchirurgie Organ der Deutschsprachigen Arbeitsgemeinschaft fur Mikrochirurgie der Peripher. Nerven und Gefasse Organ der V... 49 (2017) 37–41. https://doi.org/10.1055/s-0042-121416.

[470] C. Plaass, S. Ettinger, L. Sonnow, S. Koenneker, Y. Noll, A. Weizbauer, J. Reifenrath, L. Claassen, K. Daniilidis, C. Stukenborg-Colsman, H. Windhagen, Early results using a biodegradable magnesium screw for modified chevron osteotomies, J. Orthop. Res. 34 (2016). https://doi.org/10.1002/jor.23241.

[471] A. Yamamoto, S. Hiromoto, Effect of inorganic salts, amino acids and proteins on the degradation of pure magnesium in vitro, Mater. Sci. Eng. C. 29 (2009) 1559–1568. https://doi.org/10.1016/j.msec.2008.12.015.

[472] J. Wang, F. Witte, T. Xi, Y. Zheng, K. Yang, Y. Yang, D. Zhao, J. Meng, Y. Li, W. Li, K. Chan, L. Qin, Recommendation for modifying current cytotoxicity testing standards for biodegradable magnesium-based materials, Acta Biomater. 21 (2015) 237–249. https://doi.org/10.1016/j.actbio.2015.04.011.

[473] A. Sato, Y. Shimizu, Y. Imai, T. Mukai, A. Yamamoto, C. Miura, K. Muraki, Y. Sano, N. Ikeo, M. Tachi, Initial organ distribution and biological safety of Mg 2+ released from a Mg alloy implant, Biomed. Mater. 13 (2018). https://doi.org/10.1088/1748-605X/aaa9d5.

[474] B. Acar, O. Kose, M. Unal, A. Turan, Y. alper Katı, F. Guler, Comparison of magnesium versus titanium screw fixation for biplane chevron medial malleolar osteotomy in the treatment of osteochondral lesions of the talus, Eur. J. Orthop. Surg. Traumatol. 30 (2019) 163–173. https://doi.org/10.1007/s00590-019-02524-1.

[475] O. Kose, A. Turan, M. Unal, B. Acar, F. Guler, Fixation of medial malleolar fractures with magnesium bioabsorbable headless compression screws: short-term clinical and radiological outcomes in eleven patients, Arch. Orthop. Trauma Surg. 138 (2018) 1069–1075. https://doi.org/10.1007/s00402-018-2941-x.

[476] H. Klauser, Internal fixation of three-dimensional distal metatarsal I osteotomies in the treatment of hallux valgus deformities using biodegradable magnesium screws in comparison to titanium screws., Foot Ankle Surg. 25 3 (2019) 398–405. https://doi.org/10.1016/j.fas.2018.02.005.

[477] B. Ollivere, C. Darrah, T. Barker, J. Nolan, M.J. Porteous, Early clinical failure of the

Birmingham metal-on-metal hip resurfacing is associated with metallosis and soft-tissue necrosis., J. Bone Joint Surg. Br. 91 (2009) 1025–1030. https://doi.org/10.1302/0301-620X.91B8.21701.

[478] M. Sundfeldt, L. V Carlsson, C.B. Johansson, P. Thomsen, C. Gretzer, Aseptic loosening, not only a question of wear: a review of different theories., Acta Orthop. 77 (2006) 177–197. https://doi.org/10.1080/17453670610045902.

[479] P.K. Mishra, M. Palma, B. Buechel, J. Moore, V. Davra, N. Chu, A. Millman, N.J. Hallab, T.-D. Kanneganti, R.B. Birge, E.M. Behrens, A. Rivera, K.S. Beebe, J. Benevenia, W.C. Gause, Sterile particle-induced inflammation is mediated by macrophages releasing IL-33 through a Bruton's tyrosine kinase-dependent pathway., Nat. Mater. 18 (2019) 289–297. https://doi.org/10.1038/s41563-018-0271-6.

[480] Q. Peng, K. Li, Z. Han, E. Wang, Z. Xu, R. Liu, Y. Tian, Degradable magnesium-based implant materials with anti-inflammatory activity., J. Biomed. Mater. Res. A. 101 (2013) 1898–1906. https://doi.org/10.1002/jbm.a.34494.

[481] L. Jin, C. Chen, Y. Li, F. Yuan, R. Gong, J. Wu, H. Zhang, B. Kang, G. Yuan, H. Zeng, T. Chen, A Biodegradable Mg-Based Alloy Inhibited the Inflammatory Response of THP-1 Cell-Derived Macrophages Through the TRPM7-PI3K-AKT1 Signaling Axis., Front. Immunol. 10 (2019) 2798. https://doi.org/10.3389/fimmu.2019.02798.

[482] J. Sugimoto, A.M. Romani, A.M. Valentin-Torres, A.A. Luciano, C.M. Ramirez Kitchen, N. Funderburg, S. Mesiano, H.B. Bernstein, Magnesium decreases inflammatory cytokine production: a novel innate immunomodulatory mechanism., J. Immunol. 188 (2012) 6338–6346. https://doi.org/10.4049/jimmunol.1101765.

[483] L. Sun, X. Li, M. Xu, F. Yang, W. Wang, X. Niu, In vitro immunomodulation of magnesium on monocytic cell toward anti-inflammatory macrophages., Regen. Biomater. 7 (2020) 391–401. https://doi.org/10.1093/rb/rbaa010.

[484] Z. Chen, X. Mao, L. Tan, T. Friis, C. Wu, R. Crawford, Y. Xiao, Osteoimmunomodulatory properties of magnesium scaffolds coated with β-tricalcium phosphate., Biomaterials. 35 (2014) 8553–8565. https://doi.org/10.1016/j.biomaterials.2014.06.038.

[485] F. Suska, M. Källtorp, M. Esposito, C. Gretzer, P. Tengvall, P. Thomsen, In vivo/ex vivo cellular interactions with titanium and copper., J. Mater. Sci. Mater. Med. 12 (2001) 939–944. https://doi.org/10.1023/a:1012844612753.

[486] F. Suska, M. Esposito, C. Gretzer, M. Källtorp, P. Tengvall, P. Thomsen, IL-1α, IL-1β and TNF-α secretion during in vivo/ex vivo cellular interactions with titanium and copper, Biomaterials. 24 (2003) 461–468. https://doi.org/https://doi.org/10.1016/S0142-9612(02)00359-9.

[487] M. Lindblad, M. Lestelius, A. Johansson, P. Tengvall, P. Thomsen, Cell and soft tissue interactions with methyl- and hydroxyl-terminated alkane thiols on gold surfaces, Biomaterials. 18 (1997) 1059–1068. https://doi.org/https://doi.org/10.1016/S0142-9612(97)00029-X.

[488] B. Wiese, R. Willumeit-Römer, D. Letzig, J. Bohlen, Alloying effect of silver in magnesium on the development of microstructure and mechanical properties by indirect extrusion, J. Magnes. Alloy. 9 (2021) 112–122. https://doi.org/10.1016/j.jma.2020.08.001.

[489] K. Donath, G. Breuner, A method for the study of undecalcified bones and teeth with attached soft tissues. The Säge-Schliff (sawing and grinding) technique., J. Oral Pathol. 11 (1982) 318–326. https://doi.org/10.1111/j.1600-0714.1982.tb00172.x.

[490] F. Suska, L. Emanuelsson, A. Johansson, P. Tengvall, P. Thomsen, Fibrous capsule formation around titanium and copper., J. Biomed. Mater. Res. A. 85 (2008) 888–896. https://doi.org/10.1002/jbm.a.31575.

[491] P. Bankhead, M.B. Loughrey, J.A. Fernández, Y. Dombrowski, D.G. McArt, P.D. Dunne, S. McQuaid, R.T. Gray, L.J. Murray, H.G. Coleman, J.A. James, M. Salto-Tellez, P.W. Hamilton, QuPath: Open source software for digital pathology image analysis, Sci. Rep. 7 (2017) 1–7. https://doi.org/10.1038/s41598-017-17204-5.

[492] I. Arganda-Carreras, V. Kaynig, C. Rueden, K.W. Eliceiri, J. Schindelin, A. Cardona, H.S. Seung, Trainable Weka Segmentation: A machine learning tool for microscopy pixel classification, Bioinformatics. 33 (2017) 2424–2426. https://doi.org/10.1093/bioinformatics/btx180.

[493] B. Ullmann, N. Angrisani, J. Reifenrath, J.M. Seitz, D. Bormann, F.W. Bach, A. Meyer-Lindenberg, The effects of handling and storage on magnesium based implants - First results, Mater. Sci. Eng. C. 33 (2013) 3010–3017. https://doi.org/10.1016/j.msec.2013.03.034.

[494] K.-M. Holgers, M. Esposito, M. Källtorp, P. Thomsen, Titanium in Soft Tissues, in: D.M. Brunette, P. Tengvall, M. Textor, P. Thomsen (Eds.), Titan. Med., Springer Berlin Heidelberg, Berlin, Heidelberg, 2001: pp. 513–560. https://doi.org/10.1007/978-3-642-56486-4_16.

[495] D. Zhao, A. Brown, T. Wang, S. Yoshizawa, C. Sfeir, W.R. Heineman, In vivo quantification of hydrogen gas concentration in bone marrow surrounding magnesium fracture fixation hardware using an electrochemical hydrogen gas sensor., Acta Biomater. 73 (2018) 559–566. https://doi.org/10.1016/j.actbio.2018.04.032.

[496] L. Chung, D.R.J. Maestas, F. Housseau, J.H. Elisseeff, Key players in the immune response to biomaterial scaffolds for regenerative medicine., Adv. Drug Deliv. Rev. 114 (2017) 184–192. https://doi.org/10.1016/j.addr.2017.07.006.

[497] J.M. Anderson, A. Rodriguez, D.T. Chang, Foreign body reaction to biomaterials., Semin. Immunol. 20 (2008) 86–100. https://doi.org/10.1016/j.smim.2007.11.004.

[498] P.T. Thevenot, D.W. Baker, H. Weng, M.-W. Sun, L. Tang, The pivotal role of fibrocytes and mast cells in mediating fibrotic reactions to biomaterials., Biomaterials. 32 (2011) 8394–8403. https://doi.org/10.1016/j.biomaterials.2011.07.084.

[499] E. Dondossola, B.M. Holzapfel, S. Alexander, S. Filippini, D.W. Hutmacher, P. Friedl, Examination of the foreign body response to biomaterials by nonlinear intravital microscopy., Nat. Biomed. Eng. 1 (2016). https://doi.org/10.1038/s41551-016-0007.

[500] M. Rahmati, E.A. Silva, J.E. Reseland, C. A. Heyward, H.J. Haugen, Biological responses to physicochemical properties of biomaterial surface, Chem. Soc. Rev. 49 (2020) 5178–5224. https://doi.org/10.1039/d0cs00103a.

[501] S. Svensson, M. Trobos, O. Omar, P. Thomsen, Site-specific gene expression analysis of implant-near cells in a soft tissue infection model - Application of laser microdissection to study biomaterial-associated infection., J. Biomed. Mater. Res. A.

105 (2017) 2210–2217. https://doi.org/10.1002/jbm.a.36088.

[502] Y. Zhang, J. Xu, Y.C. Ruan, M.K. Yu, M. O'Laughlin, H. Wise, D. Chen, L. Tian, D. Shi, J. Wang, S. Chen, J.Q. Feng, D.H.K. Chow, X. Xie, L. Zheng, L. Huang, S. Huang, K. Leung, N. Lu, L. Zhao, H. Li, D. Zhao, X. Guo, K. Chan, F. Witte, H.C. Chan, Y. Zheng, L. Qin, Implant-derived magnesium induces local neuronal production of CGRP to improve bone-fracture healing in rats., Nat. Med. 22 (2016) 1160–1169. https://doi.org/10.1038/nm.4162.

[503] H.S. Gill, G. Grammatopoulos, S. Adshead, E. Tsialogiannis, E. Tsiridis, Molecular and immune toxicity of CoCr nanoparticles in MoM hip arthroplasty., Trends Mol. Med. 18 (2012) 145–155. https://doi.org/10.1016/j.molmed.2011.12.002.

[504] F.K.-M. Chan, K. Moriwaki, M.J. De Rosa, Detection of necrosis by release of lactate dehydrogenase activity., Methods Mol. Biol. 979 (2013) 65–70. https://doi.org/10.1007/978-1-62703-290-2_7.

[505] A. Mazur, J.A.M. Maier, E. Rock, E. Gueux, W. Nowacki, Y. Rayssiguier, Magnesium and the inflammatory response: potential physiopathological implications., Arch. Biochem. Biophys. 458 (2007) 48–56. https://doi.org/10.1016/j.abb.2006.03.031.

[506] W.A. Marasco, E.L. Becker, J.M. Oliver, The ionic basis of chemotaxis. Separate cation requirements for neutrophil orientation and locomotion in a gradient of chemotactic peptide., Am. J. Pathol. 98 (1980) 749–768.

[507] K.A. Lapidos, E.C. Woodhouse, E.C. Kohn, L. Masiero, Mg(++)-induced endothelial cell migration: substratum selectivity and receptor-involvement., Angiogenesis. 4 (2001) 21–28. https://doi.org/10.1023/a:1016619414817.

[508] A. Aguirre, A. González, J.A. Planell, E. Engel, Extracellular calcium modulates in vitro bone marrow-derived Flk-1+ CD34+ progenitor cell chemotaxis and differentiation through a calcium-sensing receptor., Biochem. Biophys. Res. Commun. 393 (2010) 156–161. https://doi.org/10.1016/j.bbrc.2010.01.109.

[509] S. Choi, K.-J. Kim, S. Cheon, E.-M. Kim, Y.-A. Kim, C. Park, K.K. Kim, Biochemical activity of magnesium ions on human osteoblast migration., Biochem. Biophys. Res. Commun. 531 (2020) 588–594. https://doi.org/10.1016/j.bbrc.2020.07.057.

[510] F. Suska, C. Gretzer, M. Esposito, L. Emanuelsson, A. Wennerberg, P. Tengvall, P. Thomsen, In vivo cytokine secretion and NF-kappaB activation around titanium and copper implants., Biomaterials. 26 (2005) 519–527. https://doi.org/10.1016/j.biomaterials.2004.02.066.

[511] Y. Wu, M. Yuan, J. Song, X. Chen, H. Yang, Hydrogen Gas from Inflammation Treatment to Cancer Therapy, ACS Nano. 13 (2019) 8505–8511. https://doi.org/10.1021/acsnano.9b05124.

[512] A.-M. Galow, A. Rebl, D. Koczan, S.M. Bonk, W. Baumann, J. Gimsa, Increased osteoblast viability at alkaline pH in vitro provides a new perspective on bone regeneration, Biochem. Biophys. Reports. 10 (2017) 17–25. https://doi.org/https://doi.org/10.1016/j.bbrep.2017.02.001.

[513] W. Liu, T. Wang, C. Yang, B.W. Darvell, J. Wu, K. Lin, J. Chang, H. Pan, W.W. Lu, Alkaline biodegradable implants for osteoporotic bone defects—importance of microenvironment pH, Osteoporos. Int. 27 (2016) 93–104.

https://doi.org/10.1007/s00198-015-3217-8.

[514] R. Schwarzer, D. Tondera, W. Arnold, K. Giese, A. Klippel, J. Kaufmann, REDD1 integrates hypoxia-mediated survival signaling downstream of phosphatidylinositol 3-kinase., Oncogene. 24 (2005) 1138–1149. https://doi.org/10.1038/sj.onc.1208236.

[515] E.L. Silva, S. V Lamaka, D. Mei, M.L. Zheludkevich, The Reduction of Dissolved Oxygen During Magnesium Corrosion., ChemistryOpen. 7 (2018) 664–668. https://doi.org/10.1002/open.201800076.

[516] P. Zartner, M. Buettner, H. Singer, M. Sigler, First biodegradable metal stent in a child with congenital heart disease: evaluation of macro and histopathology., Catheter. Cardiovasc. Interv. Off. J. Soc. Card. Angiogr. Interv. 69 (2007) 443–446. https://doi.org/10.1002/ccd.20828.

[517] J. Mao, L. Chen, Z. Cai, S. Qian, Z. Liu, B. Zhao, Y. Zhang, X. Sun, W. Cui, Advanced Biomaterials for Regulating Polarization of Macrophages in Wound Healing, Adv. Funct. Mater. 32 (2022) 2111003. https://doi.org/https://doi.org/10.1002/adfm.202111003.

[518] E.M. O'Brien, G.E. Risser, K.L. Spiller, Sequential drug delivery to modulate macrophage behavior and enhance implant integration, Adv. Drug Deliv. Rev. 149–150 (2019) 85–94. https://doi.org/https://doi.org/10.1016/j.addr.2019.05.005.

[519] W. Qiao, K.H.M. Wong, J. Shen, W. Wang, J. Wu, J. Li, Z. Lin, Z. Chen, J.P. Matinlinna, Y. Zheng, S. Wu, X. Liu, K.P. Lai, Z. Chen, Y.W. Lam, K.M.C. Cheung, K.W.K. Yeung, TRPM7 kinase-mediated immunomodulation in macrophage plays a central role in magnesium ion-induced bone regeneration., Nat. Commun. 12 (2021) 2885. https://doi.org/10.1038/s41467-021-23005-2.

[520] M.P. Kwesiga, A.A. Gillette, F. Razaviamri, M.E. Plank, A.L. Canull, Z. Alesch, W. He, B.P. Lee, R.J. Guillory, Biodegradable magnesium materials regulate ROS-RNS balance in pro-inflammatory macrophage environment, Bioact. Mater. 23 (2023) 261–273. https://doi.org/10.1016/j.bioactmat.2022.10.017.

[521] D.B. Gurevich, K.E. French, J.D. Collin, S.J. Cross, P. Martin, Live imaging the foreign body response in zebrafish reveals how dampening inflammation reduces fibrosis., J. Cell Sci. 133 (2019). https://doi.org/10.1242/jcs.236075.

[522] S.A. Eming, P. Martin, M. Tomic-Canic, Wound repair and regeneration: mechanisms, signaling, and translation., Sci. Transl. Med. 6 (2014) 265sr6. https://doi.org/10.1126/scitranslmed.3009337.

[523] K.L. Spiller, S. Nassiri, C.E. Witherel, R.R. Anfang, J. Ng, K.R. Nakazawa, T. Yu, G. Vunjak-Novakovic, Sequential delivery of immunomodulatory cytokines to facilitate the M1-to-M2 transition of macrophages and enhance vascularization of bone scaffolds., Biomaterials. 37 (2015) 194–207. https://doi.org/10.1016/j.biomaterials.2014.10.017.

[524] D.B. Gurevich, C.E. Severn, C. Twomey, A. Greenhough, J. Cash, A.M. Toye, H. Mellor, P. Martin, Live imaging of wound angiogenesis reveals macrophage orchestrated vessel sprouting and regression, EMBO J. 37 (2018) e97786. https://doi.org/https://doi.org/10.15252/embj.201797786.

[525] M. Alikhani, C.M. Maclellan, M. Raptis, S. Vora, P.C. Trackman, D.T. Graves,

Advanced glycation end products induce apoptosis in fibroblasts through activation of ROS, MAP kinases, and the FOXO1 transcription factor., Am. J. Physiol. Cell Physiol. 292 (2007) C850-6. https://doi.org/10.1152/ajpcell.00356.2006.

[526] U. Adhikari, X. An, N. Rijal, T. Hopkins, S. Khanal, T. Chavez, R. Tatu, J. Sankar, K.J. Little, D.B. Hom, N. Bhattarai, S.K. Pixley, Embedding magnesium metallic particles in polycaprolactone nanofiber mesh improves applicability for biomedical applications., Acta Biomater. 98 (2019) 215–234. https://doi.org/10.1016/j.actbio.2019.04.061.

[527] A.A. Oliver, M. Sikora-Jasinska, A.G. Demir, R.J. Guillory, Recent advances and directions in the development of bioresorbable metallic cardiovascular stents: Insights from recent human and in vivo studies, Acta Biomater. 127 (2021) 1–23. https://doi.org/https://doi.org/10.1016/j.actbio.2021.03.058.

[528] S. Arabnejad, B. Johnston, M. Tanzer, D. Pasini, Fully porous 3D printed titanium femoral stem to reduce stress-shielding following total hip arthroplasty, J. Orthop. Res. 35 (2017) 1774–1783. https://doi.org/https://doi.org/10.1002/jor.23445.

[529] A. Lons, S. Putman, G. Pasquier, H. Migaud, E. Drumez, J. Girard, Metallic ion release after knee prosthesis implantation: a prospective study, Int. Orthop. 41 (2017) 2503–2508. https://doi.org/10.1007/s00264-017-3528-9.

[530] M.F. López, A. Gutiérrez, J.A. Jiménez, Surface characterization of new non-toxic titanium alloys for use as biomaterials, Surf. Sci. 482–485 (2001) 300–305. https://doi.org/https://doi.org/10.1016/S0039-6028(00)01005-0.

[531] M. Abdel-Hady Gepreel, M. Niinomi, Biocompatibility of Ti-alloys for long-term implantation, J. Mech. Behav. Biomed. Mater. 20 (2013) 407–415. https://doi.org/https://doi.org/10.1016/j.jmbbm.2012.11.014.

[532] B. Prediger, T. Mathes, C. Probst, D. Pieper, Elective removal vs. retaining of hardware after osteosynthesis in asymptomatic patients—a scoping review, Syst. Rev. 9 (2020). https://doi.org/10.1186/s13643-020-01488-2.

[533] R. Viehe, D.J. Haupt, M.W. Heaslet, S. Walston, Complications of screw-fixated chevron osteotomies for the correction of hallux abducto valgus., J. Am. Podiatr. Med. Assoc. 93 (2003) 499–502. https://doi.org/10.7547/87507315-93-6-499.

[534] A. Boulos, S.F. DeFroda, J.E. Kleiner, N. Thomas, J.A. Gil, A.I.J. Cruz, Inpatient orthopaedic hardware removal in children: A cross-Sectional study., J. Clin. Orthop. Trauma. 8 (2017) 270–275. https://doi.org/10.1016/j.jcot.2017.06.020.

[535] I.I. Onche, O.E. Osagie, S. INuhu, Removal of orthopaedic implants: indications, outcome and economic implications., J. West African Coll. Surg. 1 (2011) 101–112.

[536] L.E. Claes, Mechanical characterization of biodegradable implants, Clin. Mater. 10 (1992) 41–46. https://doi.org/https://doi.org/10.1016/0267-6605(92)90083-6.

[537] M.E. Maguire, J.A. Cowan, Magnesium chemistry and biochemistry, Biometals. 15 (2002) 203–210. https://doi.org/10.1023/A:1016058229972.

[538] M.P. Staiger, A.M. Pietak, J. Huadmai, G. Dias, Magnesium and its alloys as orthopedic biomaterials: A review, Biomaterials. 27 (2006) 1728–1734. https://doi.org/10.1016/j.biomaterials.2005.10.003.

[539] J. Liu, Y. Lin, D. Bian, M. Wang, Z. Lin, X. Chu, W. Li, Y. Liu, Z. Shen, Y. Liu, Y. Tong, Z. Xu, Y. Zhang, Y. Zheng, In vitro and in vivo studies of Mg-30Sc alloys with different phase structure for potential usage within bone, Acta Biomater. 98 (2019) 50–66. https://doi.org/https://doi.org/10.1016/j.actbio.2019.03.009.

[540] D. Tie, R.G. Guan, H.N. Liu, A. Cipriano, Y.L. Liu, Q. Wang, Y.D. Huang, N. Hort, An in vivo study on the metabolism and osteogenic activity of bioabsorbable Mg-1Sr alloy, Acta Biomater. 29 (2016) 455–467. https://doi.org/10.1016/j.actbio.2015.11.014.

[541] J. Walker, S. Shadanbaz, T.B.F. Woodfield, M.P. Staiger, G.J. Dias, Magnesium biomaterials for orthopedic application: A review from a biological perspective, J. Biomed. Mater. Res. - Part B Appl. Biomater. 102 (2014) 1316–1331. https://doi.org/10.1002/jbm.b.33113.

[542] H. Leonhardt, A. Ziegler, G. Lauer, A. Franke, Osteosynthesis of the Mandibular Condyle With Magnesium-Based Biodegradable Headless Compression Screws Show Good Clinical Results During a 1-Year Follow-Up Period., J. Oral Maxillofac. Surg. (2020). https://doi.org/10.1016/j.joms.2020.02.025.

[543] F. Feyerabend, J. Fischer, J. Holtz, F. Witte, R. Willumeit, H. Drucker, C. Vogt, N. Hort, Evaluation of short-term effects of rare earth and other elements used in magnesium alloys on primary cells and cell lines, Acta Biomater. 6 (2010) 1834–1842. https://doi.org/10.1016/j.actbio.2009.09.024.

[544] I. Johnson, D. Perchy, H. Liu, In vitro evaluation of the surface effects on magnesium-yttrium alloy degradation and mesenchymal stem cell adhesion, J. Biomed. Mater. Res. Part A. 100A (2012) 477–485. https://doi.org/https://doi.org/10.1002/jbm.a.33290.

[545] J. Hofstetter, E. Martinelli, A.M. Weinberg, M. Becker, B. Mingler, P.J. Uggowitzer, J.F. Löffler, Assessing the degradation performance of ultrahigh-purity magnesium in vitro and in vivo, Corros. Sci. 91 (2015) 29–36. https://doi.org/https://doi.org/10.1016/j.corsci.2014.09.008.

[546] A. Atrens, M. Liu, N.I. Zainal Abidin, Corrosion mechanism applicable to biodegradable magnesium implants, Mater. Sci. Eng. B. 176 (2011) 1609–1636. https://doi.org/https://doi.org/10.1016/j.mseb.2010.12.017.

[547] Z. Qiao, Z. Shi, N. Hort, N.I. Zainal Abidin, A. Atrens, Corrosion behaviour of a nominally high purity Mg ingot produced by permanent mould direct chill casting, Corros. Sci. 61 (2012) 185–207. https://doi.org/https://doi.org/10.1016/j.corsci.2012.04.030.

[548] N.I.Z. Abidin, B. Rolfe, H. Owen, J. Malisano, D. Martin, J. Hofstetter, P.J. Uggowitzer, A. Atrens, The in vivo and in vitro corrosion of high-purity magnesium and magnesium alloys WZ21 and AZ91, Corros. Sci. 75 (2013) 354–366. https://doi.org/10.1016/j.corsci.2013.06.019.

[549] P. Han, P. Cheng, S. Zhang, C. Zhao, J. Ni, Y. Zhang, W. Zhong, P. Hou, X. Zhang, Y. Zheng, Y. Chai, In vitro and in vivo studies on the degradation of high-purity Mg (99.99wt.%) screw with femoral intracondylar fractured rabbit model, Biomaterials. 64 (2015) 57–69. https://doi.org/10.1016/j.biomaterials.2015.06.031.

[550] L. Chen, Z. Lin, M. Wang, W. Huang, J. Ke, D. Zhao, Q.Q. Yin, Y. Zhang, Treatment of trauma-induced femoral head necrosis with biodegradable pure Mg screw-fixed pedicle iliac bone flap, J. Orthop. Transl. 17 (2019) 133–137.

https://doi.org/10.1016/j.jot.2019.01.004.

[551] C.-C. Wong, P.-C. Wong, P.-H. Tsai, J.S. Jang, C.-K. Cheng, H.-H. Chen, C.-H. Chen, Biocompatibility and Osteogenic Capacity of Mg-Zn-Ca Bulk Metallic Glass for Rabbit Tendon-Bone Interference Fixation, Int. J. Mol. Sci. 20 (2019). https://doi.org/10.3390/ijms20092191.

[552] S.Y. Cho, S.W. Chae, K.W. Choi, H.K. Seok, Y.C. Kim, J.Y. Jung, S.J. Yang, G.J. Kwon, J.T. Kim, M. Assad, Biocompatibility and strength retention of biodegradable Mg-Ca-Zn alloy bone implants, J. Biomed. Mater. Res. - Part B Appl. Biomater. 101 B (2013) 201–212. https://doi.org/10.1002/jbm.b.32813.

[553] P. Ding, Y. Liu, X. He, D. Liu, M. Chen, In vitro and in vivo biocompatibility of Mg–Zn–Ca alloy operative clip, Bioact. Mater. 4 (2019) 236–244. https://doi.org/10.1016/j.bioactmat.2019.07.002.

[554] K.Y. Renkema, R.T. Alexander, R.J. Bindels, J.G. Hoenderop, Calcium and phosphate homeostasis: Concerted interplay of new regulators, Ann. Med. 40 (2008) 82–91. https://doi.org/10.1080/07853890701689645.

[555] N. Li, Y. Zheng, Novel Magnesium Alloys Developed for Biomedical Application: A Review, J. Mater. Sci. Technol. 29 (2013) 489–502. https://doi.org/10.1016/j.jmst.2013.02.005.

[556] Z.J. Li, X.N. Gu, S.Q. Lou, Y.F. Zheng, The development of binary Mg-Ca alloys for use as biodegradable materials within bone., Biomaterials. 29 (2008) 1329–1344. https://doi.org/10.1016/j.biomaterials.2007.12.021.

[557] I. Basu, M. Chen, J. Wheeler, R.E. Schäublin, J.F. Löffler, Segregation-driven exceptional twin-boundary strengthening in lean Mg–Zn–Ca alloys, Acta Mater. 229 (2022) 117746. https://doi.org/https://doi.org/10.1016/j.actamat.2022.117746.

[558] M. Deng, L. Wang, D. Höche, S. V Lamaka, C. Wang, D. Snihirova, Y. Jin, Y. Zhang, M.L. Zheludkevich, Approaching “stainless magnesium” by Ca micro-alloying, Mater. Horizons. 8 (2021) 589–596. https://doi.org/10.1039/D0MH01380C.

[559] P.D. Saltman, L.G. Strause, The role of trace minerals in osteoporosis., J. Am. Coll. Nutr. 12 (1993) 384–389. https://doi.org/10.1080/07315724.1993.10718327.

[560] A. Školáková, T. Lovaši, J. Pinc, Z. Kačenka, L. Rieszová, Z. Žofková, The Effect of Zinc and Calcium Addition on Magnesium Alloy, Manuf. Technol. 20 (2020) 668–676. https://doi.org/10.21062/MFT.2020.107.

[561] J. Löffer, U. P, W. C., B. M, F. H, Process and apparatus for vacuum distillation of high-purity magnesium, WO2013 107644-A1, 2013.

[562] D. Qi, J. Su, S. Li, H. Zhu, L. Cheng, S. Hua, X. Yuan, J. Jiang, Z. Shu, Y. Shi, J. Xiao, 3D printed magnesium-doped β-TCP gyroid scaffold with osteogenesis, angiogenesis, immunomodulation properties and bone regeneration capability in vivo, Biomater. Adv. 136 (2022) 212759. https://doi.org/https://doi.org/10.1016/j.bioadv.2022.212759.

[563] N. Abay Akar, G. Gürel Peközer, G. Torun Köse, Fibrous bone tissue engineering scaffolds prepared by wet spinning of PLGA., Turkish J. Biol. = Turk Biyol. Derg. 43 (2019) 235–245. https://doi.org/10.3906/biy-1904-63.

[564] R.A. Thibault, L. Scott Baggett, A.G. Mikos, F.K. Kasper, Osteogenic Differentiation

of Mesenchymal Stem Cells on Pregenerated Extracellular Matrix Scaffolds in the Absence of Osteogenic Cell Culture Supplements, Tissue Eng. Part A. 16 (2009) 431–440. https://doi.org/10.1089/ten.tea.2009.0583.

[565] K.M.M. Hasan, N. Tamanna, M.A. Haque, Biochemical and histopathological profiling of Wistar rat treated with Brassica napus as a supplementary feed, Food Sci. Hum. Wellness. 7 (2018) 77–82. https://doi.org/https://doi.org/10.1016/j.fshw.2017.12.002.

[566] A. Andretta, M.E.M. Schieferdecker, R.R. Petterle, E. dos Santos Paiva, C.L. Boguszewski, Relations between serum magnesium and calcium levels and body composition and metabolic parameters in women with fibromyalgia, Adv. Rheumatol. 60 (2020) 18. https://doi.org/10.1186/s42358-020-0122-4.

[567] S.M. van Gaalen, M.C. Kruyt, R.E. Geuze, J.D. de Bruijn, J. Alblas, W.J.A. Dhert, Use of Fluorochrome Labels in In Vivo Bone Tissue Engineering Research, Tissue Eng. Part B Rev. 16 (2009) 209–217. https://doi.org/10.1089/ten.teb.2009.0503.

[568] L. Jenö, L. Géza, A simple differential staining method for semi-thin sections of ossifying cartilage and bone tissues embedded in epoxy resin., Mikroskopie. 31 (1975) 1–4.

[569] J. Hofstetter, M. Becker, E. Martinelli, A.M. Weinberg, B. Mingler, H. Kilian, S. Pogatscher, P.J. Uggowitzer, J.F. Löffler, High-strength low-alloy (HSLA) Mg-Zn-Ca alloys with excellent biodegradation performance, Jom. 66 (2014) 566–572. https://doi.org/10.1007/s11837-014-0875-5.

[570] M.N. Lee, H.-S. Hwang, S.-H. Oh, A. Roshanzadeh, J.-W. Kim, J.H. Song, E.-S. Kim, J.-T. Koh, Elevated extracellular calcium ions promote proliferation and migration of mesenchymal stem cells via increasing osteopontin expression, Exp. Mol. Med. 50 (2018) 1–16. https://doi.org/10.1038/s12276-018-0170-6.

[571] A. Fazel Anvari-Yazdi, K. Tahermanesh, S.M.M. Hadavi, T. Talaei-Khozani, M. Razmkhah, S.M. Abed, M.S. Mohtasebi, Cytotoxicity assessment of adipose-derived mesenchymal stem cells on synthesized biodegradable Mg-Zn-Ca alloys, Mater. Sci. Eng. C. 69 (2016) 584–597. https://doi.org/https://doi.org/10.1016/j.msec.2016.07.016.

[572] L. Song, Chapter One - Calcium and Bone Metabolism Indices, in: G.S.B.T.-A. in C.C. Makowski (Ed.), Elsevier, 2017: pp. 1–46. https://doi.org/https://doi.org/10.1016/bs.acc.2017.06.005.

[573] L. Hou, Z. Li, Y. Pan, L. Du, X. Li, Y. Zheng, L. Li, In vitro and in vivo studies on biodegradable magnesium alloy, Prog. Nat. Sci. Mater. Int. 24 (2014) 466–471. https://doi.org/10.1016/j.pnsc.2014.09.002.

[574] K. Kawamoto, T. Suzuki, T. Nagano, T. Kawamoto, K. Gomi, A Study of Bone Formation around Titanium Implants Using Frozen Sections, J. Hard Tissue Biol. 30 (2021) 165–174. https://doi.org/10.2485/jhtb.30.165.

[575] A. Myrissa, N.A. Agha, Y.Y. Lu, E. Martinelli, J. Eichler, G. Szakács, C. Kleinhans, R. Willumeit-Römer, U. Schäfer, A.-M.M. Weinberg, G. Szakacs, C. Kleinhans, R. Willumeit-Romer, U. Schafer, A.-M.M. Weinberg, In vitro and in vivo comparison of binary Mg alloys and pure Mg, Mater. Sci. Eng. C-Materials Biol. Appl. 61 (2016) 865–874. https://doi.org/10.1016/j.msec.2015.12.064.

[576] X. Lu, Z. Wu, K. Xu, X. Wang, S. Wang, H. Qiu, X. Li, J. Chen, Multifunctional

Coatings of Titanium Implants Toward Promoting Osseointegration and Preventing Infection: Recent Developments., Front. Bioeng. Biotechnol. 9 (2021) 783816. https://doi.org/10.3389/fbioe.2021.783816.

[577] R. Trindade, T. Albrektsson, P. Tengvall, A. Wennerberg, Foreign Body Reaction to Biomaterials: On Mechanisms for Buildup and Breakdown of Osseointegration., Clin. Implant Dent. Relat. Res. 18 (2016) 192–203. https://doi.org/10.1111/cid.12274.

[578] R. Trindade, T. Albrektsson, S. Galli, Z. Prgomet, P. Tengvall, A. Wennerberg, Osseointegration and foreign body reaction: Titanium implants activate the immune system and suppress bone resorption during the first 4 weeks after implantation, Clin. Implant Dent. Relat. Res. 20 (2018) 82–91. https://doi.org/https://doi.org/10.1111/cid.12578.

[579] T.M. Liu, E.H. Lee, Transcriptional Regulatory Cascades in Runx2-Dependent Bone Development, Tissue Eng. Part B Rev. 19 (2012) 254–263. https://doi.org/10.1089/ten.teb.2012.0527.

[580] Y. Yu, H. Lu, J. Sun, Long-term in vivo evolution of high-purity Mg screw degradation — Local and systemic effects of Mg degradation products, Acta Biomater. 71 (2018) 215–224. https://doi.org/10.1016/j.actbio.2018.02.023.

[581] C. Janning, E. Willbold, C. Vogt, J. Nellesen, A. Meyer-Lindenberg, H. Windhagen, F. Thorey, F. Witte, Magnesium hydroxide temporarily enhancing osteoblast activity and decreasing the osteoclast number in peri-implant bone remodelling, Acta Biomater. 6 (2010) 1861–1868. https://doi.org/10.1016/j.actbio.2009.12.037.

[582] T.A. Huehnerschulte, J. Reifenrath, B. von Rechenberg, D. Dziuba, J.M. Seitz, D. Bormann, H. Windhagen, A. Meyer-Lindenberg, In vivo assessment of the host reactions to the biodegradation of the two novel magnesium alloys ZEK100 and AX30 in an animal model, Biomed. Eng. Online. 11 (2012) 1–20. https://doi.org/10.1186/1475-925X-11-14.

[583] D.H.K. Chow, J. Wang, P. Wan, L. Zheng, M.T.Y. Ong, L. Huang, W. Tong, L. Tan, K. Yang, L. Qin, Biodegradable magnesium pins enhanced the healing of transverse patellar fracture in rabbits., Bioact. Mater. 6 (2021) 4176–4185. https://doi.org/10.1016/j.bioactmat.2021.03.044.

[584] C. Pautke, T. Tischer, S. Vogt, C. Haczek, H. Deppe, A. Neff, H.-H. Horch, M. Schieker, A. Kolk, New advances in fluorochrome sequential labelling of teeth using seven different fluorochromes and spectral image analysis, J. Anat. 210 (2007) 117–121. https://doi.org/https://doi.org/10.1111/j.1469-7580.2006.00660.x.

ACKNOWLEDGEMENTS

I would like to thanks the financial bodies that support for my Ph.D research:

The Horizon 2020 Programme, Marie Słodowska-Curie Actions (MSCA) under the project "Promoting patient safety by a novel combination of imaging technologies for biodegradable magnesium implants, MgSafe", agreement 811226.

The MagMAX project entitled "Development of Advanced Magnesium Alloys for Multifunctional Applications in Extreme Environments" No. V4/JAPAN/15MagMAX/2022 is financed by the National Centre for Research and Development in Poland in the frame of Visegrad Group (V4)-Japan Joint Research Program-Advanced Materials.

I would like to express my gratitude to those who provided support and assistance throughout my Ph.D. journey. Firstly, I thank my supervisor, Professor Wojciech Święszkowski, for his constant guidance, support, and motivation. His vision, and dedication to my academic career growth were valuable for my Ph.D. progress. I would like to extend my sincere gratitude to Dr. inż. Tomasz Płociński for his invaluable guidance, patience, feedback, and assistance during my research, as well as his support throughout the extensive hours I spent conducting imaging and analysis in the microscope rooms at Narbutta.

I express my gratitude to Professor Regine Willumeit, the main coordinator of the MgSafe project, for her invaluable guidance and support. Thank you for your scientific expertise and inspirational role as a woman in science. I really appreciated her for opening the doors of her lab at the Institute of Metallic Biomaterials, hereon, Geesthacht, Germany.

Thank you to Dr. Heike Helmholz for her invaluable assistance during my *in vitro* investigations, as well as for her guidance and insightful discussions. Thank you to Anke Borkam-Schuster and Monika Luczak for their technical support during my secondment at the biological characterization lab at the Institute of Metallic Biomaterials, Hereon, Geesthacht, Germany.

A special thanks to Dr. inż. Anna Dobkowska. Thank you for being friendly and supportive over these years in Warsaw. Your assistance has contributed to my research achievements and has been invaluable in my day-to-day living in Warsaw. Thanks for generously sharing your knowledge and expertise and for always being accessible for personal and scientific exchanges.

I would like to thank all members of the Biomaterials group for their assistance throughout my time in Warsaw. Grateful acknowledgments are extended to Alessia, Marina, Pasquale, and David for their close friendship during challenging moments and the enjoyable experiences shared. I will forever remember and really appreciate your invaluable support.

I also want to thank Alexandra Zielinska, Marlene Gonzalez, and Przemek Suchecki for their valuable assistance during my visits to Bitnara lab.

Thank you to all members of the MgSafe network for the productive collaboration during my Ph.D. research. I extend my gratitude to the entire team of coauthors from the Department of Biomaterials, Institute of Clinical Sciences, Sahlgrenska Academy, University of Gothenburg, namely Peter Thomsen, Anders Palmquist, Omar Omar, and Furqan Ali Shah. Thank you, Heithem Ben Amara, for your friendship and insightful chats.

I would like to express my gratitude to my close friend, Valeria, for her invaluable emotional and mental support. I am thankful for the numerous video conversations we had to share our experiences during our PhD journey and for the memorable memories we created together during this significant chapter of our lives.

Thank you to all the administrative staff at the Faculty of Material Science and Engineering for your assistance during my Ph.D time.

Most importantly, I express my gratitude to my parents, Clemente and Sofia, as well as my beloved brother Fernando, for their unwavering support and presence throughout my life. Throughout our conversations, you consistently listened to me, provided support, and demonstrated belief in me. Your encouragement has served as a constant source of inspiration, motivating me to improve every day.

Curriculum vitae

Diana Clemencia Martinez Guerrero
Born on January 08th 1983 in Bogota, Colombia

EDUCATION

2019-2024. PhD candidate at Warsaw University of Technology, Faculty of Material Science and Engineering

Field of Study: Material Science

PhD thesis: Mg-based biodegradable implants: From surface characterization to tissue-implant interface evaluation after *in vitro* and *in vivo* degradation

Supervisor: Prof. Wojciech Święszkowski

2017-2018. Master student at The University of Sheffield, Department of Material Science and Engineering

Field of Study: Material Science

Master thesis: Fucoidan as an alternative natural source for osteoblast differentiation and its potential to be used as a biomaterial for bone regeneration

Supervisior: Prof. Gwendolen Reilly

2009-2011. Postgraduate student at the Universidad Nacional de Colombia, Faculty of Dentistry

Field of study: Oral Rehabilitation

Thesis: Comportamiento biomecánico de coronas individules implantosoportadas, comparado con restauraciones ferulizadas sobre implantes de oseintegración en el sector posterior

Supervisor: Dr. Jorge Pardo

2000-2004. Bachelor student at the Universidad Nacional de Colombia, Faculty of Dentistry

Field of Study: Dentistry

Thesis: Analisis costo-efectivo de AINEs COX-1 and AINES COX-2 para el manejo del dolor postoperatorio de procedimiento de cirugia oral.

Supervisor: Dr Eduardo Low

TRAININGS AND INTERSHIPS:

31.05-02.06.2022r. Bioretec Ltd.

Training in the life cycle of medical devices.

Training as part of the Mg Safe Project.

01-03.03.2022r. University of Gothenburg, Sahlgrenska Academy, Institute of Clinical Sciences, Department of Biomaterials
Histology and Gene expression.
Training as part of the MgSafe project.

22-24.11.2021r. Institute of Metallic Biomaterials, Helmholtz-Zentrum hereon.
Career Planning and Application Training.
Training as part of the MgSafe project.

16-18.06.2021r. Warsaw University of Technology, Faculty of Material Science and Engineering.
Introduction of surface sensitive methods, orrelation between measured parameters and material properties.
Training as part of the MgSafe project

16-17.12.2020r Consiglio Nazionale delle Ricerche
Molecular Imaging Technologies for Biodegradable Bone Implants
Training as part of the MgSafe project

12-15.01.2020r. University of Gothenburg, Sahlgrenska Academy, Institute of Clinical Sciences, Department of Biomaterials
Raman spectroscopy of mineralized tissues

01.09-27.10.2020r Department of Biomaterials characterization, Institute of Metallic Biomaterials, Helmholtz-Zentrum hereon.
Intership for *in vitro* tests to study magnesium-based biomaterials degradation
Training as part of the MgSafe project

02-06.12.2019. Medical University of Graz
Animal handling, operation techniques; Writing scientific communications I; Personal Learning Environment
Training as part of the Mg Safe Project

INVOLVEMENT IN PROJECTS

2022-2024. “Development of Advanced Magnesium Alloys for Multifunctional Applications in Extreme Environments” No. V4-JAPAN/2/15MagMAX/2022 financed by the National Centre for Research and Development in Poland in the frame of Visegrad Group (V4)-Japan Joint Research Program-Advanced Materials.

2019- 2022. "Promoting patient safety by a novel combination of imaging technologies for biodegradable magnesium implants" European Union´s Horizon 2020 programme under the Marie Sklodowska-Curie grant agreement No. 811226.

LIST OF PUBLICATIONS

Chapter in this thesis

Martinez, D. C.; Borkam-Schuster, A.; Helmholz, H.; Dobkowska, A.; Luthringer -Feyerabend, B.; Plocinski, T.; WIllumeit-Römer, R., Swieszkowski, W. *Bone cells influence the degradation interface of Mg-based materials: Insights from multimodal in vitro analysis*. (*Accepted in **Acta Biomaterialia**, Available online 19 August 2024*). https://doi.org/10.1016/j.actbio.2024.08.015.

Martinez, D. C., Dobkowska, A., Marek, R., Cwieka, H., & Swi, W. (2023). *In vitro* and *in vivo* degradation behavior of Mg-0.45Zn-0.45Ca (ZX00) screws for orthopedic applications. ***Bioactive Materials***, 28, 132–154. https://doi.org/10.1016/j.bioactmat.2023.05.004.

Ben, H., **Martinez, D. C**., Shah, F. A., Johansson, A., Emanuelsson, L., Norlindh, B., Willumeit-r, R., Swieszkowski, W., Palmquist, A., Omar, O., & Thomsen, P. (2023). Magnesium implant degradation provides immunomodulatory and proangiogenic effects and attenuates peri-implant fibrosis in soft tissues. ***Bioactive Materials***, 26, 353–369. https://doi.org/10.1016/j.bioactmat.2023.02.014.

Okutan B, Schwarze UY, Berger L, **Martinez D.C**., Herber V, Suljevic O, Plocinski T, Swieszkowski W, Santos SG, Schindl R, Löffler JF, Weinberg AM, Sommer NG. (2023). The combined effect of zinc and calcium on the biodegradation of ultrahigh-purity magnesium implants. ***Biomater Adv. Mar***;146:213287. https://doi: 10.1016/j.bioadv.2023.213287.

Other publications:

H. Ben, **D.C. Martinez**, K. Iskhakova, L. Emanuelsson, B. Norlindh, A. Johansson, D.C.F. Wieland, B. Zeller-Plumhoff, R. Willumeit-Römer, T. Plocinski, W. Swieszkowski, F.A. Shah, A. Palmquist, P. Thomsen, Multifaceted response to immunomodulatory magnesium implants: Osteopromotion at the interface and adipogenesis in the bone marrow. (Accepted in **Biomaterials**, Available online 30 August 2024). https://doi.org/10.1016/j.biomaterials.2024.122779.

Dobkowska, A., Lofaj, F., Gonzalez, M., **Martinez D.C**., kulikowski, K., Paradiso, A., Idaszek, J., Gubicza, J., Jenei, P.,K abátová, M., Kvetková, Lisnichuk, M., Inoue, S., Kawamura, Y. Swieszkowski, W. Structural, mechanical, corrosion, and early biological assessment of tantalum nitride coatings deposited by reactive HiTUS. (***Surface and Coatings Technology**, 493 (part 2), 131267). https://doi.org/10.1016/j.surfcoat.2024.131267.*

Filiz, Y., Arslan, Y., Duran, E., Saglam-metiner, P., Horozoglu, S., Paradiso, A., **Martinez, D. C**., Sabour-takanlou, M., Heljak, M., Jaroszewicz, J., Biray-avci, C., Swieszkowski, W., & Yesil-celiktas, O. (2024). Decellularized plant-derived vasculature-on-a-chip interacting with breast cancer spheroids to evaluate a dual-drug therapy. ***Applied Materials Today***, 36, 102015. https://doi.org/10.1016/j.apmt.2023.102015.

Górecka, Ż., Idaszek, J., Heljak, M., **Martinez, D. C**., Choińska, E., Kulas, Z., & Święszkowski, W. (2023). Indocyanine green and iohexol loaded hydroxyapatite in poly(L-lactide-co-caprolactone)-based composite for bimodal near-infrared fluorescence- and X-ray-based imaging. ***Journal of Biomedical Materials Research - Part B Applied Biomaterials***, 1–15. https://doi.org/10.1002/jbm.b.35313

Gupta, D., **Martinez, D. C**., Angel, M., Hearnden, V. L., & Reilly, G. C. (2024). The Effects of Fucoidan Derived from Sargassum filipendula and Fucus vesiculosus on the Survival and Mineralisation of Osteogenic Progenitors. ***International Journal of Molecular Sciences***, 25, 1–23. https:// doi.org/10.3390/ijms25042085.

Gupta, D.; Silva, M.; Radziun, K.; **Martinez, D.C**.; Hill, C.J.; Marshall, J.; Hearnden, V.; Puertas-Mejia, M.A.; Reilly, G.C. (2020). Fucoidan Inhibition of Osteosarcoma Cells is Species and Molecular Weight Dependent. **Mar. Drugs**, 18, 104. https://doi.org/10.3390/md18020104

Manuscripts under review:

Mota-Silva, E.; **Martinez, D.C**.; Basta, G.; Babonni, S.; del Turco, S., Fragnito, D.; Salvatore, S.; Kusmic, C.; Leon, R.; Panetta, D.; Campanella, B.; Onor, M., T Plocinski, W Swieszkowski, L Menichetti. Monitoring osseointegration and degradation of Mg-Alloy implants through plasma biomarkers of inflammation and bone regeneration. (*Under review in* ***Journal of Tissue Engineering***).

Short communications- Conference participations:

DC Martinez, A Dobkowska, A. Paradiso, D Drozdenko, A Farkas, K Mathis, K Pucia, A Kaminski, Y Kawamura, W Swiszkowski. Exploring the biocompatibility and corrosion properties of a novel Mg-Ca-Zn-Y-Mn alloy for orthopedic implant materials. 16th Symposium on Biodegradable Metals, Kraków-Poland. August 25-30, 2024. (**Poster and Oral presentation**).

DC Martinez, A Borkam-Schuster, H Helmholz, B Luthringer -Feyerabend, T Plocinski, R Willumeit-Römer, W Swieszkowski. Surface morphology and dynamic changes in the element distribution in the corrosion layer induced by direct monoculture and co-culture models of osteoblasts (OBs) and osteoclasts (OCs) on pure Mg and WE43 alloy. 33rd Annual Conference of European Society for Biomaterials, Davos-Switzerland. September 4-8, 2023 (**Oral presentation**).

DC Martinez, A Paradiso, A Dobkowska, E Choinska, J Kubasek, W Swieszkowski. Cytotoxicity and biocorrosion behavior of Mg-ZnCa-Mn-Y alloy containing long-period stacking ordered phases under physiological conditions. 33rd Annual Conference of European Society for Biomaterials, Davos-Switzerland. September 4-8, 2023 (**Poster presentation**).

DC Martinez, A Dobkowska, R Marek, J Jaroszewicz, T Plocinski, H Helmholz, R Willumeit, W Swieszkowski. *In vitro* and *in vivo* degradation performance of ZX00 screw for bone implant applications. 14th Symposium on Biodegradable Metals, Alicante-Spain. August 24-29, 2022. (**Oral presentation**).

DC Martinez, H Helmholz, A Borkam-Schuster, B Luthringer-Feyerabend, T Plocinski, R Willumeit-Römer, W Swieszkowski. *In vitro* assessment of the degradation interface of pure Mg by

direct osteoblast and osteoclast monoculture and coculture. TERMIS EU Chapter, Kraków June 28-July 01, 2022. (**Poster presentation**).

E Mota-Silva; **DC Martinez**; C Kusmic; G Basta; T Plocinski, W Swieszkowski, L Menichetti: Magnesium implant degradation for bone tissue regeneration − Circulating biomarkers of inflammation and bone regeneration in a rodent model. TERMIS EU Chapter, Kraków June 28-July 01, 2022. (**abstract**).

DC Martinez, H Ben Amara, A Palmquist, O Omar, T Plocinski, P Thomsen, W Swieszkowski: *In vivo* interaction between biodegradable magnesium implants and soft tissue Part I: Time-related changes in thickness and composition of the corrosion layer. 13th Symposium on Biodegradable Metals, August 2021 (**Oral Presentation**).

Paradiso Alessia, Volpi Marina, Walejewska Ewa, **Martinez Guerrero Diana Clemencia**, Łojkowski Maciej, Costantini Marco, Święszkowski Wojciech*: Biofabricated wet-spun core-shell hydrogel fibers for microvascular tissue engineering.* Tissue Engineering and Regenerative Medicine International Society (TERMIS) European Chapter Conference 2023 2023. *(***abstract***)*.

Paradiso Alessia, Volpi Marina, **Martinez Guerrero Diana Clemencia**, Walejewska Ewa, Costantini Marco, Święszkowski Wojciech: *Microfluidic-assisted co-axial wet-spinning extrusion of microvascularized hydrogel fibers with low viscous bioinks*, 5th Novel Fluidic Technologies Workshop with an Emphasis on Tissue Engineering 2023 (**abstract**).

LIST OF FIGURES

LIST OF SUPPLEMENTARY FIGURES

LIST OF TABLES

LIST OF SUPPLEMENTARY TABLES